

GIS BASED SEISMIC HAZARD MAPPING OF TURKEY

A THESIS SUBMITTED TO  
THE GRADUATE SCHOOL OF NATURAL AND APPLIED SCIENCES  
OF  
MIDDLE EAST TECHNICAL UNIVERSITY

BY

ALİ ANIL YUNATCI

IN PARTIAL FULFILLMENT OF THE REQUIREMENTS  
FOR  
THE DEGREE OF DOCTOR OF PHILOSOPHY  
IN  
CIVIL ENGINEERING

OCTOBER 2010

Approval of the thesis:

**GIS BASED SEISMIC HAZARD MAPPING OF TURKEY**

submitted by **ALİ ANIL YUNATCI** in partial fulfillment of the requirements for the degree of **Doctor of Philosophy in Civil Engineering Department, Middle East Technical University** by,

Prof. Dr. Canan ÖZGEN  
Dean, Graduate School of Natural and Applied Sciences

\_\_\_\_\_

Prof. Dr. Güney ÖZCEBE  
Head of Department, Civil Engineering

\_\_\_\_\_

Prof. Dr. K. Önder ÇETİN  
Supervisor, Civil Engineering Dept., METU

\_\_\_\_\_

Assoc. Prof. Dr. Bora ROJAY  
Co-Supervisor, Geological Engineering Dept., METU

\_\_\_\_\_

**Examining Committee Members:**

Prof. Dr. Tamer TOPAL  
Geological Engineering Dept., METU

\_\_\_\_\_

Prof. Dr. K. Önder ÇETİN  
Civil Engineering Dept., METU

\_\_\_\_\_

Prof. Dr. Bilge SİYAHİ  
Earthquake and Structural Engineering Dept.,  
Gebze Institute of Technology

\_\_\_\_\_

Assoc. Prof. Dr. Sinan AKKAR  
Civil Engineering Dept., METU

\_\_\_\_\_

Asst. Prof. Dr. Zeynep GÜLERCE  
Civil Engineering Dept., METU

\_\_\_\_\_

Date: October 25, 2010

**I hereby declare that all information in this document has been obtained and presented in accordance with academic rules and ethical conduct. I also declare that, as required by these rules and conduct, I have fully cited and referenced all material and results that are not original to this work.**

**Name, Last name: Ali Anıl Yunatçı**

**Signature :**

## **ABSTRACT**

### **GIS BASED SEISMIC HAZARD MAPPING OF TURKEY**

Yunatçı, Ali Anıl

Ph.D., Department of Civil Engineering

Supervisor: Prof. Dr. K. Önder Çetin

Co-Supervisor: Assoc. Prof. Dr. Bora Rojay

October 2010, 399 pages

Efficiency of probabilistic seismic hazard analysis mainly depends on the individual successes of its complementing components; such as source characterization and ground motion intensity prediction. This study contributes to major components of the seismic hazard workflow including magnitude – rupture dimension scaling relationships, and ground motion intensity prediction. The study includes revised independent models for predicting rupture dimensions in shallow crustal zones, accompanied by proposals for geometrically compatible rupture area-length-width models which satisfy the rectangular rupture geometry assumption. Second main part of the study focuses on developing a new ground motion prediction model using data

from Turkish strong ground motion database. The series of efforts include, i) compilation and processing of a strong motion dataset, ii) quantifying parameter uncertainties of predictive parameters such as magnitude and source to site distance; and predicted accelerations due to uncertainty in site conditions and response, as well as uncertainty due to random orientation of the sensor, iii) developing a ground response model as a continuous function of peak ground acceleration and shear wave velocity, and finally, iv) removing bias in predictions due to uneven sampling of the dataset. Auxiliary components of the study include a systematic approach to source characterization problem, with products ranging from description of systematically idealized and documented seismogenic faults in Anatolia, to delineation, magnitude-recurrence parameterization, and selection of maximum magnitude earthquakes. Last stage of the study covers the development of a custom computer code for probabilistic seismic hazard assessment which meets the demands of modern state of practice.

Keywords: Seismic hazard, ground motion prediction, seismic source characterization, ground response, earthquake rupture dimension.

## ÖZ

# TÜRKİYE’NİN COĞRAFI BİLGİ SİSTEMİ TABANLI SİSMİK TEHLİKE HARİTALAMASI

Yunatıcı, Ali Anıl

Doktora, İnşaat Mühendisliği Bölümü

Tez Yöneticisi: Prof. Dr. K. Önder Çetin

Ortak Tez Yöneticisi: Doç. Dr. Bora Rojay

Ekim 2010, 399 sayfa

Olasılıksal sismik tehlike analizinin verimliliği büyük oranda, sismik kaynak tanımlaması ve yer sarsıntısı şiddeti tahmini gibi birbirini tamamlayan ana bileşenlerinin tekil başarısına bağlıdır. Bu çalışma, tehlike analizi akışının, deprem büyüklüğü – kırılma boyutu ilişkileri ve yer sarsıntısı şiddeti tahmini gibi ana bileşenlerine katkıda bulunmaktadır. Aktif sığ kabuk yapılarında gerçekleşen depremlerin kırık boyutlarını tahmin etmeye yönelik, yenilenmiş bağımsız tahmin modellerine, dikdörtgen kırılma geometrisini sağlayan bağımlı alan-uzunluk-genişlik modelleri önerisi eşlik etmektedir. Çalışmanın ikinci ana kısmını, Türkiye’de

gerçekleşen depremlerin kuvvetli yer hareketi kayıtları kullanılarak geliştirilen yeni bir yer hareketi şiddeti tahmin bağıntısı oluşturmaktadır. Sarf edilen bir dizi çaba; i) kuvvetli yer hareketi veritabanının derlenmesi ve işlenmesini, ii) deprem büyüklüğü ve saha-kaynak mesafesi gibi tahmin edici parametrelerin içerdiği belirsizliklerle beraber, tahmin edilen parametre olan yer ivmesinin kati olmayan saha koşulları belirlenmesi ve kaydedici sensörün rastgele konumlandırılması nedeniyle içerdiği belirsizlikleri nicelemeyi, iii) maksimum yer ivmesi ve kayma dalgası hızının sürekli fonksiyonu olan bir zemin tepki modeli geliştirmeyi, ve son olarak, iv) denk olmayan örnekleme sonucu oluşan model meyilini temizlemeyi içermektedir. Çalışmanın yardımcı bileşenlerinden biri de Anadolu'daki deprem üretebilen fayların basitleştirilerek konumlarının belirlenmesi, büyüklük – tekrar ilişkilerinin hesaplanması, ve maksimum deprem büyüklüklerinin belirlenmesi gibi ürünlerin sunulduğu kaynak karakterizasyonu problemine getirilen sistematik yaklaşımdır. Çalışmanın son aşaması, olasılıksal sismik tehlike analizinde modern uygulama standartlarının gereksinimlerini karşılayan bir bilgisayar kodunun geliştirilmesini kapsamaktadır.

Anahtar Kelimeler: Sismik tehlike, yer hareketi tahmini, sismik kaynak karakterizasyonu, zemin tepkisi, kırık boyutu..

To My Family



## ACKNOWLEDGEMENTS

I would like to express my sincere thanks to Dr. Kemal Önder Çetin for his generosity in sharing his knowledge and farsighted decision making skills during the progress of this work. His guidance and never-ending motivation, combined with patience have supplied invaluable momentum towards the accomplishment of the dissertation. I wholeheartedly believe that the traces of academic and social skills he has been trying to transfer do inspire younger academicians.

Thanks are greatly expanded to Dr. Bora Rojay for his co-supervision. Working with Dr. Rojay has helped me to gain an insight on bringing solutions to engineering problems while working at a different scale, from a different perspective.

Dr. Norman Abrahamson is greatly acknowledged for hosting me during my short stay at UC Davis. He was generous to share his ideas and feedback about the second chapter of this work; as well as introducing me to newly emerging concepts in earthquake engineering.

Thanks are also due to Dr. Tamer Topal and Dr. Sinan Akkar for providing valuable feedback and comments during the thesis progress committee meetings. Dr. M. Yener Özkan, who has never hesitated to share his wisdom, with an exceptional nobleness, has scraped unforgettable anecdotes in my memory, during my prolonged stay at METU. What I've learned from him is definitely not limited to the MSc. research topic we've completed.

Funding for this study was provided by BAP Project Code: BAP-08-11-DPT2002K120510-COG-05. DPT's support under the Scientific HR Development Program is gratefully acknowledged.

I also wish to thank my friends whom I shared the office space with; for their friendship in and out of the laboratory, encouragement and patience. Ms. Fatma Özkahriman, Mr. Deniz Ülgen, Dr. Ersan Yıldız, Mr. Rıza Savaş Özkuzukıran, Dr. Ali Fırat Çabalar, Mr. Serkan Üçer, Ms. Sevinç Ünsal Oral and Ms. Menzer Pehlivan are greatly acknowledged. My warmest thanks also goes to many friends at the geotechnical laboratory as well METU-CE family, for sharing their brilliant ideas and companionship, as well as reserving their computers for me during a certain phase of my study.

Last, but not the least, thanks are due to the members of my family. Their unconditional support and sacrifice has made it possible for me to complete this task. Without the love and support they have given to me; this work would be simply impossible, and would lack the strongest cause as well. A great ratio of my persistence is due to the encouragement I've taken from my mother Ferda Yunatçı, my grandparents, my wife İpek Yunatçı and all of my remaining family members. I also want to thank Dr. Nevin Çelebi, Dr. Füsün Acartürk and countless family friends for supporting me through this journey.

## TABLE OF CONTENTS

ABSTRACT.....	iv
ÖZ.....	vi
ACKNOWLEDGEMENTS.....	ix
TABLE OF CONTENTS.....	xi
LIST OF TABLES.....	xvii
LIST OF FIGURES.....	xix
CHAPTERS	
1. INTRODUCTION.....	1
1.1 RESEARCH STATEMENT.....	1
1.2 LIMITATIONS OF PREVIOUS STUDIES.....	1
1.3 SCOPE OF THIS STUDY.....	8
2. MAGNITUDE – RUPTURE DIMENSION SCALING FOR SHALLOW CRUSTAL REGIONS USING EXPANDED GLOBAL DATABASE.....	11
2.1 THEORETICAL BASIS FOR MAGNITUDE – RUPTURE DIMENSION SCALING.....	11
2.2 OVERVIEW OF EXISTING RELATIONSHIPS.....	15
2.3 DATABASE COMPILATION.....	25
2.3.1 Data Sources and Spatial Distribution.....	25
2.3.2 Compilation of Source Parameters.....	27
2.3.2.1 Earthquake Magnitude and Seismic Moment.....	27
2.3.2.2 Focal Depth.....	28
2.3.2.3 Style of Faulting.....	29
2.3.2.4 Dip Angles.....	32
2.3.3 Rupture Dimensions.....	33
2.3.3.1 Rupture Area.....	35

2.3.3.2	Rupture Width.....	37
2.3.3.3	Rupture Length and Aspect Ratio.....	37
2.4	PROBABILISTIC MODELS FOR MAGNITUDE – RUPTURE DIMENSION SCALING.....	40
2.4.1	Independent Models of A, RW and RL.....	40
2.4.1.1	Independent Model for Rupture Area.....	40
2.4.1.2	Independent Model for Rupture Length.....	46
2.4.1.3	Independent Model for Rupture Width.....	51
2.4.2	Conditional Models of A, RW and RL.....	53
2.4.3	Bilinear logA and Aspect Ratio Models.....	62
3.	SEISMIC SOURCE CHARACTERIZATION FOR TURKEY.....	71
3.1	BRIEF SUMMARY OF REGIONAL TECTONICS.....	71
3.1.1	Introduction.....	71
3.1.2	Major Tectonic Structures.....	73
3.1.2.1	North Anatolian Fault Zone.....	74
3.1.2.2	East Anatolian Fault Zone.....	75
3.1.2.3	Dead Sea Fault Zone.....	76
3.1.2.4	South Aegean Arc.....	77
3.1.2.5	Cyprean Arc.....	77
3.1.2.6	Bitlis Suture.....	78
3.1.3	Neotectonic Provinces.....	78
3.2	SEISMIC SOURCE CHARACTERIZATION FROM HAZARD ASSESSMENT PERSPECTIVE.....	81
3.2.1.	Previous Efforts in Seismic Source Characterization for Turkey.....	83
3.3	INSTRUMENTAL MACROSEISMICITY CATALOGUES.....	88
3.3.1.	Magnitude-Recurrence Relationships for Seismic Sources.	95
3.3.1.1	Effect of Catalogue Completeness on Recurrence Relations.....	97

3.4	GEOMETRIC CHARACTERIZATION.....	98
3.4.1.	Introduction.....	98
3.4.2.	Geometric Characterization for Active Faults in Turkey....	100
3.5	CALCULATION OF MAXIMUM MAGNITUDES.....	107
3.6	CALCULATION OF RECURRENCE PARAMETERS.....	109
3.6.1.	Problem Definition.....	109
3.6.2.	Quantifying Epicenter Location Uncertainty.....	110
3.6.3.	Criteria for Assigning Events to Defined Seismic Sources.	113
3.6.4.	Choice of Regression Method.....	117
3.6.5.	Aftershock Filtering.....	119
4.	GROUND MOTION PREDICTION MODEL USING DATA FROM TURKISH STRONG GROUND MOTION DATABASE.....	125
4.1	MOTIVATION AND SCOPE.....	125
4.1.1.	Current State of Ground Motion Prediction Models.....	125
4.1.2	Scope of Current Study.....	127
4.2	DATA PROCESSING.....	130
4.2.1	Event Selection and Initial Screening Criteria.....	130
4.2.2	Strong Ground Motion Record Processing.....	136
4.2.2.1	Effect of Filter Type on Processed Strong Ground Motions.....	143
4.2.2.2	Identification of Apparent Errors in Waveforms.	144
4.2.3	Relationships Between Horizontal Components of Ground Motion.....	145
4.2.3.1	Trial Runs Using Time Histories of Analogue and Digital Origin.....	148
4.2.3.2	Relations Between Different Definitions of Horizontal Ground Motion for Turkish Dataset..	152
4.2.3.3	Uncertainty in Spectral Acceleration Due to Rotation of Ground Motion Components.....	164

4.2.4	Style of Faulting.....	165
4.2.5	Earthquake Magnitude.....	171
4.2.6	Source to Site Distance Metrics.....	176
4.2.6.1	Re-Evaluation of Source-to-Site Distance Metrics Using Batch Simulations.....	178
4.2.6.2	Performance Evaluation of Source to Site Distance Relationships.....	186
4.2.7	Site Classification and 1-D Ground Response Analyses.....	189
4.2.7.1	Brief Overview of Modeling Ground Response in GMPEs.....	189
4.2.7.2	Data Sources for Site Classification of National Strong Ground Motion Stations.....	190
4.2.7.3	Resolving Conflicts in Station Metadata and Coordinates.....	192
4.2.7.4	Discussion on Site Classification Preferences.....	194
4.2.7.5	Generic Soil Profiles for 1-D Ground Response Analyses.....	198
4.2.8	Summary of Strong Ground Motion Dataset.....	203
4.2.9	Comparison of Dataset With Local and Global GMPE Models.....	211
4.3	GROUND MOTION PREDICTION MODEL.....	216
4.3.1	Site Response Model.....	216
4.3.1.1	Introduction and Background on Similar Models.....	216
4.3.1.2	Dataset Formation.....	218
4.3.1.3	Reliability Models in Quantifying Parameter Uncertainty and Removing Bias Due to Dataset Compilation.....	221
4.3.1.4	Ground Response Model Results.....	225

4.3.2	Formulation of Ground Motion Prediction Model.....	236
4.3.2.1	Style of Faulting Parameter.....	239
4.3.2.2	Hanging Wall Effects.....	239
4.3.2.3	Modeling Inexact Descriptive Parameters and Weighting Scheme.....	241
4.3.2.4	Error Terms for the Ground Motion Prediction Model.....	242
4.3.3	Evaluation of Motion Prediction Model Results.....	244
4.3.3.1	Magnitude and Distance Scaling.....	244
4.3.3.2	Style of Faulting Scaling.....	250
4.3.3.3	Shear Wave Velocity Scaling.....	251
4.3.3.4	Quantifying Model Uncertainty.....	253
4.3.3.5	Effect of Removing Sampling Bias.....	258
5.	SEISMIC HAZARD ASSESSMENT SOFTWARE.....	261
5.1	PROBABILISTIC SEISMIC HAZARD ANALYSIS.....	261
5.1.1	Mathematical Formulation of PSHA.....	263
5.2	PSHA SOFTWARE FOR HAZARD CALCULATIONS.....	266
5.2.1	Existing PSHA Software and Cause for Authoring a New Computer Code.....	267
5.2.2	Capabilities of the Custom PSHA Code.....	268
5.2.3	Rules for Locating Ruptures and Subdivision of Area Sources.....	270
5.2.3.1	Locating Ruptures Along Linear Faults.....	270
5.2.3.2	Locating Ruptures for Area Sources.....	272
5.2.4	Flow of the Computer Code.....	274
5.2.4.1	Description of “hazardmain.m”	275
5.2.4.2	Description of Remaining Functions	278
6.	SUMMARY AND CONCLUSION.....	281
	REFERENCES.....	286

APPENDICES

A. GLOBAL RUPTURE DIMENSION SCALING DATASET.....	308
B. RECURRENCE RELATION PLOTS FOR SEISMIC SOURCES.....	328
C. PROPERTIES OF GENERIC SOIL PROFILES.....	346
D. SUMMARY OF GMPE DATASET.....	379
CURRICULUM VITAE.....	397



## LIST OF TABLES

### TABLES

Table 2.2-1.	Wells and Coppersmith (1994) model coefficients for various types of rupture dimension definitions.....	16
Table 2.2-2.	Illustration of geometric incompatibility in Wells and Coppersmith (1994) model predictions.....	18
Table 2.4-1.	Summary of model coefficients and performances of limit state functions tested for independent log-rupture area prediction.....	42
Table 2.4-2.	Summary of model coefficients and performances of limit state functions tested for independent log-rupture length prediction...	47
Table 2.4-3.	Summary of model coefficients and performances of limit state functions tested for independent log-rupture width prediction....	51
Table 2.4-4.	Illustration of geometric incompatibility in independent model predictions.....	54
Table 2.4-5.	Summary of model coefficients and performances of limit state functions tested for conditional rupture area prediction.....	57
Table 2.4-6.	Summary of model coefficients and performances of limit state functions tested for conditional rupture width prediction (polynomial models).....	57
Table 2.4-7.	Summary of model coefficients and performances of limit state functions tested for conditional rupture width prediction (power models).....	58
Table 2.4-8.	Summary of model coefficients and performances of limit state function tested for bilinear rupture area prediction.....	64
Table 2.4-9.	Summary of model coefficients and performances of limit state function tested for bilinear aspect ratio prediction.....	66
Table 3.6-1.	Maximum likelihood estimates for average epicentral distance uncertainty.....	112

Table 3.6-2.	Summary of source characterization for linear segments.....	121
Table 3.6-3.	Summary of source characterization for area sources.....	124
Table 4.2-1.	Event list for GMPE dataset, composed of records which passed first screening.....	132
Table 4.2-2.	List of suspected aftershock events removed from the strong ground motion dataset.....	134
Table 4.2-3.	Descriptive parameters of candidate records for demonstrating relationship between different definitions of horizontal ground motion.....	149
Table 4.2-4.	Summary of fault plane solutions available through various agencies.....	169
Table 4.2-5.	Model coefficients for the $r_{jb} - r_{epi}$ relationship.....	183
Table 4.2-6.	Comparison of different methods for source to site distance simulations.....	187
Table 4.2-7.	Comparison of COV values for different methods of source to site distance simulations.....	188
Table 4.2-8.	Summary of key parameters for generic soil profiles used in 1-D ground response analyses.....	199
Table 4.3-1.	Summary of the weighting factors used to eliminate uneven sampling in the ground response model.....	224
Table 4.3-2.	Model coefficients for site response function.....	226
Table 4.3-3.	Model coefficients for peak and 5% damped spectral acceleration response (GMRotD50 component).....	238
Table 4.3-4.	Correlation vector for peak and spectral values of rock acceleration.....	243
Table 4.3-5.	Model error terms.....	255

## LIST OF FIGURES

### FIGURES

Figure 2.1-1.	Illustration of stress drop on a fault (reproduced from McGuire, 2004).....	13
Figure 2.2-1.	Variation of rupture area prediction as a function of style of faulting for Wells and Coppersmith (1994) model.....	17
Figure 2.2-2.	Bilinear magnitude scaling relation by Hanks and Bakun (2002).....	21
Figure 2.2-3.	Comparison of Dowrick and Rhoades (2004) study with Hanks and Bakun (2002) model.....	23
Figure 2.2-4.	Magnitude dependence of aspect ratio in Dowrick and Rhoades (2004) model.....	23
Figure 2.2-5.	Stein (2008) magnitude-area scaling model.....	24
Figure 2.3-1.	Spatial distribution of events included in the magnitude – rupture dimension relationship dataset.....	26
Figure 2.3-2.	Magnitude-frequency distribution of rupture dimension dataset.....	28
Figure 2.3-3.	Focal depth distribution of rupture dimension dataset.....	29
Figure 2.3-4.	Style of faulting scheme used for categorizing events without any rake angle.....	31
Figure 2.3-5.	Rake angles remapped into a linear representation of faulting mechanism.....	32
Figure 2.3-6.	Style of faulting frequency distribution of the rupture dimension dataset.....	32
Figure 2.3-7.	Dip angle frequency distribution of the rupture dimension dataset.....	33
Figure 2.3-8.	Magnitude-area distribution of the current dataset.....	36
Figure 2.3-9.	Magnitude-area distribution with style of faulting bins.....	36

Figure 2.3-10.	Magnitude-area distribution separated with tectonic regions of occurrence.....	37
Figure 2.3-11.	Magnitude-area distribution separated with tectonic regions of occurrence.....	38
Figure 2.3-12.	Magnitude – rupture length distribution for the dataset.....	39
Figure 2.3-13.	Magnitude – aspect ratio distribution with dip angle bins.....	39
Figure 2.4-1.	Proposed relationship for independent log-rupture area.....	43
Figure 2.4-2.	Median log-area predictions for different faulting styles.....	43
Figure 2.4-3.	Normalized residuals vs. measured log-rupture area.....	44
Figure 2.4-4.	Normalized residuals vs. dip angle.....	45
Figure 2.4-5.	Normalized residuals vs. moment magnitude.....	45
Figure 2.4-6.	Normalized residuals vs. style of faulting parameter.....	46
Figure 2.4-7.	Proposed relationship for independent log-rupture length.....	47
Figure 2.4-8.	Median log-rupture length predictions for different faulting styles.....	48
Figure 2.4-9.	Measured vs. predicted comparison for rupture length model	49
Figure 2.4-10.	Normalized residuals vs. dip angle (rupture length model)....	49
Figure 2.4-11.	Normalized residuals vs. magnitude (rupture length model)..	50
Figure 2.4-12.	Normalized residuals vs. style of faulting (rupture length model).....	50
Figure 2.4-13.	Proposed relationship for independent log-rupture width.....	52
Figure 2.4-14.	Measured vs. predicted comparison for rupture width model.	52
Figure 2.4-15.	Normalized residuals vs. dip angle (rupture width model)....	53
Figure 2.4-16.	Proposed relationship for conditional log-rupture area model	58
Figure 2.4-17.	Proposed relationship for conditional log-rupture width model.....	59
Figure 2.4-18.	Variation of logRL with respect to median estimates of logA and log RW A.....	60
Figure 2.4-19.	Measured vs. predicted values of conditional logRW.....	60
Figure 2.4-20.	Measured vs. predicted values of conditional logA.....	61

Figure 2.4-21.	Normalized residuals of conditional rupture width model against SOFP.....	61
Figure 2.4-22.	Bilinear rupture area model.....	64
Figure 2.4-23.	Measured vs. predicted values in bilinear rupture area model.	65
Figure 2.4-24.	Measured vs. predicted values in rupture area model.....	66
Figure 2.4-25.	Measured vs. predicted values in aspect ratio model.....	67
Figure 2.4-26.	Measured vs. predicted values in rupture area model.....	68
Figure 2.4-27.	Measured vs. predicted values in rupture area model.....	69
Figure 3.1-1.	Simplified tectonic map of Turkey showing major neotectonic structures (reproduced and modified from Rojay et al., 2001).....	72
Figure 3.1-2.	Active fault map of Turkey (reproduced from Şaroğlu et. al., 1992).....	74
Figure 3.2-1.	Source characterization which forms the basis for the current earthquake code for Turkey (modified from Gülkan et al., 1993).....	84
Figure 3.2-2.	Nationwide source characterization for Turkey (Demircioğlu et al., 2007).....	85
Figure 3.2-3.	Seismic source characterization used by Deniz (2006).....	86
Figure 3.2-4.	Seismic source characterization used by Kayabalı (2002).....	87
Figure 3.2-5.	Seismic source characterization used by Ulusay (2004).....	88
Figure 3.3-1.	(a) Focal depth and (b) magnitude distribution for Deniz (2006) and KOERI (2010) datasets.....	90
Figure 3.3-2.	Catalogue completeness analysis for the Deniz (2006) and Kalafat et al. (2010) datasets.....	91
Figure 3.3-3.	Macroseismicity distribution for Turkey and neighboring regions (Kalafat et al., 2010).....	94
Figure 3.3-4.	Magnitude pdf for truncated exponential model.....	96
Figure 3.3-5.	Effect of catalogue completeness problem on recurrence relations.....	97

Figure 3.4-1.	Illustrative example for source characterization.....	99
Figure 3.4-2.	Linear faults and projections of down-dip geometry for Turkey.....	104
Figure 3.4-3	Linear faults and projections of down-dip geometry for Turkey (zoomed image on the Western Anatolia Tectonic Province).....	105
Figure 3.4-4.	Area sources modeled for Turkey.....	106
Figure 3.5-1.	Rupture length calculation as a function of total fault length..	108
Figure 3.6-1.	Quantifying average error in epicenter location.....	111
Figure 3.6-2.	Quantifying average error in epicenter location (variation against event date).....	113
Figure 3.6-3.	Distribution of events with multiple source intersections.....	115
Figure 3.6-4.	Multiple source intersections at Western Anatolia.....	116
Figure 3.6-5.	Recurrence parameters obtained through MLE and LSE for Dinar.....	118
Figure 3.6-6.	Effect of aftershock filtering on recurrence parameters of Karaburun Segment.....	119
Figure 4.2-1.	Spatial distribution of event epicenters as proposed by KOERI.....	135
Figure 4.2-2 .	Distribution of number of events along the 1976-2006 timeline.....	136
Figure 4.2-3.	Distribution of number of records along the 1976-2006 timeline.....	136
Figure 4.2-4.	Response function of a high-pass causal Butterworth filter, for cutoff frequency of 0.10 Hz, using different filter orders..	137
Figure 4.2-5.	Processed time history traces of 20/10/2005 Seferihisar Earthquake (BRN Station, longitudinal component).....	141
Figure 4.2-6.	5% damped elastic response spectra for longitudinal component of 20/10/2005 Seferihisar event, recorded at BRN station.....	142

Figure 4.2-7.	Fourier amplitude spectra for raw and processed records of 20/10/2005 Seferihisar (M=5.86) earthquake, recorded at BRN station (longitudinal component).....	143
Figure 4.2-8.	Comparison between pseudo acceleration response spectra of four sample ground motions (GMRotDpp component).....	150
Figure 4.2-9.	Comparison between pseudo acceleration response spectra of sample ground motions (GMRotDpp and GMRotIpp components).....	151
Figure 4.2-10.	GMRotD100 / GMRotD50 values for different periods.....	153
Figure 4.2-11.	GMRotD50 / GM values for different periods.....	154
Figure 4.2-12.	GMRotI50 / GMRotD50 values for different periods.....	155
Figure 4.2-13.	SRSS / GMRotD50 values for different periods.....	156
Figure 4.2-14.	GMLarger50 / GMRotD50 values for different periods.....	157
Figure 4.2-15.	SN/SP values for different periods.....	158
Figure 4.2-16.	SP / GMRotD50 values for different periods.....	159
Figure 4.2-17.	SN / GMRotD50 values for different periods.....	160
Figure 4.2-18.	Dependence of horizontal ground motion component ratios on source to site distance and earthquake magnitude.....	161
Figure 4.2-19.	Variation of ratios between different definitions of horizontal component of ground motion, as a function of period.....	162
Figure 4.2-20.	Median values of GMRotD parameter with standard error bars.....	165
Figure 4.2-21.	Focal mechanism solutions for the complete HRVD catalog (clipped for region covering Anatolia).....	167
Figure 4.2-22.	Focal mechanism solutions for the complete EMMA catalog (clipped for region covering Anatolia).....	167
Figure 4.2-23.	Focal mechanism solutions for 3/2/2002 Sultandağı Earthquake.....	168
Figure 4.2-24.	Frequency distribution of SOFP in the compiled dataset.....	170

Figure 4.2-25.	Uncertainty in moment magnitude parameter.....	173
Figure 4.2-26.	Moment magnitude uncertainty as summarized by Moss and Kiureghian (2003).....	173
Figure 4.2-27.	Moment magnitude uncertainty as a function of event date....	174
Figure 4.2-28.	Estimated median moment magnitudes with error bars.....	175
Figure 4.2-29.	Illustrative description of various distance metrics used in GMPE models (Erdoğan, 2008).....	176
Figure 4.2-30.	Randomly generated observation points for source to site simulations.....	179
Figure 4.2-31.	Illustration of location, depth, dip, and rupture dimension uncertainty for a scenario with a given earthquake magnitude.....	180
Figure 4.2-32.	Sample bin data for $R_{jb}$ - $R_{epi}$ relationships ( $M=6.5$ , $Rake=$ $30^0$ ).....	181
Figure 4.2-33.	Effect of magnitude on scatter of $R_{jb} - R_{epi}$ relationships.....	181
Figure 4.2-34.	Median predictions for the $R_{epi}$ - $R_{jb}$ model plotted against scattered data from different magnitude bins (normalized representation).....	184
Figure 4.2-35.	Median predictions for the $R_{epi}$ - $R_{jb}$ model plotted against..... scattered data from different magnitude bins (unnormalized representation).....	185
Figure 4.2-36.	Distribution of strong ground motion recording stations used in the current dataset.....	194
Figure 4.2-37.	Measured and correlation-predicted shear wave velocity profiles.....	196
Figure 4.2-38.	Residuals of $V_s$ values against depth from surface.....	197
Figure 4.2-39.	Modulus degradation curves for clays (Vucetic and Dobry, 1991).....	201
Figure 4.2-40.	Damping curves for clays (Vucetic and Dobry, 1991).....	201
Figure 4.2-41.	Modulus degradation curves for cohesionless materials.....	202



Figure 4.2-42.	Damping curves for cohesionless materials.....	202
Figure 4.2-43.	Site response procedure using generic profiles.....	203
Figure 4.2-44.	Effect of signal processing on the useable period range.....	204
Figure 4.2-45.	Closest distance to rupture vs. $pga_{rock}$ scatter with median values and computed parameter uncertainties.....	205
Figure 4.2-46.	Epicentral distance vs. $pga_{rock}$ scatter with median values and computed parameter uncertainties.....	205
Figure 4.2-47.	Boore-Joyner distance vs. $pga_{rock}$ scatter with median values and computed parameter uncertainties.....	206
Figure 4.2-48.	Boore-Joyner distance vs. $SA_{rock}$ scatters for $T=0.2$ s and $T=1.0$ s.....	206
Figure 4.2-49.	Magnitude v.s $pga_{rock}$ distribution.....	208
Figure 4.2-50.	Magnitude vs. $R_{rup}$ scatter of NGA flatfile data and Turkish SGM datasets.....	208
Figure 4.2-51.	Magnitude vs. $R_{epi}$ scatter of Abrahamson and Silva (2008) NGA and Turkish SGM datasets.....	209
Figure 4.2-52.	Percentage of events falling between the defined magnitude - distance bins for the current dataset.....	209
Figure 4.2-53.	Percentage of events falling between the defined magnitude - distance bins for Abrahamson and Silva (2008) dataset.....	210
Figure 4.2-54.	Magnitude vs. $R_{jb}$ scatter for different NEHRP site classes....	210
Figure 4.2-55.	Magnitude vs. $R_{jb}$ scatter for different style of faulting classes.....	211
Figure 4.2-56.	Comparison of normalized residuals for different GMPE models, prior to model development.....	214
Figure 4.3-1.	Dataset used for developing ground response model (PGA)...	219
Figure 4.3-2.	Dataset used for developing ground response model ( $T=0.2s$ ).....	220
Figure 4.3-3.	Dataset used for developing ground response model ( $T=1.0$ s).....	220

Figure 4.3-4.	$pga_{rock}$ - $pga_{soil}$ scatter plot.....	227
Figure 4.3-5.	Median curves for the current model in the $V_{s30}=360$ -760 m/s range.....	227
Figure 4.3-6.	Median curves for the current model in the $V_{s30}=180$ -360 m/s range.....	227
Figure 4.3-7.	Comparison of Seed et al. (1997) model for sites falling within NEHRP B and C classes.....	229
Figure 4.3-8.	Comparison of Seed et al. (1997) model for sites falling within NEHRP D and E classes.....	229
Figure 4.3-9.	Comparison of Choi and Stewart (2005) model for sites falling within NEHRP B and C classes.....	230
Figure 4.3-10.	Comparison of Choi and Stewart (2005) model for sites falling within NEHRP D and E classes.....	230
Figure 4.3-11.	Cross –comparison of median estimates from different models at NEHRP B/C boundary.....	231
Figure 4.3-12.	Cross –comparison of median estimates from different models at a typical NEHRP D site.....	232
Figure 4.3-13.	Impact of weighting on the predicted median amplification curves for $V_{s30}=180$ m/s, $V_{s30}=270$ m/s, and $V_{s30}=360$ m/s.....	233
Figure 4.3-14.	Average values of normalized residual plots as a function of spectral period.....	234
Figure 4.3-15.	Normalized residual plots as a function of $pga_{rock}$ .....	234
Figure 4.3-16.	Normalized residual plots as a function of $V_{s30}$ .....	235
Figure 4.3-17.	Magnitude-distance scaling for the proposed model.....	245
Figure 4.3-18.	Normalized residuals of GMPE model for peak component and spectral values.....	246
Figure 4.3-19.	Comparison of current study and NGA models at reference rock condition.....	248
Figure 4.3-20.	Comparison of current study and models developed using local data at $V_{s30}= 760$ m/s equivalent site conditions.....	249

Figure 4.3-21.	Effect of style of faulting on peak acceleration.....	251
Figure 4.3-22.	Effect of shear wave velocity on peak acceleration.....	252
Figure 4.3-23.	Effect of shear wave velocity on spectral acceleration.....	253
Figure 4.3-24.	Effect of removing parameter uncertainties (M=5).....	254
Figure 4.3-25.	Effect of removing parameter uncertainties (M=7.5).....	255
Figure 4.3-26.	Comparison of sigma values at rock sites (M=6.5).....	256
Figure 4.3-27.	Variation of sigma as a function of $V_{s30}$ (M=6.5).....	257
Figure 4.3-28.	Ratio of soil and rock sigma values modeled using different studies.....	258
Figure 4.3-29.	Effect of weighting on magnitude-distance scaling.....	259
Figure 4.3-30.	Effect of weighting on ground motion intensity curves for different minimum magnitude thresholds used in datasets.....	260
Figure 5.1-1.	Basic steps of PSHA (from Finn et al., 2004).....	262
Figure 5.2-1.	Illustration of a normally distributed continuous variable truncated at both ends.....	269
Figure 5.2-2.	Simulation of rupture along a fault: a) polyline representation of the fault, b) Location of discrete rupture centers along the fault for given earthquake magnitude, c) Sketch of first and last ruptures along the fault.....	271
Figure 5.2-3.	Variation of number of rupture location simulations as a function of segment length.....	272
Figure 5.2-4.	Illustration of area source geometry and subdivision of polygon geometry.....	273
Figure 5.2-5.	Simplified flowchart of PSHA software.....	274
Figure 5.2-6.	Sample triple deaggregation output of PSHA software.....	279
Figure 5.2-7.	Sample hazard curve for PGA.....	280

# **CHAPTER 1**

## **INTRODUCTION**

### **1.1 RESEARCH STATEMENT**

The aim of this study is to develop enhanced engineering tools for the assessment of seismic hazard at a selected site or region, to eventually prepare national seismic hazard maps for Turkey. Within the designated scope, it is intended to bring improvements to the available components of seismic hazard framework including, i) earthquake magnitude – rupture dimension scaling, ii) ground motion prediction equations, with particular emphasis on treatment of uncertainties and modeling local site response, iii) source characterization at a national scale with the utilization of top notch data available, and iv) development of a custom computer code from the rough, for calculation of hazard.

### **1.2 LIMITATIONS OF PREVIOUS STUDIES**

Seismic hazard studies constitute the initial step in seismic risk assessment and mitigation, and provide the basis for the seismic demand for the design of engineered structures. The basic questions that are expected to be answered in this multi-disciplinary field are the time and location of probable earthquakes, the ground motion intensity from these events and effects on structures. State of the art hazard

and risk assessment methodology answers all but the first part of this series of questions.

The source parameters in a seismic hazard study as well as travel path effects are unexceptionally subject to uncertainties. The probabilistic seismic hazard framework originally introduced by Cornell (1968) and partially evolved by cooperated research with UNAM (Universidad Nacional Autonoma de Mexico) group (Mc Guire, 2008), survives as a robust tool for engineering use. Despite numerous counter-ideas represented in Krinitzsky (1993a), Krinitzsky (1993b), Krinitzsky (1993c), Krinitzsky (2002a), Krinitzsky (2002b), Mualchin and Krinitzsky (2003), Hatheway (2003), Castaños and Lomnitz (2002) as well as many others, mostly originating from misconception of the fundamental concepts; the reputation of probabilistic seismic hazard (PSHA) methodology and its close interaction with deterministic methods mostly used in decision-making has remained solid over decades, and the framework has succeeded to remain valid.

Recent developments in the field of engineering seismology and expansion of global strong ground motion databases, with partial support from more detailed field investigations and batch data processing tools have revealed that the key concept in improving the prediction of design ground motion intensity parameter is conducting advanced treatment to the components of a seismic hazard study, rather than the probabilistic framework itself. The results presented herein focus on two major components of a seismic hazard study; seismic source characterization and modeling ground motion intensity.

Given an earthquake magnitude and style of faulting, there exist empirical relationships to predict the rupture dimensions to be used in a hazard study. The predicted parameters are either rupture area, rupture width, or rupture length sometimes divided into two subcategories as surface and subsurface rupture length. The set of relationships by Wells and Coppersmith (1994) are undoubtedly the most

commonly used tools for shallow crustal regions. Wells and Coppersmith (1994) relations provide predictions for all of the forementioned rupture dimension parameters and their uncertainties around the median, also verifying empirical data with theoretical constant median static stress drop models. Nevertheless, inconsistencies among the predicted parameters arise when the relations are utilized in a hazard analysis. Wells and Coppersmith (1994) present a set of relationships of rupture dimensions as a function of magnitude and style of faulting that are regressed independently and using different datasets. Thus, for a given earthquake magnitude, the predicted rupture dimensions fail to yield geometrically compatible results among width, length and area; assuming the basic principle of rectangular rupture. The current workaround to the problem in hazard assessment practice is to divide the predicted rupture area to either rupture length or rupture width predictions.

Another issue in Wells and Coppersmith (1994) relationships is the utilization of separate regression bins for each style of faulting. For every data point in the sample space, corresponding style of faulting is assessed using a discrete bin for the relevant rake angles, and different models having the same functional form with varying coefficients are proposed. Such simple approaches may be considered relatively robust, provided that the dataset is not sparse and regressions are substantially insensitive to binning. Wells and Coppersmith (1994) relations possessing dataset populations for a specific style of faulting, composing as low as 14% of the total number of events representing all faulting styles for the rupture dimension of interest raises the question of sensitivity in the results. An alternative proposal is the continuous representation of style of faulting by introducing a style of faulting parameter, as will be shown in this text.

One of the main concerns in Wells and Coppersmith (1994) relations is the effect of large magnitude earthquakes on rupture dimension predictions and its possible effect on the uncertainty of the model. Better predictions in the high magnitude range requires expansion of the dataset especially over  $M$  (moment magnitude) 7.5.

Expansion of the dataset in the prescribed range will enable further discussion of whether total uncertainty in the model decreases with increasing magnitude. A re-evaluation of Triep and Sykes (1996) catalogue merged with Hanks and Bakun (2002) and Hanks and Bakun (2008) datasets provide a slightly expanded high quality dataset.

Another major point of discussion in the source characterization stage is the geometric characterization of faults, accompanied by their earthquake recurrence parameters. In literature, pathway to a correct representation of seismic sources is largely established. Factors such as details of geometric delineation, representation of source regions, establishing systematic rules for maximum earthquake producing capabilities, compiling seismicity catalogues and selecting the probability density functions for recurrence characteristics have been thoroughly studied. Nevertheless, an inevitable point to consider in source characterization, while finalizing the parameters for design is the application of expert judgment. While assessing the constraints to the extreme values of a parameter, vast amount of field data or analytical work reduces the epistemic uncertainty, which in turns decreases the total uncertainty in the model. The application of these rules of thumb has not yet been fully implemented in seismic hazard assessment studies for Turkey at a regional scale.

Besides preliminary studies by Bath (1979) and Karnik and Klima (1993) focused on assessing the recurrence parameters in Turkey using superficially selected rectangular boundaries, systematic characterization of modern seismic hazard assessment studies for Turkey begins with Gülkan et al. (1993). Gülkan et al. (1993) has characterized seismic sources in Turkey with 19 area sources, excluding area zones representing background seismicity. While this representation may seem sufficient at a regional scale for mapping purposes, it is evident that the calculated hazard is considerably sensitive to source characterization at near-fault sites; and cannot be comfortably used in site specific hazard studies.

A revised form of Erdik et al. (1999) compilation has been used in Bommer et al. (2002) aimed at developing a model for earthquake loss insurance. Bommer et al. (2002) compilation introduces a more comprehensive evaluation of offshore seismic sources. Bommer et al. (2002) brings a major improvement to earlier models by introducing sub-zones, in which the rupture locations of higher magnitude events are binned into a more constrained geometry. Demircioğlu et al. (2007) uses the same approach with area sources. Deniz (2006) uses an extended version of source characterization proposed by Bommer et al. (2002), with a more systematic framework for maximum magnitude determination.

Kayabalı (2002) proposed another version of seismic source characterization for Turkey, by compiling data mostly from Erdik et al. (1985) and Yalıtırak et al. (1998). Kayabalı (2002) model utilizes an expert judgment in assessing the maximum earthquake magnitudes for each source, assuming a fraction of total fault length has ruptured. The decision for fault segmentation along a fault zone is crucial at this point, and directly affects the maximum magnitude selections for sources such as North Anatolian Fault Zone; in which the segmentation was not applied. Similar considerations for the demand of more detailed characterization exist for the extensional neotectonic regime in the Aegean Region; which is characterized by a single wide source area. Kayabalı and Akın (2003) represents a revised version of source characterization for Turkey, in which the area source is exempted and a more detailed delineation is used.

Study by Ulusay et al. (2004) has proposed the utilization of single magnitude scenarios corresponding to maximum magnitude for assessing design hazard levels, mainly using segmented linear sources compiled from Şaroğlu et al. (1992). As a conclusion for the defined active faults in Turkey, the major challenge in characterization remains to be a systematic approach in decision making. Macroseismicity catalogue for Turkey has revealed that the location uncertainty of



focal points of events can reach over 10 kilometers; thus introducing an ambiguity in assigning those events to each seismic source. Up to the present, this has impacted both the geometric characterization choices as well as direct effect on recurrence values, and caused a bias towards using area zonations for the possible rupture location determination within the hazard scenarios.

The third major research area in this study is the prediction of ground motion intensity. All modern prediction relationships are based on estimating the peak or spectral value of the ground motion parameter of interest; as a function of earthquake magnitude, source to site distance, local soil conditions and additional variables such as style of faulting, hanging wall effect, etc.

There is a steady improvement on addressing the issues to be resolved and building a cooperative effort since the proposal of the set of ground motion prediction relationships for shallow active crustal regions by Abrahamson and Silva (1997), Boore et al. (1997), Campbell (1997), and Sadigh et al. (1997). A second set of prediction relationships have been recently released as the NGA (Next Generation Attenuation) project, by four groups; Abrahamson and Silva (2008), Boore and Atkinson (2008), Campbell and Bozorgnia (2008) and finally, Choi and Youngs (2008). The NGA effort has attempted to bring improvements on i) constructing models that work over a broad magnitude and distance range, ii) applicability for the prediction of peak and spectral values over a broader spectral range and for different definitions of horizontal components of ground motion, iii) characterization of local site effects using more detailed models and site classification schemes, iv) enhancing the model form by introducing new parameters such as the depth to bedrock units and depth to top of rupture.

Introduction of ground motion prediction equations based on locally compiled and processed data for earthquakes that have occurred in Turkey or partly from Euro-Mediterranean region has rapidly emerged after the 1999 Kocaeli earthquake. Studies

by Gülkan and Kalkan (2002), Kalkan and Gülkan (2004), Ulusay et al. (2004), Özbey et al. (2004), Akkar and Bommer (2010), Akkar and Çağnan (2010) have displayed a steady and remarkable progress in expanding the datasets, processing raw data and utilizing more sophisticated parameters in site characterization. Median estimates of these local relationships are almost always different from those of Western US relationships and this has been mainly attributed to the characteristics of motions forming the strong ground motion database in Turkey. While this may be empirically true as the high magnitude ground motions in the local database is heavily dominated by 1999 Kocaeli and Düzce events showing weaker intensities; there is no seismological evidence that this trend is likely to be supported by prospective high magnitude events that will occur in the future. Thus, constructing a model that represents the most likely ground motion intensity for the given predictive parameters will be more representative if an equal weighting procedure of data points is used. This is often an issue that is overlooked, especially for databases having less number of recordings compared to global models and dominated by a few events. Global versus local model discussions are greatly triggered by median estimate comparisons of ground motion prediction equations, and the results in this study point that the path to resolving this issue is through debating on how to construct and statistically treat GMPE (ground motion prediction equation) databases.

Another crucial topic in GMPE models is the variability term. Considering seismic hazard analyses, the impact of aleatory variability on the calculated hazard, especially for long return period ground motion levels are extremely large. While one way of avoiding the discussion of physically possible extremes of ground motion intensity is through truncating the ground motion at a reasonable value that conforms to the empirical findings; a better solution from the ground up is through obtaining more accurate representations of the aleatory variability term. Assuming that the same model is used; hence there is no difference in epistemic uncertainty, it is within expectations that variability term in GMPE's derived using less number of events will be higher than global GMPE's using higher number of recordings. This has been

the case so far for GMPE's derived using data from events which took place in Turkey.

The aleatory variability term for GMPE's also contains the uncertainty inherent to the predictive parameters itself; thus overstating the order of actual aleatory variability unless treated. The author of this study attempts to evaluate the order of parameter uncertainty for earthquake magnitude, source to site distance, ground motion intensity due to orientation of the horizontal components, and finally ground motion intensity at rock due to uncertainty in site response procedure followed herein. This in turn, will lead to a reduction in the overstated variability term; contributing to the discussion of hazard levels at long return periods.

### **1.3 SCOPE OF THIS STUDY**

Following this introduction, Chapter 2 presents a magnitude rupture-dimension scaling model using a compiled global database. Events from Wells and Coppersmith (1994) database are merged with Triep and Sykes (1996) catalog, supplemented with rupture dimensions from NGA dataset, Hanks and Bakun (2002) and finally Hanks and Bakun (2008). The new dataset contains a higher number of rupture dimensions from large magnitude events, enabling the discussion of heteroscedastic (predictive parameter dependent) variability term. The proposed relationships are derived using a single bin for style of faulting; providing a continuous representation of earthquake mechanism without the need for subdivision of the database. The proposed models conform to the simplest assumption of rectangular rupture geometry; in other words, among the predictions of rupture area, rupture width and rupture length; it is sufficient to calculate any two of the parameters to consistently yield the third.

Chapter 3 summarizes the seismic source characterization for Turkey. Introduction and brief overview of the local macroseismicity catalogue is followed by the procedure to obtain the linear and area source characterization for defined faults.

Geometric characterization, recurrence models and parameters, maximum earthquake magnitude selections for each source are systematically described. The produced information, undoubtedly containing a certain amount of epistemic uncertainty is to be used for seismic hazard calculations at a nationwide scale. Chapter 3 also presents a discussion on level of detailing used in seismic source characterization on the calculated hazard at near-fault sites.

Following source characterization presented in Chapter 3, Chapter 4 focuses on the ground motion prediction model proposed using data from earthquakes in Turkey. Review of existing relations, data compilation efforts, data processing using the recordings meticulously selected from raw strong ground motion databases is followed by the discussion and evaluation of parameter uncertainties of predictive variables in the model. The parameters subject to uncertainty modeling are the earthquake magnitude, source to site distance which is evaluated using a series of simulations for probable rupture dimensions, fault orientation and rupture location along a fault. Uncertainties in the predicted variable (ground motion intensity parameter) as a consequence of variability in orientation of the horizontal component, and the site response procedure are also studied. A noteworthy sub-topic in Chapter 4 is the soil response model developed using the same dataset utilized in GMPE; which attempts to model the soil to rock amplification ratios of spectral acceleration values as a continuous function of peak ground motion parameter at defined rock level and average shear wave velocity at the top 30 m of the profile ( $V_{s30}$ ). Chapter 4 proceeds with the final proposal of the GMPE model which inhibits a new soil response model, uncertainty treatment using variability of the predictive parameters, application of weighting factors for avoiding sampling bias in a relatively small dataset. The model is compared to the recent studies, derived using both local and global datasets, and ends with a discussion.

Chapter 5 is devoted to the construction of a custom software tool that is suitable for preparing the national seismic hazard maps for various ground motion return periods having significance in current state of practice, for both peak and spectral intensities. Production of a complete seismic hazard computation tool; that is capable of handling multiple sources; either area or linear sources with polyline definitions is summarized. Properties and limitations of series of scripts are discussed in detail; and sample output is presented towards the end of the chapter.

Chapter 6 concludes the study by summarizing the main findings and proposed tools, with comments and reference for future work.

## **CHAPTER 2**

# **MAGNITUDE – RUPTURE DIMENSION SCALING FOR SHALLOW CRUSTAL REGIONS USING EXPANDED GLOBAL DATABASE**

### **2.1 THEORETICAL BASIS FOR MAGNITUDE – RUPTURE DIMENSION SCALING**

Empirical relationships between earthquake magnitude and rupture dimension parameters such as the rupture area, rupture width, rupture length and average rupture displacement are an inevitable component of hazard assessment. Although there are remarkably valuable empirically-based studies in the literature related to earthquake magnitude – rupture dimension scaling, there are still fields of discussion which require further attention; such as modeling aleatory variability at larger magnitudes, physical constraints on the parameters imposed by crustal thickness and geometrical compatibility of predicted rupture dimensions. Chapter 2 begins with a brief overview of seismological parameters related to magnitude – rupture dimension scaling, proceeds with a summary of previous efforts, and concludes with a thorough presentation of current effort to enhance the existing relationships.

Seismic moment for an event,  $M_0$ , expressed in units of dyne.cm is given by:

$$M_0 = \mu A D \quad (2-1)$$

In Equation 2-1,  $\mu$  is the shear modulus of the ruptured material in dyne/cm<sup>2</sup> units having a representative value of  $3 \times 10^{11}$  dyne/cm<sup>2</sup>. Terms “log<sub>10</sub>” and “log” are used interchangeably, and refer to base-10 logarithm. Also recall that the well known relation between moment magnitude  $M$  (since moment magnitude is instrument independent measure of source parameter, it will be denoted as “ $M$ ” in the text) and seismic moment is expressed by Hanks and Kanamori (1979):

$$M = \frac{2}{3} \log_{10}(M_0) - 10.7 \quad (2-2)$$

Equation 2-2 can be rearranged as:

$$\log_{10} M_0 = 1.5M + 16.05 \quad (2-3)$$

Substituting Equation 2-3 into Equation 2-1 will yield new information about the relation of earthquake magnitude with average fault slip for an event:

$$M = \frac{2}{3} \log_{10}(A) + \frac{2}{3} \log_{10}(D) + \frac{2}{3} \log_{10}(\mu) - 10.7 \quad (2-4)$$

The most critical step in discussing empirically based magnitude scaling relationships is the introduction of stress drop parameter. A brief remark on stress drop parameter is that, it relates rupture area  $A$ , and rupture displacement,  $D$ . A comprehensible definition of the stress drop is given by Abrahamson (2009): “Stress drop of an earthquake event describes the compactness of the seismic release in space and/or time. A high stress drop indicates that the moment release is tightly compacted in space and/or time. A low stress drop indicates that the moment release

is spread out in space and/or time” (Abrahamson, 2009). McGuire (2004) presents a simplified illustration of the definition of stress drop by plotting stress accumulation on a fault during and after the event (Figure 2.1-1).

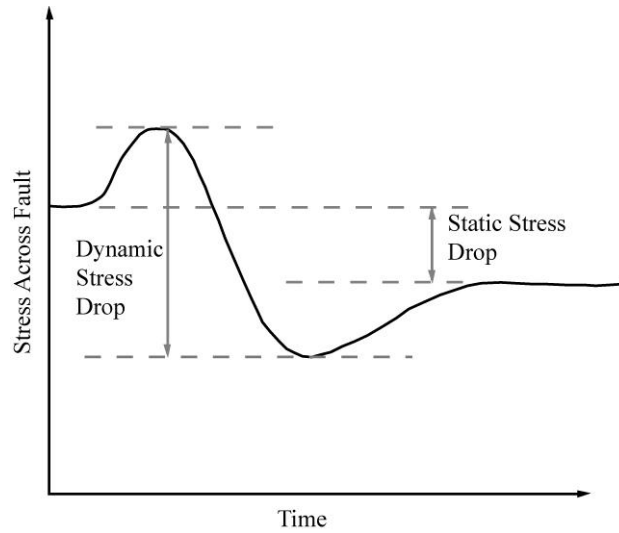


**Figure 2.1-1. Illustration of stress drop on a fault (reproduced from McGuire, 2004)**

For the simplest assumption of circular rupture geometry, the static stress drop at the center of rupture is given by:

$$\Delta\sigma_{circ} = \frac{7 \cdot 10^{-6}}{16} \cdot \pi^{1.5} \cdot \mu \cdot \frac{D}{\sqrt{A}} \quad (2-5)$$

In Equation 2-5,  $\Delta\sigma$  is in bars (Kanamori and Anderson, 1975). Kanamori and Anderson (1975) present a set of expressions with different constants corresponding to various rupture geometries. Findings of Sato (1972) support this proposition by introducing a scale factor of  $(L/W)^{-0.15}$ , where L and W are rupture length and width, respectively. Abrahamson (2009) merges two expressions and rearranges into Equation 2-6 by the assumption that a rectangular rupture with an aspect ratio of 1 ( $L=W$ ) is analogous to the case for circular crack:

$$\Delta\sigma_{rec} = \frac{7 \cdot 10^{-6}}{16} \cdot \pi^{1.5} \cdot \mu \cdot \frac{D}{\sqrt{A}} \cdot \left(\frac{L}{W}\right)^{-0.15} \quad (2-6)$$



Aspect ratio value of 5 suggests that stress drop given by Equation 2-6 is approximately 22% smaller than for a circular crack (Equation 2-5 and 2-6). This value rises up to 30% for an aspect ratio of 10.

If the stress drop expression is simplified one step further, such that the dependence on aspect ratio and dependence of  $D/(A)^{1/2}$  on magnitude are ignored; Equation 2-4 can be rewritten as:

$$M = \log(A) + \frac{2}{3}\log(c_1) - 3.05 \quad (2-7)$$

where  $\mu=3 \times 10^{11}$  dyne/cm<sup>2</sup> and  $c_1=D/(A)^{1/2}$ . Constant median static stress drop reduces Equation 2-7 to its simplest form as presented in Equation 2-8.

$$M = \log(A) + b \quad (2-8)$$

In Equation 2-8, b is a constant that depends on the median stress-drop (Abrahamson, 2009).

Empirical data has supported the constant stress drop model for small to moderate size earthquakes. On the other hand, physical constraints to the rupture dimensions begin to arise for large earthquakes in the crustal zone for continental regions. A closer examination for large events has revealed that the slope of Equation 2-8 may deviate from unity, once the maximum rupture width is reached along the down-dip direction. This also implies that the average fault slip, D for an event scales differently for large earthquakes. Two different approaches exist for modeling D scaling for large events; L-model and the W-model. The L-model suggests that, D is proportional to the rupture length, and will increase even if the full fault width is reached. On the contrary, D value in W-model is constrained by the fault width. Empirical evidence collected so far has supported the L-model. Further discussion on the application of L-model in practice will be supplied in the proceeding section, and

full discussion on theoretical basis can be tracked in Scholz (1982), Yin and Rogers (1996), and Wang and Ou (1998).

## **2.2 OVERVIEW OF EXISTING RELATIONSHIPS**

Proposal of correlating earthquake magnitude with rupture parameters such as length and displacement dates back to over a half century (Tocher, 1958; Iida, 1959; Chinnery, 1969). Wells and Coppersmith (1994) lists a series of published empirical relationships which attempt to relate earthquake magnitude to various fault rupture parameters such as surface rupture length, maximum surface displacement, total fault length, etc. (Tocher, 1958; Iida, 1959; Albee and Smith, 1966; Chinnery, 1969; Ohnaka, 1978; Slemmons, 1977, 1982; Acharya, 1979; Bonilla and Buchanon, 1970; Bonilla et. al., 1984; Slemmons et al., 1989). Numerous studies which relate magnitude with rupture length, rupture width, rupture area as inferred from different methods of data analysis have also contributed to the current state of the art (Utsu and Seki, 1954; Utsu, 1969; Kanamori and Anderson, 1975; Wyss, 1979; Singh et al. (1980); Purcaru and Berckhemer, 1982; Scholz, 1982; Wesnousky, 1986; and Darragh and Bolt, 1987). These studies listed in Wells and Coppersmith (1994) has been the building blocks of larger scale studies with cautiously compiled datasets.

Undoubtedly, Wells and Coppersmith (1994) set of relationships for the prediction of rupture dimension parameters for shallow crustal regions, is the most widely used tool in modern seismic hazard assessment studies. Wells and Coppersmith (1994) have presented a meticulous effort in quantifying and documenting the reliability of data to be included into their dataset for regressions.

Wells and Coppersmith (1994) database represents events shallower than 40 km at continental interplate or intraplate regions, with an approximate magnitude cutoff of M 4.5 at lower end. Events from subduction zones, plate interfaces, or oceanic slabs

are excluded, which fits perfectly for our practical use of events taking place all over Anatolian Plate. Data from stable continental regions defined as regions of continental crust that have no significant Cenozoic tectonism or volcanism are included.

For the sake of compactness of the text, only the results from the magnitude - rupture area, rupture width and rupture length models are covered; hence prediction models in which maximum or average fault displacement act the predictive variables are excluded from discussion. Table 2.2-1 summarizes the Wells and Coppersmith (1994) relations for the prediction of surface rupture length (SRL), subsurface rupture length (RLD), downdip rupture width (RW) and rupture area (A), all having units of either km or km<sup>2</sup>, as a function of moment magnitude, M. Coefficients for the regressions are summarized in Table 2.2-1, with the exception of rupture area models.

**Table 2.2-1. Wells and Coppersmith (1994) model coefficients for various types of rupture dimension definitions**

Equation	SOF <sup>(1)</sup>	# of Events	a <sup>(2)</sup>	b <sup>(2)</sup>	$\sigma_{\log RD}$ <sup>(3)</sup>
$\log(\text{SRL})=a+bM$	All	77	-3.22	0.69	0.22
$\log(\text{RLD})=a+bM$	All	167	-2.44	0.59	0.16
$\log(\text{RW})=a+bM$	All	153	-1.01	0.32	0.15
$\log(\text{A})=a+bM$	All	148	-3.49	0.91	0.24
$\log(\text{A})=a+bM$	SS	83	-3.42	0.90	0.22
$\log(\text{A})=a+bM$	R	43	-3.99	0.98	0.26
$\log(\text{A})=a+bM$	N	22	-2.87	0.82	0.22

<sup>1</sup>: SS: Strike-slip, N: Normal, R: Reverse

<sup>2</sup>: Standard errors of coefficients are not shown

<sup>3</sup>:  $\sigma_{\log RD}$ : aleatory variability value of Rupture Dimension of interest

Difference among the predictions of rupture area as a function of magnitude for Wells and Coppersmith (1994) models is slightly notable for three main types of faulting style, for magnitudes below  $M=6.5$ . Figure 2.2-1 shows the rupture area predictions in linear scale for strike-slip, normal and reverse fault subsets of the Wells and Coppersmith (1994) model, obtained from independent regressions. In Figure 2.2-1, the solid line represents model with all faulting styles included in the dataset (148 events). Model for strike-slip events (83 events) is plotted using dash-dots. Reverse fault and normal fault models are calculated using 43 and 22 events respectively. This brings the question whether the observed difference at smaller magnitudes is due to the seismological characteristics of faulting, or a bias in regressions with sample sets having uneven number of data.

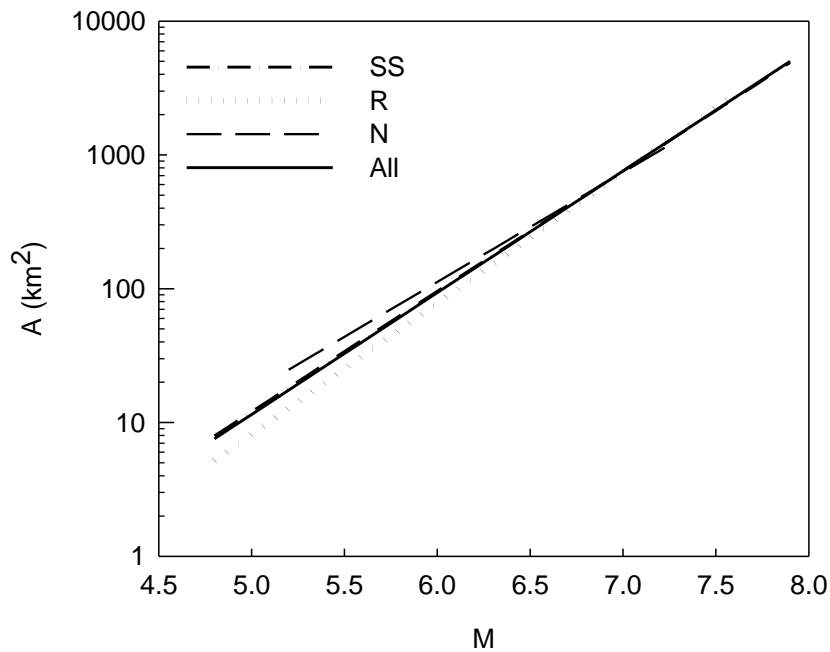


**Figure 2.2-1. Variation of rupture area prediction as a function of style of faulting for Wells and Coppersmith (1994) model**

Another general subject of discussion is the geometrical compatibility of predictions for rupture area, rupture length and rupture width. Given the most basic assumption of rectangular rupture geometry, and excluding small magnitude events with circular ruptures, predicted rupture area for an earthquake magnitude is expected to satisfy

the product of rupture width and rupture length predictions. This basic compatibility is required for hazard assessment studies, while running simulations for source to site distance calculations. However, meeting such a compatibility is far from expectations when the rupture width, rupture length and rupture area models are regressed independently. An illustrative example is given in Table 2.2-2, where a comparison between the rupture areas obtained using the product of rupture width and length is compared to the prediction made by the magnitude - rupture area relationship itself. A moderate and a large earthquake magnitude are chosen for comparison. Even though percent difference is more or less the same, the absolute difference is more distinguishable in large magnitude earthquakes.

**Table 2.2-2. Illustration of geometric incompatibility in Wells and Coppersmith (1994) model predictions**

Magnitude M	SOF	RL (km)	RW (km)	RLxRW (km <sup>2</sup> )	A (km <sup>2</sup> )	Percent Difference
5.5	All	6.4	5.6	35.9	32.7	9.8 %
7.5	All	96.6	24.6	2371.4	2162.7	9.6%

Among the three fundamental parameters for defining the rupture geometry for rectangular ruptures, a necessity arises for sub categorization of the rupture length. Rupture length is either reported as surface rupture length, which is the trace of rupture observed on the ground surface, or the subsurface rupture length. Wells and Coppersmith (1994) reports that the distinction of primary surface ruptures due to intersection of fault plane with the surface was made from secondary fractures due to ground shaking, landslides, etc. Nevertheless, it is within expectations that a significant amount of variability exists in parameter estimations of rupture lengths due to numerous factors such as method of analysis, measurement errors, and loss of field evidence from old events. On the contrary, reporting of an approximate ratio of 0.75 between the surface rupture length and subsurface rupture length for an event, in

accordance with the findings of Wells and Coppersmith (1994), holds reasonable for most practical purposes.

Similar study by Somerville et al. (1999) supports the constant stress drop scaling, yielding Equation 2-9:

$$M = \log(A) + 3.95 \quad (2-9)$$

Anderson et al. (1996) proposed the introduction of an extra parameter in the magnitude – rupture dimension relationships, the annual slip rate. Anderson et al. (1996) model estimates earthquake magnitude as a function of rupture length and annual slip rate.

L-model in earthquake magnitude scaling has gained support through verification by empirical data for large magnitude earthquakes, as first stated in Section 2.1. Recalling that L-model represents the continuity of increasing average fault displacement proportional to rupture length, and rupture width is constrained by physical boundaries of the crust for regions outside subduction zones ( $RW_{max}$ ), Equation 2-10 and Equation 2-11 were introduced (Hanks and Bakun, 2002):

$$D = \alpha RL \quad (2-10)$$

$$A = RL \cdot RW_{max} \quad (2-11)$$

In Equations 2-10 and 2-11,  $\alpha$  is a scaling coefficient between rupture length and seismic slip, and  $RW_{max}$  is the maximum downdip width of the rupture, constrained by the thickness of the crust. Substituting Equation 2-10 and 2-11 into Equation 2-4 and rearranging yields Equation 2-12 and Equation 2-13 respectively:

$$M = \frac{4}{3} \log_{10}(RL) + \frac{2}{3} \log_{10}(RW_{max}) + \frac{2}{3} \log_{10}(\alpha) + \frac{2}{3} \log_{10}(\mu) - 10.7 \quad (2-12)$$

$$M = \frac{4}{3} \log_{10}(RL) + b_1 = \frac{4}{3} \log_{10}(A) + b_2 \quad (2-13)$$

Interpretation of Equation 2-13 is self explanatory; for an L-model, theoretical slope for an M(A) function becomes 4/3. A recent study by Hanks and Bakun (2002) utilizes a bilinear model; preferring a combination of constant stress drop model for smaller magnitude events, and L-model for large earthquake scaling.

Hanks and Bakun (2002) have commented on the constant stress drop scaling of Wells and Coppersmith (1994) relations by considering the effect of systematic estimation bias on the calculated hazard levels for earthquakes having magnitudes greater than or equal to M=7. Hanks and Bakun (2002) have run regressions on a subset of Wells and Coppersmith (1994) database consisting of strike-slip events, with the addition of 5 large events having magnitude greater than or equal to M=7.85 (Figure 2.2-2).

Final form of the bilinear function with fixed slopes at unity and 4/3 is presented in Equation 2-14. Transition magnitude corresponds to M=6.71.

$$M = \log(A) + 3.98 \quad A \leq 537 \text{ km}^2$$

$$M = \frac{4}{3} \log(A) + 3.07 \quad A > 537 \text{ km}^2 \quad (2-14)$$

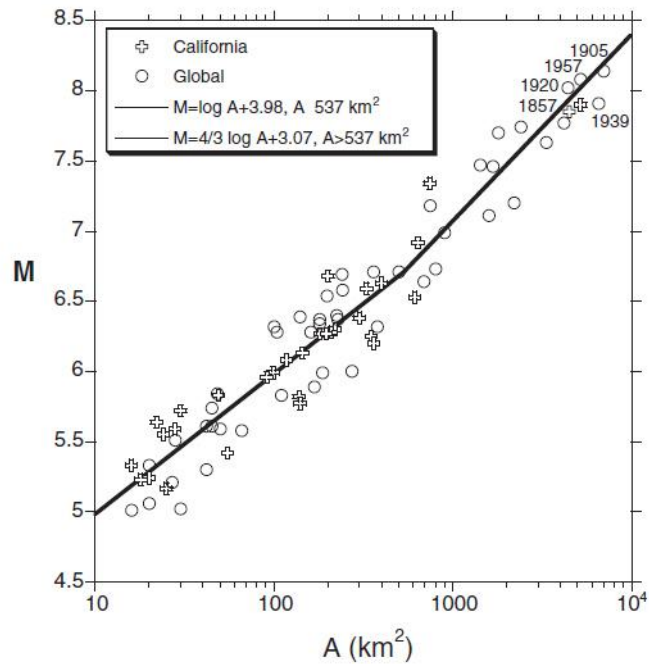


**Figure 2.2-2. Bilinear magnitude scaling relation by Hanks and Bakun (2002)**

Hanks and Bakun (2008) have reevaluated their previous study by adding data from 7 large earthquakes having magnitudes between  $M=7.06$  and  $M=7.88$ . L-model scaling was verified without further modifications to the coefficients of the Hanks and Bakun (2008) model.

Ellsworth (2003) is another valuable attempt in modeling magnitude rupture dimension scaling. USGS Working Group on California Earthquake Probabilities (2003) summarizes efforts of Ellsworth (2003); in which a linear function was considered to be the most appropriate for defining magnitude log-area relationship. Strike slip data compiled from literature was regressed for events having rupture areas greater than  $500 \text{ km}^2$ , and the following expression was derived:

$$M = \log(A) + 4.2 \quad A > 500 \text{ km}^2 \quad (2-15)$$



Ellsworth (2003) has also carried out a remarkable study on defining the parameter uncertainties on both  $M$  and  $\log(A)$ . The study has made use of data analysis from published literature, and came up with a value of  $\sigma_M=0.12$ ; which is far below the general expectation of standard error value, for the case when the contribution of parameter uncertainty to the total error is ignored. A typical value of 0.20 or greater is valid for most well known relationships.

Regional variance in magnitude – rupture dimension relationships have been stated by various researchers (Acharya, 1979; Bonilla et al., 1984; Dowrick and Rhoades, 2004). A recent study is by Dowrick and Rhoades (2004), which performed a systematic study to investigate the possible regional variability in magnitude – rupture dimension relationships.

The study utilizes event data collected from New Zealand earthquakes, excludes the events from subduction zone interfaces, and includes events that took place wholly in crustal or subduction zones. Figure 2.2-3 shows the regressions of magnitude versus rupture area for New Zealand data, compared with Hanks and Bakun (2002) model which includes data from multi regions such as California, Japan and China. The study compares and contrasts rupture width, rupture area and rupture length models; eventually describing the variability in terms of aspect ratio (Figure 2.2-4).  $L_{sub}/W$  term is the ratio of subsurface rupture length to rupture width, and  $W_{max}$  is the maximum downdip rupture width. Dowrick and Rhoades (2004) do not conclude with any solid explanation of the regional variability; however mainly focuses on possible cause as a difference in crustal structure.

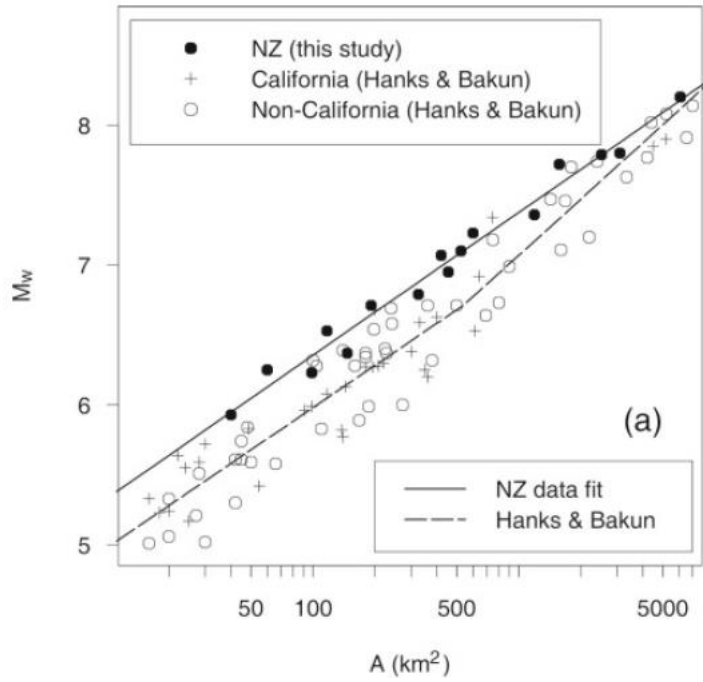


**Figure 2.2-3. Comparison of Dowrick and Rhoades (2004) study with Hanks and Bakun (2002) model**

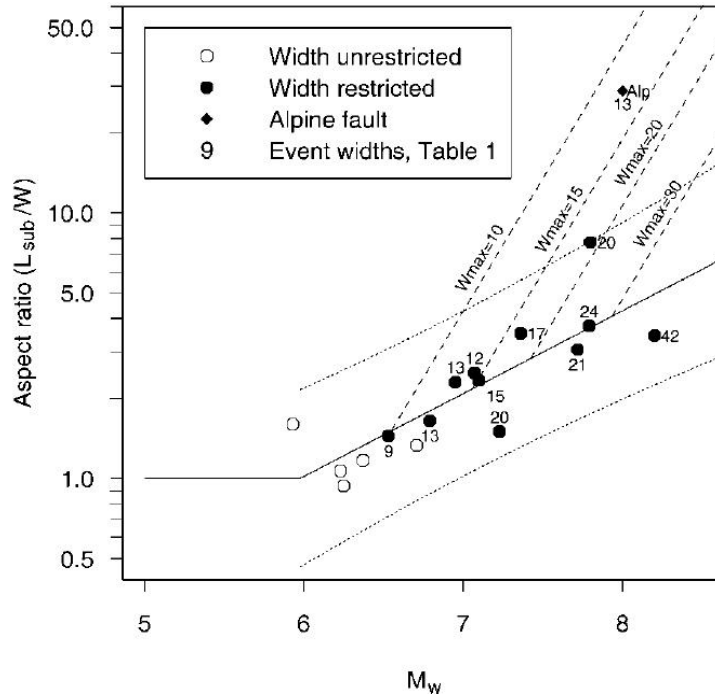


**Figure 2.2-4. Magnitude dependence of aspect ratio in Dowrick and Rhoades (2004) model**

Stein (2008), as part of the effort by the 2007 Working Group for California Earthquake Probabilities, re-evaluated the current situation of the magnitude – area relationships in the UCERF-2 (Uniform California Earthquake Rupture Forecast) collaboration. Stein (2008) commented that log-linear model by Somerville (2006), developed using teleseismic and strong motion inversions of coseismic slip of recent earthquakes, are biased in terms of inversions and the trimming preferences of fault rupture area parameters in regions of no or low seismic slip. Somerville (2006) yields similar results with Wells and Coppersmith (1994) relationships. Using data from the Hanks and Bakun (2008) study, Stein (2008) proposed a new fit using the power law which enables transitional slope change in the magnitude – rupture area relationship (Figure 2.2-5). Avoiding the breakpoint value of 537 km<sup>2</sup> in a bilinear model, Stein (2008) developed Equation 2-16. Performance of power function in high magnitude range is concluded to be satisfactory; and the error is partially attributed to the parameter uncertainty inherent in events dating back to almost a century.

$$M = 4.2775 \cdot A^{0.0726} \quad (2-16)$$

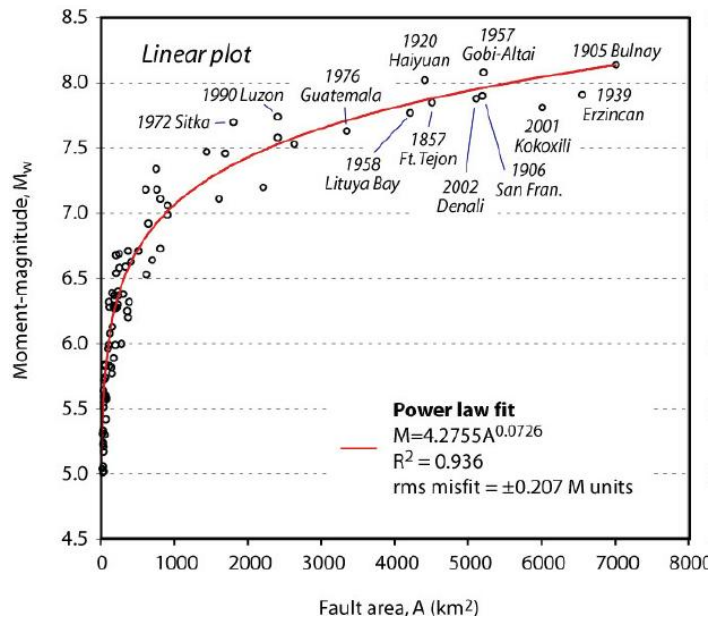


Figure 2.2-5. Stein (2008) magnitude-area scaling model

## **2.3 DATABASE COMPILATION**

A global database of earthquake rupture dimensions as well as complementary parameters defining the event source characteristics for 192 earthquakes is compiled from published literature. The data represents shallow focus events having reported depths less than 30 km, with an exception of 2 events. The lower bound moment magnitude for the database is  $M=5.5$ , representing a non-intentional cutoff value that covers the needs in a seismic hazard assessment. Upper bound magnitude reaches as high as  $M=8.20$ . Tectonic setting for the earthquakes considered herein are restricted to shallow crustal events; subduction zone events, earthquakes occurring within oceanic slabs and plate interface earthquakes are out of scope of the study. Each earthquake included in the database consists of main and auxiliary data fields such as name, location, epicentral coordinates, focal depth, type and size of reported earthquake magnitude, style of faulting in either reported rake angle term or mechanism, dip angle of the ruptured fault, subsurface rupture length, downdip rupture width and seismic moment compatible average displacement over the fault plane. Parameters which are reported for a certain proportion of the events in the database such as surface rupture length and static stress drop are also compiled where available. An extended presentation of the dataset used in magnitude – rupture dimension scaling relationships developed under this study is given in Table A.1 and Table A.2 in Appendix A.

### **2.3.1 Data Sources and Spatial Distribution**

The main data source for the earthquakes is the Wells and Coppersmith (1994) database (abbreviated as WC94 hereafter), supplemented by Triep and Sykes (1996) online catalog (TS96 hereafter) where necessary. Events from active continental regions tagged as “a” or “i” in Triep and Sykes (1996) catalog were included. For events with undefined tectonic region tags, data was carefully screened and events that were compatible with defined criteria were added. Screening of Triep and Sykes

catalog (1996) as well as data from recent literature enabled inclusion of events eliminated from WC94 database due to unreliable or missing rupture dimensions.

Attention was given to distinguishing subduction zone events from crustal events, especially for earthquakes in Japan and North America; by referring to field reports and published literature (Kawasumi, 1950; Richter et al., 1958; Shor and Roberts, 1958; Green and Bloch, 1971; Abe, 1974; Magistrale et al., 1989; Westaway and Smith, 1989; Caskey et al., 1996; Thatcher et al. 1997; Young et al. 2002; Caskey et al. 2004; Taymaz and Tan, 2005). Table A.1 lists the sources of data for each event. Source data was compiled from various regions of the world, including Europe, North America, Asia, Central and South America, Africa, Middle East, Japan, Taiwan and Philippines, as well as Oceania; covering continental Australia, New Zealand, New Guinea, Figure 2.3-1 presents the spatial distribution of 192 events forming the dataset.

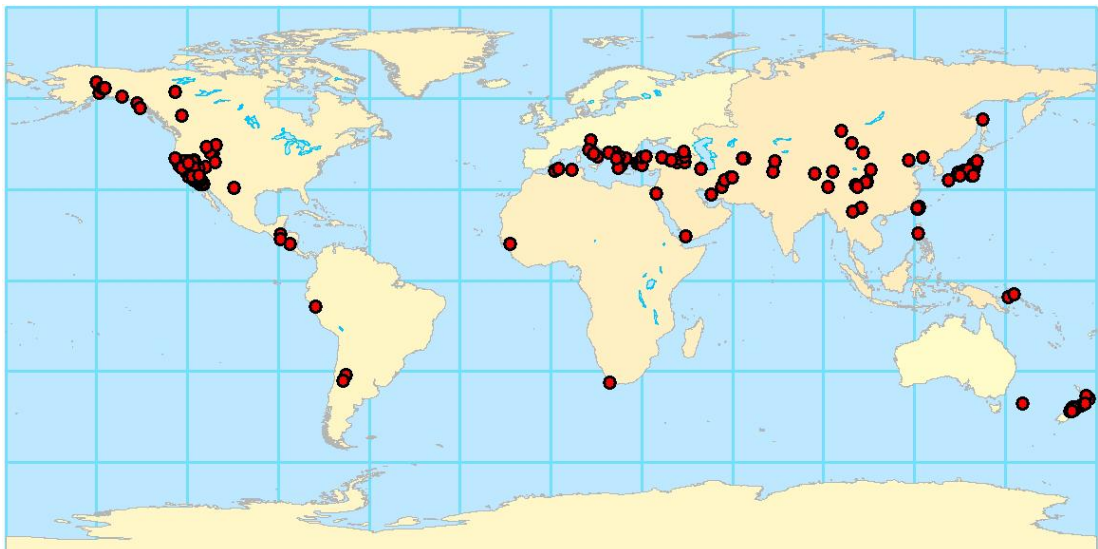


**Figure 2.3-1. Spatial distribution of events included in the magnitude – rupture dimension relationship dataset**

For events which WC94 data was compatible with Triep and Sykes (1996) (TS96) catalog, metadata was referred to TS96 listing. Rupture dimensions from the past

decade were mainly compiled from the NGA (Next Generation of Attenuation Relations Project) strong motion database flatfile (Chiou et al., 2008). Several large magnitude shallow crustal events were added from Hanks and Bakun (2002), and Hanks and Bakun (2008) respectively. Ellsworth (2003) compilation was reviewed for any data inconsistencies and expansion opportunities. Data from Geller (1976), Scholz (1982), as well as Dowrick and Rhoades (2004) for crustal New Zealand earthquakes were utilized for assessment and possible inclusion to our dataset. Similarly, data from subduction zone events and unreliable estimates as reported by Dowrick and Rhoades (2004) were excluded.

For events which published literature documented several non-unique estimates of rupture dimensions, all relevant values and their sources were recorded for comparison and final selection. Events that lacked any of the downdip rupture width or subsurface rupture length were directly excluded from the dataset. Additional discussion on the uncertainty arising from data reported by various references, and various aspects bringing in data quality issues such as event date, event magnitude and method of obtaining the rupture dimensions will be discussed in the following sections.

### **2.3.2 Compilation of Source Parameters**

#### *2.3.2.1 Earthquake Magnitude and Seismic Moment*

Moment magnitude was selected as the primary magnitude measure to define the earthquake size. For 2 cases out of 192 records in the compiled database, only surface wave magnitude was reported, hence either the seismic moment or the moment magnitude was missing. Considering that, for many of the events included either in the WC94 or TS96 datasets, which are the primary sources of data for the current dataset, the reported moment magnitudes are already converted from another magnitude scales; relationships presented in Heaton et al. (1982) were utilized for

surface wave magnitude to moment magnitude conversion for those 2 events. Thus, especially for older events, one would easily state that the order of uncertainty in magnitude estimates is basically unknown. Table A.1 summarizes the method for determining the moment magnitude for each event. For events with tag “A”, moment magnitude  $M$  is directly reported. Tag “B” stands for calculation of  $M$  through seismic moment ( $M_0$ ) reported in the NGA database or the Harvard CMT catalog (2010). Tag “C” represents moment magnitude calculation using  $M_0$  reported in TS96 database. Finally, tag “D” represents 2 events with other magnitude scales; converted to  $M$ . Frequency distribution of moment magnitude values is presented in Figure 2.3-2.

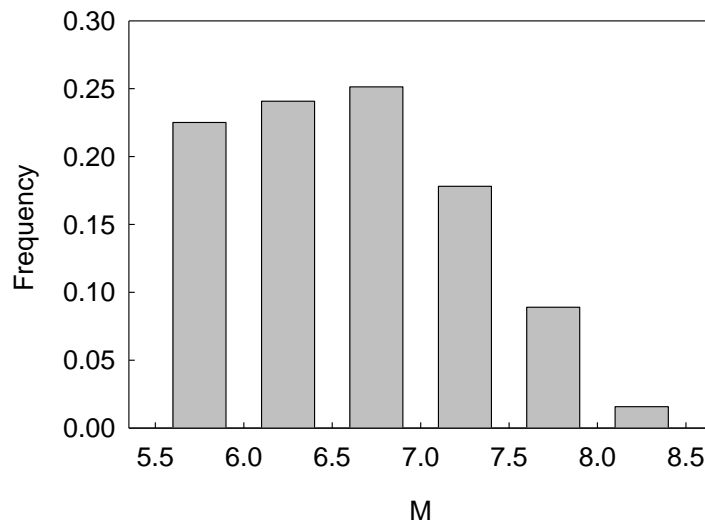


**Figure 2.3-2. Magnitude-frequency distribution of rupture dimension dataset**

### 2.3.2.2 Focal Depth

Events in the magnitude – rupture dimension scaling dataset consist of shallow focus events; with values ranging from 2 km to 30 km. Two events having focal depths larger than 30 km were investigated and concluded to be in regions of crustal activity; therefore truncation not necessary. Average focal depth of the dataset is 11 km, and its variation as a function of moment magnitude is presented in Figure 2.3-3.

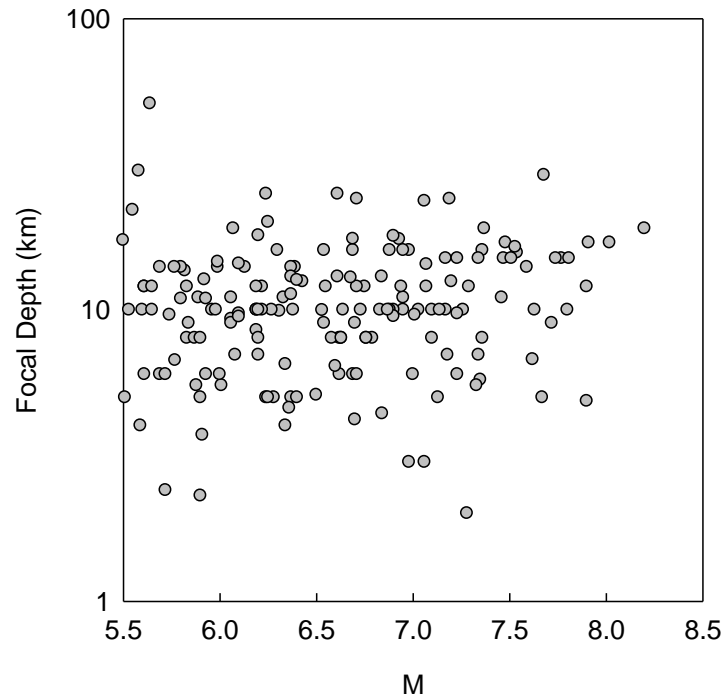


**Figure 2.3-3. Focal depth distribution of rupture dimension dataset**

### *2.3.2.3 Style of Faulting*

In predicting the rupture dimensions associated with earthquake size, WC94 has attempted to model the style of faulting using discrete bins and independent regressions. This approach limits the sample size of each regression statistically, while obscuring the smooth, natural transition between earthquake mechanisms using sharp selection criteria among normal, strike-slip, and reverse faults.

In the selection of best estimates of source parameters, parameter uncertainty is assumed to be zero for seismic moment, style of faulting, dip angle and rupture dimensions respectively. However, we attempt to classify the parameter selections based on the extent and quality of available data.



Data Class A: A different modeling criteria using the rake angles associated with the most probable focal plane obtained through focal mechanism solutions was preferred. For cases with the published focal mechanism solutions, such as the Harvard CMT (Centroid Moment Tensor), the primary plane using the strike and dip directions as determined by the actual fault geometry were picked. Style of faulting inferred using procedures in accordance with Data Class A constitutes 49% of the dataset.

Data Class B: There are several events which the relevant earthquake reports were inaccessible. For such cases, the arithmetic mean of the two possible rake angles for the specific event, suggested by the published focal mechanism, was calculated. Since the difference between two options of the rake angles were almost always in the range of 3-4 degrees on average, reaching a maximum value of 10 degrees at rare circumstances; simple averaging was not considered to induce considerable uncertainty on the variable and impact the results. 40 out of 192 cases belong to Data Class B.

Data Class C: There were 58 cases which the style of faulting was only defined as either “normal”, “reverse” or “strike-slip”. For such events, the median values of available rake angles included in our catalog were assigned; being consistent with style of faulting scheme used in WC94 and NGA, to events which lacked reported rake angle estimates. The binned style of faulting scheme is reflected by 30 degree arcs as summarized in Figure 2.3-4. The classification makes no distinction among the tectonic regime where the earthquake occurred, namely compressional, transpressional or extensional.

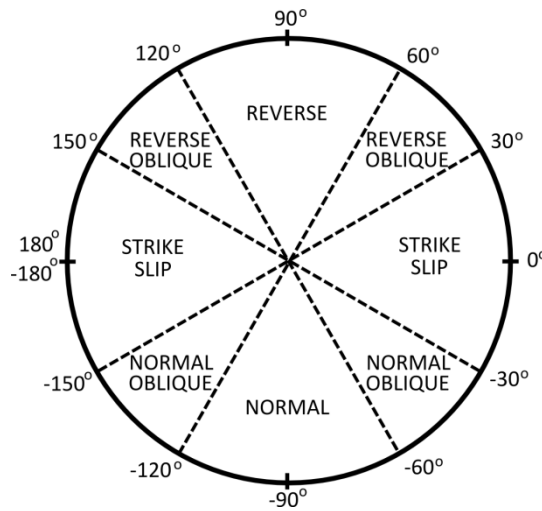


**Figure 2.3-4. Style of faulting scheme used for categorizing events without any rake angle**

A point worth noting is, reported focal mechanism solutions are the best estimates of the source parameters, already incorporating uncertainty that is often not reflected to the reader, also not quantified in this study.

The rake angle convention associated with dominant slip direction of a fault rupture is composed of two half circle transitions distinguishing between transition to either normal or reverse mechanisms from an origin defined by pure strike-slip mechanism; that is also capable of differentiating the left lateral and right lateral slip directions. For the purpose of utilizing the current scheme to be used in the proposed models as a less complicated continuous parameter, whole circle is remapped into a “**Style of Faulting Parameter**”, that takes the value of “0” for a normal fault, “1” for a reverse fault, and any value between 0 and 1 for intermediate slip styles including strike-slip. Letting  $\lambda$  be the reported rake angle compatible with the general sign convention, transformation required for rake angles falling in each quadrant of the circle is schematized in Figure 2.3-5. Figure 2.3-6 presents the style of faulting histogram of the current dataset.

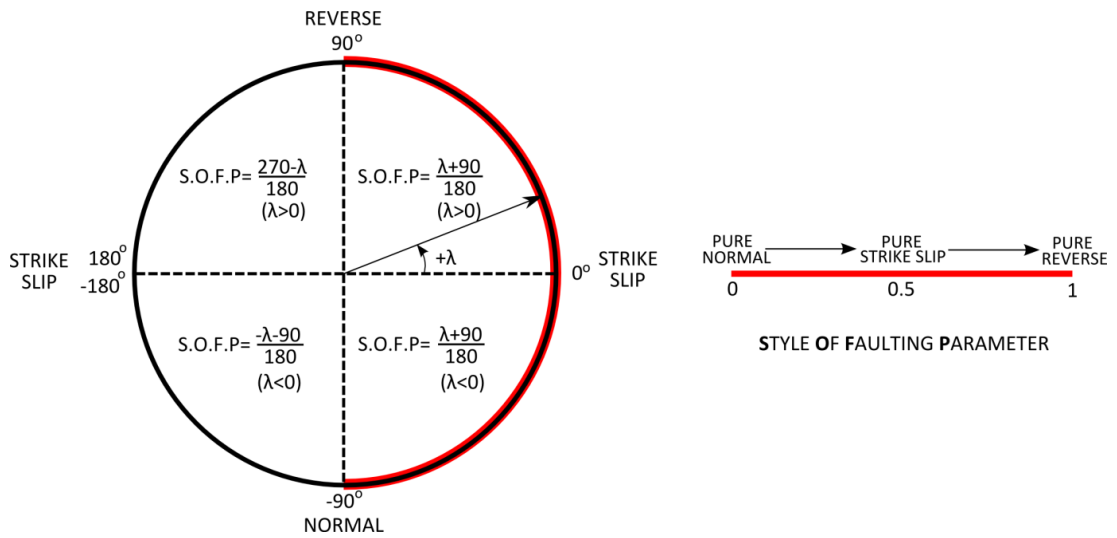


**Figure 2.3-5. Rake angles remapped into a linear representation of faulting mechanism**

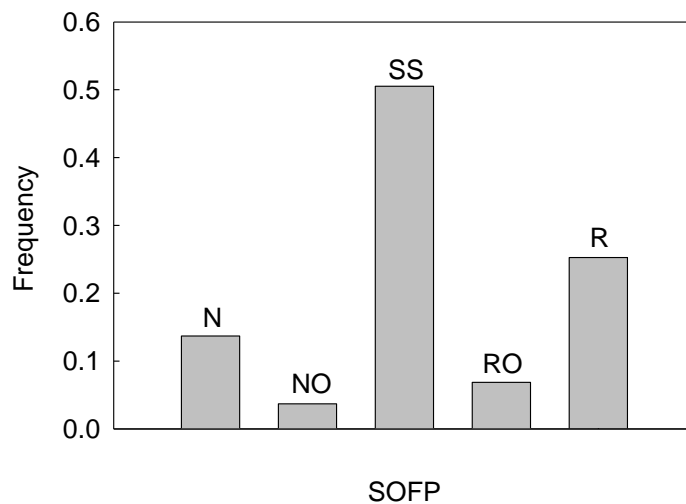


**Figure 2.3-6. Style of faulting frequency distribution of the rupture dimension dataset**

#### 2.3.2.4 Dip Angles

Selection of dip angles for each event was completed using the same procedure for style of faulting. There were 47 events (24%) with missing dip angles; and representative values calculated using the median dip angle for the relevant style of

faulting in the dataset were assigned to those events. Events having dip angles assigned with respect to the assumption given above are marked with ‘\*’ symbol in Table A.2. Frequency distribution of dip angles in the dataset is presented in Figure 2.3-7.

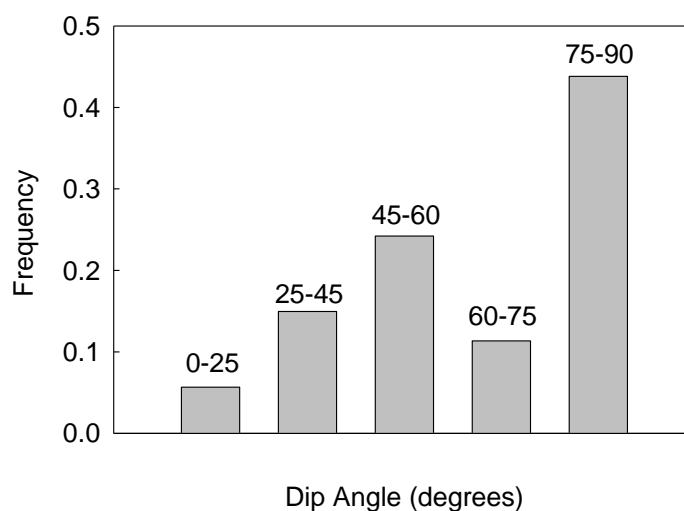


**Figure 2.3-7. Dip angle frequency distribution of the rupture dimension dataset**

### **2.3.3 Rupture Dimensions**

This section contains a brief description and discussion of rupture dimension parameters. One of the vital characteristics of rupture dimension data available in published literature is that the set of parameters are not fully independent. Depending on the earthquake date and available data, various methods exist for inferring rupture dimensions. Choice of methods is closely correlated with the age of earthquake and availability of instrumental data. Rupture dimension determination based on analysis of aftershock distribution, geodetic modeling, teleseismic inversion, field data or a combination of these methods is possible. For events which took place before instrumental data were available, even the most basic source parameters such as earthquake magnitude may be inferred from the assumed traces of field evidence, such as the 1857 Fort Tejon, USA, and 1905 Bulnay, Mongolia earthquakes. For

some of large magnitude events which the rupture is assumed to reach the crust thickness, rupture width is restricted to the measured downdip crustal thickness without further instrumental evidence (Dowrick and Rhoades, 2004).

Almost all of the rupture dimension data available in published literature contain sources of reported parameters, most of them being originated from various methods, and inhibiting sources of uncertainty that are hard to quantify. Referring back to Equations 2-1 and 2-5; relating seismic moment, moment magnitude, average displacement on fault surface, and average static stress drop using assumptions of ruptures having different geometrical patterns; one needs an independent set of measurements for each of the source parameters to fully understand the nature of the phenomenon. However, this is not the case in practice, and also valid in the current dataset. For most of the cases, missing rupture parameters are derived from a more restricted set of available parameters. The dataset used in this study contains reported rupture dimensions that fully comply with rectangular assumption. Such an idealization is acceptable; especially considering that the magnitude cutoff value is chosen as  $M=5.5$ ; truncating lower magnitude events that are more likely to exhibit elliptical or circular rupture patterns.

Column tagged as “Remark” summarizes the criteria for rupture dimension selection. For events with multiple reporting of rupture dimensions by various sources; a systematic approach was followed towards selecting the values from more recent studies. For events with reported average displacement along the fault; rupture length and width pair was chosen among the ones that satisfy Equation 2-1, in the case of multiple dimension reporting. Such a preference certainly brings a bias; however the possible effect is ignored.

Data from the NGA flatfile represents subsurface rupture length. For events with missing subsurface rupture length, surface rupture length was assigned where available; overriding the average relationship between surface and subsurface rupture

length proposed by Wells and Coppersmith (1994). A cross comparison was made for rupture area calculated using rupture width-length pair; and through Equation 2-1 where average fault displacement from any published source was available. Agreements in predictions were satisfactory (Table A.1), although prior information on possible dependency of reported parameters is partly responsible for compatibility.

### *2.3.3.1 Rupture Area*

Variation of earthquake magnitude with rupture area is presented in Figure 2.3-8. Gray dots represent the current database, for which the probabilistic prediction model is to be established. Underlying series represent the WC94 dataset used for rupture area regressions. Figure 2.3-8 shows solid evidence on the expansion of dataset towards the larger magnitude extreme. Theoretical relation from the constant stress drop model is superimposed in Figure 2.3-8; demonstrating that the curve over predicts the rupture area for events having magnitudes greater than  $M=7.5$ . Distribution of events with respect to style of faulting is shown in Figure 2.3-9.

Another point of discussion in the literature is the regional variability of magnitude – rupture dimension scaling relationships. Acharya (1979) has made an attempt to demonstrate regional variability, and further discussion on modeling and/or differentiating regional tendencies in data is out of scope of this thesis. Nevertheless, Figure 2.3-10 is presented to display fundamental information on magnitude area data binned with respect to various tectonic regions.

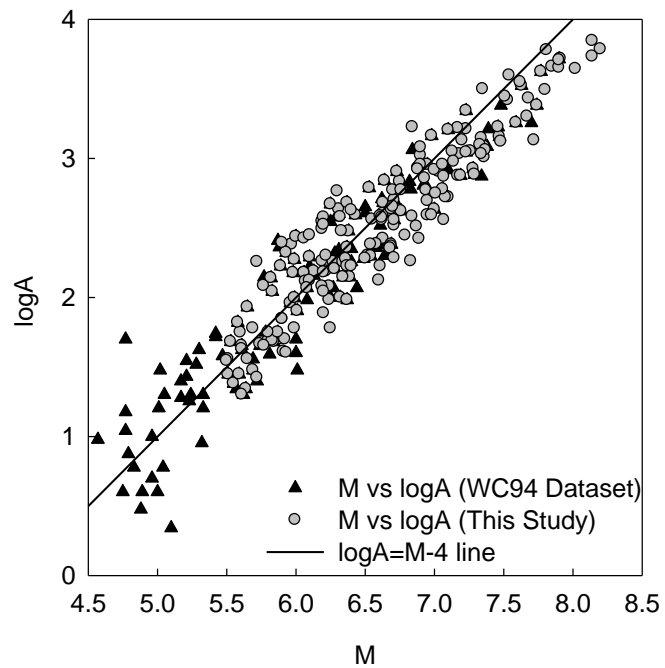


**Figure 2.3-8. Magnitude-area distribution of the current dataset**

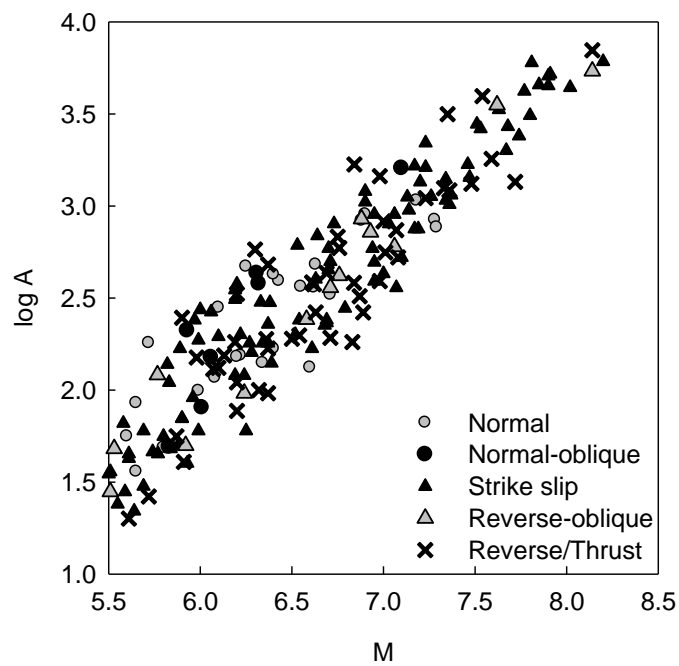


**Figure 2.3-9. Magnitude-area distribution with style of faulting bins**

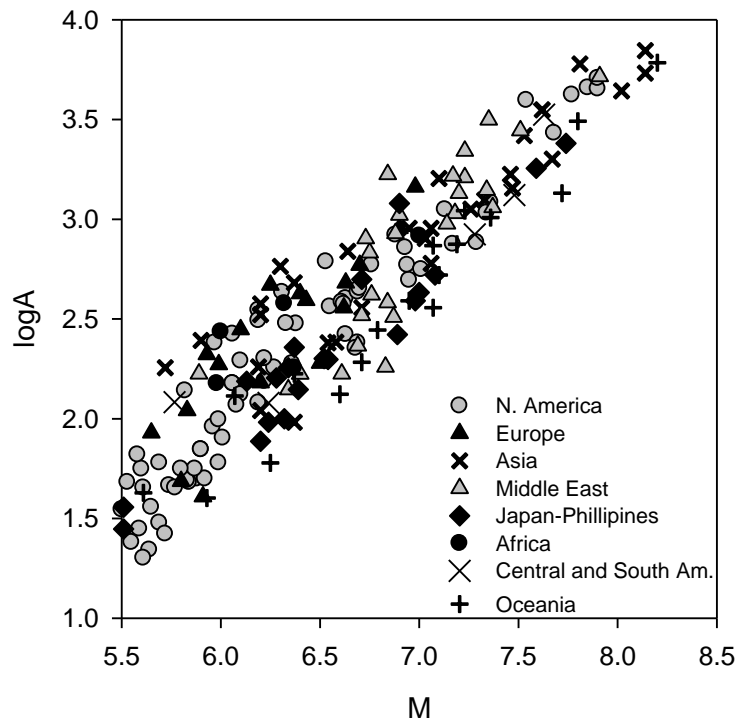


**Figure 2.3-10. Magnitude-area distribution separated with tectonic regions of occurrence**

### 2.3.3.2 Rupture Width

Recalling the constant stress drop model and L-model discussions, observing the distribution of rupture width data becomes crucial. Figure 2.3-11 clearly presents the field evidence of rupture width saturation for high magnitudes. This phenomenon is valid for shallow events from active crustal zones; and excludes behaviour from subduction zone earthquakes.

### 2.3.3.3 Rupture Length and Aspect Ratio

Variation of rupture length with respect to moment magnitude is presented in Figure 2.3-12. Data are observed to follow a linear trend. Aspect ratio for the dataset is sometimes overlooked, yet an important parameter. Aspect ratio is defined as in



Equation 2-17. Variation of aspect ratio against magnitude, binned with respect to assigned dip angles is presented in Figure 2.3-13, showing obvious evidence of L-model validity. The term “ $\delta$ ” in Figure 2.3-13 stands for dip angle.

$$AR = \frac{RL}{RW} \quad (2-17)$$

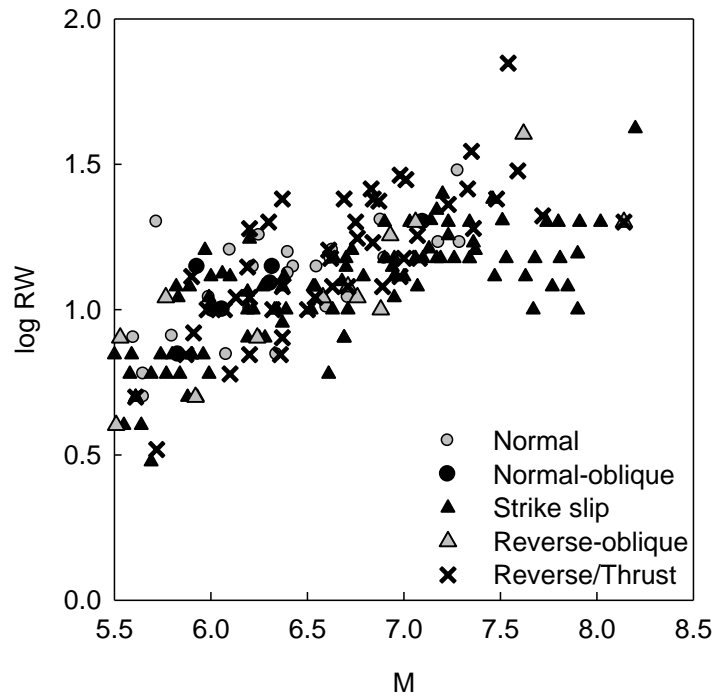


**Figure 2.3-11. Magnitude-area distribution separated with tectonic regions of occurrence**

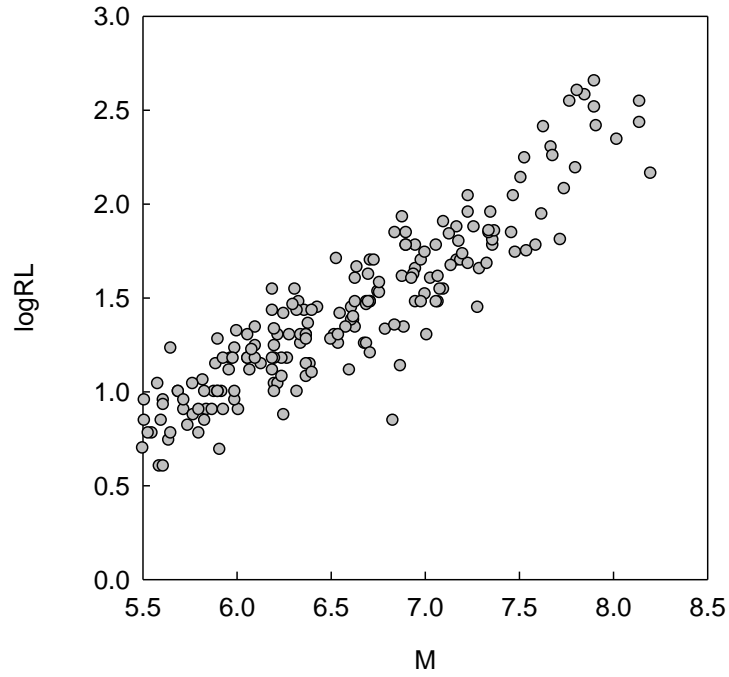


**Figure 2.3-12. Magnitude – rupture length distribution for the dataset**

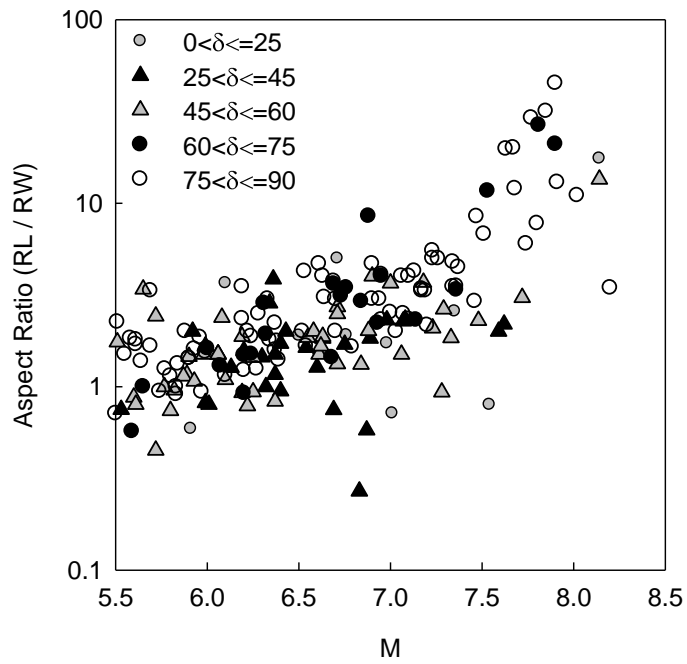


**Figure 2.3-13. Magnitude – aspect ratio distribution with dip angle bins**

## 2.4 PROBABILISTIC MODELS FOR MAGNITUDE – RUPTURE DIMENSION SCALING

### 2.4.1 Independent Models of A, RW and RL

#### 2.4.1.1 Independent Model for Rupture Area

Maximum likelihood methodology was utilized to model magnitude – rupture dimension relationships. This section contains the details of the probabilistic assessment framework including the maximum likelihood methodology. The first step in developing a probabilistic model is to select a limit state expression that captures the essential parameters of the problem. The model for the limit state function has the general form  $g = g(\mathbf{x}, \Theta)$  where  $\mathbf{x}$  is a set of descriptive parameters and  $\Theta$  is the set of unknown model parameters. Inspired by available models in literature, as well as the trends in the presented databases, and theoretical background; a suite of functional forms have been tested, some of which are listed in Table 2.4-1. Among these models, the following functional form is adopted as the limit state function for log-rupture area prediction.

$$g(M, SOFP, \Theta) = \log A_{\text{measured}} - (\theta_1 + \theta_2 M + \theta_3 SOFP) \mp \varepsilon_{\log A} \quad (2-18)$$

where  $\theta_i$  is the set of unknown model parameters.

The proposed model includes a random model correction term ( $\varepsilon$ ) to account for the facts that i) possible missing descriptive parameters with influence on rupture area may exist; and ii) the adopted mathematical expression may not have the ideal functional form. It is reasonable and also convenient to assume that  $\varepsilon$  has normal distribution with zero mean for the aim of producing an unbiased model (i.e., one that in the average makes correct predictions). The standard deviation of  $\varepsilon$ , denoted

as  $\sigma_\varepsilon$ , however is unknown and must be estimated. The set of unknown parameters of the model, therefore, is  $\Theta = (\theta, \sigma_\varepsilon)$ .

where  $\sigma_\varepsilon$  can be also modeled as a function of one of the predictive parameters,  $M$ .

$$g(M, SOFP, \theta, \sigma_\varepsilon) = \log A_{\text{measured}} - (\theta_1 + \theta_2 M + \theta_3 SOFP) \mp \varepsilon_{\log A} \quad (2-19)$$

Assuming the value of logarithm of rupture area obtained after the analyses to be statistically independent, the likelihood function for “k” analyses where exact ratio values are available (i.e., values at the end of the analyses are available), can be written as the product of the probabilities of the observations.

$$L_{\log A}(\theta, \sigma_\varepsilon) = \prod_{i=1}^k P[g_{\log A, i}(\cdot) = 0] \quad (2-20)$$

Suppose the values of  $M$ ,  $SOFP$  at each data point are exact, i.e. no measurement or estimation error is present, noting that  $g(\dots) = \hat{g}(\dots) + \varepsilon_i$  has the normal distribution with mean  $\hat{g}$  and standard deviation  $\sigma_\varepsilon$ , then the likelihood function can be written as:

$$L_{\log A}(\theta, \sigma_\varepsilon) = \prod_{i=1}^k \varphi \left[ \frac{\hat{g}_{\log A}(M, SOFP, \theta)}{\sigma_{\varepsilon_{\log A}}} \right] \quad (2-21)$$

where  $\varphi[\cdot]$  is the standard normal probability density function. Note that the above is a function of the unknown parameters. The final form of the model takes the form:

$$\log A = \theta_1 + \theta_2 M + \theta_3 SOFP \quad (2-22)$$

where  $\sigma_\varepsilon$  is defined as  $\sigma_\varepsilon = \theta_4 + \theta_5 M$

**Table 2.4-1. Summary of model coefficients and performances of limit state functions tested for independent log-rupture area prediction**

Trial #	Model Coefficients					Remarks	$\Sigma_{lh}$
	$\theta_1$	$\theta_2$	$\theta_3$	$\theta_4$	$\theta_5$		
1	-3.041	0.843	-	0.212	-	Homoscedastic sigma model with no SOFP	25.25
2	-3.024	0.848	-0.090	0.211	-	Homoscedastic sigma model with SOFP	26.59
3	-2.998	0.843	-0.073	0.597	-0.059	Heteroscedastic sigma model with SOFP	31.66
4	-4.018	1	-0.134	0.410	-0.027	Model 3 with slope ( $\theta_2$ ) fixed to unity	8.14

Table 2.4-1 also summarizes parameter coefficients and corresponding values of maximum likelihood functions for 4 trial models. Noting that smaller  $\sigma$ , and higher likelihood value ( $\Sigma_{lh}$ ) are the indications of a superior model, hence Trial #3 produces the best predictions for independent log-rupture area models. Proposed median log-rupture area relationship (Trial #3) along with  $\pm 1$  standard deviation boundaries are presented schematically in Figure 2.4-1; superposed on compiled data pairs. Figure 2.4-1 denotes predictions for typical strike-slip faulting; SOFP fixed at 0.5. Sensitivity of the predictions with respect to variation in faulting style is presented in Figure 2.4-2. Although plotting in log-scale partly covers the significance of faulting style parameter, a careful interpretation reveals that normal faults produce approximately 18% larger rupture areas than fully reverse faults for a given moment magnitude. On the contrary, WC94 estimates a completely different pattern:

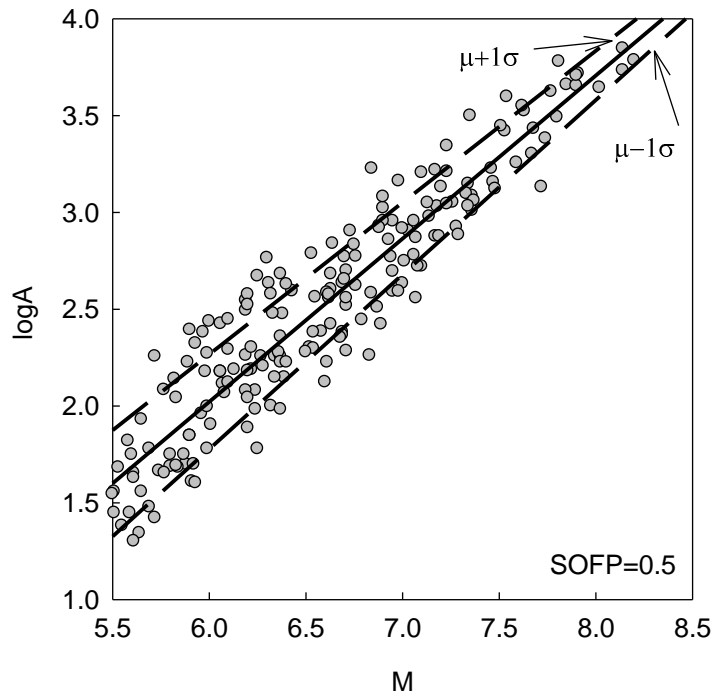


**Figure 2.4-1. Proposed relationship for independent log-rupture area**

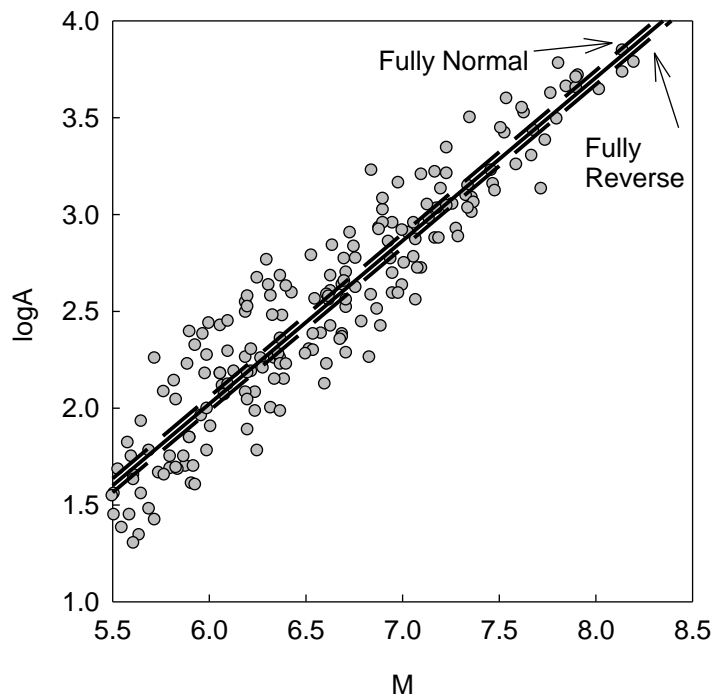


**Figure 2.4-2. Median log-area predictions for different faulting styles**

A glance at WC94 magnitude-log rupture area relationships reveals that for a moderate magnitude value of  $M=5.5$ , rupture area for a normal faulting is approximately 73% larger than that for a reverse event. At a higher magnitude of  $M=7.0$ , difference becomes non-existent. This brings the question of whether the significant variation with respect to magnitude and style of faulting in WC94 relationships is a consequence of the rupture mechanism itself; or a possible bias caused by running separate regressions for different faulting styles having uneven sample sizes. Thorough discussion of WC94 models, focusing on binning style of faulting has been made by Yunatçı and Cetin (2009), and will not be repeated here.

Residuals for the current independent, log-linear rupture area model exhibits an unbiased trend for  $A$  greater than  $10^{1.75}$  km<sup>2</sup>. However, for smaller events ( $A < 10^{1.75}$  km<sup>2</sup>), proposed relationship is judged to be conservatively biased (Figure 2.4-3). Figures 2.4-4 through 2.4-6 present normalized residual plots against dip angle, magnitude and style of faulting parameter, respectively.

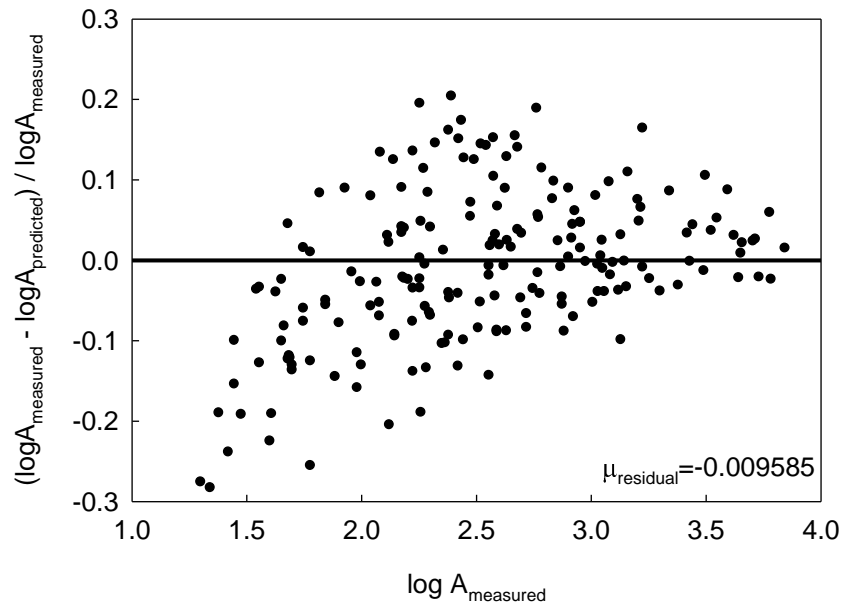


**Figure 2.4-3. Normalized residuals vs. measured log-rupture area**

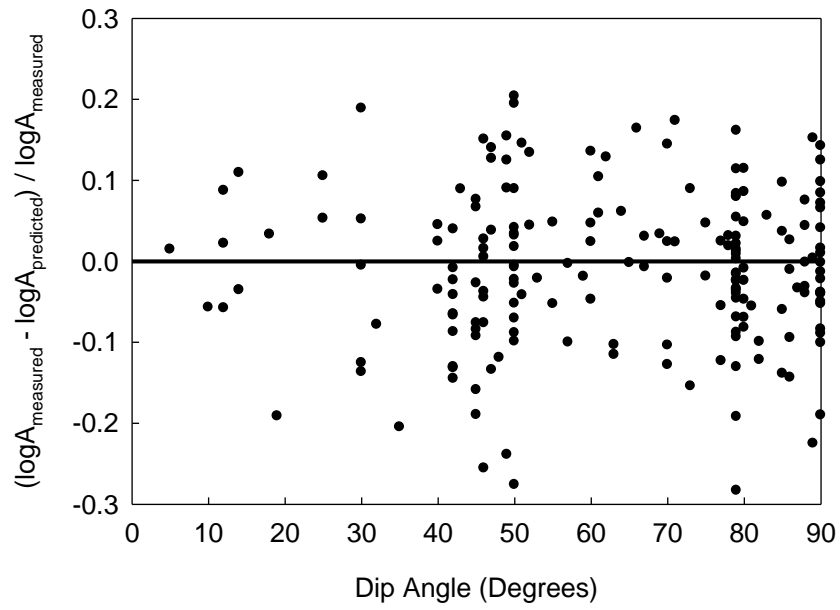


**Figure 2.4-4. Normalized residuals vs. dip angle**

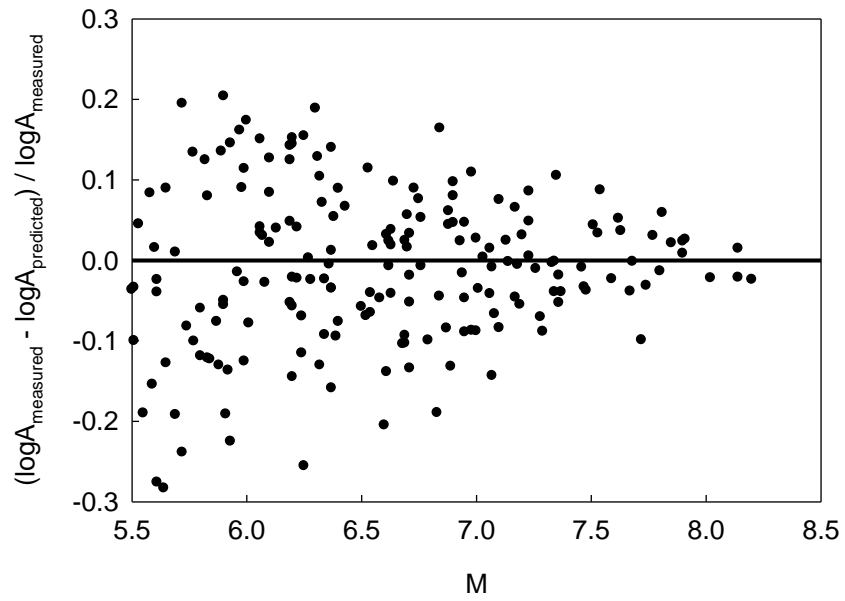


**Figure 2.4-5. Normalized residuals vs. moment magnitude**



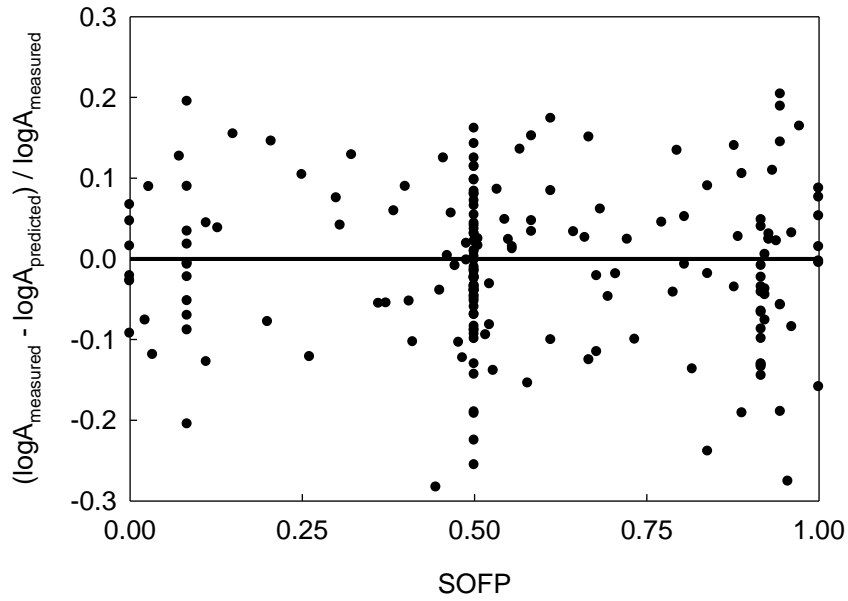


**Figure 2.4-6. Normalized residuals vs. style of faulting parameter**

*2.4.1.2 Independent Model for Rupture Length*

Mathematical framework for magnitude – log rupture length relationships follows the same procedure as the log-area model discussed in the preceding section. The limit state function for predicting rupture length takes the form:

$$g(M, SOFP, \Theta) = \log RL_{\text{measured}} - (\theta_1 + \theta_2 M + \theta_3 SOFP) \mp \varepsilon_{\log RL} \quad (2-22)$$

where

$$\sigma_{\varepsilon} = \theta_4 \quad (2-23)$$

Model coefficients for the two trials yielding the best likelihood estimates are presented in Table 2.4-2. Trial #2 is chosen as the independent log-rupture length model. Proposed median log-rupture length relationship (Trial #2) along with  $\pm 1$  standard deviation boundaries are presented schematically in Figure 2.4-7; superposed on compiled data pairs. Figure 2.4-7 denotes predictions for typical

strike-slip faulting; SOFP fixed at 0.5. Sensitivity of the predictions with respect to variation in faulting style is presented in Figure 2.4-8.

**Table 2.4-2. Summary of model coefficients and performances of limit state functions tested for independent log-rupture length prediction**

Trial #	Model Coefficients				Remarks	$\Sigma_{lh}$
	$\theta_1$	$\theta_2$	$\theta_3$	$\theta_4$		
1	-2.603	0.612	-	0.172	Homoscedastic sigma model with no SOFP	65.708
2	-2.580	0.619	-0.123	0.169	Homoscedastic sigma model with SOFP	69.514

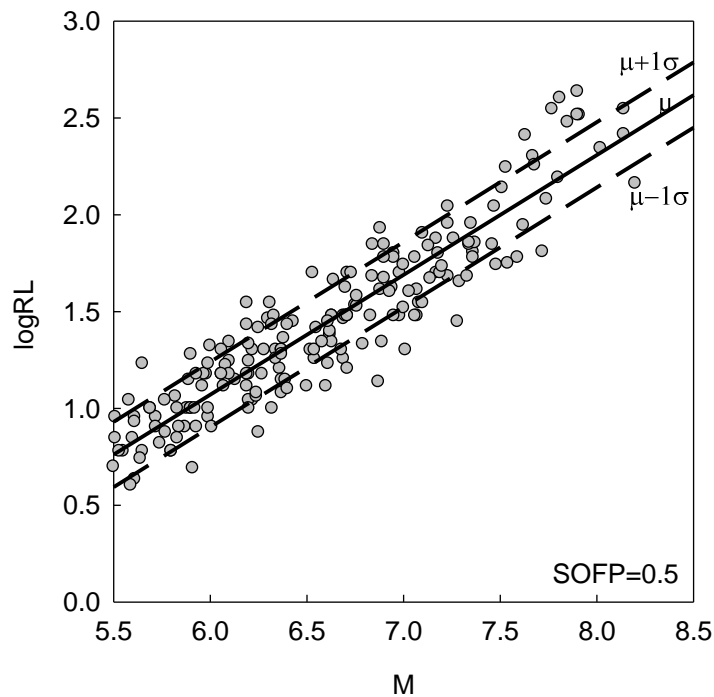


**Figure 2.4-7. Proposed relationship for independent log-rupture length**

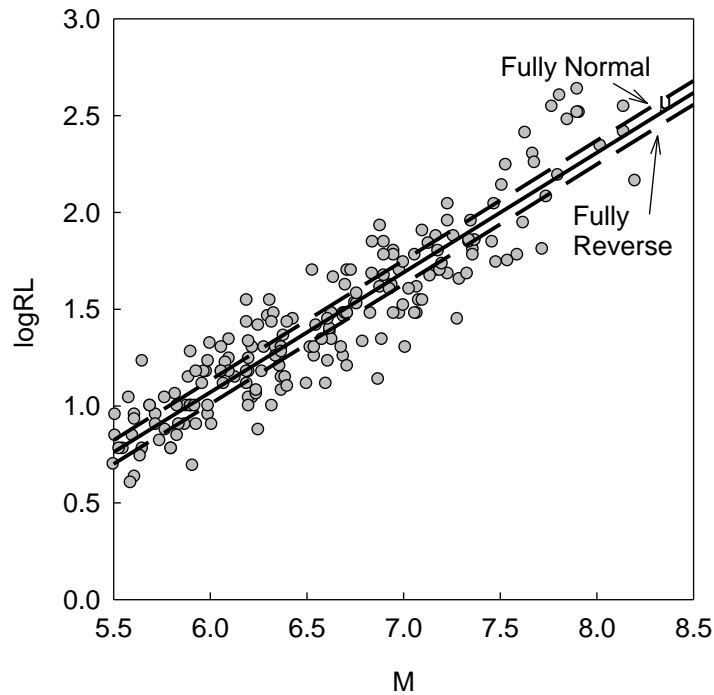


**Figure 2.4-8. Median log-rupture length predictions for different faulting styles**

Interpretation on effects of faulting style reveals that, normal faults produce approximately 33% larger rupture lengths than fully reverse faults for a given moment magnitude, in this model.

Examination of residuals for the current independent, log-linear rupture length model exhibits a slight over prediction at small rupture length range; as well as under prediction at high rupture lengths (Figure 2.4-9). Figures 2.4-10 through 2.4-12 present normalized residual plots against dip angle, magnitude and style of faulting parameter, respectively. These figures suggest an unbiased model with an absolute average normalized residual of 0.0104.

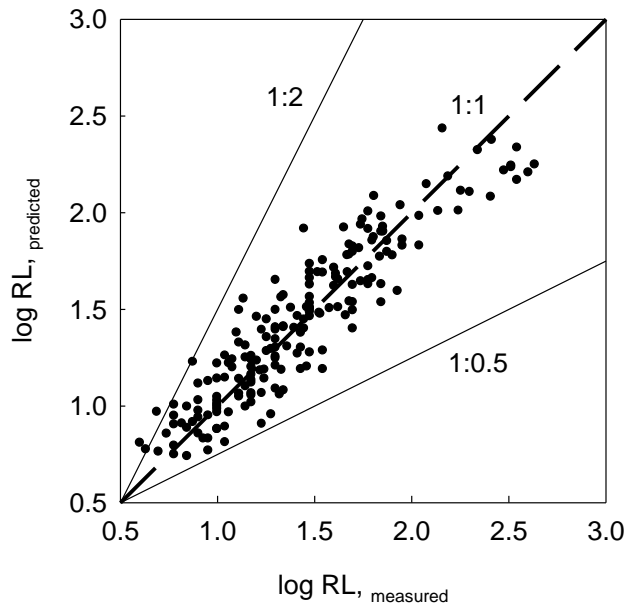


**Figure 2.4-9. Measured vs. predicted comparison for rupture length model**

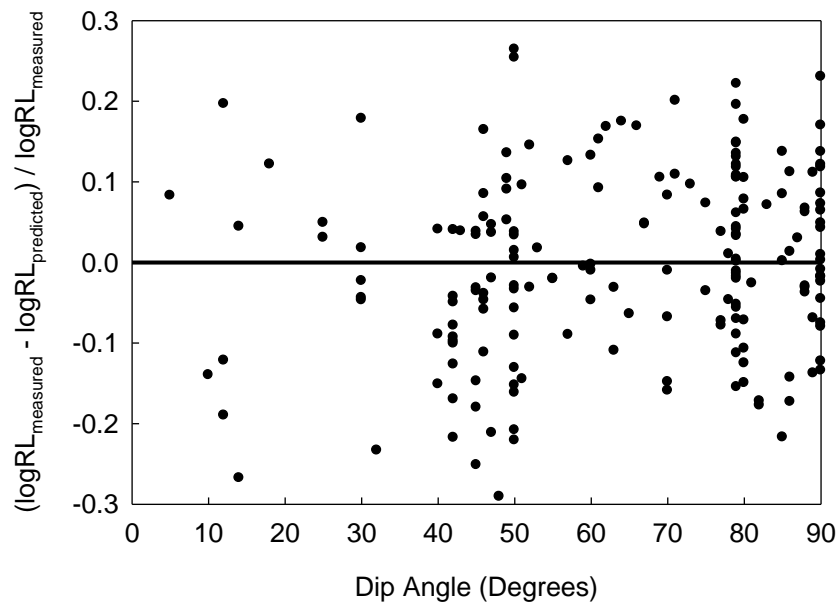


**Figure 2.4-10. Normalized residuals vs. dip angle (rupture length model)**

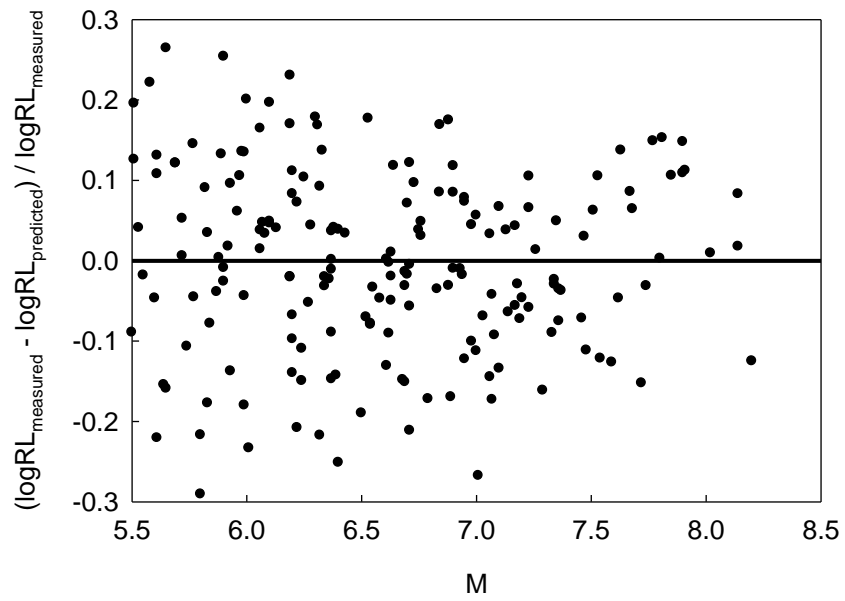


Figure 2.4-11. Normalized residuals vs. magnitude (rupture length model)

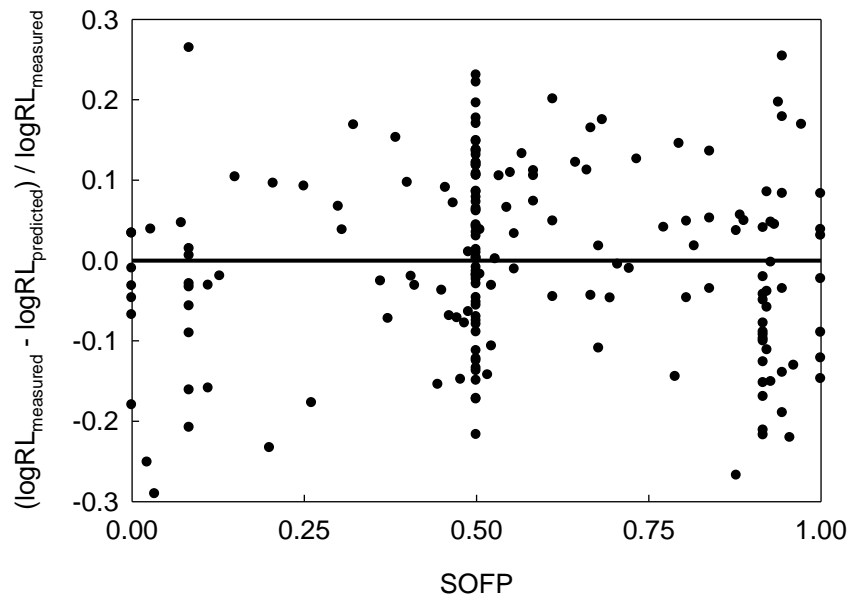


Figure 2.4-12. Normalized residuals vs. style of faulting (rupture length model)

### 2.4.1.3 Independent Model for Rupture Width

Final model for independent likelihood estimates of rupture dimensions is the rupture width. In the rupture width model, observed data indicates that, utilization of a log-linear functional form may not be sufficient in capturing the saturation trend at higher magnitudes (Figure 2.4-13). Hence, a higher order magnitude term was added as Trial #2 during parameter estimation. Results of Trial #1 are tabulated for comparison; with the chosen functional form as presented in Trial #2 in Table 2.4-3. Limit state function is given in Equations 2-24 and 2-25.

$$g(M, \Theta) = \log RW_{\text{measured}} - (\theta_1 + \theta_2 M + \theta_3 M^2 + \theta_4 M^3) \mp \varepsilon_{\log RW} \quad (2-24)$$

$$\sigma_\varepsilon = \theta_5 \quad (2-25)$$

**Table 2.4-3. Summary of model coefficients and performances of limit state functions tested for independent log-rupture width prediction**

Trial #	Model Coefficients					Remarks	$\Sigma_{lh}$
	$\theta_1$	$\theta_2$	$\theta_3$	$\theta_4$	$\theta_5$		
1	-0.476	0.237	-	-	0.154	Log-linear model	86.361
2	-11.425	4.461	-0.523	0.021	0.146	3 <sup>rd</sup> order polynomial model	96.920

Proposed median log-rupture width relationship (Trial #2) along with  $\pm 1$  standard deviation boundaries are presented schematically in Figure 2.4-13; superposed on compiled data pairs. Similar to the case in rupture dimension relationships presented in previous sections, examination of residuals for the current independent, log-linear rupture width model exhibits over prediction at small rupture length range; as well as under prediction at high rupture lengths (Figure 2.4-14).

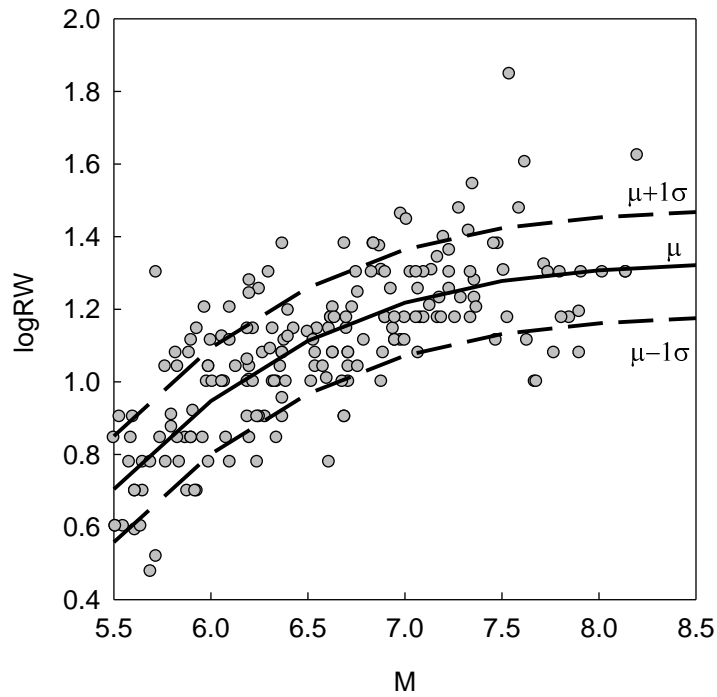


**Figure 2.4-13. Proposed relationship for independent log-rupture width**

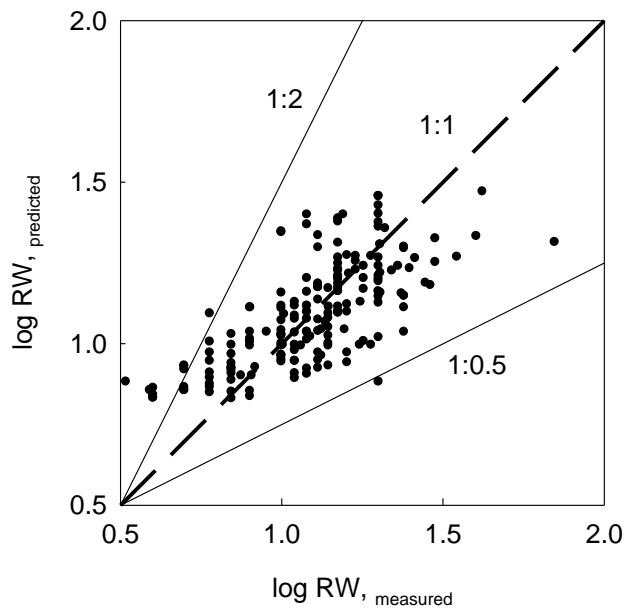


**Figure 2.4-14. Measured vs. predicted comparison for rupture width model**

Figure 2.4-15 presents normalized residual plots against dip angle. Trend in residuals against dip angle is more pronounceable in the proposed model. The case is

unsurprisingly similar for the plot of residuals against style of faulting (excluded from this text), a parameter closely correlated with dip angle. Alternative limit state functions incorporating dip angle or style of faulting parameter were used in trial likelihood estimates, and the outcome was worse than the proposed models in terms of statistical values.

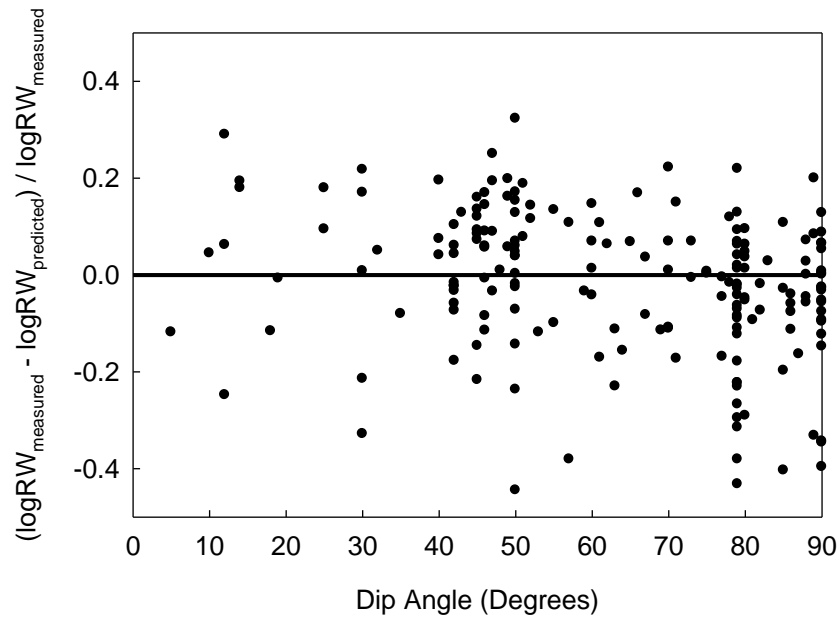


**Figure 2.4-15. Normalized residuals vs. dip angle (rupture width model)**

### 2.4.2 Conditional Models of A, RW and RL

Referring to Table 2.2-2 which demonstrates the geometrical incompatibility between model predictions of rupture dimensions, a similar comparison can be made for the results of independently optimized models in Section 2.4.1. Table 2.4-4 summarizes the comparison of products of rupture length and rupture model predictions against rupture area predictions for three magnitudes; for a SOFP of 0.5. Unlike the 9% difference in a typical WC94 relationship, ratio between the median estimates rises up to 53%. The drastic increase in geometric incompatibility among models is mainly attributed to the functional form chosen for the rupture width. Given the selection of log-linear rupture width model that yields a lower value of



likelihood estimate, instead of power function; the ratio between the two alternative rupture area predictions would fall to 3%.

**Table 2.4-4. Illustration of geometric incompatibility in independent model predictions**

Magnitude	SOFP	RL (km)	RW (km)	RLxRW (km <sup>2</sup> )	A (km <sup>2</sup> )	RLxRW/A
M 5.5	0.5	5.8	6.1	35	40	0.88
M 6.5	0.5	24.1	17.5	422	279	1.51
M 7.5	0.5	100	29.7	2970	1941	1.53

Overlooking the discussion of whether the shift in compatible estimates carries any engineering significance, an attempt was made to obtain a model automatically satisfying geometrical compatibility. Considering the fact that measured rupture dimensions were reported such that the basic rectangular rupture criterion is met, and the calculated average fault displacement as well as moment magnitude satisfies Equation 2-1; the likelihood function was modified to maximize the probabilities of occurrences of rupture area and rupture area dependent rupture width limit state functions simultaneously.

Equation 2-26 presents the limit state function for log- rupture area. Equations 2-28 and 2-29 present limit state functions for the two trial alternatives of the functional form of the rupture width model; one being either a lower or higher order polynomial; and the proceeding form representing the power curve.

$$g_{\log A}(M, SOFP, \Theta) = \log A_{\text{measured}} - (\theta_{1,A} + \theta_{2,A}M + \theta_{3,A}SOFP) \mp \varepsilon_{\log A} \quad (2-26)$$

where

$$\sigma_{\varepsilon, \log A} = \theta_{4,A} + \theta_{5,A}M \quad (2-27)$$

$$g_{\log RW}(M, \Theta) = \log RW_{\text{reference}} - (\theta_{1,RW} + \theta_{2,RW}M + \theta_{3,RW}M^2 + \theta_{4,RW}M^3) \mp \varepsilon_{\log RW, RL|A} \quad (2-28)$$

and

$$g_{\log RW}(M, \Theta) = \log RW_{\text{reference}} - \left( \frac{M + \theta_{1,RW}}{\theta_{2,RW} + \theta_{3,RW}M} \right) \mp \varepsilon_{\log RW, RL|A} \quad (2-29)$$

where

$$\sigma_{\varepsilon, \log RW, RL|A} = \theta_{5,RW} \quad (2-30)$$

Note that the error term in both limit state functions for rupture width are conditioned on rupture area prediction. Notation used in error terms also imply the conditional error of rupture width and rupture length combined. Since the basic relation stated in Equation 2-11 holds true, imposing a third condition on rupture length would be redundant. The key point in Equations 2-28 and 2-29 is the purpose of minimization of the error between the rupture width model predictions, using a “reference” value of  $\log RW$ ; instead of the directly measured (or calculated from other parameters) values in the dataset; as in the case of independent models. The values of  $\log RW_{\text{reference}}$  are calculated using the predicted values of the rupture area model; optimized simultaneously with the rupture width model. The expression  $\log RW_{\text{reference}}$  is calculated using the basic relationship between stress drop and other source parameters for rectangular rupture geometry:

$$\log RW_{\text{reference}} = \frac{2M_0}{\pi \cdot A_{\text{predicted}} \cdot \Delta\sigma} \quad (2-31)$$

where  $M_0$  is the seismic moment compatible with the final selection of moment magnitude  $M$  in the dataset,  $A_{\text{predicted}}$  is the predicted rupture area using the limit state function in Equation 2-26, and  $\Delta\sigma$  is the average static stress drop. Reversing Equation 2-31, average static stress drop is inferred using the measured or calculated values of average fault displacement, measured rupture width, and shear modulus.

$$\Delta\sigma = \frac{2 \cdot \mu \cdot \bar{D}}{\pi RW_{\text{measured}}} \quad (2-32)$$

As long as there are inevitable dependent measurements or calculations of source parameters in published literature compiled from various sources using different techniques, the above expression holds true as the optimum solution to the compatibility problem; if such framework is preferred. The next step in building the framework is the expression of the likelihood function to maximize the probabilities of occurrences of products of limit state functions. Equation 2-33 is the likelihood expression for the problem, and Equation 2-34 represents the same expression in the form of standard normal probability density function. Last, but not the least; probability density function for the conditional rupture width model was truncated at down-dip widths corresponding to 30 km depth from surface (conforming to the approximate crustal thickness in the tectonic environments studied), using the dip angle for each observation.

$$L_{\log A, \log RW | \log A}(\theta, \sigma_\varepsilon) = \prod_{i=1}^k P[g_{\log A, i}(\cdot) g_{\log RW, i}(\cdot) = 0] \quad (2-33)$$

$$L_{\log A, \log RW | A} = \prod_{i=1}^k \varphi \left[ \frac{\hat{g}_{\log A}(M, SOFP, \theta_A)}{\sigma_{\varepsilon_{\log A}}} \right] \cdot \varphi \left[ \frac{\hat{g}_{\log RW}(M, \theta_{RW})}{\sigma_{\varepsilon_{\log RW, RL | RA}}} \right] \quad (2-34)$$

Among numerous candidate models, 6 of them were chosen to be represented for the conditional rupture dimension results. Table 2.4-5 condenses the results for rupture area models. Tables 2.4-6 and 2.4-7 summarize the model coefficients and likelihood values for conditional rupture width models; grouped by the form of the functional

form used. Table 2.4-6 represents the models which Equation 2-28 was used as the limit state function, whereas Table 2.4-7 is prepared for models having Equation 2-29 as their limit state function. Trial #6 was chosen to be the most appropriate model among the candidates. Evaluation of results indicates that there is a minor adjustment to the coefficients of the rupture area model. Effect of conditioning is relatively more pronounced in rupture width models, when Trial #2 in independent rupture width model and Trial #3 in Table 2.4-6 are compared.

**Table 2.4-5. Summary of model coefficients and performances of limit state functions tested for conditional rupture area prediction**

Trial #	Model Coefficients for logA					Remarks	$\Sigma_{lh}$
	$\theta_{1,A}$	$\theta_{2,A}$	$\theta_{3,A}$	$\theta_{4,A}$	$\theta_{5,A}$		
1	-2.973	0.826	-	0.221	-	linear model on logA	10.507
2	-3.128	0.850	-	0.599	-0.058	Heteroscedastic sigma on logA	15.019
3	-2.969	0.825	-	0.221	-	3 <sup>rd</sup> order polynomial in logRW	14.094
4	-2.976	0.826	-	0.221	-	Power function on logRW	14.925
5	-3.133	0.851	-	0.599	-0.058	Power function on log RW	19.431
6	-3.119	0.852	-0.039	0.590	-0.057	SOFP in logA	19.744

**Table 2.4-6. Summary of model coefficients and performances of limit state functions tested for conditional rupture width prediction (polynomial models)**

Trial #	Model Coefficients for conditional logRW					$\Sigma_{lh}$
	$\theta_{1,RW A}$	$\theta_{2,RW A}$	$\theta_{3,RW A}$	$\theta_{4,RW A}$	$\theta_{5,RW A}$	
1	-0.582	0.261	-	-	0.349	10.507
2	-0.427	0.236	-	-	0.351	15.019
3	-12.848	4.894	-0.557	0.0021	0.341	14.094

**Table 2.4-7. Summary of model coefficients and performances of limit state functions tested for conditional rupture width prediction (power models)**

Trial #	Model Coefficients for conditional logRW				$\Sigma_{lh}$
	$\theta_{1,RW A}$	$\theta_{2,RW A}$	$\theta_{3,RW A}$	$\theta_{4,RW A}$	
4	-5.264	-3.095	0.637	0.340	14.925
5	-5.283	-3.306	0.668	0.341	19.431
6	-5.281	-3.296	0.667	0.341	19.744

Proposed median log-rupture area relationship for the joint probability model along with  $\pm 1$  standard deviation boundaries are presented schematically in Figure 2.4-16; superposed on compiled data pairs. Median line and standard deviation boundaries are plotted for a typical style of faulting parameter of 0.5. Similarly, Figure 2.4-17 presents the proposed relationship for conditional log-rupture width model. Note that  $\pm 1$  standard deviation boundaries cover the aleatory variability of log-rupture length and width combined. Encapsulate all the observation points for originally reported rupture width values by the sigma boundaries shall not be misleading.

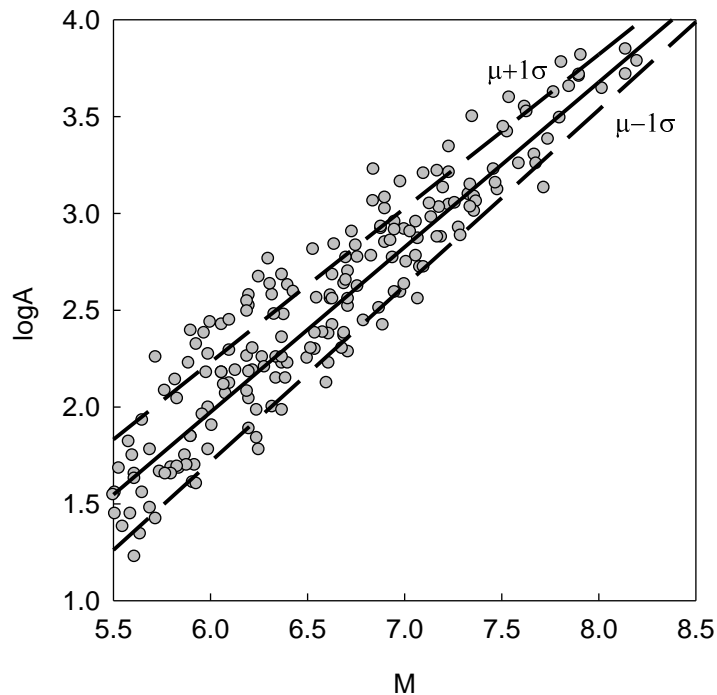


**Figure 2.4-16. Proposed relationship for conditional log-rupture area model**

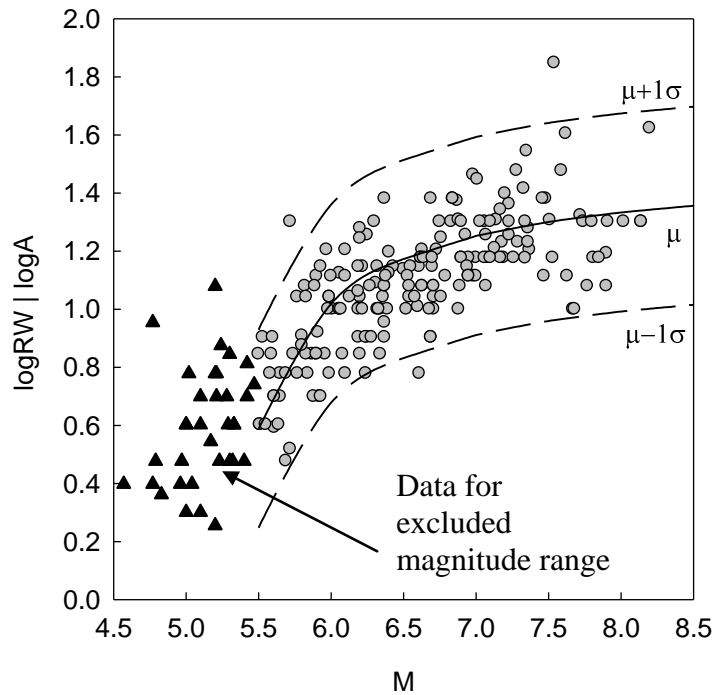


**Figure 2.4-17. Proposed relationship for conditional log-rupture width model**

Also shown in Figure 2.4-17 is the exempted subset of rupture width data having moment magnitude values less than  $M=5.5$ . The relevant plot gives obvious evidence on the implied unconservatism if the proposed curve is intended to be used for magnitudes less than  $M=5.5$ , through extrapolation. Once  $\log A$  and  $\log RW$  models are obtained,  $\log RL$  model can be automatically calculated using difference between two predictions. Assuming that median values of  $\log A$  and  $\log RW|A$  are present in a scenario, corresponding  $\log RL$  estimate is shown in Figure 2.4-18.

Comparison of measured values and model predictions for rupture width and rupture area models are given in Figures 2.4-19 and 2.4-20 respectively. Normalized residual plot as a function of SOFP indicates an unbiased model with respect to style of faulting (Figure 2.4-21).

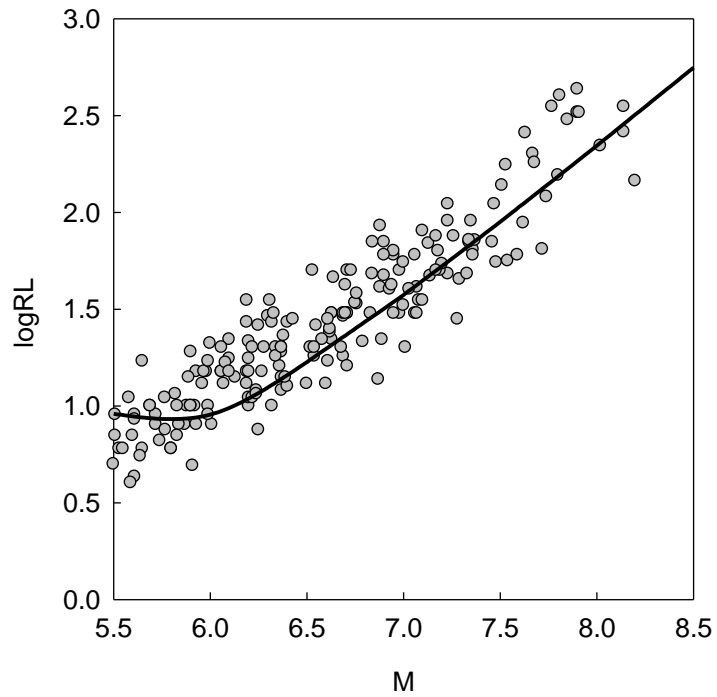


**Figure 2.4-18. Variation of  $\log RL$  with respect to median estimates of  $\log A$  and  $\log RW|A$**

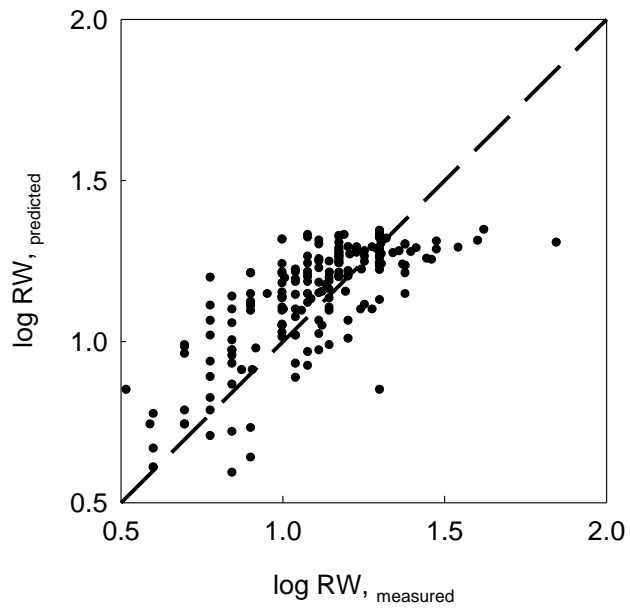


**Figure 2.4-19. Measured vs. predicted values of conditional  $\log RW$**

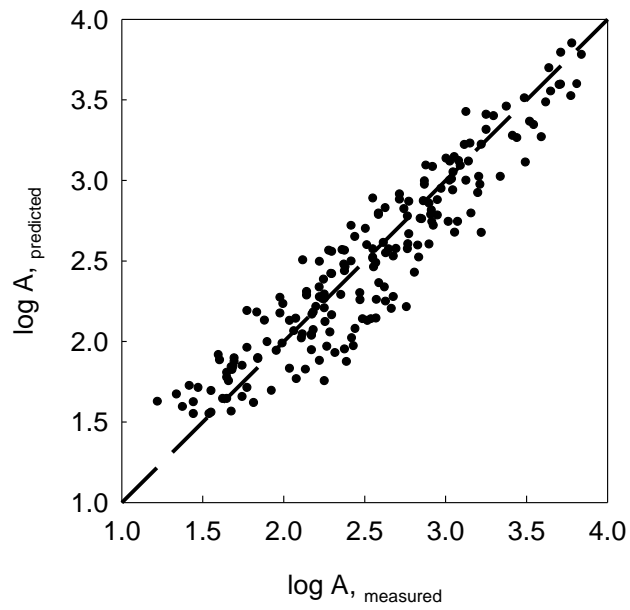


**Figure 2.4-20. Measured vs. predicted values of conditional logA**

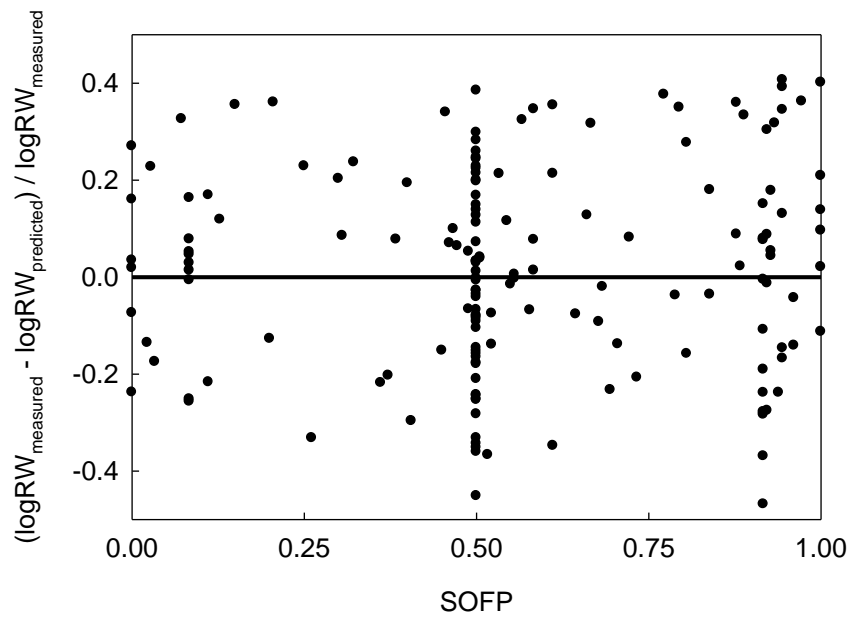


**Figure 2.4-21. Normalized residuals of conditional rupture width model against SOFP**



### 2.4.3 Bilinear logA and Aspect Ratio Models

The third and last approach in magnitude – rupture dimension scaling is the utilization of bilinear rupture area model accompanied by a bilinear aspect ratio model in which the breakpoint magnitudes are defined as a function of dip angle of the fault. Based on the results of the independent optimization and a more complex procedure utilizing joint probability, this approach is mainly motivated by the following facts:

- i) Rupture width of large magnitude earthquakes at active crustal regions are restricted by the thickness of the crust. Compiled event database suggests that the L-model is valid at large magnitudes. Direct impact of the rupture geometry pattern which is compatible with the L-model can be tracked from the magnitude – rupture area data, as well as aspect ratio observations.
- ii) For the rupture area model, recent studies such as Hanks and Bakun (2002, 2008) have implemented bilinear models. On the contrary, Stein (2008) has preferred to model the transition between the constant stress drop and L-models using a power curve; capturing the smoothness. This study implements bilinear model using an optimization search for the breakpoint.
- iii) Rupture width models presented in the previous sections lacked a direct implementation of dip angle of the fault. An indirect implementation attempt was made to use SOFP, which is a correlated parameter with dip angle. However results have yielded the SOFP supported models used for rupture width estimation as insignificant, from statistical point of view.

Limit state function for the proposed bilinear rupture area model is as follows:

$$g_{\log A}(M, \Theta) = \log A_{\text{measured}} - \begin{cases} \theta_1 + \theta_2 M; & M \leq M_b \\ \theta_3 + \theta_4 (M - M_b); & M > M_b \end{cases} \mp \varepsilon_{\log A} \quad (2-35)$$

$$\varepsilon_{\log A} = \theta_5 \quad (2-36)$$

Also keep in mind that,  $\theta_3$  is a function of  $\theta_1$ ,  $\theta_2$ , and  $M_b$  in order to preserve continuity of the function:

$$\theta_3 = \theta_1 + \theta_2 M_b \quad (2-37)$$

Visual examination of the magnitude breakpoint symbolizing transition from constant stress drop model to L-model revealed that a value in the range of  $M=6.5$  to  $M=6.7$  assigned to  $M_b$  would be a reasonable starting point. Independent likelihood estimates on a subset of the current database in the magnitude range of  $M=5.5$  –  $M=6.7$  revealed that the slope, namely  $\theta_2$  was 0.87 for a breakpoint of 6.7, and this value converged to unity for breakpoint magnitude of 6.5. Sensitivity analysis has proven that fixing  $\theta_2=1$  would be a reasonable choice; both considering the fact that the overall optimization and the  $M_b$  value are determined using the whole dataset covering  $M=5.5$  –  $M=8.2$  ranges, and the theoretical discussion made in Section 2.1. A similar sensitivity analysis has been conducted for the second portion of Equation 2-35, and the slope modeled by the  $\theta_4$  coefficient was fixed to 0.75; supporting Hanks and Bakun (2002) model at its fullest. Model coefficients for the bilinear rupture area model are presented in Table 2.4-8. Median estimate and  $\pm 1$  sigma boundary curves are presented in Figure 2.4-22. Comparison of measured values and model predictions, along with 1:1 line is presented in Figure 2.4-23.

**Table 2.4-8. Summary of model coefficients and performances of limit state function tested for bilinear rupture area prediction**

Trial #	Model Coefficients					Remarks	$\Sigma_{lh}$
	$\theta_1$	$\theta_2$	$\theta_3$	$\theta_4$	$\theta_5$		
1	-4.018	1	2.682	0.75	0.219	$M_b = 6.7$	19.508

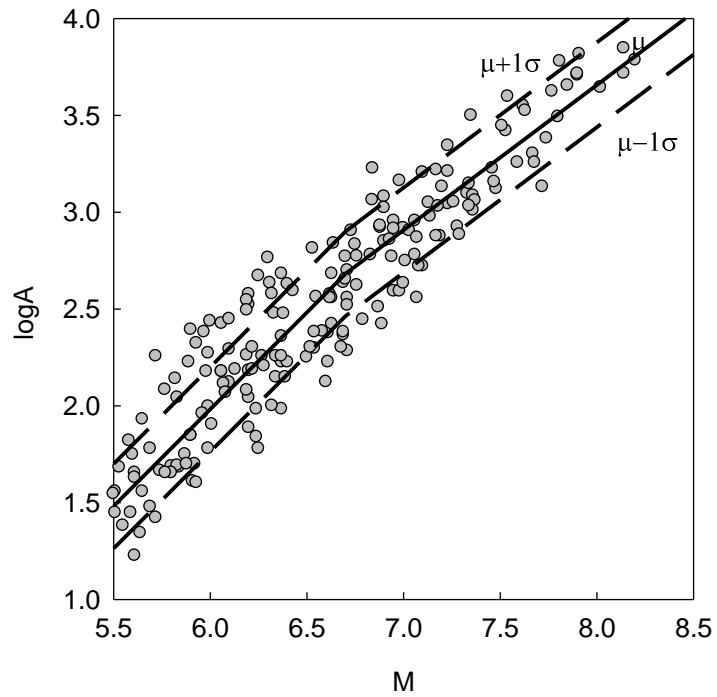


**Figure 2.4-22. Bilinear rupture area model**

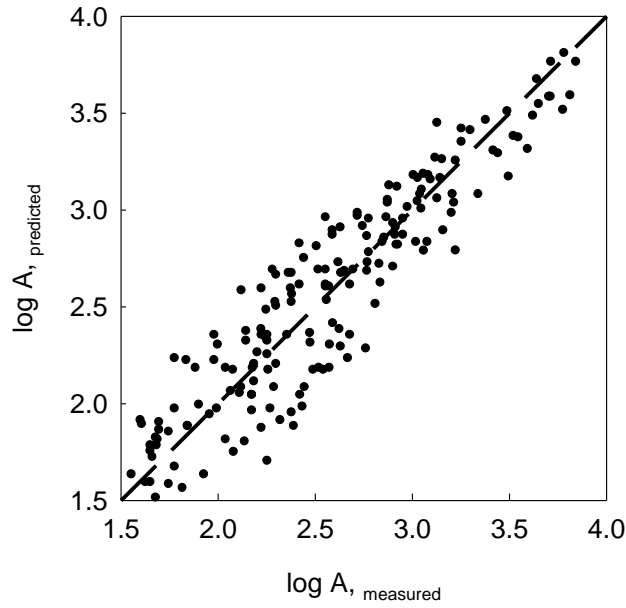


**Figure 2.4-23. Measured vs. predicted values in bilinear rupture area model**

Limit state functions for the proposed log-aspect ratio model is as follows:

$$g_{logAR}(M, \delta, \theta) = \log AR_{measured} - \begin{cases} \theta_1 + \theta_2(M - M_b); & M < M_1(\delta) \\ \theta_1 + \theta_2[M_1(\delta) - M_b] + \theta_3[M - M_1(\delta)]; & M \geq M_1(\delta) \end{cases} \mp \varepsilon_{logAR} \quad (2-38)$$

$$\varepsilon_{logAR} = \theta_4 \quad (2-39)$$

where

$$M_1(\delta) = \frac{-2\log(\sin\delta)}{\theta_3 - \theta_2} + M_b \quad (2-40)$$

In Equations 2-38 - 2-40,  $M_b$  was finally fixed at  $M=6.7$ . Optimization of  $M_1(\delta)$  was made using an iterative procedure. Slope of the log-aspect ratio model in the L-model range, namely model coefficient  $\theta_3$  was fixed at 0.75. Results of the likelihood estimate are presented in Table 2.4-9. Figure 2.4-24 summarizes the aspect ratio

model result; where the median estimates for various dip angles are plotted against magnitude. Notice how optimization has yielded different magnitude breakpoints for a range of dip angles switching to the L-model. Comparison of measured values and model predictions for the aspect ratio model is presented in Figure 2.4-25. Additional analysis has revealed that the correlation coefficient (0.177) between the residuals of aspect ratio and area models indicates loose correlation.

**Table 2.4-9. Summary of model coefficients and performances of limit state function tested for bilinear aspect ratio prediction**

Trial #	Model Coefficients				Remarks	$\Sigma_{lh}$
	$\theta_1$	$\theta_2$	$\theta_3$	$\theta_4$		
1	0.2604	0.2033	0.75	0.219	$M_b = 6.7$	14.183

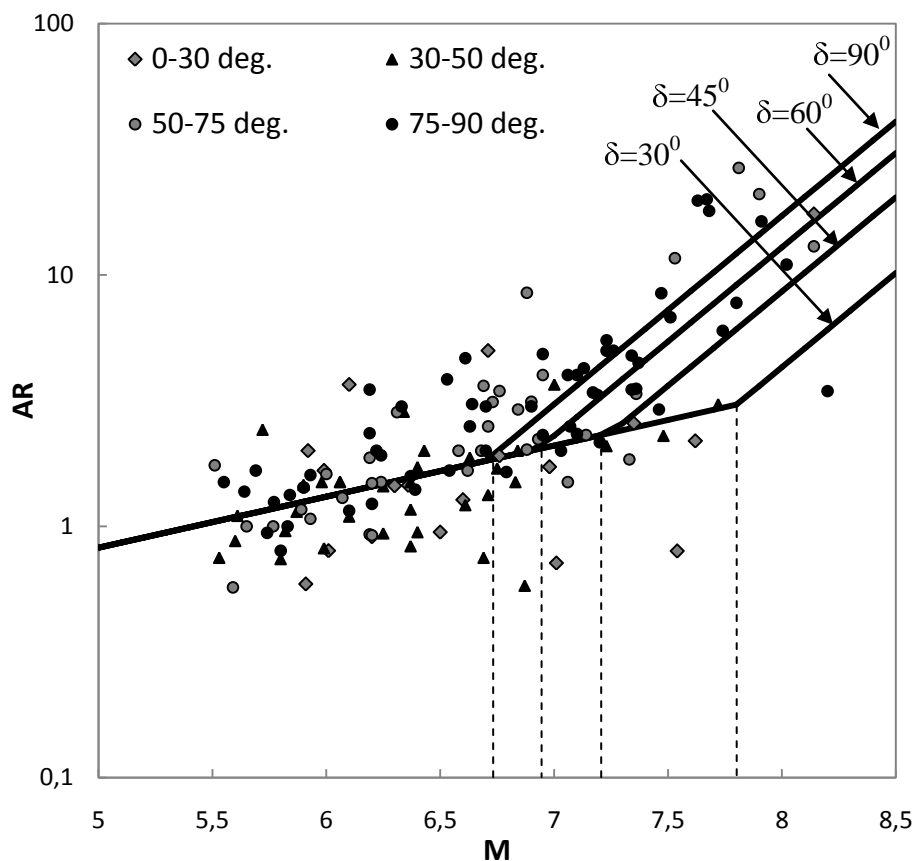


**Figure 2.4-24. Measured vs. predicted values in rupture area model**

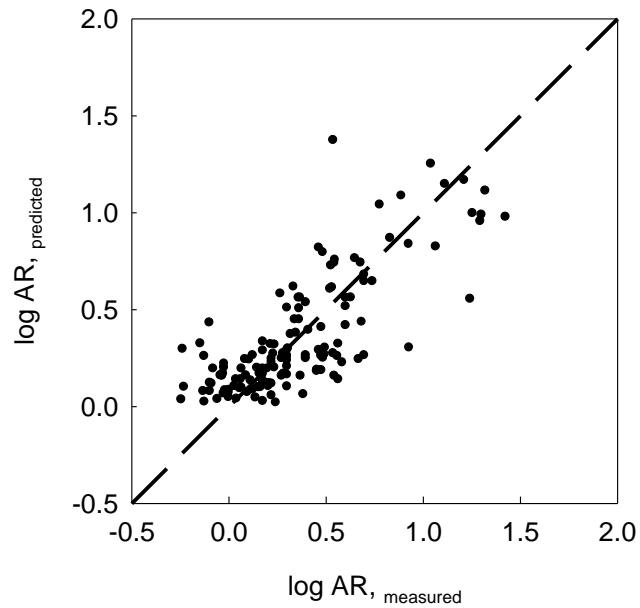


**Figure 2.4-25. Measured vs. predicted values in aspect ratio model**

Recalling Equations 2-11 and 2-17; describing the basic relationships among rupture dimension parameters, relationships for rupture length and rupture width can be calculated directly from the results of bilinear area and aspect ratio models. Rearranging Equations 2-11 and 2-17 by taking the base-10 logarithms of both sides yield:

$$\log A = \log RW + \log RL \quad (2-41)$$

and

$$\log AR = \log RL - \log RW \quad (2-42)$$

Rupture length can be expressed by adding Equations 2-41 and 2-42 and rearranging in the following form:

$$\log RL = \frac{1}{2}(\log A + \log AR) \quad (2-43)$$

Similarly, rupture width is expressed as in Equation 2-44.

$$\log RW = \frac{1}{2}(\log A - \log AR) \quad (2-44)$$

The median values for  $\log RL$  and  $\log RW$  are calculated by simply substituting the median estimates of  $\log A$  and  $\log AR$  into Equations 2.43 and 2-44. This model also preserves the basic geometric compatibility between rupture dimensions for the rectangular rupture assumption. Residuals of the  $\log RL$  and  $\log RW$  models, directly inferred from  $\log A$  and  $\log AR$  models are presented in Figures 2.4-26 and 2.4-27.

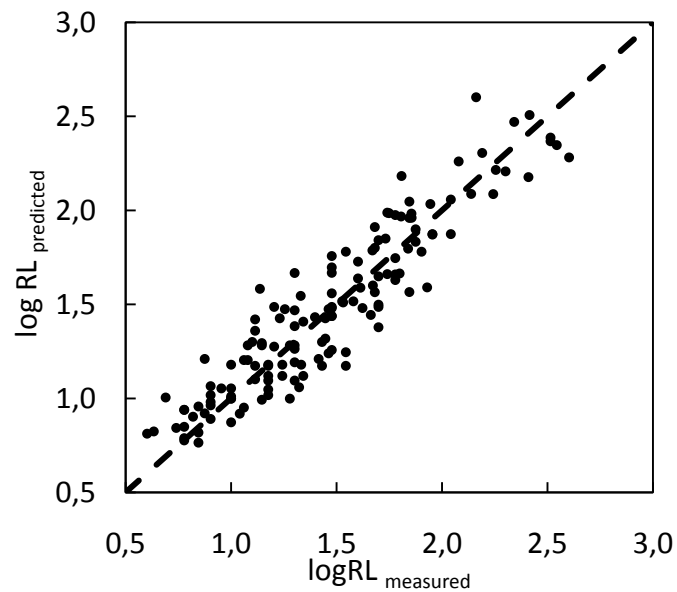


**Figure 2.4-26. Measured vs. predicted values in rupture area model**

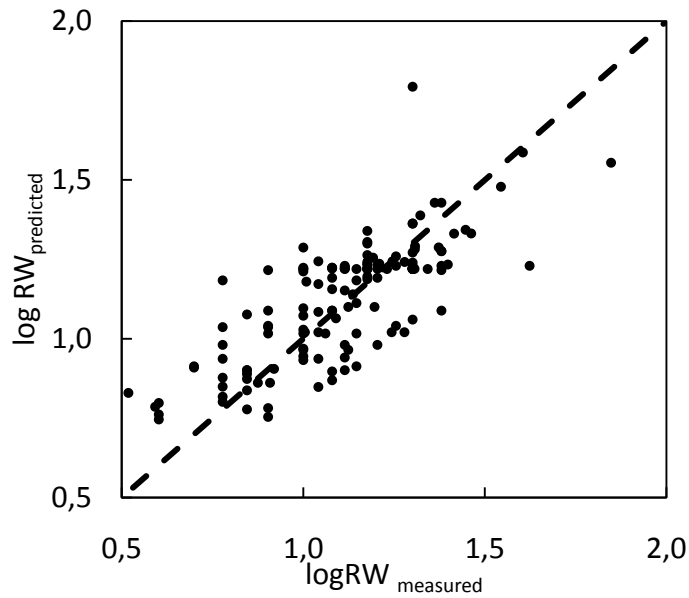


**Figure 2.4-27. Measured vs. predicted values in rupture area model**

The expression for the variance of rupture length and rupture width, in the form of sum of two random variables can be derived using the following method.

$$Var[y] = \sum_{i=1}^n \sum_{j=1}^n \left( \frac{\partial y}{\partial x_i} \cdot \frac{\partial y}{\partial x_j} \right) \cdot \rho_{i,j} \cdot \sigma_i \sigma_j \quad (2-45)$$

In the above expression,  $\frac{\partial y}{\partial x_i}$  stands for the derivative of the function  $y$  with respect to the  $i^{\text{th}}$  random variable  $x$ .  $\sigma_i$  is simply the standard deviation of  $i^{\text{th}}$  random variable, and  $\rho_{i,j}$  is the correlation coefficient between  $x_i$  and  $x_j$ . Assuming that aspect ratio and rupture area ( $x_1$  and  $x_2$ ) are uncorrelated, variance expression for rupture length reduces to the open form as shown in Equation 2-46. Note that the specific case studied herein yields the same expression for the variance of  $logRW$ . This result is different from the non unique variances of models that would have been obtained through independent regression of rupture length and rupture width.



$$Var[\log RL] = \left(\frac{\partial \log RL}{\partial \log A}\right)^2 \cdot \sigma_{\log A}^2 + \left(\frac{\partial \log RL}{\partial \log AR}\right)^2 \cdot \sigma_{\log AR}^2 = \frac{1}{4}(\sigma_{\log A}^2 + \sigma_{\log AR}^2) \quad (2-46)$$

Substitution of standard deviations of bilinear rupture area and dip dependent aspect ratio models yields the following magnitude of variance in the  $\log RL$  and  $\log RW$  expressions

$$Var[\log RL] = Var[\log RW] = \frac{1}{4}(0.2186^2 + 0.2194^2) = 0.02398 \quad (2-47)$$

and

$$\sigma_{\log RL} = \sigma_{\log RW} = \sqrt{0.02398} \cong 0.155 \quad (2-48)$$

## **CHAPTER 3**

### **SEISMIC SOURCE CHARACTERIZATION FOR TURKEY**

#### **3.1 BRIEF SUMMARY OF REGIONAL TECTONICS**

##### **3.1.1 Introduction**

This section provides a brief introduction on the neotectonic features of Turkey; a region undergoing active deformation controlled by collisional convergence, and westward tectonic escape of the Anatolian Block. The major neotectonic structures dominating the dynamic behavior are the dextral (right-lateral) North Anatolian Fault Zone (NAFZ), sinistral (left-lateral) East Anatolian Fault Zone and the Aegean-Cyprean Arc. African-Arabian and Eurasian plates collide over Anatolia, and this interaction governs the westward escape of the Anatolian wedge. All of the faulting styles, namely strike-slip, normal and reverse; as well as associated structures can be observed in this geography. This section will dominantly cover the topics of regional neotectonics in the context which is summarized by Bozkurt (2001), which provides a compact synthesis of the general characteristics of the region.

“Of the three major elements governing the neotectonics of Turkey, South Aegean-Cyprean Arc is a convergent plate boundary where the African Plate to the south is subducting beneath the Anatolian Plate to the north. Dextral North Anatolian Fault

Zone and sinistral East Anatolian Fault Zone complete the deformation mechanism; by moving the Anatolian Plate, a wedge of amalgamated fragments of crust, moves westward away from the collision zone between the Arabian and Eurasian Plates, at a rate of approximately 20 mm/year” (Bozkurt, 2001). Bozkurt (2001) summarizes that this activity is the result of interactions between northward moving African and Arabian Plates, and the relatively stable Eurasian Plate. Point “K” in Figure 3.1-1 is the Karlova junction; where the the two strike slip fault zones meet.

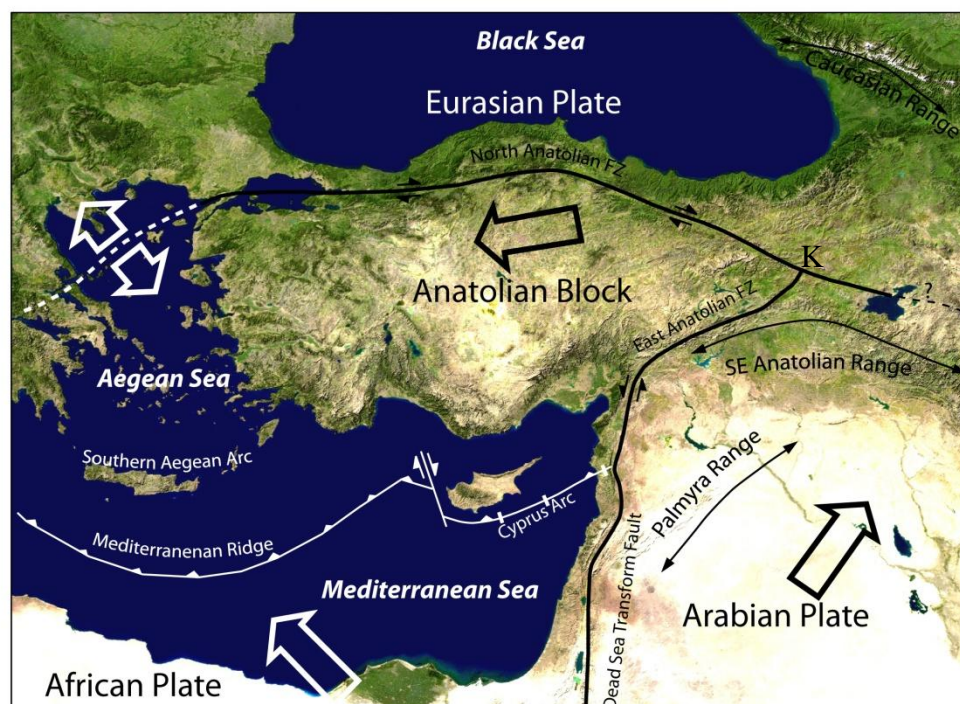


**Figure 3.1-1. Simplified tectonic map of Turkey showing major neotectonic structures (reproduced and modified from Rojay et al., 2001)**

In Figure 3.1-1, bold lines with half arrows are strike slip faults with arrows showing relative movement directions. Bold lines with triangles indicate an active subduction zone; and the tips of the triangles show dipping directions of the subducting slab. Block arrows show the directions of the relative plate movements.

The westward movement of the Anatolian Plate is not purely translational; the velocity vectors have shown that the movement is accompanied by a certain amount of counter clockwise rotational component (Westaway, 1994). Bozkurt (2001) also allows a brief introduction to controversial views on the driving force behind the westward tectonic escape; indicating a possible contribution of slab-fall forces caused by the subduction along south of the Aegean to Mediterranean Ridge.

The scope of this text is beyond the explanation of dynamics in the paleotectonic period in Anatolia and neighboring regions; which gave rise to the active tectonic structures that are in turn, the sources of recent seismicity. Section 3.1.2 presents brief information on the major structures mentioned herein.

### **3.1.2 Major Tectonic Structures**

This section provides a concise summary of major tectonic structures of Anatolia. Basic information on generation mechanisms, style of deformation, presence of splay faults and remarkable records of historical seismicity will be presented for North Anatolian Fault Zone (Zone I in Figure 3.1-2), East Anatolian Fault Zone (Zone II in Figure 3.1-2), Dead Sea Fault Zone (Zone III in Figure 3.1-2), South Aegean Arc (Zone IV in Figure 3.1-2), Cyprean Arc (Zone V in Figure 3.1-2) and Bitlis Suture (Zone VI in Figure 3.1-2), respectively. Although not being totally up to date, active fault map of General Directorate of Mineral Research and Exploration-MTA (Şaroğlu et. al., 1992) serves as a valuable guide for the delineation of active faults (Figure 3.1-2). Figure 3.1-2 is presented for the purpose of enabling easier tracking of the fault zone descriptions.

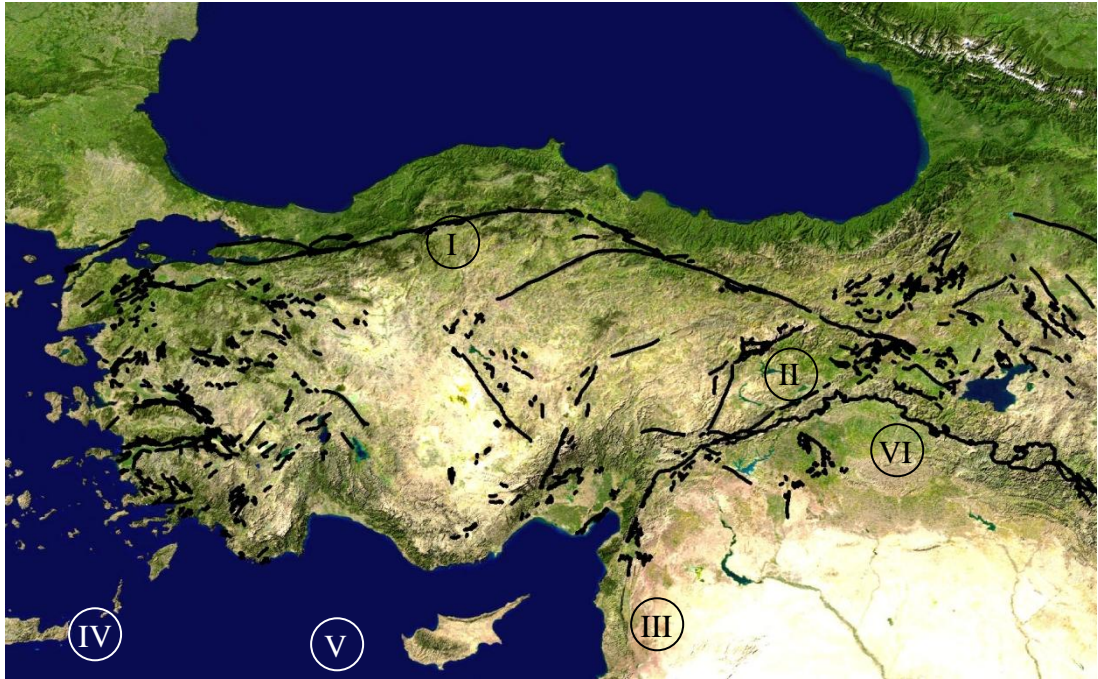


**Figure 3.1-2. Active fault map of Turkey (reproduced from Şaroğlu et. al., 1992)**

### *3.1.2.1 North Anatolian Fault Zone*

The North Anatolian Fault Zone is one of the most well studied tectonic features of the world. It has been the host of numerous destructive earthquakes in Anatolian history. Evidence from written recordings, as compiled by Ambraseys and Finkel (2006) emphasize the ongoing activity, from historical earthquakes that occurred between 1500 and 1800. Although the data gathered from historical earthquakes using methods other than field evidence may be biased in terms of proximity of the event to civilized settlements; there exists no doubt that destructive historical events have affected regions along the North Anatolian Fault Zone. Moreover, collected instrumental data have proven the activity of the fault zone, beginning from 1939 Erzincan earthquake (M=7.9), propagating along west with 1942 Erbaa-Niksar (M=7.1), 1943 Tosya (M=7.6), 1944 Bolu-Gerede (M=7.3), 1957 Abant (M=7), 1967 Mudurnu Valley (M=7.1), 1992 Erzincan (M=6.8), 1999 Kocaeli (M=7.4) and Düzce earthquakes (Bozkurt, 2001).

The North Anatolian Fault Zone extends from Greece in the west to the Karliova triple junction in the east, along a distance of approximately 1500 km (Item “I” in Figure 3.1-2). The transform fault zone forms the boundary between the Eurasian Plate and Anatolian Plate. The surface structure of the fault is easily traceable from morphology, and inhibits the presence of second order splay faults. Within the content of this study, being aware of the fact that slip rates and earthquake activity of the two classifications may differ significantly, secondary seismogenic faults characterized for seismic hazard assessment are defined under the primary segments of the North Anatolian Fault Zone. The zone corresponding to the southeast of Karliova triple junction is not considered to be the termination point of the NAFZ.

Glancing to the western boundary; on the other hand, NAFZ splays into two major branches; the southern branch lies almost parallel to the southern boundary of the Marmara Sea, while the northern branch propagates through the Marmara Sea before bending south and running through the Aegean Sea. Among the controversial proposals on the age of the fault zone, Barka and Cadinsky-Cade (1988) dates NAFZ to approximately 5 million years, which is comparable with the observed total slip on the fault. Bozkurt (2001) summarizes the estimated annual slip rates on the fault using the results from geological studies and GPS velocity measurements. A reasonable present-day value of 15-25 mm/year is found to be acceptable.

Study by Stein et al. (1997) shows that the stress transfer after the 1999 Kocaeli earthquake has triggered the 12 November 1999 Düzce earthquake towards east; and the amount of strain accumulated towards west is expected to be released by a future rupture along the northern branch of the NAFZ in Sea of Marmara (Bozkurt, 2001).

#### *3.1.2.2 East Anatolian Fault Zone*

The East Anatolian Fault Zone is approximately 500 km long, and trends in the northeast direction. Northern boundary is determined by the Karliova triple junction

and the southern boundary progresses towards Kahramanmaraş and Antakya to meet Dead Sea Fault Zone (Item “II” in Figure 3.1-2). The EAFZ is a transform fault, and style of faulting is left lateral (sinistral). The faults are aligned parallel, subparallel, sometimes oblique to the general trend. Faults which are aligned oblique to the northeast alignment possess an oblique component in style of faulting; which is an expected behavior considering the orientation of plate boundaries and major principal stress direction. Working together with the NAFZ, EAFZ contributes to the westward tectonic escape of the Anatolian Plate. The debate on the age of EAFZ falls into four categories; with estimates ranging from Late Miocene to Quaternary. The same discussion is closely related to the total slip in the neotectonic period; thus values fall in the range of 10 mm/year (Reilinger et al., 1997) to 25-35 mm/year (Taymaz et al., 1991). A few of the significant ruptures of the EAFZ during the last century can be listed as the 22 May 1971 Bingöl (M=6.8), 1986 Sürgü (M=6.0), and 1 May 2003 Bingöl (M=6.4) earthquakes (Bozkurt, 2001).

Besides Karlıova, another significant triple junction exists at the southern boundary of EAFZ, where the African, Arabian and Anatolian Plate meet at Kahramanmaraş region (Rojay et al., 2001). While the continuation of the EAFZ at the southern boundary, either towards the Dead Sea Fault Zone, or Cyprus via Osmaniye and Iskenderun is a subject of intense debate, from seismic hazard point of view, the Dead Sea segments, offshore zone towards Cyprus and parallel faults along Karataş, Osmaniye and Yumurtalık are modeled as independent sources each having their magnitude-recurrence characteristics. A remarkable amount of seismicity exists in this region as well, hosting the 1998 Adana-Ceyhan (M=6.2) event as well as many other moderate magnitude earthquakes (Bozkurt, 2001).

### *3.1.2.3 Dead Sea Fault Zone*

The Dead Sea Fault Zone is a 1000 km long transform fault zone trending in north-south direction (Item “III” in Figure 3.1-2) (Bozkurt, 2001). Style of faulting is left-

lateral, and the zone consists of en-echelon strike slip faults with pull-apart basins. Dead Sea Fault Zone serves as the separating plate boundary between African and Arabian Plates. The differential movement by these two plates constitutes the slip rate on the Dead Sea Fault Zone. Regional dynamics suggest the age of the fault zone to be much older than NAFZ and EAFZ, with estimates ranging from Early Miocene to Late Miocene (Bozkurt, 2001).

Contrasting proposals on the approximate slip magnitude range from 10-20 km to 110 km, and include comments on a two staged slip phases with quiescence between (Bozkurt, 2001). The portion of the Dead Sea Fault which exposes hazard of significant magnitude, on the area of interest to this study is modeled.

#### *3.1.2.4 South Aegean Arc*

Bozkurt (2001) defines the general characteristics of the South Aegean Arc as a converging boundary between African and Anatolian plates in the Eastern Mediterranean, where subduction takes place from Mediterranean Ridge to South Aegean Arc. (Item “IV” in Figure 3.1-2). Western extension of the Aegean Arc is marked by the Ionian Trench. Eastern part acts as a transform fault, where Pliny and Strabo trenches are present. Approximate age of active subduction is proposed to be in the order of 5 million years to 26 million years (Bozkurt, 2001).

#### *3.1.2.5 Cyprean Arc*

The Cyprean Arc is a major plate boundary, separating Anatolian Plate to the north and African Plate to the south in the eastern Mediterranean. Instrumental seismicity data has proved the continuation of the Aegean Arc towards west of Cyprus, where subduction of the oceanic crust takes place (Item “V” in Figure 3.1-2). A similar contraction takes place in the southern boundary of Cyprus. The behavior is proposed to be changing nature to strike-slip faulting to the east of Cyprus. Bozkurt (2001)



defines the zone to the east of Cyprus as a location where a significant amount of controversy occurs. This ambiguity, mainly collected in four distinct views on the nature of deformation, directly affects the engineering applications for earthquake and tsunami hazard assessment studies. Comparison of a few of the studies on the structure and mode of deformation of the Cyprean Arc clearly demonstrates the epistemic uncertainty among ongoing efforts (Ambraseys and Adams, 1993; Pınar and Kalafat, 1999; Harrison et al., 2004). The differences in models have been directly reflected to engineering studies (Erdik et al. 1999; Kythreoti and Pilakoutas, 2000; Salamon et al., 2007; Yolsal et al., 2007; Çağnan and Tanırca, 2009).

#### *3.1.2.6 Bitlis Suture*

Bozkurt (2001) gives a concise definition of the Bitlis Suture as follows: “During the Middle Miocene to early Late Miocene, Arabian and Eurasian Plates collided along the Bitlis-Zagros Suture Zone. This has resulted in the uplift of mountains along the suture, and the quite shallow marine environments were converted to molasse basins. The Bitlis Suture is a complex continent-continent and continent-ocean collisional boundary that lies north of fold-and-thrust belt of the Arabian platform and extends from southeastern Turkey to Zagros Mountains in Iran” (Item “VI” in Figure 3.1-2).

### **3.1.3 Neotectonic Provinces**

The term “neotectonic provinces” will be used for explaining tectonic structures and seismic activity at regions other than the major fault zones composing the intraplate boundaries. East Anatolian Contractive Province, North Anatolian Province, Central Anatolian Province and Western Anatolia are the four main areas of seismic activity that lie within the major fault zones.

Bozkurt (2001) summarizes the East Anatolian Contractive Province as the area to east of Karliova triple junction, characterized by a north-south compressional

tectonic regime. “Strike-slip faults of left-lateral and right-lateral deformation are the basic structural elements of the region. The faults are seismically active and form the source for many earthquakes. Some of the major earthquakes in the last century are 1924 Pasinler (M=6.8), 1975 Lice (M=6.6), 1976 Çaldıran (M=7.3), 1983 Horasan-Narman (M=6.8), 1986 Doğanşehir earthquakes (M=5.8 and M=5.6)” (Bozkurt, 2001).

To the north of the North Anatolian Fault Zone, North Anatolian Province is located as a zone of low seismicity, characterized by a number of strike slip faults along east-west direction. Bartın Fault has caused a major event in the area (M=6.8) in September 1968, causing damage. Barka and Reilinger (1997) have proposed a value of 5 mm/year slip rate on the Bartın Fault. Evaluation of the annual slip rate and overall activity of the area indicates a possible emerging zone that is analogous to the NAFZ (Bozkurt, 2001).

Shifting to the southern boundary of the NAFZ, Central Anatolia is a specific geography undergoing north-south and north-northeast, south-southwest contraction. The mode of deformation is controlled by the dynamics of the tectonic escape of the Anatolian Plate; counter clockwise rotation has been contributing to the generation of splay faults from NAFZ and EAFZ; as well as forming new structures within the plate. Numerous second order faults with oblique slip deformation exist towards the eastern boundary of the province. Splay faults from the NAFZ tend to propagate in the east-west direction for some distance, and then bend southwards to the Anatolian Plate in north-north east direction. Considering the direction of major principal stress, it becomes fairly easy to predict that faults trending in east-west directions display strike-slip character; whereas the north-east trending sections are subject to oblique-slip deformation. Among the major neotectonic structures in Central Anatolia; Malatya-Ovacık, Tuz Gölü, Eskişehir fault zones are to name a few. A noteworthy shear zone, Central Anatolian Fault Zone also exists; beginning from Erzincan, running through Sivas, Kayseri into the Mediterranean Sea. The evolution,

thus the slip rate and activity of the Central Anatolian Fault Zone is proposed to be in an increasing trend, considered within the geologic time scale (Bozkurt, 2001).

Sparse seismic activity is observed in one of the major structures of the region; namely the Tuz Gölü Fault Zone. The quietness of the structure during the instrumental period forms a challenge for earth scientists and engineers to assign the parameters for earthquake generation capability of the fault. The fault zone is composed of strike-slip faults with a considerable normal component (Bozkurt, 2001). Event in eastern part of the Central Anatolian province having the largest magnitude in the instrumental period is recorded as 1938 Kırşehir event.

Progressing towards west, northwest-southeast trending Eskişehir Fault Zone is a dextral structure with considerable amount of normal component. It extends from Uludağ to Afyon (Bozkurt, 2001). The greatest rupture during the instrumental period is the 1956 Eskişehir Earthquake ( $M=6.5$ ).

Bozkurt (2001) defines the basic characteristics of the western parts of the Central Anatolian Tectonic Province as faults formed by northeast-southwest and northwest-southeast trending cross graben and horst structures. These structures are dominantly normal, with a strike-slip oblique component. Isparta Angle forms the transition boundary between the extending Western Anatolia and the Central Anatolian Zone. Dinar, Civril, Akşehir, Afyon, Burdur grabens and their bounding faults, as well as the Fethiye-Burdur Fault Zone are the major structures of the area.

Bounded by Eskişehir Fault Zone and the Isparta Angle, western part of Anatolia is an extremely active region undergoing extension at a measured rate (30-40 mm/year) larger than the transformational slip rate of the NAFZ (15-25 mm/year). Approximately east-west trending grabens and bounding normal faults are the most remarkable features of the tectonic region. Edremit, Bergama (Bakırçay), Kütahya, Gediz, Küçük Menderes, Büyük Menderes and Gökova (Muğla) grabens make up the

main structures, being hosts to numerous large magnitude earthquakes. The largest event measured during the instrumental period is the 1970 Gediz Earthquake (M=7.2).

### **3.2 SEISMIC SOURCE CHARACTERIZATION FROM HAZARD ASSESSMENT PERSPECTIVE**

This section provides concise information on the fundamentals of seismic source characterization for hazard assessment studies. The essence of source characterization is interpreting the knowledge produced by earth science studies to engineering parameters for design. Basic questions to be answered in source characterization of faults from hazard perspective is the location of the faults, style of faulting, annual rate of slip (creep) along the fault, maximum earthquake producing capabilities, and frequency of events for each earthquake magnitude bin.

For some faults which are intensely studied, collecting these parameters of interest is unquestionably easier. However, even for earthquake hotspots such as the North Anatolian Fault Zone, an inevitable amount of epistemic uncertainty exists in parameter determination. Variability of estimated annual slip rates forms an excellent example for this case. Further simplification by the assumption of uniform creep rate along the whole fault zone for a typical study lacks correct addressing of the total uncertainty for design purposes.

For the simplest case of delineation of active faults, segmentation in terms of hazard concern is crucial. Within this text, the term “segmentation” refers to the distinction of fault geometry that is likely to rupture independently from the other “segments” nearby. Taking the NAFZ for instance, it is unlikely that the 1500 km long system will rupture at once. A segment in a zone consisting of strike-slip faults may be partially separated from the adjacent geometry through a pull-apart basin and a

rhomb secondary normal fault. For the specific case, the essential question to be answered is whether the accumulated stress along the fault, often non-uniformly distributed, is adequate for rupturing the defined geometry simultaneously in adjacent segments. Since the initial geostatic stresses cannot be accurately resolved, the answer to the question is often unclear in many circumstances; hence the decision of segmentation is significantly influenced by expert opinion.

Defining segments for the rupture scenarios of linear or planar fault systems is closely related to parameterizing the earthquake producing capabilities of each fault. As studied in Chapter 2 with detail, release of the accumulated seismic moment is related to moment magnitude of an earthquake; hence moment magnitude is also a function of the rupture dimension parameters. This fact acts as a basis for a convenient tool in determining the maximum earthquake magnitudes for a fault. Using the rupture dimension scaling relationships, the maximum magnitude earthquake for a fault can be estimated by utilizing empirical correlations. Noting that the estimate of  $M$  as a function of rupture length is not exact, it has a distribution around the median. Additionally, “fault length” is not always equivalent to “rupture length” for a structure.

Regarding the past earthquakes, unless a detailed field investigation and trench studies suggest the presence of pre-instrumental large magnitude events, the only valuable information at hand becomes the seismicity catalogue for the last century. From the general principle that large magnitude events occur rarely, and keeping in mind that the maximum magnitude events approximately correspond to events having return periods of about 10000 years or more, the possibility of having encountered the largest possible earthquake on a fault during a century is infinitesimal for active regions in Turkey. While written records may provide valuable information about the felt intensity of the event at civilized settlements, magnitude parameter has to be justified from a different source. Combining all these data in a model for hazard assessment requires a systematic and reasonable approach,

which will inevitably include epistemic uncertainty. The details of approach followed in defining the maximum earthquake magnitudes in this study is explained in the proceeding sections.

Last but not the least; the engineer has to gain an understanding of the relative rate occurrences of different earthquake magnitudes for each defined seismic source. Modern seismic hazard studies incorporate multiple magnitude scenarios, each contributing with their own probability of occurrences, during calculations. Even if the problem is suitable for utilizing a single scenario earthquake, such as in the case of conventional microzonation studies, a probabilistic hazard study should accompany to extract the dominant scenario for the problem. The readers are referred to Chapter 5 for thorough description of the hazard integral. Calculating the relative rates of occurrences of earthquakes having different magnitudes requires a careful assessment of instrumental seismicity. The main factors influencing the results are the effect of aftershocks, catalogue completeness and the magnitude scale. These issues will be addressed within the current chapter. Another problem in practice is the assignments of the events to each specific source, taking account the variability of the reported epicenter. A solution proposal to this problem is also supplied within the current report.

### **3.2.1 Previous Efforts in Seismic Source Characterization for Turkey**

Modern seismic source characterization attempts for Turkey are relatively recent, having a history of about only two decades. Starting from the first well-known characterization attempt which was used for developing the recent earthquake code of Turkey (Gülkan et al., 1993) this section provides a brief presentation of various studies which demonstrate that a unique solution to the problem has not been developed yet.

Gülkan et al. (1993) has characterized seismic sources in Turkey with 19 area sources, and additional area zones representing background seismicity. While this

representation may seem sufficient at a regional scale for mapping purposes, it is evident that the calculated hazard is considerably sensitive to source characterization at near-fault sites; and cannot be comfortably used in site specific hazard studies. While not stated explicitly, Gülkan et al. (1993) model assumes that the earthquakes occur as point sources within the defined area boundaries (Figure 3.2-1).

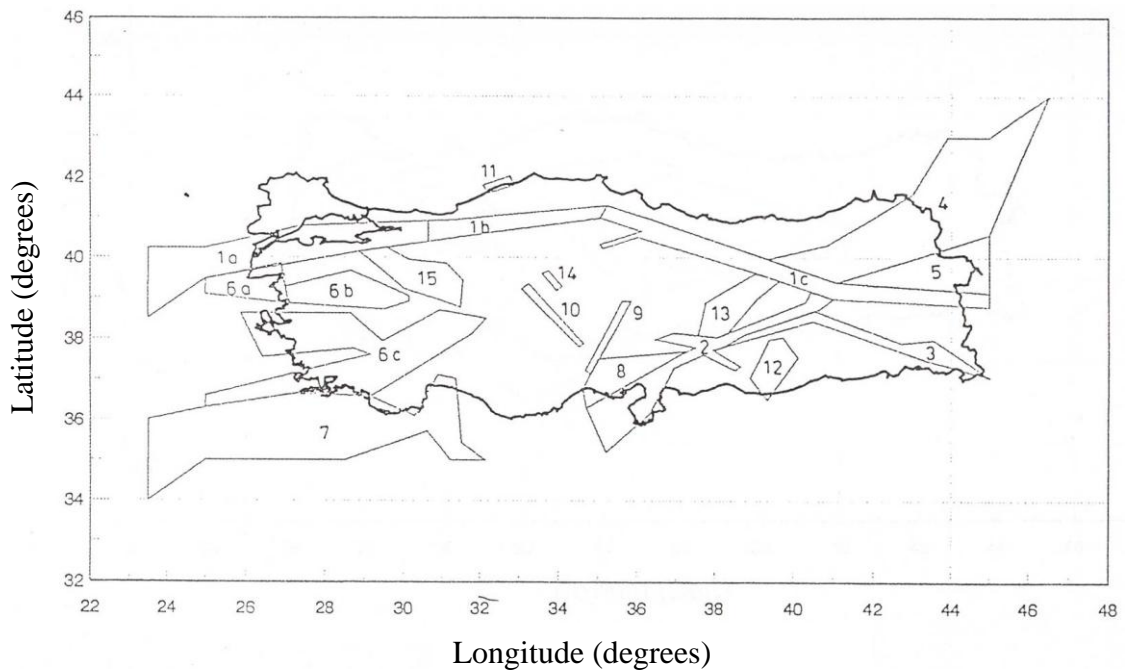


**Figure 3.2-1. Source characterization which forms the basis for the current earthquake code for Turkey (modified from Gülkan et al., 1993)**

A revised form of Erdik et al. (1999) compilation has been used in Bommer et al. (2002) aimed at developing a model for earthquake loss insurance. Bommer et al. (2002) compilation introduces a more comprehensive evaluation of offshore seismic sources. Bommer et al. (2002) brings a major improvement to earlier models by introducing sub-zones, in which the rupture locations of higher magnitude events are binned into a more constrained geometry. Demircioğlu et al. (2007) uses the same approach with area sources (Figure 3.2-2).

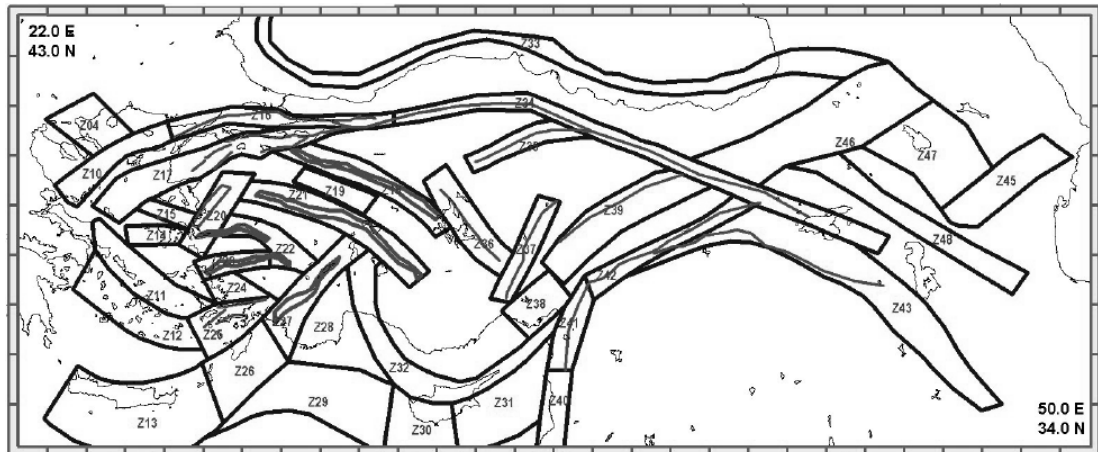


**Figure 3.2-2. Nationwide source characterization for Turkey (Demircioğlu et al., 2007)**

Deniz (2006) uses an extended version of source characterization proposed by Bommer et al. (2002), with a more systematic framework for maximum magnitude determination (Figure 3.2-3). Deniz (2006) describes the  $M_{\max}$  determination procedure as follows: “If the observed maximum magnitude ( $M_{\max, \text{obs}}$ ) is greater than the magnitude value based on expert opinion, the observed value is taken. If the opposite is valid the difference between the two is examined. The value assigned by the expert is taken if the difference is less than or equal to 0.5 magnitude units, otherwise the value of  $[(\text{observed}+0.5) + \text{expert}]/2$  is taken.”

Commenting on Deniz (2006) maximum magnitude determination procedure with an example; provided that the maximum observed earthquake magnitude for a source is  $M=6.5$  and the expert opinion corresponds to  $M=7.2$ , the final proposal would be  $M=7.1$ ; which indicates a bias towards expert opinion. Alternatively, if  $M_{\max, \text{obs}}$  is greater than the expert opinion;  $M_{\max, \text{obs}}$  automatically becomes  $M_{\max}$  value for design, which can be under predicting the actual value since the instrumental data collected from earthquakes are limited to 100 years. This will probably have negligible effect on faults with limited earthquake producing capabilities; however will significantly bias predictions for known active faults if the “expert opinion”



proposes smaller values than actual. Deniz (2006) study, in addition, makes a valuable contribution to earthquake catalogue compilation and processing; focusing on aftershock filtering, magnitude conversion and completeness analysis.

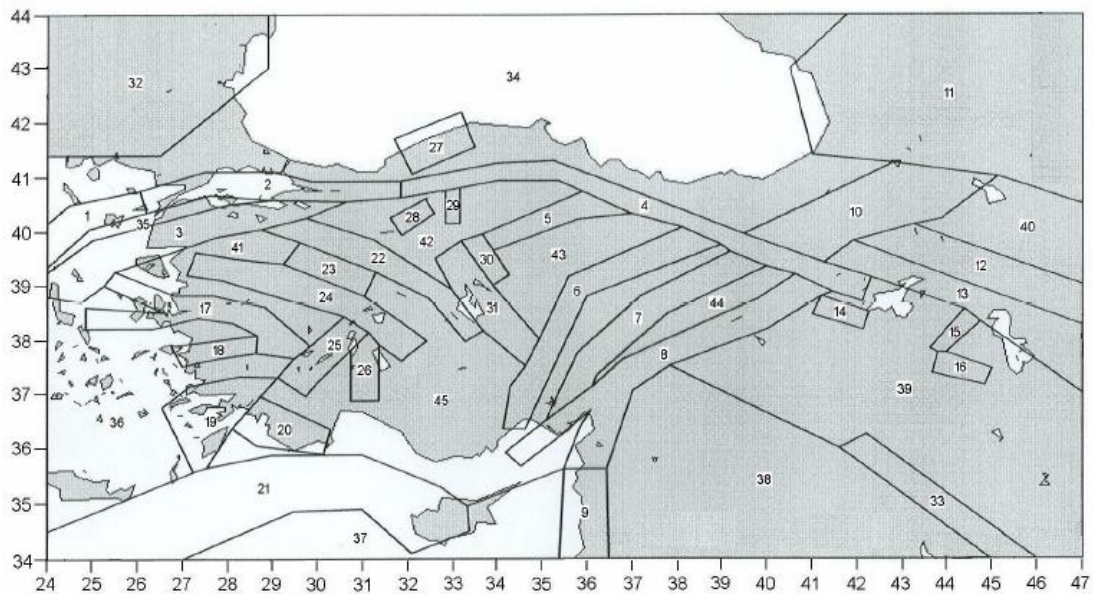


**Figure 3.2-3. Seismic source characterization used by Deniz (2006)**

Kayabalı (2002) has proposed another version for seismic source characterization for Turkey, by compiling data mostly from Erdik et al. (1985) and Yalırak et al. (1998). Kayabalı (2002) model utilizes an expert judgement in assessing the maximum earthquake magnitudes for each source, assuming a fraction (one-third) of total fault length has ruptured. The study does not present any information whether the median magnitude or any percentile above the median is used for assigning the  $M_{max}$  value. The decision for fault segmentation along a fault zone is crucial at this point, and directly affects the maximum magnitude selections for sources such as North Anatolian Fault Zone; in which the segmentation was not applied (Figure 3.2-4). Similar considerations for the demand of more detailed characterization exist for the extensional neotectonic regime in the Aegean Region; which is characterized by a single wide source area. Kayabalı and Akın (2003) represents a revised version of

source characterization for Turkey, in which the area source is exempted and a more detailed delineation is used.

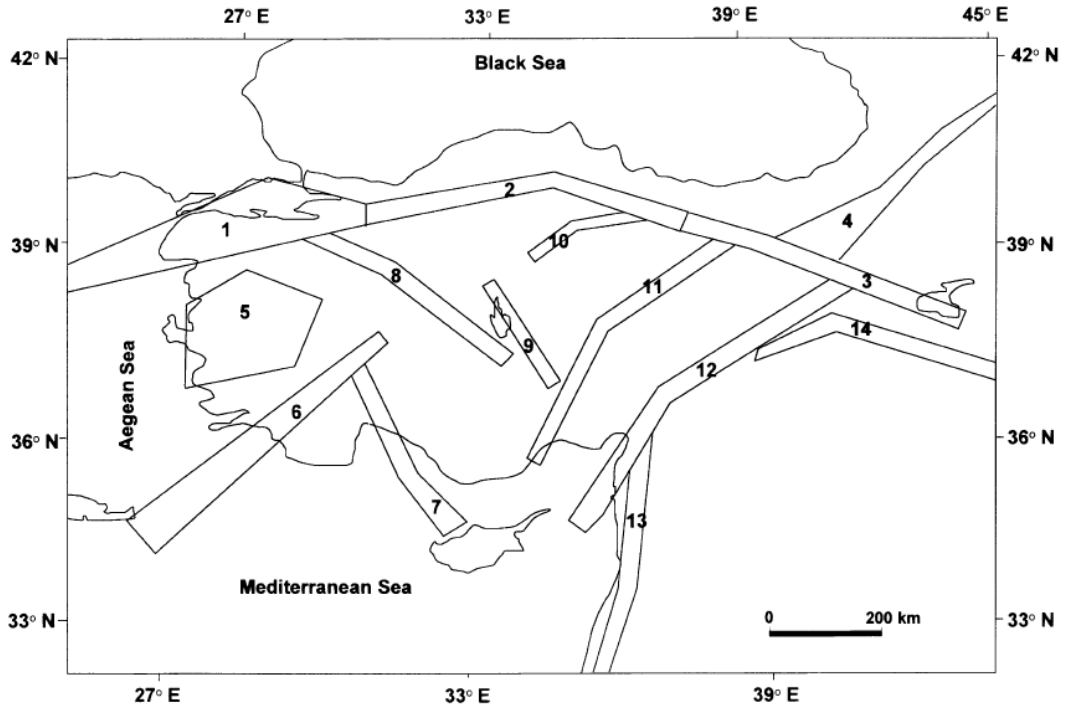


**Figure 3.2-4. Seismic source characterization used by Kayabalı (2002)**

Study by Ulusay et al. (2004) has proposed the utilization of single magnitude scenarios corresponding to maximum magnitude for assessing design hazard levels, mainly using segmented linear sources compiled from Şaroğlu et al. (1992) (Figure 3.2-5).

As a conclusion for the defined active faults in Turkey, the major challenge in characterization remains to be a systematic approach in decision making. Macroseismicity catalogue for Turkey has revealed that the location uncertainty of focal points of events can reach over 10 kilometers; thus introducing an ambiguity in assigning those events to each seismic source. Up to the present, this has impacted both the geometric characterization choices as well as direct effect on recurrence

values, and caused a bias towards using area zonations for the possible rupture location determination within the hazard scenarios.

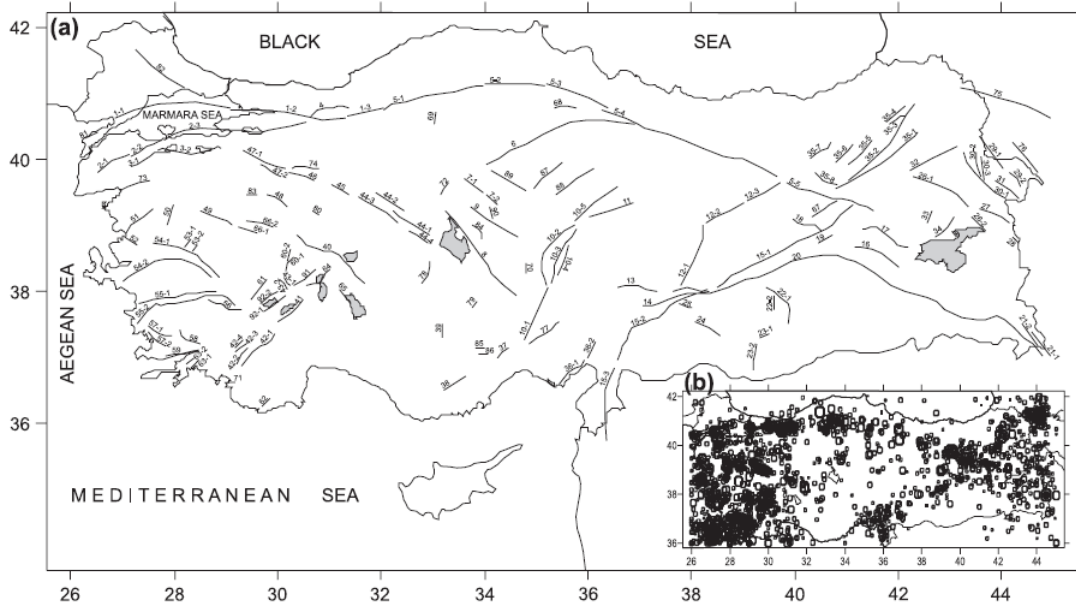


**Figure 3.2-5. Seismic source characterization used by Ulusay et al. (2004)**

### **3.3 INSTRUMENTAL MACROSEISMICITY CATALOGUES**

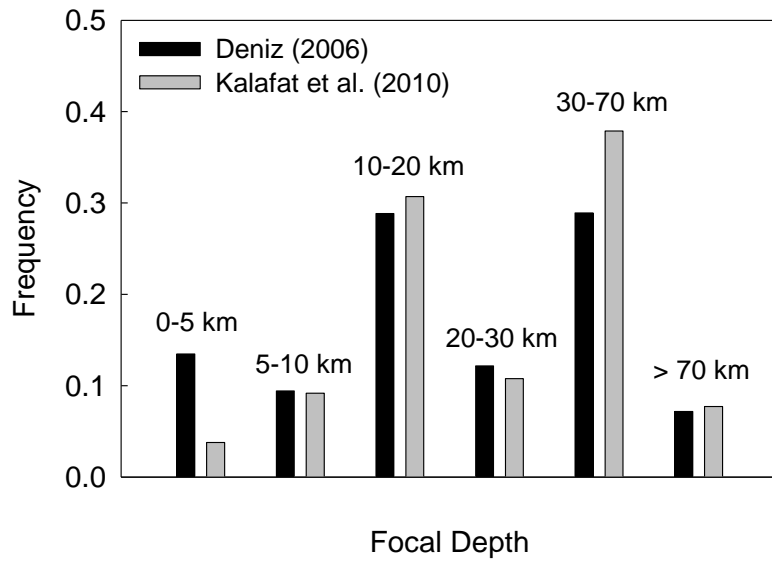
Selection of a seismicity catalogue for determining the recurrence parameters for seismic sources requires careful interpretation. It is essential that the data points in the catalogue should not represent any duplicate events, if the dataset is a compilation of event catalogues from different sources. In other words, same events recorded in different contributing catalogues with slightly varying metadata such as the event time, coordinates and magnitude should be identified and filtered. Having compiled reliable data into a single bin, the magnitude scale chosen for each data point should be unique.

Compilation of a new seismicity catalogue from scratch is out of scope of this study. Nevertheless, two recent compilations of decent quality by Deniz (2006) and Boğaziçi University Kandilli Observatory and Earthquake Research Institute-KOERI Kalafat et al. (2010) are analysed in terms of key properties and catalogue completeness.

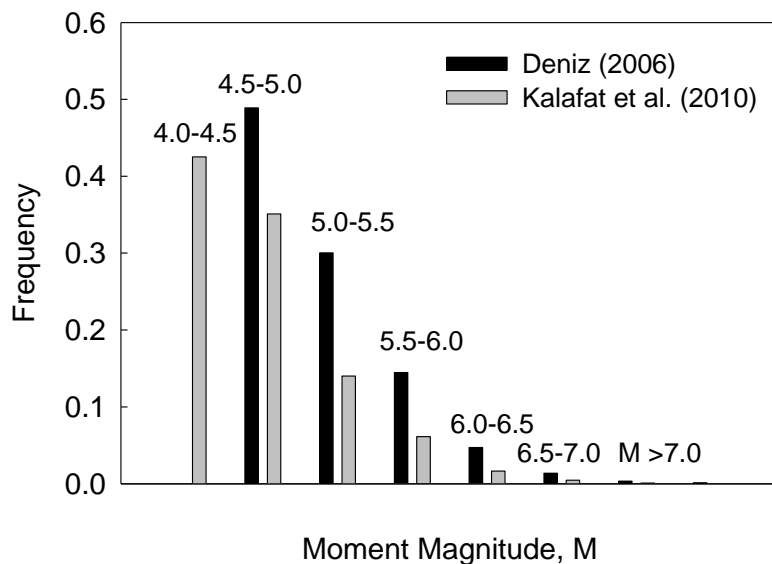
Deniz (2006) compilation is composed of 7 different data sources, with limited catalogues from İnan et al. (1996) to more comprehensive compilations such as the KOERI (2004), ISC and USGS catalogues. Data from different sources were homogenized for obtaining the final form of the catalogue. The dataset contains 4752 events having magnitudes greater than or equal to  $M=4.5$ . Although the catalogue has been screened for foreshock and aftershock identification, the presented raw form does not contain further processing, except magnitude conversion.

In KOERI catalogue, earthquakes with magnitudes of 4.0 and larger that occurred in Turkey and its surroundings ( $32-45^{\circ}$  N /  $23-48^{\circ}$  E) during the period 1900-2005 were compiled. The number of earthquakes having magnitudes greater than or equal to  $M$  4 is 8011, after filtering data of questionable quality. The study area includes the regions that have high seismic activity; Eastern Mediterranean, Aegean, the Balkans, East of Marmara Sea and its surroundings, Central and Northeast Anatolia, Eastern and Southeastern Anatolia, Cyprus and Iranian-Iraq border, Caucasus (Kalafat et al., 2010). All magnitude data, with a total number of 8010, have been converted to moment magnitude scale,  $M$ .

Frequency distribution of magnitude bins and focal depth for each catalogue is presented in Figure 3.3-1. Two catalogues do not show notable differences in focal depth distribution. On the other hand, effect of lower magnitude cutoff on the frequency distribution can be clearly observed from Figure 3.3-1b.



(a)



(b)

**Figure 3.3-1. (a) Focal depth and (b) magnitude distribution for Deniz (2006) and Kalafat et al. (2010) datasets**

Another significant issue regarding the seismicity catalogues is the completeness problem. Before the flourishing dates of wide-spread global seismometer networks, events with low magnitudes were either not measured or reported. When data covering whole instrumental period are analyzed in terms of magnitude distribution,

the actual rate of low magnitude events are lower than expected. This, in fact, arises from treating all the magnitude bins in the catalogue as if they possess the same completeness period. A simple data analysis for both catalogues of concern reveals the following (Figure 3.3-2):

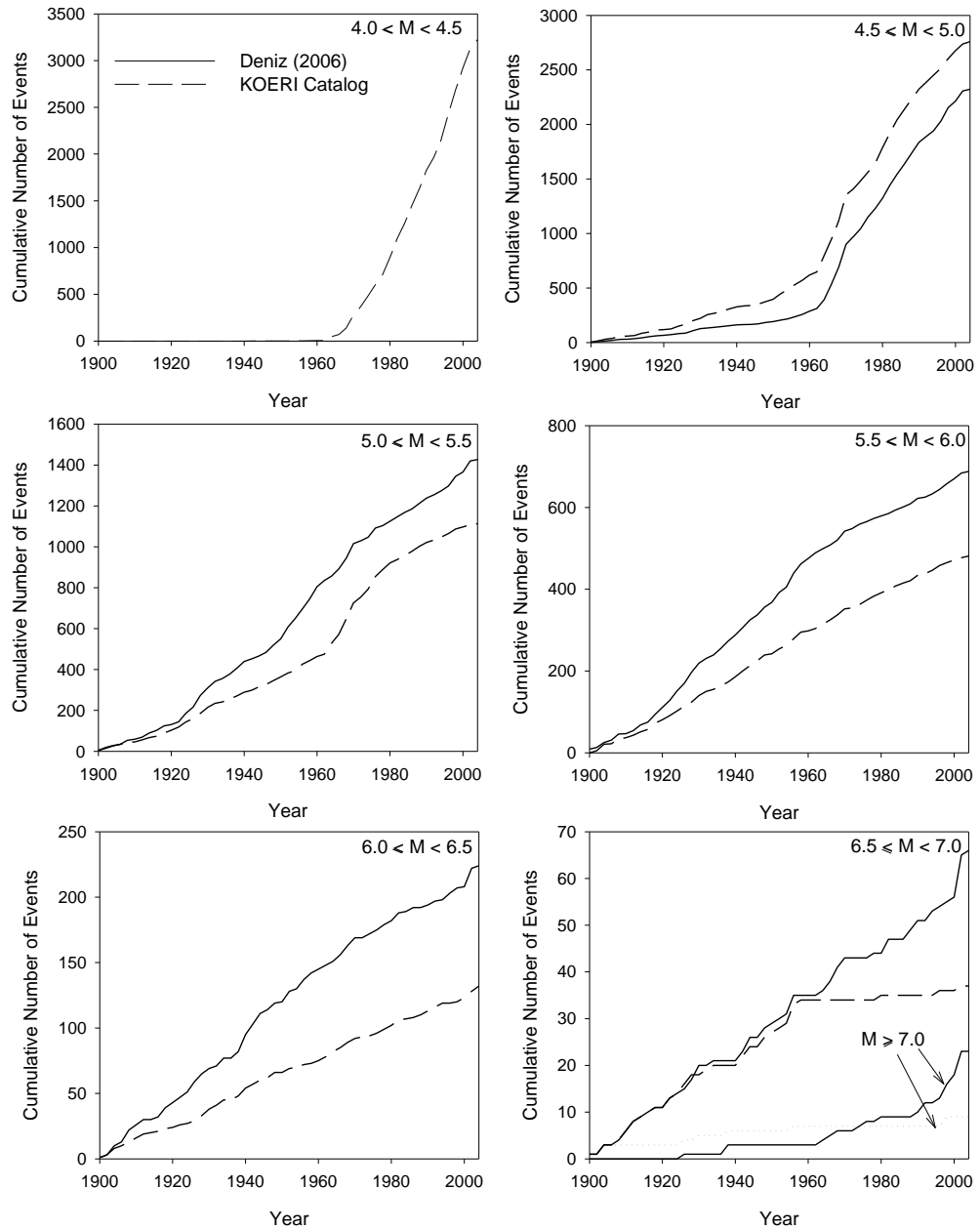


**Figure 3.3-2. Catalogue completeness analysis for the Deniz (2006) and Kalafat et al. (2010) datasets**

In Figure 3.3-2, Deniz (2006) and Kalafat et al. (2010) seismicity catalogues are binned with respect to moment magnitude,  $M$ . Cumulative number of events for that bin as a function of increasing date of occurrence are plotted for each bin. Examining  $M=4.0-4.5$  bin for the Kalafat et al. (2010) catalogue reveals that, before 1960, none of the events for the magnitude bin of interest were reported.

The completeness problem is slightly pronouncable for both catalogues in the  $M=4.5-5.0$  bin, and primarily vanishes after  $M=5.0$ . However, another incompatibility in cumulative event buildup with time becomes evident at large magnitudes. There is a particular difference between the event buildup trends of two catalogues, for magnitude above  $M=6.5$ . The reason behind this case was thoroughly investigated and the following evidences were found:

- i) Some of the high magnitude events are duplicates in Deniz (2006) catalogue. A closer investigation reveals that, the records for 17 August 1999 Kocaeli and 26 December 1939 Erzincan events are included as duplicate events, Erzincan event also being located off the related fault trace. This is a possible consequence of misinterpretation of the algorithm for unifying event data from different source catalogues. One of the major consequences of using such data will result in overpredicting large magnitude activity at an area. Events with lower magnitudes were not checked against any possible errors.
- ii) For the 22 July 1967 Mudurnu Valley earthquake, error introduced in the previous item does not exist. However, probably due to utilization of different magnitude scale conversion relationships for Deniz (2006) and Kalafat et al. (2010) catalogues, events are shifted to be included in different magnitude bins. Deniz (2006) uses its own scale conversion relationship derived by orthogonal regression, whereas Kalafat et al. (2010) does not provide detailed information regarding their preference.

Based on these evidences, Kalafat et al. (2010) catalogue was chosen to be included in this study. Glancing back to the completeness analysis problem, a procedure similar to Stepp (1972) was followed by computing the rate of each magnitude over the time period for which it is complete. The transition zone for  $M=4.5-5.0$  was neglected in Figure 3.3-2, and the renormalization of rates was applied for events falling into the  $M=4.0-4.5$  bin. While, Deniz (2006) applies a different catalog completeness correction factor to the events falling within each seismic source independently, this study proposes the utilization of a single value for the  $M=4.0-4.5$  range, which is chosen as 40 years (1965-2005 period).

The proceeding section contains introductory information about magnitude-recurrence values for a seismic source, which will enable the demonstration of catalogue completeness correction on a sample source.

The final selection of regionwide macroseismicity catalogue compiled by Kalafat et al. (2010) reveals the following distribution (Figure 3.3-3). Events having unatcmagnitudes lower than  $M 4.0$  are excluded.



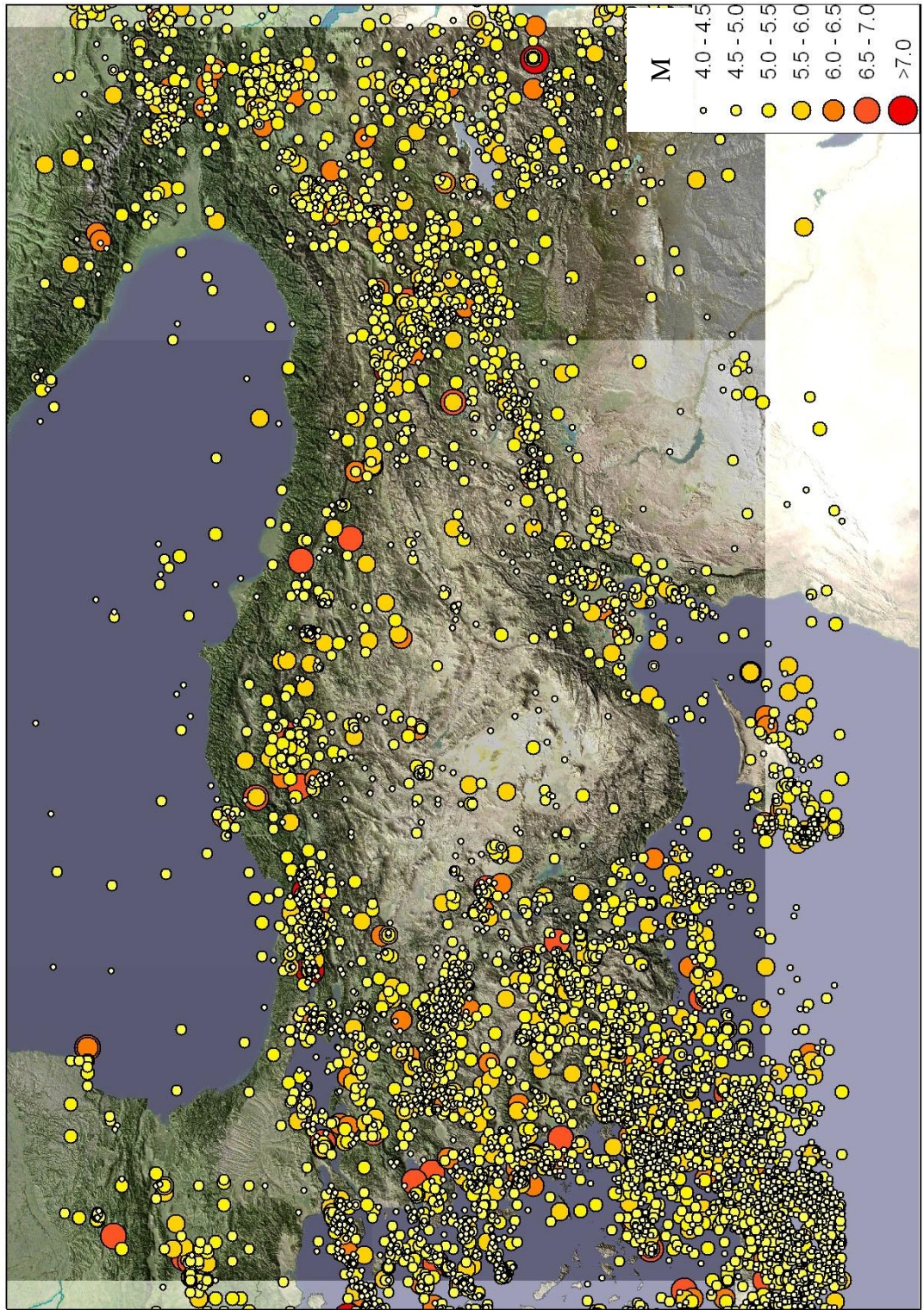


**Figure 3.3-3. Macroseismicity distribution for Turkey and neighboring regions (Kalafat et al., 2010)**

### 3.3.1 Magnitude-Recurrence Relationships for Seismic Sources

The essence of magnitude – recurrence relationships lies in the assumption that a seismic source is capable of generating earthquakes having various magnitudes, over a time period. If an ideal fault was to generate a single magnitude earthquake each time it ruptured, then the probability of rupture being equal to that value would be equal to unity. In reality, there is no doubt that seismic sources generate events in a magnitude range, represented by a probability density function (pdf). The magnitude pdf, hence, expresses the relative number of events having different magnitudes that occur on a modeled seismic source. Truncated exponential and characteristic earthquake models exist, however this text will only refer to the truncated exponential pdf for description of the phenomenon. Magnitude pdf will be denoted as  $f_m(m)$ , and its inclusion into the hazard integral is presented in Chapter 5.

The truncated exponential model is based on the conventional Gutenberg-Richter magnitude recurrence relation. The Gutenberg-Richter relationship is expressed by Equation 3-1:

$$\log N(M) = a - bM \quad (3-1)$$

In Equation 3-1,  $N(M)$  is the cumulative number of earthquakes with magnitude greater than or equal to  $M$ . Parameter “ $a$ ” corresponds to logarithm rate of the earthquakes above magnitude “0” and “ $b$ ” parameter is the slope.

Similarly, for a truncated exponential distribution, pdf is expressed as:

$$f_{m,TE}(m) = \frac{\beta \cdot e^{-\beta(M-M_{min})}}{1 - e^{-\beta(M_{max}-M_{min})}} \quad (3-2)$$

where

$$\beta = b \cdot \ln (10) \quad (3-3)$$

Magnitude density function expressed in Equation 3-2 defines the relative rate of different earthquake magnitudes on a seismic source. The distribution is truncated at a selection of minimum magnitude,  $M_{\min}$ , and maximum magnitude  $M_{\max}$  (Figure 3.3-4).

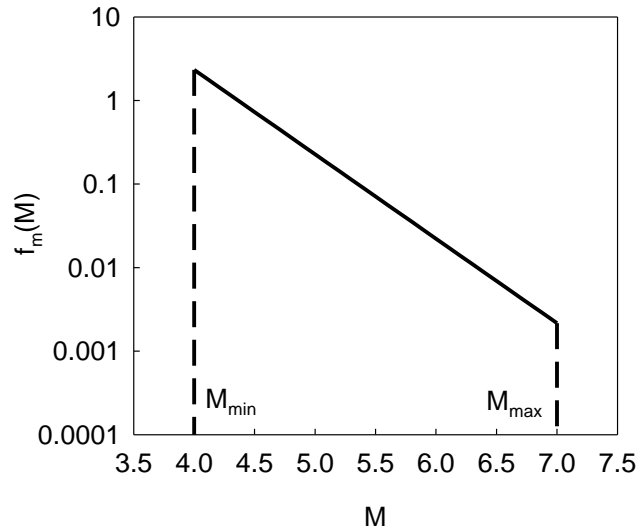


**Figure 3.3-4. Magnitude pdf for truncated exponential model**

Calculation of the rate of earthquakes equal to or above a magnitude is done by a parameter denoted as  $N(M_{\min})$ , defining the “activity” of the fault, accompanying the probability distribution functions. Two approaches exist for determining  $N(M_{\min})$ , i) calculating activity rate based on instrumental seismicity data, and ii) annual slip rate on a fault. This study focuses on parameter determination using instrumental seismicity data. This is achieved by fitting a truncated exponential model to the macroseismicity data using the Kalafat et al. (2010) catalogue, after distributing events to the related seismic sources. Thus, recurrence relation simply yields as the expression:

$$N(M) = N(M_{\min}) \int_{m=M}^{M_{\max}} f_m(m) dm \quad (3-4)$$

### 3.3.1.1 Effect of Catalogue Completeness on Recurrence Relations

Based on previous discussions and the definition of recurrence relations, impact of catalogue completeness on recurrence relations is presented by an example. The sample seismic source is taken as Central Anatolia Background Source-2, of which the details for source zonations will be given later in this chapter. Figure 3.3-5 presents the observations for annual rate of events having magnitudes greater than or equal to  $M$ . The light series are the uncorrected series, and the period of catalogue completeness is taken as 105 years for the whole magnitude range. On the other hand, a correction has been applied to the bold series, representing the modified rates for  $M < 4.5$ . Under-representing the rate of small magnitude events would have yielded a linear fit having a lower slope, and difference in annual rates would be in the order of two (recall that the  $N(M)$  axis is plotted in log scale).

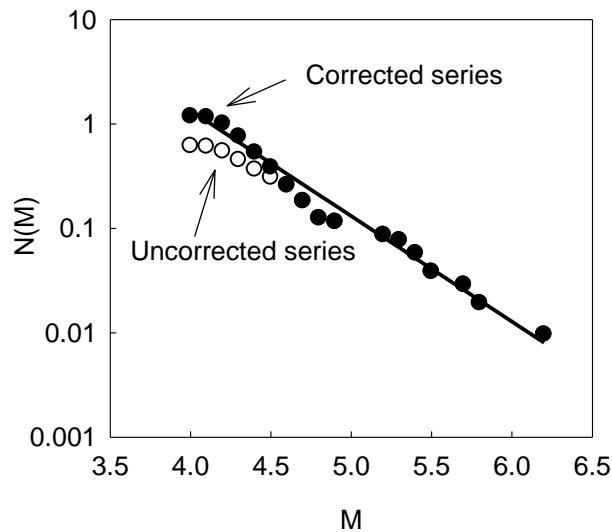


**Figure 3.3-5. Effect of catalogue completeness problem on recurrence relations**

## 3.4 GEOMETRIC CHARACTERIZATION

### 3.4.1 Introduction

Geometrical idealization of seismic sources can be made by dividing sources into three main categories that are point, line and area models, respectively. Separating area sources aside, point sources expressed in terms of source zones and line sources will be given attention in our case. The section begins with a brief descriptive example of how geometrical characterization may be made given a set of mapped faults. However, one should always note that such characterizations are made by utilizing fault evidence and epicenter distribution of past events together. Generally, if the spatial distribution of events cannot be attributed to a fault segment or system, it is considered to be a part of the background seismicity, which can be represented by area sources (polygons). Characterization considerations can also be based on the level of detail required and source-site distance. Modeling the geometry of the seismic source depends on a number of factors, including the uncertainty and complexity of the collected field data, as well as precision required for the analysis which may directly rely upon the distance between the source and site. For instance, consider a series of parallel to sub-parallel fault segments mapped using field work (Figure 3.4-1).

In Figure 3.4-1, four active fault segments are identified, and they belong to a three stage horst-graben system as shown in the cross section tagged A-A'. In this specific example, the faults can be characterized using three different source geometry models, depending on the behavior and analysis options. In Model 1, it is assumed that the creep rate estimates (as computed by in-situ geological measurements and radiometric dating of samples) of different segments show variability that is precisely quantified; and the site where the hazard is to be computed is relatively near to the sources. The solution can be proposed by modeling the faults as linear sources each having different parameters.

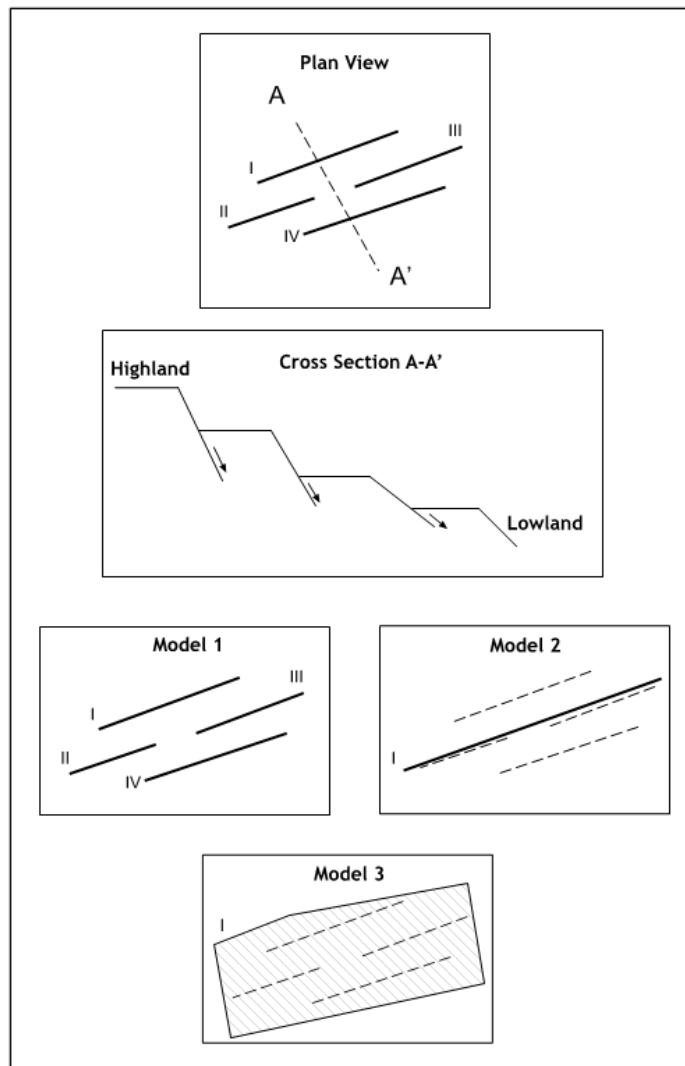


**Figure 3.4-1. Illustrative example for source characterization**

Glancing at Model 2, a major fault segment and minor faults lying parallel to it are observed. The major source is predicted to be the location of the main rupture event, and the minor faults have been interpreted as propagations due to the main rupture and surface topography (e.g. sloped surface). The solution offered in such a case might be modeling the main fault only, considering the site is away from the source and ground displacement hazards is out of concern. In the last scenario named as Model 3, either, there is a lack of information about the geometry and seismicity rates of the faults, or detailed modeling is not required since the sources are at a great

distance from the site; thus, area representation will comfortably be an appropriate choice.

### **3.4.2 Geometric Characterization for Active Faults in Turkey**

There has been considerable amount of argument going on the definition of the active fault. Although there is general agreement concerning the use of the terms “active fault” to describe a fault that poses a current earthquake threat and “inactive fault” to describe one on which past earthquake activity is unlikely to be repeated, there is no consensus as to how fault activity should be evaluated. Kramer (1996) compiles the studies to define an active fault, as follows:

The California Division of Mines and Geology defines an active fault as one that has produced surface displacement within Holocene time (approximately 10000 years). For dams, U.S Army Corps of Engineers has used a time period of 35000 years. U.S Bureau of Reclamation has used 100,000 years. The U.S Nuclear Regulatory Commission, on the other hand, has used the term “capable fault” for those that exhibit

- i) Movement at or near the ground surface at least once within the past 35000 years or movement of a recurring nature within the past 50000 years.
- ii) Macroseismicity instrumentally determined with records of sufficient precision to demonstrate a direct relationship with the fault; or
- iii) A structural relationship to a capable fault according to characteristics (1) and (2) above, such that movement on one could reasonably be expected to be accompanied by movement on the other.

A reasonable conclusion without restricting activity definitions into certain time periods was suggested by Cluff and Cluff (1984); proposing six classes and five subclasses of fault activity based on characteristics such as slip rate, slip per event, rupture length, earthquake size, and recurrence interval.

Without going into further discussion on the definition of active faults, this section summarizes the criteria for geometric characterization of faults, discussing the segmentation concept, zonations for point sources, and the framework for computing the maximum earthquake magnitudes for each source. The essence of geometric characterization is keeping a balance between the detailed fault mapping from field evidence, and simplified form intended for engineering use. Excessive detailing of active faults in hazard studies requires the same amount of detail in field evidence such as the activity rate, geometry, faulting style, and creep rate. In circumstances which a compilation is made over a large region, some amount of simplification becomes necessary. However, such idealization needs to be in a manageable order, so that any oversimplification that will impact hazard results is avoided. Expert judgement plays an important role at this stage, while obeying the rules of a simple framework becomes extremely helpful.

For the well studied fault systems in different neotectonic provinces of Turkey, linear modeling was preferred. Segmentation of the faults, with particular emphasis on determining the maximum earthquake magnitudes were made using the spatial distribution of pull-apart basins, morphology, angular distortions in the alignment of the fault, location of horst and graben systems, as well as careful observations of distribution of past seismicity. Utilization of linear sources was selected in faults covering the North Anatolian Fault Zone, East Anatolian Fault Zone, horst and graben systems throughout Western Anatolia, and many parts of Central Anatolian Region.



For regions where surface traces of the faults were fragmented and closely spaced, point source models (readers are referred to Chapter 5 for full description) were used as area zones. For area zones, seismicity is uniformly distributed along the defined plane geometry, fixed at a certain focal depth over the area covered by polygon boundaries.

Delineation of on-land faults was relatively easier than characterizing faults offshore. For offshore faults, except few sources in the Mediterranean Sea, area sources were preferred. Boundary definitions for offshore faults are a synthesis of several studies. Zonations in the North Aegean Sea was mainly influenced by the results of Saatçılar et al. (1999) study, supported by the evidence in Oçakoğlu et al. (2005). Possible offshore traces of on-land faults in the Karaburun-Sığacık-Seferihisar region were verified from Benetatos et al. (2006) and Aktar et al. (2007). Results from the studies listed above also helped in determining the boundaries for Hellenic Trench and Pliny-Strabo Trenches. Sources for tectonic evidence in the Cyprean Arc were mentioned in Section 3.1.2.5, hence will not be repeated here.

As a complement to the linear fault segmentation in continental Anatolia, some sources of seismicity were preferred to be modeled as point sources. These include the Bitlis Suture Zone, a wide compressional zone of distributed seismicity, Caucasus compressional zone, fragmented North East Anatolian Fault covering Erzurum and Horasan regions, Burdur-Fethiye axis and finally, Köyceğiz region.

Events not falling within the boundaries of linear segments (incorporating the down-dip width up to 30 km depth), or specifically defined area sources were included to background seismicity zones. Background seismicity zones are areal in geometry, and divided into 10 regions. These include the background seismicity in the Aegean Sea, West Anatolia, West and East Mediterranean, South East Anatolia, East Anatolian Fault Zone (EAFZ), Black Sea, North Anatolian Fault Zone (NAFZ), and two regions for Central Anatolia. The criteria for assigning individual events to each

source for determining the recurrence parameters based on historical seismicity is presented in Section 3.6 of the current chapter.

Simplest assumption of a linear fault characterization does not include the geometrical characterization along the down-dip direction. Being aware of the fact that down-dip slope may be a variable along depth from surface, especially for faults having normal style of faulting (steeper at higher depths), this study proposes the inclusion of a constant slope down-dip representation of the fault. The characterization may be used for a possible propagation of rupture scenarios along the down-dip plane of the fault, as well as playing an important role in computing the recurrence parameters, as presented in Section 3.6.

As the next step, linear fault segments were assigned a characteristic dip angle, based on the relevant style of faulting. Some strike-slip faults with highly steep dip angles were assigned a value of  $90^{\circ}$ . Other faults with dominant strike-slip nature were assigned a typical angle of  $70^{\circ}$ . Faults having a normal or reverse character were assigned an average dip angle of  $40^{\circ}$ . These values were double checked from the average sample dip angle values of the global rupture dimension scaling dataset used in Chapter 2 for each faulting style. Additionally, focal mechanism solutions of earthquakes, which were included in the strong ground motion database of Turkey (please refer to Chapter 4) were investigated for the relevant fault, where available. Dip angles from the primary axis of focal mechanism solutions were in close agreement with other findings, verifying the choice of  $90^{\circ}$ - $70^{\circ}$ - $40^{\circ}$  dip angle set.

Linear fault traces, with surface projections of modeled down-dip geometry up to 30 km focal depth are plotted in Figure 3.4-2. The numbers refer to detailed descriptions of fault parameters summarized in Table 3.6-2. A blowout of Figure 3.4-2, focusing on densely spaced faults of Western Anatolia is presented in Figure 3.4-3, for better viewing. Similarly, Figure 3.4-4 includes the identification and distribution of area sources, including background seismicity, with details presented in Table 3.6-3.

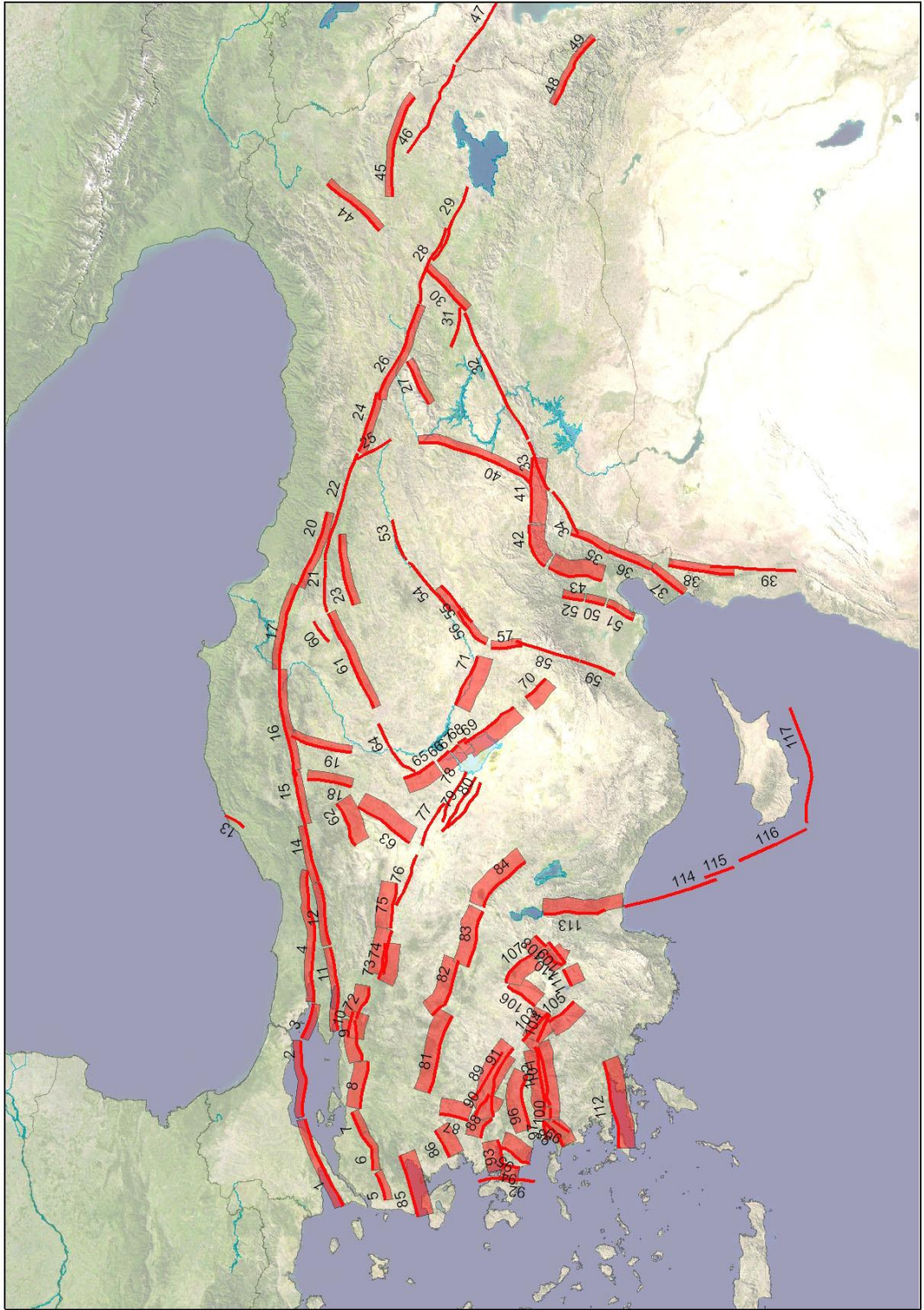


**Figure 3.4-2. Linear faults and projections of down-dip geometry for Turkey**

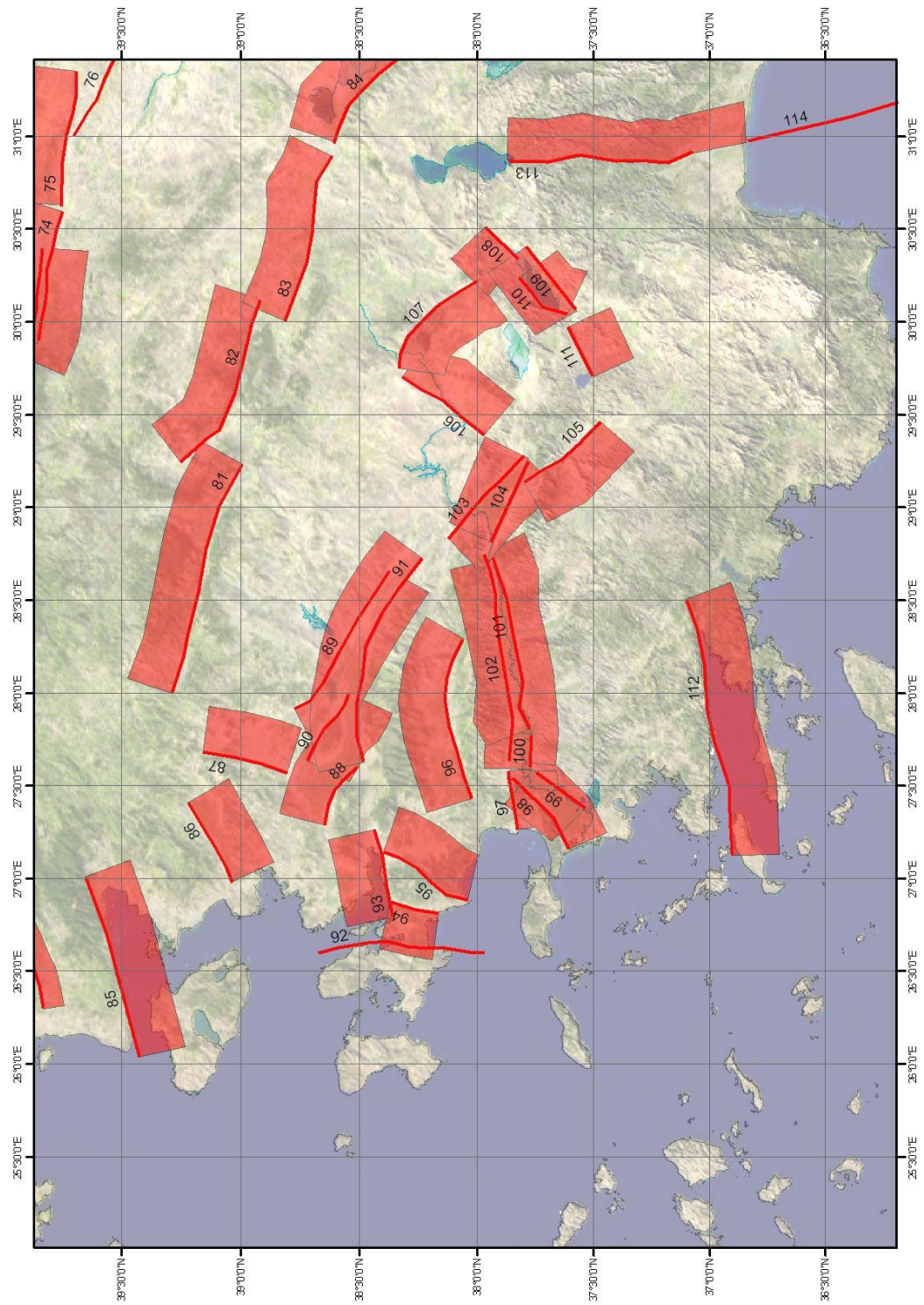


**Figure 3.4-3. Linear faults and projections of down-dip geometry for Turkey (zoomed image on the Western Anatolia Tectonic Province)**

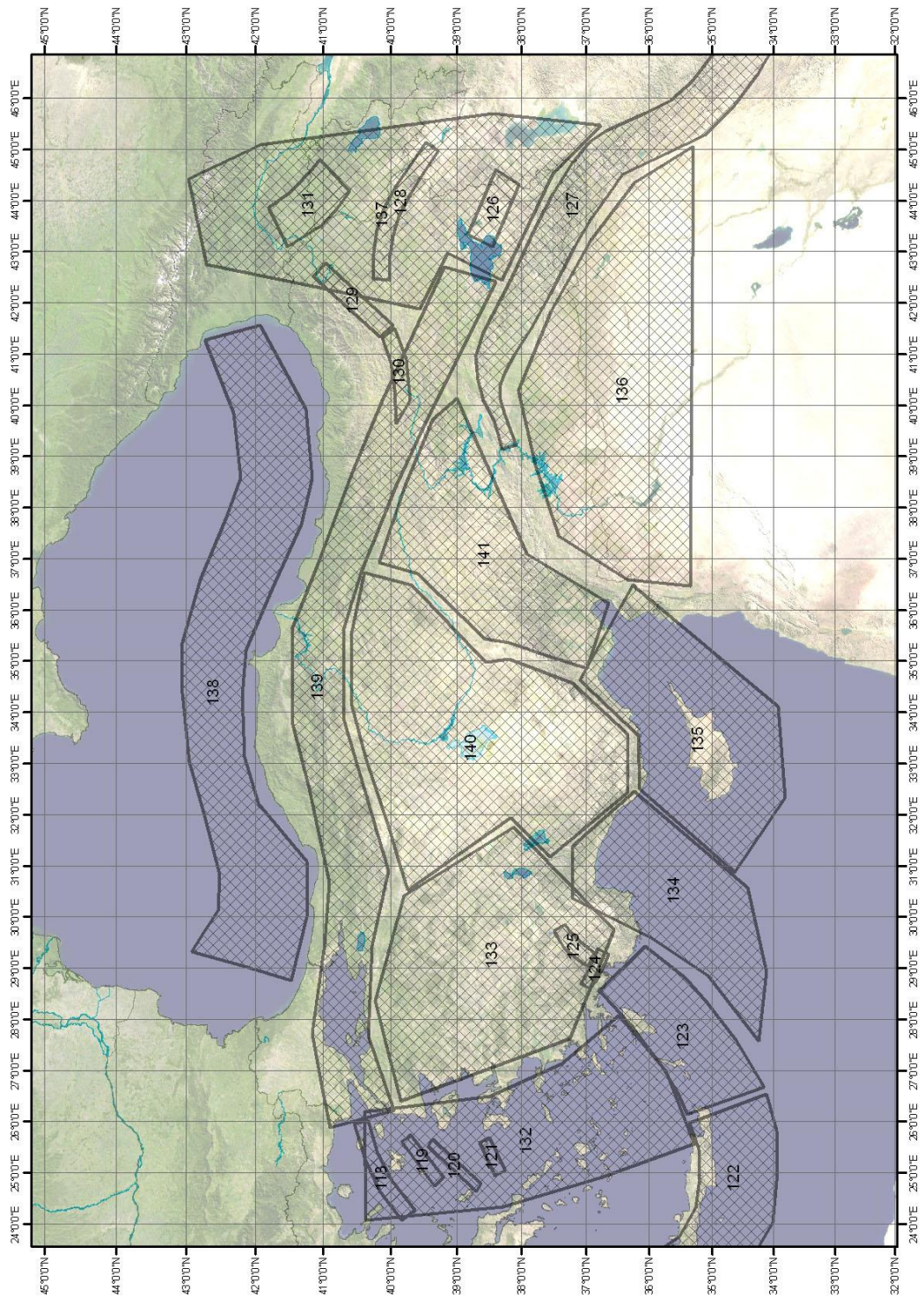


**Figure 3.4-4. Area sources modeled for Turkey**

### 3.5 CALCULATION OF MAXIMUM MAGNITUDES

Calculation of maximum magnitudes for all of 141 sources was completed within a specific framework. Previous knowledge on magnitude-rupture dimension relationships has revealed that moment magnitude of an earthquake is directly related with the length of rupture. Since there is aleatory variability around the estimate of  $M$ , given the exact rupture length; the question to be answered is the selection of number of standard deviations above the median for assigning the maximum earthquake magnitude for that rupture.

Conventional worst-case approach incorporates assigning a value of 2-standard deviations above the median magnitude estimate, since the procedure targets estimation of the extreme value of earthquake magnitude that the fault will generate in its entire lifetime, during the current neotectonic period. Nevertheless, there are no well established rules on defining the “rupture length”, given the total “fault length”. Faults with extremely well studied background information (through stress modeling or historical field evidence) may be an exception for yielding values with less uncertainty. As a general approach, the success of taking the whole fault length or a certain fraction into consideration, and calculating either the median or a higher percentile of moment magnitude for design will directly depend on the fault segmentation preferences.

A series of alternatives considering the rupture length selection and aleatory variability of rupture dimension relationships were studied, and consequent maximum magnitude selections were evaluated in the light of physical limitations and observed distribution of seismicity in the instrumental period. Given the fact that our proposal of truncating the rupture length to the total fault length for the cases which a rupture length (either median or a higher percentile) exceeds the defined fault length in a hazard scenario (please refer to Chapter 5 for software assumptions),

the dependence of  $M_{\max}$  selection on the choice of fault segmentation is once again verified.

Detailed analysis of maximum magnitude earthquake values has yielded the final selection criteria:

- i) Proportion of the total defined fault segment length likely to rupture in the maximum magnitude event is defined by the following piecewise function (Equation 3-5 and Figure 3.5-1):

$$\begin{aligned} \frac{RL}{FL} &= 1 & FL &\leq 30 \text{ km} \\ \frac{RL}{FL} &= \left( \frac{-FL}{45} + \frac{5}{3} \right) & 30 \text{ km} &\leq FL \leq 45 \text{ km} \\ \frac{RL}{FL} &= \frac{2}{3} & FL &\geq 45 \text{ km} \end{aligned} \quad (3-5)$$

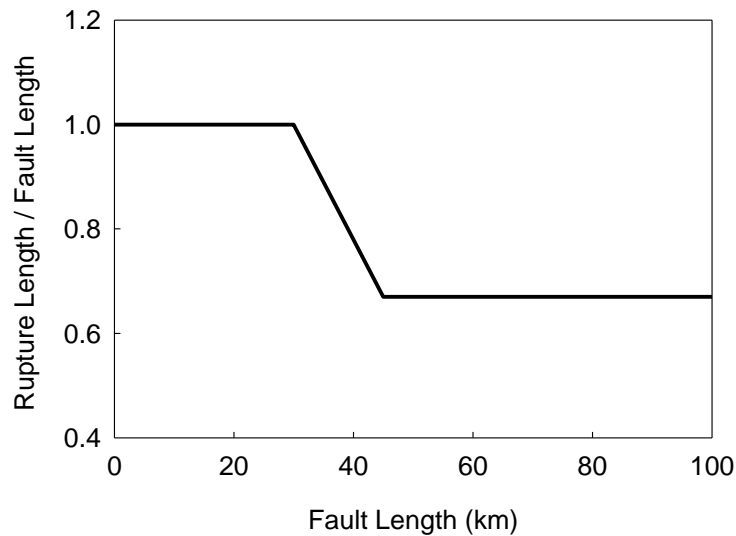


**Figure 3.5-1. Rupture length calculation as a function of total fault length**

- ii) For linear sources,  $M_{\max}$  is calculated as the median + 1 standard deviation value of  $M$ , using rupture length obtained through Equation 3-5. For 21% of the sources, fault length segmentation was modified in an

iterative manner to yield the median magnitude corresponding to the original (unmodified) rupture length, as  $M_{\max}$ . This modification was solely based on expert opinion for the cases applied.

- iii) Re-examining historical seismicity during the last 105 years has assured that the  $M_{\max}$  selection was equal or greater than the observed maximum earthquake,  $M_{\max, \text{obs}}$ .
- iv) For smaller area sources and background seismicity zones,  $M_{\max}$  was calculated as  $M_{\max, \text{obs}} + 0.5$ , representing half magnitude units, or approximately 2-2.5 standard deviations above the median magnitude in widely accepted magnitude – rupture dimension relationships in which rupture area or rupture length is the predictive variable.

Minimum magnitude,  $M_{\min}$  for all sources was chosen to be  $M=4.0$ . List of  $M_{\max, \text{obs}}$  and final  $M_{\max}$  selections for linear and area sources is presented in Tables 3.6-2 and 3.6-3 respectively.

## **3.6 CALCULATION OF RECURRENCE PARAMETERS**

### **3.6.1 Problem Definition**

The last stage in seismic source characterization is the calculation of recurrence parameters for each source. Once the method of selection of parameter calculation through observed seismicity is made, the basic problem of assigning individual events to each source remains to be solved. With vast amount of events automatically excluded from the intersection set after a line-point query, general practice to assign events to sources is to sketch a wider region around linear faults, often in accordance with the spatial density of earthquakes around the fault.



Such a selection intrinsically assumes that delineated sources have some amount of location uncertainty, and attributes the scarcity of the line-point intersection set to a shift (or enlargement) of the location of the source. Even if the rupture propagation for a hazard scenario proceeds in the way it should for a linear source, assessment of recurrence parameters are done in a non-systematic manner. This section attempts to investigate the solution in terms of quantifying the location uncertainty of the earthquakes, instead of using delineated seismic sources.

### **3.6.2 Quantifying Epicenter Location Uncertainty**

The fundamental assumption in quantifying epicenter location uncertainty for a single event is, treating the differences in epicenter estimates of different seismological agencies as a source for epistemic uncertainty. In reality, some of the event parameters reported by different agencies make use of data retrieved from common stations in the global network, while some agencies directly report approved parameter estimates from other networks. Another assumption in quantifying epicenter coordinate uncertainty is treating reported parameters from a single agency as exact estimates; neglecting the order of parameter uncertainty. Combining all these, it can be concluded that epistemic uncertainty of parameters assessed using values reported by different agencies for an event is underestimated at an uncertain degree.

This study utilizes epicenter data compiled from 72 earthquakes included in the strong ground motion database of Turkey (please refer to Chapter 4 for full dataset). Epicenter location uncertainty was computed using one of the agencies, namely the predictions of Kandilli Observatory Earthquake Research Institute (KOERI) as the reference epicenter (Kalafat et al., 2010). Predictions of six reliable networks were used to compute the difference in spherical distances to KOERI predictions. Auxiliary agencies were HRVD (Harvard University), ISC (International Seismological Center, UK), NEIC (National Earthquake Information Center, USGS,

USA), ETHZ (Swiss Seismological Center, Zurich, Switzerland), MEDNET (Mediterranean Very Broadband Seismographic Network) and EMSC (Centre Seismologique Euro-Mediterraneen, France). Data for all 72 events were not present from all agencies, thus calculations were done for the ones that were available. Arithmetic averages of differences between the KOERI prediction and the remaining 6 agencies for each event, plotted against earthquake magnitude  $M$ , is presented in Figure 3.6-1. Apparent reason for events with magnitudes lower than 5.0 having a lower order of average epicentral difference is a result of averaging values of fewer agencies, where the small prediction differences between KOERI and ISC becomes dominant. Since biased underestimation of the error is not desired, this study excludes data from magnitudes lower than 5.0 while finalizing the error magnitude. Table 3.6-1 summarizes the results of 4 functional forms fitted to the data above  $M$  5.0. Of the 4 functions presented, Trial 1 has the greatest likelihood of occurrence. However, data trend, and difference between the predictions of Trial 4 at both magnitude extremes suggest the restriction of average error to a constant value. This value is chosen as 9 km.

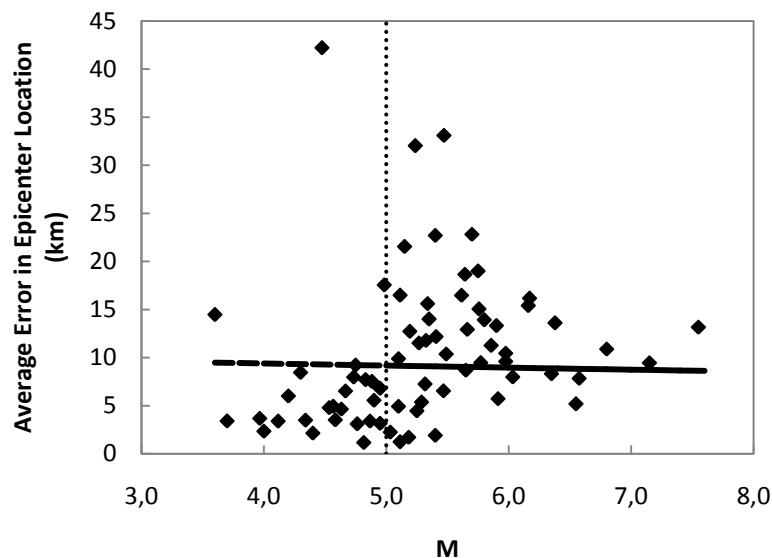


**Figure 3.6-1. Quantifying average error in epicenter location**

**Table 3.6-1. Maximum likelihood estimates for average epicentral distance uncertainty**

Trial #	Trial Function	$\Sigma_{lh}$
1	$\Delta r_{epi} = -1.403 \ln(M) + 14.499$ $\sigma_{\Delta r_{epi}} = 6.86$	-153.845
2	$\Delta r_{epi} = 1.01 \ln(M) + 10.135$ $\sigma_{\Delta r_{epi}} = 40.08 - 19.33 \ln(M)$	-148.547
3	$\Delta r_{epi} = 13.968e^{-0.0257M}$ $\sigma_{\Delta r_{epi}} = 6.86$	-153.837
4	$\Delta r_{epi} = 10.318e^{-0.0236M}$ $\sigma_{\Delta r_{epi}} = 40.815 - 19.74 \ln(M)$	-148.529

Deeper investigation of average difference in epicentral distances as a function of event date revealed the investigated parameter as insignificant. Data were separated into 2 bins, pre-1990 and post-1990 events. The average value of average error in epicentral distances, were found to be 7.9 km and 11.22 km, respectively (Figure 3.6-2). Standard deviations of samples of pre-1990 and post-1990 bins were calculated to be 5.27 km and 8.16 km. A test for values obtained through bins with different sample populations (20 and 52, respectively) were carried out in the following order:

$$\sigma_{\Delta r_{pre1990}} / \sigma_{\Delta r_{post1990}} = 0.646 \quad (3-6)$$

and

$$\sqrt{\frac{N_{pre1990}}{N_{post1990}}} = \sqrt{\frac{20}{52}} = 0.62 \quad (3-7)$$

Equations 3-6 and 3-7 approximately yield the same results, indicating that sample size is insignificant in explaining the difference between the sample standard deviations of values in the pre-1990 and post-1990 bins.

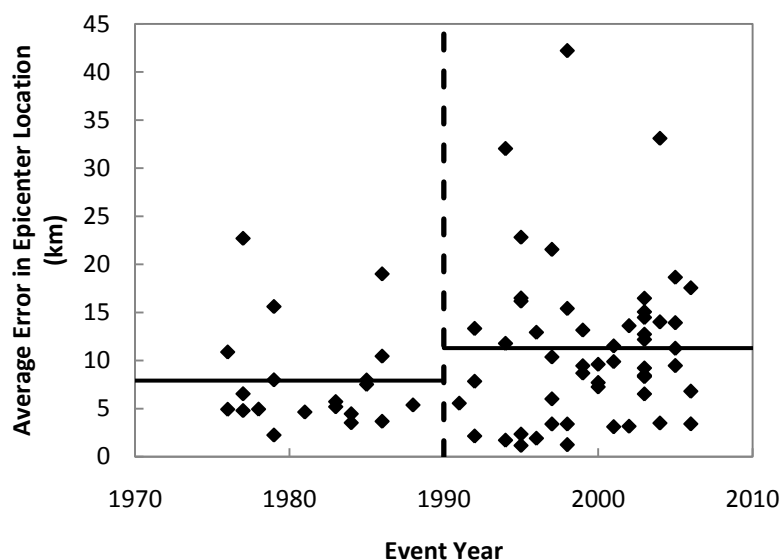


**Figure 3.6-2. Quantifying average error in epicenter location (variation against event date)**

### **3.6.3 Criteria for Assigning Events to Defined Seismic Sources**

Having quantified the average error in epicenter determination as 9 km, spatial queries were made for each defined source geometry; searching for an intersection between the i) surface projections of linear sources (incorporating the down-dip geometry as well) and epicenters with defined buffer zones, and ii) area sources and buffers of event epicenters. Event epicenters were upgraded from a point representation to circles having radii equivalent to the quantified location error. Three different multiples of the calculated 9 km average error was applied to define the buffer zones. Careful interpretation of results using scaling values of 1, 1.5 and 2 revealed that utilizing a scale value of 1.5, hence defining the radii of the buffer

zones around epicenters as 13.5 km established a reasonable balance in assigning some of the off-fault events to defined sources.

Nevertheless, converting point representations of epicenters into buffer zones resulted in the consequence of multiple intersections with seismic source geometry. Any lack of intent towards fixing such a result would have yielded in overrepresented fault activities; with chaotic manipulations at any magnitude range. Hence, the next step involved identification of multiple intersections using a series of custom authored MATLAB code that made use of the spatial query results completed in a geographic information system software package.

The total number of 1004 multiple intersection events were assigned to a single source, manually, using the following procedure (Figure 3.6-3):

- i) For events with large magnitudes, historical seismicity reports were scanned and the event was assigned to the suitable fault.
- ii) For other events, low magnitude earthquakes that were likely to be the aftershocks of a larger magnitude earthquake were identified. This was accomplished by examining the metadata of large magnitude events having close dates to the likely aftershocks. If a match was found, lower magnitude events with multiple source intersections were assigned to that source, for prospective aftershock filtering process.
- iii) If any evidence of aftershock identification was not found, events were distributed according to their proximities to each intersecting source.
- iv) For offshore area sources such as the intersection zone of Aegean Arc and Pliny-Strabo Trenches, intersecting events consisting of a large dataset were distributed evenly between the sources, ensuring that the magnitude distributions of two sets were as close as possible.

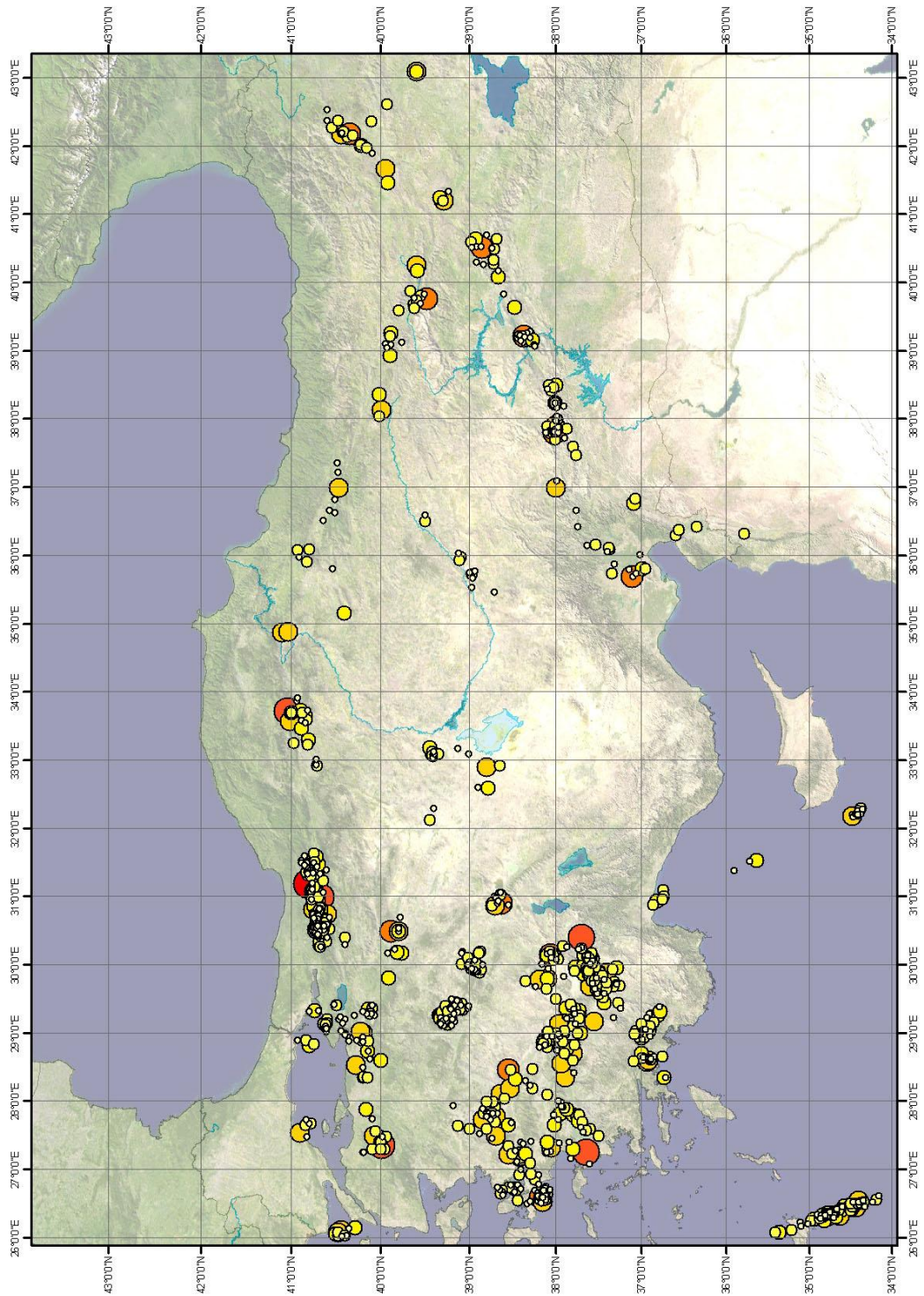


**Figure 3.6-3. Distribution of events with multiple source intersections**

The framework introduced so far worked successfully for strike-slip faults, however, extra measures had to be taken for horst-graben systems in Western Anatolia. Distribution of events having multiple intersections with seismic sources is zoomed in to the Western Anatolia region in Figure 3.6-4. Factors such as presence of narrow grabens as compared to the order of uncertainty assigned to the events, and characteristics of faults shallowly dipping towards each other at the boundaries of horst-graben systems prevents the utilization of above criteria, for the determination of recurrence parameters. A structurally reasonable workaround to this problem was found through merging facing faults of a host-graben system in every valley. The recurrence parameters were calculated using a single (merged) dataset for the faults in the same graben system, and the resulting total activity from the recurrence analysis was distributed to the defined segments, in proportional to segment lengths. Such a proposal is found to be meaningful, considering that longer faults accumulate larger strain energy over time, and are likely to be more active than shorter faults.

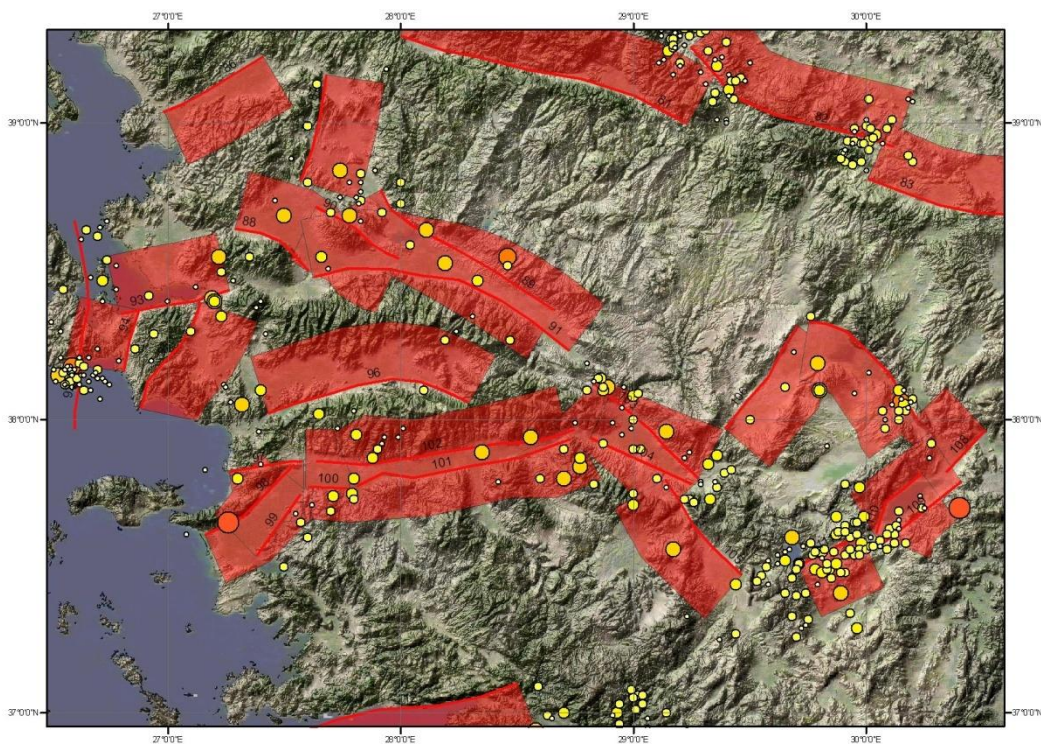


**Figure 3.6-4. Multiple source intersections at Western Anatolia**

The proposal for horst-graben systems was applied for Burdur, Çivril-Dinar, Denizli, Büyük Menderes and Turgutlu-Alaşehir systems individually (Tables 3.6-2 and 3.6-3).

A similar problem also existed for linear faults in regions where recorded seismicity was relatively low. For those cases, running independent regressions on separated catalogues with sparse datasets yielded in unreasonable results in adjacent segments of the fault. Once more, the seismicity catalogues for those regions were merged and the resulting fault activity was distributed as a function of segment length, between each fault. This procedure was applied to Çan Fault, Demirtaş Fault, Bolu-Abant Fault, Tosya Fault, Gölbaşı and Narlı Faults, Kahramanmaraş-Islahiye and Islahiye Kırıkhan Faults, Dead Sea Fault, Sürgü and Göksun Faults, Yüksekova Fault, Sivas-Karakuz and Karakuz-Felahiye Faults, Subaşı-Karakaya, Yahyalı-Subaşı and Mersin Yahyalı Faults, Sungurlu Fault, Tuz Gölü Fault, Bozüyük Fault, Eskişehir Fault and finally, Cihanbeyli Fault (Tables 3.6-2 and 3.6-3).

#### **3.6.4 Choice of Regression Method**

Two methods are available for predicting the recurrence parameters of each source, the ordinary least squares method and the maximum likelihood method. In the ordinary least squares regression, regression parameters are obtained so that the sum of squares of the differences between the observed and estimated values is minimized. This method does not make any distinction between the data points in the entire magnitude range, thus data from a rare event may shift predicted values from the observed ones in the low magnitude range, compared to the maximum likelihood method. In the maximum likelihood method, the procedure involves maximizing the likelihood of fit of the predicted function to the observed data (Weicherdt, 1980). Such framework ensures that the residuals between the predicted function and the observed values are minimal at the lower bound magnitudes.



Restating the fact that low magnitude events happen more frequently than larger extremes for the seismic source, choosing the maximum likelihood methodology inherently leads to relying on trend generated by lower magnitude earthquakes. Thus, the return period of large magnitude events from the model predictions become dependent on the trend of lower magnitude data. Ensuring that the return rates of large events, computed using the more pronounced effect of more frequent events are supported by other tectonic evidence (annual slip rate, for instance), this trade off yields to be a reasonable choice. Another point worth mentioning is the choice of predicted variable. If the optimization is done on “logarithm of annual number of events greater than or equal to  $M$ ”, than the difference between the predictions of ordinary least squares (LSE) and maximum likelihood method (MLE) diminishes. This study involves optimizing “annual number of events greater than or equal to  $M$ ”. Previous studies have proved that the slope of the recurrence relation, “ $b$ ” generally lies between 0.8 and 1.2 for active crustal zones. Results of optimizations using both methods have generally produced more reasonable values for “ $b$ ”, when the maximum likelihood estimate was used. Figure 3.6-5 shows a case for Dinar source. The thin black series is ordinary least squares estimate, having “ $a$ ” value of 4.139 and “ $b$ ” value of 1.0. For the maximum likelihood estimates, “ $a$ ” and “ $b$ ” values are 3.305 and 0.814, respectively.

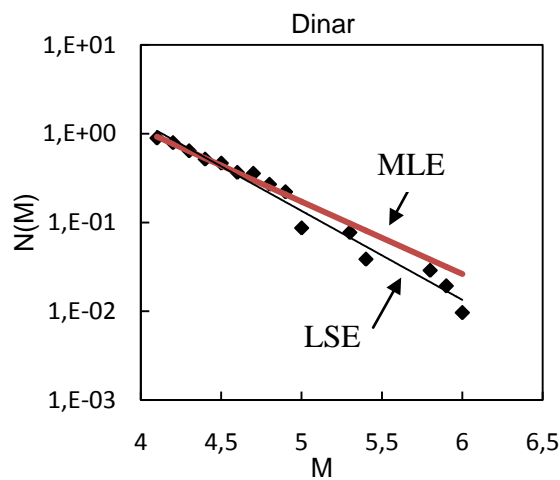


**Figure 3.6-5. Recurrence parameters obtained through MLE and LSE for Dinar**

### 3.6.5 Aftershock Filtering

Aftershock filtering of events from each source was completed manually. Automated time-space window algorithms proposed by Gardner and Knopoff (1974), Prozorov and Dziewonski (1982), Savage and Rupp (2000), and Kagan (2002a) were not utilized. Figure 3.6-6 presents least squares and maximum likelihood estimates of recurrence parameters, before and after dependent events were removed. MLE estimate of “a” and “b” before any removal process (catalogue completeness correction had already been applied) were calculated to be 4.65 and 1.14 respectively. These values were altered to 3.71 and 0.99.

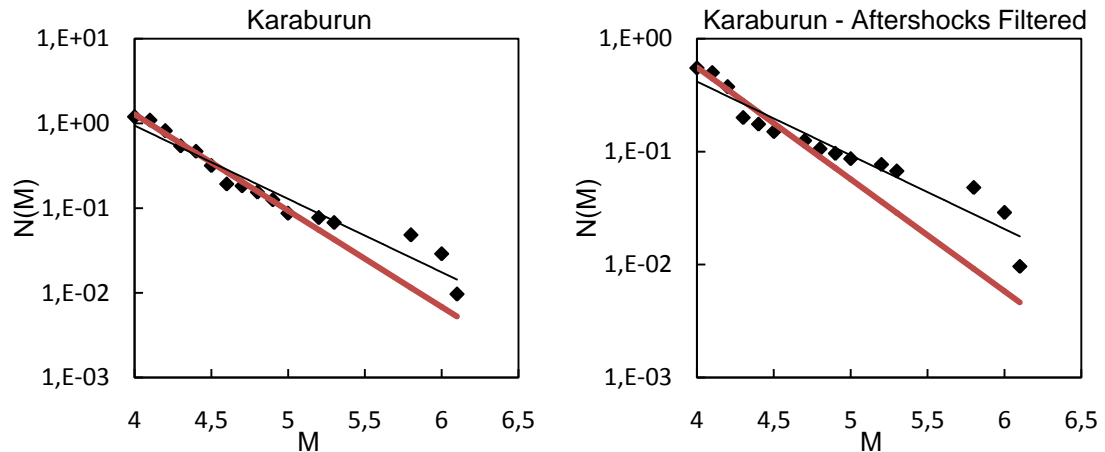


**Figure 3.6-6. Effect of aftershock filtering on recurrence parameters of Karaburun Segment.**

In the dataset, there were two fault segments identified, without any instrumental seismicity assigned on them. For Avanos Fault, “b” value was assumed to be the same “b” value for the nearby Kayseri-Tatlıpınar Fault, and the activity parameter was halved. Same procedure was applied for Sivrihisar Fault. The reference fault for completing missing parameters for Sivrihisar Fault was chosen to be Cihanbeyli Fault.

Having completed all processing related with seismic source characterization of faults, key parameters are presented in Table 3.6-2 for linearly characterized segments, and Table 3.6-3 for area sources. Recurrence plots of all sources are presented in Appendix B. Explanation of abbreviations are as follows:

For identification of the major fault system, or the neotectonic province that the source belongs to; the following were used:

- NAFZ: North Anatolian Fault Zone. Splay faults from the NAFZ were also included under this tagging.
- EAFZ: East Anatolian Fault Zone. Parallel faults to the EAFZ near the south border (Adana, Ceyhan, Osmaniye regions) were also tagged as EAFZ.
- NA: North Anatolian Tectonic Province. Bartın Fault is included under this group.
- EA: Eastern Anatolian Province. Strike-slip fault systems in Eastern Anatolia and sources in Southeastern Anatolia were included in this group. Faults, forming the boundary between the NA and EA, were chosen to be tagged under the topic EA.
- CA: Central Anatolian Province. Faults along the boundary beginning from İnönü Fault to Isparta Angle were also included under this group.
- EX: Western Anatolia Extensional Province.
- OS: OS stands for offshore faults, generally characterized as area sources.
- BG: BG stands for the background seismicity zones throughout continental and offshore Anatolia.

**Table 3.6-2. Summary of source characterization for linear segments**

ID Number	Name	Tectonic Setting	FL (km)	$M_{\max, \text{obs}}$	$M_{\max}$	LSE a	LSE  b	MLE a	MLE  b
1	Mürefte	NAFZ	128	6.9	7.3	2.21	0.62	2.53	0.69
2	Marmara (W)	NAFZ	104	5.7	7.5	3.86	1.05	4.37	1.16
3	Marmara (E)	NAFZ	49	6.2	7.1	2.36	0.75	3.91	1.09
4	Adapazarı	NAFZ	178	7.5	7.5	1.89	0.53	4.11	1.02
5	Çan-A	NAFZ	39	6.8	7.1	1.63	0.55	1.79	0.58
6	Çan-B	NAFZ	54	6.8	7.1				
7	Çan-C	NAFZ	35	6.8	7.1				
8	M.K.Paşa	NAFZ	66	6.2	7.1	2.08	0.67	3.44	0.97
9	Bursa	NAFZ	57	5.7	7.2	2.72	0.79	5.67	1.47
10	Demirtaş	NAFZ	36	5.7	7.1				
11	İznik	NAFZ	114	4.8	7.5	8.06	2.12	9.30	2.40
12	Mudurnu-Abant	NAFZ	86	6.7	7.4	3.31	0.81	3.72	0.90
13	Bartın	NA	30	6.0	7.1	2.28	0.74	3.38	0.98
14	Bolu-Abant (W)	NAFZ	77	5.3	7.3	1.07	0.47	1.02	0.46
15	Bolu-Abant (E)	NAFZ	74	6.6	7.3				
16	Tosya (W)	NAFZ	146	6.8	7.7	2.58	0.70	2.43	0.66
17	Tosya (E)	NAFZ	116	5.6	7.5				
18	Orta	NAFZ	61	6.0	7.2	1.69	0.64	7.98	2.10
19	Çankırı	NAFZ	85	5.8	7.2	2.37	0.75	3.20	0.94
20	Niksar	NAFZ	106	6.7	7.5	0.94	0.46	2.44	0.80
21	Amasya-Erbaa*	NAFZ	69	5.4	7.1	4.41	1.20	5.53	1.45
22	Koyulhisar	NAFZ	151	6.0	7.7	1.52	0.57	1.61	0.59
23	Tokat	NAFZ	98	6.7	7.1	0.06	0.30	2.56	0.88
24	Suşehri-Erzincan	NAFZ	84	5.9	7.4	2.23	0.80	1.82	0.71
25	Suşehri-Akkaya	NAFZ	54	6.2	7.2				
26	Erzincan	NAFZ	142	7.6	7.7	2.54	0.64	2.81	0.69
27	Ovacık	NAFZ	67	5.3	7.2	1.22	0.59	1.02	0.55
28	Erzincan-Varto	NAFZ	112	6.0	7.1	3.06	0.76	2.20	0.57
29	Erzincan-Van	NAFZ	113	6.0	7.5	2.87	0.82	2.89	0.82
30	Bingöl	EAFZ	80	6.1	7.4	2.39	0.71	2.34	0.70
31	Bingöl-B	EAFZ	57	6.4	7.2	1.38	0.55	2.11	0.71
32	Hazar	EAFZ	197	6.0	7.5	4.13	1.01	4.70	1.14
33	Gölbaşı	EAFZ	74	5.3	7.3	5.85	1.49	4.39	1.15
34	Narlı	EAFZ	71	4.8	7.3				
35	K.Maraş-İslahiye	EAFZ	61	5.3	7.2	2.61	0.80	2.03	0.67
36	İslahiye-Kırıkhan	EAFZ	65	5.1	7.3				
37	Kırıkhan-Antakya	EAFZ	59	5.6	7.2	2.02	0.70	2.23	0.74
38	Dead Sea-A	EAFZ	96	4.5	7.5	1.78	0.75	1.78	0.75
39	Dead Sea-B	EAFZ	126	4.5	7.3				
40	Malatya	EAFZ	169	5.3	7.3	2.73	0.83	4.11	1.13

**Table 3.6-2. (continued) Summary of source characterization for linear segments**

ID Number	Name	Tectonic Setting	FL (km)	$M_{max, obs}$	$M_{max}$	LSE a	LSE  b	MLE a	MLE  b
41	Sürgü	EAFZ	92	6.0	7.4	3.85	0.98	4.62	1.15
42	Göksun	EAFZ	65	5.5	6.9				
43	Osmaniye	EAFZ	79	5.7	7.1	3.70	0.99	5.09	1.31
44	Horasan	EA	96	6.5	7.2	2.93	0.75	3.07	0.79
45	Ağrı	EA	142	5.7	7.3	2.59	0.77	2.83	0.82
46	Çaldıran	EA	141	6.3	7.4	2.50	0.71	2.00	0.60
47	Çaldıran-B	EA	141	6.3	7.6	3.87	1.01	2.93	0.79
48	Yüksekova-A	EA	58	5.9	7.1	2.91	0.86	4.14	1.14
49	Yüksekova-B	EA	53	5.9	7.2				
50	Ceyhan-A	CA	28	6.0	7	2.93	0.86	5.51	1.45
51	Ceyhan-B	CA	44	5.6	7.1	4.92	1.34	4.90	1.31
52	Kozan-Göksun	CA	31	5.4	7.1	1.91	0.73	2.06	0.76
53	Sivas-Karakuz	CA	59	4.9	7.2	4.29	1.20	4.29	1.20
54	Karakuz-Felahiye	CA	89	4.9	7.1				
55	Kayseri-Tatlıpınar	CA	66	4.9	7.1				
56	Subaşı-Karakaya	CA	62	4.9	7				
57	Yahyalı-Subaşı	CA	44	5.4	7				
58	Mersin-Yahyalı	CA	94	5.6	7.4	2.07	0.75	1.22	0.56
59	Mersin-Pozantı	CA	53	5.6	7.2	1.71	0.66	2.16	0.76
60	Çorum-Amasya	CA	34	6.9	7.1				
61	Sungurlu	CA	143	5.7	7.1	* (Merged with ID No. 21)			
62	Güdül	CA	63	4.4	7.1	5.34	1.58	5.34	1.58
63	Kazan	CA	86	4.8	7.2	4.32	1.32	4.32	1.32
64	Kırıkkale	CA	85	5.3	7.1	2.14	0.76	1.49	0.62
65	Bala	CA	49	5.4	6.9	3.96	1.12	3.06	0.90
66	Tuz Gölü-A	CA	21	4.4	6.9	7.30	2.01	7.30	2.03
67	Tuz Gölü-B	CA	13	4.4	6.7				
68	Tuz Gölü-C	CA	14	4.4	6.7				
69	Tuz Gölü-D	CA	85	4.4	7.1				
70	Niğde	CA	39	4.2	7	6.00	1.76	6.00	1.74
71	Avanos**	CA	74	-	7.1	2.15	1.20	2.15	1.20
72	İnönü	CA	48	5.3	7.1	4.80	1.32	4.80	1.30
73	Bozüyük	CA	51	6.2	7.1	2.12	0.65	1.62	0.54
74	Eskişehir-A	CA	61	6.2	7.2				
75	Eskişehir-B	CA	63	5.3	7.2				
76	Sivrihisar**	CA	76	-	7.2	1.33	0.85	1.10	0.75
77	Cihanbeyli-A	CA	68	5.5	7.1	2.65	0.85	2.20	0.75
78	Cihanbeyli-B	CA	77	5.5	7.1				
79	Cihanbeyli-C	CA	88	5.5	7.1				
80	Cihanbeyli-D	CA	80	5.5	7.2				
81	Kütahya	CA	112	6.0	7.2	5.76	1.31	5.76	1.30

**Table 3.6-2. (continued) Summary of source characterization for linear segments**

ID Number	Name	Tectonic Setting	FL (km)	$M_{\max, \text{obs}}$	$M_{\max}$	LSE a	LSE  b	MLE a	MLE  b
82	Emet	CA	87	6.2	7.1	5.14	1.13	5.14	1.15
83	Afyon	CA	81	6.0	7.1	2.58	0.75	3.85	1.03
84	Akşehir	CA	88	6.5	7.3	2.75	0.75	2.81	0.75
85	Edremit	EX	87	6.7	7.3	2.07	0.62	4.33	1.12
86	Bergama	EX	43	6.9	7.1	1.20	0.53	4.04	1.17
87	Kırkağaç	EX	41	6.0	7.1	3.91	1.01	4.49	1.13
88	Manisa	EX	33	5.5	6.8	3.10	0.81	3.43	0.88
89	Akhisar	EX	80	6.1	7.3				
90	Akhisar-B	EX	37	5.5	7				
91	Turgutlu-Alaşehir	EX	104	6.1	7.4				
92	Karaburun	EX	79	6.1	6.9	2.23	0.65	3.71	0.99
93	İzmir	EX	42	5.8	7.1	3.08	0.82	2.82	0.77
94	Urla	EX	23	6.0	6.9	1.59	0.62	6.56	1.72
95	Seferihisar	EX	47	6.0	6.9	1.95	0.62	2.60	0.77
96	K. Menderes	EX	79	6.3	6.9	1.88	0.63	3.27	0.94
97	Selçuk	EX	28	4.3	7	2.68	0.70	3.02	0.78
98	Söke	EX	44	6.5	7				
99	B. Menderes-(S)-A	EX	29	5.8	7.1				
100	B. Menderes-(S)-B	EX	16	5.8	6.8				
101	B. Menderes-(S)-C	EX	84	5.8	7.4				
102	B. Menderes-(N)	EX	99	5.8	7.1				
103	Denizli-Buldani-(N)	EX	53	5.6	7.2	3.53	0.89	2.86	0.74
104	Denizli-South	EX	42	5.6	7.1				
105	Denizli-Yumrutaş	EX	47	5.6	7.1	3.24	0.88	2.78	0.78
106	Çivril	EX	48	5.9	7.1	4.14	1.00	3.31	0.81
107	Dinar	EX	58	6.0	7.1				
108	Gönen-Burdur	CA	22	6.6	6.9	3.13	0.84	3.84	0.98
109	Burdur	CA	38	6.6	7.1				
110	Burdur-North-A	CA	30	6.6	7.1				
111	Burdur-North-B	CA	26	6.6	7	4.61	1.09	4.61	1.11
112	Muğla	EX	125	6.3	7.2	4.63	1.03	4.63	1.03
113	Isparta-Antalya	CA	90	5.9	7.1	3.41	0.93	4.86	1.26
114	Antalya-Med. S.-A	OS	140	5.9	7.4	3.56	0.93	3.95	1.02
115	Antalya-Med. S.-B	OS	46	5.0	7.1				
116	Med.-W. of Cyprus	OS	111	6.5	7.5	2.12	0.68	4.66	1.24
117	Cyprus Arc	OS	175	6.3	7.3	4.25	1.14	4.25	1.14

**Table 3.6-3. Summary of source characterization for area sources**

ID Number	Name	Tectonic Setting	$M_{\max, \text{obs}}$	$M_{\max}$	LSE a	LSE  b	MLE a	MLE  b
118	Aegean Sea-A	OS	6.2	6.7	4.76	1.08	4.76	1.06
119	Aegean Sea-B	OS	6.2	6.7	4.29	1.05	3.39	0.85
120	Aegean Sea-C	OS	6.8	7.3	3.48	0.86	5.39	1.27
121	Aegean Sea-D	OS	5.8	6.3	4.80	1.19	4.80	1.17
122	Aegean Arc	OS	7.3	7.8	5.96	1.14	5.96	1.16
123	Pliny-Strabo Trenches	OS	6.8	7.3	5.67	1.10	5.67	1.12
124	Köyceğiz	CA	5.4	5.9	5.09	1.22	5.09	1.23
125	Burdur-Fethiye	CA	6.0	6.5	4.73	1.15	5.06	1.22
126	Van-Başkale	EA	7.1	7.6	3.77	1.00	2.73	0.76
127	Bitlis-Zagros	EA	6.7	7.2	4.89	1.03	4.88	1.04
128	Iğdır-Doğubayazıt	EA	6.1	6.6	3.75	0.96	3.55	0.91
129	Narman	EA	6.2	6.7	3.83	0.94	3.04	0.77
130	Erzurum	EA	6.0	6.5	3.67	0.93	3.47	0.88
131	Caucasus	EA	6.2	6.7	3.67	0.87	2.21	0.55
132	BG (Aegean Sea)	BG	7.2	7.7	5.12	1.00	5.12	1.01
133	BG (W. Anatolia Ext.)	BG	6	6.5	3.99	0.88	3.81	0.84
134	BG (W. Mediterranean)	BG	6.5	7	3.98	0.88	4.14	0.91
135	BG (E. Mediterranean)	BG	6.3	6.8	4.26	0.95	5.15	1.16
136	BG (SE Anatolia)	BG	5.9	6.4	3.99	0.96	4.69	1.12
137	BG (EAFZ)	BG	7.1	7.6	3.82	0.81	3.81	0.80
138	BG (Black Sea)	BG	5.5	6	2.90	0.80	2.08	0.62
139	BG (NAFZ)	BG	6.5	7	3.51	0.77	3.27	0.72
140	BG (C. Anatolia-A)	BG	6.4	6.9	3.36	0.82	3.15	0.77
141	BG (C. Anatolia-B)	BG	6.5	7	4.01	0.98	4.17	1.01

## **CHAPTER 4**

### **GROUND MOTION PREDICTION MODEL USING DATA FROM TURKISH STRONG GROUND MOTION DATABASE**

#### **4.1 MOTIVATION AND SCOPE**

##### **4.1.1 Current State of Ground Motion Prediction Models**

This chapter develops a ground motion prediction model (GMPE), by using strong ground motion records from Turkey. The most basic definition for a GMPE covers the estimation of a selected ground motion intensity parameter as a function of earthquake magnitude, source to site distance, soil type and other predictive parameters where applicable. Numerous strong ground motion prediction models have been developed for various regions of the world, incorporating data retrieved from local and/or global earthquakes. Douglas (2001) compilation of GMPE models until year 2000 covers the historical development of the concept, including but not limited to the improvements in addressing aleatory variability in predictions, introduction of additional source parameters, and the predicted parameter itself. Type of estimated ground motion intensity parameter has flourished from intensity measures to peak ground acceleration, until the introduction of spectral parameters as well as peak ground velocity began to meet the rising demands of modern structural design methodologies.



With the dissemination of the world-wide strong ground motion networks, data collected per unit time have rapidly burst. Such collection of data, especially after the 1997 series of ground motion prediction models developed for Western US (Abrahamson and Shedlock, 1997), initiated extensive efforts for the compilation of local datasets from various regions of the world. Although record processing and systematic parameter estimation of local databases have assisted the expansion of global datasets, developing GMPE's using isolated local sets has brought up important topics of discussion. This study does not intend to bring the debate of strong ground motion characteristics between shallow crustal zones and subduction zone events (as modeled by Atkinson 1997; Atkinson and Boore, 2003). The focus of attention is the debate concerning the strong ground motion variation within similar tectonic environments.

A similar discussion was based on the findings of Gülkan and Kalkan (2002), later revised in Kalkan and Gülkan (2004); as well as Ulusay et al., (2004) and Özbey et al. (2004). The major conclusion of models developed using earthquakes from Turkey is lower ground motion intensity in median predictions, compared with GMPE's developed using global datasets. Apparent explanation of this property is the low intensity of ground motion motions from the 1999 Kocaeli and Düzce events at near-fault sites (Erdik and Durukal, 2001; Akkar and Gülkan, 2002). As will be presented in proceeding sections, number of events from 1999 Kocaeli and Düzce events is remarkably high in proportion, to the total number of data in the Turkish strong ground motion catalogue; posing an impact on predicted median ground motion intensities.

The Next Generation Attenuation (NGA) project (Power et al., 2008) has been the second wave in evoking re-evaluation of the GMPE's developed from European data. NGA - European GMPE compatibility in general terms has been verified by Campbell and Bozorgnia (2006), Stafford et al. (2008) and Scasserra et al. (2009);

however Bommer et al. (2010) stress the considerable differences between median predictions.

Another emerging subject of concern is the lower bound magnitude selection in GMPE's (Douglas, 2003a; and Bommer et al., 2007). This study leaves related discussion towards the end of the chapter.

Of the several leaps that NGA project has brought into attention, attempts on correct addressing of epistemic uncertainties, and aleatory variability terms come one step forward. A significant amount of effort has been put into quantifying the contributing sources of aleatory variability term, sigma; including modeling parameter uncertainty (Moss and Kiureghian, 2006) and providing complete definition for sources of variability in a ground motion (Atik et al., 2010).

Integrating more complex models for site response, introduction of additional parameters in the functional form, and discussions on defining the horizontal component of ground motions within the NGA project are valuable contributions to the current state of research and practice in the field.

Glancing back to the Turkish strong ground motion catalogue, a substantial effort has recently been put in record processing, evaluation of source and source-path parameters. Result of the study by Akkar et al. (2010) has enabled the public domain online access to the processed data.

#### **4.1.2 Scope of Current Study**

Chapter 4 of the current study focuses on developing a GMPE using data from strong ground motion database of Turkey. The empirical ground motion prediction model includes, i) enhanced representation of uncertainty regarding source (M) and path (source-to-site distance) parameters, ii) discussion about definition of horizontal

component of ground motion, iii) framework for site characterization for cases which detailed site information is missing, iv) development of a ground response model as a continuous function of peak ground acceleration and  $V_{s,30}$ ; average shear wave velocity at the top 30 m, and v) application of a weighting scheme for avoiding choice based sampling bias in the predicted parameter.

The model also include discussions of style of faulting, possible integration of hanging wall component into functional form, representation of the aleatory variability term as a function of one or more of predictive parameters (heteroscedastic sigma).

Chapter 4 progressively examines all of the issues listed above, concluding with the presentation of the final form of the equation, providing a comparison with local and global models in the light of topics pronounced in Section 4.1.1.

More specifically, the evolution path of the proposed model includes the following steps, listed in an easily traceable format:

- i) Compilation of raw accelerometric data, extracted from the complete suite of strong ground motion records from Turkey. Data include strong ground motions from shallow crustal regions.
- ii) Processing of horizontal strong ground motion records, computation of peak and 5% damped elastic spectral parameters.
- iii) Investigating the relationship between different definitions of horizontal component of ground motions in the Turkish dataset, and comparison with findings from published literature. This step also involves quantifying uncertainty of spectral values of ground motion intensity due to random orientation of horizontal components.

- iv) Quantifying parameter uncertainty in earthquake magnitude, using estimates of different seismological agencies operating worldwide.
- v) Quantifying parameter uncertainty in source to site distance,  $R$ , using analytical simulations of variable rupture dimensions and location of rupture along the fault. Review of relationships among different definitions of source to site distance.
- vi) Parameterizing style of faulting, investigation on hanging wall effects.
- vii) Modeling local ground response effects; using data retrieved from stations of which limited information on local site characteristics is available.
- viii) Developing a ground response model as a continuous function of maximum component of ground acceleration and average shear wave velocity of the upper 30 m, namely  $V_{s30}$ . Comparison of available models with recently developed alternatives in the literature.
- ix) Applying a weighting scheme to avoid choice-based sampling bias in the dataset, allowing homogenous representation of data from all magnitude and distance bins in the dataset. This framework enables a statistical treatment for datasets compiled from local events, having non-uniform distribution throughout their key predictive parameters.

## **4.2 DATA PROCESSING**

### **4.2.1 Event Selection and Initial Screening Criteria**

The current section covers brief explanation about the initial criteria for strong ground motion selection that is to be included in the dataset, as well as compilation of relevant parameters such as magnitude, focal depth and site characteristics. The study aims to predict the ground motion parameters for moderate to large magnitude earthquakes, as far as the damage producing capability of such events is concerned. The current effort tends to avoid inclusion of strong ground motion parameters having very small magnitudes into the calculations. However, this rule is systematically defined as a function of earthquake magnitude.

At the time of database compilation, a true relational database composed of processed local ground motion records was not available, thus previous empirical studies such as Kalkan and Gülkan (2004), Özbey et.al (2004), Ulusay et al. (2004), were taken as references while selecting which events and records to include into the dataset. The results, were sceptically reviewed using the ERD (General Directorate of Disaster Affairs – Earthquake Research Department, recently re-organized as AFAD – Disaster and Emergency Management Agency) raw dataset. Ground motion records belonging to KOERI (Bosphorus University – Kandilli Observatory and Earthquake Research Institute and İTÜ (İstanbul Technical University) arrays, as well as temporary stations established by IRIGM (Universite Joseph Fourier, Grenoble, France) and LDEO (Lamont-Doherty Earth Observatory, Columbia University, USA) after, 1999 Kocaeli and Düzce earthquakes for cases which the initial criteria were met.

Initial criteria can be summarized as follows:

Assuming that all the other data are considered as correct (or reliable), include the record to the dataset if;

- i) Any of the two horizontal components of recorded (raw) acceleration is larger than 0.05 g, regardless of earthquake magnitude.
- ii) Any of the two horizontal components of recorded (raw) acceleration is larger than 0.03 g, provided that reported magnitude (still not converted to moment magnitude) is greater than or equal to 5.0.
- iii) Any of the two horizontal components of recorded (raw) acceleration is larger than 0.02 g, provided that reported magnitude (still not converted to moment magnitude) is greater than or equal to 5.5.
- iv) For Kocaeli and Düzce records, few exceptions were tolerated and records having unprocessed absolute acceleration values slightly smaller than 0.02 g were still included.

The unorganised ERD catalogue, which was personally obtained from GDDA digitally, was thoroughly searched as a final screening, to be sure that any useful data had not been accidentally skipped. Apparent aftershock motions from 20 events were filtered out from the dataset. The final list of events includes 179 recordings from 72 events.

Current set is considered to represent earthquake ground motion levels that have created light to heavy damage in the past, and are likely to do so for future events. Basically, the dataset consists of records from large and moderate magnitude earthquakes, and some from small magnitude events that have produced ground

motions which are worth including into the dataset. Table 4.2-1 presents list of events, which were eligible for further investigation. Table 4.2-2 contains the exclusions from the dataset, as a consequence of aftershock identification. Listed magnitudes are mean parameter estimates for moment magnitude; fully explained in Section 4.2.3.

**Table 4.2-1. Event list for GMPE dataset, composed of records which passed first screening**

EQID	YEAR	MO/DY	Time (GMT)	Earthquake Name	M	Number of Recordings
1	1976	08/19	01:12:40	Denizli	5.10	1
2	1976	11/24	12:22:00	Çaldıran	6.80	1
3	1977	10/05	05:34:43	Çerkeş	5.40	1
4	1977	12/09	15:53:37	İzmir	4.53	1
5	1977	12/16	07:37:29	İzmir	5.47	1
6	1978	09/21	19:37:48	Malatya	4.57	1
7	1979	04/11	12:14:27	Muradiye	5.03	1
8	1979	05/28	09:27:33	Bucak	6.03	1
9	1979	07/18	13:12:23	Dursunbey	5.34	1
10	1981	06/30	07:59:08	Hatay	4.63	1
11	1983	07/05	12:01:27	Biga	5.91	3
12	1983	10/30	04:12:28	Horasan-Narman	6.55	2
13	1984	03/29	00:06:01	Balıkesir	4.58	1
14	1984	06/17	07:48:00	Foça	5.25	1
15	1985	08/12	02:54:44	Kığı	4.88	1
16	1985	12/06	22:35:29	Köyceğiz	4.73	1
17	1986	05/05	03:35:38	Malatya	5.98	1
18	1986	06/01	06:43:09	Kuşadası	3.97	1
19	1986	06/06	10:39:47	Sürgü (Malatya)	5.75	2
20	1988	04/20	03:50:07	Muradiye	5.29	1
21	1991	02/12	09:54:58	İstanbul	4.90	1
22	1992	02/12	15:55:11	Amasya	4.40	1
23	1992	03/13	17:18:39	Erzincan	6.58	3
24	1992	11/06	19:08:09	Seferihisar	5.90	3
25	1994	01/03	21:00:30	İslahiye	5.18	1
26	1994	05/24	02:05:36	Girit	5.33	1

**Table 4.2-1. (continued) Event list for GMPE dataset, composed of records which passed first screening**

EQID	YEAR	MO/DY	Time (GMT)	Earthquake Name	M	Number of Recordings
27	1994	11/13	06:56:00	Köyceğiz	5.24	1
28	1995	01/29	04:16:57	Tercan	5.11	1
29	1995	02/26	11:33:25	Van	4.00	1
30	1995	04/13	04:08:00	Tekirdağ	4.82	1
31	1995	10/01	15:57:13	Dinar	6.17	3
32	1995	12/05	18:49:32	Erzincan	5.70	1
33	1996	04/02	07:59:20	Kuşadası	5.40	1
34	1996	08/14	01:55:02	Merzifon	5.66	2
35	1997	01/21	20:47:46	Buldan	5.15	1
36	1997	01/22	17:57:19	Hatay	5.49	2
37	1997	10/21	10:49:33	Sakarya	4.20	1
38	1997	10/25	00:38:41	Gelibolu	4.12	1
39	1998	04/04	16:16:47	Dinar	5.11	2
40	1998	04/13	19:56:28	Horasan	4.48	1
41	1998	06/27	13:55:51	Adana-Ceyhan	6.16	5
42	1998	07/09	17:36:47	Bornova	4.87	1
43	1999	08/17	00:01:39	Kocaeli	7.55	30
44	1999	11/11	14:41:24	Sapanca-Adapazarı	5.65	9
45	1999	11/12	16:57:20	Düzce	7.15	38
46	2000	06/06	02:41:51	Çankırı -Orta	5.98	1
47	2000	08/23	13:41:28	Hendek-Akyazı	5.32	4
48	2000	10/04	02:33:57	Denizli	4.83	1
49	2001	07/10	21:42:04	Erzurum-Pasinler	5.27	1
50	2001	08/26	00:41:12	Yığılca-Düzce	5.10	1
51	2001	12/02	04:11:45	Van	4.76	1
52	2002	02/03	07:11:28	Sultandağı-Çay	6.38	2
53	2002	12/14	01:02:44	Andırın	4.95	1
54	2003	03/10	04:10:07	Akyazı	3.60	1
55	2003	04/10	00:40:16	Seferihisar-Urla	5.76	1
56	2003	05/01	00:27:04	Bingöl	6.35	1
57	2003	05/21	08:21:50	Düzce	4.30	1
58	2003	06/09	17:44:03	Bandırma	4.67	1
59	2003	07/06	19:10:28	Saros Kör.	5.61	1
60	2003	07/23	04:56:02	Buldan-Denizli-1	5.19	2
61	2003	07/26	01:00:56	Buldan-Denizli-2	4.75	1



**Table 4.2-1. (continued) Event list for GMPE dataset, composed of records which passed first screening**

EQID	YEAR	MO/DY	Time (GMT)	Earthquake Name	M	Number of Recordings
62	2003	07/26	08:36:49	Buldan-Denizli-3	5.41	2
63	2004	04/13	21:47:23	Bolu	4.34	1
64	2004	08/04	03:01:07	Çiftlikköy-Muğla	5.47	1
65	2004	12/20	23:02:15	Ula-Muğla	5.35	2
66	2005	01/23	22:36:06	Antalya-Kaş Aç.	5.77	1
67	2005	06/06	07:41:30	Karlıova	5.64	1
68	2005	10/17	09:46:56	Seferihisar-İzmir	5.80	1
69	2005	10/20	21:40:02	Seferihisar-İzmir	5.86	2
70	2006	02/08	05:24:26	Sakarya	3.70	1
71	2006	10/20	18:15:58	Manyas	4.95	1
72	2006	10/24	14:00:22	Gemlik Körfezi	4.98	9

**Table 4.2-2. List of suspected aftershock events removed from the strong ground motion dataset**

EQID	YEAR	MO/DY	Time (GMT)	Earthquake Name
AF1	1992	03/15	16:16:25	Pülümür
AF2	1994	05/24	02:18:34	Girit
AF3	1994	11/13	07:58:16	Köyceğiz
AF4	1995	09/26	14:58:08	Dinar
AF5	1995	09/26	15:18:22	Dinar
AF6	1995	09/27	14:15:54	Dinar
AF7	1995	10/01	21:14:42	Dinar
AF8	1995	10/01	16:28:53	Dinar
AF9	1995	10/01	18:02:55	Dinar
AF10	1995	10/03	07:38:10	Dinar
AF11	1995	10/05	16:15:21	Dinar
AF12	1995	10/06	16:15:57	Dinar
AF13	1995	10/11	04:44:59	Dinar
AF14	1995	12/04	18:52:40	Erzincan
AF15	1996	08/14	02:59:40	Merzifon
AF16	1998	07/04	02:15:47	Yüreğir-Adana
AF17	1998	07/04	09:24:22	Yüreğir-Adana
AF18	2002	02/03	09:26:43	Sultandağı-Çay

**Table 4.2-2. (continued) List of suspected aftershock events removed from the strong ground motion dataset**

EQID	YEAR	MO/DY	Time (GMT)	Earthquake Name
AF19	2003	07/26	13:31:36	Buldan-Denizli-4
AF20	2004	08/04	14:18:48	Çiftlikköy-Muğla-2

Spatial distribution of 72 events eligible for initial screening on time history characteristics and source parameters is presented in Figure 4.2-1. Event epicenters are referred to Kandilli Observatory and Earthquake Research Institute (KOERI) solutions. Distribution of events and total number of records in the strong ground motion dataset, as a function of event year are presented in Figure 4.2-2 and Figure 4.2-3.



**Figure 4.2-1. Spatial distribution of event epicenters as proposed by KOERI**

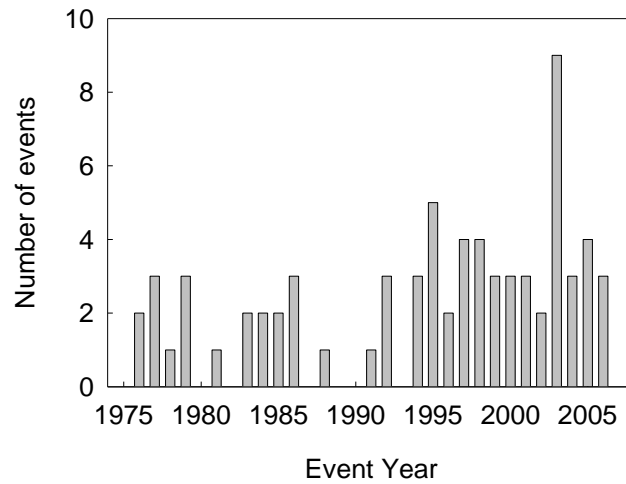


**Figure 4.2-2. Distribution of number of events along the 1976-2006 timeline**

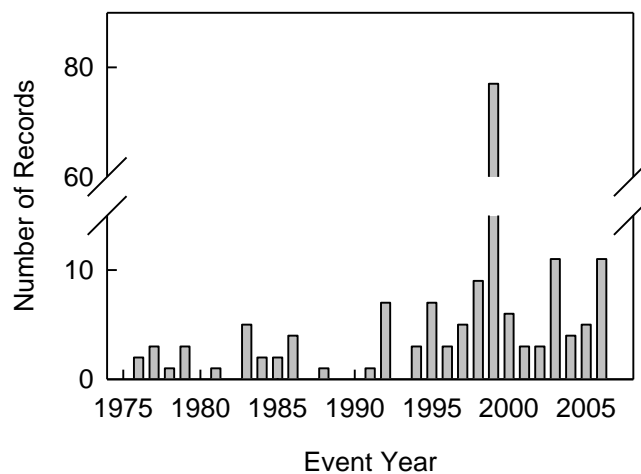


**Figure 4.2-3. Distribution of number of records along the 1976-2006 timeline**

#### 4.2.2 Strong Ground Motion Record Processing

Turkish National Strong Ground Motion Network was first established in 1973, by Earthquake Research Department of General Directorate of Disaster Affairs (Erdoğan, 2008). First strong motion record in the database is recorded as the 19/08/1976 Denizli event ( $M=5.1$ ), by an analog SMA-1 instrument. Since its first establishment, the network has gradually expanded and upgraded in instrument

quality, with the addition of denser local arrays. As stated in Section 4.2.1, strong ground motion data in raw form is also retrieved from KOERI, ITU, IRIGM and LDEO networks in raw form; offered through the ESD (Ambraseys et al., 2002).

This section focuses on the procedure followed in time history processing, and identification of common problems in time traces. A set of MATLAB codes were generated to carry out the routine record processing tasks for the chosen dataset. The functions, which will be described more in detail in the following subsections, perform record processing steps such as mean removal, digital bandpass filtering, Fourier amplitude computation, computation of signal+noise to noise ratio (SNR) for digital records with pre-event memory, and elastic response spectrum ordinates which are presented in the form of generated plots with automatic labeling. The functions are accompanied by routine input-output tasks such as opening a strong ground motion file with specified format (either the file format offered by ERD or ESD), storing contents into arrays as variables and finally, printing to a postscript document file or an image file. The runs can be completed automatically using a batch file, however choosing the final filter cutoff values requires an iterative approach that has to be implemented manually. Strong ground motion processing scheme used follows the basic steps listed below:

- i) Zeroth order correction is done by removing the mean of whole record from the raw data for analog records, in acceleration time history. The criterion is different for records obtained from digital instruments. Digital instruments provide a pre-event memory; a certain portion of the record that is buffered and stored before the waves from the actual ground motion arrives at the site. Therefore, it can be used for the purpose of identifying the noise content of the instrument in the steady, non-excited state. As it can be inferred from the above explanation; mean of the pre-event portion is subtracted from the raw record to yield the mean corrected data for digital instruments. Pre-event buffer duration is defined

manually, using detailed visual examination which ensures that the p-wave triggering phase is not accidentally clipped. Pre-event trace is supplied for some of the records stored by digital instruments (33%); and is unfortunately not available for any of the analogue instruments. Any form of resampling of the time history is not applied.

- ii) Ratio of Fourier amplitude spectrum of whole record to the Fourier amplitude spectrum of the portion defined as pre-event memory; which eventually represents the characteristics of background noise in the signal, is calculated. The output is stored to be used as an assistant in the selection of the filter parameters. The transition frequency which the signal+noise to noise ratio stays constantly above a selected value can be used as a reference during the high-pass filter cutoff. This value is generally accepted as 3.
- iii) Next step is the selection of filter type, filter order and low-pass and high-pass filter frequencies; so that portion of the signal that is considered as being unrepresentative of the original ground motion is excluded in frequency domain. This is accomplished through Fourier transformation of the mean removed form of the time domain signal, applying the filter and inverting the signal into time domain. Causal Butterworth filter of order 2 (as defined by “p” in this text) is used. Figure 4.2-4 presents the response function of a causal (single pass) high-pass Butterworth filter, cutoff value chosen as 0.10 Hz, for different filter orders.

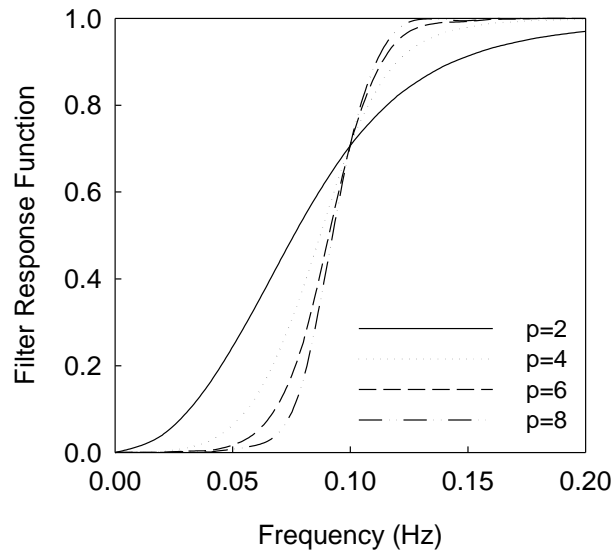


**Figure 4.2-4. Response function of a high-pass causal Butterworth filter, for cutoff frequency of 0.10 Hz, using different filter orders.**

Steps followed in strong ground motion processing are analogous to the guidelines proposed by Boore and Bommer (2005). Boore and Bommer (2005) outline the criteria for selecting the high-pass frequency value in the filter by the judgment of where the long-period portion of the record Fourier amplitude spectrum deviates from the tendency to decay in proportion to the reciprocal of the frequency squared ( $f^2$ ). The rationale behind the selection is summarized as follows: “Whether one assumes the single corner-frequency model of Brune (1970, 1971) or the more complex models with two corner frequencies, seismological theory dictates that at low frequencies, the Fourier amplitude spectrum of acceleration decays according to  $f^2$  (by virtue of the fact that the long-period displacement time series radiated from earthquakes will be pulse-like, ignoring residual displacements, and the Fourier amplitude spectrum of the displacement pulse will therefore be finite at zero frequency)” (Boore and Bommer, 2005). Selection of appropriate cutoff frequency requires an iterative approach; using an eye-fit of the  $f^2$  model. Special care is signified for strong ground motions recorded at near-fault regions from large magnitude earthquakes, such as in the case of 1999 Kocaeli and Düzce events, for

the reason that they possess higher content in low frequency components of the waveform.

Low-pass filter frequency is chosen using the framework, this time using the inverse;  $1/f^2$  eyeball fit. Natural frequency of the seismometer is also considered when selecting the low-pass frequency. Motions recorded at “rock” sites are re-evaluated so that any high frequency content inherent in the ground motion itself is not accidentally filtered.

The last step in strong ground motion processing involves, linear baseline correction over the whole time domain applied to the velocity trace, if necessary. Time history traces and the Fourier amplitude spectra of raw and processed records are plotted and stored, 5% damped elastic response spectrum parameters for a suite of spectral periods are calculated and stored. Velocity and displacement time histories are visually checked, ensuring they represent the characteristic waveform for an earthquake.

Sample time history plot of processed record for the longitudinal component of the 20/10/2005 Seferihisar Earthquake ( $M=5.86$ ) recorded at Bornova (BRN) station presented in Figure 4.2-5. Similarly, 5% damped elastic response spectra for the same record is presented in Figure 4.2-6. Figure 4.2-7 shows the  $f^2$  and  $1/f^2$  eye-fit used in the final selection of cutoff frequencies, on Fourier amplitude spectra of mean removed and processed records for the same sample ground motion. Black series represent the raw form, whereas dashed red series are plotted for the processed waveform.

Useable period range of ground motions after filtering is defined by the factor 1.25; denoting that comfort zone for cutoff frequencies should be reserved to account for the gradual roll-off of the filter response function in frequency domain (Figure 4.2-4).

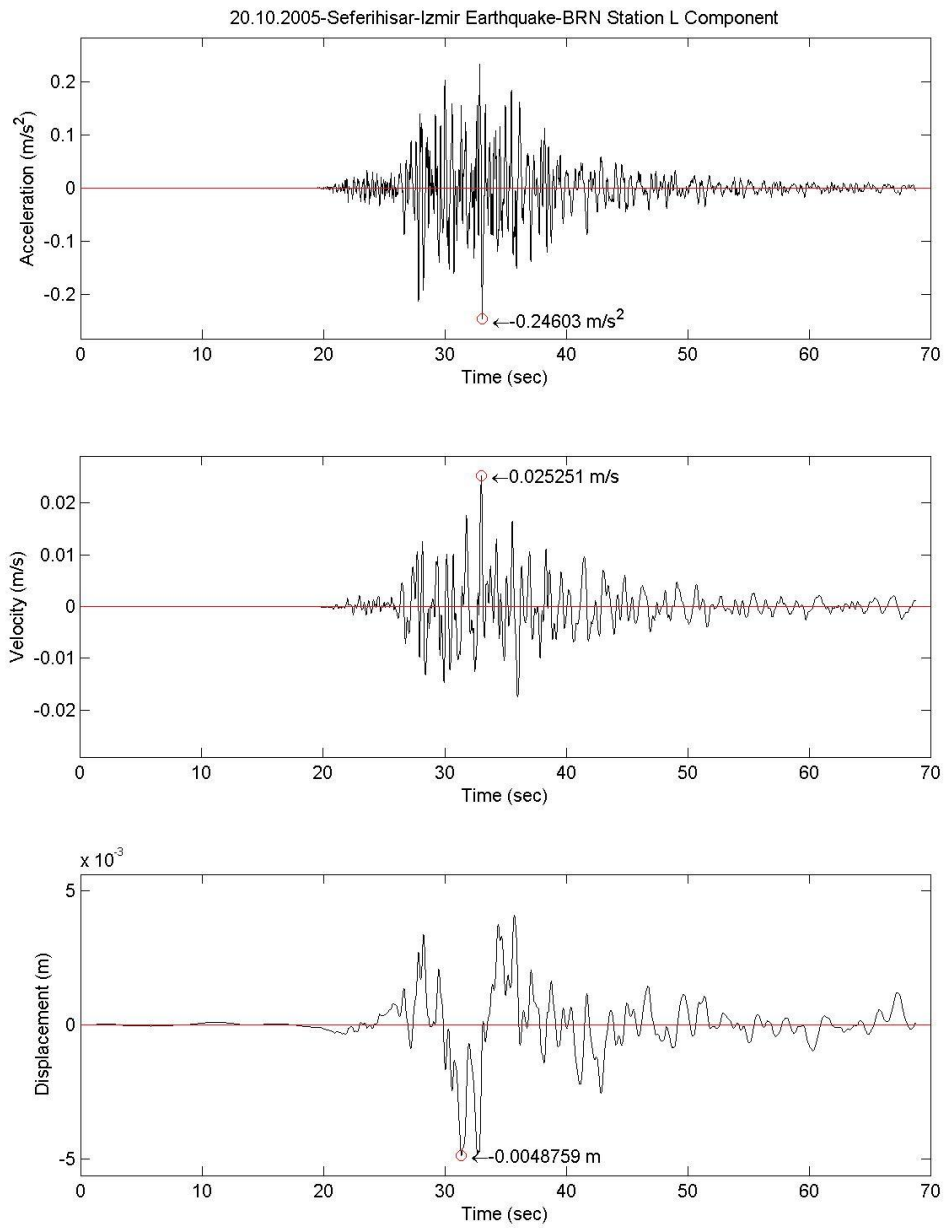


**Figure 4.2-5. Processed time history traces of 20/10/2005 Seferihisar Earthquake (BRN Station, longitudinal component)**



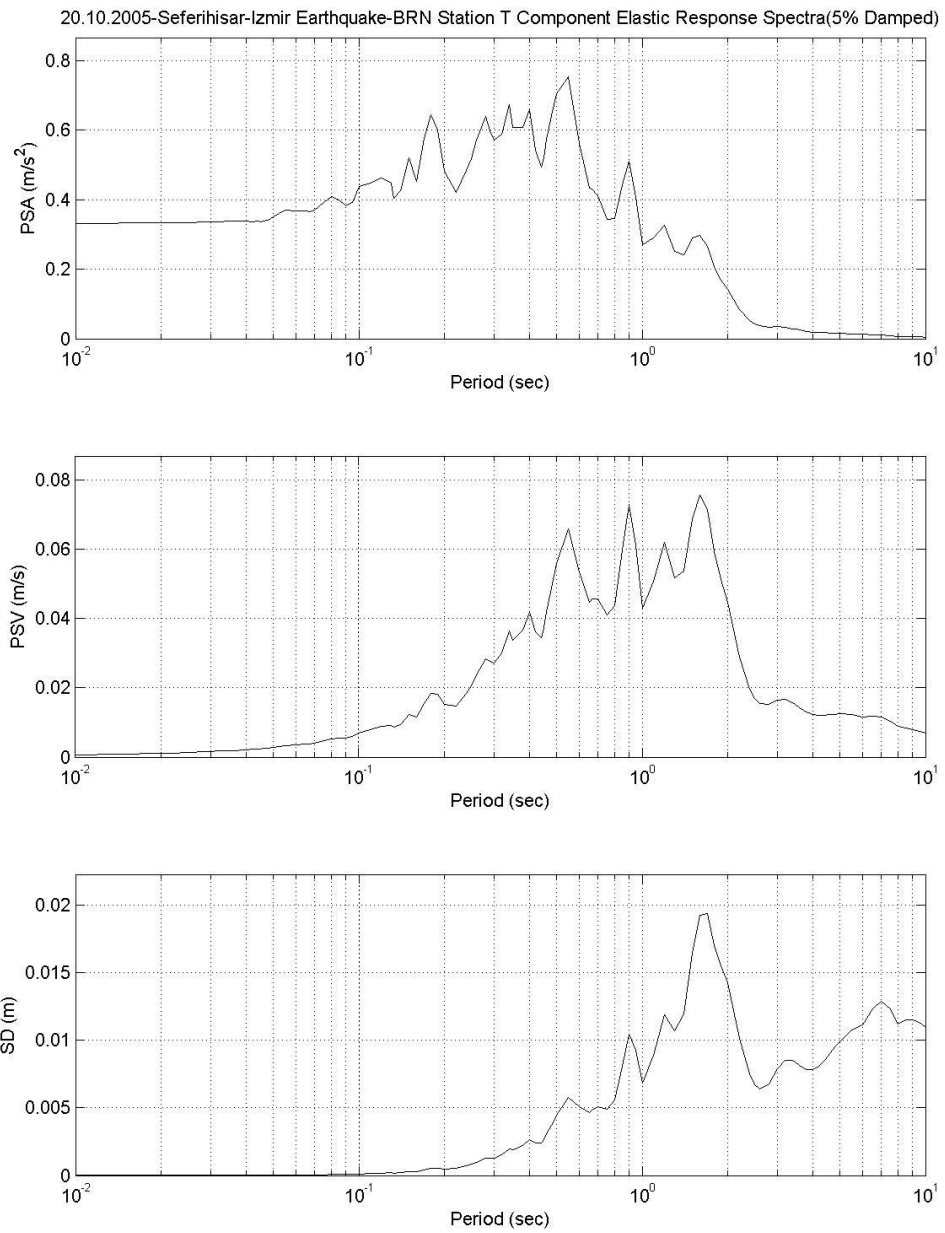


**Figure 4.2-6. 5% damped elastic response spectra for longitudinal component of 20/10/2005 Seferihisar event, recorded at BRN station.**

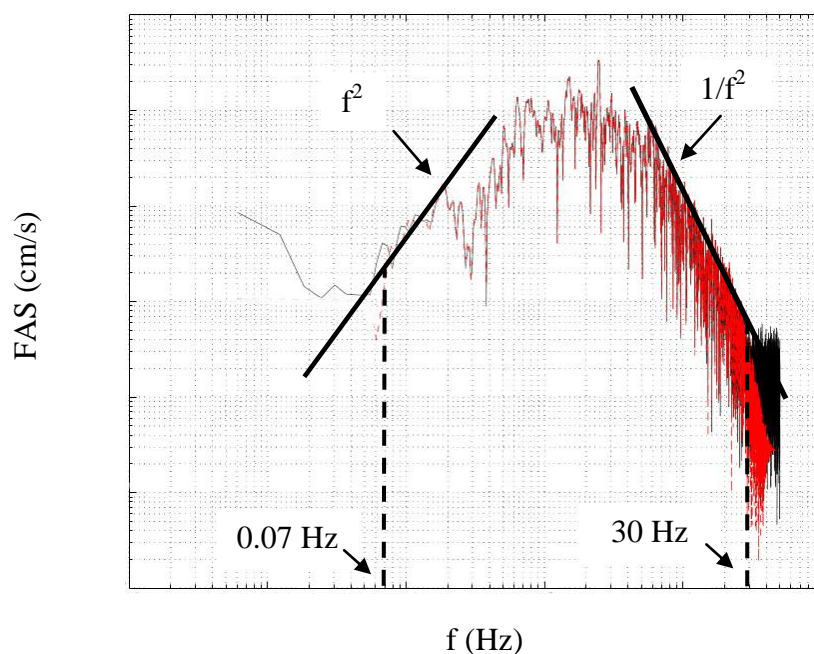


**Figure 4.2-7. Fourier amplitude spectra for raw and processed records of 20/10/2005 Seferihisar (M=5.86) earthquake, recorded at BRN station (longitudinal component)**

Type of filter used in the described function is casual. Acausal filtering (two way forward and reverse filtering as Abrahamson and Silva, 1997 describe) is not applied in this case. Comments on effects of causal and acausal filtering on peak values as spectral values are well studied in Boore and Akkar (2003), and Akkar and Bommer (2006).

#### 4.2.2.1 *Effect of Filter Type on Processed Strong Ground Motions*

Impact of filter type (causal and acausal) and choice of high-pass frequency cutoffs on the elastic and inelastic demand parameters have been thoroughly studied in literature (Boore and Akkar, 2003; Boore, 2005; Boore and Bommer, 2005; Akkar and Bommer, 2006). The main outcomes of these studies suggest that correct

application of acausal filtering (two way filtering that causes no distortion in phase) requires zero paddings to be added and conserved; and the selection between causal and acausal filter types begin to impact the elastic spectral displacement parameters at high periods; roughly above 1 s.

As will be listed in the conclusion section of data processing stage; filter cutoffs naturally constrain the useable period range in spectral parameter predictions; since the contribution of selected components are neutralized in the frequency domain. This procedure decreases the number of records included in the dataset for the period range considered. In other words, the overall evaluation yields less number of data points for the period range which the impact of acausal and causal filtering techniques are distinguishable. Thus, the ground motion prediction equation development attempt will be limited to the spectral period range, implicitly bounded by the selection of filter cutoffs. Therefore the discussion of filtering technique becomes less critical as data in that frequency range is already exempted from the model.

#### 4.2.2.2 *Identification of Apparent Errors in Waveforms*

The strong ground motion dataset compiled herein contains a significant amount of recordings from analogue instruments (61 in number, %34 of total), which some extra inadequacies such as S-wave triggering, incomplete waveform may exist. As long as a waveform was considered to be conserving the component when absolute maximum was reached at a site upon visual check; that waveform was used in determining the peak acceleration parameters. However, exclusion of such waveforms from the GMPE development became inevitable for spectral parameters and peak parameters of velocity and displacement.

Boore and Bommer (2005) and Erdoğan (2008) after Douglas (2003b) systematically list the major types of problems in waveforms, mainly as a consequence of errors or

shifts in the digitization process, low resolution of the recording instrument, recording of successive events in a single waveform, spikes common in pre-event memory segment, or the late triggering of accelerographs.

Visual check implemented within the confines of this study identified 10 accelerograms to be excluded from the dataset presented in Table 4.2-1, simply as a result of a combination of irrecoverable S-wave triggering, uneven triggering time in horizontal components, early termination and severe resolution problems.

Two time histories exhibited apparent signs of instantaneous spikes in the pre-event segment; and those spikes were neutralized manually using the average values of acceleration at neighbor time intervals.

Out of 179 records, 16 accelerograms retrieved from SMA-1 instruments suffered from S-wave triggering. While accepting that including those records in spectral parameter predictions are questionable; records were conserved in the dataset for inclusion to the acceleration model. This decision was based on visual examination of the waveform.

### **4.2.3 Relationships Between Horizontal Components of Ground Motion**

One of the key parameters in ground motion prediction equations is the definition of the horizontal component of ground motion that was often overlooked while making comparisons between various models. Numerous types of definitions have been put into practical use, such as the random horizontal component, arithmetic average of horizontal components, geometric mean, strike normal and strike parallel components, larger component, and the recently introduced rotation independent components of ground motion.

A quick look at the choice of horizontal components for the GMPE's developed using Turkish dataset (or a combination of Turkish and European datasets in the case

of Akkar and Bommer, 2010) reveals that either geometric mean definition (Özbey et al., 2004; Akkar and Bommer, 2010), or larger component definition is preferred (Ulusay et al., 2004; Kalkan and Gülkan, 2004).

Choice of horizontal ground motion component depends on the specific engineering application. Geometric mean of two orthogonal horizontal components of motion is usually utilized in assessing the response value; although it is not necessarily the most representative definition of the forces imposed on the structure. Some applications may require maximum response in a given direction.

The NGA project has initiated the discussion of rotation independent measures of ground motion, and its relation with other definitions. Two companion papers by Boore et al. (2006) and Beyer and Bommer (2006) introduce the concept and calculation process of orientation independent measures of ground motion, while providing guidelines for conversion to other definitions of horizontal ground motion. These efforts were later expanded by Watson-Lamprey and Boore (2007), focusing on the relationships between “GMRotIpp” definition (Boore et al., 2006), and arbitrary, strike normal, maximum rotated components. Huang et al. (2008) is one of the most recent works on the subject, showing particular emphasis on the selection of suitable definitions for ground motions at near-fault sites.

This section attempts to answer the question of whether the relationships calculated using the whole or subset of the NGA dataset is applicable to the Turkish ground motion dataset. For the case of rotated ground motion definitions, uncertainty in the geometric mean due to rotation is also quantified. For the specific purpose, ground motion intensity values for maximum and spectral components of processed strong ground motions were calculated, for a suite of definitions defined below:

- i) Geometric Mean: Geometric mean is defined as the square root of products of response spectral values of two horizontal components. It is

equivalent to the arithmetic average taken using the logarithms of spectral values (Equation 4-1).

$$GM = \sqrt{SA_{h,1} \cdot SA_{h,2}} \quad (4-1)$$

- ii) **GMRotDpp:** GMRotDpp is based on the set of geometric means computed from the as-recorded orthogonal horizontal ground motions, rotated through all possible non-redundant rotation angles. The post fix “pp” stands for the pp<sup>th</sup> percentile of the set of geometric means for a given spectral period. GMRotD50 corresponds to median, and GMRotD00 and GMRotD100 correspond to minimum and maximum values of rotated geometric means respectively. Calculation steps for GMRotDpp are presented in Boore et al. (2006), and will not be repeated here. However, a simple explanation involves the calculation of geometric means of two orthogonal horizontal components, in the as-recorded and rotated orientations along 0<sup>o</sup>-89<sup>o</sup>; obtaining the distribution of geometric means, and finally taking the pp<sup>th</sup> percentile as the design value.
- iii) **GMRotIpp:** While developing GMRotDpp for various periods in the spectral band, different rotation angles corresponding to pp<sup>th</sup> percentiles are present. Boore et al. (2006) makes a modification to the GMRotDpp, incorporating unique rotation angle for all useable period range, minimizing the spread of the rotation dependent geometric mean. NGA GMPE models are developed for the GMRotI50 values. Similar
- iv) **LargerRotDpp:** LargerRotDpp is the pp<sup>th</sup> percentile larger horizontal component of rotated orthogonal ground motions. Instead of calculating the geometric mean as in GMRotDpp, larger of the two components is chosen. Rotation angle corresponding to each spectral period is different.

- v) SN-SP: Strike normal and strike parallel components of ground motion are calculated using the orientation of the sensor and azimuth alignment of the causative fault for every earthquake event. For the GMPE dataset compiled for Turkey, causative fault azimuth is chosen either from the available focal mechanism solutions for the particular event, or the approximate alignment of the mapped fault. The base fault map considered is the seismogenic fault map compiled in Chapter 3. Procedure for determining the primary axis of the focal mechanism solution is summarized in proceeding sections.
  
- vi) SRSS Component: SRSS is computed from the unrotated 2-D trace of the ground motion. Square root of sums of squares of two horizontal components is calculated for each data point in time-history trace, and the maximum value is chosen. In other words, maximum of “n” resultant vectors of acceleration in a time history trace is the SRSS component.

#### 4.2.3.1 *Trial Runs Using Time Histories of Analogue and Digital Origin*

Before conducting batch runs on the Turkish strong ground motion dataset, few sample runs demonstrating the relationship between spectral values of horizontal ground motion definitions are presented. Four candidate time histories are selected from the dataset. Selections reflect the quest for possible instabilities in the parameters defined in Section 4.2.3, caused by time histories acquired from an i) non-problematic analogue instrument, ii) S-wave triggered analogue instrument, iii) non-problematic digital instrument, and iv) non-problematic digital instrument with an expected polarization between ground motion components at a near-fault site. Table 4.2-3 presents the key information for candidate records.  $T_{\text{usable}}$  is the usable period range after filtering.

**Table 4.2-3. Descriptive parameters of candidate records for demonstrating relationship between different definitions of horizontal ground motion**

Record ID	Related Event and Record	$T_{usable}$ (s)	Instrument Type	Remarks
A	4/4/1998 Dinar Earthquake (M=5.0), recorded at DIN Station with $r_{epi}=12$ km, +L component rotated $64^0$ with respect to SN direction.	0.063 s - 3.2 s	SMA-1	Non-problematic record
B	12/2/1991 İstanbul Earthquake (M=5.1), IST station with $r_{epi}=33$ km, +L component rotated $0^0$ with respect to SN direction.	0.063 s - 1.6 s	SMA-1	S-wave triggering defect
C	26/7/2003 Buldan Earthquake (M=5.5), DAT1 Station with $r_{epi}=20$ km, +L component rotated $40^0$ with respect to SN direction.	0.042 s - 16 s	ETNA	Non-problematic record
D	1/5/2003 Bingöl-Karlıova Earthquake (M=6.4), BNG Station with $r_{epi}=4.8$ km, +L component rotated $63^0$ with respect to SN direction.	0.05 s - 4.0 s	GSR-16	Non-problematic record at a near-fault site

Comparison between the pseudo acceleration response spectra of four sample ground motions, focusing on the upper, 50<sup>th</sup> percentile, and lower bounds of geometric means due to rotation is presented in Figure 4.2-8. Although spectra are plotted for the complete period range, reliable comparison should be based on the differences within the usable period range; defined by  $T_{usable}$ . Variability of GMRotDpp among four samples seems to be a little higher for analogue records; however a systematic quantification was not made for its justification in the whole dataset. Since variability in geometric mean due to rotation is quantified and separated from



aleatory variability term in GMPE model, this does not impose any threat on the overall stability of the model.

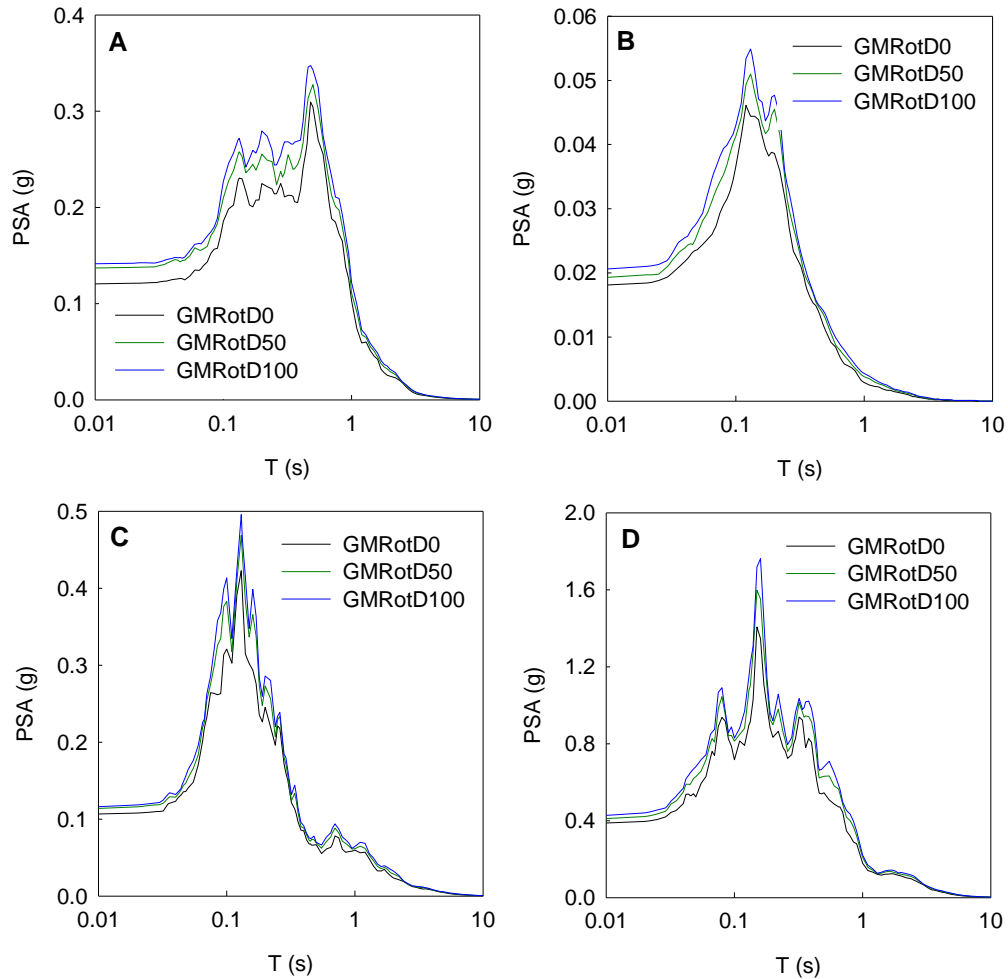


**Figure 4.2-8. Comparison between pseudo acceleration response spectra of four sample ground motions (GMRotDpp component)**

Second set of comparison is done for the GMRotDpp and GMRotIpp components. Ground motions “A” and “C” are chosen for this purpose. Side by side comparison in Figure 4.2-9 yields that the difference between the GMRotI50 and GMRotD50 are negligible, whereas a distinguishable variation exists between minimum and maximum values of rotation dependent and independent measures of ground motion.

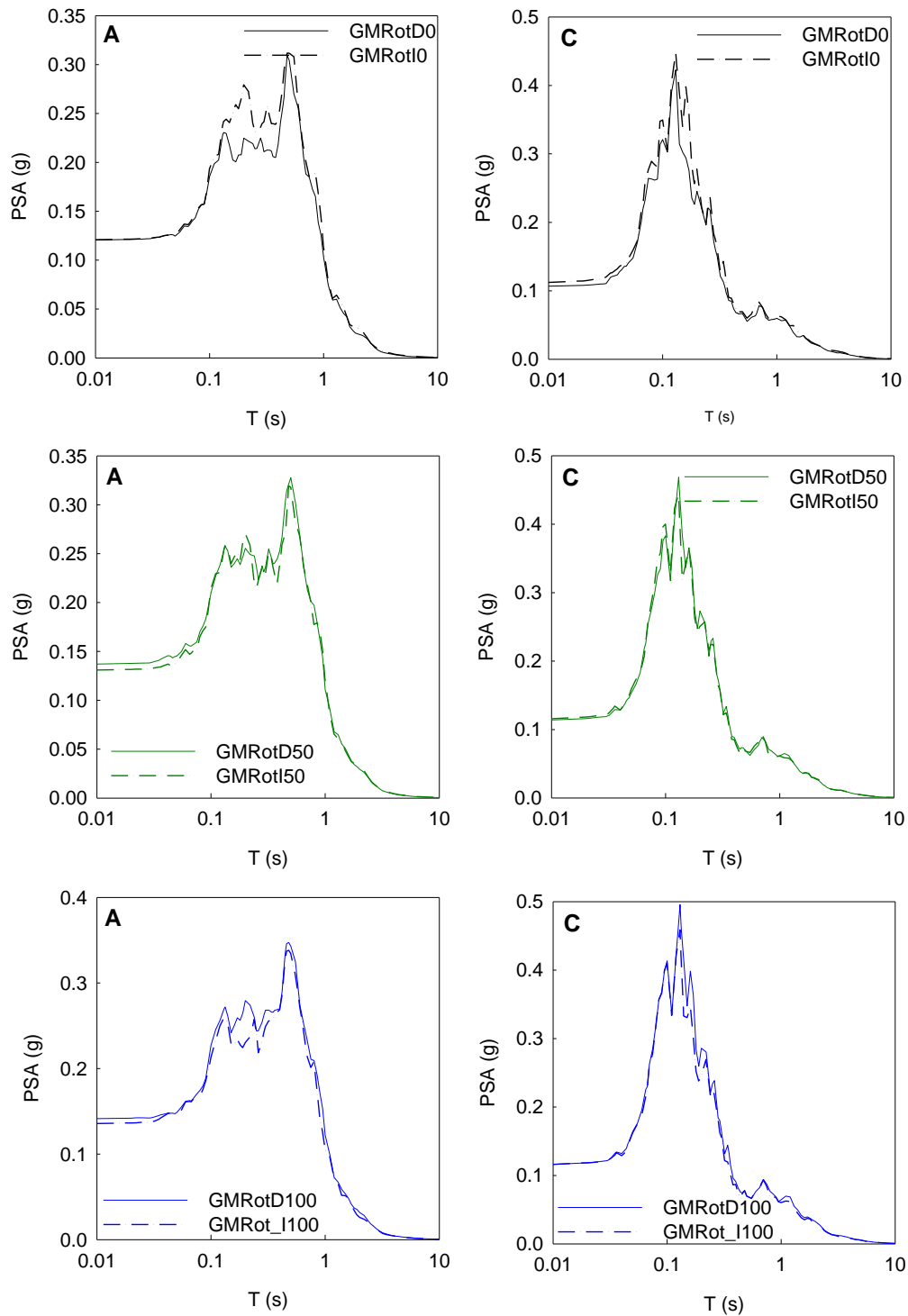


**Figure 4.2-9. Comparison between pseudo acceleration response spectra of sample ground motions (GMRotDpp and GMRotIpp components)**

Further comparison of analogue and digital records, by means of unrotated-rotated geometric means, larger horizontal components and strike normal-parallel orientations did not expose any systematic errors or instabilities leading to unphysical values in response. Hence, analogue records are considered to be safe for use in calculating rotated definitions of ground motion.

#### *4.2.3.2 Relations Between Different Definitions of Horizontal Ground Motion for Turkish Dataset*

This section covers the results of batch processing made for calculating the ratios between different definitions of horizontal ground motion, and associated variability due to rotation of orthogonal axes, where applicable. Calculations are made for peak ground acceleration (as-recorded motion after standard signal processing, and using waveforms having the same record length in both horizontal directions), and 16 spectral periods ( $T=0.02$  s,  $0.03$  s,  $0.04$  s,  $0.05$  s,  $0.075$  s,  $0.1$  s,  $0.15$  s,  $0.20$  s,  $0.25$  s,  $0.30$  s,  $0.40$  s,  $0.50$  s,  $0.75$  s,  $1.0$  s,  $1.5$  s,  $2.0$  s). The first set of results present all the data points for  $T=0$  s,  $T=0.2$  s,  $T=0.5$  s, and  $T= 2.0$  s. Ratios of interest are  $GMRotD100 / GMRotD50$ ,  $GMRotD50 / GM$  (unrotated),  $GMRot150 / GMRot D50$ ,  $SRSS / GMRotD50$ ,  $GMLarger50 / GMRotD50$ ,  $SN / SP$ ,  $SP / GMRotD50$ , and finally,  $SN / GMRotD50$ . Calculations are made using a purpose specific MATLAB script developed within the content of this study.

Figures 4.2-10 through 4.2-17 present ratios between different measures of horizontal ground motion, for four different periods along the spectral band. The horizontal axes stand for the unrotated geometric mean. A linear trendline, constrained at zero slope (constant value) is plotted for each sample; representing the average ratio for that period. Arithmetic average of the ratios for each set, as well as sample standard deviations is calculated to assess the spectral variation of ratios. Dependence of ratios as a function of source to site distance and earthquake magnitude are also investigated. Results show that, for almost all of the parameters

under inquiry, there is a decreasing trend of the ratios both as a function of distance and magnitude. Figure 4.2-18 presents only two cases for  $GMLarger50 / GMRotD50$  for peak ground acceleration; chosen on purpose for demonstrating the most pronounced trend among all the ratios considered. Weaker or stronger dependence on magnitude and distance is also a function of spectral period. Nevertheless, developing a general model for calculating ratios between different definitions of horizontal ground motion components is out of scope of this study. Beyer and Bommer (2006) and Watson-Lamprey and Boore (2007) present more detailed work on the subject.

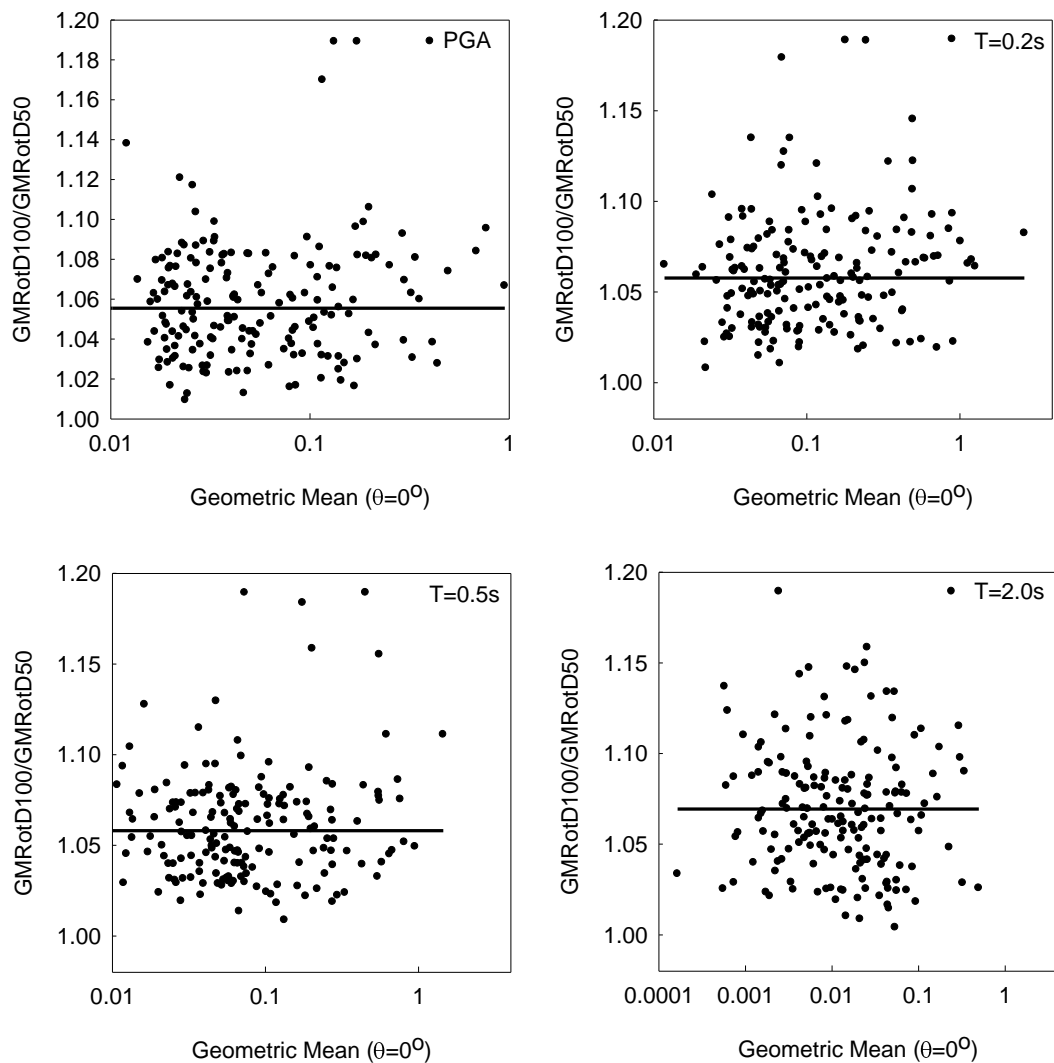


**Figure 4.2-10.  $GMRotD100 / GMRotD50$  values for different periods**

A quick examination shows that  $GMRotD100 / GMRotD50$  ratio stays at 1.06 (Figure 4.2-10), with a slight variation as a function of period. Unsurprisingly, overall  $GMRotD50 / GM$  (unrotated geometric mean) ratio is generally around 1.01 or less; indicating that  $GMRotD50$  can be comfortably used as a substitute for  $GM$  in rough  $GMPE$  comparisons (Figure 4.2-11).

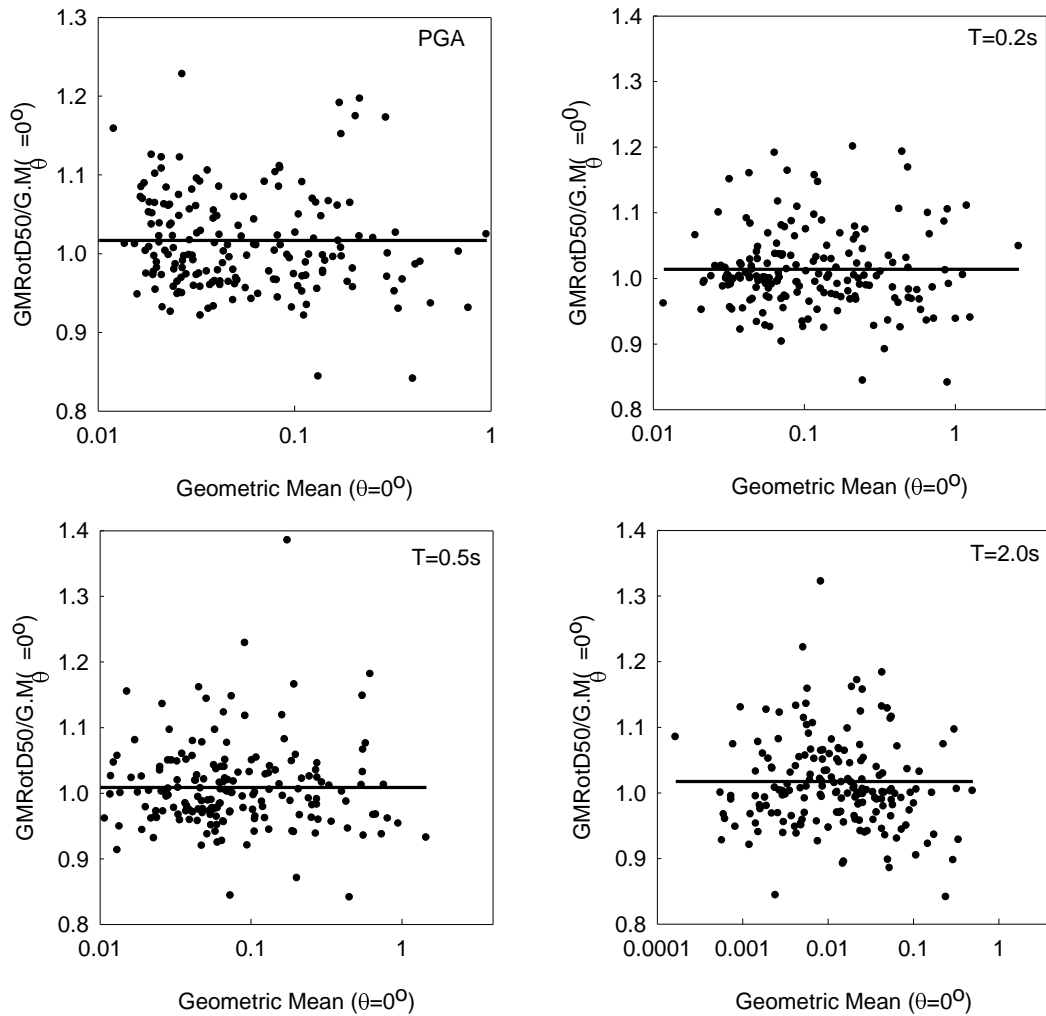


**Figure 4.2-11.  $GMRotD50 / GM$  values for different periods**

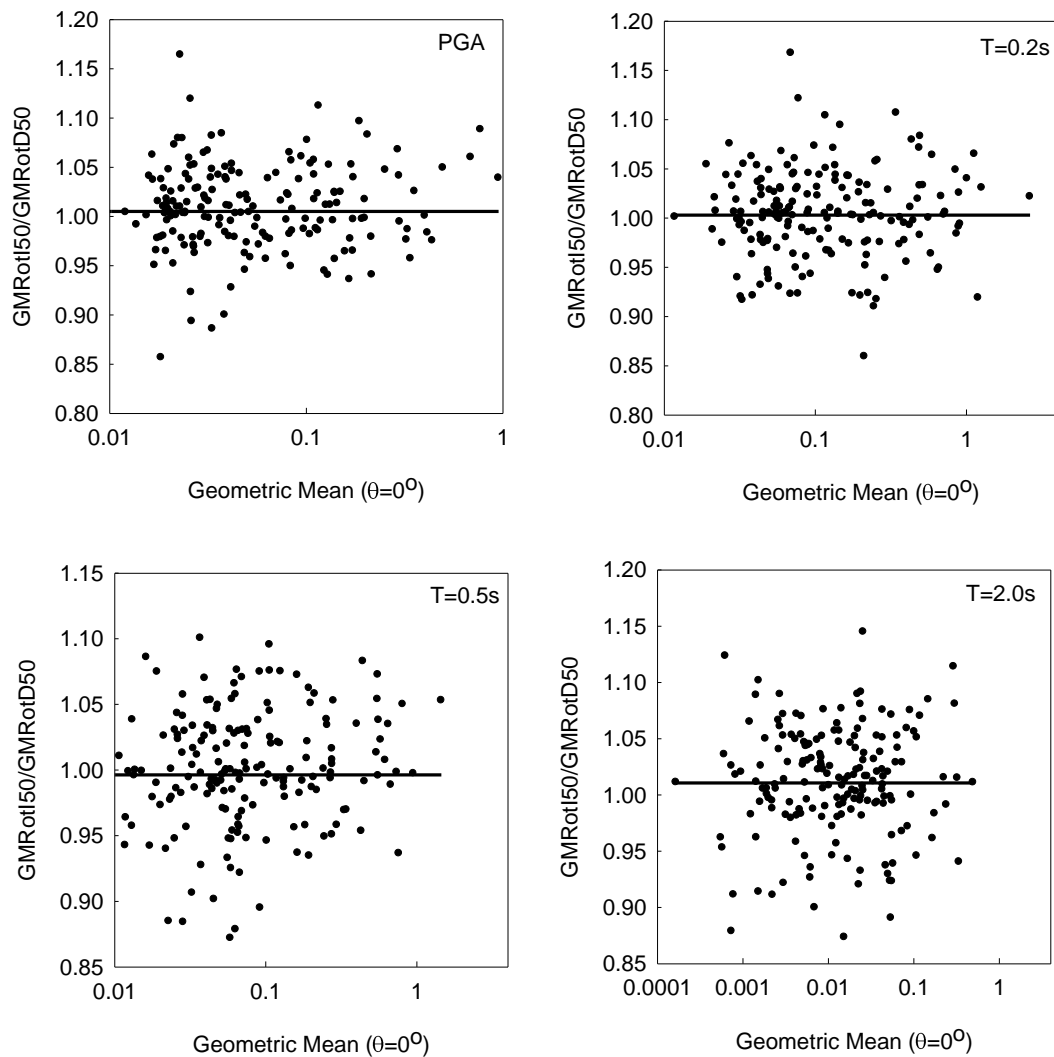


**Figure 4.2-12. GMRotI50 / GMRotD50 values for different periods**

Results of Figure 4.2-12 suggest that GMRotI50 and GMRotD50 have a negligible difference for the usable period range considered. In a case by case basis, GMRotI50 / GMRotD50 ratio, as well as ratios considered in previous comparisons, fall within a broader band. For the case of GMRotI50 / GMRotD50, this band is between -10% and +10%.

The average ratio between SRSS component and GMRotD50 is more dramatic at all periods. The average ratio varies between 1.25 and 1.37; indicating a systematic increase over spectral period (Figure 4.2-13).

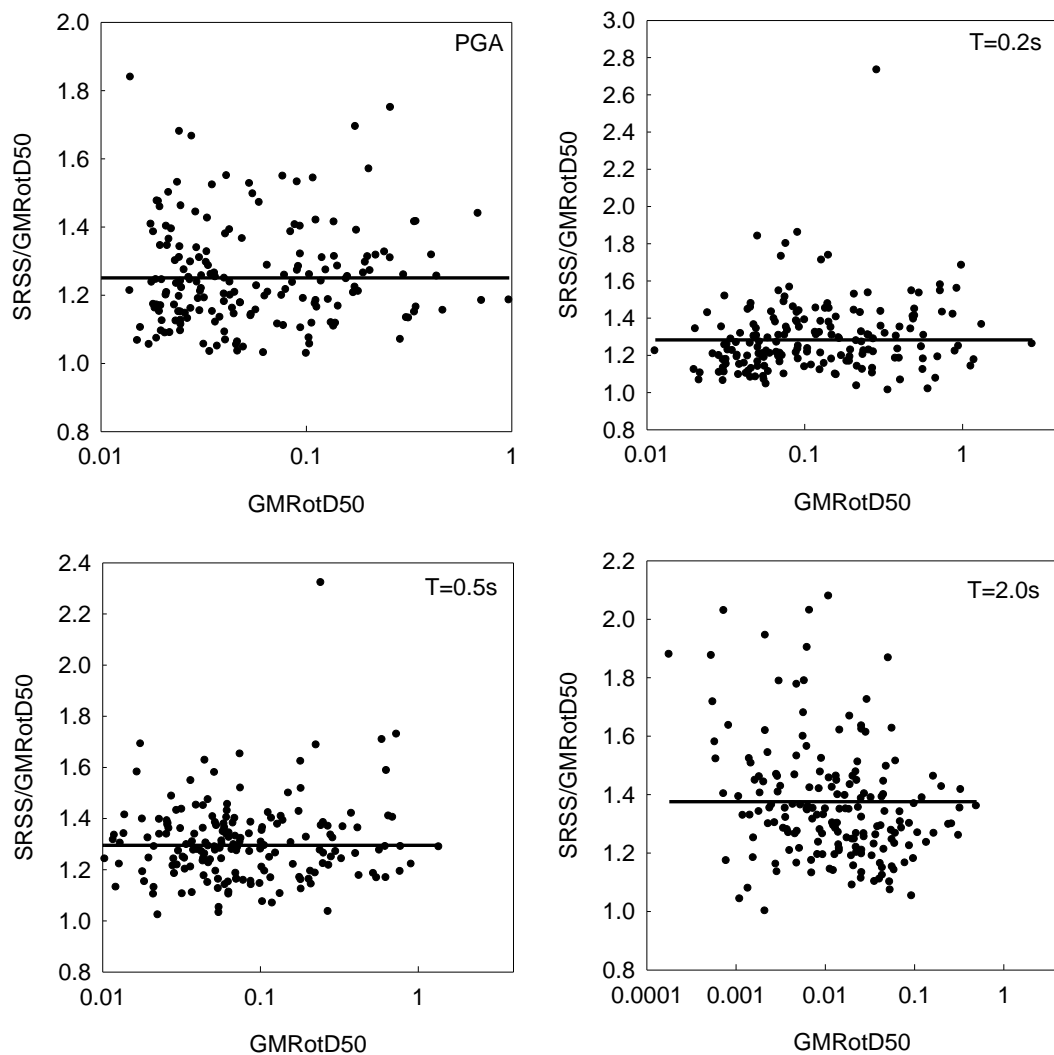
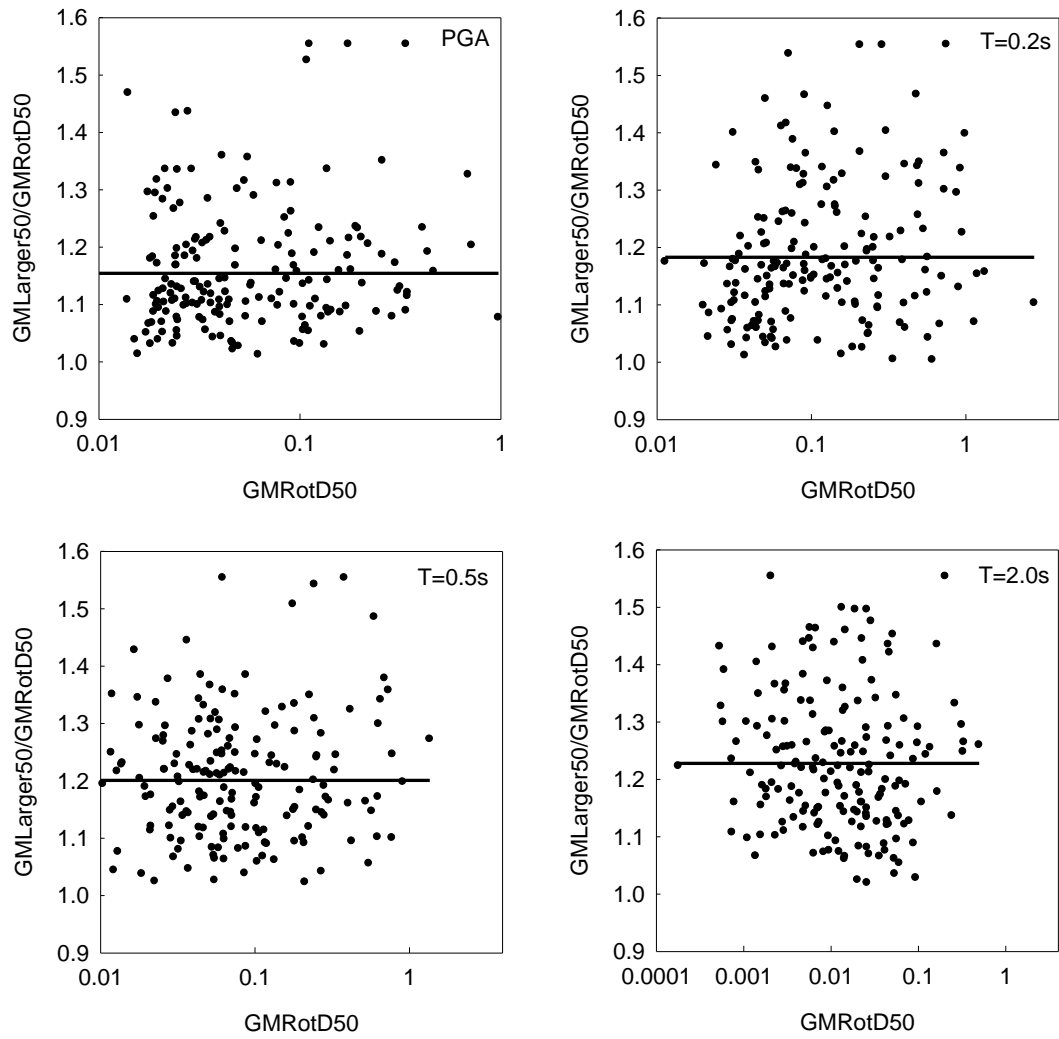


**Figure 4.2-13. SRSS / GMRotD50 values for different periods**

Case for the 50<sup>th</sup> percentile of the rotated larger component and GMRotD50 is smoother. The average ratio varies from 1.15 to 1.22, once again, increasing with higher periods (Figure 4.2-14).

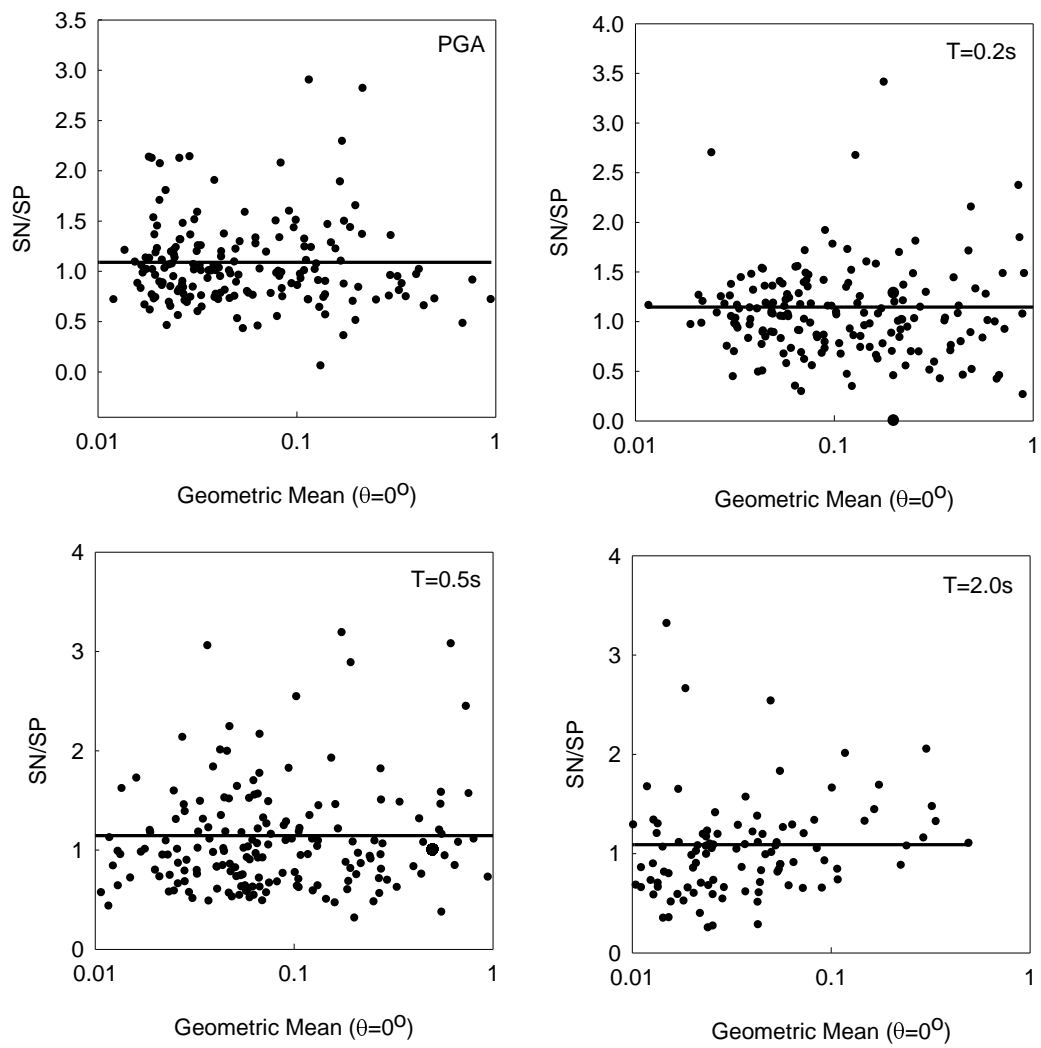
Strike normal components are 10-15% greater than the strike parallel components, depending on period (Figure 4.2-15). Variations of SP / GMRotD50 and SN / GMRotD50 are compatible with the results of SN / SP (Figures 4.2-16, 4.2-17), as expected.

Figure 4.2-19 presents the spectral variation of median ratios between different definitions of horizontal component of ground motion, with error bars representing the sample standard deviation of ratios at each period.



**Figure 4.2-14. GMLarger50 / GMRotD50 values for different periods**





**Figure 4.2-15. SN/SP values for different periods**

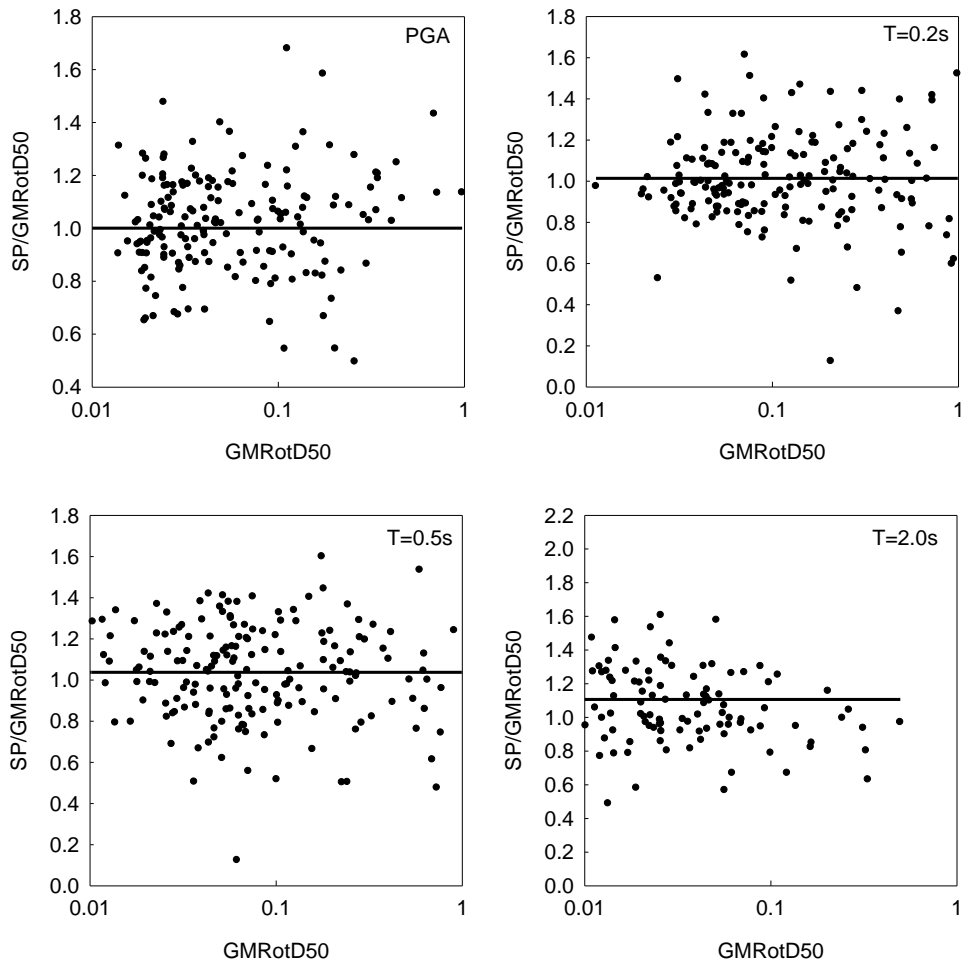


**Figure 4.2-16. SP / GMRotD50 values for different periods**

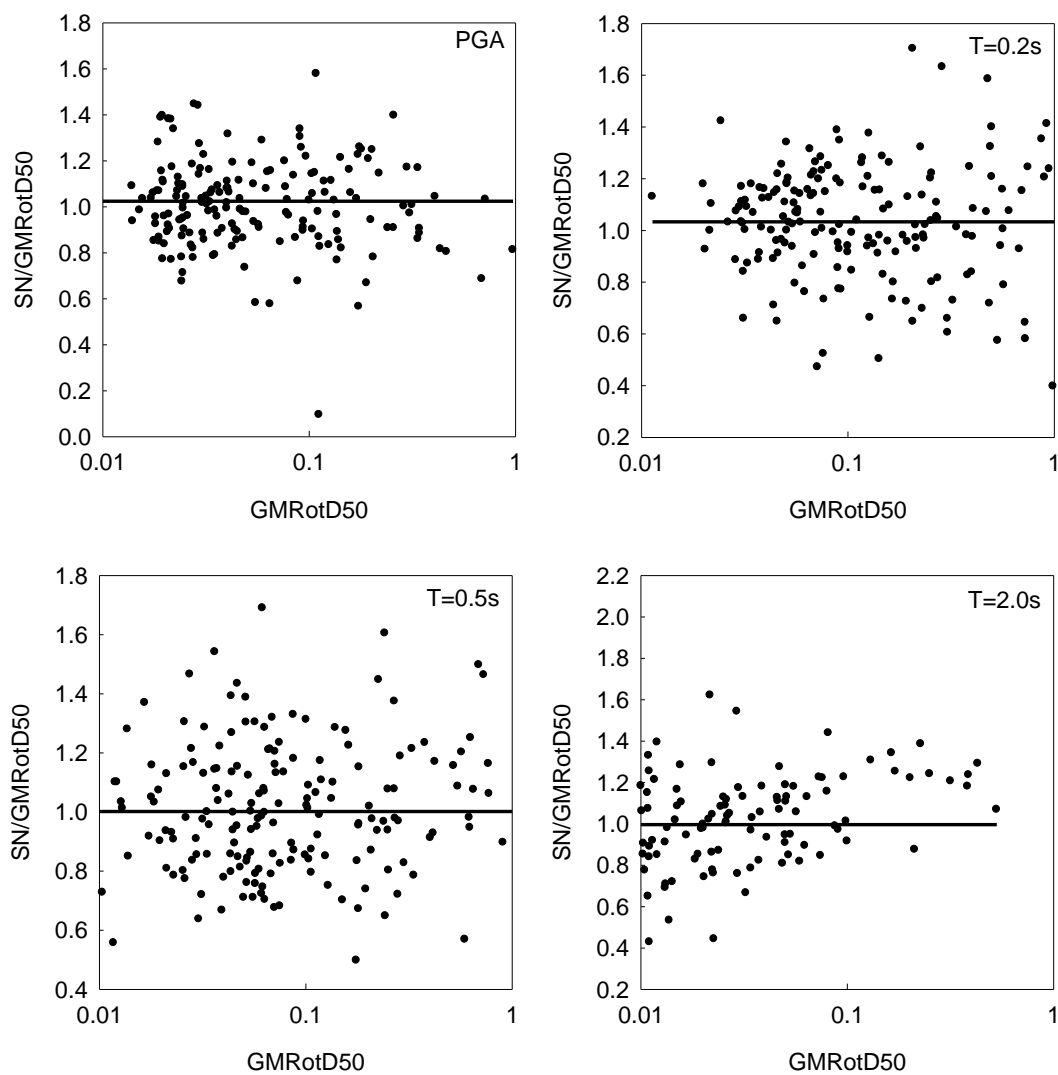


**Figure 4.2-17. SN / GMRotD50 values for different periods**

GMRotD100 / GMRotD50, GMRotD50 / GM, GMRotI50 / GMRotD50 comparisons do not exhibit any significant variation of median and standard deviation values along spectral period. On the other hand, GMLarger50 / GMRotD50, SRSS / GMRotD50, SN / SP polarization becomes more dominant at higher periods. While this may be mostly attributed to the nature of the ground motion definition used, an

unquantified portion may be responsible for the filtering preferences at periods higher than 1 s. This proposal has not been verified and awaits further investigation.

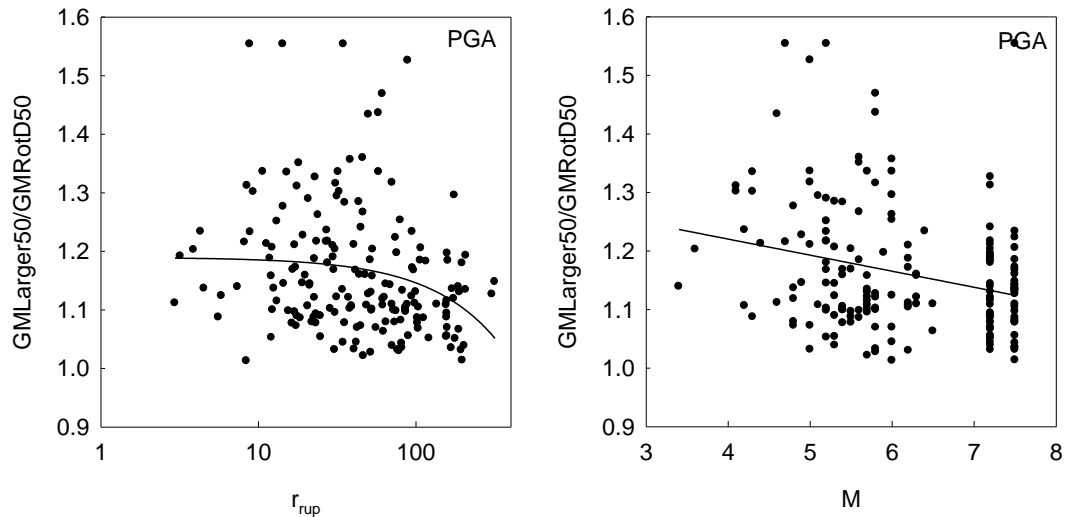


**Figure 4.2-18. Dependence of horizontal ground motion component ratios on source to site distance and earthquake magnitude**

In Figure 4.2-19, blue outlined circles in the GMRotI50 / GMRotD50 comparison is the result of the Boore et al. (2006) study. There is an unperceivable difference between two findings.

Beyer and Bommer (2006) findings for SN / GM (noted as FN / GM<sub>xy</sub>), SP / GM (noted as FP / GM<sub>xy</sub>), and GMLarger50 / GM (noted as Env<sub>xy</sub> / GM<sub>xy</sub>) conform to the findings of this study in general. Although Env<sub>xy</sub> is defined as the unrotated envelope, previous knowledge between the ratios of unrotated geometric mean and 50<sup>th</sup> percentile geometric mean enables a general comparison between Env<sub>xy</sub> of Beyer and Bommer (2006) and GMLarger50 of this study. As the last item, “MaxD” definition corresponds to GMRotI100 in this text, and MaxD / GM<sub>xy</sub> ratio trend of Beyer and Bommer (2006) suggest values between 1.2 and 1.33 (read from graph). This contradicts with the current finding of 1.06.

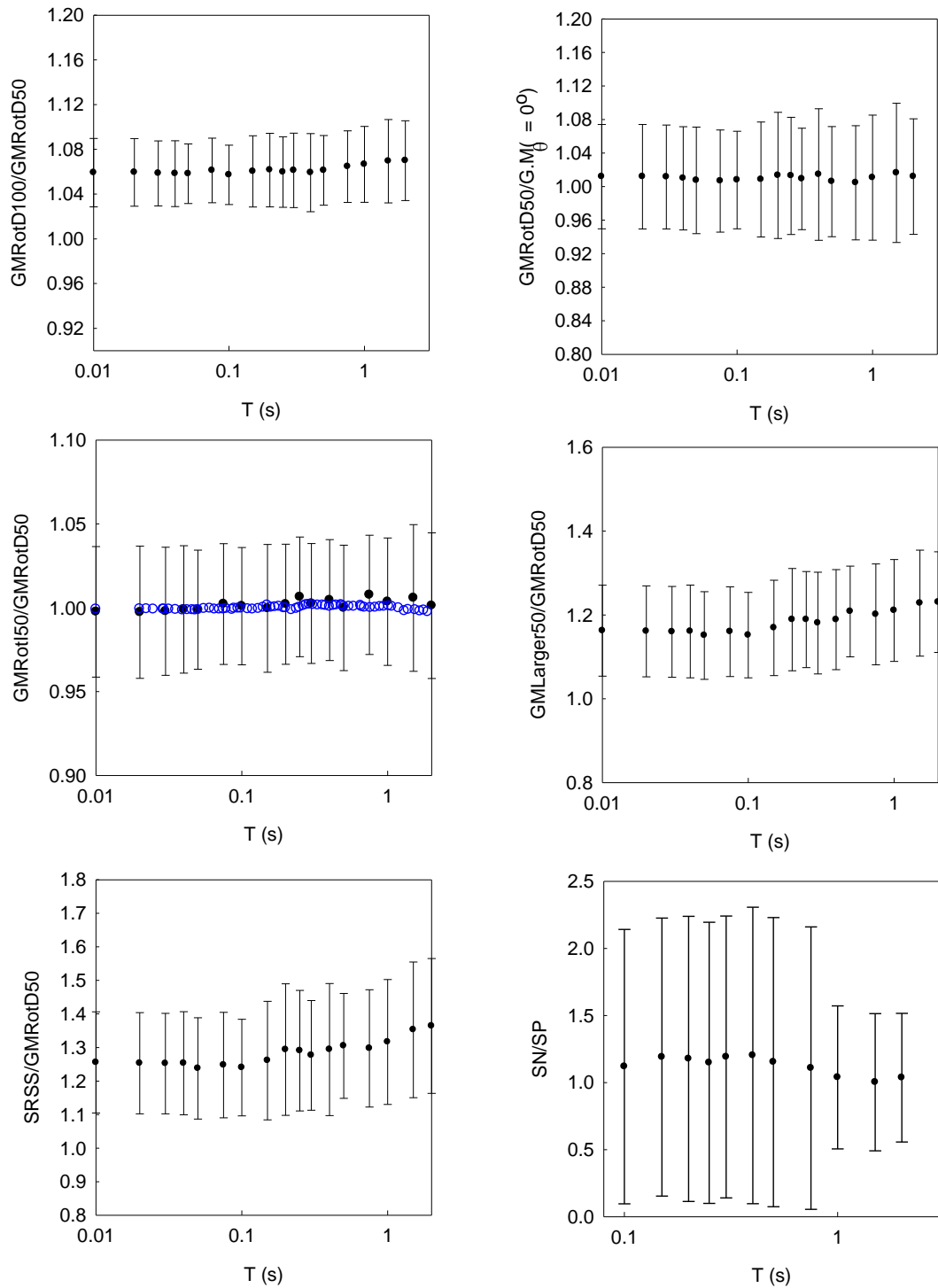


**Figure 4.2-19. Variation of ratios between different definitions of horizontal component of ground motion, as a function of period**

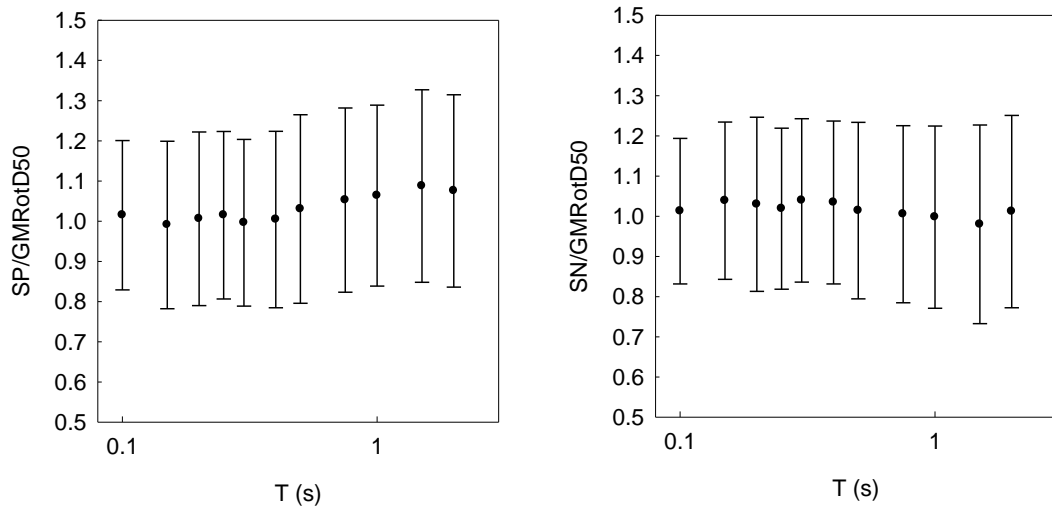


**Figure 4.2-19. (continued) Variation of ratios between different definitions of horizontal component of ground motion, as a function of period**

Examination of the error bars reveals that; for SRSS / GMRotD50, SP/GMRotD50, and SN/GMRotD50, there is a slight increase in sample standard error with increasing period. Excessive standard error in SN / SP ratio is a consequence of several outliers shown in Figure 4.2-15. Observable reduction in standard error for periods above 1 s is a consequence of reduced sample size due to filtering preferences. This effect became evident only in SN/SP comparisons, although applied for all parameters under examination.

A final warning on relationships between the above listed components is about the use of ratios on modifying GMPE's developed different measures of horizontal ground motion. While these general findings roughly indicate modification factors applied on median estimates, the correct implementation requires the procedure described in Beyer and Bommer (2006), since the modification requires treatment on median and sigma values simultaneously.

#### 4.2.3.3 *Uncertainty in Spectral Acceleration Due to Rotation of Ground Motion Components*

For definitions of rotated ground motion components, such as the GMRotDpp, the application field may require utilization of any pp<sup>th</sup> percentiles due to rotation. In GMRotD50, median value of the rotated geometric means is computed; however GMPE's may require higher percentiles to be implemented. Either selection does not involve quantification of parameter uncertainty due to rotation of two orthogonal components.

The aim of this section is to introduce the concept of parameter uncertainty modeling of rotational components of SA (spectral acceleration). The philosophy behind the preference of this study is to quantify the variability in natural logarithm of SA, the commonly used parameter to be predicted in GMPE's, due to rotation over non-redundant angles.

Choice for the predicted parameter in the current proposal of GMPE is GMRotD50. Modeling of uncertainty in  $\ln(\text{SA})$  due to rotation enables a reduction in the model error term of the final GMPE. Since the impact of uncertainty on hazard values at long exposure periods is of critical concern to analysts, any contribution to this topic is crucial.

Previous work on the subject was carried out by Moss and Kiureghian (2006). A feasibility analysis incorporating parameter uncertainties of peak ground acceleration and moment magnitude was carried out using the functional form of Campbell et al. (1997) GMPE was used.

Figure 4.2-20 presents the variation in geometric mean due to rotation of orthogonal peak ground acceleration components, as a function of moment magnitude. Relevant values are also computed for the natural logarithm of peak and spectral values, and

will be used for reducing the model error during GMPE development. The notation chosen for sigma value due to rotational variability of the horizontal component is  $\sigma_{\ln S_a, \theta}$ .

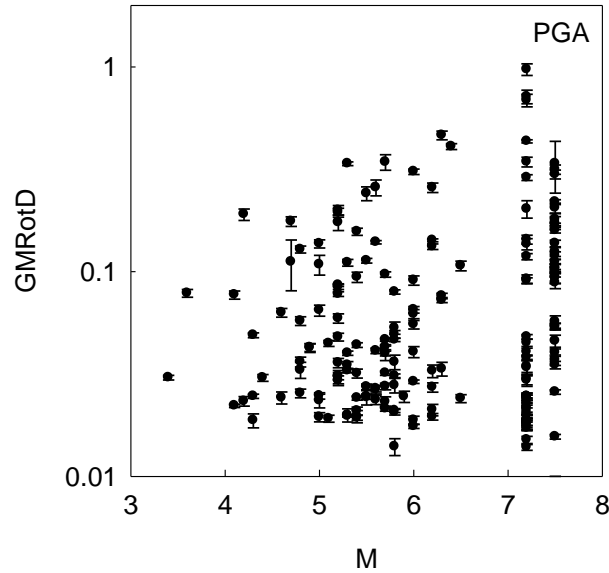


**Figure 4.2-20. Median values of GMROtD parameter with standard error bars**

#### 4.2.4 Style of Faulting

Style of faulting is one of the major parameters in GMPE's, often modeled in the form of dummy variables, using the simple, yet non-unique, classification system: normal, strike-slip and reverse. Besides re-grouping of certain fault classes into broader bins in GMPE functional forms, various preferences in defining the transition between styles of faulting classes exist.

Bommer et al. (2003) has stated that using different schemes to classify fault ruptures into various categories, leads to uncertainty and ambiguity regarding the nature and extent of the effect of focal mechanism on ground motions. Bommer et al. (2003) provides a compilation of fault classification schemes used in literature, and emphasizes on the effect of sampling bias on the calculated ratio of spectral



accelerations between data collected from events having different faulting types. Factors such as variation of the dataset for peak and spectral parameters, absence of normal fault data for California earthquakes, ambiguities in classifying rupture mechanisms of oblique nature, and effect of statistical uncertainty caused by splitting of datasets into categories of different faulting style, are considered to have an effect on the estimated ratios between the relative intensities of ground motions generated by different types of faults, for the same magnitude, distance, and soil type.

GMPE models using local earthquake data have mostly ignored the style of faulting parameter. Ulusay et al. (2004), Kalkan and Gülkan (2004) have preferred to exclude a term for style of faulting. Özbey et al. (2004) relationship does not require a faulting parameter, since the dataset is composed of records from the 1999 earthquake sequence. On the other hand, Akkar and Bommer (2010), utilizing local data as well as earthquakes from European and Middle East, and Akkar and Çağnan (2010) relationships incorporate dummy variables for “reverse”, “normal” or “strike-slip” classes. Utilization of dummy variables in the final functional forms of 1997 series of Western U.S GMPE’s and the NGA models were also favoured.

In the light of factors such as avoiding statistical uncertainty, by subdivision of the sample space into smaller sets of faulting styles, and bypassing ambiguity in non-unique classification systems; this study prefers to use a continuous parameter characterizing transition from normal to reverse faulting. An appropriate parameter enabling smooth transition is chosen as the style of faulting parameter (SOFP) used in Chapter 2. Assessing the SOFP parameters for the events included in the GMPE dataset requires the utilization of; i) focal mechanism solutions, provided by either the Harvard CMT (Centroid Moment Tensor) method or other methods preferred by various seismological agencies, ii) utilization of focal mechanism solutions for other events on the same fault segment, to complete missing information about the faulting style of the event included in the current dataset, and iii) completing the missing data using the general characteristics of the tectonic setting. For item ii, complete Harvard

CMT Catalog and EMMA (Euro-Mediterranean Earthquake Mechanisms of the Mediterranean Area) database were independently mapped (Figures 4.2-21 and 4.2-22).

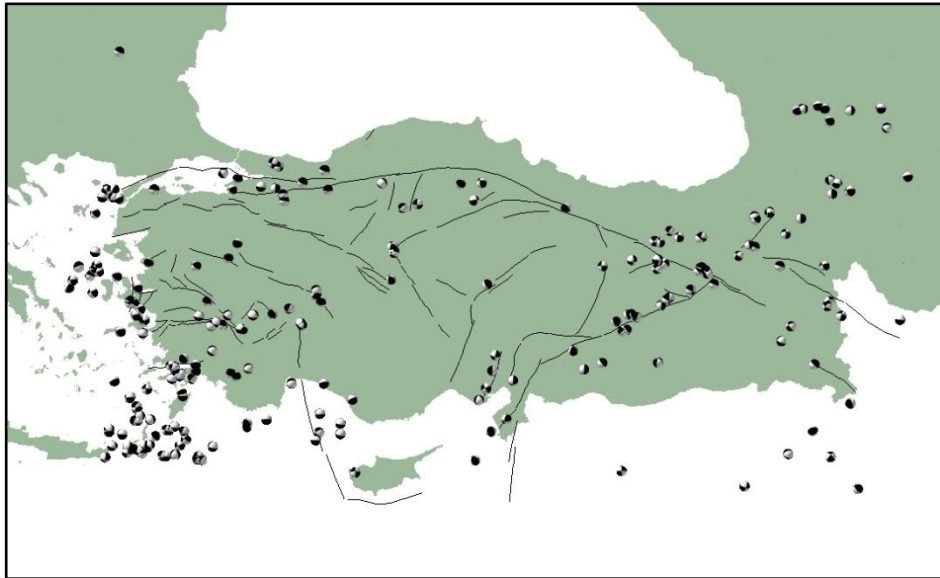


**Figure 4.2-21. Focal mechanism solutions for the complete HRVD catalog (clipped for region covering Anatolia)**

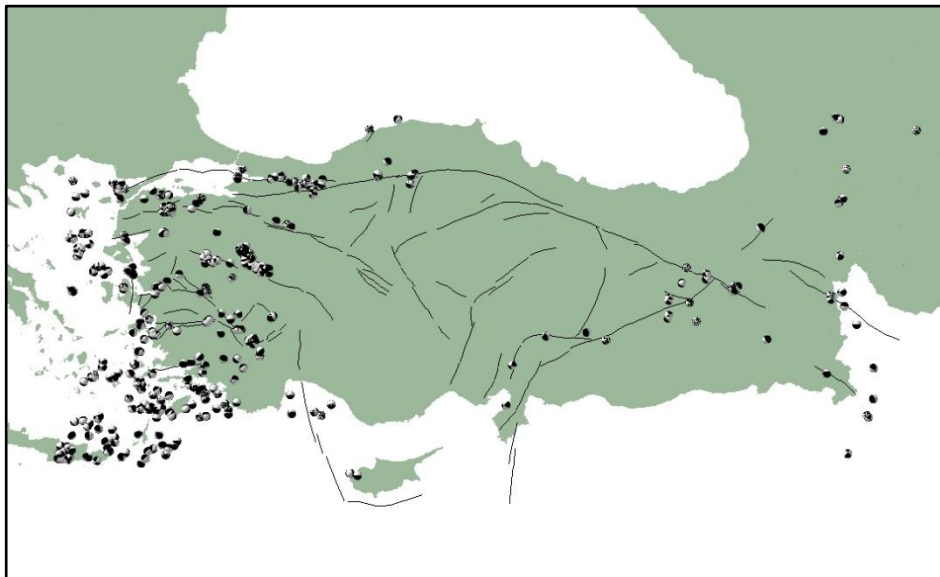


**Figure 4.2-22. Focal mechanism solutions for the complete EMMA catalog (clipped for region covering Anatolia)**

Focal mechanism solutions as provided by several dependable seismological agencies were compiled. These agencies are listed as HARVARD (CMT Solutions), USGS NEIC, MED-NET, Swiss ETHZ, CSEM, and MOS (Moscow). The data has been compiled from internet databases, with crosschecking where applicable. The available data possesses strike, dip and slip plane solutions. The primary fault plane was selected upon comparisons with seismogenic fault alignments in the epicenter region. For cases with more than fault plane solution were available, rake angles for primary planes were converted to style of faulting parameter (SOFP), and arithmetic average was taken as the final parameter for the GMPE dataset. Figure 4.2-23 presents a specific case for the 3/2/2002 Sultandağı Earthquake. The figure shows epicenter locations resolved by HRVD, KOERI, MEDNET, USGS-NEIC, and CSEM; as well as published focal mechanism solutions. Decision of whether the focal mechanism solutions were compatible with the tectonic evidence was made, and any exclusion was applied where necessary.

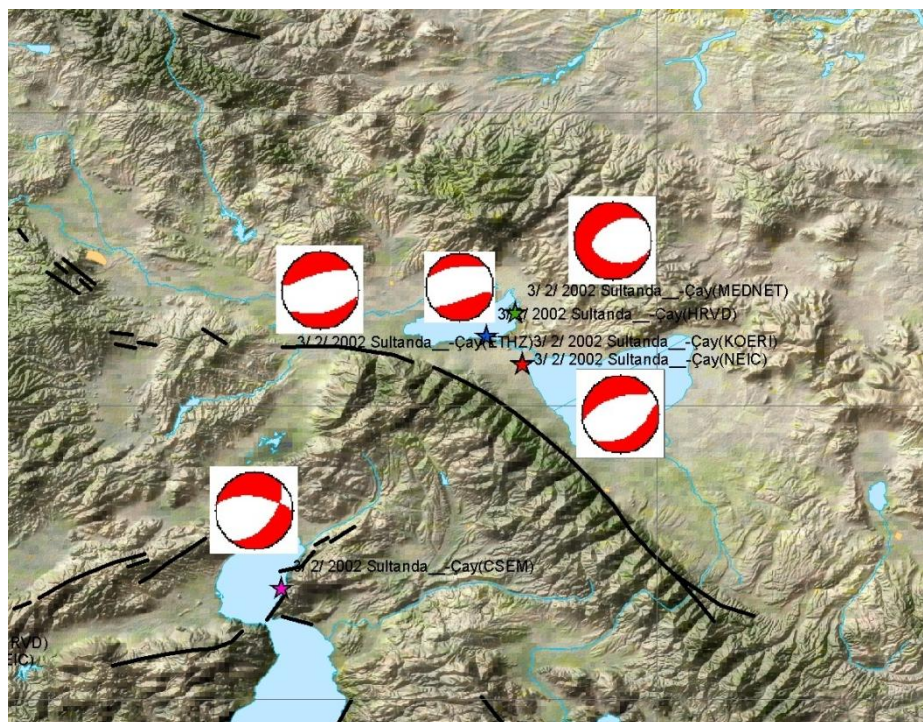


**Figure 4.2-23. Focal mechanism solutions for 3/2/2002 Sultandağı Earthquake**

Before SOFP parameterization was done, 45 events (62%) was classified as SS (strike-slip), 16 (22%) as N (normal), 1 as R (reverse), and 10 as oblique-slip events. This distribution is significantly different from the Western US databases, in which data from reverse events are considerably higher in number, and normal fault data is very sparse.

Distribution of events with focal mechanism solutions, as a function of number of fault plane data available from different seismological agencies are tabulated below:

**Table 4.2-4. Summary of fault plane solutions available through various agencies**

Number of Different Agencies for a Single Event	Number of Events	Percentage of Events
1	18	36%
2	17	34%
3	8	16%
4	5	10%
5	2	4%
Total	50	100%

There are numerous cases where the fault plane solutions are missing in the literature. Specifically, 22 out of 72 candidate events lack focal mechanism solution data. Those 22 events belong to single station recorded events, corresponding to roughly 12% of the total number of strong ground motion records in the dataset.

Among the 22 events with missing fault plane solutions, 12 (54%) are in SS (strike-slip) category, 5 are in N (normal) category, and 5 are in oblique category. An extensive literature survey was performed to assess the nature of faulting of events with missing focal mechanism solutions. Earthquake epicenter estimates from various agencies were critically evaluated. These data were combined with evidence

collected from published literature including, but not limited to, Kalafat (1989) and Kalafat (1995). Earthquake reports from MTA (General Directorate of Mineral Research and Exploration), KOERI, EERI, and ERD (GDDA) were consulted. In particular, information was gathered from Ateş and Bayülke (1982) for the 1976 Denizli Earthquake, Durukal et al. (1998) for the 1995 Dinar Earthquake, Grosser et al. (1998) for 1992 Erzincan Earthquake, Özalaybey et al. (2002) and Polat et al. (2002) for 1999 Kocaeli main event, Ocakoğlu et al. (2005) and Uzel and Sözbilir (2008) for 2005 Sığacık Gulf events.

For events which the style of faulting was assessed by tectonic evidence, style of faulting parameter (SOFP) was assigned using the mean SOFP calculated from the subset of events with available rake angles, for the relevant class of faulting. For normal faults, value of 0.09 was assigned; similarly, strike slip faults were assigned 0.477. Frequency distribution of SOFP for all records (reflecting multiple SOFP counts coming from a single event) is presented in Figure 4.2-24.

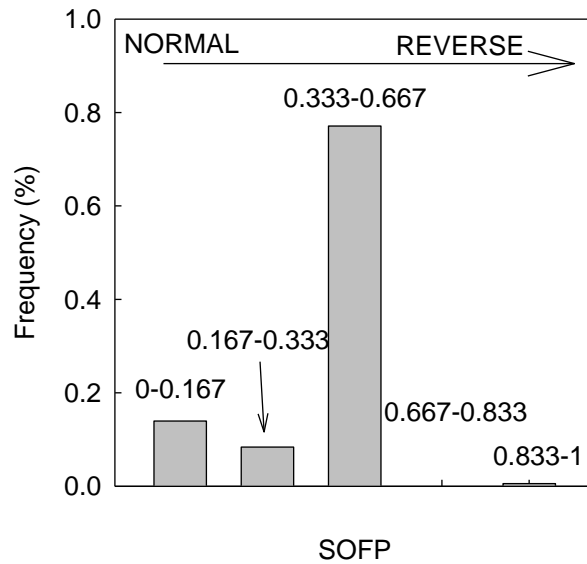


**Figure 4.2-24. Frequency distribution of SOFP in the compiled dataset**

#### 4.2.5 Earthquake Magnitude

This section contains brief information about the procedures followed in compiling earthquake magnitude data in various scales, magnitude conversion principles, evaluation of magnitude uncertainty in the dataset, and finally proposed values of median magnitude and related uncertainties.

Data sources for magnitude were KOERI, HARVARD, ISC, USGS-NEIC, ETHZ, MEDNET, EMSC, ATH (Athens Observatory, Greece), MOS (Moscow), THE (Thessaloniki, Greece), DHMR (Dhamar, Yemen), BJI (Beijing, China), IASPEI (Physics Dept., University of Colorado, Boulder, CO), ROM (Rome, Italy), EIDC (Experimental International Data Center, Virginia), GBZT (Gebze, Turkey), LDG (Lodge, Alabama, USA), MDD (Madrid, Spain), IGIL (Gilhagi, Iceland), IDC (Isla del Cano, Costa Rica), GRAL (Lebanon), SYO (Syowa Base, Dronning Maud Land, Antarctica), BGS (British Geological Survey, Edinburgh, UK), HLW (Helwan, Egypt), CRAAG (Centre de Recherche en Astronomie, Astrophysique et Geophysique, Algeria), SOF (Sofia, Bulgaria). Total number of data from agencies except the first listed 7, were very sparse; there were almost no data for events which took place before last two decades.

Earthquake magnitudes reported in units of local magnitude;  $M_L$ , surface-wave magnitude;  $M_S$ , body-wave magnitude;  $M_b$  were converted to moment magnitude;  $M$ , using the results of study by Heaton et al., (1982). Duration magnitude,  $M_d$  was converted to  $M$  using the relationship proposed by Ulusay et al., (2004). Epistemic uncertainty due to different models for magnitude conversion was assumed to zero, and conversion factors for the given model was taken to be exact (model error term of the magnitude conversion relationship used was ignored).

More specifically, data from HRVD, ETHZ, KOERI, MEDNET and EMSC were already reported in moment magnitude scale. Conversion was applied to data

retrieved from ISC, partly for USGS-NEIC (38%), and most of the remaining agencies.

Variability in moment-tensor solution for a given earthquake was also neglected. Moss and Kiureghian (2006) list possible sources of uncertainty in moment tensor solutions as, i) the utilization of different inversion techniques, ii) sample size difference in measuring events with large or small magnitudes, and iii) signal quality of the records acquired from large magnitude events. Using data from same stations by different agencies for an event is considered to correlate the predictions.

The only form of uncertainty considered in moment magnitude parameter was the epistemic uncertainty due to different parameter reporting of the same event by different agencies. Magnitude data was collected for every event, through detailed query of databases from various agencies. Magnitude predictions at scales other than moment magnitude were converted to  $M$ , using the relationships presented above.

Median and standard deviation of moment magnitude values for each event was computed using the reported best estimates of moment magnitude values. A subset of all the listed agencies was used, consisting of KOERI, HRVD, ISC, ETHZ, KOERI, ETHZ, MEDNET and EMSC predictions. Mean value of coefficient of variation calculated using each data point was 0.03; highest being slightly above 0.1 for a single event out of 72.

Figure 4.2-25 presents the variation of magnitude uncertainty as a function of moment magnitude. Several trials of functional form fitting to the data trend revealed that a constant value was satisfactory, evaluated as  $\sigma_M=0.17$ . This finding contradicts with Moss and Kiureghian (2006), and Moss (2009) findings, indicating that there is a decreasing trend in parameter uncertainty of  $M$  as a function of increasing earthquake magnitude (Figure 4.2-26).

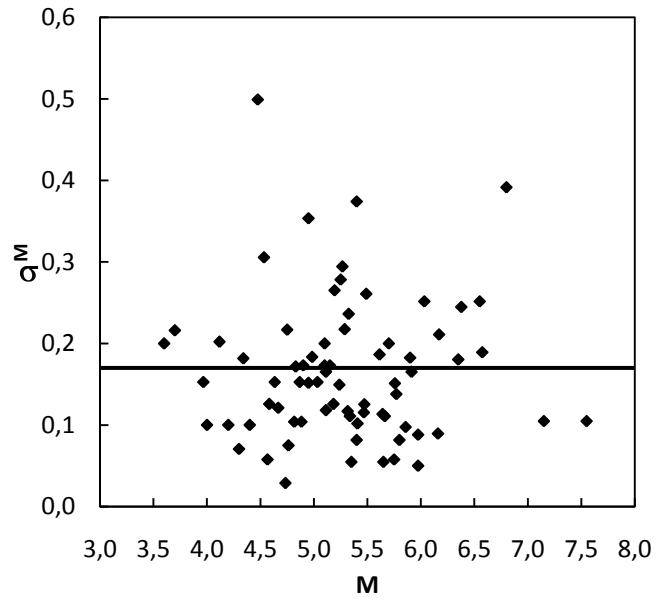


**Figure 4.2-25. Uncertainty in moment magnitude parameter**

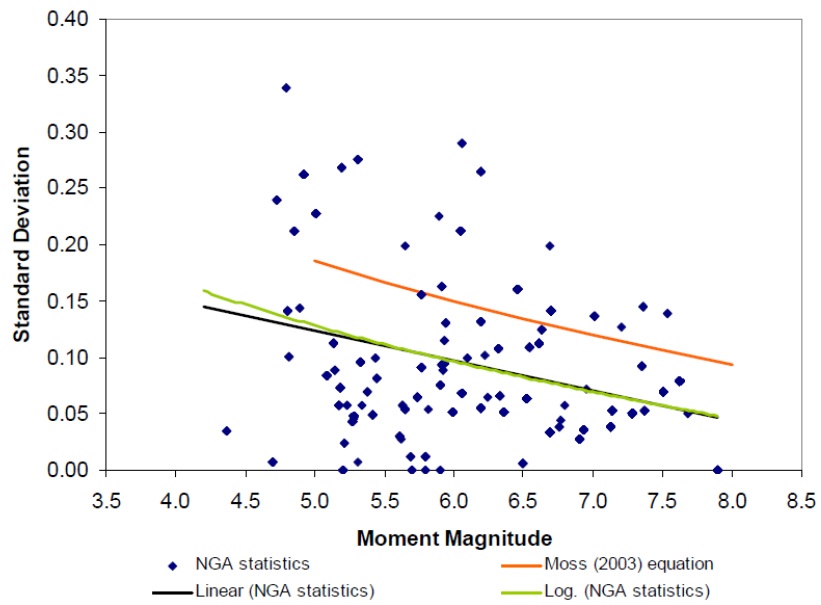


**Figure 4.2-26. Moment magnitude uncertainty as summarized by Moss and Kiureghian (2006)**



Examination of variation of  $\sigma_M$  against year of earthquake does not prove any reduction in sigma values with expanding seismometer network, or increased sample size in standard deviation calculations, for the current dataset (Figure 4.2-27).

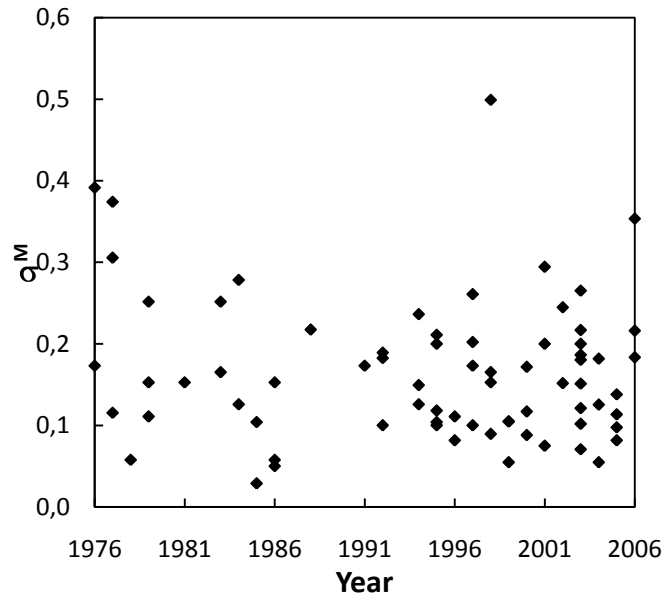


**Figure 4.2-27. Moment magnitude uncertainty as a function of event date**

Final form of magnitude uncertainty quantification is presented in Figure 4.2-28, showing median estimates of  $M$ , and error bars corresponding to 1 standard deviation value for each event. Recall that, due to relatively sparse sample size of reliable moment magnitude estimates for the Turkish dataset, the average value of  $\sigma_M$ , being equal to 0.17 magnitude units is assigned as the constant value of parameter uncertainty in the current GMPE model. Assigning individual parameter uncertainties to each event requires a more thorough understanding and quantification of sources of error, thus this preference was overlooked. Factors such as possible inter-dependency of magnitude estimates of multiple seismological agencies, eventually that will result in underestimation of epistemic uncertainty, also needs to be quantified.

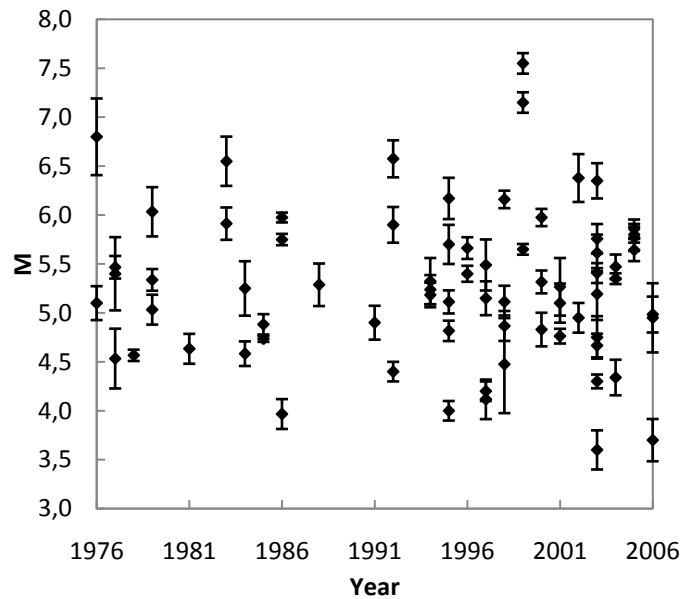


**Figure 4.2-28. Estimated median moment magnitudes with error bars**

Results obtained by processing local data has shown that, superposing uncertainty in moment tensor solution with a representative value of  $\sigma_{M,T}=0.081$  proposed by Kagan (2002b), would result in a higher estimate of total uncertainty due to moment magnitude; as compared to overall representative value yielded by NGA data (Figure 4.2-26). Thus, it becomes possible to state that predicted values of moment magnitude uncertainty from local data already inhibits unknown level of uncertainty due to magnitude scale conversion, and possibly increased statistical uncertainty due to reduced sample size used while calculating related parameters. To partly answer this question, a second set of data with increased number of samples (including all the listed agencies utilizing mostly converted magnitude scales) was evaluated.  $\sigma_M$  value increased to 0.22, indicating that moment magnitude conversion procedures are more likely dominate the increased variability in our dataset.

Final selection of parameter uncertainty of moment magnitude is  $\sigma_M = 0.17$  and superposition of uncertainty due to methods in moment tensor solutions is disregarded in this study.

#### 4.2.6 Source to Site Distance Metrics

A relationship between different measures of source to site distance and their respective implementations in GMPE's is another topic of discussion in GMPE models. Abrahamson and Shedlock (1997) present an outline of several different metrics used to measure distance in strong ground motion attenuation studies. The most common distance metrics are  $R_{jb}$ , the closest horizontal distance to the vertical projection of the rupture,  $R_{rup}$  the closest distance to the rupture surface,  $R_{seis}$  the closest distance to the seismogenic rupture surface,  $R_{epi}$  the closest distance to the epicenter, and  $R_{hyp}$  the hypocentral distance (Abrahamson and Shedlock 1997).  $R_x$  distance has also been recently introduced to model the hanging wall parameter in the NGA series, used by Abrahamson and Silva (2008) and Chiou and Youngs (2008) models. Combination of more than one distance metrics is also possible. For instance, Abrahamson and Silva (2008) model has utilized  $R_{rup}$  as the major distance metric, however also implemented  $R_{jb}$  to their hanging wall scaling function. Illustrative reminder for various distance metrics is presented in Figure 4.2-29.

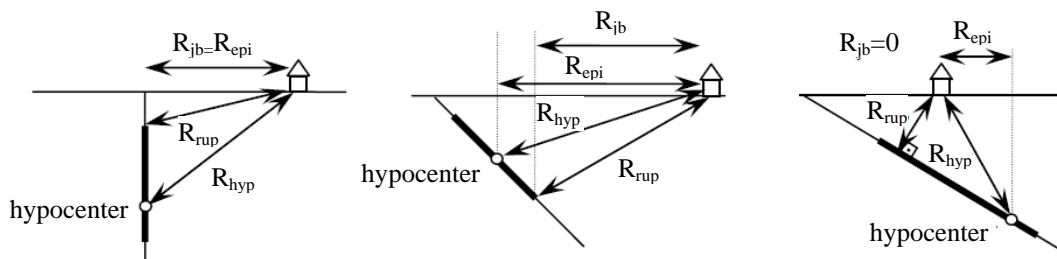


**Figure 4.2-29. Illustrative description of various distance metrics used in GMPE models (Erdoğan, 2008)**

Determination of the hypocentral location for an event involves the processing of waveforms collected at various stations distributed over an area, and an approximation on the best possible choice; with a given uncertainty. This approximation is closely related with magnitude calculation, indicating that moment magnitude and distance terms are not fully independent. However, in source to site

distance determination, this study excludes the epistemic uncertainty in epicentral location. Rather than modeling the average epicentral distance error for defining the buffer zones as in Chapter 3, estimates from a single seismological agency are selected for progress. The agency is selected as KOERI, having epicentral location predictions compatible with the alignment and position of tectonic structures in the field. On the contrary, HRVD epicenter estimates can be classified as the other extreme, mostly pointing to off-fault locations.

Having considered the hypocentral (or epicentral) location as a fixed point, another form of uncertainty that is of importance to the hazard analyst is the relationship between different distance metrics. Scherbaum et al. (2004) studied the relationship of these distance metrics and ran simulations to assess the relative variability.  $R_{jb}$  was treated as the baseline distance metric and the variation of  $R_{rup}$ ,  $R_{seis}$ ,  $R_{epi}$ , and  $R_{hyp}$  were calculated using simulated ruptures along a rupture plane scaled to magnitude. Main variables of the simulations were as follows:

- i) Scherbaum et al. (2004) rupture geometry for an event is assumed to be rectangular; width and length are generated using the Wells and Coppersmith (1994) relationships.
- ii) Depth distribution of hypocenters is modeled using a truncated normal distribution, later modified by a half cosine wave.
- iii) The simulations were performed in different-magnitude bins with center values varying from 4.75 to 8.25 in steps of  $\Delta M=0.25$ . The individual magnitude values were randomly selected from a uniform distribution within the bin margins.
- iv) For each bin, 100 fault planes were generated for which the hypocentral depths were randomly sampled from a truncated normal distribution.

- v) For all scenarios the top of the seismogenic zone was modeled at 3 km. The bottom was at 20 and 25 km for strike-slip and dipping events, respectively. Dip angles were selected randomly for each fault type, based on a given median and standard deviation defined by truncated normal distribution.

Subsequently, for each event, 200 randomly selected observation points were generated within a distance range of 300 km plus the average fault length for that magnitude bin (Scherbaum et al., 2004).

#### *4.2.6.1 Re-Evaluation of Source-to-Site Distance Metrics Using Batch Simulations*

This study attempts to re-evaluate the relationships between different distance metrics, by running simulations that are analogous to Scherbaum et al. (2004); however implementing randomization of different parameters obeying different distributions. Properties of the simulation parameters are as follows:

- i) Strike axis of the fault is aligned  $45^{\circ}$  to the north. 100 observation points are distributed randomly around the strike axis, over an area of 400 km x 400 km dimensions. Randomization of observation points is made by generating 100 linearly spaced points along the strike axis, then rotating randomly over  $360^{\circ}$  circle (Figure 4.2-30).
- ii) Simulations are made for magnitudes  $M=4.0$  to  $M=8.0$ , in half magnitude intervals. For each magnitude interval, rupture dimensions are also generated randomly. A preliminary version of the magnitude-rupture dimension relationships summarized in Chapter 2 was used. The relationship incorporates SOFP (style of faulting parameter). Rupture area and rupture width were sampled using normal distribution, truncated at -3

and +3 standard deviations. Rupture length was calculated as the ratio of rupture area to rupture width. Thus, probability of occurrence of a specific length-width scenario was calculated using the product of probabilities of occurrences of individual (area and width) values of rupture dimensions.

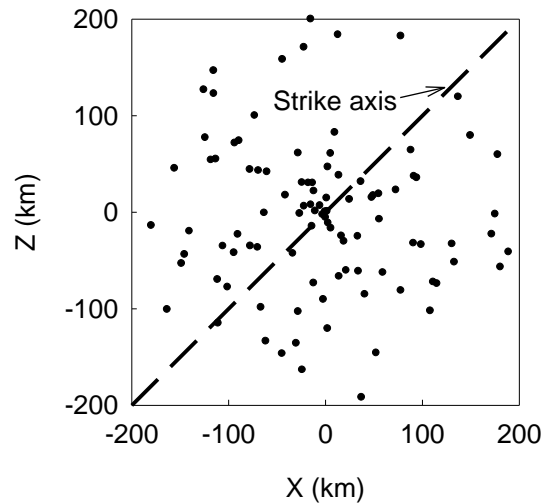


**Figure 4.2-30. Randomly generated observation points for source to site simulations**

- iii) Focal depth was sampled at 3, 5, 10, 15, 20, 25 and 30 km, respectively. Probability of each depth scenario was the same.
- iv) Rake angles were uniformly sampled from SOFP=0 to SOFP=1, using 13 bins.
- v) Dip angles were uniformly sampled at  $10^0$  intervals. Boundaries were rather wide,  $30^0$ - $80^0$  for normal faults, and  $10^0$ - $80^0$  reverse faults.
- vi) Location of the hypocenter on the generated rupture area was also randomized. Keeping the hypocentral point fixed, simulations were done by shifting the rupture plane (considering dipping) in two dimensions. Bottom edge of the rupture cannot extend beyond the defined  $z_{\max}$  value

of 30 km. Similarly, top edge of the rupture can extend along the ground surface.

The total number of simulations, excluding multiplicative factors from randomization of rupture dimensions and shifting of rupture location, reached up to 507870, and required the utilization of enormous amount of runtime distributed to multiple CPUs. The program to conduct the simulations, and compute the different source to site metrics was prepared from scratch, using MATLAB.

Values of individual distance metrics (excluding the epicentral and hypocentral distance that are taken as exact), obtained through simulations contain the quantification of variability due to uncertainty of rupture location on the defined fault plane, and the variability superposed by rupture geometries having different aspect ratios (consequence of sampling of rupture area and rupture width from magnitude – rupture dimension relationships). However, median values of the distance estimates from each data point are considered in developing the global model. Figure 4.2-31 presents an illustrative explanation of the simulation procedure used:

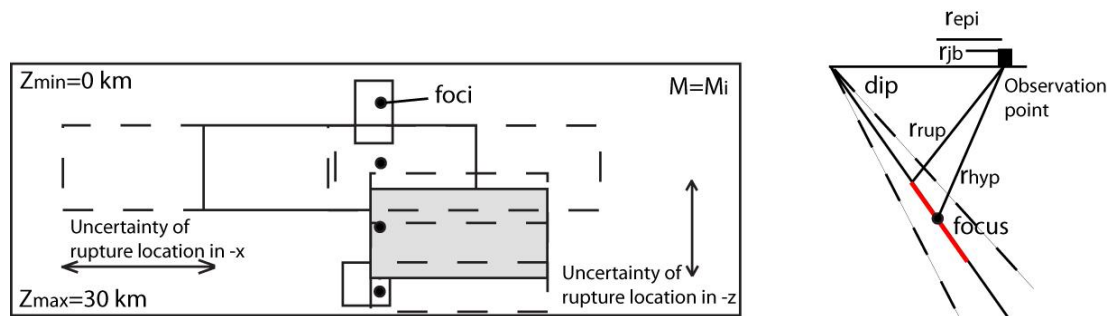


**Figure 4.2-31. Illustration of location, depth, dip, and rupture dimension uncertainty for a scenario with a given earthquake magnitude**

Simulation results from over 500000 scenarios were collected and merged. Unprocessed data was batch-plotted for every magnitude, and rake angle bin; both in

normalized and unnormalized forms. Figure 4.2-32 presents the relationship between  $R_{epi}$  and  $R_{jb}$ . For the sake of simplicity, results from  $R_{epi} - R_{hyp}$ ,  $R_{rup} - R_{jb}$ ,  $R_{rup} - R_{hyp}$ ,  $R_{rup} - R_{epi}$ ,  $R_{jb} - R_{hyp}$  relationships are undisclosed. Impact of earthquake magnitude on the scatter of normalized  $R_{jb} - R_{epi}$  relationship is presented in Figure 4.2-33. Switch from the  $M=5.5$  bin to  $M=7.5$  bin explodes the amount of scatter in the data. The scatter is also a function of dip angles.

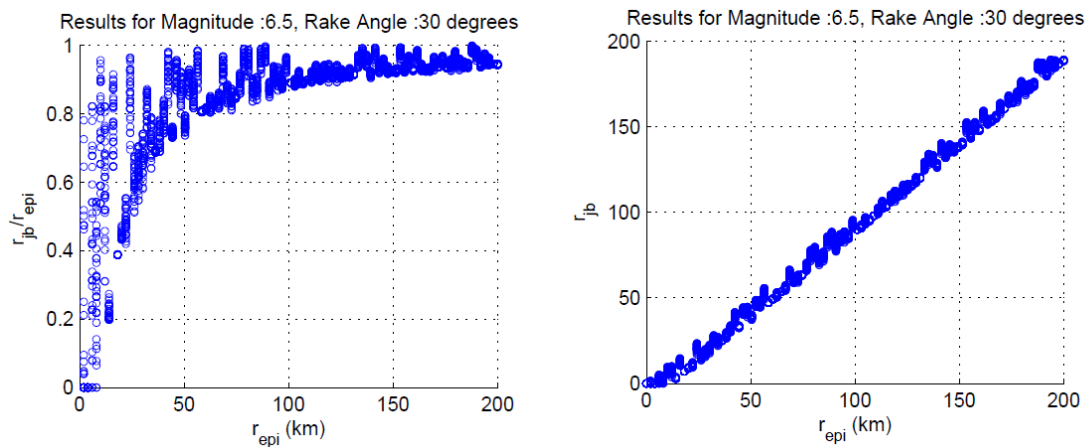


**Figure 4.2-32. Sample bin data for  $R_{jb} - R_{epi}$  relationships ( $M=6.5$ ,  $Rake= 30^{\circ}$ )**

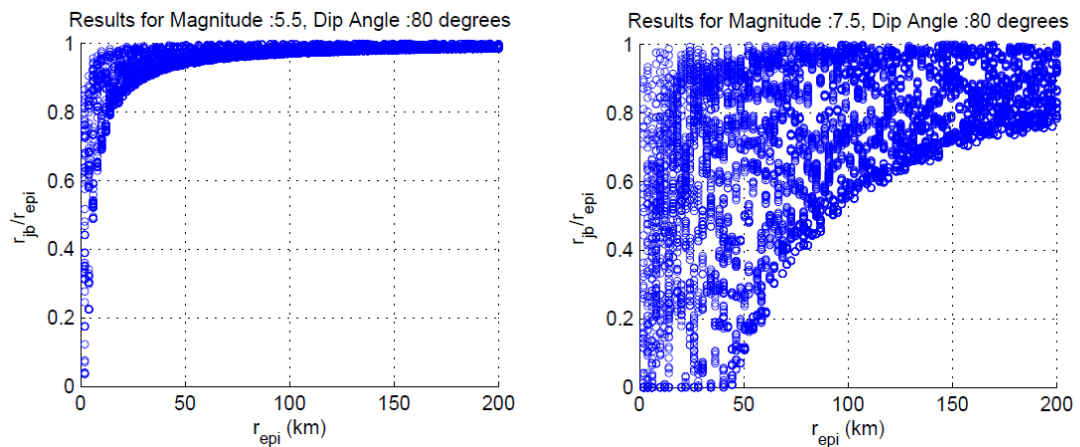


**Figure 4.2-33. Effect of magnitude on scatter of  $R_{jb} - R_{epi}$  relationships**



In order to develop a model stating the relationship between two distance metrics, 24 different functional forms were studied. For demonstration purposes, optimization results for relation between  $R_{epi}$  and  $R_{jb}$  is presented. Effect of excluding higher bound magnitudes on the order of model error was also studied; and the final decision was made for keeping the high magnitude data ( $M=8.0$ ) in the optimization. Out of 24 functional forms, the following was selected, based on the maximum likelihood values, and capabilities to satisfy the constraints imposed by the definitions of distance metrics (Equation 4-2). Extreme outliers above 10 standard deviation values were interactively excluded from the optimization, for the stability of model coefficients. In Equation 4-2,  $M$  is the moment magnitude;  $\delta_{dip}$  is the dip angle of the fault. The optimization is made on  $\ln(r_{jb})$ . Model error term is given in Equation 4-3.

$$\ln(r_{jb}) = \ln(r_{epi}) + \ln(r_{epi} + \theta_1 + \theta_2 \cdot \ln(M)) - \ln(r_{epi} + \theta_3 + \theta_4 \cdot \ln(M) + \theta_5 \cdot \ln(\delta_{dip}) + \theta_6 \cdot e^{\theta_7 \cdot M}) \quad (4-2)$$

$$\sigma \ln_{r_{jb}} = \theta_8 + \theta_9 \cdot \ln(r_{epi}) + \theta_{10} \cdot \ln(M) \quad (4-3)$$

Results of the maximum likelihood estimates, and related model coefficients are presented in Table 4.2-5. Final form of the model is presented in Equations 4-4 and 4-5.

$$\ln(r_{jb}) = \ln(r_{epi}) + \ln(r_{epi} + 7.154 + 1.708 \cdot \ln(M_w)) - \ln(r_{epi} + 6.778 - 2.963 \cdot \ln(M_w) + 0.746 \cdot \ln(\delta_{dip}) + 0.316 \cdot e^{0.660 \cdot M_w}) \quad (4-4)$$

$$\sigma \ln_{r_{jb}} = 0.261 - 0.082 \cdot \ln(r_{epi}) + 0.128 \cdot \ln(M_w) \quad (4-5)$$

For different magnitude bins, using a representative dip angle value of  $45^0$ , median predictions of the model was plotted. Figure 4.2-34 divides the data into 9 magnitude

bins for better representation. Blue scatter represents the data, and the solid red lines are the median predictions for given magnitudes. For low magnitude events,  $R_{jb} / R_{epi}$  ratio is close to unity except near-rupture distance range, as expected. The distance range dominating variability in the data increases with increasing magnitude.

**Table 4.2-5. Model coefficients for the  $r_{jb} - r_{epi}$  relationship**

Model coefficient	Value
$\theta_1$	7.154
$\theta_2$	1.708
$\theta_3$	6.778
$\theta_4$	-2.963
$\theta_5$	0.746
$\theta_6$	0.316
$\theta_7$	0.660
$\theta_8$	0.261
$\theta_9$	-0.082
$\theta_{10}$	0.128
MLE	167237

A different form of representation was used in Figure 4.2-35, exhibiting the distribution of measured (simulation results) and predicted  $R_{jb}$  values (model results). Both axes represent natural logarithms of  $R_{jb}$  values.

Decision making process on the implementation of median and associated variability terms of source to site distance parameter to the GMPE model will be based on performance evaluation of Scherbaum et al. (2004) and the currently developed relationships. This will be covered in Section 4.2.6.2.

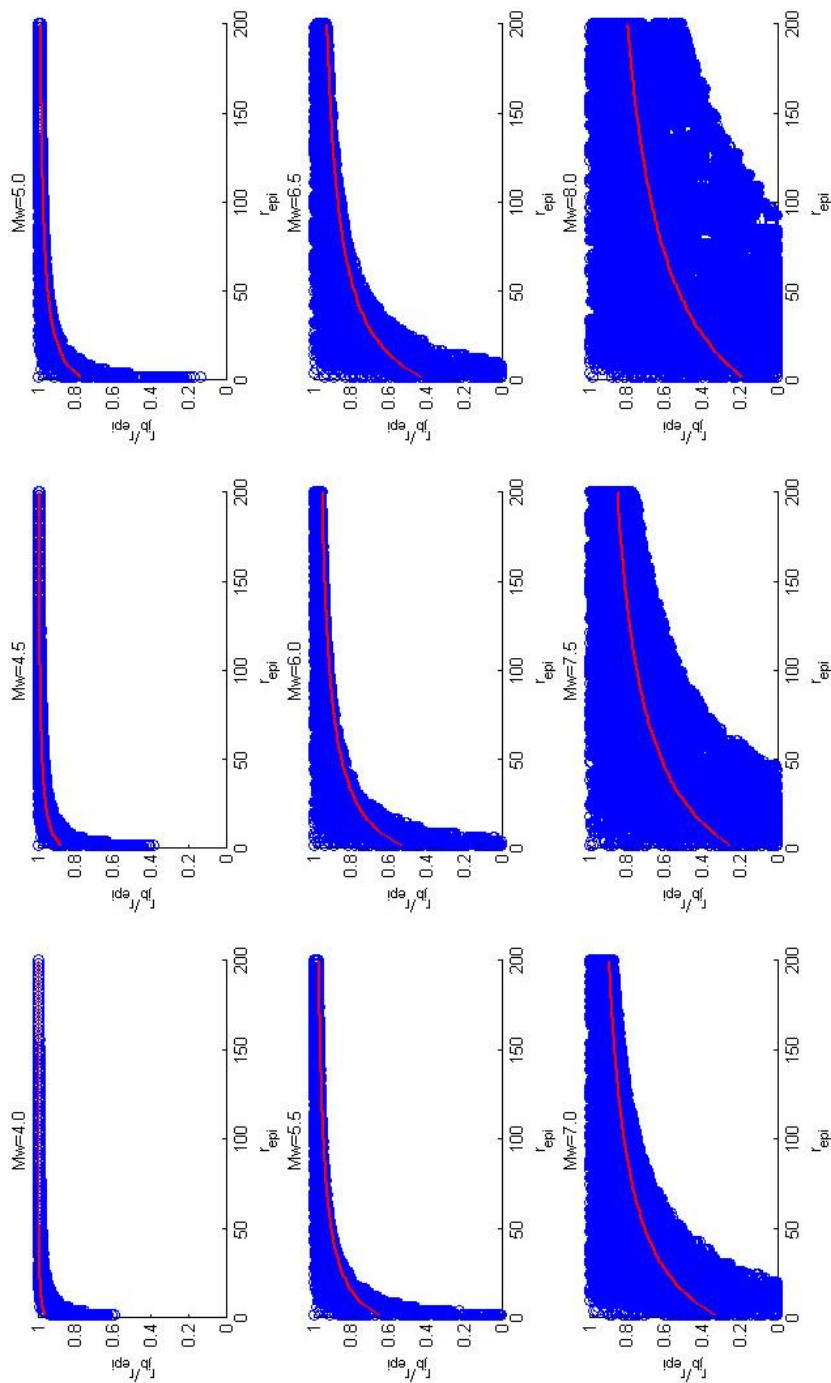


**Figure 4.2-34. Median predictions for the  $R_{\text{epi}}\text{-}R_{\text{jb}}$  model plotted against scattered data from different magnitude bins (normalized representation)**

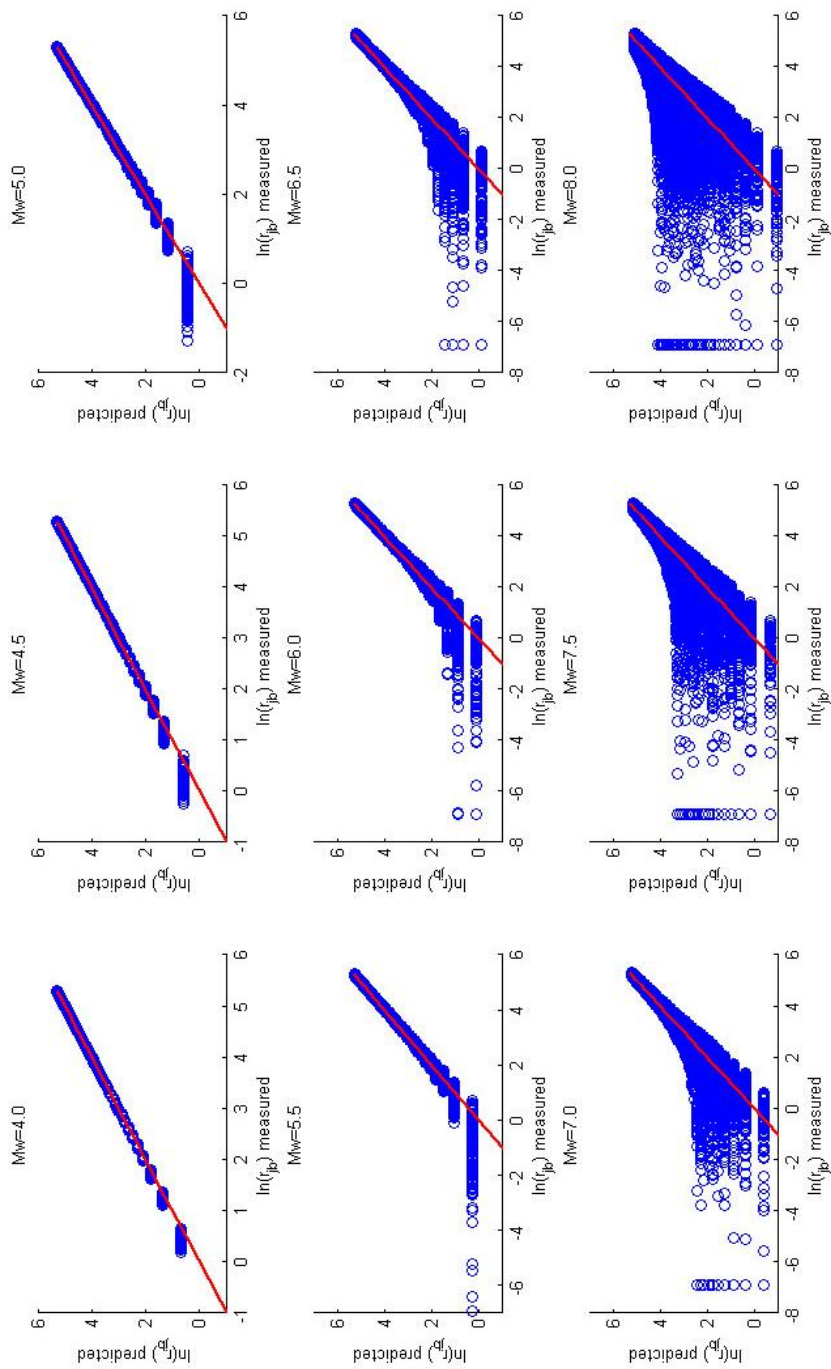


**Figure 4.2-35. Median predictions for the  $R_{epi}$ - $R_{jb}$  model plotted against scattered data from different magnitude bins (unnormalized representation)**

#### 4.2.6.2 Performance Evaluation of Source to Site Distance Relationships

This section covers the results of a set of source to site simulations made using different models and methods. First two models to be compared are the Scherbaum et al. (2004) and the currently developed model introduced within this text. The basis of comparison will be the relationship between  $R_{epi}$  and  $R_{jb}$ . A third set of controlling simulations is based on excluding global models, hence exempting variability superposed by additional predictive variables and the model itself. Thus, the sole contributor of variability for  $R_{jb}$  becomes the variability imposed by the shifted (in both axes) location of rupture on the fault, and the aspect ratio for the rupture, as a consequence of sampling rupture area and rupture width through empirical scaling relationships. The global model developed within this study does not contain quantification of above listed uncertainties, and reflects the variability of the model itself.

The comparison set contains 12 selected scenarios. Values from Scherbaum et al. (2004), abbreviated as “S04” and the recently developed model are compared to results of individual data simulations carried out on a case specific basis (Table 4.2-6). Notice that for Equations 4-4 and 4-5, maximum likelihood estimates are made for natural logarithm of  $R_{jb}$ . The median value was converted to  $R_{jb}$  using the exponential function, and the total error term ( $\sigma \ln R_{jb}$ ) was converted to  $\sigma R_{jb}$  using the first order approximation. Thus, for the specific case of natural logarithm function,  $\sigma \ln R_{jb}$  corresponds to coefficient of variation of  $R_{jb}$ .

Examining Table 4.2-6 reveals that median values of  $R_{jb}$  predictions from two models and the control case are close, especially for small to moderate magnitude earthquakes. However, for large magnitude events, difference is pronounced for some of the cases (trial numbers 6, 9, 10).

**Table 4.2-6. Comparison of different methods for source to site distance simulations**

No	M	R <sub>epi</sub> (Exact)	δdip (Deg.)	μR <sub>jb</sub> (km) <b>S04</b>	σR <sub>jb</sub> (km) <b>S04</b>	μR <sub>jb</sub> (km) <b>Eq. 4-4</b>	σR <sub>jb</sub> (km) <b>Eq. 4-5</b>	μR <sub>jb</sub> (km) <b>Case Specific</b>	σR <sub>jb</sub> (km) <b>Case Specific</b>
1	4.5	76.5	85	75.5	0.9	74.7	7.3	75.7	0.9
2	5.1	39.9	85	38.6	1.0	36.6	6.1	38.4	2.1
3	5.1	14	85	11.5	1.0	11.8	3.0	12.7	1.4
4	5.5	73.4	60	70.3	1.7	68.0	8.6	70.6	2.5
5	6.7	14	85	6.7	8.2	7.6	2.2	7.01	2.1
6	7.1	14	85	3.1	13.6	6.5	1.9	6.9	1.7
7	7.1	56.8	85	40.1	16.9	40.1	7.2	34.8	14.9
8	7.1	76.5	85	58.2	17.7	57.9	9.0	55.5	15.3
9	7.1	14	85	3.1	13.6	6.5	1.9	6.3	1.9
10	7.1	14	60	0.41	12.1	6.6	1.9	2.5	3.2
11	7.5	73.4	60	45.4	23.3	50.6	8.4	47	8.9
12	7.5	9.15	60	Error	Error	3.1	1.1	5.5	1.6

Another descriptive statistical parameter to check is the coefficient of variation. COV values for the 12 events are summarized in Table 4.2-7. Results indicate that the COV values for small magnitude events predicted using Equations 4-4 and 4-5 are relatively higher than the two other predictions. On the other hand, it is obvious that Scherbaum et al. (2004) model yields extremely high values of COV for large events; which eventually makes it unacceptable for utilization in parameter uncertainty quantification of source to site distance. Equations 4-4 and the case specific control runs yield comparable results.

Recalling that uncertainties from both models have different origins, the quantification of source to site distance uncertainty using the case specific approach

was selected in GMPE development. In the compiled dataset, parameters such as focal depth, strike angle, dip angle, as well as earthquake magnitude are available. Considering these parameters are exact, independent simulations were run for each case, instead of utilizing available model predictions. Magnitude uncertainty quantified in Section 4.2.5 was ignored in distance simulations.

**Table 4.2-7. Comparison of COV values for different methods of source to site distance simulations**

No	M	R <sub>epi</sub> (Exact)	$\delta$ dip (Deg.)	COV S04	COV Eq. 4-4	COV Case Specific
1	4.5	76.5	85	0.01	0.10	0.01
2	5.1	39.9	85	0.03	0.17	0.05
3	5.1	14	85	0.08	0.25	0.11
4	5.5	73.4	60	0.02	0.13	0.04
5	6.7	14	85	1.22	0.29	0.30
6	7.1	14	85	4.40	0.30	0.25
7	7.1	56.8	85	0.42	0.18	0.43
8	7.1	76.5	85	0.30	0.16	0.28
9	7.1	14	85	4.44	0.30	0.30
10	7.1	14	60	29.73	0.30	1.31
11	7.5	73.4	60	0.51	0.17	0.19
12	7.5	9.15	60	-	0.34	0.30

#### 4.2.7 Site Classification and 1-D Ground Response Analyses

Local site response term in ground motion prediction equations has been subject to steadily increasing attention among researchers. Selection of most appropriate site classification system, uncertainties and missing data regarding the local soil conditions of strong ground motion stations, integration of empirically based ground response models into GMPE's have brought huge steps in model development, that was once characterized by an ambiguous definition of "rock" vs. "soil". This section does not intend to provide complete background information on the development of ground response models used in GMPE's; however a brief introduction will be supplied.

The emphasis will be given on the procedures followed to compile site characteristics of strong ground motion stations, comparison between predictions of various studies, tracking and completing missing site information, tracking incompatibilities in the metadata supplied by header lines of the accelerogram files, and developing a systematic approach for generic site characterization aimed at 1-D equivalent linear analyses.

##### 4.2.7.1 *Brief Overview of Modeling Ground Response in GMPEs.*

During the early stages of steady evolution of local site response term in GMPEs, implementation of most basic, yet ambiguous definition of "soil" and "rock", as well as an amplification factor defined with respect to a reference  $V_{s30}$  were used. In the Abrahamson and Silva (1997) model, definition of "rock", was indeed a representation of intact rock, weathered rock and shallow stiff soils melted in the same pot, an important factor for cross comparison that was unknown to most users worldwide. Campbell (1997) used the definitions "hard rock", "soft rock", and "soil"; whereas Boore et al. (1997) implemented a continuous representation in terms of  $V_{s30}$  value.



Glancing at local models, Kalkan and Gülkan (2004) followed the same approach with Boore et al. (1997). Özbey et al. (2004) used dummy variables for NEHRP soil classes, whereas Ulusay et al. (2004) preferred the basic definition of “rock”, “soil” and “soft-soil”. A more recent work by Akkar and Bommer (2010) uses the “rock”, “stiff soil”, and “soft soil” classification; almost in one to one correspondence with Ulusay et al. (2004). As the last representative, Akkar and Çağnan (2010) model implements Boore and Atkinson (2008) modification of the Choi and Stewart (2005) study; enabling a continuous representation of ground response factor in terms of  $V_{s30}$  and  $pea_{cock}$  (peak ground acceleration on rock).

More detailed discussion on ground response models will be supplied in the proceeding sections; however, in order to develop, or even use an existing model, the essential parameter to be clarified is the local site conditions.

#### *4.2.7.2 Data Sources for Site Classification of National Strong Ground Motion Stations*

An extensive literature survey was performed to compile the existing data on classification of national strong ground motion stations. Among the references used, Kalkan and Gülkan (2004), Zare and Bard (2002), Rathje et al. (2003), ESD (European Strong Motion Database, Ambraseys et al., 2002), Sandıkkaya (2008) in conjunction with Sandıkkaya et al. (2009), are to name a few.

Initial comparison was done by separating the recent results of testing and classification on strong ground motion sites by Sandıkkaya et al. (2010) and Akkar et al. (2010) from previous studies. Non-unique classification systems used and contradictory parameterization used in earlier works restricted the reliability of compiled data. To give an example, REF (Refahiye) station operated by ERD-GDDA was classified as “soft soil” by Kalkan and Gülkan (2004). Same station is

considered to be under “stiff soil” class by the European Strong Motion Database, and falls into NEHRP C Class according to Akkar et al. (2010).

Rathje et al. (2003) includes shear wave velocity profiles obtained using SASW measurement for temporary strong ground motion stations installed after the 1999 Kocaeli main shock. It also provides SASW results for some of the sites near Istanbul and Kocaeli Bay Area; reaching up to a total number of 18 characterizations. Characterizations of 10 sites operating within BYT-NET and DAT-NET local dense arrays in Yalova and Denizli regions provide boring log information.

Out of 179 total recordings for 72 candidate events were recorded by 114 different stations operated by various agencies such as ERD-GDDA, KOERI, ITU, IRIGM, and LDEO. Out of 179 accelerograms, 109 (61%) were recorded on sites characterized using MASW studies and site borings by Sandıkkaya (2008), later summarized in Akkar et al. (2010). Details of site characterization were obtained from online dissemination of strong ground motion database of Turkey (DAPHNE), accessed via <http://kyh.deprem.gov.tr/ftpt.htm>. Above listed references for site classification were not satisfactory in covering the complete list of stations that required characterization within the confines of this study. Thus, a supplementary stage of work was put into act, implementing an overlay analysis of surface geology maps of MTA (Directorate of Mineral Research and Exploration), 1:25000 scale topographical maps of various regions, water-well logs recorded and archived by DSI (State Hydraulic Works), online mapping platforms providing satellite images, and spoken communication with local government authorities (including, but not limited to meteorological stations, public works and settlement offices at provinces, hospitals, and post offices) on the locations of strong ground motion stations. During the compilation of data, critical ambiguities on location, name, and type of instrument installed in strong ground motion stations were also resolved. Next section discusses the details in identifying and solving missing, or conflicting data.

#### 4.2.7.3 *Resolving Conflicts in Station Metadata and Coordinates*

Careful investigation conducted on metadata supplied by the header lines of accelerograms revealed several issues to be resolved, regarding the correct names of the establishments where strong ground motions were located, type of instrument recording the accelerogram, and coordinates of the station. Since any misinterpretation of data would have led to unquantifiable magnitudes of error in source to site distance calculations, or local site conditions of the stations; extreme care was shown in addressing the problems.

First type of problem was the incompatibility of station names and/or coordinates between two records from the same station at different time intervals. For some of the records, metadata indicated a change in instrument type also, mainly biased towards upgrading from analog to digital. Further investigation of station coordinates presented by the earlier version of ERD website, at the time of compilation of data, also addressed incompatibilities between the recent list and the values indicated within accelerogram headers. Meticulous effort in tracking the inconsistencies was initially bounded by 21 stations (ERZ: Erzurum, GOL: Gölbaşı, HRS: Horasan, CER: Çerkeş, IZM: İzmir, MLT: Malatya, MUR: Muradiye, HTY: Hatay, TKR: Tekirdağ, IST: İstanbul, AMS: Amasya, ERC: Erzincan, VAN: Van, BRD: Burdur, CYH: Ceyhan, Göynük: GYN, IZN: İznik, BLK: Balıkesir, BNG: Bingöl, and BDR: Bodrum). A revised stage of effort was expanded throughout all the station list; through conducting a specialized study for cases which the defined location coordinates did not coincide with the geographical locations of the actual establishments spotted on online maps.

The main points of suspect in the reason of incompatibilities were, i) deinstallation and reinstallation of stations at different government agencies over time (e.g. shifting from meteorological station to the local government palace, with station identification code remaining the same), ii) shifting of stations to the new settlement

of the same agency within the same city (moving of the agency settlement), iii) upgrading of the instrument at the same location, transition from older SMA-1's to new digital accelerographs, iv) name and function changes in the local government building, meanwhile keeping the properties and location of the instrument same, and finally, v) other possible changes.

To resolve these issues, case by case study was performed for each location; overlaying information on surface geology and 1:25000 scale maps mostly showing important buildings within towns, cities. Local government authorities, including chiefs of meteorological stations, officials at city public works and settlement offices, headmen at villages, government palaces (city court like office gatherings where the municipality, province or district governorship were contacted by phone. Several questions were asked; including verification of the exact recent location of the instrument, and history of the instrument (shifts, deinstallations, reinstallations). Answers given to these questions were collected and analysed.

The results indicate that, there were even multiple location changes of the instrument over time, and each record from that instrument in our database was collected from different part of the city, town, or village. This certainly has effect on the local site characteristics, and source to site distance calculations. All of the conflicts were solved, and the correct location of the instrument at the time of those particular events were compiled and recorded. Abbreviated instrument codes were appended a suffix "A" or "B" where necessary, for healthier tracking. It is worth noting that some of these stations are inactive.

Figure 4.2-36 presents the spatial distribution of strong ground motion stations included in the current dataset.

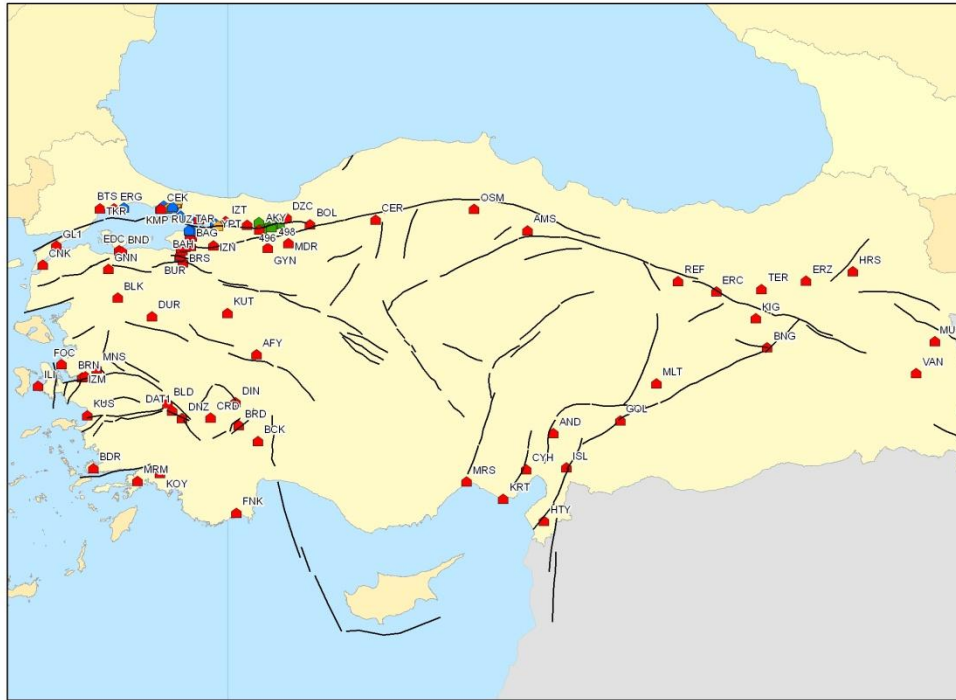


**Figure 4.2-36. Distribution of strong ground motion recording stations used in the current dataset**

#### 4.2.7.4 Discussion on Site Classification Preferences

As stated in Section 4.2.7.2, out of 179 candidate records to be included in GMPE model, 109 of them have site characterizations based on detailed data collected from the recent study by Sandıkkaya (2008) and Sandıkkaya et al. (2009). Even with the several additions from SASW, BYT-NET and DAT-NET sites, a considerable amount of sites still need to be characterized based on limited amount of measured data.

The current GMPE model initiates the site characterization procedure using NEHRP categories, and builds the ground response model on this preference. As stated earlier, some of the sites have measurements available, while others do not. For sites with absent (already ignoring classifications reported in Kalkan and Gülkan (2004), and

Zare and Bard (2002)) soil classes, best predictions were based on examining surface geology, topography, and partially utilizing deep-water well logs mostly driven at deep alluvial basins of Turkey. For sites which comfortable predictions of distinct NEHRP classes could not be made, predictions were weighted between two neighboring classes. Weights assigned to sites with double NEHRP classes cover 11% of the whole dataset. Weighting factors were chosen as multiples of 0.25; generating three types of schemes; 1-0, 0.75-0.25, and 0.50-0.50.

In order to provide a consistent framework for ground response analyses, full soil profile data was exempted from further use for instrumentally characterized sites. Instead, only the NEHRP classes corresponding to available data were calculated and substituted in place of older predictions based on semi-judgemental procedures, where applicable. The difference between predictions from two methods conformed to a shift of single class in almost all of the cases. A bias was not observed towards either stiffer/denser or softer/looser classes.

In order to test the applicability of MASW generated shear wave velocity measurements, a comparison of shear wave velocity profiles, summarized by Sandıkkaya (2008) and Akkar et al. (2010), with shear wave velocity values predicted from measured SPT blow counts is made. For cohesive materials, relationship proposed by Dickenson (1994) was used:

$$V_s = 100(N)^{1/3} \text{ (m/s)} \quad (4-6)$$

Similarly, Dickenson (1994) proposes Equation 4-7 for cohesionless soils:

$$V_s = 80(N)^{1/3} \text{ (m/s)} \quad (4-7)$$

Shear wave velocity values from MASW tests were compared with predictions of SPT-based relationships. Overburden correction was not applied to the SPT blow

counts. Assumed energy ratio of 45% was converted to 60% prior to substitution into Equations 4-6 and 4-7. Figure 4.2-37 presents two sample profiles from total number of 52 stations considered. Black series with triangle markers are the results of MASW measurements. Blue series with rhombus markers are  $V_s$  predictions using the empirical relationships. Data from DZC (Düzce) and DIN (Dinar) are two good representatives of the overall data trend; indicating a relative overestimation of MASW values below 20 m depth.

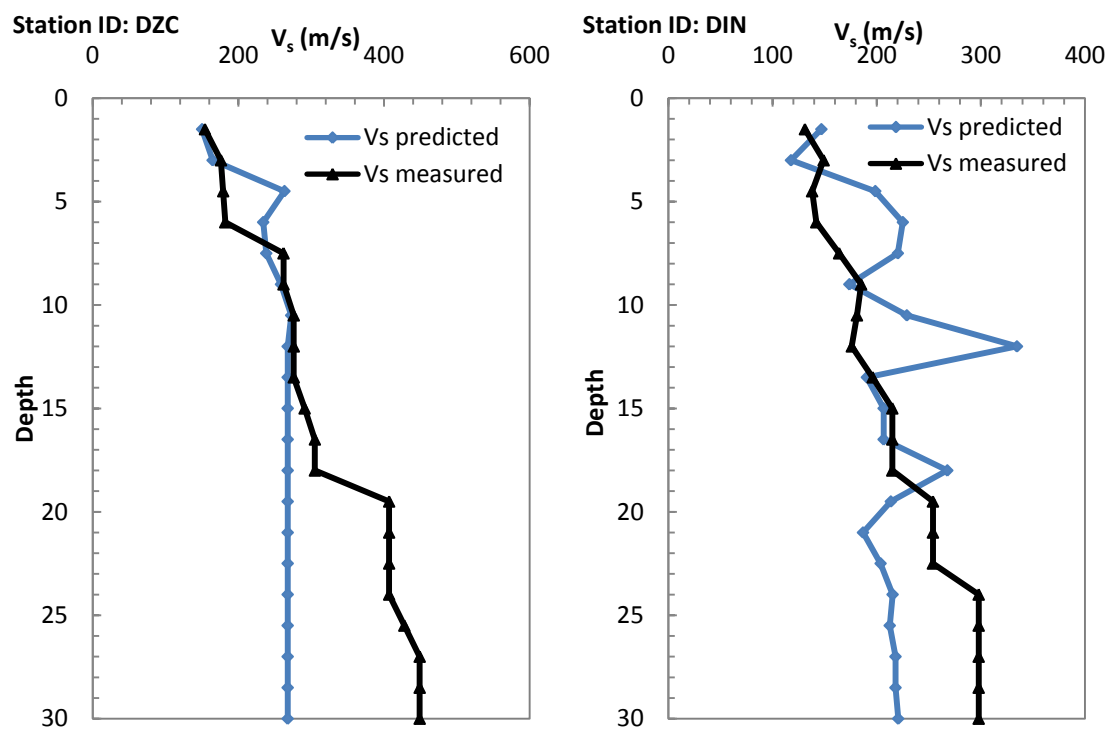


**Figure 4.2-37. Measured and correlation-predicted shear wave velocity profiles**

Residuals of shear wave velocity measurements, for every measurement point throughout 52 profiles, are presented in Figure 4.2-38. Data binning was performed for 3 categories of NEHRP classes, assigned using the  $V_s$  values predicted by MASW measurements.

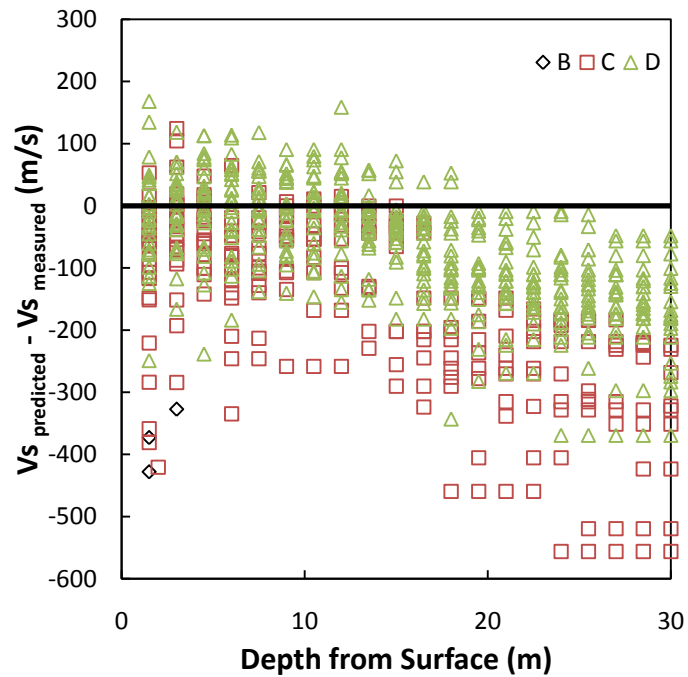


**Figure 4.2-38. Residuals of  $V_s$  values against depth from surface**

Profile information from MASW measurements, as well as additional data from SASW and borehole logs, provide valuable data for site classification. However, the question about adequacy of MASW data at depths below 20 m, and truncation of the profile at 30 m limits the modeling of deep stiff or soft soil sites in ground response analyses; unless extrapolation is made. Even when parameter uncertainty of soil stratum thickness, modulus degradation properties are neglected, all of these remaining factors bring inevitable amount of uncertainty to ground response analyses. Combining data points from stations, of which class predictions are made using less reliable methods (topography, surface geology, etc), requires a new approach that covers uncertainty in site classifications.



#### 4.2.7.5 *Generic Soil Profiles for 1-D Ground Response Analyses*

Having variable amount of information on local soil characteristics of each of the strong ground motion recording stations, a systematic approach was used to account for uncertainty imposed by ground response. Recalling that the simplest, yet the most comprehensive parameter that reveals information for all of the strong ground motion stations is the NEHRP classification system in the current dataset; a suite of representative soil profiles were developed.

Generic profiles were generated for NEHRP soil classes of B, C, D, and E, representing transition from rock to softer or looser soil types. Each soil class was represented by 7 different profiles, most of them being modified versions of actual cases, taken from Cetin and Seed (2000). Modified versions of Police Station and Soccer Field sites from Cetin et al. (2004) were also implemented, together with the modified version of Sapanca Hotel site (Cetin et al., 2002) to represent some of the NEHRP E class sites. Several sites with  $V_s$  profiles modeled using SASW testing (Rathje et al., 2003) were modified and enriched to obtain NEHRP D sites. Profiles for NEHRP B sites were developed completely artificially, accounting for the natural transition of the shear wave velocity as a function of depth from surface.

Key parameters of the generic soil profiles are tabulated in Table 4.2-8.  $H_{\text{profile}}$  is the total height of the profile in meters,  $T_p$  is the fundamental vibration period of the soil column.  $V_s$  represents average shear wave velocity of the whole column, until proposed bedrock is reached, and  $V_{s,30}$  is the average shear wave velocity of the upper 30 meters. Examination of mean values of  $V_{s,30}$  and  $T_p$  for each NEHRP class, as well as individual profile parameters, exhibits a smooth transition from stiffer/denser to softer/looser sites, meanwhile conforming to the overall representative values. Complete information about the shear wave velocity profiles of generic sites are presented in Figure C.1-C.28 (Appendix C). Related parameters

and soil types used for each layer are also summarized in Tables C.1-C.28 (Appendix C).

**Table 4.2-8. Summary of key parameters for generic soil profiles used in 1-D ground response analyses**

No	ID	H <sub>profile</sub> (m)	T <sub>p</sub> (s)	V <sub>s</sub> (m/s)	V <sub>s,30</sub> (m/s)	μV <sub>s,30</sub> (m/s)	μT <sub>p</sub> (s)
1	B1	30	0.16	769	769	992	0.13
2	B2	30	0.13	955	955		
3	B3	30	0.1	1245	1245		
4	B4	30	0.09	1323	1323		
5	B5	30	0.11	1065	1065		
6	B6	33	0.16	838	762		
7	B7	32.5	0.15	895	826		
8	C1	80	0.50	637	362	540	0.31
9	C2	35	0.17	817	717		
10	C3	46	0.3	621	523		
11	C4	51	0.34	593	495		
12	C5	55	0.47	472	395		
13	C6	30	0.20	595	595		
14	C7	30	0.17	690	690		
15	D1	34	0.5	277	252	250	0.66
16	D2	90	1.11	326	188		
17	D3	49	0.71	276	223		
18	D4	46	0.55	338	214		
19	D5	59	0.79	302	231		
20	D6	60	0.65	369	290		
21	D7	25	0.34	296	355		
22	E1	82.5	1.80	184	102	138	1.59
23	E2	63	1.19	211	151		
24	E3	80	2.14	150	105		
25	E4	54	0.89	243	179		
26	E5	103.5	2.28	181	120		
27	E6	70	1.38	202	140		
28	E7	95	1.48	256	168		

The next step in performing the 1-D ground response analyses is the selection of dynamic soil properties for each layer. The preference was made on using Vucetic and Dobry (1991) curves for cohesive soils. Modulus degradation and damping as a function of shear strain for a set of PI (plasticity index) values is presented in Figures 4.2-39 and 4.2-40. Similarly, for cohesionless soils, gravel curve was adopted from Seed et al. (1986), rock curve from Schnabel (1973), and sand curves for three bins of mean effective stresses from Seed and Idriss (1970) and Seed et al. (1986), respectively (Figures 4.2-41 and 4.2-42).

1-D equivalent linear ground response analyses are performed using SHAKE computer code, written by Schnabel et al. (1972). A purpose specific computer script was prepared to perform the generation of multiple input files, run SHAKE code, collect the results by reading the output files, and finally organize them for further processing. With total number of SHAKE runs reaching over 10000, developing a customized interface became inevitable. Analyses were performed for all horizontal ground motion components (longitudinal and transverse) of GMPE dataset, and for all 28 generic sites, intended for possible extended use. Signal processed ground motions were given at surface level, and the results were collected for motion at rock level. Time histories at rock level were baseline corrected prior to further use. Rotated definitions of horizontal ground motion components were then recalculated at rock level using the results of ground response analyses. The full procedure for batch ground response analyses is illustrated in Figure 4.2-43.

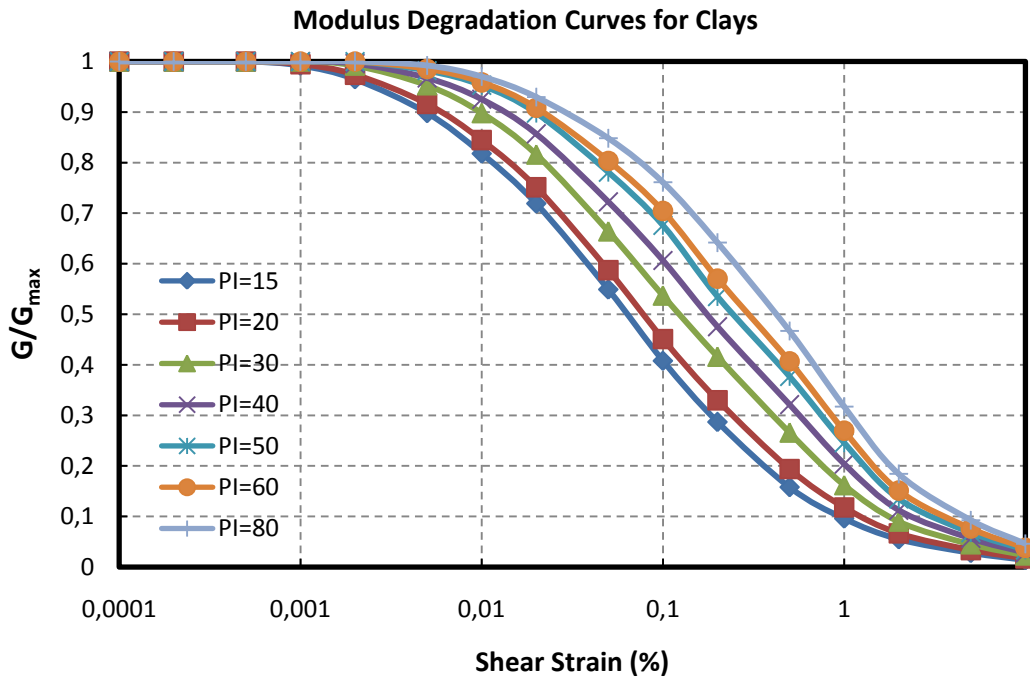


Figure 4.2-39. Modulus degradation curves for clays (Vucetic and Dobry, 1991)

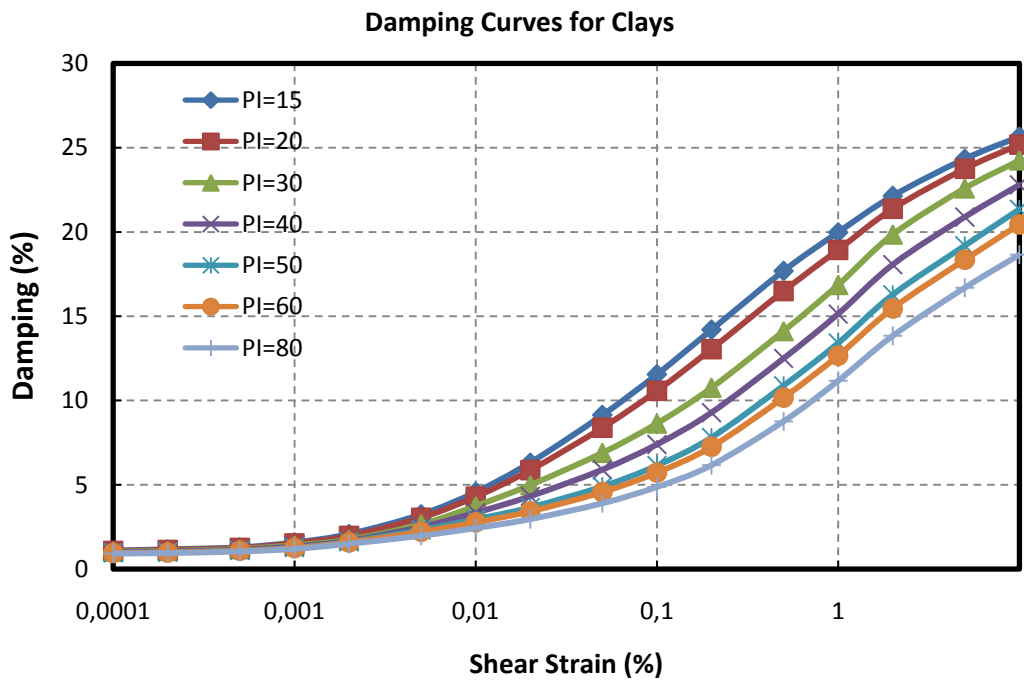


Figure 4.2-40. Damping curves for clays (Vucetic and Dobry, 1991)

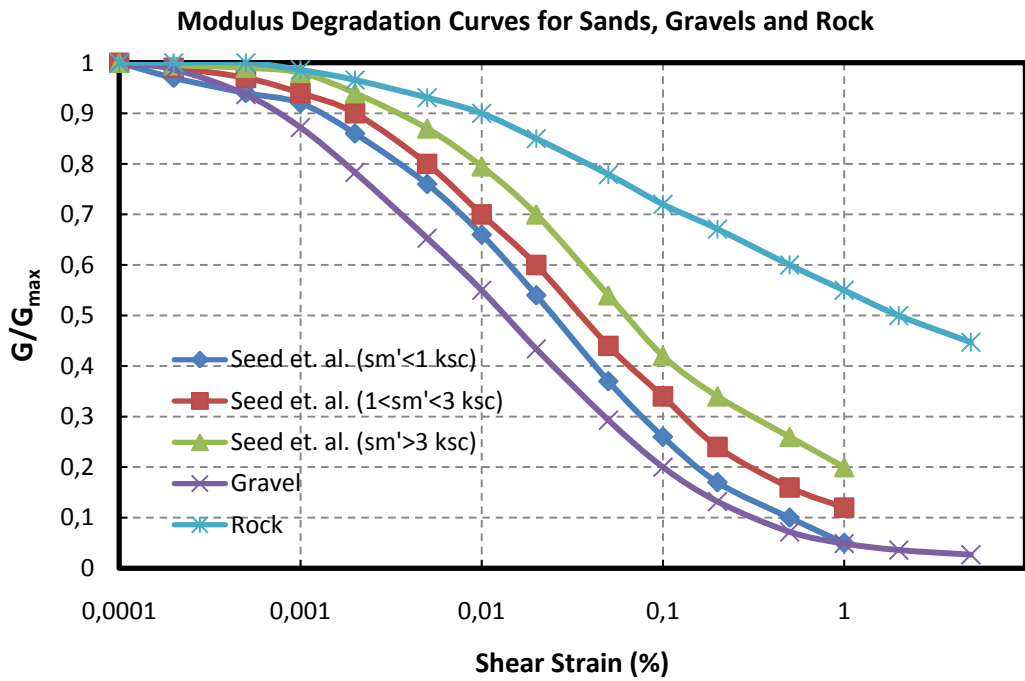


Figure 4.2-41. Modulus degradation curves for cohesionless materials

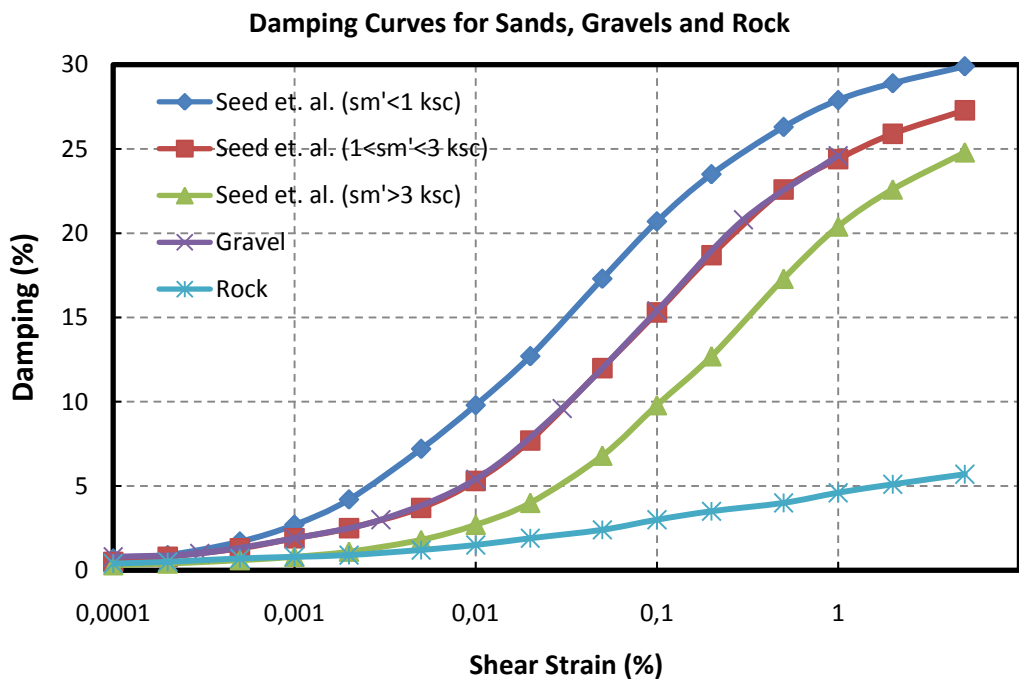
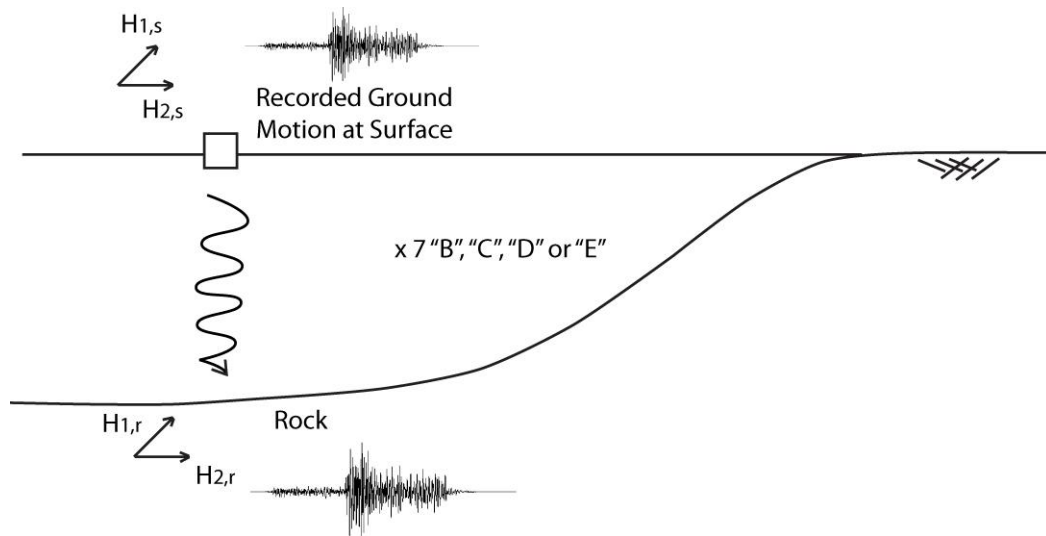


Figure 4.2-42. Damping curves for cohesionless materials



**Figure 4.2-43. Site response procedure using generic profiles**

#### **4.2.8 Summary of Strong Ground Motion Dataset**

An effort was spent in compiling a dataset for strong ground motions complying with defined GMPE model criteria. Processing of time histories, quantifying uncertainties in peak and spectral acceleration parameters due to random orientation of the site with respect to the incoming wavefront, magnitude uncertainty, and relationships between source to site distance metrics, site classification procedure, and a general approach towards defining the ground response effects shaped the final dataset. This section summarizes the outcome of the data processing attempt.

Tabulated data, listing the key parameters of each event, record, and station is presented in Appendix D. Tables D.1, and D.2 summarize the key aspects of each event and record, including, but not limited to filter cutoffs, name of recording station, source to site distance metrics. Table D.3 is reserved for providing a summary of general characteristics of strong ground motion stations.

As discussed in Section 4.2.2, choice of frequency cutoff during filtering has a direct affect on the useable period range of spectral values. Recalling that the filter response function (Figure 4.2-4) has a gradual roll-off, a comfort zone should be provided when selecting the useable period range. Frequency values ranging from 1.2-1.25 are generally accepted (Chiou et al., 2008), with 1.25 made as the final selection in the current study. To give an example, a ground motion component bandpass filtered at 0.08 Hz and 25 Hz has a useable frequency range of 0.10 Hz – 20 Hz, corresponding to 0.05 s – 10 s in terms of spectral period. Useable period range for a record is based on the mutual limits bounded by filter cutoffs of both horizontal components. Since the number of data eligible for use rapidly decreases below 0.10 s and 2 s, in order to prevent any instability due to statistical uncertainty, the author has decided to develop the GMPE model for periods falling between the defined limits, in addition to peak component of acceleration (Figure 4.2-44).

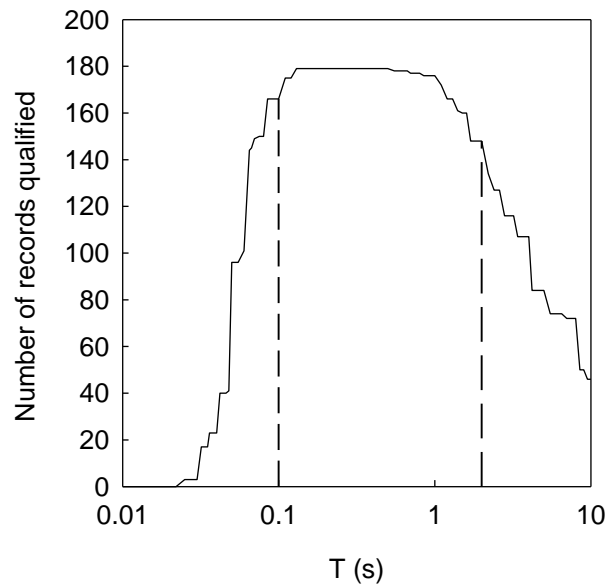


**Figure 4.2-44. Effect of signal processing on the useable period range**

Scatter of closest distance to rupture metrics, computed using the case specific approach, previously explained in Section 4.2.6, with respect to peak ground acceleration at rock (GMRotD50 component) is shown Figure 4.2-45. Left side of

the figure presents the median values of GMRotD50 (excluding parameter uncertainty in pga due to site response) and  $R_{rup}$ . Right section of the figure presents the case with parameter uncertainties of the data revealed. Similarly,  $pga_{rock}$  scatter is plotted with respect to  $R_{epi}$  and  $R_{jb}$  in Figures 4.2-46 and 4.2-47. Spectral values of acceleration, (SA) at  $T=0.2$  s and  $T=1.0$  s are presented in Figure 4.2-48.

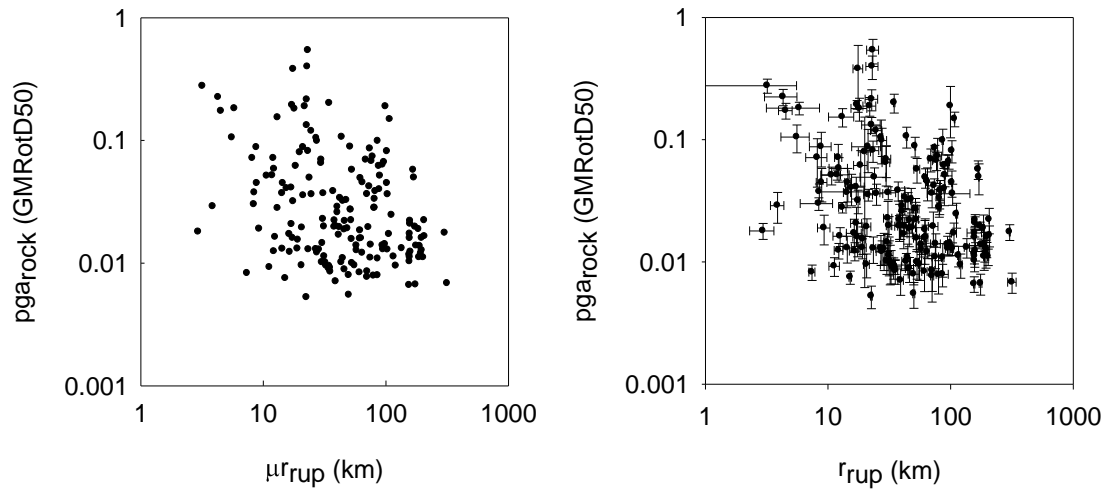


**Figure 4.2-45. Closest distance to rupture vs.  $pga_{rock}$  scatter with median values and computed parameter uncertainties**

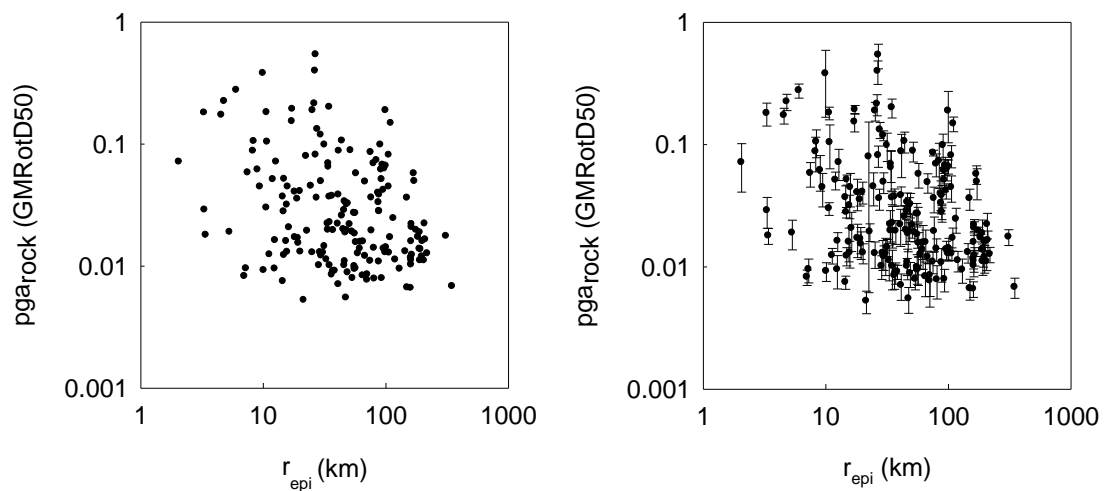


**Figure 4.2-46. Epicentral distance vs.  $pga_{rock}$  scatter with median values and computed parameter uncertainties**



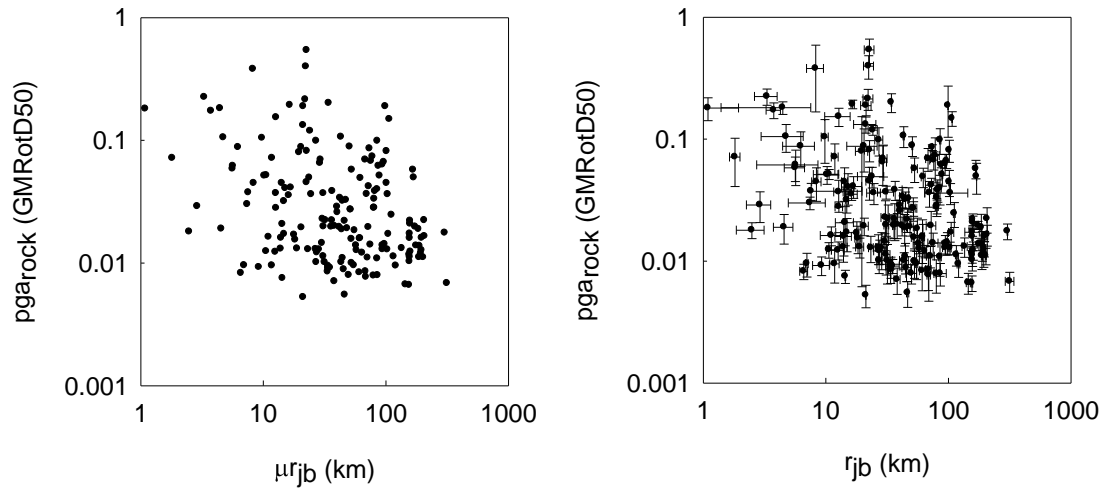


**Figure 4.2-47. Boore-Joyner distance vs.  $pga_{rock}$  scatter with median values and computed parameter uncertainties**

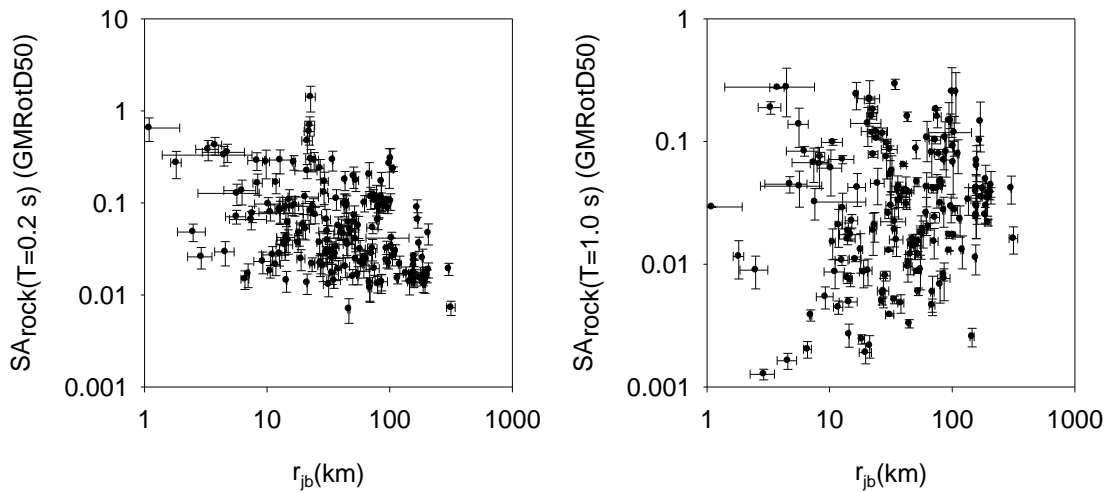


**Figure 4.2-48. Boore-Joyner distance vs.  $SA_{rock}$  scatters for  $T=0.2$  s and  $T=1.0$  s**

Examination of moment magnitude distribution with respect to  $pga_{rock}$  values brings up the discussion about homogenous distribution of magnitude values in the dataset. Turkish strong ground motion dataset lacks a significant gap in the  $M=6.5 - M=7.0$  range (Figure 4.2-49). In order to compare our restricted dataset with that of the NGA flatfile, two series of scatter were superposed (Figure 4.2-50). Black dots

represent the currently compiled dataset, and the underlying red crosses represent the whole NGA flatfile. Subset of the NGA flatfile, representing Chi-Chi Earthquake aftershocks are marked as blue. Selected records included in the Abrahamson and Silva (2008) NGA model does not imply a significant change in the data scatter (Figure 4.2-51). A simple quantification of the number of records falling within prescribed magnitude – distance bins is presented in Figures 4.2-52 and 4.2-53 for the current and Abrahamson and Silva (2008) datasets, respectively. Although there is a slight variation among the NGA models, a preliminary data analysis reveals the imbalance in completeness of data representation.

Distribution of data with respect to defined NEHRP site classes is presented in Figure 4.2-54. In the scatter plot, for sites with weighted classification schemes, priority in symbolization was given to the option with higher weight assigned. For the case of equal weighting, option with stiffer/denser classification was preferred for demonstration purposes. NEHRP B sites compose 14% of the dataset, with dominance of NEHRP C sites (37%) and NEHRP D sites (44%). 5% of the total records were recorded on NEHRP E sites.

A similar dominance was observed in strike slip faults, controlling the dataset with 76% weight (Figure 4.2-55). Abbreviation “NO” stands for normal faults with oblique component. Similarly, “SN” is for strike slip with normal component, and “SR” is for strike slip with reverse component. Classification of style of faulting is presented in forms of predefined bins, however the model incorporates SOFP (style of faulting parameter) introduced in Chapter 2.

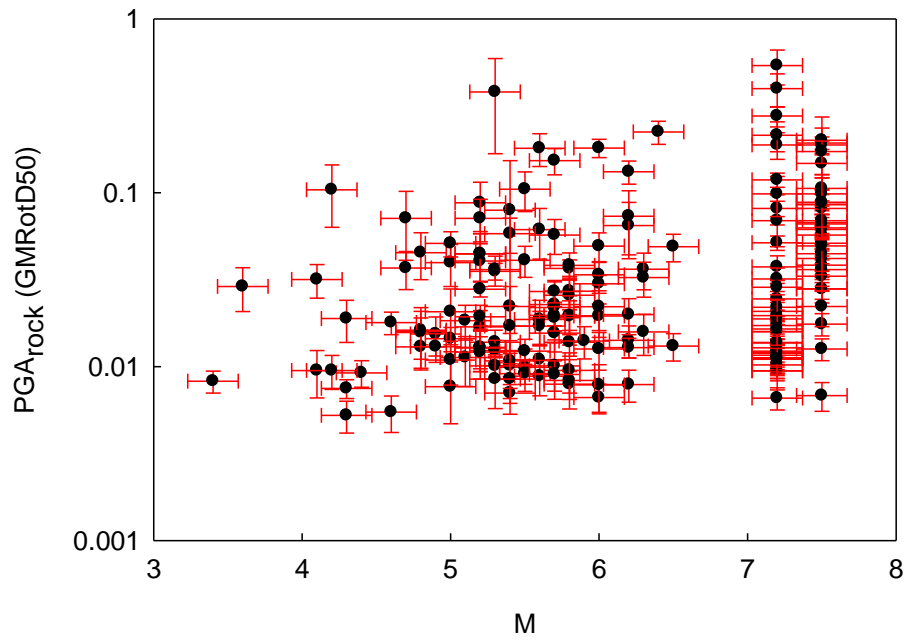


**Figure 4.2-49. Magnitude vs.  $p_{ga_{rock}}$  distribution**

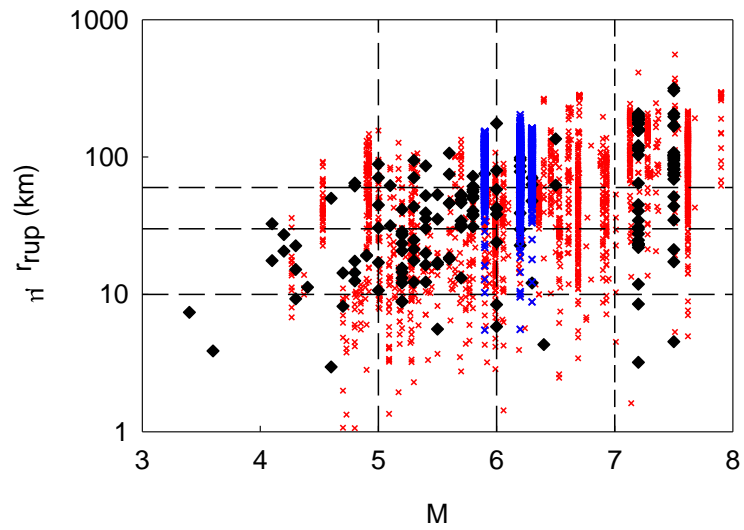


**Figure 4.2-50. Magnitude vs.  $R_{rup}$  scatter of NGA flatfile data and Turkish SGM datasets**

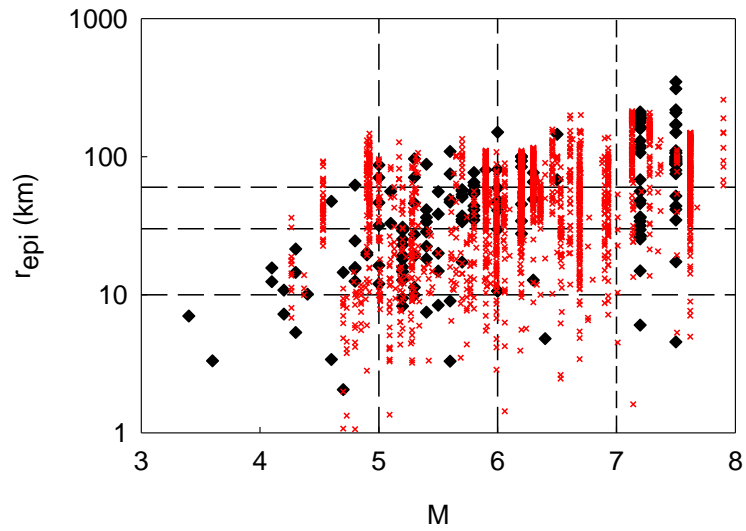


**Figure 4.2-51. Magnitude vs.  $R_{epi}$  scatter of Abrahamson and Silva (2008) NGA and Turkish SGM datasets**

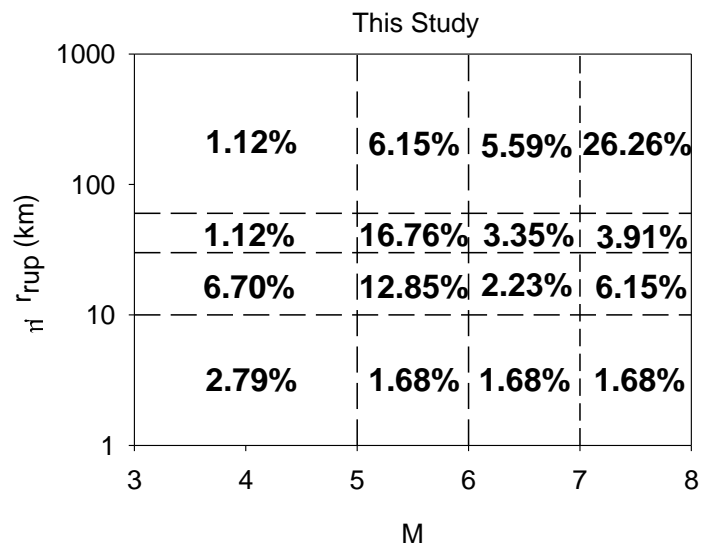


**Figure 4.2-52. Percentage of events falling between the defined magnitude - distance bins for the current dataset**

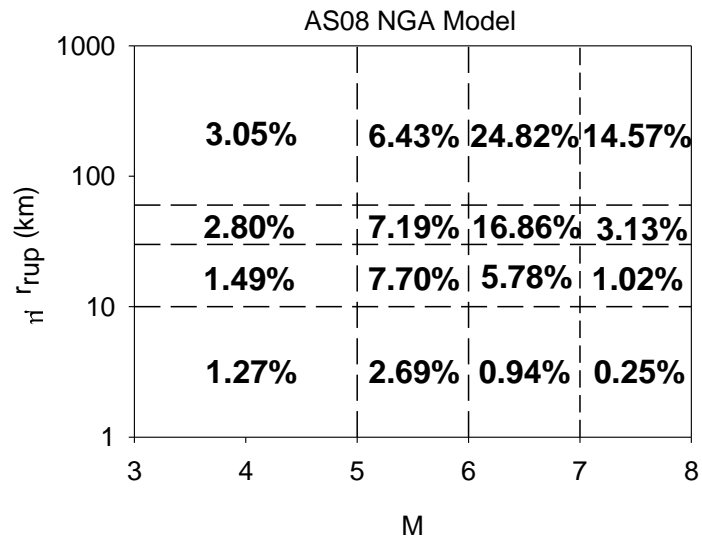


Figure 4.2-53. Percentage of events falling between the defined magnitude - distance bins for Abrahamson and Silva (2008) dataset

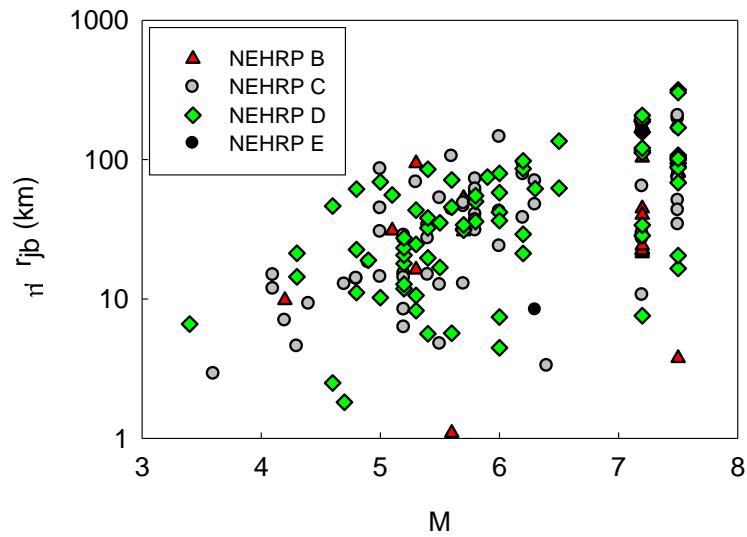
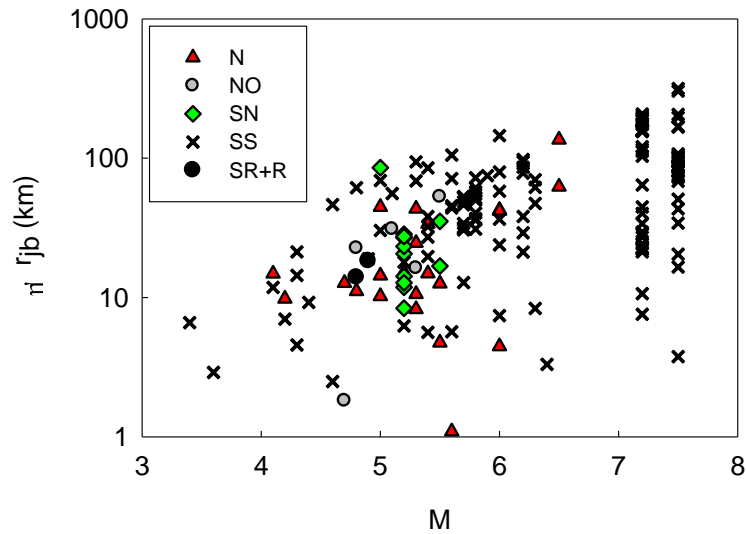


Figure 4.2-54. Magnitude vs.  $R_{jb}$  scatter for different NEHRP site classes



**Figure 4.2-55. Magnitude vs.  $R_{jb}$  scatter for different style of faulting classes**

#### 4.2.9 Comparison of Dataset With Local and Global GMPE Models

Having observed the trends in fully processed dataset, subsequent step prior to developing the models is to examine how the compiled local data compares to the predictions of previously developed local and global relationships. For this purpose, measured values of ground motion on the soil surface are taken as a reference to calculate the residuals. Results from 7 ground motion prediction models are presented. For models which predictions can be made for spectral ordinates, residuals are presented for  $T=0.2$  s and  $T=1.0$  s, in addition to the peak ground acceleration. Compatibility between definitions of measured acceleration parameters and reference GMPE models is ensured. Additionally, possible ambiguity between source to site distance metrics and style of faulting is avoided. Hanging wall effect is ignored.

However, an inevitable source of incompatibility arises from the different site classification parameterization in GMPE models. Comparisons for GMPEs using soil-rock or soft soil-stiff soil-rock schemes were made by adapting the NEHRP site classes to the best suitable match. To give an example, “rock” was taken in correspondence with NEHRP B, “soil” with C and D, and “soft soil” with NEHRP E.

An alternative to making comparisons at soil level, would be using the deconvolved rock ground motions and compare with “rock” predictions. However, definitions for “rock” in GMPE models, expressed in terms of shear wave velocity for convenient discussion, are highly variable. Reference shear wave velocity for rock definition of Abrahamson and Silva (1997) roughly corresponds to 550 m/s. NEHRP B/C boundary soils represent a shear wave velocity of 760 m/s, whereas Abrahamson and Silva (2008) models the reference rock level at  $V_s = 1100$  m/s. Empirical scaling factors are required for converting rock definitions to a common scale, a step that will incorporate additional level of uncertainty. Since the sole aim of residual comparison is to get a grasp of the relative magnitudes of ground motion intensity between models and the current dataset; comparisons through soil definitions were found to be adequate. Median shear wave velocity of generic sites falling to each NEHRP category was used for comparison.

Figure 4.2-56 summarizes the scatter and trend in residuals, computed from median estimates of the following GMPE models, and the current dataset. Median estimates of each ground motion model are calculated using the consistent definitions of source to site distance and horizontal component of acceleration. The overall summary begins with the 1997 series of ground motion prediction equations, including Abrahamson and Silva (1997) (AS97 in figure), Boore et al. (1997) (BJF97 in figure) and Campbell (1997) (C97 in figure). Data trends indicate that there is a constant overestimation by the prediction equations, except for magnitudes below M 4.0; which is not a real indicative of the performance. Normalized residuals; calculated as the ratio of difference between measured and predicted values, to the measured value; indicate differences up to %100. Factor is a function of spectral period in most cases.

Özbey et al. (2004) model (OZ04 in figure) tends to underestimate the measured values for magnitudes lower than the event magnitudes of 1999 Kocaeli and Düzce

events; which is within expectations since the basis of the model is the 1999 event series.

Kalkan and Gülkan (2004) model (KG04 in figure) constantly overestimates measured values at all periods, difference almost vanishing near high magnitude events.

Ulusay et al. (2004) (U04 in figure), and Akkar and Bommer (2010) models (AB10 in figure) provide better fits to the measured values than equations examined previously; however the magnitude of average difference is still notable. Ulusay et al. (2004) model overestimates the data by 16% in the lowest magnitude range, and underestimates by 19% at the high magnitude boundary. On the contrary, Akkar and Bommer (2010) model exhibits a steady increase in overestimation of pga, from negligible difference to 20%, as a function of increasing magnitude. This value increases to 32% for  $T=0.2$  s. Completely different pattern is observed for  $T=1.0$  s (52%-22% difference).

Trials of two models from the NGA set, namely the Boore and Atkinson (2008) (BA08 in figure) model and Campbell and Bozorgnia (2008) (CB08 in figure) model yield poor performances in terms of coherence to the measured values.

Trends of residuals plotted with respect to source to site distance signify similar trends, and are not presented in this text.



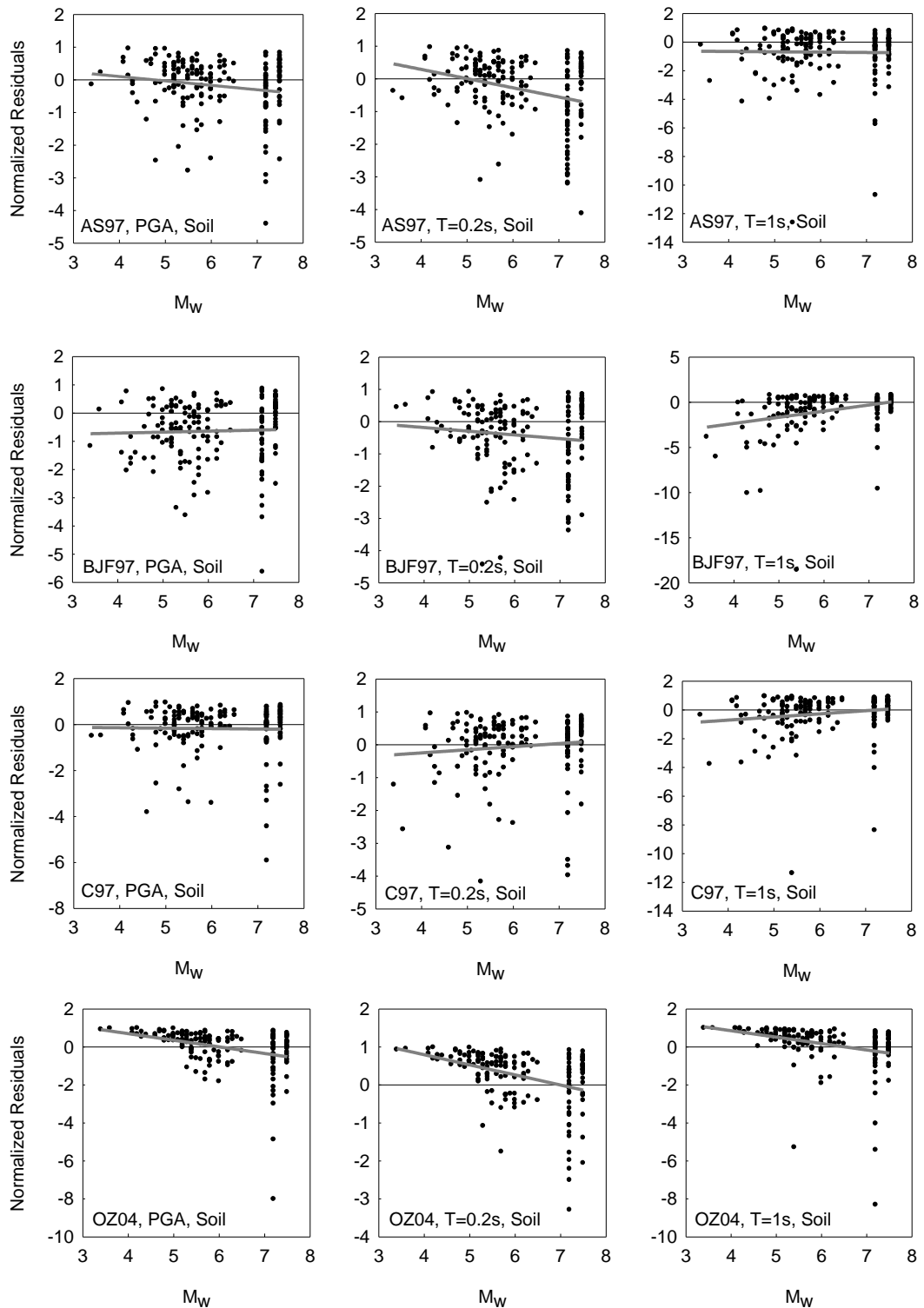


**Figure 4.2-56. Comparison of normalized residuals for different GMPE models, prior to model development**

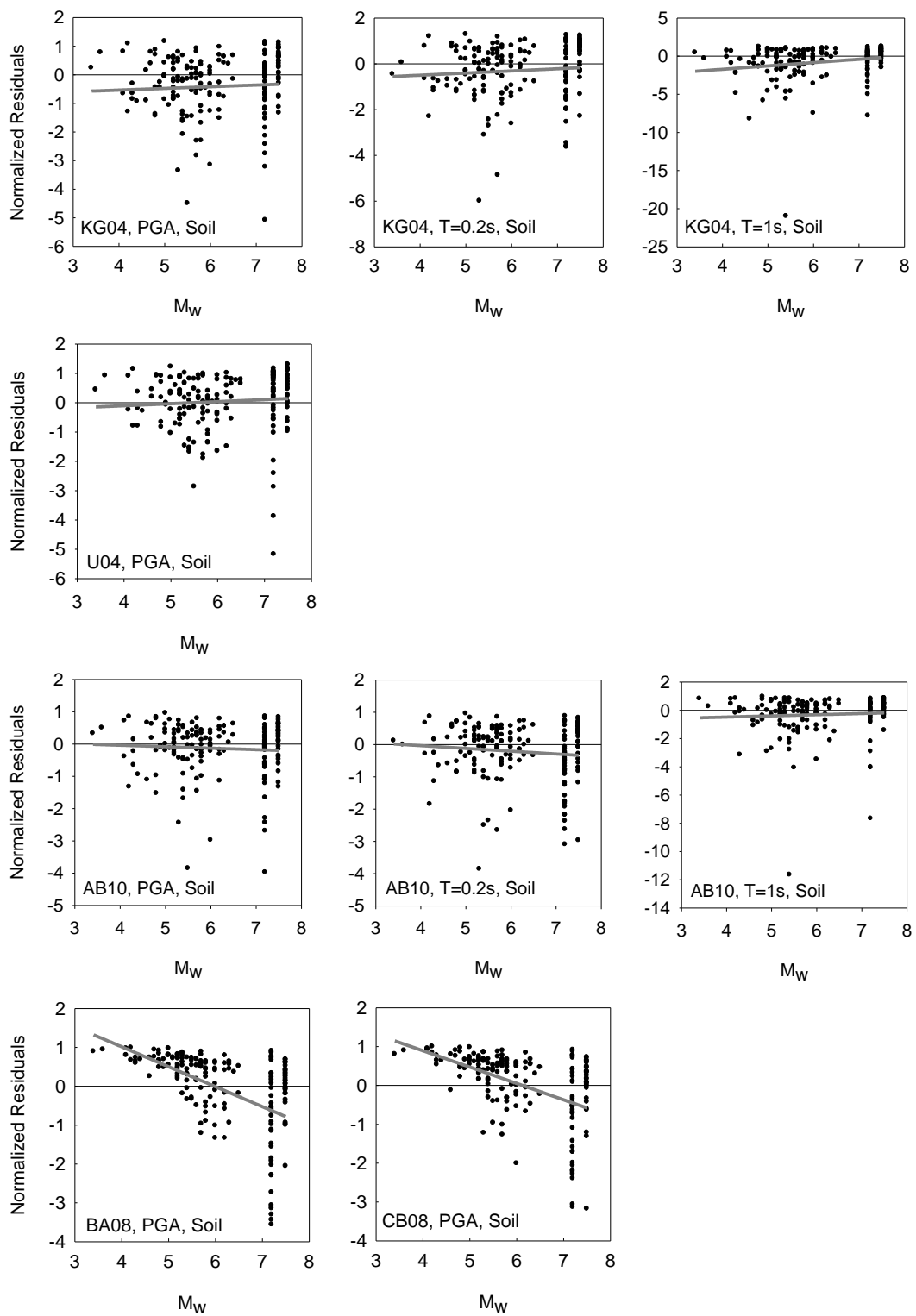


**Figure 4.2-56. (continued) Comparison of normalized residuals for different GMPE models, prior to model development**

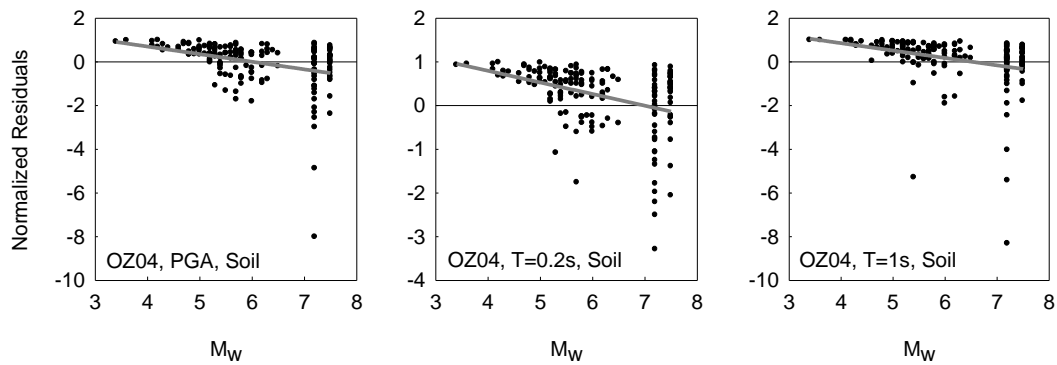


**Figure 4.2-56. (continued) Comparison of normalized residuals for different GMPE models, prior to model development**

### 4.3 GROUND MOTION PREDICTION MODEL

This section discusses the development stages of the ground motion prediction model. Before progressing with the model development, a concise summary is provided on the reliability methods used throughout the remaining part of the text. In addition to the maximum likelihood formulation provided in Chapter 2; further discussion on likelihood formulation with parameter uncertainty and choice based sampling will be made. Chapter 4, will then proceed with the brief presentation of the site response model developed using the results of 1-D site response analyses on generic profiles. Final form of the model will be provided towards the end of Section 4.3.

#### 4.3.1 Site Response Model

##### 4.3.1.1 Introduction and Background on Similar Models

Until present, site response term in ground motion prediction equations were either modeled using dummy variables for different site classes, or continuous function of  $V_{s30}$  normalized with respect to a reference shear wave velocity value. Amplification of peak ground parameters as a nonlinear function of  $pga_{rock}$  were studied for a

unique scheme of site classes defined by Seed et al. (1997), however did not have direct implementation in the GMPE models. The later generation of ground response models attempted to include both the input ground motion intensity and site classification in robust estimation of peak and spectral amplification factors. Choi and Stewart (2005) have performed a remarkable progress on the subject and led the way to further developments.

Using results from 1-D ground response analyses performed on generic soil sites, we develop empirical relationships to predict nonlinear amplification factors for 5% damped response spectral acceleration as a continuous function of average shear wave velocity of the upper 30 m,  $V_{s30}$ , and the peak ground acceleration defined at rock level. The functional form chosen is motivated from previous studies, and is similar to the form used by Choi and Stewart (2005). Choi and Stewart (2005) have presented their basic form as follows:

$$\ln(F) = c \ln\left(\frac{V_{s30}}{V_{ref}}\right) + b \ln\left(\frac{pga_{rock}}{0.1}\right) \quad (4-8)$$

where “F” or “Amp” (will be named “Amp” hereafter)

$$F = \frac{SA_{soil}}{SA_{rock}} \quad (4-9)$$

Model parameters  $c$  and  $V_{ref}$  are period dependent constants, and  $b$  is a step wise function binned with respect to  $V_{s30}$ , including period dependent parameters and  $V_{s30}$  as predictive variables. Boore and Atkinson (2008) have implemented a simpler form of Choi and Stewart (2005) model, with a slight modification on the “b” function. However,  $V_{ref}$  was fixed to 760 m/s without further refinement of remaining parameters. A similar effort was carried out by Walling et al. (2008), whose spectral amplification factors with respect to base  $pga_{rock}$  value defined at  $V_s = 1100$  m/s were successfully implemented to the Abrahamson and Silva (2008) model.

This study simply prefers the utilization of an exponential function for the nonlinear response term, “b” expressed in Equation 4-8. As stated earlier, results of previous studies have influenced the choice of the base model, and nonlinearity of spectral acceleration amplification / deamplification was chosen to be controlled by a function not exhibiting any kinks. Effect of inexact observations of predictive parameters such as  $V_{s30}$  and  $pga_{rock}$ ; due to site response on generic sites were also incorporated to separate parameter uncertainty from model error. After a brief introduction on dataset formation for site response model, Section 4.3.1.2 presents the data, and Section 4.3.1.3 presents the basic formulation of the ground response model; and discusses on the improvements as a consequence of quantifying uncertainties of inexact observations and removing any effects due to possible non homogenous sampling.

#### *4.3.1.2 Dataset Formation*

Although the basic function for the representation of the nonlinear ground response is analogous to the forms used by Choi and Stewart (2005) and Walling et al. (2008); the method for collecting and processing raw data is different. This study directly implements the results of the ground response analyses performed on generic soil sites introduced in Section 4.2.7.5. Since the number of data lying within the NEHRP E range is significantly lower than the rest of the site categories (5% of total), GMPE dataset was artificially expanded by using results of additional generic runs performed on NEHRP E sites, with input ground motions from the GMPE dataset having peak ground accelerations at soil, above 0.1 g. The same approach was followed for NEHRP B, C, and D sites to prevent problems due to statistical uncertainty in the expected nonlinear response range. With this expansion, 229 data points were produced for peak parameters; relevant number being lower for spectral periods subject to restrictions by filter cutoffs.

Keeping in mind that each data point actually carries parameter uncertainty in peak ground acceleration at rock and shear wave velocity, as a consequence of ground response analysis from 7 (or 14 for multiple characterizations with weighting factors) characteristic sites for each NEHRP class; it can be concluded that the total number of data points used to generate the descriptive statistics is above 1600. One of the major assumptions in the model is that the correlation due to performing response analyses on multiple sites (7 or 14), with the same input acceleration time history is ignored. Amplification ratio for each spectral period is calculated using Equation 4-9. GMRotD50 definition is used for calculating amplification ratios, and observed parameter of amplification is assumed to be an exact estimate, bypassing propagated uncertainty due to  $SA_{rock}$ . Figures 4.3-1 to 4.3-3 present the data scatter for amplification of peak ground acceleration, and spectral accelerations at  $T=0.2$  s and  $T=1.0$  s; color coded with respect to NEHRP classifications. Current definition for  $SA_{rock}$  is approximately equal to the acceleration intensity collected at  $V_s=1250$  m/s.

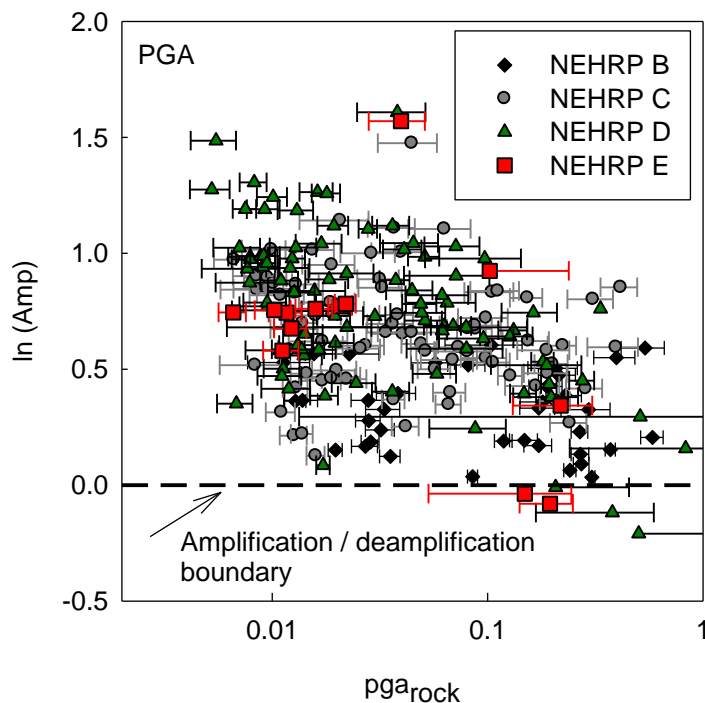


**Figure 4.3-1. Dataset used for developing ground response model (PGA)**

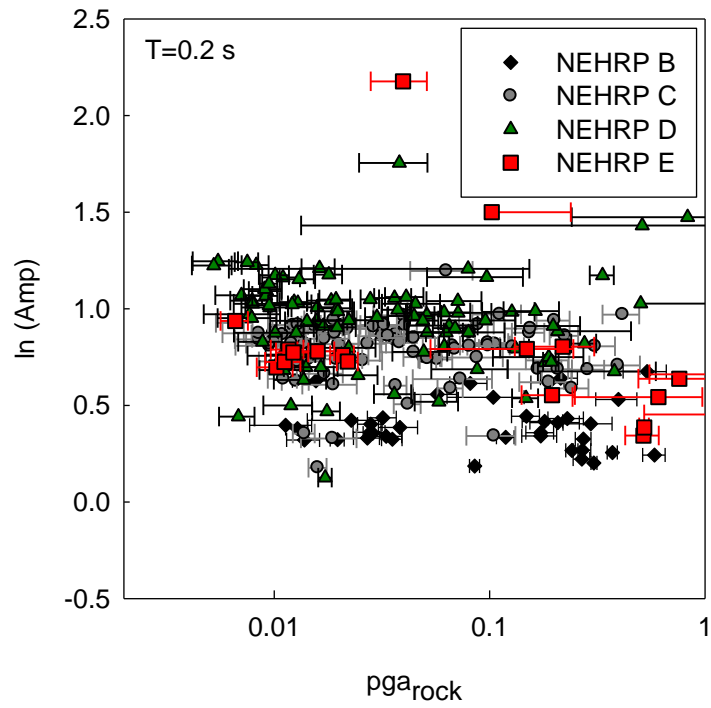


Figure 4.3-2. Dataset used for developing ground response model ( $T=0.2$  s)

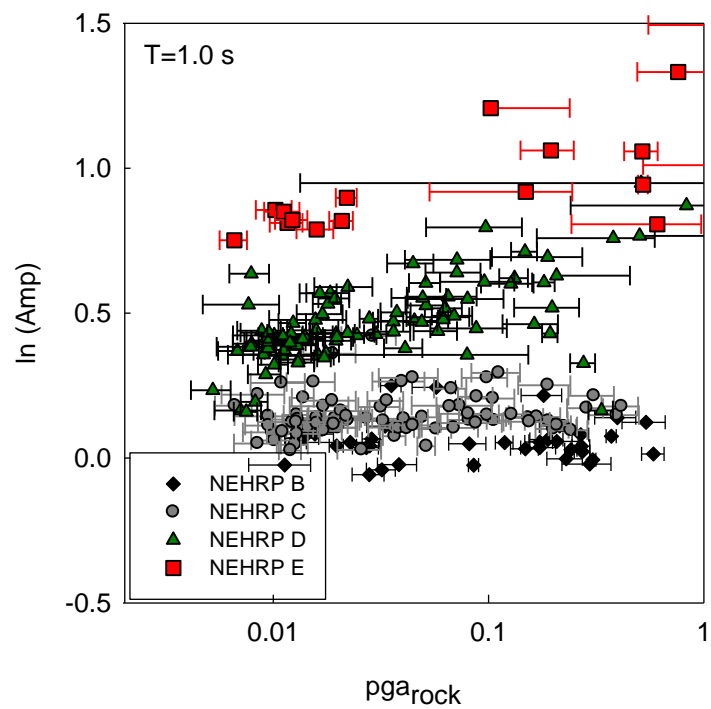


Figure 4.3-3. Dataset used for developing ground response model ( $T=1.0$  s)

A brief examination of Figures 4.3-1 through 4.3-3 unsurprisingly, yet obviously displays the amplification / deamplification behavior of all types of soils under varying intensities of rock ground motion. For PGA, under high intensity of shaking, few data points fall below the boundary line defining amplification / deamplification. Amplification at low levels of shaking intensity is higher at higher frequency response range, without any evident distinction between site classes. At  $T=1.0s$ , where the average site periods of NEHRP D and E classes converge to the spectral response period, amplification factors as high as 2.7 to 3 can be observed; and a clear distinction can be made on the relative amplifications of different classes.

#### *4.3.1.3 Reliability Models in Quantifying Parameter Uncertainty and Removing Bias Due to Dataset Compilation*

Mathematical representation of the uncertainties regarding predictive variables, such as  $pga_{rock}$  and  $V_{s30}$  are discussed in this section. Before proceeding with the revised form of likelihood estimation, a quick reminder on definitions of sources of uncertainty is presented. Sources of error can be listed as measurement/estimation errors; also named as parameter uncertainty within this text, model errors, and statistical errors; which was discussed in Chapter 2.

Measurement / estimation errors arise from the uncertainty in measurements, and estimation. Considering the specific case of ground response, uncertainty in  $V_{s30}$  comes from the scatter of  $V_{s30}$  values of the suite of generic sites used in site response analyses. Uncertainty in  $pga_{rock}$ , (or  $\ln pga_{rock}$ ) due to site response conducted using a single input soil motion on, 7 or 14 possible generic sites falling within the best estimates of site classification, is obtained similarly.



Imperfect models; both due to missing descriptive parameters in the functional form, or building an imperfect type of formulation using adequate number of parameters, leads to model uncertainty (Cetin, 2000).

Statistical size of estimated parameters of a model generates statistical uncertainty. Sample of observations having finite size imposes additional uncertainty into the model, due to statistical error in estimating the parameters.

Having made a brief introduction on the types of uncertainty for the specific problem, the base formulation of the limit state function for the proposed ground response model is presented as follows:

$$g(pga_{rock}, V_{s30}, \theta, \sigma_\varepsilon) = \ln(\text{Amp})_{\text{measured}} - \left\{ \theta_1 \ln\left(\frac{V_{s30}}{\theta_2}\right) + \theta_3 [e^{-\theta_4 \ln(V_{s30})} - e^{-\theta_4 \ln(\theta_2)}] \ln\left(\frac{pga_{rock}}{\theta_5}\right) \right\} \mp \varepsilon_{\ln(\text{Amp})} \quad (4-10)$$

Corresponding likelihood equation can be written as follows:

$$L_{\ln(\text{Amp})}(\theta, \sigma_\varepsilon) = \prod_{i=1}^k \varphi \left[ \frac{\hat{g}_{\ln(\text{Amp})}(pga_{rock}, V_{s30}, \theta)}{\sigma_{\varepsilon_{\ln(\text{Amp})}}} \right] \quad (4-11)$$

Next step in the process is incorporating statistically independent inexact observations to the model. In the ground response model, measurement uncertainty in  $pga_{rock}$  value, computed from a single input motion – NEHRP classified profile set pair (7 or 14 samples) is assumed to be fully independent, regardless of the same input motion used for that pair. The companion parameter for incorporating measurement uncertainty is  $V_{s30}$ . Each estimation or measurement can be written in terms of a mean value and zero-mean random error term, assuming that measurements do not have systematic error.

$$V_{s30,i} = \widehat{V}_{s30,i} + e_{V_{s30,i}} \quad (4-12)$$

$$pga_{rock,i} = \widehat{pga}_{rock,i} + e_{pga_{rock,i}} \quad (4-13)$$

where  $e_{V_{s30,i}}$  and  $e_{pga_{rock,i}}$  represent the measurement error terms, being normally distributed.

Total variance is written as the sum of model error  $(\sigma_\epsilon)^2$  and errors due to observations  $(\sigma_e)^2$ . Variance of observational error contributor in  $\ln(\text{Amp})$  function, due to parameter errors of  $pga_{rock}$  and  $V_{s30}$  is calculated using the first order approximation using Taylor's series expansion. Details of the procedure are presented in Cetin (2000).

Another issue encountered in model development of the ground response function, using the relatively limited and non-homogenously sampled GMPE dataset is the over-representation of low intensity ground motions over the higher ones. Only 26% of the deconvolved median  $pga_{rock}$  values were above 0.05 g in the dataset, and an evident imbalance exists between number of soft and stiffer soil profiles, even after expansion of the dataset in favor of NEHRP E sites. Cetin (2000) defines this as a sampling disparity problem, and attempts to correct the uneven sampling by weighting the likelihood functions as described in Manski and Lerman (1977). This study follows the same approach, and defines the weighting factors by dividing the dataset into two dimensional  $pga_{rock}$  (median) and NEHRP class bins (best estimate or stiffer option when weighted multiple options were present). Details of the weighting procedure are not covered in this text; however weighting matrices used for data falling within each spectral period is presented in Table 4.3-1. Note that sum of weighting factors for each period sums up to the total number of bins; 12.

**Table 4.3-1. Summary of the weighting factors used to eliminate uneven sampling in the ground response model**

Period (s)	NEHRP Site Class	pga <sub>rock</sub> Bins		
		≤0.1g	0.1 < pga <sub>rock</sub> ≤ 0.3	>0.3 g
PGA & T=0.15 s - 0.5s	B	0.461	0.523	1.569
	C	0.124	0.560	2.614
	D	0.105	0.784	1.307
	E	0.871	1.961	1.120
T=0.50 s	B	0.461	0.523	1.568
	C	0.126	0.560	2.613
	D	0.109	0.784	1.306
	E	0.871	1.960	1.120
T=0.75 s	B	0.456	0.553	1.549
	C	0.127	0.553	2.581
	D	0.106	0.774	1.291
	E	0.968	1.936	1.106
T=1.0 s	B	0.455	0.553	1.548
	C	0.129	0.553	2.581
	D	0.106	0.774	1.290
	E	0.968	1.936	1.106
T=1.5 s	B	0.506	0.542	1.519
	C	0.141	0.542	2.531
	D	0.113	0.759	1.519
	E	0.844	1.898	1.085
T=2.0 s	B	0.578	0.578	1.502
	C	0.144	0.536	2.503
	D	0.123	0.751	1.502
	E	0.834	1.877	1.073

#### 4.3.1.4 Ground Response Model Results

Presentation of model results for the  $\ln(\text{Amp})$  function required two consecutive steps of process. First stage results indicated an extremely high sensitivity to model coefficient  $\theta_3$ , and  $\theta_5$  (Equation 4-10) was affected as a function of period, with no significant improvement in the overall maximum likelihood estimate. Subsequent refinement included fixing of  $\theta_5$  with respect to its value at  $T=0$  s, and re-evaluating  $\theta_3$ , as well as other model coefficients. The last step consisted of fitting a higher order natural logarithm function to the  $\theta_3[e^{-\theta_4 \ln(V_{s30})} - e^{-\theta_4 \ln(\theta_2)}]$  term in Equation 4-10,  $V_{s30}$  being the predictive parameter and, model coefficients varying for each period. Additionally, coefficients  $\theta_1$  and  $\theta_2$  were smoothed along period. Re-substituting the simplified/smoothed parameter set did not affect the stability of the likelihood function. Equation 4-14 presents the final form of the function, and Table 4.3-2 summarizes the model parameters for 11 spectral periods and the peak component of ground acceleration; with weighting scheme applied, and inexact observations in  $\text{pga}_{\text{rock}}$  and  $V_{s30}$  implemented.

$$\ln(\text{Amp}) = \left\{ \theta_1 \ln \left( \frac{V_{s30}}{\theta_2} \right) + b [\ln(\text{pga}_{\text{rock}}) - \theta_7] \right\} \mp \sigma_{\ln(\text{Amp})} \quad (4-14)$$

where

$$b = \theta_3 + \theta_4 \ln(V_{s30}) + \theta_5 \ln^2(V_{s30}) + \theta_6 \ln^3(V_{s30}) \quad (4-15)$$

Error term is expressed as:

$$\sigma_{\ln(\text{Amp}),TOTAL}^2 = \sigma_{\varepsilon}^2 + \sigma_e^2 \quad (4-16)$$

where  $\sigma_{\varepsilon}^2$  is the model error, and variance of  $\ln(\text{Amp})$  due to inexact observations is:

$$\sigma_e^2 = \left[ \left( \frac{\partial \ln(Amp)}{\partial V_{s30}} \right)^2 \cdot \sigma_{V_{s30}}^2 + \left( \frac{\partial \ln(Amp)}{\partial pga_{rock}} \right)^2 \cdot \sigma_{pga_{rock}}^2 \right] \quad (4-17)$$

**Table 4.3-2. Model coefficients for site response function**

T (s)	$\theta_1$	$\theta_2$	$\theta_3$	$\theta_4$	$\theta_5$	$\theta_6$	$\theta_7$	$\sigma_\epsilon$
PGA	2.577	1303	0.0654	-0.2807	0.0378	0	12.09	0.282
0.1	1.038	1464	0.4262	-0.2661	0.0284	0	12.09	0.239
0.15	0.482	1522	-1.2247	0.6328	-0.1232	0.0081	12.09	0.284
0.2	0.089	1560	-0.8289	0.4319	-0.0833	0.0054	12.09	0.267
0.25	-0.176	1581	-0.5489	0.2886	-0.0551	0.0035	12.09	0.290
0.3	-0.341	1586	-0.386	0.2052	-0.0379	0.0023	12.09	0.264
0.4	-0.475	1558	0.0584	-0.013	0.0007	0	12.09	0.154
0.5	-0.480	1489	0.0005	-0.00006	0	0	12.09	0.210
0.75	-0.560	1225	0.5183	-0.2811	0.0523	-0.0032	12.09	0.146
1	-1.115	945	-0.3306	0.1689	-0.0177	0	12.09	0.095
1.5	-1.997	672	-0.3577	0.2485	-0.0298	0	12.09	0.147
2	-0.938	732	0.8444	-0.4569	0.0905	-0.0062	12.09	0.195

Results of the ground response model for PGA are presented using the  $pga_{rock} - pga_{soil}$  plot, a format which truly reflects the nonlinear behavior. Figure 4.3-4 presents the scatter of  $pga_{rock}$  vs.  $pga_{soil}$ , before any model was superposed. Figure 4.3-5 shows the median estimates of the current model for  $V_{s30}$  values of 760 m/s, representing the NEHRP B/C boundary,  $V_{s30}=560$  m/s, average value for a C site, and  $V_{s30}=360$  m/s, lower bound for C sites. Considering the fact that average  $V_{s30}$  value for NEHRP B generic sites in our dataset was 992 m/s, overestimation of amplification of black filled NEHRP B data series by the  $V_{s30}=760$  m/s curve, should not be misleading. Glancing at Figure 4.3-6, the nonlinear response behavior and deamplification of peak ground acceleration at soil surface was captured by median curves for the  $V_{s30}=180-360$  m/s range.  $V_{s30}=270$  m/s curve, representing the average shear wave velocity for a NEHRP D site, deamplifies rock ground motion for accelerations above 0.5 g, and similar behavior is observed around 0.25 g for the NEHRP D/E boundary range, using the  $V_{s30}=180$  m/s curve.

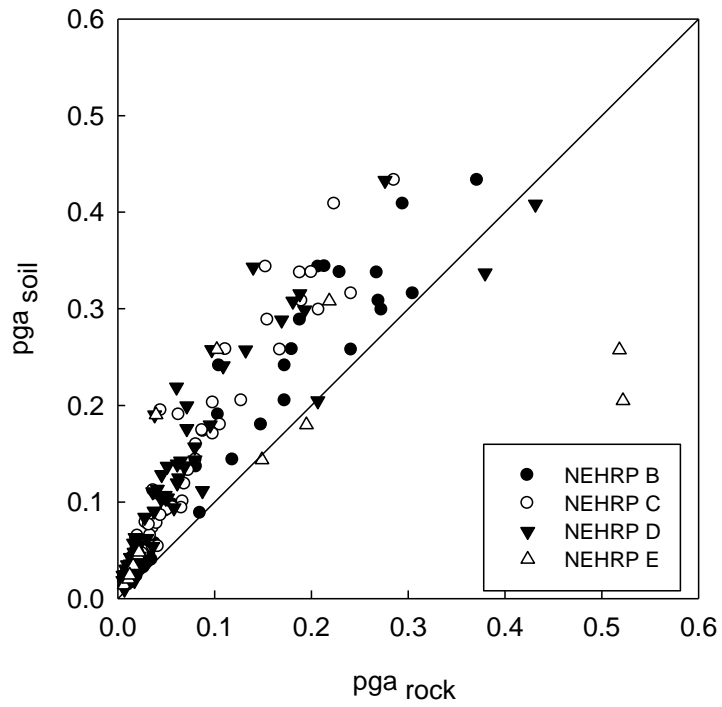


**Figure 4.3-4.  $pga_{rock}$ - $pga_{soil}$  scatter plot**

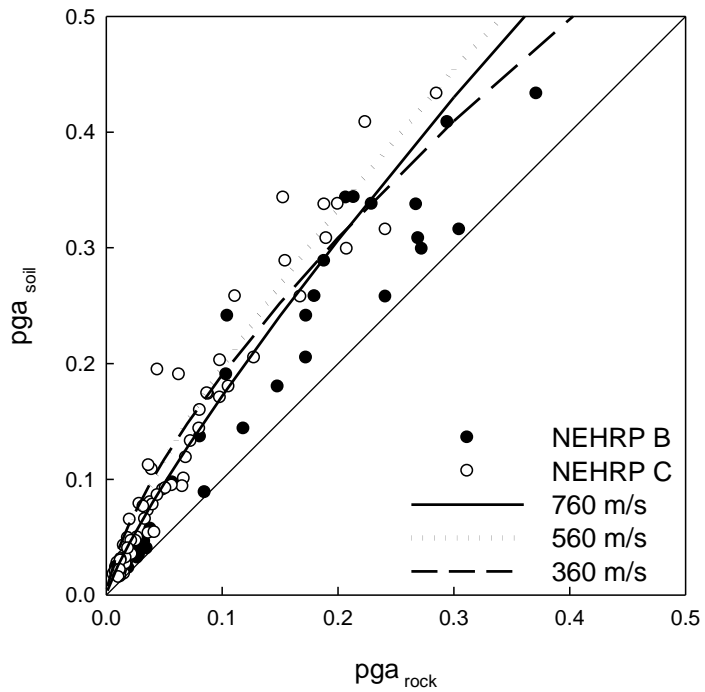


**Figure 4.3-5. Median curves for the current model in the  $V_{s30}=360-760$  m/s range**

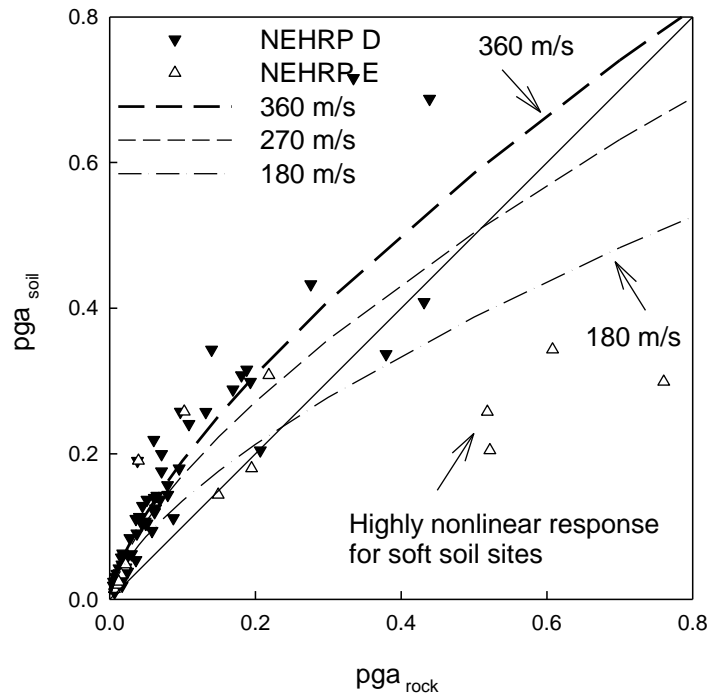


**Figure 4.3-6. Median curves for the current model in the  $V_{s30}=180\text{-}360$  m/s range**

In order to make a comparison between the current data trend and various significant models in literature, results by Seed et al. (1997) (S97 in figures), and Choi and Stewart (2005) (CS05 in figure) were plotted.

Figure 4.3-7 demonstrates that Seed et al. (1997) “AB” curve for soft (weathered) rock, almost perfectly fits the data trend for NEHRP B sites. On the contrary, B, C1, C2 group curve underestimates the amplification by a ratio of almost 50%, except low shaking intensities (below 0.1 g). Data trend and Seed et al. (1997) curves for softer/looser sites are comparable (Figure 4.3-8). Figures 4.3-9 and 4.3-10 show median estimates from Choi and Stewart (2005) A-1 model. Amplification factors from all of the above models are normalized with respect to compatible  $pga_{rock}$  definition collected at  $V_s=1250$  m/s.

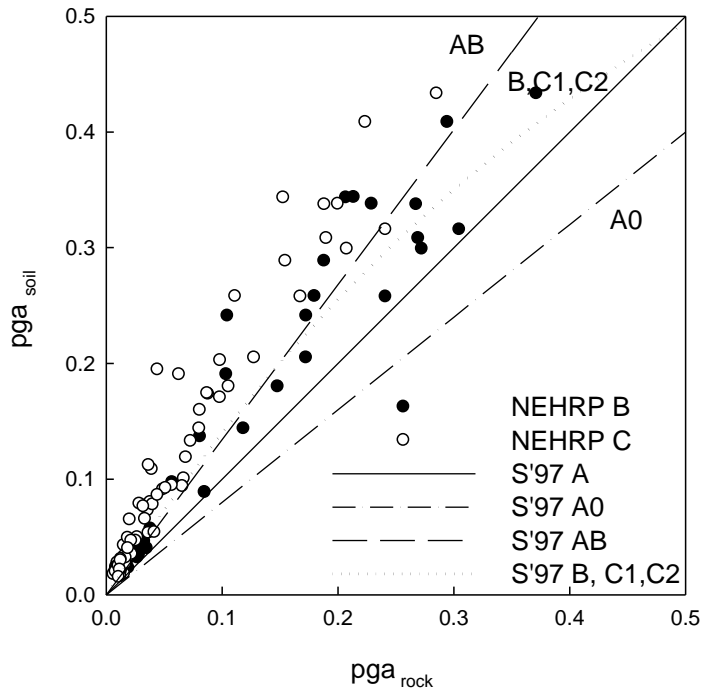


**Figure 4.3-7. Comparison of Seed et al. (1997) model for sites falling within NEHRP B and C classes**

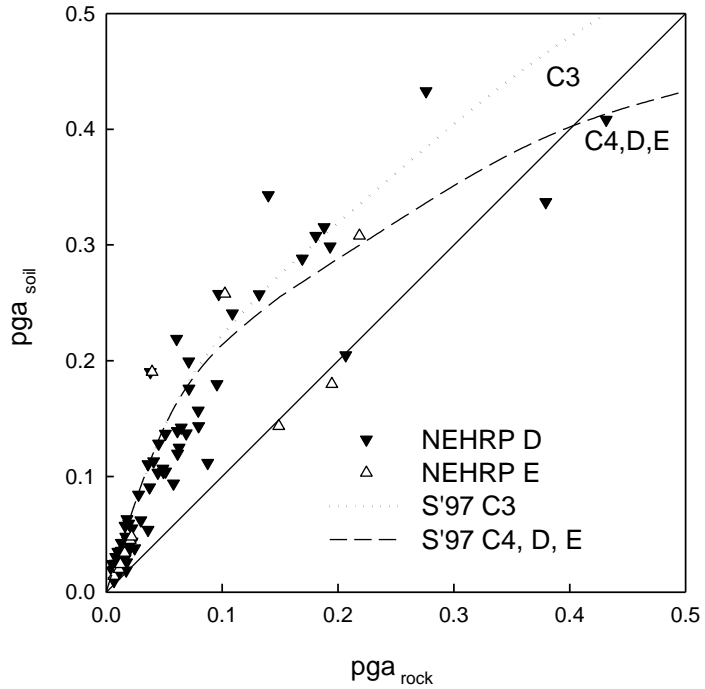


**Figure 4.3-8. Comparison of Seed et al. (1997) model for sites falling within NEHRP D and E classes**



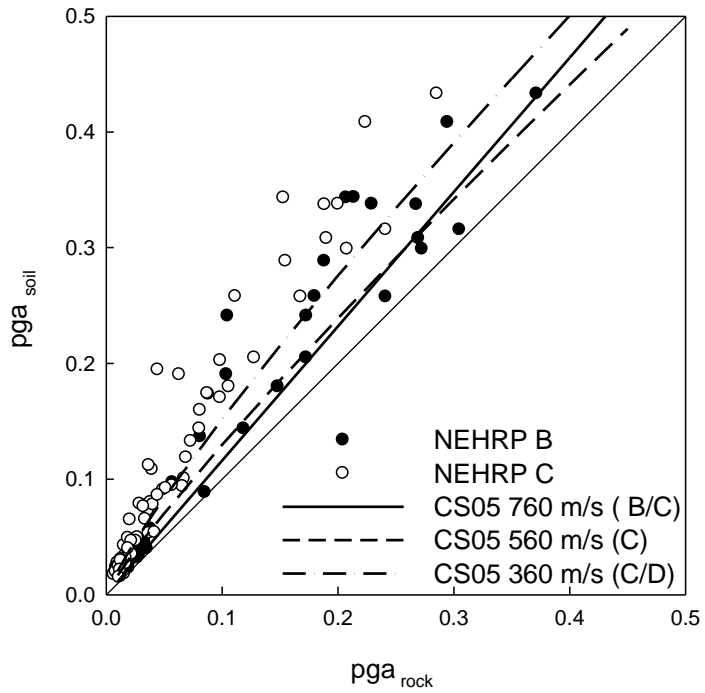


**Figure 4.3-9. Comparison of Choi and Stewart (2005) model for sites falling within NEHRP B and C classes**

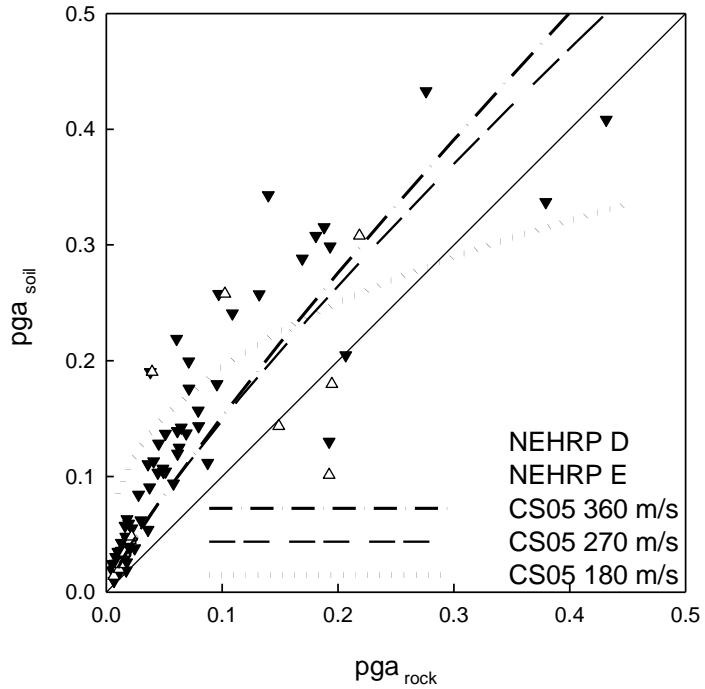


**Figure 4.3-10. Comparison of Choi and Stewart (2005) model for sites falling within NEHRP D and E classes**

A cross comparison is made among the model developed by the effort in this study, Seed et al. (1997) model, and Choi and Youngs (2005) study; for two selected shear wave velocity values. Median estimates at NEHRP B/C boundary ( $V_{s30}=760$  m/s) suggest that the current model overamplifies ground motion significantly higher than the remaining models. For a selected  $pga_{rock}$  value of 0.2 g, Choi and Stewart (2005), Seed et al. (1997), and the current study yield  $pga_{soil}$  values of 0.23 g, 0.27 g, and 0.31 g, respectively (Figure 4.3-11).

Last series of comparisons are made for  $V_{s30}=270$  m/s, representing a typical NEHRP D site. Model results indicate that, despite the notable variability in the intensity of amplification above 0.1 g, all models succeed to reflect the increasing level of expected nonlinear response (Figure 4.3-12).

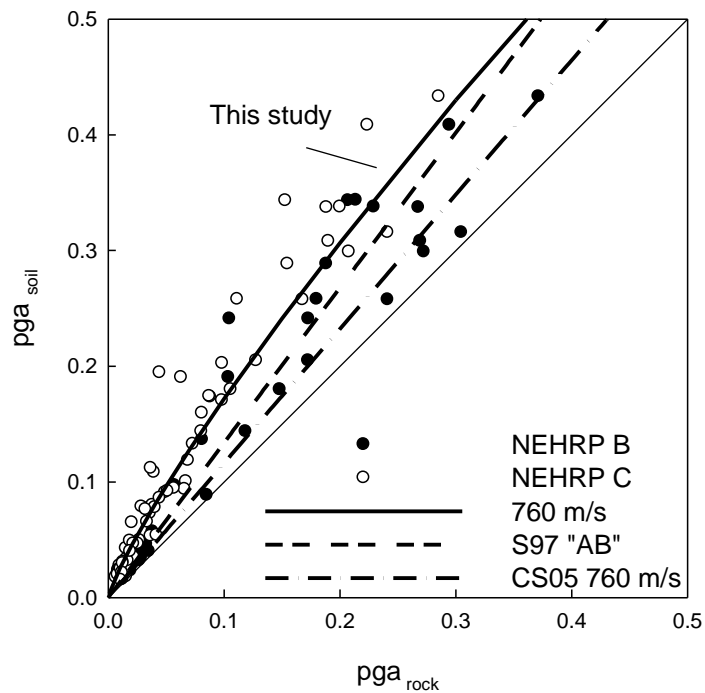


**Figure 4.3-11. Cross –comparison of median estimates from different models at NEHRP B/C boundary**

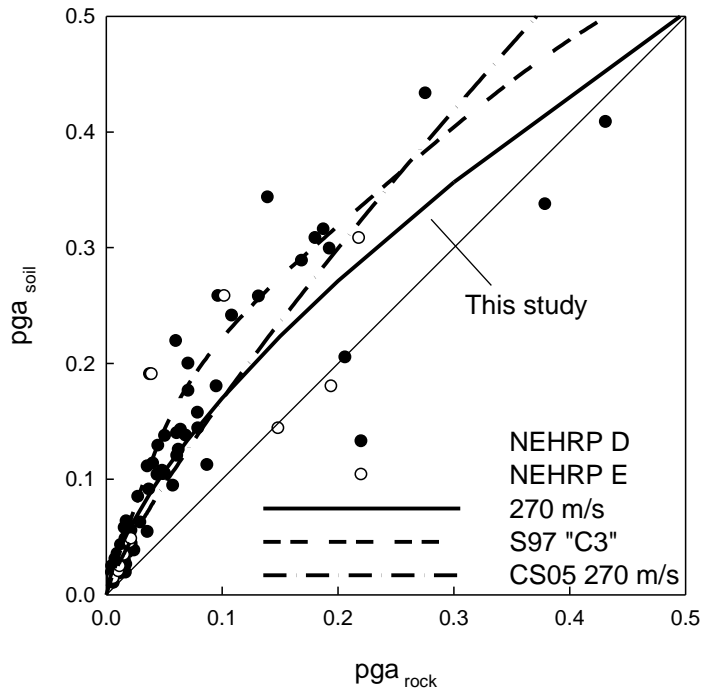


**Figure 4.3-12. Cross –comparison of median estimates from different models at a typical NEHRP D site**

Impact of applying a weighting scheme, to balance the uneven sampling of data points at every defined intensity-site class bin is presented in Figure 4.3-13. Dashed series represent final selections of the model, and solid lines represent the series obtained without performing any modifications.

Contribution of modeling parameter uncertainties of  $pga_{rock}$  and  $V_{s30}$  has also had a beneficial impact on the estimated model error. For PGA amplification; namely  $\ln(\text{Amp})_{T=0}$ ,  $\sigma_{\epsilon}$  (model error) was calculated to be 0.361 using exact estimates of descriptive variables. Incorporating inexact estimates to the likelihood formulation yielded a reduced value of 0.282. Choi and Stewart (2005) present values of model uncertainty in  $\ln(\text{Amp})$ , equal to or above 0.55.

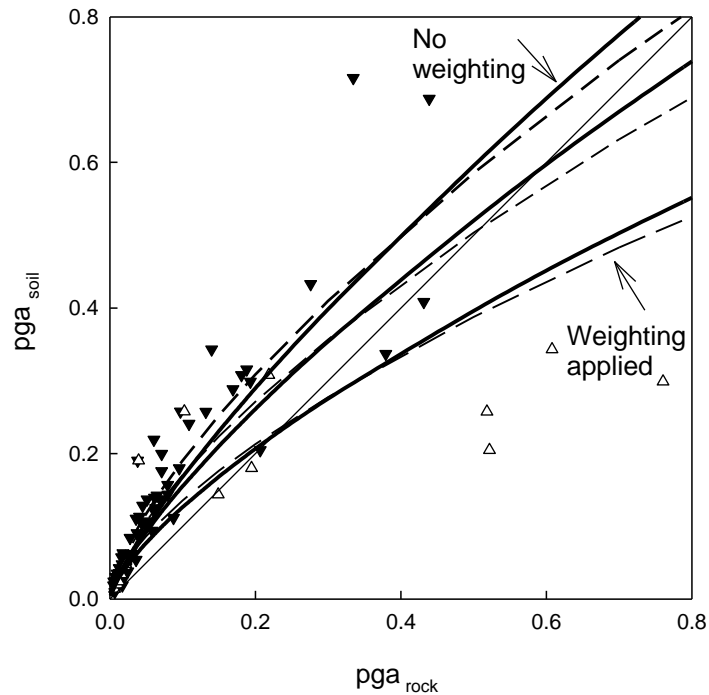


**Figure 4.3-13. Impact of weighting on the predicted median amplification curves for  $V_{s30}=180$  m/s,  $V_{s30}=270$  m/s, and  $V_{s30}=360$  m/s**

Average residuals for the proposed model, plotted as a function of spectral period, and binned with respect to site categories are presented in Figure 4.3-14. Average error generally lies within the minus and plus 20% range, with a systematic overprediction at PGA, and larger scatter with respect to site class after  $T=1.0$  s. For the final word in this section, Figures 4.3-15 and 4.3-16 present the complete normalized residual plots computed from measured and predicted spectral values of soil acceleration; as a function of  $pga_{rock}$  and  $V_{s30}$ . Errors greater than 100% do exist, however are clipped out of the graphs.

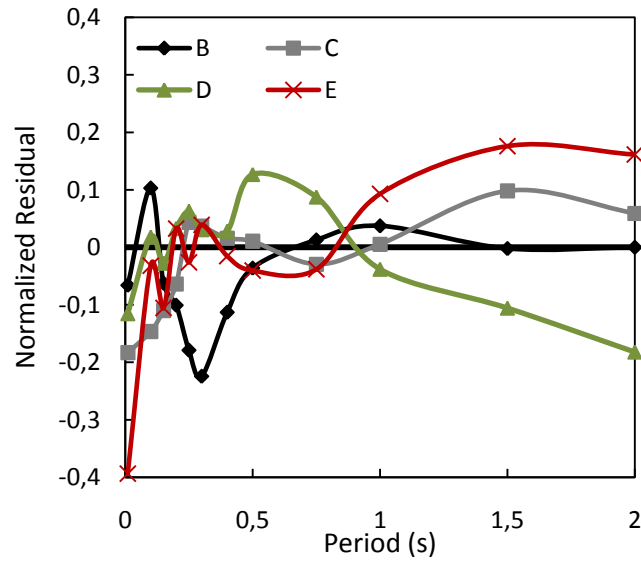


**Figure 4.3-14. Average values of normalized residual plots as a function of spectral period**

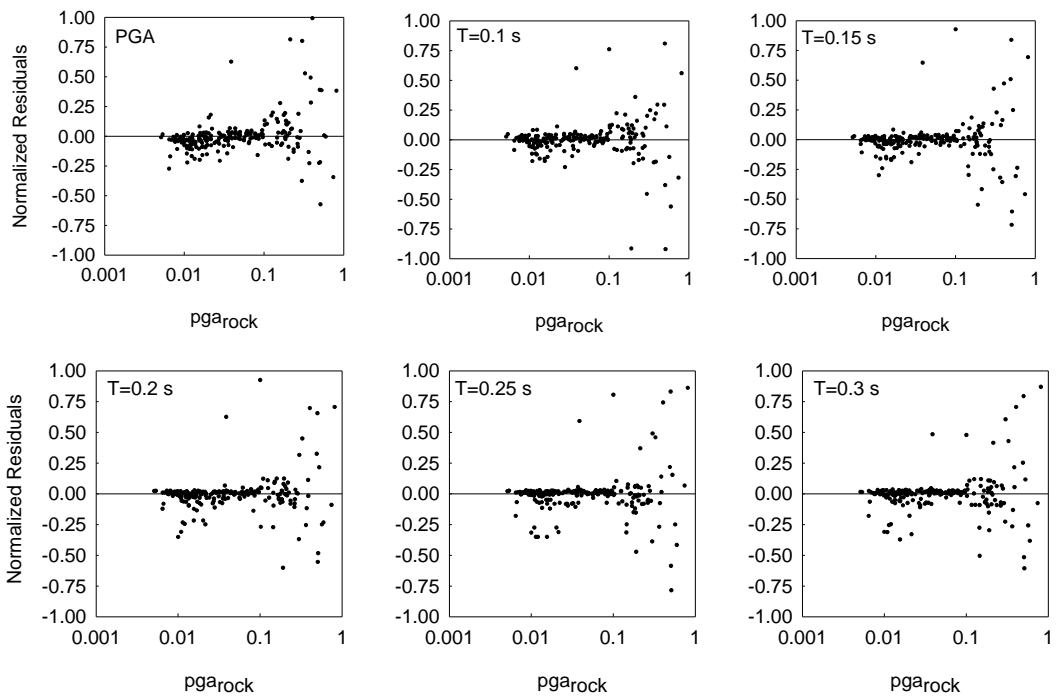


**Figure 4.3-15. Normalized residual plots as a function of  $pga_{rock}$**

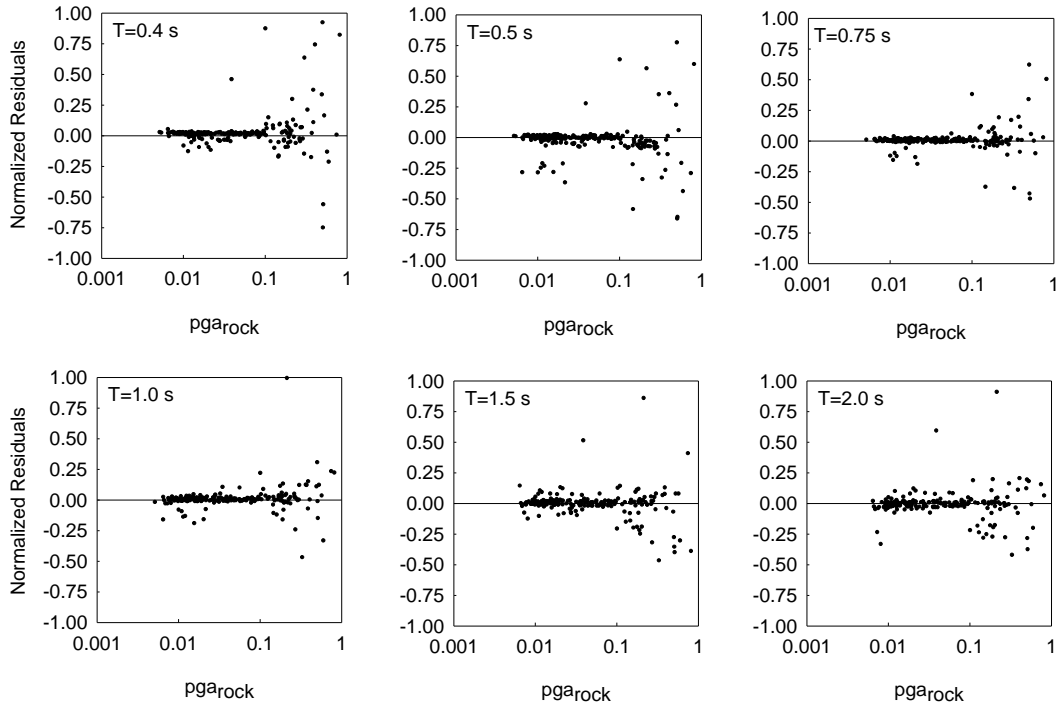


**Figure 4.3-15. (continued) Normalized residual plots as a function of  $pga_{rock}$**

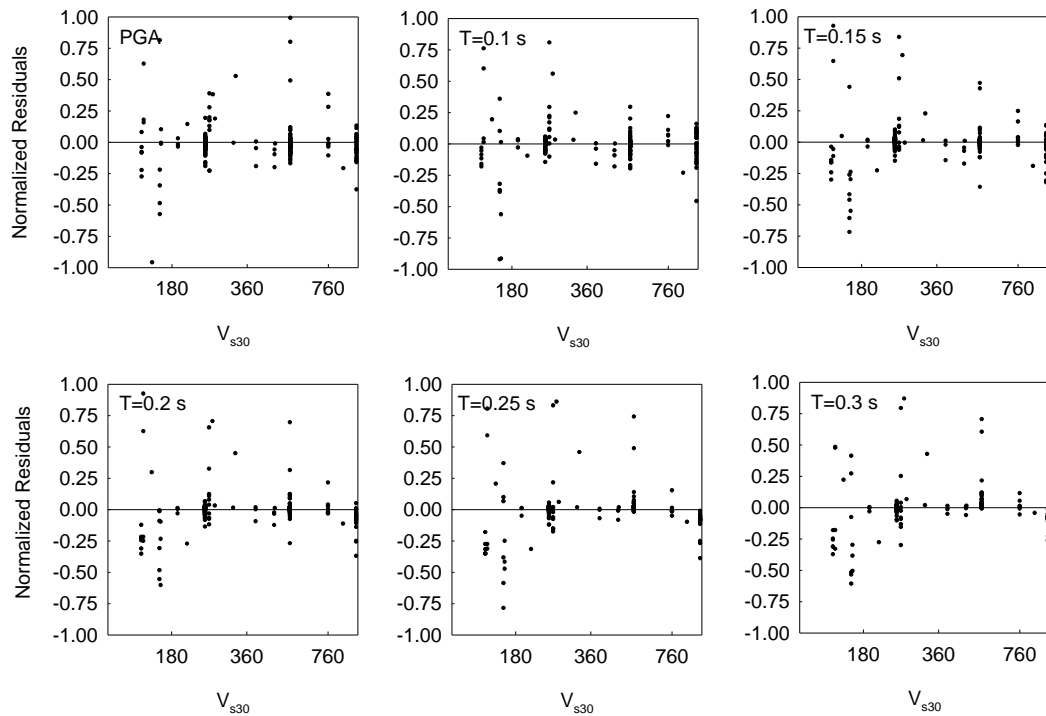


**Figure 4.3-16. Normalized residual plots as a function of  $V_{s30}$**

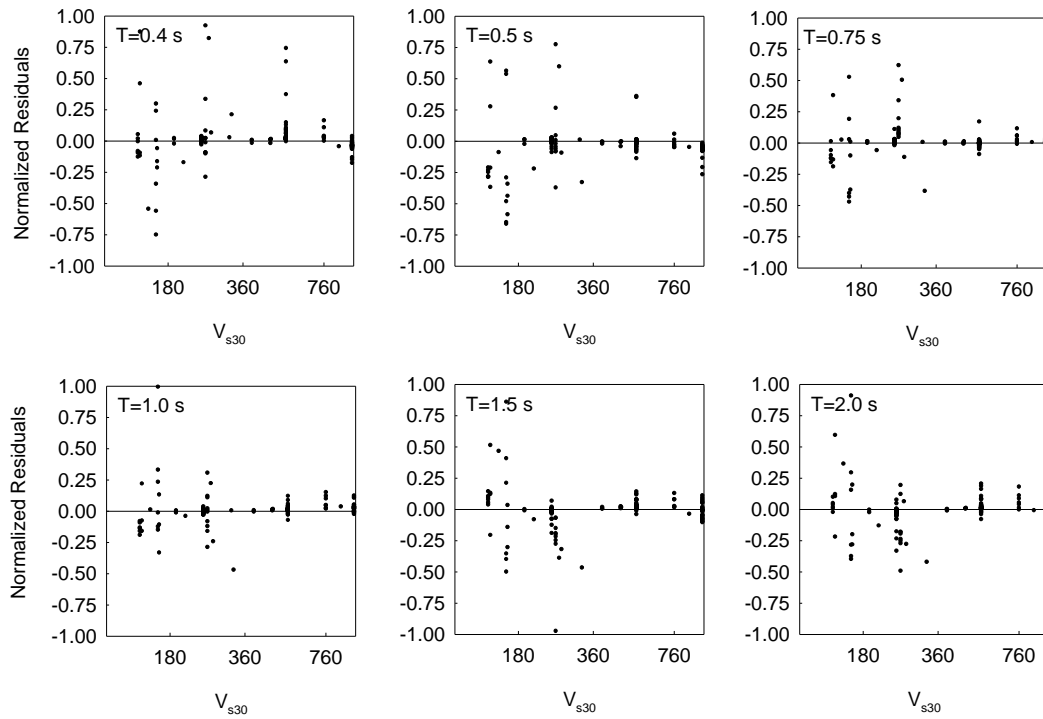


**Figure 4.3-16. (continued) Normalized residual plots as a function of  $V_{s30}$**

### 4.3.2 Formulation of Ground Motion Prediction Model

Ground motion prediction model, for estimating the peak and 5% damped spectral parameters of horizontal component of acceleration conforms to the following restrictions defined by the dataset formation and waveform processing steps:

- i) In addition to the peak parameters, reliable spectral period range that will avoid any bias from statistical uncertainty is determined to be the 0.1 s – 2.0 s interval.
- ii) The proposed model covers the  $M=3.4 - M=7.5$  magnitude range. However, only two events exist for magnitudes lower than  $M=4.0$ , hence the reliable magnitude interval is determined as  $M=4.0 - M=7.5$ .

- iii) The equation applies for events with shallow focus, hence should not be used in subduction zones.
- iv) Although a descriptive parameter for style of faulting is implemented, data for reverse faulting is almost non-existent. Ground motion intensity estimates for reverse faults should be critically reviewed.
- v) Ground motion prediction equation is developed for the GMRotD50 definition of horizontal ground motion, and, for rock sites; corresponding to a material having  $V_s=1250$  m/s shear wave velocity. Predictions of median ground motion estimates, and corresponding standard deviation values at soil sites utilizes the companion ground response model presented in Section 4.3.1.

Basic functional forms of the 1997 generation of ground motion prediction equations were studied. Additionally, recently developed NGA models, incorporating more descriptive parameters were investigated. As will be explained in the following sections, two separate weighting schemes were experimented and the most appropriate basic functional form of the equation was determined as follows:

$$\ln(SA_{\text{rock}}) = \theta_1 + \theta_2(M - 6.2) + \theta_3(M - 6.2)^2 + [\theta_4 + \theta_5(M - 6.2)] \ln \sqrt{R_{jb}^2 + \theta_6^2} + \theta_7 SOFP + \sigma_\varepsilon \quad (4-18)$$

where  $\theta_i$  and  $\sigma_\varepsilon$  are model coefficients and model error terms, respectively.  $M$  is the moment magnitude,  $R_{jb}$  is the Joyner-Boore distance, and  $SOFP$  is the style of faulting parameter; previously discussed in Chapter 2.

In Equation 4-18, geometrical spreading is a function defined by the product of magnitude and natural logarithm of  $R$ . All the terms, including model error is period



dependent, and is obtained using independent likelihood estimates. Although smoothing has been applied on the resulting coefficients, neither the median estimate, nor the error term and likelihood value was altered remarkably. Model error term  $\sigma_\varepsilon$ , was modeled as a magnitude dependent function. Choosing a heteroscedastic sigma function enhanced model results, and was in good agreement with the order of sigma values proposed in NGA relationships. The linear dependence on magnitude is parameterized as follows:

$$\sigma_\varepsilon = \theta_8 + \theta_9 M \quad (4-19)$$

Smoothed model coefficients for peak and 5% damped spectral values of acceleration response are presented in Table 4.3-3. Value of period independent coefficient  $\theta_7$ , regressed for PGA and kept constant for all other periods, is assigned as 0.0628.

**Table 4.3-3. Model coefficients for peak and 5% damped spectral acceleration response (GMRotD50 component)**

T	$\theta_1$	$\theta_2$	$\theta_3$	$\theta_4$	$\theta_5$	$\theta_6$	$\theta_8$	$\theta_9$
PGA	0.7674	0.2511	-0.0480	-1.0987	0.1635	11.034	0.875	-0.040
0.1	1.6772	0.0817	0.0000	-1.2389	0.1832	13.278	0.913	-0.041
0.15	2.3841	-0.0520	-0.0156	-1.3613	0.2148	17.735	0.913	-0.044
0.2	2.9220	-0.0245	-0.0421	-1.4495	0.2201	18.793	1.164	-0.076
0.25	2.1480	0.5602	-0.0222	-1.2570	0.0854	14.393	1.007	-0.052
0.3	1.7886	0.7137	-0.0345	-1.1742	0.0455	14.103	0.873	-0.035
0.4	1.6001	0.5691	-0.119	-1.134	0.1093	13.648	1.037	-0.054
0.5	0.6218	0.7023	-0.1192	-0.9253	0.085	9.918	1.019	-0.051
0.75	-0.2737	0.7295	-0.2250	-0.7426	0.1013	7.137	1.382	-0.115
1	-0.6055	0.8140	-0.2262	-0.7128	0.1103	6.603	1.453	-0.126
1.5	-1.000	1.1854	-0.2376	-0.7326	0.0419	8.325	1.091	-0.080
2	-1.6142	0.8868	-0.3417	-0.6704	0.1279	1.419	0.617	0.010

#### *4.3.2.1 Style of Faulting Parameter*

The procedure for fixing the style of faulting coefficient is subjective. The initial value is the result of optimization performed on PGA ( $T=0$ ). For higher periods, using neither a dummy variable for faulting style, nor the continuous SOFP representation yielded results that were compatible with the expected physical behavior; indicating that reverse faulting for a given magnitude and distance should produce relatively higher shaking intensity. This condition, also in agreement with the results of NGA relationships, was only satisfied for  $T=0$  period. Since the current dataset dominantly contains records from normal and strike-slip faulting; the results for reverse faulting were, in fact an extrapolation from the existing conditions. Given the fact that, observing noteworthy difference between events from strike slip faults and normal faults is inherently sensitive to dataset formation (Bommer et al., 2003); slight dependence on SOFP parameter for PGA probably vanished for higher periods for the current study. The final decision was to fix the model coefficient controlling SOFP at all periods, rather than neglecting it at all. Moreover, statistical benefit of fixing and keeping the descriptive parameter was higher than excluding it, since a slight improvement in the likelihood of the model was observed.

#### *4.3.2.2 Hanging Wall Effects*

Another descriptive parameter used in 1997 series of Western U.S relationships and NGA project is the hanging wall effect. Hanging wall effect is partly covered by the choice of source to site distance metrics. This study utilizes  $R_{jb}$  distance measure, implicitly accounting for the hanging wall phenomenon. Nevertheless, a feasibility study in the form of a screening procedure was applied to assess the approximate number of records subjected to hanging wall effects. The procedure consists of the following steps:

- i) For events with published dip angles (obtained using focal mechanism solutions) greater than  $70^{\circ}$ , the effect was considered to be negligible; referring to the taper function used in Abrahamson and Silva (1997). For events with unpublished focal mechanisms, but assigned faulting style, strike-slip events were removed.
- ii) Events having magnitudes lower than M 5.5 were removed (Abrahamson and Silva, 1997). Although the limit for the taper function was updated as M=6.0 in the Abrahamson and Silva (2008) model, the decision was made on behalf of conservatism.
- iii) As source to site distance increases, effect of hanging wall steadily diminishes. Abrahamson and Somerville (1996) study has defined a  $R_{rup}$  threshold of 40 km. Description of the procedure is also summarized in the NGA flatfile. Orientation of the site with respect to the rupture and dipping direction is also of critical importance. Application of criteria defined in Abrahamson and Somerville (1996), required certain assumptions. Simplification was made, by assuming that the rupture plane for a given event was located in the middle of the focal point published by KOERI, and relevant rupture dimensions were obtained from median estimates of Wells and Coppersmith (1994) relations. Locating the rupture plane and surface projection was completed using the strike and dip data for a given event.
- iv) After the simplified screening procedure was applied, a total number of 14 records from 2 events qualified, with a dominance of the 1999 Düzce event. 10 of the events were in the footwall, and 4 events were falling in the hanging wall zone. Average dip angle reported for Düzce event by various agencies was  $66^{\circ}$ , close to the selected cutoff dip angle.

Based on the factors listed above, hanging wall parameter was excluded from further quantification; since it would not possibly improve our results. The new source to site distance definition “ $R_x$ ” used in Abrahamson and Silva (2008) model was not studied.

#### *4.3.2.3 Modeling Inexact Descriptive Parameters and Weighting Scheme*

Similar to the companion study for ground response model, effect of inexact observations of moment magnitude,  $M$  and source to site distance measure,  $R_{jb}$  was modeled in predictive parameters. Additionally, uncertainty in  $\ln SA_{rock}$  due to random orientation of the horizontal component, brought by the preferred definition of GMRotD50 was accounted for. Last, but not the least, uncertainty in rock ground motion intensity, due to utilization of generic sites and site response procedures were separated from total uncertainty. Mathematical expression for the contributors of complete error term will be provided.

Two separate weighting schemes were applied, to account for the uneven sampling problem. First trial was based on establishing uneven magnitude and distance bins; and the second approach was based on directly implementing weighting factors using  $pga_{rock}$  distribution. Out of two methods, second approach yielded better results in terms of residuals. The threshold for weighting was chosen as 0.05 g. For records having  $pga_{rock}$  values below 0.05 g,  $W_{<0.05g}$  was assigned 0.415. Similarly,  $W_{>0.05g}$  was assigned a value of 1.585, adding up to total number of 2 weighting units. These factors are valid for the peak component of ground motion, however were slightly modified for spectral values due to uneven sample size of records at each period.

#### 4.3.2.4 Error Terms for the Ground Motion Prediction Model

Variance for the error term proposed ground motion model can be expressed as the sum of variances of the model error and inexact observations (Equation 4-20).

$$\sigma_{\ln SA_{rock,TOTAL}}^2 = \sigma_{\varepsilon}^2 + \sigma_{INEXACT}^2 \quad (4-20)$$

where

$$\sigma_{INEXACT}^2 = \sigma_{\ln SA_{rock|Site}}^2 + \sigma_{\ln SA_{rock|\theta}}^2 + \left[ \left( \frac{\partial \ln SA_{rock}}{\partial M} \right)^2 \sigma_M^2 + \left( \frac{\partial \ln SA_{rock}}{\partial R_{jb}} \right)^2 \sigma_{R_{jb}}^2 \right] \quad (4-21)$$

In Equation 4-21,  $\sigma_{\ln SA_{rock|Site}}^2$  is the variance in  $\ln SA_{rock}$  due to site response applied on generic profiles,  $\sigma_{\ln SA_{rock|\theta}}^2$  is the variance in  $\ln SA_{rock}$  due to random orientation of the site with respect to the wavefront. Ground motion prediction model is developed for the GMRotD50 definition, thus randomness in rotation angle is incorporated to the error term. Terms in brackets quantifies the variance of  $\ln SA_{rock}$  due to inexact observations of moment magnitude, M, and source to site distance,  $R_{jb}$ . Correlation between these two variables is assumed to be zero. Having separated the error due to measurements from the total error, the term  $\sigma_{\varepsilon}^2$  reflects the magnitude of model error left, and can be calculated from Equation 4-19.

While this defines the error quantification for rock sites with a reference  $V_s$  of 1250 m/s; an extra step is required to express the magnitude of propagated error to soil sites. For this purpose, integration of the ground response amplification model to the ground motion prediction equation becomes mandatory. Overlooking the mathematical details, period dependent expression for the calculation of standard deviation value for soil sites is presented in Equation 4-22.

$$\begin{aligned} \sigma_{\ln SA_{Soil}}^2 = & \\ & \sigma_{\ln SA_{rock}}^2 + \sigma_{\ln Amp}^2 + \left( \frac{\partial \ln Amp}{\partial \ln pga_{rock}} \right)^2 \sigma_{\ln pga_{rock}}^2 + \\ & 2 \left( \frac{\partial \ln Amp}{\partial \ln pga_{rock}} \right) \sigma_{\ln SA_{rock}} \sigma_{\ln pga_{rock}} \rho_{\ln SA_{rock}, \ln pga_{rock}} \end{aligned} \quad (4-22)$$

where  $\rho_{\ln SA_{rock}, \ln pga_{rock}}$  is the correlation of residuals between lnPGA and lnSA at any other period. Table 4.3-4 presents the correlation coefficients between the model residuals of peak horizontal acceleration with that of spectral values. Corresponding values for Abrahamson and Silva (2008) model are presented in the right column for comparison. The values are shown to be in good agreement.

**Table 4.3-4. Correlation vector for peak and spectral values of rock acceleration**

$\rho$	<b>This Study</b>	<b>AS08</b>
<b>PGA</b>	1.00	1.00
<b>0.1s</b>	0.94	0.93
<b>0.15s</b>	0.92	0.90
<b>0.2s</b>	0.91	0.87
<b>0.25s</b>	0.90	0.86
<b>0.3s</b>	0.87	0.84
<b>0.4s</b>	0.85	0.82
<b>0.5s</b>	0.81	0.78
<b>0.75s</b>	0.71	0.68
<b>1s</b>	0.60	0.61
<b>1.5s</b>	0.50	0.50
<b>2s</b>	0.45	0.43

### 4.3.3 Evaluation of Motion Prediction Model Results

This section provides a brief overview on the ground motion prediction equation model developed using records from Turkish dataset. The first series of figures provide a general sense of the magnitude – distance decay, spectral shape and intensity of spectral parameters. We investigate the variation of peak and spectral amplitudes with respect to predictive parameters, such as magnitude, source to site distance and style of faulting. Presenting the variation of amplitudes with respect to different site conditions; controlled by two parameters, peak ground acceleration value on rock; and  $V_{s30}$ , composes the next step. In addition to the model results from this study, comparison with some of the recent relationships developed using global and local datasets is provided. Impact of applying weighting factors to establish even sampling conditions, and its consequence on selection of lower magnitude thresholds is discussed. Standard error term of the ground motion model is presented, and a routine evaluation is made on the order of model uncertainty decrement.

#### 4.3.3.1 *Magnitude and Distance Scaling*

Figure 4.3-17 presents the median curves for magnitude – distance scaling, plotted for strike slip faulting (SOF<sub>P</sub>=0.5). The curves are drawn for a reference site condition having a  $V_{s30}$  value of 1250 m/s. The proposed curves partially capture the magnitude saturation for  $M > 7$ ; nevertheless a solid evidence is yet to be observed. Saturation of ground motion intensity at short source to site distance range is evident.

Normalized residuals, expressed in form of difference between measured and predicted values of  $\ln(SA)$ , divided by the measured value, is presented in Figure 4.3-18 for the peak component and two representative spectral periods ( $T=0.2$ , and  $T=1.0$ ). Residuals are plotted as a function of two key descriptive parameters, magnitude and distance. The results suggest the model is fairly unbiased in terms of magnitude and distance.

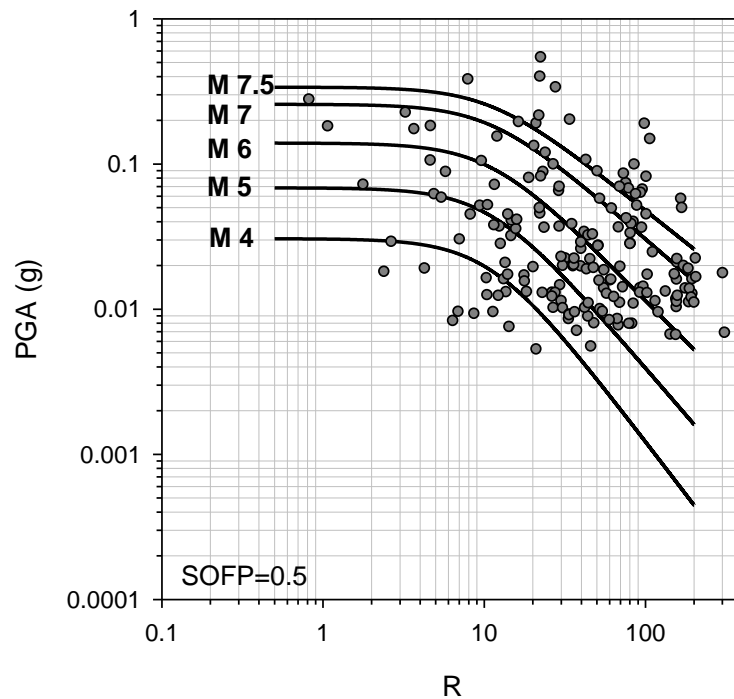


**Figure 4.3-17. Magnitude-distance scaling for the proposed model**

Several data points exceeding the -1 and +1 factors for residuals are clipped out of the plot. Examination of average values of residuals suggest that the success of the model is more evident at lower periods and the peak component; in which the value does not exceed a thousandth, and a visible trend along magnitude and distance is not observable. However, in the case of higher periods, the average value of normalized residuals point to 6% error, with a slight trend along predictive parameters (Figure 4.3-18).

Comparison of magnitude and distance dependence of peak component of horizontal ground motion, with four of the NGA models is presented in Figure 4.3-19. Solid lines represent results of this study, while thin dashed lines are the predictions of other models. In order to avoid ambiguities arising from different distance definitions used, the scenarios are based on a strike slip fault with  $90^{\circ}$  dip angle, which provides a common base for distance comparison. All of the NGA models are predicting GMRotI50 component, however, we have already shown that difference between



GMRotI50 and GMRotD50 is comfortably negligible for our dataset and spectral period range.

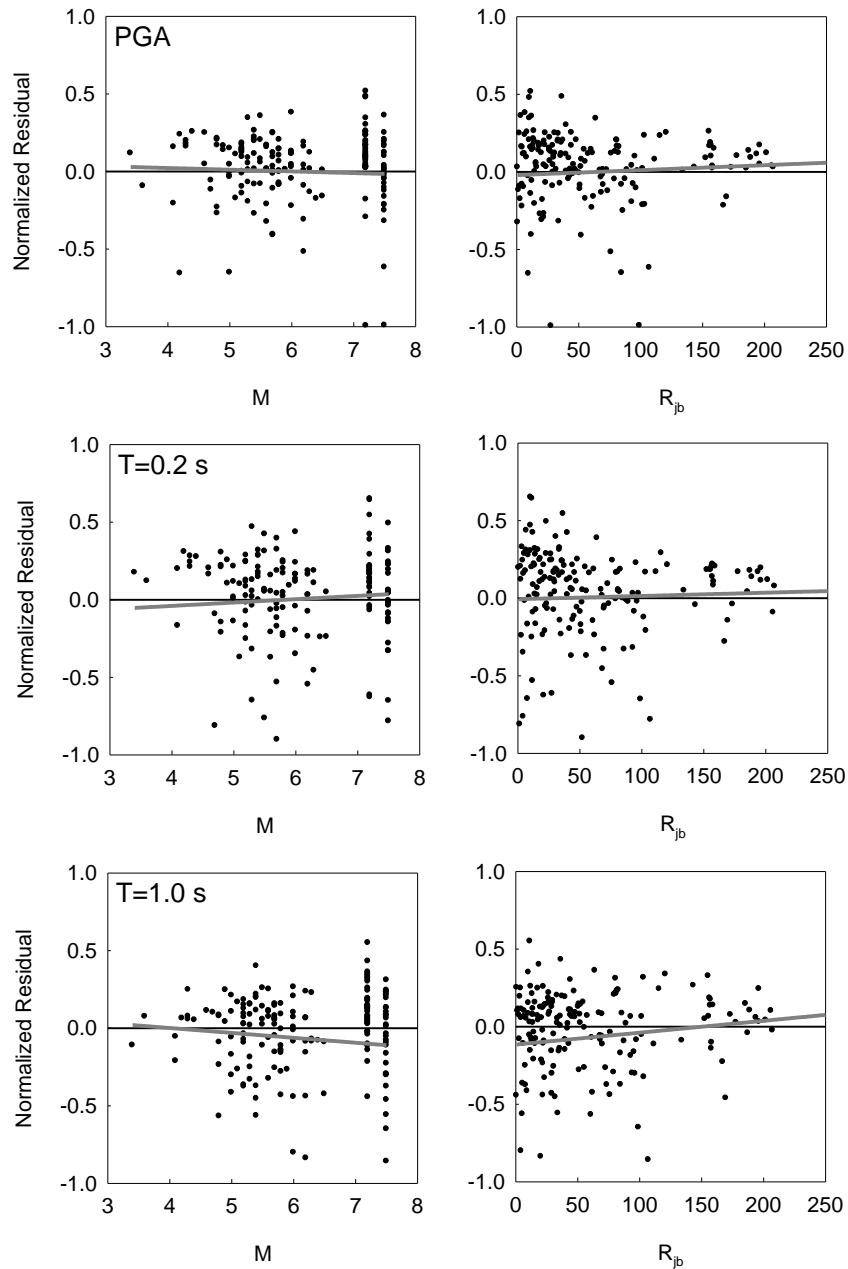


**Figure 4.3-18. Normalized residuals of GMPE model for peak component and spectral values**

The comparisons are made for a reference  $V_{s30}$  of 1250 m/s in all models. For the missing descriptive parameters in the NGA models, median estimates are substituted.

Abrahamson and Silva (2008) (AB08 in figures) presents the median relationship between  $V_{s30}$  and depth to  $V_s$  1 km/s;  $Z_{1.0}$  parameter. This relationship was used in conjunction with the depth to 2.5 km/s parameter;  $Z_{2.5}$  present in Campbell and Bozorgnia (2008) (CB08 in figure). Depth to top of rupture ( $Z_{TOR}$ ) is also a recently introduced predictive parameter, present in all models compared herein, but the Boore and Atkinson (2008) (BA08) study.  $Z_{TOR}$  controls the amplified intensity of ground motion due to rupture not reaching the surface; and has a significant impact on the predictions as modeled by Abrahamson and Silva (2008). For comparisons, we assume that rupture has reached the surface for all scenarios, regardless of earthquake magnitude, which in reality; may not be the case.

Results of comparisons point to a very good match between our predictions and NGA models, for 10-100 km distance range. The only exception comes from the Chiou and Youngs model (CY08 in figure), in which there is a stronger decay of pga against distance. The main focus of unconformity is at distances smaller than 10 km. All of the NGA models significantly overestimate shaking intensities at close distances for small magnitude events, compared to the model from this study. Recalling that NGA datasets contains events larger than  $M=5$ , it is within expectations that mismatching predictions at  $M=4$ ; or even  $M=5$  are acceptable. Intensity predictions at short distances, for magnitudes equal to or above  $M=6$  become more comparable, for the reference rock condition. Effect of integrating site response model will be discussed in Section 4.3.3.3.

Nevertheless, second series of pga comparisons is made using the results of prediction models developed using local data, or a combination of local, European, and Middle East earthquakes; as in the case of Akkar and Bommer (2010). The results are presented for 3 different models; Ulusay et al. (2004), Kalkan and Gülkan (2004) and Akkar and Bommer (2010) (Figure 4.3-20). Özbey et al. (2004) study is excluded from comparisons, since it is an event-specific model utilizing records from the 1999 series of events.

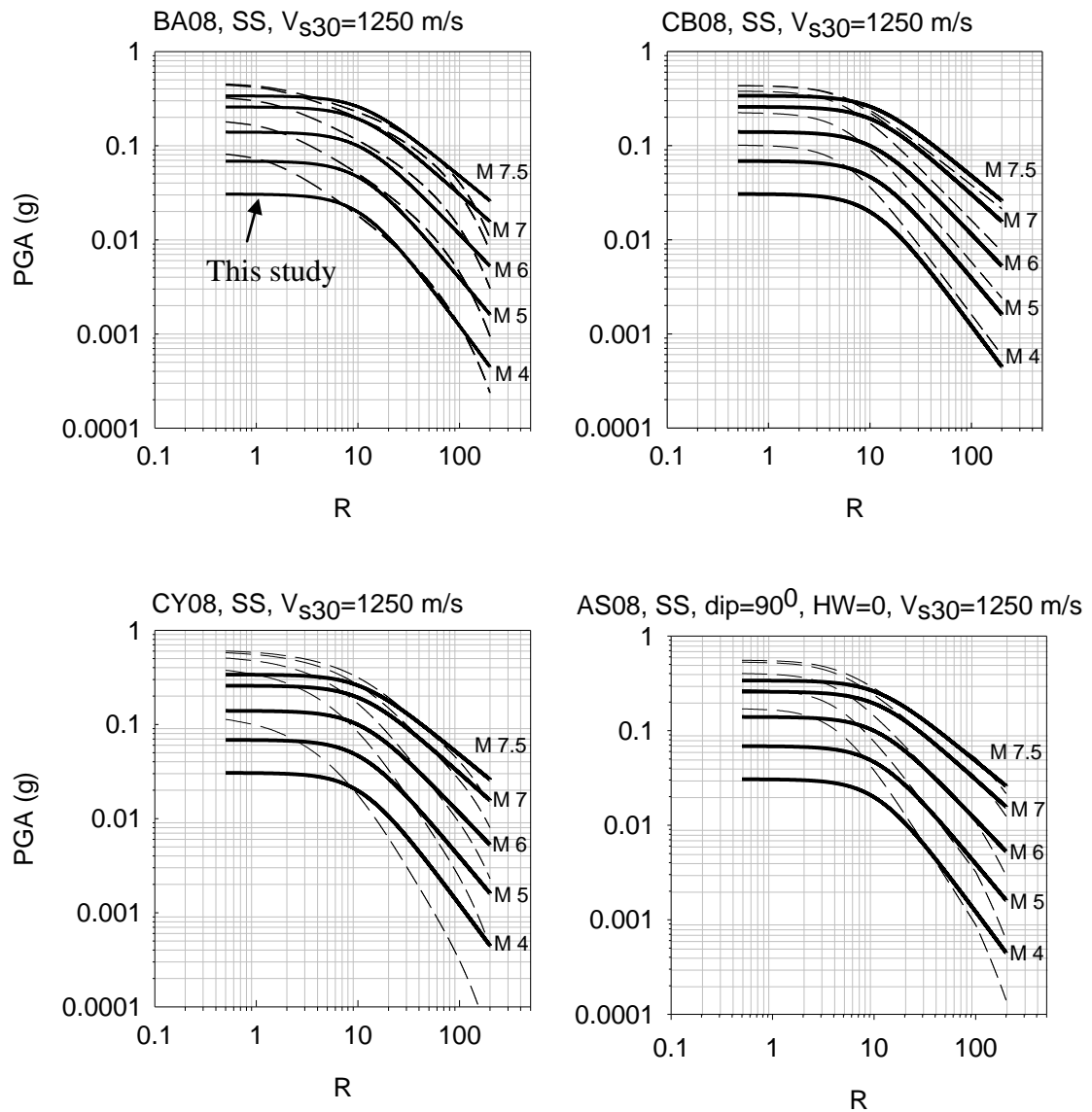


**Figure 4.3-19. Comparison of current study and NGA models at reference rock condition**

The first assumption in cross comparisons between the local models and this study is on  $V_s$  scaling. Figure 4.3-20 presents median estimates for the NEHRP B/C boundary, characterized typically by  $V_{s30}$  value of 760 m/s. Series in bold represent the findings of this study. “Rock” definition from the Ulusay et al. (2004) model is assumed to be roughly corresponding to the assigned shear wave velocity range.

Ulusay et al. (2004) and Kalkan and Gülkan (2004) models predict the larger component of horizontal motion, thus their predictions for the given scenarios were scaled to GMRotD50 values, in order to ensure compatibility. Any conversion between  $R_{epi}$  and  $R_{jb}$  was not made while comparing the Ulusay et al. (2004) model. Our results are fairly comparable to Ulusay et al. (2004) in the 20-100 km range. Above this limit, Ulusay et al. (2004) exhibits a more rapid decay of ground motion. At near-fault distances, predictions from this study are significantly higher than Ulusay et al. (2004); however convergence occurs for higher magnitudes.

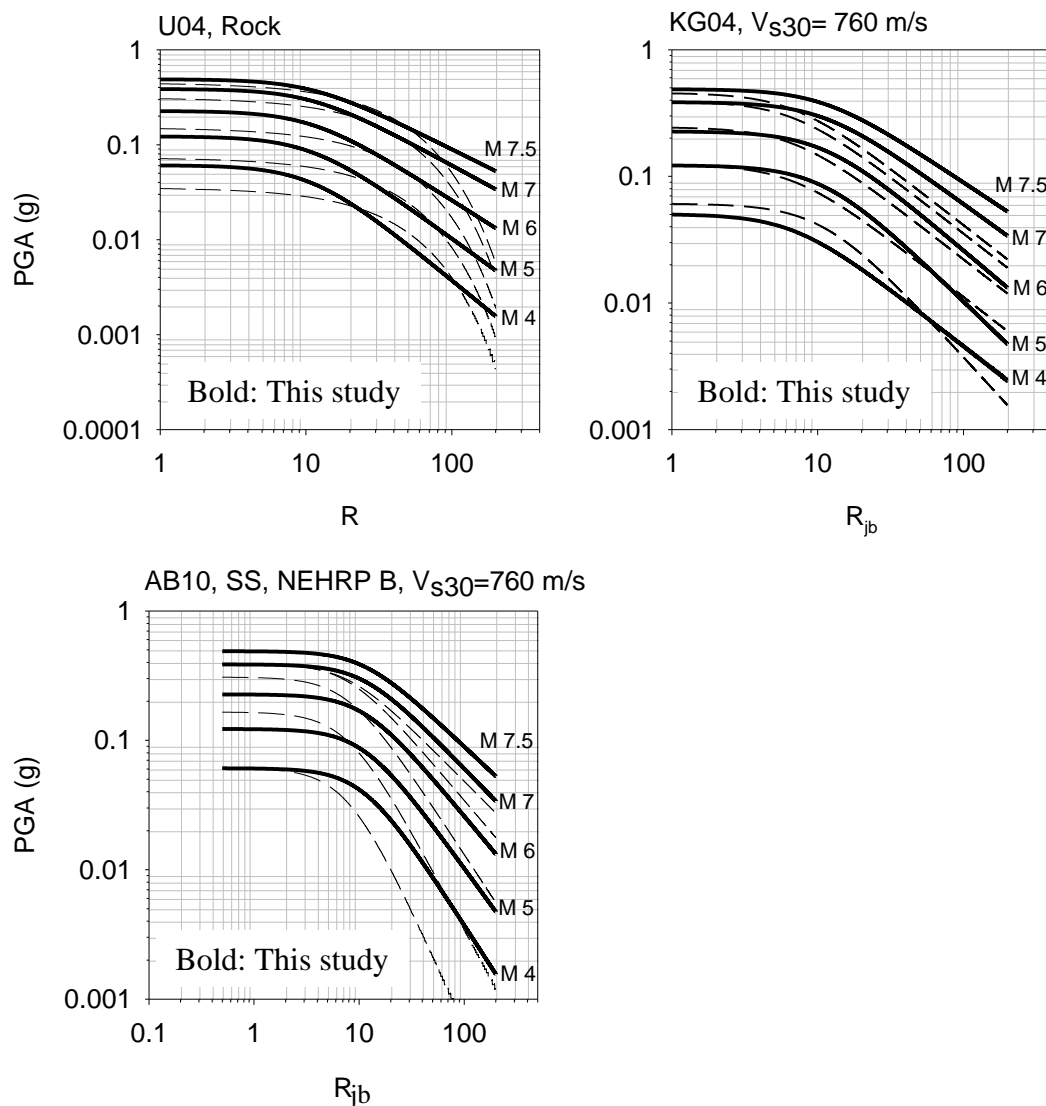


**Figure 4.3-20. Comparison of current study and models developed using local data at  $V_{s30}=760$  m/s equivalent site conditions**

The overall coherency between the Kalkan and Gülkan (2004) model and this study is more pronounced at lower magnitudes. However, for magnitudes  $M=7$  or above, Kalkan and Gülkan (2004) model falls off more rapidly with distance. To give an example, for  $M=7$ , at  $R_{jb}=30$  km, KG04 model predicts 0.102 g, while results from this study refers to a value of 0.158 g. Differences of this order has inevitable impacts on engineering design parameters.

Akkar and Bommer (2010) model originates from a combination of local, European and Middle East datasets. Difference in distance scaling is more evident in lower magnitudes, and there is a stronger agreement in shaking intensities at higher magnitude near-fault events. Although the model predictions are extrapolated below  $M=5$  for illustrative purposes, a reliable comparison cannot be made among the models, since the Akkar and Bommer (2010) dataset does not include events below  $M=5$ .

#### 4.3.3.2 *Style of Faulting Scaling*

The procedure for calculating style of faulting parameter was previously discussed in Section 4.3.2.1. Model results verify the relatively low dependence of shaking intensities on style of faulting. For a moment magnitude value of  $M=6$ , which represents the average magnitude in our dataset, variation of peak ground acceleration at rock level, as a function of source to site distance is plotted (Figure 4.3-21).

For distances up to 5 km, the average ratio of predictions between a full reverse fault and a full normal fault is found to be 1.06, and this ratio steadily decreases with increasing distance.

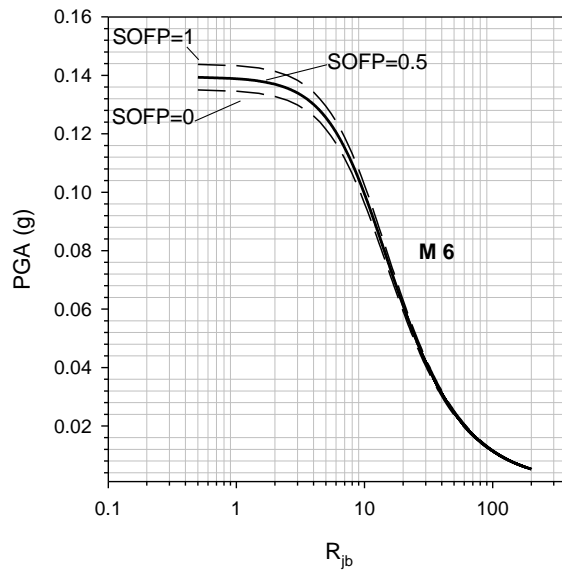


**Figure 4.3-21. Effect of style of faulting on peak acceleration**

#### 4.3.3.3 Shear Wave Velocity Scaling

The proposed ground motion prediction equation implements the site effect term using the ground response model developed in Section 4.3.1. Median predictions at soil sites, and corresponding standard deviation terms are directly based on the currently developed models. Ground motion intensities predicted at reference rock sites are substituted in ground response model to yield peak and spectral parameters for soil sites. Figure 4.3-22 presents 5% damped elastic spectral acceleration values for profiles ranging from NEHRP B to D/E classes. Similar to the discussion made on deamplification of peak components at soft sites under high shaking intensities in Section 4.3.1.4, similar behavior is observed at short periods in the spectrum. Figure 4.3-22 also signifies the verification of general facts about dynamic soil response, demonstrating higher amplification rates in the overall; with particular increase in response at higher period range for softer soils. The scenario spectra used corresponds to a strike slip fault rupturing at  $M=6.5$ , and recorded at  $R_{jb}=15$  km.

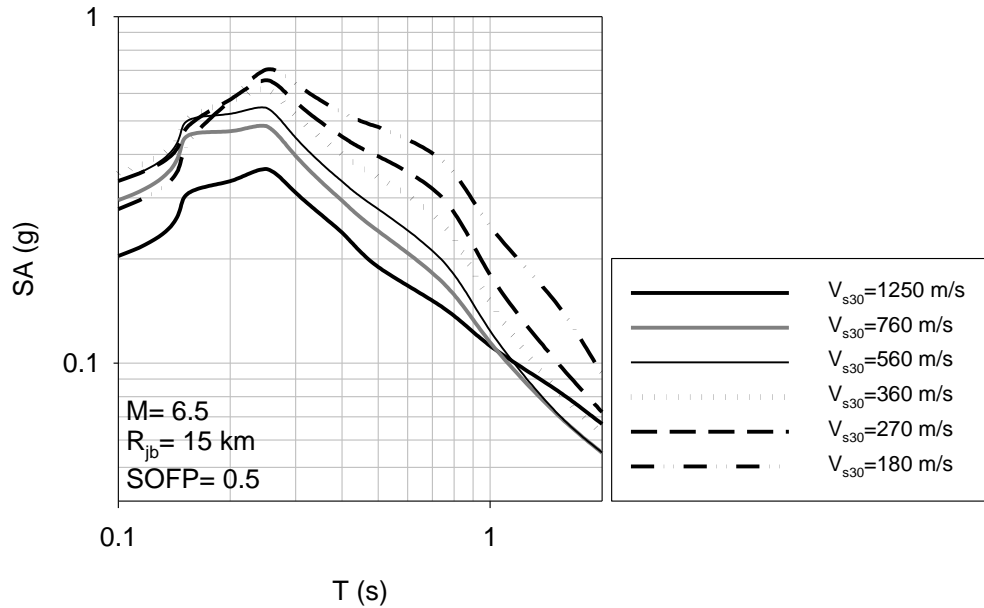


**Figure 4.3-22. Effect of shear wave velocity on peak acceleration**

Having completed comparisons between the NGA models and this study on peak parameters, we superpose the ground response model on the base equation and calculate the response spectral values at different site conditions (Figure 4.3-23). Application of the proposed site response model, acts as an upper bound curve to the spectra from NGA models, for shear wave velocity values greater than or equal to 360 m/s, beginning from  $T=0.1$  s and continuing to higher periods. Response at  $T=0.1$  s is unsystematically lower than some or, all of the NGA models. Response curves begin to decay more rapidly than those of NGA models, for NEHRP D or softer sites, and periods above  $T=1$  s.

Recalling that, prior to developing the model, residuals computed using the recorded ground surface accelerations and NEHRP site categories reflected an overestimation of the NGA model. The case is reversed here, and function of the ground response model developed using equivalent linear site response analysis on the results is highlighted.

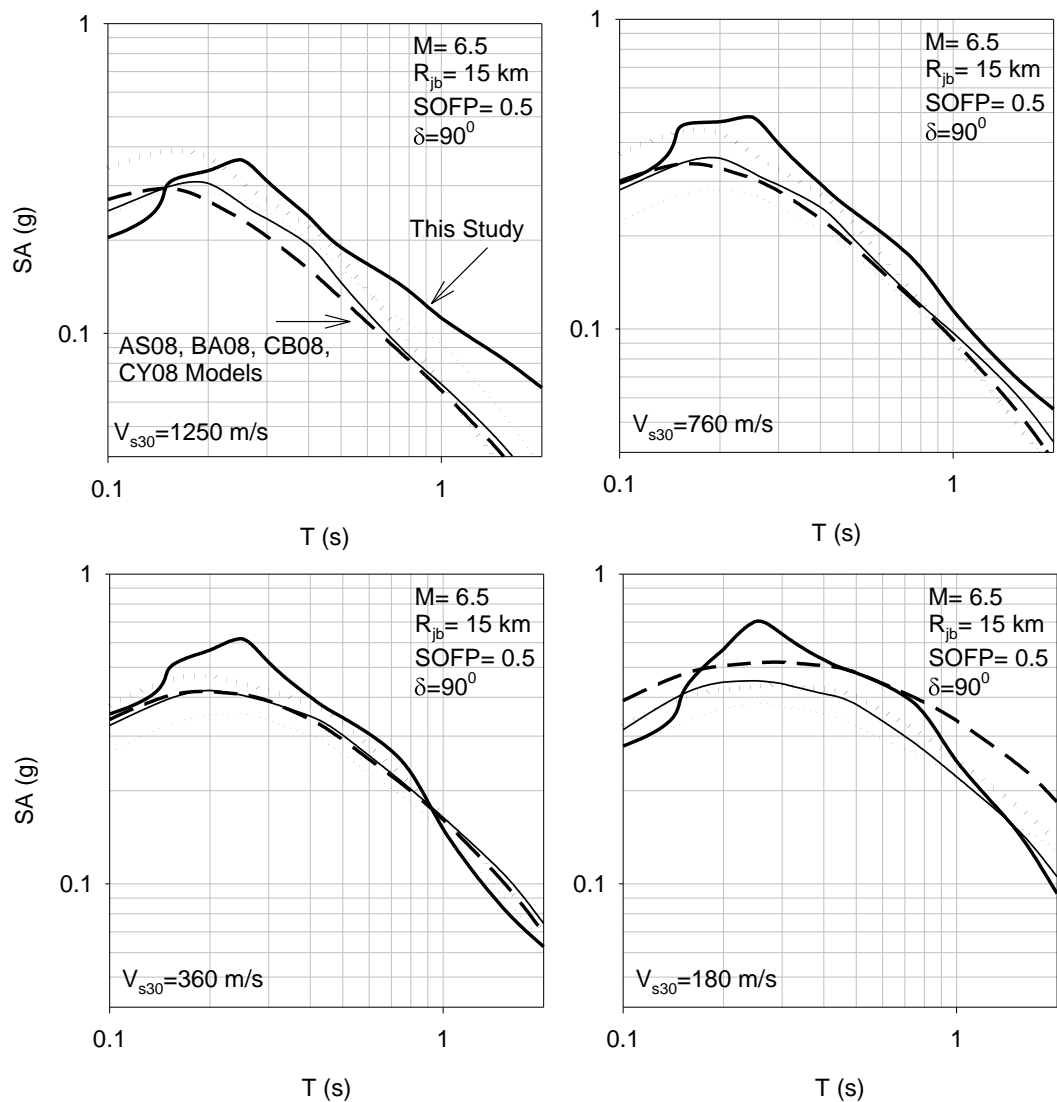


**Figure 4.3-23. Effect of shear wave velocity on spectral acceleration**

#### 4.3.3.4 Quantifying Model Uncertainty

This section discusses the results of quantifying and separating parameter uncertainty from total error term; and defining the remainder standard deviation expression as the model error term. The results are investigated for two typical magnitude scenarios,  $M=5$  and  $M=7$  (Figures 4.3-24 and 4.3-25). Solid thick series are the median curves for peak ground acceleration. Outermost boundary (dashed series)



presents the minus and plus 1 standard deviation bands for magnitudes  $M=5$  and  $M=7.5$ , prior to treatment with respect to inexact parameter estimates. For  $M=5$ , model error term for peak component was calculated to be  $\sigma_{\ln p_{ga, rock}} = 0.780$ , before any parameter uncertainty was removed. Corresponding value for  $M=7$  was 0.687. When only parameter uncertainty in natural log acceleration, due to the site response framework was applied, values dropped down to 0.704 and 0.624, respectively. Progressive effect of removing parameter uncertainties due to rotation, and moment magnitude and source to site distance was found to be relatively insignificant compared to the impact of site response procedures. However, impact of standard error term on the calculated hazard for ground motions of long return periods is crucial in design procedures, and this reduction is also worth value. Summary of the reduction in sigma term is presented in Table 4.3-5.

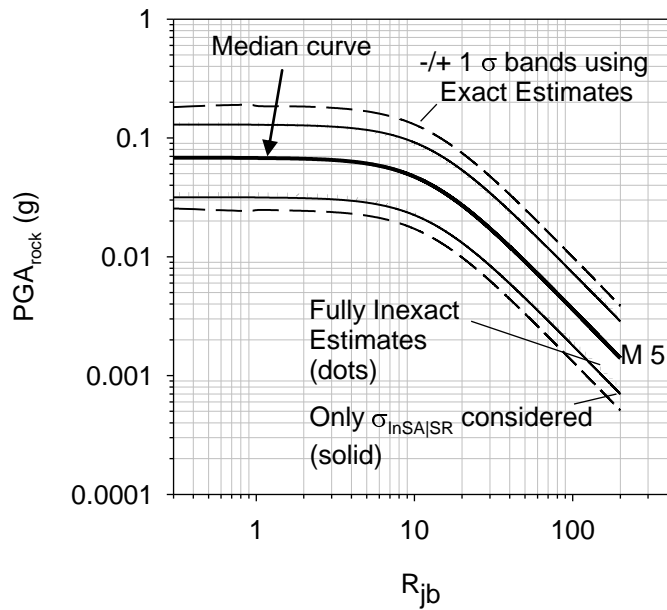


**Figure 4.3-24. Effect of removing parameter uncertainties (M=5)**

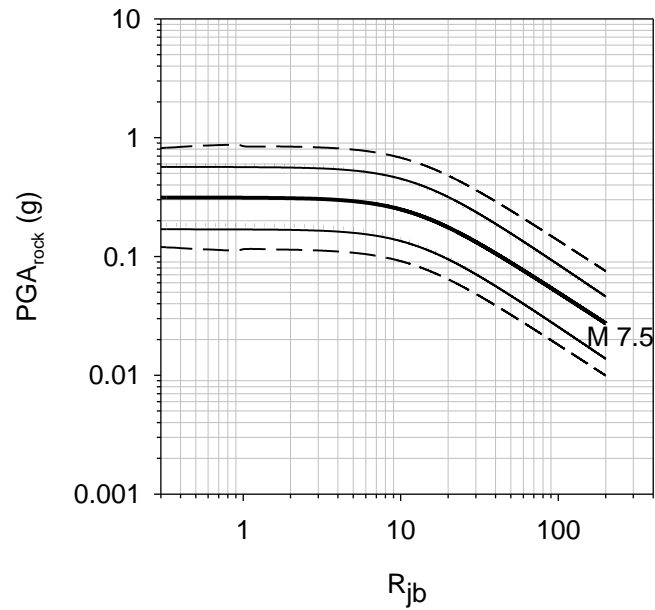


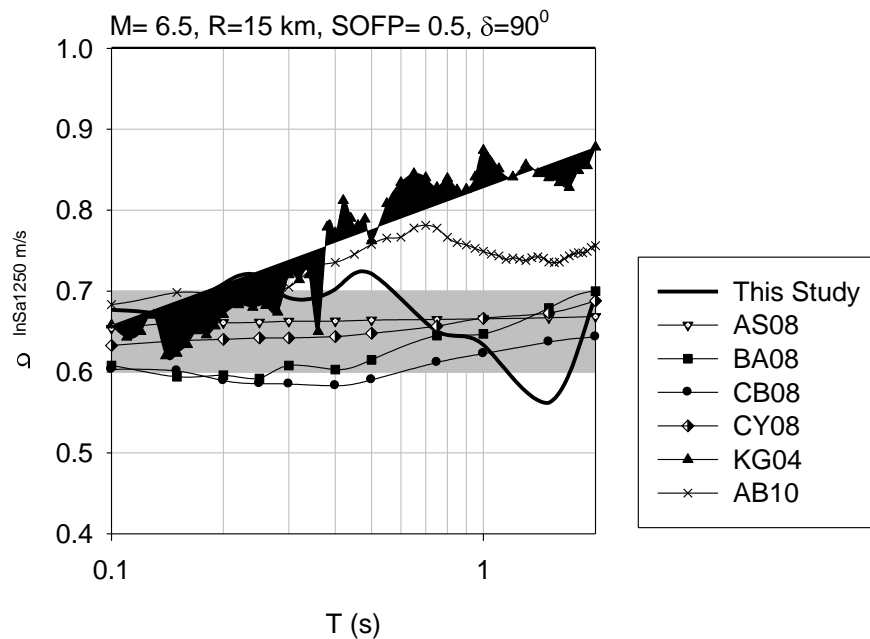
Figure 4.3-25. Effect of removing parameter uncertainties (M=7.5)

Table 4.3-5. Model error terms

$\sigma_{\ln SA_{rock}}$			
	Exact Estimate	Inexact Estimate (Only Site Response Framework)	Inexact Estimate (All)
M=5	0.780	0.704	0.677
M=7	0.687	0.624	0.597

Second part of this section is devoted to the presentation of results regarding the relative magnitudes of standard error terms of various recent ground motion prediction equations. For this purpose, standard error terms of AS08, BA08, CB08, CY08, KG04 and AB10 models go under investigation. Figure 4.3-26 presents a scenario for M 6.5; and the variation of  $\sigma_{\ln SA_{rock}}$  is plotted as a function of spectral period for a reference  $V_{s30}$  value of 1250 m/s. The 0.6-0.7 band is shaded in gray,

representing the general interval for most recent prediction equations. NGA models follow the 0.6-0.7 band, with CB08 equation exhibiting the lowest of them all. KG04 and AB10 models give comparable results with the global trend up to  $T=0.3$  s period, however yield increased estimates of sigma for longer periods of vibration. Model developed in this study is quite comparable with NGA models. Although bumps at several periods are observable, general trend lies as the approximate upper bound of the NGA models. Utilization of a relatively small dataset is concluded to be the main cause of sigma values being relatively larger than their global pairs. Given that parameter uncertainties were not quantified, the results would have been in the same order of other relationships developed using local datasets.



**Figure 4.3-26. Comparison of sigma values at rock sites (M=6.5)**

It has been previously proven that sigma value is dependent on the type of soil profile (Choi and Stewart, 2005). Given a stiff soil profile, surface response will include more uncertainty, especially in lower periods, compared to the variability of response from a softer profile. This is fairly reasonable, since part of the ground motion components are filtered out by the response of the soil column. Derivation in

Equation 4-22 enables this phenomenon to be valid in the ground motion prediction model. Figure 4.3-27 presents the variation of standard error for peak ground acceleration, as a function of  $V_{s30}$  value, for the M=6.5 scenario.

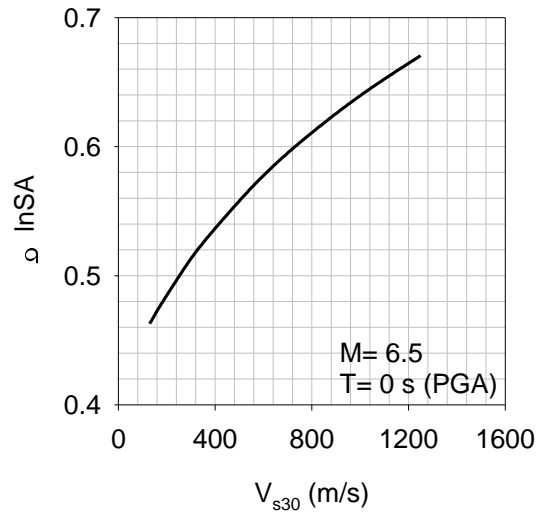


**Figure 4.3-27. Variation of sigma as a function of  $V_{s30}$  (M=6.5)**

Relation between rock sigma vs. soil sigma is perfectly demonstrated in Figure 4.3-28. Two reference  $V_{s30}$  values are chosen as 360 m/s and 1250 m/s. For the M=6.5 scenario, ratios between  $\sigma_{\ln SA_{rock}}$  values are compared. The ratio starts from 0.9 for shorter periods, and smoothly converges to unity for long periods, indicating there is simply no difference between sigma values predicted at different site classes. Results of the current study expose faster converge to unity, with a bump at T=1.5 s, which should be critically reviewed. As can be observed from Figure 4.3-28, Boore and Atkinson (2008) model does not make any differentiation between rock and soil sigmas.

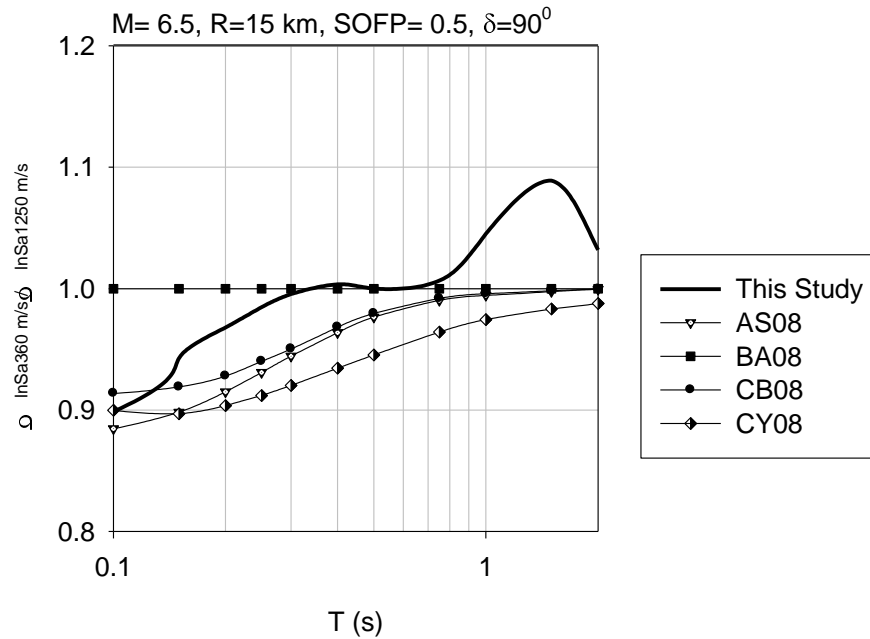


**Figure 4.3-28. Ratio of soil and rock sigma values modeled using different studies**

#### 4.3.3.5 Effect of Removing Sampling Bias

The last of the topics should be covered in presenting the results is the effect of applying the weighting scheme to remove sampling bias in the model. Since a significant amount of records are collected from the 1999 Kocaeli and Düzce events, and the gap between the  $M=6.5$  and  $M=7$  magnitude ranges point to uneven sampling in magnitude domain; a treatment was considered necessary.

Figure 4.3-29 shows the results of two cases, solid series represent weighted proposal of median  $pga_{rock}$  – distance curves, whereas dashed series are plotted for the unweighted case. It can be clearly observed that, both magnitude and distance scaling vary significantly for both cases. This result points to a noteworthy conclusion; stating that how a study samples data to be included in the optimization problem is partially responsible for the trend in results. Ground motion prediction equations developed using smaller number of data collected from various local event sets can

be easily expected to follow a different trend than global models. While regional tectonic characteristics may still play a role in model differentiations, additional comments on how the local data is treated statistically; should be a mandatory part of the solution. The procedure applied herein attempts to balance the contribution of every magnitude and distance bin equally, to come up with a model that is treated to provide the conditions of even sampling; even when databases of limited size are used.

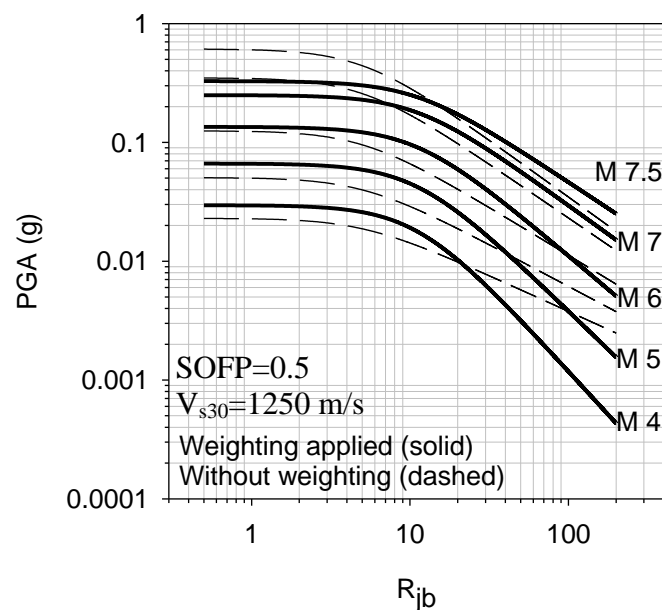


**Figure 4.3-29. Effect of weighting on magnitude – distance scaling**

Last, but not the least, effect of weighting procedure on the minimum magnitude threshold of compiled datasets is investigated. First graph in Figure 4.3-30 presents the median peak ground acceleration values as a function of source to site distance, for a suite of magnitudes. Solid lines are a recall from Figure 4.3-29, representing the original dataset of this study, without any weighting applied. Dashed series are obtained through clipping out the records from events having magnitudes lower than  $M=5$ . The impact is significant, as already been shown by other studies (Bommer et al., 2007; Akkar and Çağnan, 2010). Successful extrapolation down to  $M=4$  for the clipped dataset case is not expected, since the new sample space contains zero

records from M=4 range. Likewise, M=4 predictions from the distance independent (near-fault) decay curves are shifted from 0.02 g to 0.05 g (factor of 2.5). Similarly, M=5 predictions are shifted from 0.05 g to 0.07 g range (factor of 1.4). Predictions at higher magnitudes are relatively less affected.

For the case of weighted model development, the possible impact is re-investigated, and shown in the right side of Figure 4.3-30. Reference comparisons are made using the same distance range; however the ratio is invariant at all distance values. M=4 predictions increase from 0.029 g to 0.036 g (factor of 1.24), whereas M=5 predictions are shifted upwards by 9%. This result suggests that sampling problem can be partially eliminated using the proposed procedure.

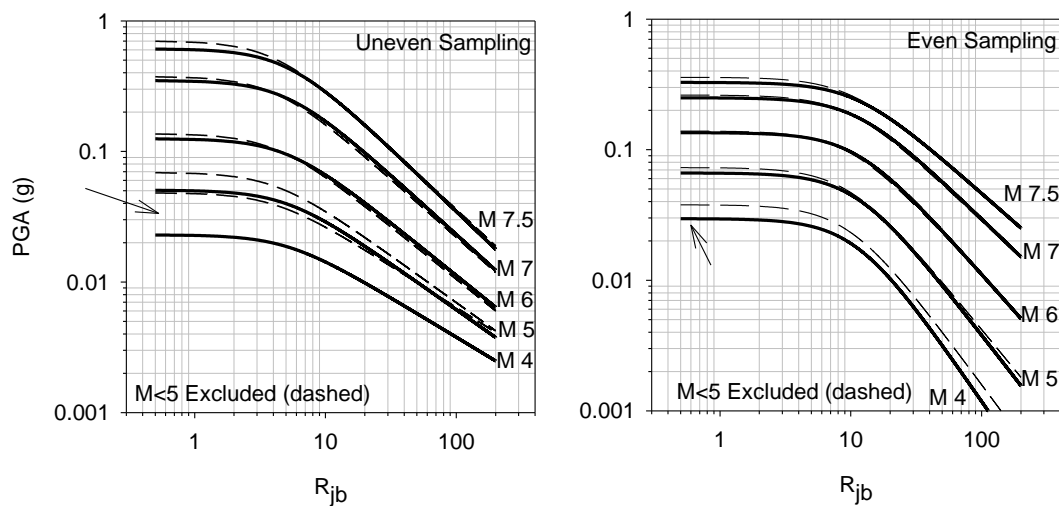


**Figure 4.3-30. Effect of weighting on ground motion intensity curves for different minimum magnitude thresholds used in datasets**

## **CHAPTER 5**

### **SEISMIC HAZARD ASSESSMENT SOFTWARE**

#### **5.1 PROBABILISTIC SEISMIC HAZARD ANALYSIS**

There exists a considerable amount of randomness in the source properties of the earthquake process; namely the magnitude, location and time of occurrence. Variation of ground motion intensity along the distance from source to the site of interest also contains randomness. The basic logic behind probabilistic seismic hazard assessment is assigning a probability distribution for every variable in the process which exhibit randomness. The probabilistic seismic hazard methodology, as described in Cornell (1968) integrates all the probabilities from each seismic source, to come up with the rate of exceedance for a selected value of ground motion intensity.

Probabilistic seismic hazard analysis has often been compared and contrasted with deterministic methods of hazard calculations. While the scope of this study is beyond rehashing this discussion; it is considered beneficial to briefly make a reasonable interpretation, in order to make a proper selection among the methods can be made on the basis of decision making purposes. McGuire (2001) discusses the role of probabilistic and deterministic issues in for decision making purposes in detail:



"Both probabilistic and deterministic methods have a role in seismic hazard and risk analyses performed for decision-making purposes. These two methods can complement one another to provide additional insights to the seismic hazard or risk problem. One method will have priority over the other; depending on how quantitative are the decisions to be made, depending on the seismic environment, and depending on the scope of the project (single site or a region). In many applications a recursive analysis, where deterministic interpretations are triggered by probabilistic results and vice versa, will give the greatest insight and allow the most informed decisions to be made" (McGuire, 2001). The procedure followed herein conforms to the fundamentals of probabilistic hazard analysis. Probabilistic seismic hazard analysis (PSHA) also serves as a valuable starting point for scenario based decision making purposes; due to its capability of presenting the deaggregated hazard. Figure 5.1-1 illustrates the basic steps involved in PSHA.

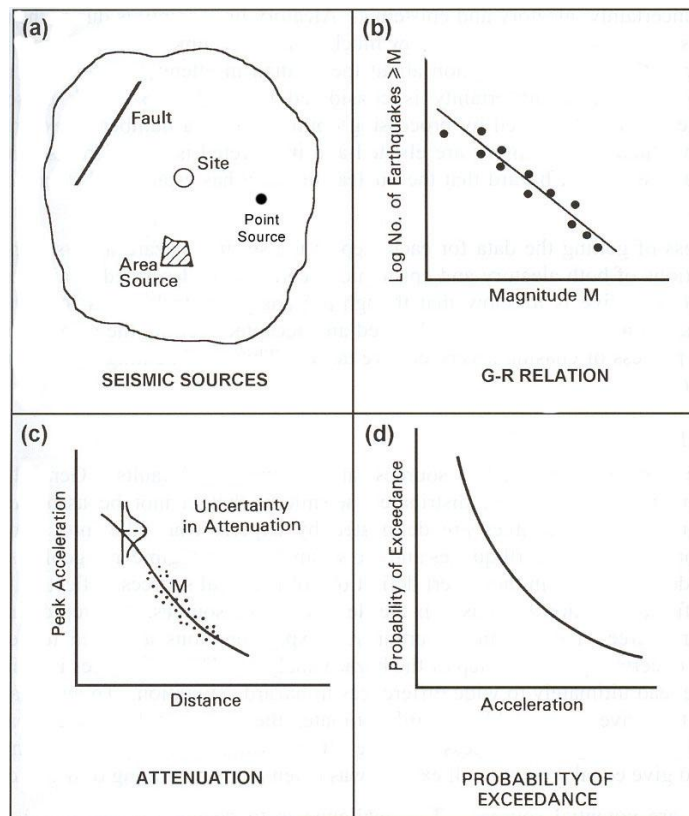


**Figure 5.1-1. Basic steps of PSHA (from Finn et al., 2004)**

### 5.1.1 Mathematical Formulation of PSHA

As briefly stated in the previous section, the basic methodology of PSHA involves calculating the frequency of specified level of ground motion (either peak or spectral values) will be exceeded at the location of interest. In a PSHA, the annual rate of events (annual rate of exceedance),  $v$ , that produces a ground motion parameter;  $Sa$  that exceeds a specified level,  $z$ , at the site is calculated. The inverse of  $v$  corresponds to the definition of return period. The calculation of the annual frequency of exceedance “ $v$ ” involves, i) the rate of earthquake of various magnitudes, ii) rupture dimensions of earthquakes, iii) the location of the earthquakes relative to the site, and iv) attenuation of the ground motion from the earthquake rupture to the site. The simplest form of hazard integral can be written for a point source at fixed depth:

$$v_i(Sa > z) = N_i(M_{min}) \int_0^\infty \int_{M_{min}}^{M_{max}} P_i(Sa > z|m, r) f_i(m) f_i(r) dm dr \quad (5-1)$$

Equation 5-1 yields the annual rate of exceedance for a single seismic source.  $P_i$  is the probability of exceedance of the specified ground motion level for the given magnitude and distance,  $f_i(m)$  and  $f_i(r)$  are the probability density functions for the magnitude and distance for that source. The integration is carried out for every possible magnitude value between  $M_{min}$  and  $M_{max}$ , and source to site distance values corresponding to the magnitude of interest.  $N_i(M_{min})$  is the annual rate of earthquakes having magnitudes greater than or equal to  $M_{min}$ . In order to explicitly demonstrate the presence of variability of the ground motion intensity parameter,  $P_i$  can be expanded as:

$$P(Sa > z|m, r) = \int_z^\infty f_{sa}(Sa, m, r) dSa \quad (5-2)$$

In Equation 5-2,  $f_{sa}$  is the probability density function of the ground motion model (GMPE). Ground motion parameters are distributed log-normally, and taking the

logarithms before utilizing the parameter in any calculation in which the normal distribution will be used provides extreme comfort. Equation 5-2 can be rewritten in the form of number of standard deviations below or above the median:

$$P(Sa > z|m, r) = \int_{\varepsilon^*}^{\infty} f_{\varepsilon}(\varepsilon) d\varepsilon \quad (5-3)$$

In Equation 5-3,  $\varepsilon$  is the number of standard deviations above or below the median ground motion,  $f_{\varepsilon}(\varepsilon)$  is the probability density function for  $\varepsilon$ ; which is essentially the standard normal distribution,  $\varepsilon^*$  is the number of standard deviation of the ground motion that yields the ground motion level  $z$ , for a given magnitude and distance (Equation 5-4). In Equation 5-4,  $\overline{Sa}$  is the median estimate of the ground motion model for a given magnitude, distance and site condition. Standard deviation term for the ground motion model is assumed to be independent of the predictive parameters for demonstration purposes (Abrahamson, 2000).

$$\varepsilon^*(M, r, z) = \frac{\ln(z) - \ln(\overline{Sa})}{\sigma(\overline{Sa})} \quad (5-4)$$

Thus, it becomes fairly self explanatory to express Equation 5-1 in the form of Equation 5-5 using the complementary standard normal distribution, which explicitly exposes the variability of the ground motion term (Abrahamson, 2000).

$$v_i(Sa > z) = N_i(M_{min}) \int_{r=0}^{\infty} \int_{M=M_{min}}^{M_{max}} \int_{\varepsilon=\varepsilon_{min}}^{\varepsilon_{max}} P_i(Sa > z|m, r, \varepsilon) f_i(m) f_i(r) f_{\varepsilon}(\varepsilon) dm dr d\varepsilon \quad (5-5)$$

Abrahamson (2000) describes the final form for a point source integral as follows: “ $P(Sa > z|m, r, \varepsilon)$  is the probability that the ground motion exceeds the test level  $z$  for magnitude  $m$ , distance  $r$ , and number of standard deviations,  $\varepsilon$ . Since the magnitude, distance and number of standard deviations fully describes the ground motion,  $P(Sa > z|m, r, \varepsilon)$  is either 0 or 1. The formulation presented herein is different from the

standard way of writing the hazard in that it explicitly denotes the variability of the ground motion.”

While this concludes the problem for area sources, in which the hypocentral locations of ruptures are located uniformly over the source boundaries; a requirement for modeling additional levels of variability emerges for linear seismic sources. For the simplest case of linear sources, additional term for rupture length, which is also subject to randomness, should be modeled. For linear sources, source to site distance becomes a function of location of rupture along the fault and magnitude of rupture (Equation 5-6).

$$v_i(Sa > z) = N_i(M_{min}) \int_{RL=0}^{RL_{max}} \int_{E_x=0}^1 \int_{m=M_{min}}^{M_{max}} \int_{\varepsilon=\varepsilon_{min}}^{\varepsilon_{max}} f_{RL_i}(m, RL) f_{E_x_i}(m, E_x) f_{m_i}(m) f_{\varepsilon}(\varepsilon) P(Sa > z | m, r(RL, E_x), \varepsilon) dRL dE_x dm d\varepsilon \quad (5-6)$$

In Equation 5-6, RL is the rupture length, and  $E_x$  is the location of rupture along the fault length, “0” and “1” representing both ends of the fault. Unlike area source idealization, site to source distance is now a function of rupture dimension and location of rupture along the fault. More complicated forms of the hazard integral are possible by introducing additional variables to be randomized.

Evolution of Equation 5-1 to 5-5 and 5-6 carries an objective for handling the M,R, $\varepsilon$  scenarios in a less error prone fashion. It enables the tedious “book keeping” process to be made in a traceable manner, thus enabling easier computer coding. Such a transformation becomes essential in deaggregating hazard.

For multiple seismic sources, the total annual rate of events with ground motions that exceed “z” at the site is just the sum of the annual rate of events from the individual sources, assuming that the sources are independent (Equation 5-7).

$$v(Sa > z) = \sum_{i=1}^{N_{source}} v_i(Sa > z) \quad (5-7)$$

Having obtained the annual rate of events, the simplest method of conversion to a probability of occurrence in a given time  $t$ , is by using the Poisson process. Discussion of Poisson assumption and time dependent models are given in literature, and will not be repeated within this text.

A typical hazard curve as shown in Figure 5.1-1 contains contributions from all of the sources and  $M, R, \varepsilon$  scenarios for a given ground motion level. For decision making purposes as summarized in McGuire (2001), it becomes essential to distinguish the controlling (dominant) scenarios within hazard and proceed with a simpler deterministic model, often used for selecting and matching time histories for time domain analyses; which utilizes results from PSHA. Deaggregation of hazard is named after Bazzurro and Cornell (1999), which simply involves breaking up hazard back to its contributing scenario pieces. One of the most basic forms of hazard deaggregation is the process implemented on magnitude ( $M$ ), distance ( $R$ ) and epsilon ( $\varepsilon$ ). Equation 5-8 formulates the expression for hazard deaggregation (Abrahamson, 2000):

$$DH(Sa > z, M_1 < M < M_2, R_1 < R < R_2, \varepsilon_1 < \varepsilon < \varepsilon_2) = \frac{\sum_{i=1}^{n_{sources}} N_i(M_{min}) \int_{r=R_1}^{R_2} \int_{m=M_1}^{M_2} \int_{\varepsilon=\varepsilon_1}^{\varepsilon_2} f_{m_i}(m) f_{r_i}(r) f_{\varepsilon}(\varepsilon) P(Sa > z | m, r, \varepsilon) dr dm d\varepsilon}{v(Sa > z)} \quad (5-8)$$

## 5.2 PSHA SOFTWARE FOR HAZARD CALCULATIONS

Calculating probabilistic seismic hazard at a site or region requires the contribution of excessive number of scenarios for every seismic source. Making use of spreadsheet calculations becomes insufficient in managing the vast amount of data; utilizing custom software for the specific purpose becomes necessary. Within this

section, a brief review of existing software is disclosed, and the guidelines for a custom authored PSHA calculation tool are introduced.

### **5.2.1 Existing PSHA Software and Cause for Authoring a New Computer Code**

Evolution of probabilistic seismic hazard software for producing site specific studies and regional hazard maps dates back to mid 1980's. One of the first widely known versions of software that was used in developing the pre-1996 hazard maps for United States is SEISRISK III (Bender and Perkins, 1987). Geographical application range for the hazard maps produced using SEISRISK III was not limited to North America; it actually extended to Italy, Iran, Turkey, and Mediterranean countries. The software basically a FORTRAN based console application requiring an input file containing all the information for fault definitions, geometrical and activity parameters, and an input table for the ground motion model to be interpolated upon during calculations. Aleatory variability term for the ground motion model had to be independent of any of the predictive parameters such as magnitude and site conditions. Faults were modeled as linear sources, and area sources were modeled as polygons; with the option to model earthquake location variability within the area source as bi dimensional normal distribution. Magnitude and distance based deaggregation could not be acquired from the outputs of the program; however it was possible to extract source based contribution to total hazard. USGS (United States Geological Survey) has terminated the development of the SEISRISK series and proceeded with newer versions of hazard software (Frankel et al., 2002) executing in a similar manner for the production of 1996, 2002 and 2008 national hazard maps.

Another notable example for hazard software can be named as CRISIS (Ordaz, 1999) developed at UNAM (Universidad Nacional Autónoma de México); however perhaps the most widely known PSHA software in the commercial market is EZ-

FRISK (Risk Engineering, 2007) which fulfills the fundamental demand from a modern PSHA through an graphical user interface.

Within the confines of this study, developing a custom tool for conducting PSHA was targeted. Legacy software such as the well known SEISRISK III is far from meeting the standards of a modern PSHA, and the learning curve for modifying the original source code to meet today's standards was considered to be extremely inefficient. Being aware of the fact that commercial PSHA software is also unsuitable for academic purposes, from the point that modification or extension of the code is impossible; an attempt was made on developing a customized tool enabling total control over the algorithm. Details of the computer code developed the national seismic hazard maps for Turkey is presented in the following section.

### **5.2.2 Capabilities of the Custom PSHA Code**

The computer code for conducting PSHA is developed using MATLAB. It contains a series of scripts lacking a graphical user interface. Main capabilities of the code are as follows:

- i) Seismic source geometry can be characterized by either polylines for linear faults, or polygons for area sources. Smoothing of rupture location boundaries as documented in SEISRISK III (Bender and Perkins, 1987) is not applied herein.
- ii) Input geometry and source characteristics are directly read from an ESRI shapefile having a ".shp" file extension. The user graphically prepares the input geometry visually; however must use a GIS software.
- iii) Each source is assigned a minimum magnitude,  $M_{\min}$ , a maximum magnitude,  $M_{\max}$ , Richter-Gutenberg parameters "a" and "b" for calculating the activity and magnitude distribution of future earthquakes.
- iv) The program is capable of handling multiple earthquake sources.

- v) The program truncates the probability density functions for magnitude-rupture dimension relationships and ground motion prediction models. Default values of truncation for rupture dimension scaling relationships are  $-2\sigma$  and  $+2\sigma$  at both ends. Default value of truncation for the ground motion prediction model is  $-3\sigma$  and  $+3\sigma$  at both ends. Bommer et al. (2004) and Bommer and Abrahamson (2006) have demonstrated that there is strong empirical evidence that truncating ground motion models below 3 standard deviations above the median will be unconservative. Similarly, truncating above 4 standard deviation values above the median value will have no significant effect on the hazard values for long return periods. An illustration for truncation of the normal distribution is presented in Figure 5.2-1.

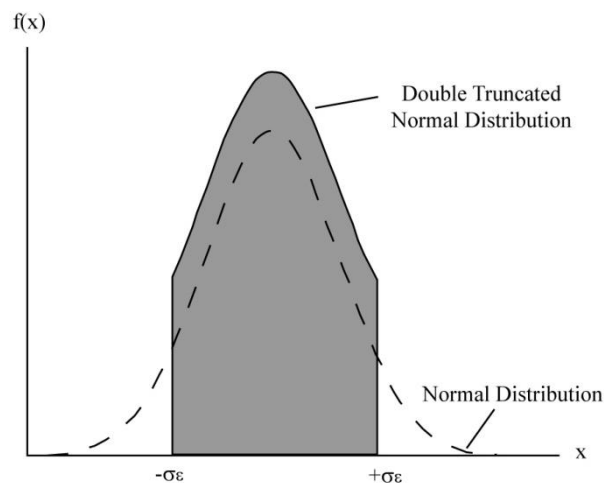


**Figure 5.2-1. Illustration of a normally distributed continuous variable truncated at both ends**

- vi) The computer code calculates two types of hazard integrals. Area sources act as point sources and comply with Equation 5-5. Linear sources are characterized by the hazard integral expressed in Equation 5-6.
- vii) Sources having closest source to site distances, that is larger than the specified threshold value are simply discarded from the calculations,



since their contribution to the hazard is negligible. Default value for the threshold is chosen as 250 km.

- viii) Time projection of hazard is carried out using the simple Poisson assumption.
- ix) The program generates the total hazard curve for a site, and interpolates on the annual hazard curve for calculating the spectral intensity values corresponding to return periods of 145 years, 475 years, 1000 years and 2500 years. These values roughly correspond to 50% probability of exceedance in 100 years, 10% probability of exceedance in 475 years, 5% probability of exceedance in 50 years, and 2% probability of exceedance in 50 years.
- x) The code deaggregates hazard as in compliance with the principles expressed in Equation 5-8, using pre-defined magnitude, distance and epsilon bins.

### **5.2.3 Rules for Locating Ruptures and Subdivision of Area Sources**

Rules for locating ruptures along linear faults are based on a few simple assumptions. One of the main rules is that the rupture length for a specific scenario cannot be greater than the fault length itself. If such a condition exists, the rupture length is set equal to the fault length, and the probability distribution function for the rupture length is truncated. Another rule is that the rupture cannot extend beyond the boundaries of faults.

#### *5.2.3.1 Locating Ruptures Along Linear Faults*

Given a rupture length for a linear fault having a definite length, the rupture location is propagated along the fault according to the following principles (Figure 5.2-2). Figure 5.2-2a shows a basic polyline representation of a fictitious fault. Node numbers and encircled segment numbers are also indicated. The algorithm behind

generating rupture centers along the fault for a given rupture length ensures that the rupture geometry cannot extend beyond the fault geometry at both ends. This is only possible when the first and last center points of the rupture are inset from each end of the fault by a distance of  $RL/2$  (Figure 5.2-2b). Note that  $RL$  (Rupture Length) is a function of magnitude and subject to randomness of both magnitude and magnitude-rupture dimension relationship within the hazard integral.

The number of centers of rupture lengths along the fault is optimized using a simple relationship which balances computer runtime, and maintains the continuity of the process by generating adequate number of scenarios such that the hazard is correctly characterized for near-fault sites without excessive fragments in the hazard curve.

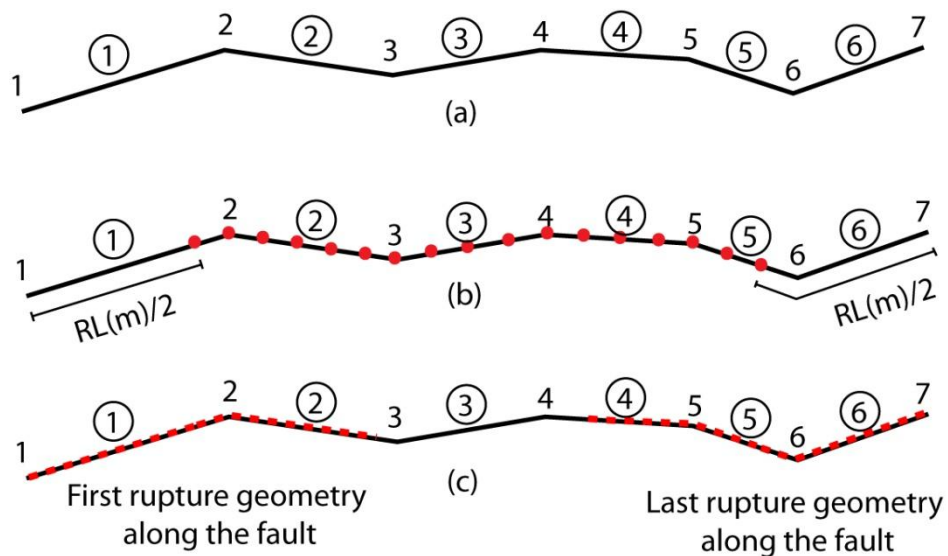


**Figure 5.2-2. Simulation of rupture along a fault: a) polyline representation of the fault, b) Location of discrete rupture centers along the fault for given earthquake magnitude, c) Sketch of first and last ruptures along the fault**

Figure 5.2-3 shows the variation of number of rupture points generated along each fault segment; which constitutes a part of the whole fault constrained by the geometric definition and shown by encircled numbers in Figure 5.2-2, as a function of segment length. The corresponding value is rounded to the nearest integer towards plus infinity. All of the exceptions in the algorithm such as the coincidence of rupture locations with nodes are successfully handled within the code.

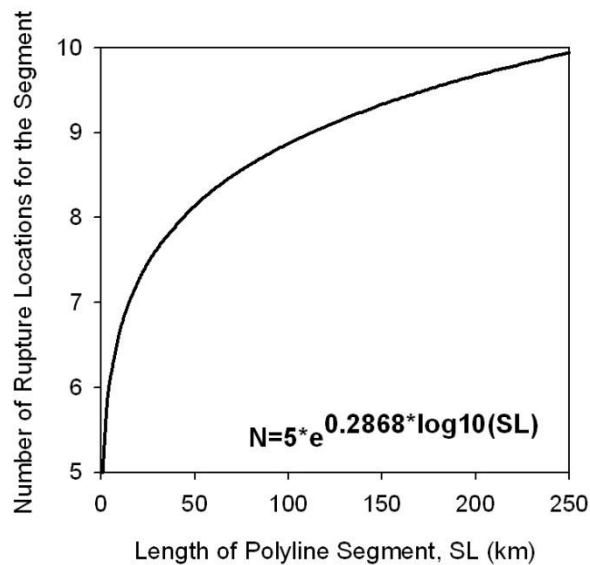


**Figure 5.2-3. Variation of number of rupture location simulations as a function of segment length**

#### 5.2.3.2 Locating Ruptures for Area Sources

As long as the area sources are defined using closed polygons, the software is capable of subdividing the area source into smaller polygons. Providing the node coordinates of any closed polygon is sufficient for generating the geometry. The algorithm functions by meshing the polygon into triangular elements with an optimized level of fineness. Another parameter for area source definition is the depth of the source. The program uses a constant value of depth for each source, thus randomness in focal depth is not considered. Figure 5.2-4 illustrates a fictitious area

source with subdivision applied. For every triangular element “i” within the source, centroid coordinates ( $x_i, y_i, \text{depth}$ ) are calculated and the distribution of source to site distance for the area source is calculated using the current set of point to point distances. It should be once again noted that the current state of practice interprets area sources as point sources.

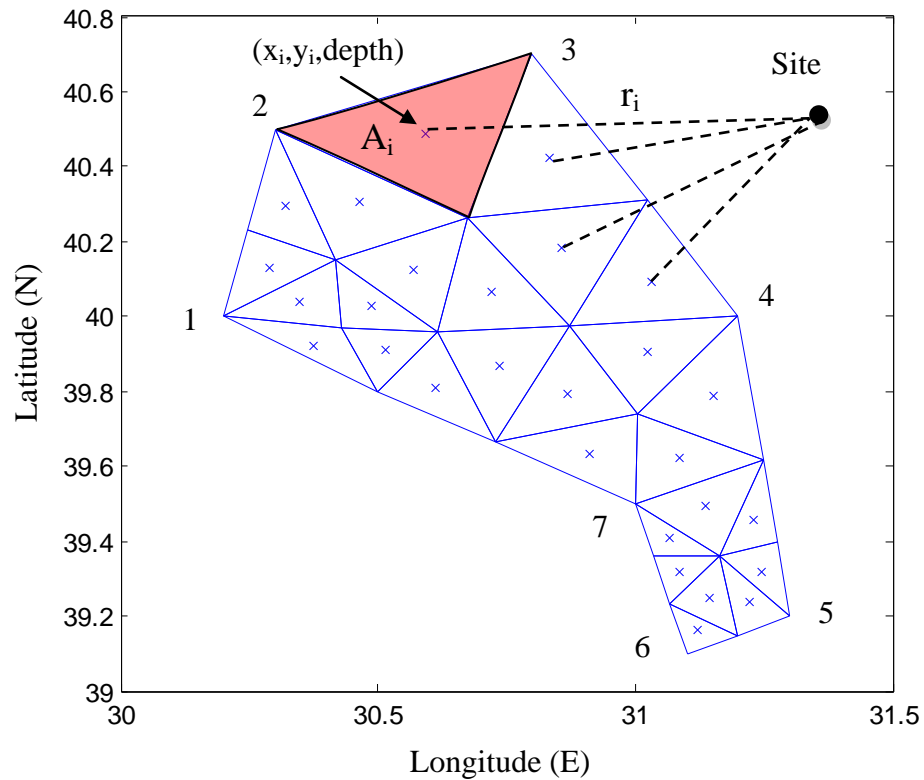


**Figure 5.2-4. Illustration of area source geometry and subdivision of polygon geometry**

For an area source, probability of rupture location being on the  $i^{\text{th}}$  element is a proportion of the area of element “i”, to the total area of the polygon (Equation 5-9).

$$f_{r,i}(r) = \frac{A_i}{\sum_{j=1}^{n_{\text{subdiv}}} A_j} \quad (5-9)$$

### 5.2.4 Flow of the Computer Code

The PSHA code presented herein is prepared from scratch, and makes use of many built in functions of MATLAB. Nevertheless, a suite of pre-processing and post-processing commands along with typical steps of a PSHA flow are implemented in addition to the main functions. This section summarizes the flowchart, and gives a brief description of each major unit (Figure 5.2-5).

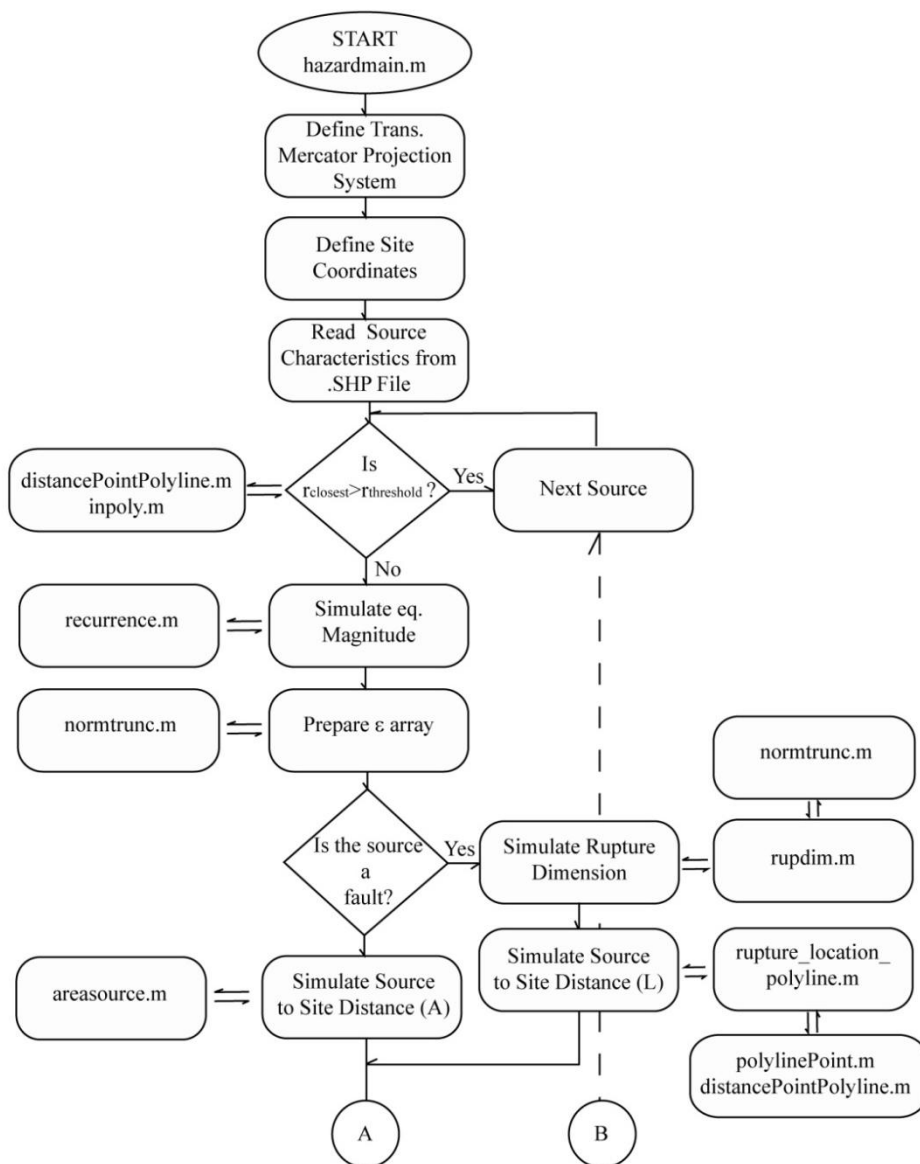
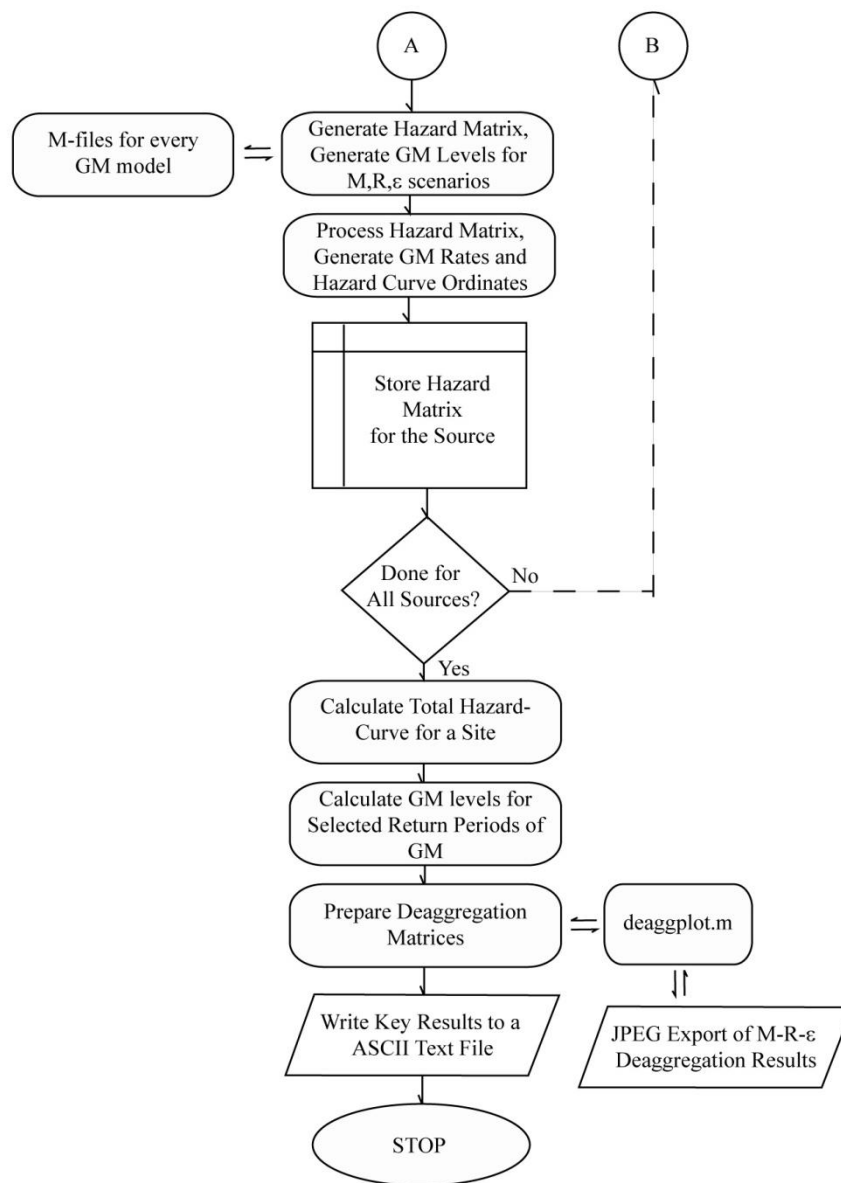


Figure 5.2-5. Simplified flowchart of PSHA software



**Figure 5.2-5. (continued) Simplified flowchart of PSHA software**

#### 5.2.4.1 Description of “hazardmain.m”

The main routine for executing the probabilistic seismic hazard code is named as “hazardmain.m”. The routine starts with defining a new projection system for converting geographical coordinates to cartesian coordinates. The projection system chosen is the Transverse Mercator, and the center meridian is assigned in conjunction

with the extent which all of the seismic sources cover spatially. A verification study has proved that the absolute source to site distance error was in the order of 1% when spherical distance definition was used for reference comparison. The routine progresses with defining the site coordinate for PSHA calculations. All coordinates are given as decimal degrees.

Next step in the procedure is reading source characteristics from an ESRI compliant external “shapefile” having an extension of “.shp”. A shapefile, by definition contains the geometry properties of faults and area sources; and any other attribute which the attribute table contains. Attributes include, but are not limited to, the minimum and maximum earthquake magnitudes for the source, recurrence parameters, style of faulting, fault name, etc. A shapefile is prepared using a GIS software compatible with the file format mentioned, and almost all of the commercial software packages are capable of reading and converting shapefiles. MATLAB is also capable of calling a shapefile within the command prompt. Utilizing the property mentioned, “hazardmain.m” reads the shapefile and automatically processes the properties of seismic sources. Any modification on the source characteristics are executed on the GIS software, while running the hazard analysis.

The next step involves determining whether the closest distance from a seismic source is smaller than the threshold value defined within the program. That is, if a seismic source is further away from the defined threshold distance, it will have negligible contribution on the ground motion levels, thus can be comfortably excluded from the analysis. The default value is defined as 250 km.

Routine “hazardmain.m” proceeds with preparing the earthquake magnitude array using the source characteristics. Similarly, it generates the epsilon array, and calls the rupture dimension generation subroutine if the source is a linearly characterized fault. For area sources, this step is skipped. Next step involves the source to site distance computations. For linear faults, “hazardmain.m” calls “rupture\_location\_polyline.m”

and simulates rupture location uncertainty as explained in Chapter 5.2.3.1. For area sources, polygon geometry is subdivided using “areasource.m” as explained in Chapter 5.2.3.2.

The main module continues with generating the hazard matrix by calling the selected ground motion prediction model. This step is mandatory for generating ground motion occurrence rates and hazard curve ordinates. Sorting columns by attributes, cumulative summation are among the routine tasks carried out. Hazard results and whole history is stored in a cell variable for further access.

Once the series of computations are carried out for all seismic sources, total hazard curve for the site of interest is calculated by summing the hazard curves. This requires an intermediate step; even resampling of ground motion intensity levels for addition of hazard curves.

Another step in processing is the interpolation on the total hazard curve for obtaining the ground motion intensity levels corresponding to the desired probability of occurrences during a specified time interval, in compliance with Poisson assumption. (Figure 5.1-1d). By default, ground motion intensity values corresponding to 145 year, 475 year, 1000 year and 2500 year ground motions are extracted from the hazard curve.

The last step is conducting the deaggregation process with pre-determined magnitude, distance and epsilon bins; for each of the ground motion intensity levels mentioned in the previous paragraph. Deaggregation plots are printed to a JPEG image file and stored on the disk drive. Key series of variables, such as hazard curve ordinates and design ground motion values are also saved on an ASCII text file.



#### *5.2.4.2 Description of Remaining Functions*

Routine “distancePointPolyline.m” computes the closest distance between a polyline and a point. The function is taken from a set of routines developed for two dimensional geometry computations in MATLAB environment (Legland, 2009).

Routine “inpoly.m” checks whether a given point is enclosed within the boundaries of a polygon. A dummy variable controls the output. The function is referenced to a set of utilities developed by Egwirda (2007).

Function “recurrence.m” produces the probability density function for earthquake magnitude. Given the slope “b” of the magnitude-recurrence relationship and the extreme values of magnitude truncation for the seismic source; the routine produces the probability density function  $f_m(m)$ . Step size for subdivision between  $M_{\min}$  and  $M_{\max}$  is a variable; the program can handle uneven subdivisions using arbitrarily assigned step sizes.

Routine “normtrunc.m” prepares a vector representing the probability density function of the standard normal distribution having median value of “0” and a variance of “1”; discretized and truncated at any desired epsilon value.

Function “rupdim.m” generates an array of rupture dimensions for a given earthquake magnitude; distributed normally with a definite variance representing aleatory variability of the magnitude-rupture dimension scaling relationship. Truncation of the distribution is also possible, and this property is achieved by calling “normtrunc.m”.

For area source characterization, “areasource.m” subdivides the polygon representing the seismic source into a mesh with triangular elements. Function “areasource.m” utilizes Egwirda’s (2009) product MESH-2D for mesh generation.

Function having the most complicated algorithm within the context of exception handling was “rupture\_location\_polyline.m”. This function carries out all the tasks defined in Chapter 5.2.3.1.

Function “polylinePoint.m” is called from “rupture\_location\_polyline.m” and is responsible for generating given number of points on a segment of a polyline. This function is part of the suite written by Legland (2009).

Last but not the least, “deaggplot.m” takes the triple deaggregation matrix on magnitude, distance and epsilon; and prepares a 3-D bar plot with vertical color coding parameterized on epsilon bins. A sample output is shown in Figure 5.2-6. Corresponding hazard curve is presented in Figure 5.2-7.

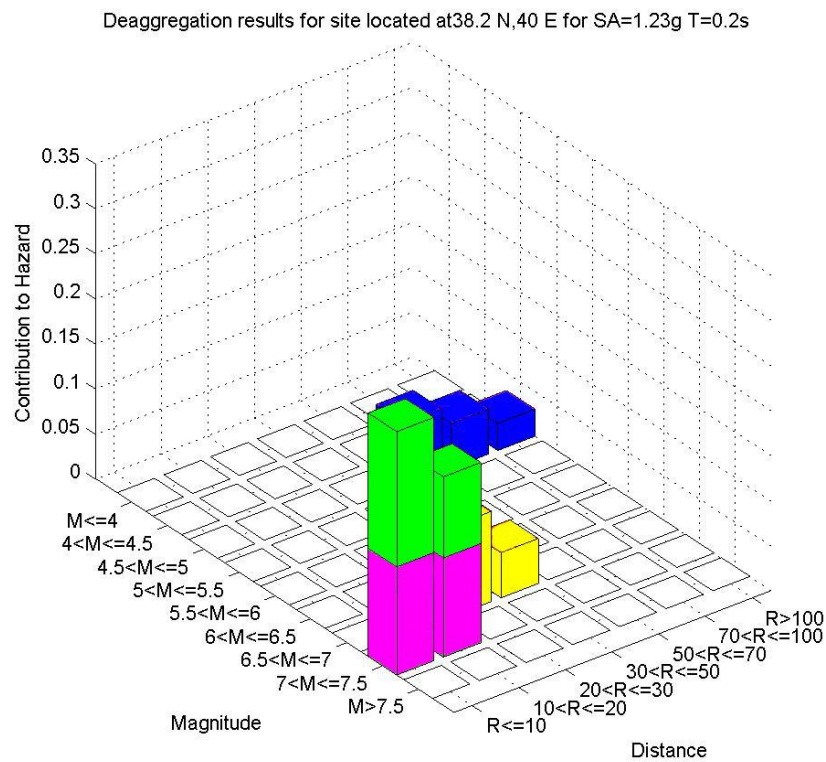


**Figure 5.2-6. Sample triple deaggregation output of PSHA software**

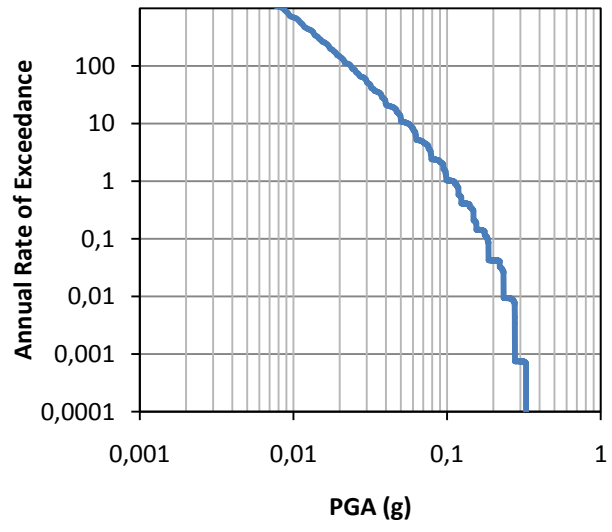


**Figure 5.2-7. Sample hazard curve for PGA**

## **CHAPTER 6**

### **SUMMARY AND CONCLUSION**

The purpose of this thesis was to develop robust and defensible tools for some of the components of seismic hazard analysis framework. These components include magnitude – rupture dimension relationships, source characterization, and ground motion intensity prediction with a particular emphasis on quantifying parameter uncertainty, removing sampling bias and modeling ground response at a higher level of detail. Additional study included the development of custom hazard software that enables implementation of the abovementioned components in practice.

Specifically, Chapter 2 was devoted to addressing the shortcomings of the magnitude – rupture dimension relationships available in literature; and a series of efforts made to improve the existing relations. First stage of the attempt included the compilation of an expanded global dataset from shallow crustal zones, including more events from higher magnitude earthquakes. Initial examination of the distribution pointed out a trend towards decreasing variability in rupture dimensions as a function of increasing earthquake magnitude; and this trend was modeled using magnitude dependent standard error terms in the log-linear rupture dimension relationships. Three separate sets of equations were derived.

The first set of equations applied a similar methodology as in the well known Wells and Coppersmith (1994) relationships; defining a log-linear relationship between magnitude and rupture dimensions. However, one of the main differences was the application of style of faulting term; which avoided the splitting of datasets into smaller ones that can be exposed to statistical uncertainty. The other, was the implementation of magnitude dependent sigma term. Reduction in sigma was favored for high magnitudes since its relevant impact on hazard estimates for long return period ground motion intensities is known to be significant.

Nevertheless, in all of the three independently optimized models for rupture area, rupture length, and rupture width; geometrical compatibility was not satisfied. In hazard studies, most common practice in simulating rupture dimensions, which eventually affects source to site distance calculations; is the assumption of rectangular rupture geometry. Given independent relationships of rupture length and width, the product of those dimensions for a specific magnitude and style of faulting will not satisfy the results of rupture area predicted using an independently optimized procedure, even when the dataset for all three is kept the same. A solution to this problem was achieved using two alternative procedures. First of the relationships included maximizing the joint probability of rupture area parameter and rupture width, given that rupture area. The second approach implemented the concept of aspect ratio modeling and L-scaling. This concept is applicable under the assumption that once the maximum rupture width restricted by crustal structure is reached; rupture dimension scaling depends on the length of rupture. This approach includes the implementation of fault dip angles to calculate the magnitude dependent limits for reaching the highest possible rupture width.

Next step in the study focused on developing a systematic framework for source characterization of active faults in Anatolia. The first step in this stage was to identify the active faults, and develop a systematic simplification method to idealize seismogenic sources. The philosophy behind the simplification was that, when

sufficient data could not be collected to assess basic engineering parameters for a fault segment, or macroseismic activity during the last century exhibited a non-existent to extremely low pattern; faults were idealized. Idealization preferences are discussed in detail within the main text body. Geometric characterization, and segmentation concept directly affects the rupture location simulations and maximum magnitudes assigned to a source. Special attention was given during characterization process, evaluating historical seismicity and recurrence patterns. The resulting fault characterization is intended for engineering use, and does not stand for the complete active fault map of Anatolia.

While calculating the recurrence parameters for defined sources, location uncertainty of epicenter solutions were evaluated and implemented systematically. Factors such as catalog completeness were taken into account. The resulting product is a base input for seismic hazard studies.

Third major step of the study was the development of a new ground motion prediction equation, using strong ground motion data compiled from earthquakes in Turkey. An initial screening procedure was followed to select the candidate records to be included in the strong ground motion dataset. Standard signal processing procedures were applied to process the collected raw waveforms. Peak and 5% damped elastic spectral components of acceleration were calculated, for all major definitions of horizontal component of ground motion. Relationships between the measures of horizontal ground motion were found to be in agreement with similar studies conducted on global datasets. For definitions of horizontal ground motion involving randomly oriented geometric means, uncertainty in accelerations due to rotation were evaluated. Choice of horizontal ground motion definition should be a function of the requirements of the specific design task and structure under consideration.

Earthquake magnitudes for the compiled dataset were converted to moment magnitude scale. This study also includes the quantification of magnitude uncertainty, calculated for events from the currently compiled dataset. While the magnitude of standard error is comparable with the findings in literature, values from this study does not contain additional uncertainties in moment magnitude due to moment tensor solutions.

Next step in ground motion prediction equations is the computation of source to site distances using simulations. Simulations include variability in rupture dimensions, focal depth and position of focal point on the rupture plane. While a separate set of model is developed for predicting the source to site dimensions using parameters such as magnitude and dip angle; range of variability inherent in the model restricts its applicability at high earthquake magnitudes. Thus, the conclusion is based on the preference of performing specific simulations for each event and site pair; since the only source of uncertainty is the variability of rupture dimensions and location of focal point on the rupture plane.

Following source to site distance simulations, special attention was given to modeling local site effects. Stages of the framework constituted of classification of sites; considering secondary options where necessary, generating multiple generic site profiles for each soil class, conducting 1-D equivalent linear site response analyses on generic sites; and finally defining the acceleration intensity at the reference rock level. Results of ground response analyses were used to develop an amplification model as a continuous function of peak ground acceleration on rock, and shear wave velocity of the upper 30 m of the profile.

A new ground motion prediction model was proposed, using the strong ground motion records from earthquakes in Anatolia. Motivated by the by-products listed above, the current model presents the peak and 5% spectral acceleration values for GMRotD50 component of ground motion. Impact of separating parameter

uncertainty in predictive variables such as magnitude and source to site distance, and uncertainty in ground accelerations due to random orientation, and response due to uncertain ground characteristics are separated from total uncertainty, to yield the true model error. Correctly evaluating model error is crucial in hazard analysis, since it has a considerable effect on the design parameters, especially at long return period ground motions. Reduction in sigma values due to removal of parameter uncertainty was found to be significant. Median estimates and absolute values of model error are comparable with global prediction equations, and relatively lower than models utilizing local data.

Another treatment to the compiled dataset was removing bias in predictions, due to uneven sampling of data. Uneven sampling is evident since, I) there were gaps in the  $M=6.5 - M=7.0$  magnitude range, and ii) magnitude – distance binning of the dataset demonstrated the uneven presence of bins, eventually corresponding to unequal representation of accelerations for the dataset. Applying weighting factors dramatically changed the data trend, and the results of treatment were concluded to be satisfactory. This study also showed that, sampling of the dataset is partially responsible for the shift in ground motion predictions due to different lower magnitude thresholds chosen.

Last part of the thesis study focused on development of a custom probabilistic seismic hazard software from scratch. The software, running on MATLAB; reads the inputs of the site characterization from a SHP file, a common file format in GIS applications. Current abilities of the code include all basic requirements for a modern hazard study, including deaggregation of hazard. Linear and source zones of point rupture can be defined. Future plans include developing a graphical user interface for the program.



## REFERENCES

- Abe, K. (1974). "Fault Parameters Determined by Near and Far Field Data: The Wakasa Bay Earthquake of March 26, 1963", *Bulletin of the Seismological Society of America*, Vol. 64, No. 5, pp. 1369-1382.
- Abrahamson, N.A. (2000). "State of the Practice of Seismic Hazard Evaluation, Vol. 1: Invited papers; Vol. 2: Extended abstracts", *International conference on geotechnical and geological engineering; GeoEng 2000*, Melbourne, Australia.
- Abrahamson, N. A. (2009). ECI 289 Seismic Hazard Assessment Lecture Notes, UC Berkeley, Spring 2009.
- Abrahamson, N. A., and Shedlock, K. M. (1997). "Overview", *Seism. Res. Lett.*, 68, 9-23.
- Abrahamson N. A. and Silva, W. J. (1997). "Empirical response spectral attenuation relations for shallow crustal earthquakes", *Seismological Research Letters*, 68, 94-127.
- Abrahamson, N. A., and Silva, W. (2008). "Summary of the Abrahamson & Silva NGA Ground-Motion Relations", *Earthquake Spectra*, Vol. 24, No.1, 67-97.
- Abrahamson, N. A., and Somerville, P. G. (1996). "Effects of the hanging wall and footwall on ground motions recorded during the Northridge Earthquake", *Bulletin of the Seismological Society of America*, 86, S93-S99.
- Acharya, H. K. (1979). "Regional Variations In Rupture-Length Magnitude Relationships and Their Dynamical Significance", *Bull. Seism. Soc. Am.*, 69, 2063-2084.

- Akkar, S. and Bommer J. J. (2006). "Influence of long-period filter cut-off on elastic spectral displacements," *Earthquake Engineering and Structural Dynamics* , 35(9), 1145-1165.
- Akkar, S. and Bommer, J. J. (2010). "Empirical equations for the prediction of PGA, PGV and spectral accelerations in Europe, the Mediterranean region and the Middle East", *Seismological Research Letters*, 81, 195-206.
- Akkar S. and Çağnan Z. (2010). "A local ground motion predictive model for Turkey and its comparison with other regional and global ground-motion models", accepted for publication in *Bulletin of Seismological Society of America*
- Akkar, S., Çağnan, Z., Yenier, E., Erdoğan, E., Sandıkkaya, M. A., and Gülkan, P. (2010). "The recently compiled Turkish strong-motion database: preliminary investigation for seismological parameters," *Journal of Seismology*, Vol. 14, No.3, pp. 457-479.
- Akkar, S. and Gülkan, P. (2002). "A critical examination of near-field accelerograms from the sea of Marmara region earthquakes", *Bulletin of the Seismological Society of America*, 92(1), 428-447.
- Aktar, M., Karabulut, H., Özalaybey, S., and Childs, D. (2007). "A conjugate strike-slip fault system within the extensional tectonics of Western Turkey", *Geophys J. Int.*, 171, 1363-1375.
- Albee, A. L., and Smith, J. L. (1966). "Earthquake Characteristics and Fault Activity In Southern California", R. Lung and D.W. Proctor (editors), Association of Engineering Geologists, Los Angeles Section, 9-34.
- Ambraseys, N. N., and Adams, R. D. (1993). "Seismicity of the Cyprus region", *Terra Nova*, 5, 88-94.
- Ambraseys, N. N., and Finkel, C. (2006). "The Seismicity of Turkey and Adjacent Areas. A Historical Review, 1500-1800" (in Turkish), Publication of The Scientific and Technological Research Council of Turkey, TUBITAK.

- Ambraseys, N., Smit, P., Sigbjornsson, R., Suhadolc, P. and Margaris, B. (2002). "Internet-Site for European Strong-Motion Data", European Commission, Research-Directorate General, Environment and Climate Programme.
- Anderson, J. G., Wesnousky, S. G, and Stirling, M. W. (1996). "Earthquake Size as a Function of Fault Slip Rate", *Bull. Seism. Soc. of Am.*, Vol. 86, No. 3, 683-690.
- Ateş, R. C., and Bayülke, N. (1982). "The August 1976 Denizli, Turkey, Earthquake: Evaluation of the Strong Motion Accelerograph Record", *Bulletin of the Seismological Society of America*, Vol. 72, No. 5, pp. 1635-1649.
- Atik, L. A., Abrahamson, N., Bommer, J. J., Scherbaum, F., Cotton, F., and Kuehn, N. (2010). "The Variability of Ground-Motion Prediction Models and Its Components", *Seismological Research Letters*, Vol. 81, No. 5, pp. 794-801.
- Atkinson, G. (1997). "Empirical ground motion relations for earthquakes in the Cascadia region", *Can. J. Civil Eng.* 24, 64-77.
- Atkinson, G. M., and Boore, D. M. (2003). "Empirical Ground-Motion Relations for Subduction-Zone Earthquakes and Their Application to Cascadia and Other Regions", *Bulletin of the Seismological Society of America*, Vol. 93, No.4, pp. 1703-1729.
- Barka, A. A., and Kadinsky-Cade, C. (1988). "Strike-slip fault geometry in Turkey and its influence on earthquake activity", *Tectonics*, 7, 663–684.
- Barka, A. A., and Reilinger R. (1997). "Active tectonics of the Mediterranean region: deduced from GPS, neotectonic and seismicity data", *Annali di Geophys.*, XI, 587–610.
- Bath, M. (1979). "Seismic Risk in Turkey – A preliminary Approach", *Tectonophysics*, Vol. 54. T9-T16.
- Bazzurro, P., and Cornell, C. A. (1999). "Disaggregation of seismic hazard", *Bull. Seism. Soc. Am.*, 89, 2, 501-520.

- Bender, B., and Perkins, D. M. (1987). "SEISRISK III: A Computer Program for Seismic Hazard Estimation", *USGS Bulletin No. 1772*
- Benetatos, C., Kiratzi, A., Ganas, A., Ziazia, M., Plessa, A., and Drakatos, G. (2006). "Strike-slip motions in the Gulf of Siğaçık (western Turkey): Properties of the 17 October 2005 earthquake seismic sequence", *Tectonophysics*, 426, pp. 263-279.
- Beyer, K., and Bommer, J. J. (2006). "Relationships between median values and between aleatory variabilities for different definitions of the horizontal component of motion", *Bulletin of the Seismological Society of America*, Vol. 96, pp. 1512-1522.
- Bommer, J. J., and Abrahamson, N. A. (2006). "Why do Modern Probabilistic Seismic-Hazard Analyses Often Lead to Increased Hazard Estimates?", *Bulletin of the Seismological Society of America*, Vol. 96, No. 6, pp. 1967-1977.
- Bommer, J. J., Abrahamson, N. A., Strasser, F. O., Pecker, A., Bard P-Y., Bungum, H., Cotton, F., Faeh, D., Sabetta, F., Scherbaum, F., and Studer, J. (2004). "The challenge of defining the upper limits on earthquake ground motions", *Seism. Res. Lett.*, 70, No. 1, 82-95.
- Bommer, J. J., Douglas, J., and Strasser, F. O. (2003). "Style-of-faulting in ground motion prediction equations", *Bulletin of Earthquake Engineering*, 1(2), 171-203.
- Bommer, J., Spence, R., Erdik, M., Tabuchi, S., Aydınoğlu, N., Booth, E., Del Re, D., and Peterken, O. (2002). "Development of an Earthquake Loss Model for Turkish Catastrophe Insurance", *Journal of Seismology*, Vol. 6, 431-446.
- Bommer, J. J., Stafford, P. J., and Akkar, S. (2010). "Current empirical ground-motion prediction equations for Europe and their application to Eurocode 8", *Bull. Earthquake Engineering*, 8:5-26.

- Bommer, J. J., Stafford, P. J., Alarcon, J. E., and Akkar, S. (2007). "The Influence of Magnitude Range on Empirical Ground-Motion Prediction", *Bulletin of the Seismological Society of America*, Vol. 97, No.6, pp. 2152-2170.
- Bonilla, M. G., and Buchanon, J. M.. (1970). Interim Report on World-Wide Historic Surface Faulting, *US Geol. Surv. Open-File Report 70-34*, 32 pp.
- Bonilla, M. G., Mark, R. K., and Lienkaemper, J. J. (1984). "Statistical Relations Among Earthquake Magnitude, Surface Rupture Length, and Surface Fault Displacement", *Bull. Seism. Soc. Am.*, 74, 2379-2411.
- Boore, D. M. (2005). "On Pads and Filters: Processing Strong-Motion Data", Short Note, *Bulletin of the Seismological Society of America*, Vol. 95, No.2, pp. 745-750.
- Boore D. M., and Akkar, S. (2003). "Effect of causal and acausal filters on elastic and inelastic response spectra," *Earthquake Engineering and Structural Dynamics*, 32, 1729-1748.
- Boore, D. M. and Atkinson, G. M. (2008). "Ground-Motion Prediction Equations for the Average Horizontal Component of PGA, PGV, and 5%-Damped PSA at Spectral Periods between 0.01s and 10.0s", *Earthquake Spectra*, 24, 99-138.
- Boore, D. M., and Bommer, J. J. (2005). "Processing of strong-motion accelerograms: needs, options and consequences", *Soil Dynamics and Earthquake Engineering*, Vol. 25, pp. 93-115.
- Boore, D. M., Joyner, W. B., and Fumal, T. E. (1997). "Equations for Estimating Horizontal Response Spectra and Peak Acceleration from Western North American Earthquakes: A summary of Recent Work", *Seismological Research Letters*, (68), 1, January, pp. 128-153.
- Boore, D. M., Watson-Lamprey, J., and Abrahamson, N. A. (2006). "GMRotD and GMRotI: Orientation-independent measures of ground motion", *Bulletin of the Seismological Society of America*, Vol. 96, 1502-1511.

- Bozkurt, E. (2001). "Neotectonics of Turkey – a synthesis", *Geodinamica Acta*, 14, 3-30.
- Brune, J. N. (1970). "Tectonic stress and the spectra of seismic shear waves from earthquakes", *J. Geophys Res*, 75(26):4997–5002.
- Brune J. N. (1971). "Correction", *J Geophys Res*, 76(20):5002.
- Çağnan, Z., and Tanırçan, G. B. (2009). "Seismic hazard assessment for Cyprus", *Journal of Seismology*, Vol. 14, No.2, pp. 225-246.
- Campbell, K. W. (1997). "Empirical near-source attenuation relationships for horizontal and vertical components of peak ground acceleration, peak ground velocity, and pseudo-absolute acceleration response spectra", *Seismological Research Letters*, 68, 154-179.
- Campbell K.W., and Bozorgnia, Y. (2006). "Next generation attenuation (NGA) empirical ground motion models: can they be used in Europe?", Proceedings of the 1st European Conference on Earthquake Engineering and Seismology. Geneva. Paper no. 458
- Campbell, K.W. and Bozorgnia, Y. (2008). "NGA ground motion model for the geometric mean horizontal component of PGA, PGV, PGD and 5% damped linear elastic response spectra for periods ranging from 0.01 to 10 s", *Earthquake Spectra*, 24, 139-171.
- Caskey, S. J., Wesnousky, S. G., Zhang, P., and Slemmons, D. B. (1996). "Surface Faulting of the 1954 Fairview Peak ( $M_s$  7.2) and Dixie Valley ( $M_s$  6.8) Earthquakes, Central Nevada", *Bulletin of the Seismological Society of America*, Vol. 86, No. 3, pp. 761-787.
- Caskey, S. J., Bell, J. W., Ramelli, A. R., and Wesnousky, S. G. (2004). "Historic Surface Faulting and Paleoseismicity in the Area of the 1954 Rainbow Mountain-Stillwater Earthquake Sequence, Central Nevada", *Bulletin of the Seismological Society of America*, Vol. 94, No. 4, pp. 1255-1275.

Castañós, H., and Lomnitz, C. (2002). “PSHA: is it science?”, *Engineering Geology*, 66, 315-317.

Cetin K. O. (2000). “Reliability-based assessment of seismic soil liquefaction initiation hazard”, Ph.D. Thesis, University of California, Berkeley.

Cetin K. O., Youd T. L., Bray J. D., Seed R. B., Sancio R. B., Lettis W., Yilmaz M. T., Stewart J. P., Durgunoglu H. T., and Onalp A. (2002). “Liquefaction-induced ground deformations at Hotel Sapanca during Izmit-Turkey Earthquake”, *J. of Soil Dynamics and Earthquake Eng*, 22(9-12): 1083-1092.

Cetin K. O., Youd T. L., Seed R. B., Bray J. D., Durgunoglu H. T., Lettis W., and Yilmaz M. T. (2004). “Liquefaction-induced lateral spreading at Izmit Bay during the 1999 Kocaeli (Izmit) – Turkey Earthquake”, *ASCE J. of Geotech. and Geoenviron. Eng.*, 130(12): 1300-1313.

Cetin K. O., and Seed R. B. (2000). “Earthquake-induced nonlinear shear mass participation factor, rd”, University of California, Berkeley, Geotechnical Engineering Research Report No: UCB/GT- 2000/08.

Chinnery, M. A. (1969). “Earthquake Magnitude and Source Parameters”, *Bull. Seism. Soc. Am.*, 59, 1969-1982.

Chiou, B., Darragh, R., and Gregor, N. (2008). “NGA Project Strong-Motion Database”, *Earthquake Spectra*, Volume 24, No.1, 23-44.

Chiou, B.S.-J. and Youngs, R. (2008). “An NGA model for the average horizontal component of peak ground motion and response spectra”, *Earthquake Spectra*, 24, 173-215.

Choi, Y., and Stewart, J. P. (2005). “Nonlinear site amplification as function of 30 m shear wave velocity”, *Earthquake Spectra*, 21, 1-30.

Cluff, L. S., and Cluff, J. L. (1984). “Importance of assessing degrees of fault activity for engineering decisions”, *Proceedings, 8th World Conference on Earthquake Engineering*, San Francisco, Vol.2, pp. 629-636.

- Cornell C. A. (1968). "Engineering seismic risk analysis", *Bulletin of the Seismological Society of America*, 58(5): 1583–1606.
- Darragh, R. B., and Bolt, B. A. (1987). "A Comment on the Statistical Regression Relation Between Earthquake Magnitude and Fault Rupture Length", *Bull. Seism. Soc. Am.*, 77, 1479-1484.
- Demircioğlu, M. B., Sesetyan, K., Durukal, E., Erdik, M. (2007). "Assessment of Earthquake Hazard in Turkey", *4<sup>th</sup> International Conference on Earthquake Geotechnical Engineering*, June 25-28, Thessaloniki, Greece.
- Deniz, A. (2006). "Estimation of Earthquake Insurance Premium Rates Based on Stochastic Methods", MSc. Thesis, The Graduate School of Natural and Applied Sciences, Middle East Technical University, Ankara, Turkey.
- Dickenson, S. E. (1994). "Dynamic Response of Soft and Deep Cohesive Soils During the Loma Prieta Earthquake of October 17, 1989", Dissertation Submitted in Partial Satisfaction of the Requirements for the Degree of Doctor of Philosophy, University of California at Berkeley.
- Douglas, J. (2001). "A comparative worldwide summary of strong-motion attenuation relationships for peak ground acceleration and spectral ordinates (1969 to 2000)", *ESEE Report, Imperial College of Science, London, Report 01-1* (2001).
- Douglas, J. (2003a). "A note on the use of strong-motion data from small magnitude earthquakes for empirical ground motion estimation", in *Skopje Earthquake 40 Years of European Earthquake Engineering SE-40EEE*, August, Skopje/Ohrid, Macedonia, Institute of Earthquake Engineering and Engineering Seismology.
- Douglas, J. (2003b). "What is a poor quality strong-motion record?", *Bulletin of Earthquake Engineering*, Vol. 1, pp.141-156.
- Dowrick, D. J., and Rhoades, D. A. (2004). "Relations Between Earthquake Magnitude and Fault Rupture Dimensions: How Regionally Variable Are They?", *Bulletin of the Seismological Society of America*, 94 (3), 776-788.



- Durukal E., Erdik, M., Avcı, J., Yüzügüllü, Ö., Alpay, Y., Avar, B., Zülfikar, C., Biro, T., and Mert, A. (1998). “Analysis of the Strong Motion Data of the 1995 Dinar, Turkey Earthquake”, *Soil Dynamics and Earthquake Engineering*, Vol. 17, 557-578.
- Egwirda, D. (2007). “Fast points in polygon test”, retrieved from <http://www.mathworks.com/matlabcentral/fileexchange/10391-fast-points-in-polygon-test>, last accessed October 1, 2010.
- Egwirda, D. (2009). “MESH-2D, Automatic mesh generation”, retrieved from <http://www.mathworks.com/matlabcentral/fileexchange/25555-mesh2d-automatic-mesh-generation>, last accessed October 1, 2010.
- Ellsworth, W. L. (2003). “Appendix D: Working Group on California Earthquake Probabilities, Earthquake Probabilities in the San Francisco Bay Region: 2002–2031”, *U.S. Geol. Surv. Open File Rep. 03-214* [<http://pubs.usgs.gov/of/2003/of03-214/>].
- Erdik, M., Biro, Y. A., Onur, T., Sesetyan, K. and Birgören, B. (1999). “Assessment of Earthquake Hazard in Turkey and Neighbouring Regions”, *Annali di Geofisica* 42(6), 1125–1138.
- Erdik, M., Doyuran, V., Gülkan, P., and Akkas, N. (1985). “A Probabilistic Assessment of the Seismic Hazard in Turkey”, *Tectonophysics*, 117, 295-344.
- Erdik, M., and Durukal, E. (2001). “1999 Kocaeli and Düzce, Earthquakes: Strong Ground Motion”, *XV<sup>th</sup> International Conference on Soil Mechanics and Geotechnical Engineering*, Lessons Learned from Recent Strong Earthquakes, Earthquake Geotechnical Engineering Satellite Conference, Istanbul, pp. 93-112.
- Erdoğan Ö. (2008). “Main Seismological Features of Recently Compiled Turkish Strong Motion Database” M. Sc. Thesis, Middle East Technical University, Ankara.

- Finn, W. D. L., Onur, T., and Ventura, C. E. (2004). "Microzonation: Developments and Applications", in *Recent Advances in Earthquake Geotechnical Engineering and Microzonation*, Ed. Atilla Ansal, Kluwer Academic Publishers, pp. 5-8.
- Frankel, A. D., Petersen, M. D., Mueller, C. S., Haller, K. M., Wheeler, R. L., Leyendecker, E. V., Wesson, R. L., Harmsen, S. C., Cramer, C. H., Perkins, D. M., and Rukstales, K. S. (2002). "Documentation for the 2002 Update of the National Seismic Hazard Maps", USGS Open File Report, 02-420.
- Gardner, J. K., and Knopoff, L. (1974). "Is the Sequence of Earthquakes in Southern California, with Aftershocks Removed, Poissonian?", *Bulletin of the Seismological Society of America*, Vol. 64, 1363-1367.
- Geller, R. J. (1976). "Scaling Relations for Earthquake Source Parameters and Magnitudes", *Bulletin of the Seismological Society of America*, Vol. 66, No. 5, pp. 1501-1523.
- Global Centroid Moment Tensor Project web site, <http://www.globalcmt.org>, last accessed October 1, 2010.
- Green, R. W. E, and Bloch, S. (1971). "The Ceres, South Africa, Earthquake of September 29, 1969 I. Report on Some Aftershocks", *Bulletin of the Seismological Society of America*, Vol. 61, No. 4, pp. 851-859.
- Grosser, H., Baumbach, M., Berckhemer, H., Baier, B., Karahan, A., Schelle, H., Kruger, F., Paulat, A., Michel, G., Demirtaş, R., Gençoğlu, S., and Yılmaz, R. (1998). "The Erzincan (Turkey) earthquake ( $M_s = 6.8$ ) of March 13, 1992 and its aftershock sequence", *Pure Appl. Geophys.*, 152, pp. 465–505.
- Gülkan, P., and Kalkan, E. (2002). "Attenuation Modeling of Recent Earthquakes in Turkey", *Journal of Seismology*, (6), pp. 397-409.
- Gülkan, P., Koçyiğit, A., Yüçemen, M. S., Doyuran, V., and Başöz, N. (1993). "Earthquake Zoning Map of Turkey Based on the Most Recent Data", Middle East Technical University Earthquake Engineering Research Center Report No: METU/EERC 93-01, Ankara, January 1993.

- Hanks, T. C., and Bakun, W. H. (2002). "A Bilinear Source-Scaling Model for M-log A Observations", *Bulletin of the Seismological Society of America*, 92 (5), 1841-1846.
- Hanks, T. C., and Bakun, W. H. (2008). "M- log A Observations for Recent Large Earthquakes", (Short Note), *Bulletin of the Seismological Society of America*, 98 (1), 490-494.
- Hanks, T. C., and Kanamori, H. (1979). "A Moment Magnitude Scale", *Journal of Geophysical Research*, 84, B5, 2348-2350.
- Harrison, R. W., Newell, W. L., Batıhanlı, H., Panayides, I., McGeehin, J. P., Mahan, S. A., Özhür, A., Tsiolakis, E., and Necdet, M. (2004). "Tectonic framework and Late Cenozoic tectonic history of the northern part of Cyprus: implications for earthquake hazards and regional tectonics", *Journal of Asian Earth Sciences*, 23, 191-210
- Hatheway, A. W. (2003). "Discussion on: How to obtain earthquake ground motions for engineering design", *Engineering Geology*, 67, 403-404.
- Heaton, T. H., Tajima, F., and Mori, A. W. (1982). "Estimating Ground Motions Using Recorded Accelerograms", Report by Dames & Moore to Exxon Production Research Company, Houston, TX.
- Huang, Y-N., Whittaker, A. S., and Luco, N. (2008). "Maximum Spectral Demands in the Near-Fault Region", *Earthquake Spectra*, Vol. 24, No.1, pp.319-341.
- Iida, K. (1959). "Earthquake Energy and Earthquake Fault, Nagoya University", *J. Earth Sci.*, 7, 98-107.
- İnan, E., Çolakoğlu, Z., Koç, N., Bayülke, N., and Çoruh, E. (1996). "Catalogue of Earthquakes Between 1976-1996 with Acceleration Records", *Earthquake Research Department of the General Directorate of Disaster Affairs Publications*, Ministry of Public Works and Settlement, Ankara, (in Turkish).

- Kagan, Y. Y. (2002a). "Aftershock Zone Scaling", *Bulletin of the Seismological Society of America*, Vol. 92, No. 2, 641-655.
- Kagan, Y. Y. (2002b)., "Modern California earthquake catalogs and their comparison", *Seismological Research Letters*, Vol. 73, No. 6, pp. 921-929.
- Kalafat, D. (1989). "Examination of Some Large Magnitude Recent Earthquakes in Terms of Focal Mechanism", *Earthquake Research Bulletin of General Directorate of Disaster Affairs*, No. 66, 6-33 (in Turkish)
- Kalafat, D. (1995). "Examination of Tectonic Structures of Anatolia in Terms of Earthquake Mechanisms", Ph.D Thesis, Institute of Marine Sciences and Management, Istanbul University, 217 pages (in Turkish).
- Kalafat, D., Güneş, Y., Kara, M., Deniz, P., Kekovalı, K., Kuleli, H. S., Gülen, L., Yılmaz, M., and Özel, N. M. (2010). "A revised and extended earthquake catalogue for Turkey since 1900 ( $M > 4.0$ )", last accessed via <http://www.koeri.boun.edu.tr/sismo/default.htm>, on October 1, 2010.
- Kalkan, E. and Gülkan, P. (2004). "Site-dependent spectra derived from ground motion records in Turkey", *Earthquake Spectra*, 20, 1111-1138.
- Kárník, V., and Klíma, K. (1993). "Magnitude-Frequency Distribution in the European- Mediterranean Earthquake Regions", *Tectonophysics*, Vol. 220, 309-323.
- Kanamori, H., and Anderson, D. L. (1975). "Theoretical Basis of Some Empirical Relations in Seismology", *Bull. Seism. Soc. Am.*, 65, 1073-1096.
- Kawasumi, H. (1950). "The Imaichi Earthquake of December 26th, 1949", General Description, *Bulletin of the Earthquake Research Institute*, University of Tokyo, Vol. 28, pp.355-67.
- Kayabalı, K. (2002). Modeling of Seismic Hazard for Turkey Using the Recent Neotectonic Data, *Engineering Geology*, Vol. 63, 221-232.

- Kayabali, K., and Akin, M. (2003). "Seismic Hazard Map of Turkey Using the Deterministic Approach", *Engineering Geology*, Vol. 69, 127-137.
- KOERI. (2004). Internet page of the Kandilli Observatory and Earthquake Research Institute, Boğaziçi University, Istanbul, *Catalogue*, [http://www.koeri.boun.edu.tr/sismo/veri\\_bank/mainw.htm](http://www.koeri.boun.edu.tr/sismo/veri_bank/mainw.htm), last accessed on October 1, 2010.
- Kramer, S. L. (1996). *Geotechnical Earthquake Engineering*, Prentice Hall, New Jersey.
- Krinitzsky, E. L. (1993a). "Earthquake probability in engineering – Part I: The use and misuse of expert opinion", *Engineering Geology*, 33, 257-288.
- Krinitzsky, E. L. (1993b). "Earthquake probability in engineering – Part II: Earthquake recurrence and limitations of Gutenberg-Richter b-values for the engineering of critical structures", *Engineering Geology*, 36, 1-52.
- Krinitzsky, E. L. (1993c). "The Hazard in Using Probabilistic Seismic Hazard Analysis", *Civil Engineering*, November, 60-61.
- Krinitzsky, E. L. (2002a). "How to obtain earthquake ground motions for engineering design", *Engineering Geology*, 65, 1-16.
- Krinitzsky, E. L. (2002b). "Epistemic and aleatory uncertainty: a new shtick for probabilistic seismic hazard analysis", *Engineering Geology*, 66, 157-159.
- Kythreoti, S and Pilakoutas, K. (2000). "Earthquake Risk Assessment Case Study: Cyprus", In 2nd EuroConference 'Global Change and Catastrophe Risk Management: Earthquake Risks in Europe', IIASA, Laxenburg, Austria 6-9 July 2000.
- Legland, D. (2009). *Geom2d* function package for geometric computations on planar shapes, retrieved from <http://www.mathworks.com/matlabcentral/fileexchange/7844-geom2d>, last accessed on October 1, 2010.

- Magistrale, H., Jones, L., and Kanamori, H. (1989). "The Superstition Hills, California, Earthquakes of 24 November 1987", *Bulletin of the Seismological Society of America*, Vol. 79, No. 2, pp. 239-251.
- Manski, C. F., Lerman, S. R. (1977). "The Estimation of Choice Probabilities from Choice-based Samples", *Econometrica*, Vol. 45, Issue 8, November 1977, 1977-1988.
- McGuire, R. K. (2001). "Deterministic vs. probabilistic earthquake hazards and risks", *Soil Dynamics and Earthquake Engineering*, 21, 377-384.
- McGuire, R. K. (2004). "Seismic Hazard and Risk Analysis", EERI Monograph Series, No. 10, Earthquake Engineering Research Institute.
- McGuire R. K. (2008). "Probabilistic seismic hazard analysis: Early history", *Earthquake Engineering and Structural Dynamics*, 37:329–338.
- Moss, R. E. S. (2009). "Reduced Uncertainty of Ground Motion Prediction Equations through Bayesian Variance Analysis." Pacific Earthquake Engineering Research Center, PEER, Report No. 2009/105.
- Moss, R. E. S. and Der Kiureghian, A. (2006). "Incorporating Parameter Uncertainty into Attenuation Relationships." *8th National Conference on Earthquake Engineering*, 1906 San Francisco Earthquake 100th Anniversary, April 18-22, 2006, The Moscone Center, San Francisco, USA.
- Mualchin, L., Krinitizsky, E. L. (2003). "A new and defective regulation in California for protecting critical buildings from earthquakes", *Engineering Geology*, 69, 415-419.
- Ocakoğlu, N., Demirbağ, E., and Kuşçu, İ. (2005). "Neotectonic Structures in İzmir Gulf and surrounding regions (western Turkey): Evidences of strike slip faulting with compression in the Aegean extensional regime", *Marine Geology*, 219, pp. 155-171.

- Ohnaka, M. (1978). "Earthquake-source parameters Related to Magnitude", *Geophys. J. R. Astr. Soc.*, 55, 45-66.
- Ordaz, M., Aguilar, A. and Arboleda, J. (1999). "CRISIS 99-18 ver. 1.018. Program for Computing Seismic Risk", Instituto de Ingeniería, Universidad Nacional Autónoma de México, Mexico City.
- Özalaybey, S., Ergin, M., Aktar, M., Tapırdamaz, C., Biçmen, F., and Yörük, A. (2002). "The 1999 İzmit Earthquake Sequence in Turkey: Seismological and Tectonic Aspects", *Bulletin of the Seismological Society of America*, Vol. 92, No.1, pp. 376-386.
- Özbey, C., Sarı, A., Manuel, L., Erdik, M., and Fahjan, Y. (2004). "An empirical attenuation relationship for northwestern Turkey ground motion using a random effects approach", *Soil Dynamics and Earthquake Engineering*, 24, 115-125.
- Pınar A., and Kalafat D. (1999). "Source processes and seismotectonic implications of the 1995 and 1996 Cyprus, eastern Mediterranean Region, earthquakes", *Tectonophysics* 301, 217–230.
- Polat, O., Eyidogan, H., Haessler, H., Cisternas, A., and Philip, H. (2002). "Analysis and interpretation of the aftershock sequence of the August 17, 1999, İzmit (Turkey) earthquake", *Journal of Seismology*, 6:, 287-306.
- Power, M. S., Chiou, B. S. J., Abrahamson, N. A., Bozorgnia, Y., Shantz, T., and Roblee, C. J. (2008). "An overview of the NGA project", *Earthquake Spectra* 24, 3–21.
- Prozorov, A. G., and Dziewonski, A. M. (1982). "A Method of Studying Variations in the Clustering Property of Earthquakes: Application to the Analysis of Global Seismicity", *Journal of Geophysical Research*, Vol. 87, No. B4, 2829-2839.
- Purcaru, G., and Berckhemer, H. (1982). "Quantitative Relations of Seismic Source Parameters and a Classification of Earthquakes", in *Quantification of Earthquakes*, S.J. Duda and K. Aki (Editors), *Tectonophysics*, 84, 57-128.

- Rathje E. M., Stokoe K. H. II, and Rosenblad, B. (2003). “Strong motion station characterization and site effects during the 1999 earthquakes in Turkey”, *Earthquake Spectra*, 19(3): 653–675.
- Reilinger R. E., McClusky S. C., Oral M. B., King W., Toksöz M. N. (1997). “Global Positioning, System measurements of present-day crustal movements in the Arabian–Africa-Eurasia plate collision zone”, *J. Geophys. Res.*, 102, 9983–9999.
- Richter, C. F., Allen, C. R., and Nordquist, J. M. (1958). “The Desert Hot Springs Earthquakes and Their Tectonic Environment”, *Bulletin of the Seismological Society of America*, Vol. 48, October 1958, pp. 315-337.
- Risk Engineering. (2007). “Ez-Frisk user manual (version 7.24)”, Risk Engineering, Inc., Golden, Colorado, United States of America, 365pp.
- Rojay, B., Heimann, A., and Toprak, V. (2001). “Neotectonic and volcanic characteristics of the Karasu fault zone (Anatolia, Turkey): The transition zone between the Dead Sea transform and the East Anatolian Fault Zone”, *Geodinamica Acta*, 14, 197-212.
- Saatçılar, R., Ergintav, S., Demirbağ, E., and İnan, S.. (1999). “Character of active faulting in the North-Aegean Sea”, *Marine Geology*, 160, pp. 339-353.
- Sadigh, K., Chang, C. Y., Egan, J. A., Makdisi, F., and Youngs, R. R.. (1997). “Attenuation Relationships for Shallow Crustal Earthquakes Based on California Strong Ground Motion Data”, *Seismological Research Letters*, (68), 1, January, pp. 180-189.
- Salamon, A., Rockwell, T., Ward, S. N., Guidoboni, E., and Comastri, A. (2007). “Tsunami Hazard Evaluation of the Eastern Mediterranean: Historical Analysis and Selected Modeling”, *Bulletin of the Seismological Society of America*, Vol. 97, No.3, pp. 705-724.
- Sandıkkaya, M. A. (2008). “Site classification of national strong-motion recording sites”, M.Sc. Thesis, Civil Engineering Department, Middle East Technical University, Ankara.



- Sandıkkaya, M. A., Yılmaz, M. T., Bakır, B. S., and Yılmaz, Ö. (2010). "Site classification of Turkish national strong-motion stations", *Journal of Seismology*, 14:543-563.
- Şaroğlu, F., Emre, Ö., and Kuşcu, İ. (1992). "Active Fault Map of Turkey", General Directorate of Mineral Research and Exploration, Ankara, Turkey.
- Sato, R. (1972). "Stress Drop for a Finite Fault", *J. Phys. Earth*, 20, 397-407.
- Savage, M. K., and Rupp, S. H. (2000). "Foreshock probabilities in New Zealand", *New Zealand Journal of Geology & Geophysics*, Vol. 43, 461- 469.
- Scasserra, G., Stewart, J. P., Bazzurro, P., Lanzo, G., and Mollaioli, F. (2009). "A comparison of NGA ground-motion prediction equations to Italian data", *Bulletin of the Seismological Society of America* , 99(5):2961-2978.
- Scherbaum, F., Schmedes, J. and Cotton, F. (2004). "On the conversion of source-to-site distance measures for extended earthquake source models", *Bulletin of the Seismological Society of America*, Vol. 94, pp.1053-1069.
- Schnabel, P. B. (1973). "Effects of Local Geology and Distance from Source on Earthquake Ground Motions", Ph.D Thesis, University of California, Berkeley, California.
- Schnabel, P. B, Lysmer, J., and Seed, H. B. (1972). "SHAKE: A computer program for earthquake response analysis of horizontally layered sites," Report No. EERC 72-12, Earthquake Engineering Research Center, University of California, Berkeley, California.
- Scholz, C. H. (1982). "Scaling Laws for Large Earthquakes: Consequences for Physical Models", *Bulletin of the Seismological Society of America* , 72 (1), 1-14.
- Seed, H. B., and Idriss, I. M. (1970). "Soil moduli and damping factors for dynamic response analysis." EERC Rep. 70-10, Univ. of California, Berkeley, Calif.

- Seed, H. B., Wong, R.T., Idriss, I.M., and Tokimatsu, K. (1986). "Moduli and damping factors for dynamic analyses of cohesionless soils", *J. Geotech. Engrg.*, ASCE, 112(1): 1016-1032.
- Seed, R. B., Chang, S. W., Dickenson, S. E., and Bray, J. D. (1997). "Site-Dependent Seismic Response Including Recent Strong Motion Data." Proc., Special Session on Earthquake Geotechnical Engineering, XIV International Conf. On Soil Mechanics and Foundation Engineering, Hamburg, Germany, A. A. Balkema Publ., Sept. 6-12, pp. 125-134.
- Shor, G. G., and Roberts, E. (1958). "San Miguel, Baja California Forte, Earthquakes of February, 1956: A Field Report", *Bulletin of the Seismological Society of America*, Vol. 48, No. 2, pp. 101-116.
- Singh, S. K., Bazan, E., and Esteva, L. (1980). "Expected Earthquake Magnitude from a Fault", *Bull. Seism. Soc. Am.*, 70, 903-914.
- Slemmons, D. B. (1977). "Faults and Earthquake Magnitude", U.S. Army Corps of Engineers, Waterways Experimental Station, Miscellaneous Papers S-73-1, Report 6, 1-129.
- Slemmons, D. B. (1982). "Determination of Design Earthquake Magnitudes for Microzonation", Proc. of the Third International Earthquake Microzonation Conf., Vol. 1, U.S. National Science Foundation, Washington, D.C., 119-130.
- Slemmons, D. B., Bodin, P., and Zang, X. (1989). "Determination of Earthquake Size from Surface Faulting Events", *Proc. of the International Seminar on Seismic Zonation*, Guangzhou, China, State Seismological Bureau, Beijing, 13.
- Stein R. S., Barka A. A., and Dieterich J. H. (1997). "Progressive failure on the North Anatolian fault since 1939 by earthquake stress triggering", *Geophys. J. Inter.* 128, 594–604.
- Somerville, P., Irikura, K., Graves, R., Sawada, S., Wald, D., Abrahamson, N., Iwasaki, Y., Kagawa, T., Smith, N., and Kowada, A. (1999). "Characterizing

Crustal Earthquake Slip Models for the Prediction of Strong Ground Motion”, *Seism. Res. Lett.*, 70, 59-80.

Somerville, P. (2006). “Review of magnitude-area scaling of crustal earthquakes”, Rep. to WGCEP, 22 pp, URS Corp., Pasadena.

Stafford P. J., Strasser F. O., and Bommer, J. J. (2008). “An evaluation of the applicability of the NGA models to ground motion prediction in the Euro-Mediterranean region”, *Bull. Earthquake Eng.*, 6(2):149–177.

Stein, R. S. (2008). “Earthquake Rate Model 2 of the 2007 Working Group for California Earthquake Probabilities, magnitude-area relationships”, *Appendix D in The Uniform California Earthquake Rupture Forecast, Version 2 (UCERF2)*: U.S. Geological Survey Open-File Report 2007-1437 and California Geological Survey Special Report 203 [<http://pubs.usgs.gov/of/2007/1091/>].

Stepp, J. C. (1972). “Analysis of completeness of the earthquake sample in the Puget Sound area and its effect on statistical estimates of earthquake hazard”, *Proc. of the 1st Int. Conf. on Microzonation for Safer Construction Research and Application*, Seattle, Vol. 2, pp. 897–910.

Taymaz T., Jackson J., and McKenzie D. P. (1991). “Active tectonics of the North and Central Aegean Sea”, *Geophy. J. Inter.* 106, 433–490.

Taymaz, T., and Tan, O. (2005). “Self Similarity of the Earthquakes Occurred in the Eurasia-Arabia Collision Zone”, *Engineering Journal of Istanbul Technical University*, Vol. 4, No. 6, pp. 105-115 (in Turkish).

Thatcher, W., Marshall, G., and Lisowski, M.. (1997). “Resolution of Fault Slip Along the 470-km-long Rupture of the Great 1906 San Francisco Earthquake and Its Implications”, *Journal of Geophysical Research*, Vol. 102, No. B3, pp. 5353-5367.

Tocher, D. (1958). “Earthquake Energy and Ground Breakage”, *Bull. Seism. Soc. Am.*, 48, 147-153.

- Triep, E. G., and Sykes, L. G. (1996). Catalog of shallow intracontinental earthquakes, Retrieved 7/6/2009, from <http://www.ldeo.columbia.edu/seismology/triep/intra.expl.html>
- Ulusay, R., Tuncay, E., Sönmez, H., and Gökçeoğlu, C. (2004). "An Attenuation Relationship Based on Turkish Strong Motion Data and Iso-Acceleration Map of Turkey", *Engineering Geology*, (74), pp. 265-291.
- Utsu, T. (1969). "Aftershocks and Earthquake Statistics (I), Some Parameters Which Characterize an Aftershock Sequence and Their Interrelations", *J. Faculty Sci.*, Series VII, Vol. III, Hokkaido University, Japan, 129-195.
- Utsu, T., and Seki, A. (1954). "A Relation Between the Area of Aftershock Region and the Energy of Mainshock", *J. Seism. Soc. Japan*, 7, 233-240.
- Uzel, B., and Sözbilir, H. (2008). "A First Record of a Strike-slip Basin in Western Anatolia and Its Tectonic Implication: The Cumaovası Basin", *Turkish Journal of Earth Sciences*, Vol. 17, pp. 559-591.
- Vucetic, M., and Dobry, R. (1991). "Effect of Soil Plasticity on Cyclic Response", *Journal of Geotechnical Engineering*, ASCE, Vol. 117, No. 1.
- Walling, M., Silva, W., and Abrahamson, N. (2008). "Nonlinear Site Amplification Factors for Constraining the NGA Models", *Earthquake Spectra*, Vol. 24, No.1, pp. 243-255.
- Wang, J. H., and Ou, S. S. (1998). "On Scaling of Earthquake Faults", *Bull. Of Seism. Soc. Am.*, Vol. 88, No.3, 758-766.
- Watson-Lamprey, J. A., and Boore, D. M. (2007). "Beyond Sa<sub>GMRotI</sub>: Conversion to Sa<sub>Arb</sub>, Sa<sub>SN</sub>, and Sa<sub>MaxRot</sub>", *Bulletin of the Seismological Society of America*, Vol. 97, pp. 1511-1524.

- Weichert, D. H. (1980). "Estimation of the Earthquake Recurrence Parameters for Unequal Observation Periods for Different Magnitudes", *Bulletin of the Seismological Society of America*, Vol. 70, No. 4, 1337-1346.
- Wells, D. L, and Coppersmith, K. J. (1994). "New Empirical Relationships Among Magnitude, Rupture Length, Rupture Width, Rupture Area and Surface Displacement", *Bulletin of the Seismological Society of America*, Vol. 84, No.4, pp. 974-1002.
- Wesnousky, S. G. (1986). "Earthquakes, Quaternary Faults, and Seismic Hazards in California", *J. Geophys. Res.*, 91, 12587-12631.
- Westaway, R. (1994). "Present-day kinematics of the Middle East and Eastern Mediterranean", *J. Geophys. Res.*, 99, 12071–12090.
- Westaway, R., and Smith, R. B. (1989). "Source Parameters of the Cache Valley (Logan), Utah, Earthquake of 30 August 1962", *Bulletin of the Seismological Society of America*, Vol. 79, No. 5, pp. 1410-1425.
- Wyss, M. (1979). "Estimating Maximum Expectable Magnitude of Earthquakes from Fault Dimensions", *Geology*, 7, 336-340.
- Yaltrak, C., Alpar, B., and Yüce, H. (1998). "Tectonic Elements Controlling the Evolution of the Gulf of Saros (Northeastern Aegean Sea, Turkey)", *Tectonophysics*, 300, 227-248.
- Yin, Z. M., and Rogers, G. C. (1996). "Toward a Physical Understanding of Earthquake Scaling Relations", *Pure and Applied Geophysics*, Vol. 146, No.s 3-4, 661-675.
- Yolsal, S., Taymaz, T., and Yalçiner, A. C. (2007). "Source Parameter and Historical Seismicity Related Tsunami Simulations of Hellenic and Cyprean Arc Earthquakes", (in Turkish), *6<sup>th</sup> National Conference on Coastal Engineering*, 25-28 October, 2007, pp. 509-517.
- Young, J. J, Arrowsmith, J. R., Colini, L., Grant, L.B., and Gootee, B. (2002). "Three-Dimensional Excavation and Recent Rupture History Along the

Cholame Segment of the San Andreas Fault”, *Bulletin of the Seismological Society of America*, Vol. 92, No. 7, pp. 2670-2688.

Yunatçı, A. A., and Cetin, K. O. (2009). “Empirical Magnitude – Fault Rupture Dimension Relationships: A Reevaluation”, *presented at Seismological Society of America Annual Meeting*, 8-10 April, Monterey, California.

Zaré, M. and Bard, P. Y. (2002). “Strong motion dataset of Turkey: data processing and site classification”, *Soil Dynamics and Earthquake Engineering*, Vol. 22, pp.703-718.

## **APPENDIX A**

### **GLOBAL RUPTURE DIMENSION SCALING DATASET**

#### Abbreviation List for Data Sources

GL76: Geller (1976)

SC82: Scholz (1982)

TS96: Triep and Sykes (1996)

HB02: Hanks and Bakun (2002)

EL03: Ellsworth (2003)

DR04: Dowrick and Rhoades (2004)

HB08: Hanks and Bakun (2008)

NGA: Next Generation Attenuation Project (Power et al., 2008)

**Table A.1 Fundamental parameters of the global dataset for rupture dimension scaling in crustal zones**

Event Id.	Catalog	Year	Month	Day	Name	Location	Latitude	Longitude	Depth (km)	Final M	Method for M
1	DR04	1848	10	15	Marlborough	New Zealand	-41.900	173.601	10	7.80	A
2	DR04	1855	1	23	Wairarapa	New Zealand	-41.200	175.200	19	8.20	A
3	TS96/HB02/ SC82/EL03	1857	1	9	Fort Tejon	CA,USA	35.720	-120.320	-	7.85	A
4	DR04	1888	8	31	North Canterbury	New Zealand	-42.600	172.550	8	7.10	A
5	TS96/HB02	1905	7	23	Bulnay	Mongolia	49.270	95.760	-	8.14	A
6	TS96/SC82/ EL03	1906	4	18	San Francisco	CA,USA	38.000	-123.000	12	7.90	A
7	TS96	1915	1	13	Avezzano	Italy	41.900	13.600	8	6.62	A
8	TS96/HB02	1920	12	16	Kansu	China	36.620	105.400	17	8.02	A
9	TS96/GL76	1927	3	7	Tango	Japan	35.600	135.100	-	7.08	A
10	DR04	1929	3	9	Arthur's Pass	New Zealand	-42.840	171.830	11	6.95	A
11	DR04	1929	6	16	Buller	New Zealand	-41.700	172.200	9	7.72	A
12	TS96	1930	11	25	North Izu	Japan	35.000	139.000	-	6.89	A
13	TS96	1931	8	16	Valentine	TX,USA	30.690	-104.570	10	6.31	A
14	TS96	1931	9	21	Saitama	Japan	36.100	139.200	-	6.52	A
15	DR04	1932	9	15	Wairoa	New Zealand	-38.960	177.598	8	6.79	A
16	TS96/GL76/ EL03	1933	3	11	Long Beach	CA,USA	33.600	-117.900	10	6.38	A
17	DR04	1934	3	5	Pahiatua	New Zealand	-40.550	176.290	8	7.36	A
18	TS96/HB02	1939	12	26	Erzincan	Turkey	39.700	39.410	17	7.91	A
19	TS96/NGA/ EL03	1940	5	19	Imperial Valley	CA,USA	32.760	-115.416	10	6.95	A
20	DR04	1942	6	24	Wairarapa I	New Zealand	-40.959	175.688	12	7.07	A



**Table A.1 (contd.) Fundamental parameters of the global dataset for rupture dimension scaling in crustal zones**

Event Id.	Catalog	Year	Month	Day	Name	Location	Latitude	Longitude	Depth (km)	Final M	Method for M
21	TS96/SC82/ EL03	1942	12	20	Erbaa	Turkey	40.500	36.500	10	6.90	A
22	TS96/GL76	1943	9	10	Sikano	Japan	35.500	134.200	-	7.00	A
23	TS96	1946	11	10	Ancash	Peru	-8.500	-77.800	2	7.28	A
24	TS96	1948	6	28	Fukui	Japan	36.100	136.200	16	6.98	A
25	TS96	1948	12	4	Desert Hot Spring	CA,USA	33.930	-116.380	-	5.97	A
26	TS96	1949	12	26	Imaichi	Japan	36.725	139.722	-	6.20	D
27	TS96	1951	11	18	Damxung	China	30.980	91.490	5	7.67	A
28	TS96/NGA	1952	7	21	Kern County	CA,USA	34.977	-119.033	16	7.36	A
29	TS96	1954	3	19	Arroyo Salada	CA,USA	33.280	-116.180	10	6.27	A
30	TS96	1954	7	6	Rainbow Mountain	NV,USA	39.250	-118.370	12	6.22	A
31	TS96	1954	8	23	Stillwater	NV,USA	39.330	-118.330	12	6.55	A
32	TS96	1954	12	16	Dixie Valley	NV,USA	39.670	-118.000	12	6.94	A
33	TS96	1954	12	16	Fairview Peak	NV,USA	39.300	-118.100	15	7.17	A
34	TS96	1956	2	9	San Miguel	Mexico	31.750	-115.920	-	6.63	A
35	TS96/HB02	1957	12	4	Gobi-Altai	Mongolia	45.300	99.300	-	8.14	A
36	TS96/SC82/ EL03	1958	7	10	Lituya Bay	AK,USA	58.340	-136.520	15	7.77	A
37	TS96	1959	8	18	Hebgen Lake	MT,USA	44.700	-110.800	12	7.29	A
38	TS96	1962	8	30	Cache Valley	UT,USA	41.917	-111.733	10	5.60	C
39	TS96/EL03	1963	3	26	Wakasa-Bay	Japan	35.800	135.760	5	6.28	A
40	TS96/EL03	1963	7	26	Skopje	Yugoslavia	42.100	21.400	-	5.99	A
41	TS96	1964	6	16	Niigata	Japan	38.400	139.260	14	7.59	A
42	TS96/NGA/ EL03	1966	6	28	Parkfield	CA,USA	35.955	-120.498	10	6.19	A

**Table A.1 (contd.) Fundamental parameters of the global dataset for rupture dimension scaling in crustal zones**

Event Id.	Catalog	Year	Month	Day	Name	Location	Latitude	Longitude	Depth (km)	Final M	Method for M
43	TS96	1966	8	16	Caliente-Clover Mountain	NV,USA	37.420	-114.190	30	5.58	A
44	TS96	1966	8	19	Varto	Turkey	39.170	41.560	10	6.88	A
45	TS96/EL03	1966	9	12	Truckee	CA,USA	39.440	-120.160	10	5.96	A
46	TS96	1967	1	5	Mogod	Mongolia	42.220	102.900	10	7.03	A
47	TS96/SC82	1967	7	22	Mudurnu Valley	Turkey	40.670	30.690	15	7.34	A
48	TS96/NGA/ EL03	1968	4	9	Borrego Mountain	CA,USA	33.190	-116.142	8	6.63	A
49	TS96	1968	5	24	Glasgow	New Zealand	-41.950	171.930	14	7.07	A
50	TS96/EL03	1968	8	31	Dasht-e-Bayaz	Iran	33.969	59.022	6	7.23	A
51	TS96/EL03	1968	10	29	Rampart	AK,USA	65.400	-150.100	6	6.69	A
52	TS96	1969	3	28	Alasehir Valley	Turkey	38.587	28.449	-	6.71	A
53	TS96	1969	4	28	Coyote Mountain	CA,USA	33.300	-116.300	6	5.69	A
54	TS96/EL03	1969	9	9	Gifu	Japan	35.749	136.980	4	6.34	A
55	EL01	1969	9	29	Ceres	South Africa	-33.500	19.500		6.37	A
56	TS96	1970	1	4	Tonghai	China	24.139	102.503	10	7.26	A
57	TS96	1970	3	28	Gediz	Turkey	39.182	29.488	7	7.18	A
58	TS96	1970	10	16	Akita	Japan	39.263	140.696	14	6.13	A
59	TS96/NGA	1971	2	9	San Fernando	CA,USA	34.440	-118.410	13	6.61	A
60	TS96	1972	4	10	Qir-Karzin	Iran	28.434	52.829	12	6.75	A
61	TS96/NGA/ EL03	1972	7	30	Sitka	AK,USA	56.770	-135.784	29	7.68	A
62	TS96	1972	9	3	Hamran	Pakistan	35.979	73.417	12	6.19	A
63	TS96/NGA	1972	12	23	Managua	Nicaragua	12.150	-86.270	5	6.24	A
64	TS96/EL03	1973	2	6	Luhuo	China	31.398	100.581	15	7.47	A

**Table A.1 (contd.) Fundamental parameters of the global dataset for rupture dimension scaling in crustal zones**

Event Id.	Catalog	Year	Month	Day	Name	Location	Latitude	Longitude	Depth (km)	Final M	Method for M
65	TS96	1973	2	21	Point Mugu	CA,USA	34.065	-119.035	6	5.72	A
66	TS96/EL03	1974	5	8	Izu-Oki	Japan	34.522	138.740	16	6.54	A
67	TS96	1974	8	11	Tadzhikestan	USSR	39.340	73.760	3	7.06	A
68	TS96/EL03	1975	2	4	Haicheng	China	40.700	122.800	16	6.95	A
69	TS96	1975	3	28	Pocatello Valley	ID,USA	42.061	-112.548	9	6.06	A
70	TS96/EL03	1975	4	20	Oita Prefecture	Japan	33.190	131.300	-	6.32	A
71	TS96	1975	6	30	Yellowstone	WY,USA	44.745	-110.605	6	5.88	A
72	TS96	1975	8	1	Oroville	CA,USA	39.439	-121.528	6	6.01	A
73	TS96/SC82/ EL03	1976	2	4	Motagua	Guatemala	15.270	-89.250	10	7.63	A
74	TS96	1976	4	8	Gazli, Uzbekistan	USSR	40.360	63.730	10	6.83	A
75	TS96/NGA	1976	5	6	Friuli	Italy	46.345	13.240	5	6.50	A
76	TS96	1976	5	17	Gazli, Uzbekistan	USSR	40.370	63.440	13	6.84	A
77	TS96/EL01	1976	7	27	Thangshan	China	39.570	117.980	11	7.46	A
78	TS96/EL01	1976	8	16	Songpan Huya	China	32.753	104.157	12	6.71	A
79	TS96	1976	8	17	Kawazu	Japan	34.801	138.954	5	5.51	A
80	TS96	1976	8	21	Songpan Huya	China	32.610	104.150	5	6.37	A
81	TS96/EL03	1976	8	23	Songpan Huya	China	32.480	104.100	8	6.58	A
82	NGA	1976	9	15	Friuli	Italy	46.375	13.067	4	5.91	B
83	TS96	1976	11	24	Caldiran	Turkey	39.050	44.040	15	7.23	A
84	TS96/EL03	1976	12	7	Mesa de Andrade	Mexico	31.983	-114.783	12	5.61	A
85	TS96	1977	5	31	Matata	New Zealand	-37.931	176.776	6	5.61	A
86	TS96	1977	11	23	Caucete	Argentina	-31.028	-67.767	17	7.48	A
87	TS96/EL03	1977	12	19	Bob-Tangol	Iran	30.954	56.473	11	5.89	A
88	TS96/EL03	1978	1	14	Izu-Oshima	Japan	34.809	139.259	24	6.71	A

**Table A.1 (contd.) Fundamental parameters of the global dataset for rupture dimension scaling in crustal zones**

Event Id.	Catalog	Year	Month	Day	Name	Location	Latitude	Longitude	Depth (km)	Final M	Method for M
89	TS96	1978	6	20	Thessaloniki	Greece	40.739	23.229	13	6.43	A
90	TS96/NGA	1978	8	13	Santa Barbara	CA,USA	34.399	-119.681	13	5.92	A
91	TS96/NGA	1978	9	16	Tabas-e-Golshan	Iran	33.215	57.323	6	7.35	A
92	NGA	1979	2	28	St Elias	AK,USA	60.643	-141.593	16	7.54	B
93	TS96/EL03	1979	3	15	Homestead Valley	CA,USA	34.317	-116.450	22	5.55	A
94	TS96	1979	4	15	Montenegro	Yugoslavia	42.096	19.209	3	6.98	A
95	TS96/NGA/ EL03	1979	8	6	Coyote Lake	CA,USA	37.085	-121.505	10	5.74	A
96	TS96	1979	9	19	Umbria, Norca	Italy	42.812	13.061	8	5.83	A
97	TS96/NGA/ EL03	1979	10	15	El Centro	CA,USA	32.644	-115.309	10	6.53	A
98	TS96	1979	11	14	Kurizan	Iran	33.918	59.741	25	6.61	A
99	TS96	1979	11	27	Koli	Iran	33.962	59.726	10	7.17	A
100	TS96	1980	1	24	Greenville	CA,USA	37.852	-121.815	14	5.82	A
101	NGA	1980	5	25	Mammoth Lakes-01	CA,USA	37.609	-118.846	9	6.06	B
102	NGA	1980	5	25	Mammoth Lakes-02	CA,USA	37.628	-118.927	14	5.69	B
103	TS96/EL03	1980	5	27	Mammoth	CA,USA	37.510	-118.830	14	5.99	A
104	TS96/NGA/ EL03	1980	6	9	Victoria	Mexico	32.185	-115.076	11	6.33	A
105	TS96/EL03	1980	6	29	Izu-Hanto-Toho	Japan	34.808	139.181	14	6.39	A
106	TS96	1980	10	10	El Asnam	Algeria	36.195	1.354	6	7.00	C
107	NGA	1980	11	23	Irpinia-02	Italy	40.846	15.332	7	6.20	B
108	TS96/NGA	1980	11	23	Irpinia-01	Italy	40.806	15.337	10	6.90	A
109	TS96/EL03	1981	1	23	Daofu	China	30.890	101.150	10	6.64	A
110	TS96	1981	2	24	Corinth	Greece	38.118	22.871	8	6.63	A

**Table A.1 (contd.) Fundamental parameters of the global dataset for rupture dimension scaling in crustal zones**

Event Id.	Catalog	Year	Month	Day	Name	Location	Latitude	Longitude	Depth (km)	Final M	Method for M
111	TS96	1981	3	4	Corinth	Greece	38.209	23.288	20	6.25	A
112	NGA	1981	4	26	Westmorland	CA,USA	33.100	-115.620	2	5.90	B
113	TS96	1982	12	13	Dhamer	North Yemen	14.701	44.379	7	6.34	A
114	TS96/NGA	1983	5	2	Coalinga	CA,USA	36.233	-120.310	5	6.36	A
115	TS96	1983	5	10	Taipingshan	Taiwan	24.419	121.560	2	5.72	A
116	NGA	1983	8	6	Ierissos	Greece	40.180	24.730	9	6.70	B
117	TS96/NGA	1983	10	28	Borah Peak	ID,USA	43.968	-113.899	16	6.88	A
118	TS96/EL03	1983	10	30	Pasinler	Turkey	40.330	42.187	10	6.73	A
119	TS96	1983	11	25	Tasman Sea	Australia	-40.451	155.507	19	6.07	A
120	EL03	1983	12	22	Guinea	West Africa	12.020	-13.640		6.32	A
121	TS96	1984	3	19	Gazli, Uzbekistan	USSR	40.300	63.300	10	6.87	C
122	TS96/NGA/EL03	1984	4	24	Morgan Hill	CA,USA	37.306	-121.695	9	6.19	A
123	TS96	1984	4	29	Perugia	Italy	43.260	12.558	10	5.65	A
124	TS96/NGA	1984	5	7	Lazio-Abruzzo	Italy	41.710	13.902	14	5.80	A
125	TS96	1984	8	14	Sutton, Talkeetn	AK,USA	61.857	-149.104	9	5.84	A
126	TS96/EL03	1984	9	14	Naganoken-Seibu	Japan	35.774	137.424	25	6.24	A
127	TS96/EL03	1984	11	23	Round Valley	CA,USA	37.480	-118.655	12	5.83	A
128	TS96	1985	1	26	Mendoza	Argentina	-33.060	-68.770	14	5.77	C
129	TS96/EL03	1985	5	10	New Britain	New Guinea	-5.599	151.045	24	7.19	A
130	TS96	1985	7	3	New Ireland	New Guinea	-4.439	152.828	10	7.23	A
131	TS96	1985	8	4	Kettleman Hills	CA,USA	36.118	-120.150	10	6.10	A
132	TS96	1985	10	5	Nahanni-1	Canada	62.190	-124.240	6	6.62	A
133	TS96/EL03	1985	10	27	Constantine	Algeria	36.460	6.761	6	6.00	A
134	TS96/NGA	1985	12	23	Nahanni-2	Canada	62.187	-124.243	8	6.76	A

**Table A.1 (contd.) Fundamental parameters of the global dataset for rupture dimension scaling in crustal zones**

Event Id.	Catalog	Year	Month	Day	Name	Location	Latitude	Longitude	Depth (km)	Final M	Method for M
135	TS96	1986	3	21	Prince George	BC, Canada	54.284	-121.854	10	5.53	A
136	TS96/EL03	1986	3	31	Mt Lewis	CA,USA	37.483	-121.690	51	5.64	A
137	TS96	1986	5	20	Hualien	Taiwan	24.125	121.619	11	6.37	A
138	TS96/NGA/ EL03	1986	7	8	N. Palm Springs	CA,USA	34.000	-116.612	11	6.06	A
139	TS96	1986	7	13	Oceanside	CA,USA	32.970	-117.870	8	5.87	A
140	NGA	1986	7	20	Chalfant Valley-01	CA,USA	37.577	-118.449	7	5.77	B
141	TS96/NGA/ EL03	1986	7	21	Chalfant Valley-02	CA,USA	37.538	-118.443	10	6.19	A
142	TS96	1986	9	13	Kalamata	Greece	37.014	22.176	11	5.93	A
143	TS96/NGA	1986	10	10	San Salvador	El Salvador	13.633	-89.200	11	5.80	B
144	TS96	1986	11	14	Hualien	Taiwan	23.901	121.574	6	7.33	A
145	TS96	1986	12	30	Omachi	Japan	36.666	137.896	-	5.51	A
146	TS96/NGA	1987	3	2	Edgecumbe	New Zealand	-37.920	176.760	6	6.60	A
147	TS96/NGA	1987	10	1	Whittier Narrows-01	CA,USA	34.049	-118.081	15	5.99	A
148	TS96/NGA/ EL03	1987	11	24	Superstition Hills-01	CA,USA	33.082	-115.795	10	6.22	A
149	TS96/NGA/ EL03	1987	11	24	Superstition Hills-02	CA,USA	33.022	-115.831	9	6.54	A
150	TS96	1988	8	14	Colorado Plateau	UT,USA	39.128	-110.869	17	5.50	D
151	TS96/EL03	1988	11	6	Lancang Gengma	China	22.789	99.611	10	7.10	A
152	TS96	1988	12	7	Armenia	USSR	40.987	44.185	8	6.76	A
153	TS96/NGA/ EL03	1989	10	18	Loma Prieta	CA	37.041	-121.883	17	6.93	A
154	TS96	1989	10	29	Chenoua	Algeria	36.788	2.448	10	5.98	A
155	DR04	1990	2	10	L. Tennyson	New Zealand	-42.245	172.646	6	5.93	A

**Table A.1 (contd.) Fundamental parameters of the global dataset for rupture dimension scaling in crustal zones**

Event Id.	Catalog	Year	Month	Day	Name	Location	Latitude	Longitude	Depth (km)	Final M	Method for M
156	TS96/EL03	1990	2	20	Izu-Oshima	Japan	34.706	139.252	14	6.37	A
157	TS96	1990	2	28	Upland	CA,USA	34.140	-117.700	4	5.59	A
158	DR04	1990	5	13	Weber II	New Zealand	-40.427	176.470	13	6.37	A
159	TS96/NGA	1990	6	20	Rudbar-Tarom	Iran	36.810	49.353	19	7.37	A
160	TS96/EL03	1990	7	16	Luzon	Philippines	15.679	121.172	15	7.74	A
161	NGA	1990	12	21	Griva	Greece	40.969	22.376	9	6.10	B
162	TS96	1991	4	29	Racha	Georgia	42.424	43.664	4	6.84	C
163	TS96/NGA	1991	6	28	Sierra Madre	CA,USA	34.259	-118.001	12	5.61	A
164	TS96/NGA	1992	3	13	Erzincan	Turkey	39.705	39.587	16	6.69	A
165	TS96/EL03	1992	4	23	Joshua Tree	CA,USA	33.956	-116.300	14	6.10	A
166	NGA	1992	4	25	Cape Mendocino	CA,USA	40.334	-124.229	10	7.01	B
167	TS96/EL03	1992	6	28	Big Bear	CA,USA	34.166	-116.987	13	6.68	A
168	TS96/EL03	1992	6	28	Landers	CA,USA	34.200	-116.430	7	7.34	A
169	TS96/NGA	1992	6	29	Little Skull Mtn	NV,USA	36.720	-116.286	12	5.65	A
170	TS96	1993	5	17	Eureka Valley	CA,USA	37.171	-117.775	7	6.08	A
171	NGA	1994	1	17	Northridge-01	CA,USA	34.206	-118.554	18	6.69	B
172	DR04	1994	6	18	Arthur's Pass	New Zealand	-43.008	171.476	6	6.71	A
173	NGA	1994	9	12	Double Springs	CA,USA	38.823	-119.632	5	5.90	B
174	NGA	1995	1	16	Kobe	Japan	34.595	135.012	18	6.90	B
175	NGA	1995	5	13	Kozani	Greece	40.157	21.675	13	6.40	B
176	HB08	1995	5	27	Sakhalin	Russia	53.030	142.650	24	7.06	B
177	NGA	1995	10	1	Dinar	Turkey	38.060	30.150	5	6.40	B
178	NGA	1995	11	22	Gulf of Aqaba	Saudi Arabia- Egypt	28.760	34.660	13	7.20	B
179	DR04	1995	11	24	Cass	New Zealand	-42.953	171.819	5	6.25	A

**Table A.1 (contd.) Fundamental parameters of the global dataset for rupture dimension scaling in crustal zones**

Event Id.	Catalog	Year	Month	Day	Name	Location	Latitude	Longitude	Depth (km)	Final M	Method for M
180	HB08	1997	11	8	Manyi	Tibet, China	35.330	86.960	16	7.53	B
181	NGA	1999	8	17	Kocaeli	Turkey	40.727	29.990	15	7.51	B
182	NGA	1999	9	20	Chi-Chi-04	Taiwan	23.600	120.820	18	6.20	B
183	NGA	1999	9	20	Chi-Chi	Taiwan	23.860	120.800	7	7.62	B
184	NGA	1999	9	20	Chi-Chi-02	Taiwan	23.940	121.010	8	5.90	B
185	NGA	1999	9	20	Chi-Chi-03	Taiwan	23.810	120.850	8	6.20	B
186	NGA	1999	9	22	Chi-Chi-05	Taiwan	23.810	121.080	10	6.20	B
187	NGA	1999	9	25	Chi-Chi-06	Taiwan	23.870	121.010	16	6.30	B
188	NGA	1999	10	16	Hector Mine	CA,USA	34.574	-116.291	5	7.13	B
189	NGA	1999	11	12	Duzce	Turkey	40.775	31.187	10	7.14	B
190	HB08	2001	11	14	Kokoxili (Kunlunshan)	China	35.800	92.910	15	7.81	B
191	NGA	2002	10	23	Nenana Mountain	AK,USA	63.514	-148.110	4	6.70	B
192	NGA	2002	11	3	Denali	AK,USA	63.538	-147.444	5	7.90	B



**Table A.2 Rupture dimension parameters of the global dataset for crustal zones**

Event Id.	Name	CR	Dip	SOFP	Method for SOFP	SRL (km)	RL (km)	RW (km)	A (km <sup>2</sup> )	Remark	D compatible A from Mo (sq.km)	D (cm)
1	Marlborough	OC	90	0.50	C	-	155	20	3100	Disp. comp.	3.12E+03	600
2	Wairarapa	OC	80	0.50	C	-	145	42	6090	Disp. comp.	6.17E+03	1210
3	Fort Tejon	NA	79*	0.50	C	297	380	12	4560	Disp. comp.	4.46E+03	500
4	North Canterbury	OC	90	0.50	C	-	35	15	525	Disp. comp.	5.22E+02	320
5	Bulnay	AS	5	1.00	A	-	350	20	7000	Disp. comp.	7.58E+03	800
6	San Francisco	NA	79*	0.50	C	432	450	10	4500	Not disp. comp	5.88E+03	450
7	Avezzano	EU	50*	0.08	C	20	24	15	360	Subsurface Pref.	-	-
8	Kansu	AS	90	0.50	A	230	220	20	4400	Disp. comp.	4.83E+03	830
9	Tango	JP	42*	0.92	C	14	35	15	525	Disp. comp.	5.20E+02	300
10	Arthur's Pass	OC	90	0.50	C	-	30	13	390	Disp. comp.	3.98E+02	250
11	Buller	OC	50	0.92	C	-	64.3	21	1350	Disp. comp.	1.37E+03	1040
12	North Izu	JP	42*	0.92	C	35	22	12	264	Disp. comp.	2.70E+02	300
13	Valentine	NA	62	0.32	B	-	35	12.3	431	Single Option	-	-
14	Saitama	JP	79*	0.50	C	-	20	10	200	Single Option	-	-
15	Wairoa	OC	82	0.50	C	-	21.4	13	278	Disp. comp.	2.86E+02	200
16	Long Beach	NA	79*	0.50	C	-	23	13	299	Not disp. comp	6.95E+02	20
17	Pahiatua	OC	90	0.50	C	-	60	17	1020	Disp. comp.	1.03E+03	400
18	Erzincan	ME	86	0.66	A	350	260	20	5200	Disp. comp.	4.85E+03	400
19	Imperial Valley	NA	80	0.50	A	60	45	11	495	Disp. comp.	6.63E+02	150

**Table A.2 (contd.) Rupture dimension parameters of the global dataset for crustal zones**

Event Id.	Name	CR	Dip	SOFP	Method for SOFP	SRL (km)	RL (km)	RW (km)	A (km <sup>2</sup> )	Remark	D compatible A from Mo (sq.km)	D (cm)
20	Wairarapa I	OC	86	0.50	C	-	30	12	360	Disp. comp.	3.67E+02	410
21	Erbaa	ME	79*	0.50	C	47	70	15	1050	Not disp. comp	7.48E+02	112
22	Sikano	JP	79*	0.50	C	4.7	33	13	429	Disp. comp.	4.73E+02	250
23	Ancash	SA	50*	0.08	C	21	28	30	840	Subsurface Pref.	-	-
24	Fukui	JP	42*	0.92	C	-	30	13	390	Single Option	-	-
25	Desert Hot Spring	NA	79*	0.50	C	-	15	16	240	Single Option	-	-
26	Imaichi	JP	42*	0.92	C	-	11	7	77	Single Option	-	-
27	Damxung	AS	90	0.50	A	90	200	10	2000	Subsurface Pref.	-	-
28	Kern County	NA	75	0.84	B	57	64	19	1216	Disp. comp.	1.31E+03	312.8
29	Arroyo Salada	NA	79*	0.50	C	-	15	12	180	Single Option	-	-
30	Rainbow Mountain	NA	50*	0.08	C	18	11	14	154	Subsurface Pref.	-	-
31	Stillwater	NA	50*	0.08	C	34	26	14	364	Subsurface Pref.	-	-
32	Dixie Valley	NA	79*	0.50	C	45	42	14	588	Subsurface Pref.	-	-
33	Fairview Peak	NA	79*	0.50	C	57	50	15	750	Subsurface Pref.	-	-
34	San Miguel	NA	42*	0.92	C	22	22	12	264	Subsurface Pref.	-	-
35	Gobi-Altai	AS	53	0.68	A	250	270	20	5400	Not disp. comp	1.52E+04	400
36	Lituya Bay	NA	79*	0.50	C	200	350	12	4200	Disp. comp.	5.20E+03	325
37	Hebgen Lake	NA	50*	0.08	C	26.5	45	17	765	Subsurface Pref.	-	-
38	Cache Valley	NA	46	0.00	B	-	7	8	56	Single Option	-	-

**Table A.2 (contd.) Rupture dimension parameters of the global dataset for crustal zones**

Event Id.	Name	CR	Dip	SOFP	Method for SOFP	SRL (km)	RL (km)	RW (km)	A (km <sup>2</sup> )	Remark	D compatible A from Mo (sq.km)	D (cm)
39	Wakasa-Bay	JP	79*	0.50	C	-	20	8	160	Single Option	-	-
40	Skopje	EU	79*	0.50	C	6	17	11	187	Subsurface Pref.	-	-
41	Niigata	JP	42*	0.92	C	40	60	30	1800	Subsurface Pref.	-	-
42	Parkfield	NA	90	0.50	A	38.5	35	10	350	Disp. comp.	3.57E+02	20.2
43	Caliente-Clover Mountain	NA	79*	0.50	C	-	11	6	66	Single Option	-	-
44	Varto	ME	64	0.68	B	30	85	10	850	Subsurface Pref.	-	-
45	Truckee	NA	79*	0.50	C	-	13	7	91	Single Option	-	-
46	Mogod	AS	89	0.46	A	36	40	20	800	Subsurface Pref.	-	-
47	Mudurnu Valley	ME	88	0.50	A	80	70	20	1400	Not disp. comp	3.83E+03	100
48	Borrego Mountain	NA	78	0.49	A	31	40	10	400	Disp. comp.	4.30E+02	76.7
49	Glasgow	OC	42*	0.92	C	2	41	18	738	Subsurface Pref.	-	-
50	Dasht-e-Bayaz	ME	80	0.53	A	80	110	20	2200	Not disp. comp	1.14E+03	230
51	Rampart	NA	79*	0.50	C	-	30	8	240	Single Option	-	-
52	Alasehir Valley	ME	50*	0.08	C	32	30	11	330	Subsurface Pref.	-	-
53	Coyote Mountain	NA	79*	0.50	C	-	10	3	30	Single Option	-	-
54	Gifu	JP	79*	0.50	C	-	18	10	180	Single Option	-	-
55	Ceres	AF	79*	0.50	C	-	20	9	180	Single Option	-	-
56	Tonghai	AS	86	0.50	A	48	75	15	1125	Subsurface Pref.	-	-
57	Gediz	ME	50*	0.08	C	41	63	17	1071	Subsurface Pref.	-	-
58	Akita	JP	42*	0.92	C	-	14	11	154	Single Option	-	-

**Table A.2 (contd.) Rupture dimension parameters of the global dataset for crustal zones**

Event Id.	Name	CR	Dip	SOFP	Method for SOFP	SRL (km)	RL (km)	RW (km)	A (km <sup>2</sup> )	Remark	D compatible A from Mo (sq.km)	D (cm)
59	San Fernando	NA	50	0.96	A	16	24	16	384	Disp. comp.	5.23E+02	58.8
60	Qir-Karzin	ME	45	1.00	A	20	34	20	680	Subsurface Pref.	-	-
61	Sitka	NA	90	0.50	A	-	180	15	2700	Disp. comp.	3.22E+03	384.4
62	Hamran	AS	55	0.92	A	-	13	14	182	Single Option	-	-
63	Managua	CA	80	0.50	A	5.9	15	8	120	Not disp. comp	8.23E+01	104.1
64	Luhuo	AS	87	0.50	A	89	110	13	1430	Not disp. comp	4.61E+03	130
65	Point Mugu	NA	49	0.84	B	-	8	3.3	26.4	Single Option	-	-
66	Izu-Oki	JP	42*	0.92	C	5.7	18	11	198	Subsurface Pref.	-	-
67	Tadzhikestan	AS	51	0.79	B	-	30	20	600	Single Option	-	-
68	Haicheng	AS	75	0.58	B	5.5	60	15	900	Subsurface Pref.	-	-
69	Pocatello Valley	NA	50*	0.08	C	-	15	10	150	Single Option	-	-
70	Oita Prefecture	JP	42*	0.92	C	-	10	10	100	Single Option	-	-
71	Yellowstone	NA	79*	0.50	C	-	10	5	50	Single Option	-	-
72	Oroville	NA	32	0.20	A	3.8	8	10	80	Subsurface Pref.	-	-
73	Motagua	CA	85	0.50	A	235	257	13	3341	Not disp. comp	6.95E+03	150
74	Gazli, Uzbekistan	ME	45	0.94	B	-	7	26	182	Single Option	-	-
75	Friuli	EU	12	0.94	A	-	19	10	190	Disp. comp.	2.12E+02	99
76	Gazli, Uzbekistan	ME	46	0.92	B	-	22.5	17	382.5	Single Option	-	-
77	Thangshan	AS	80	0.47	A	10	70	24	1680	Subsurface Pref.	-	-
78	Songpan Huya	AS	59	0.71	B	-	30	12	360	Single Option	-	-

**Table A.2 (contd.) Rupture dimension parameters of the global dataset for crustal zones**

Event Id.	Name	CR	Dip	SOFP	Method for SOFP	SRL (km)	RL (km)	RW (km)	A (km <sup>2</sup> )	Remark	D compatible A from Mo (sq.km)	D (cm)
79	Kawazu	JP	79*	0.50	C	-	9	4	36	Single Option	-	-
80	Songpan Huya	AS	45	1.00	A	-	12	8	96	Single Option	-	-
81	Songpan Huya	AS	60	0.69	B	-	22	11	242	Single Option	-	-
82	Friuli	EU	19	0.89	A	-	4.9	8.3	40.7	Disp. comp.	4.86E+01	56.4
83	Caldiran	ME	80	0.54	A	55	90	18	1620	Subsurface Pref.	-	-
84	Mesa de Andrade	NA	79*	0.50	C	-	9	5	45	Single Option	-	-
85	Matata	OC	79*	0.50	C	-	8.5	5	42.5	Single Option	-	-
86	Caucete	SA	46	0.92	B	-	55	24	1320	Single Option	-	-
87	Bob-Tangol	ME	60	0.57	A	12	14	12	168	Disp. comp.	2.13E+02	12
88	Izu-Oshima	JP	18	0.64	A	3.2	50	10	500	Subsurface Pref.	-	-
89	Thessaloniki	EU	45	0.00	B	19.4	28	14	392	Subsurface Pref.	-	-
90	Santa Barbara	NA	30	0.82	A	-	10	5	50	Disp. comp.	5.97E+01	47.5
91	Tabas-e-Golshan	ME	25	0.89	A	85	90	35	3150	Disp. comp.	3.76E+03	105.4
92	St Elias	NA	12	1.00	A	-	56	70	3948	Disp. comp.	4.71E+03	162.1
93	Homestead Valley	NA	90	0.50	A	3.9	6	4	24	Not disp. comp	1.58E+02	5
94	Montenegro	EU	14	0.93	B	-	50	29	1450	Single Option	-	-
95	Coyote Lake	NA	80	0.52	A	14.4	6.6	7	46.2	Disp. comp.	5.52E+01	27.6
96	Umbria, Norca	EU	79*	0.50	C	-	10	11	110	Single Option	-	-
97	El Centro	NA	80	0.50	A	30.5	51	12	612	Disp. comp.	7.75E+02	30.1
98	Kurizan	ME	85	0.53	B	17	28	6	168	Subsurface Pref.	-	-

**Table A.2 (contd.) Rupture dimension parameters of the global dataset for crustal zones**

Event Id.	Name	CR	Dip	SOFP	Method for SOFP	SRL (km)	RL (km)	RW (km)	A (km <sup>2</sup> )	Remark	D compatible A from Mo (sq.km)	D (cm)
99	Koli	ME	90	0.50	A	65	75	22	1650	Subsurface Pref.	-	-
100	Greenville	NA	49	0.46	A	6.2	11.5	12	138	Subsurface Pref.	-	-
101	Mammoth Lakes-01	NA	50	0.31	A	-	15	10	150	Disp. comp.	1.79E+02	25.7
102	Mammoth Lakes-02	NA	90	0.50	A	-	10	6	60	Disp. comp.	7.16E+01	17.9
103	Mammoth	NA	45	0.00	A	-	9	11	99	Single Option	-	-
104	Victoria	NA	90	0.50	A	-	30	10	300	Disp. comp.	3.58E+02	32.7
105	Izu-Hanto-Toho	JP	86	0.52	A	-	14	10	140	Single Option	-	-
106	El Asnam	AF	46	0.88	B	31.2	55	15	825	Subsurface Pref.	-	-
107	Irpinia-02	EU	70	0.00	A	-	15	10.1	151.5	Disp. comp.	1.81E+02	41.3
108	Irpinia-01	EU	60	0.00	A	38	60	15	900	Disp. comp.	8.41E+02	99.5
109	Daofu	AS	90	0.50	A	44	46	15	690	Subsurface Pref.	-	-
110	Corinth	EU	47	0.13	B	15	30	16	480	Not disp. comp	6.36E+02	51.8
111	Corinth	EU	49	0.15	B	13	26	18	468	Subsurface Pref.	-	-
112	Westmorland	NA	90	0.50	A	-	10	7	70	Disp. comp.	8.35E+01	31.7
113	Dhamer	ME	45	0.00	B	15	20	7	140	Subsurface Pref.	-	-
114	Coalinga	NA	30	1.00	A	-	27	7	189	Disp. comp.	2.10E+02	61.7
115	Taipingshan	AS	50*	0.08	C	-	9	20	180	Single Option	-	-
116	Ierissos	EU	83	0.47	A	-	42	14	588.2	Disp. comp.	7.02E+02	59.8
117	Borah Peak	NA	52	0.11	A	34	41	20.3	832.3	Disp. comp.	9.93E+02	78.7
118	Pasinler	ME	73	0.40	B	12	50	16	800	Subsurface Pref.	-	-

**Table A.2 (contd.) Rupture dimension parameters of the global dataset for crustal zones**

Event Id.	Name	CR	Dip	SOFP	Method for SOFP	SRL (km)	RL (km)	RW (km)	A (km <sup>2</sup> )	Remark	D compatible A from Mo (sq.km)	D (cm)
119	Tasman Sea	OC	67	0.93	B	-	13	10	130	Single Option	-	-
120	Guinea	AF	61*	0.25	C	-	27	14	378	Single Option	-	-
121	Gazli, Uzbekistan	ME	45	0.96	A	-	14	24	323	Single Option	-	-
122	Morgan Hill	NA	90	0.50	A	-	27	11.5	310.5	Disp. comp.	3.70E+02	19.5
123	Perugia	EU	50*	0.08	C	-	17	5	85	Single Option	-	-
124	Lazio-Abruzzo	EU	48	0.03	A	-	6.0	8.1	48.6	Disp. comp.	5.80E+01	32.3
125	Sutton, Talkeetn	NA	77	0.48	A	-	8	6	48	Single Option	-	-
126	Naganoken-Seibu	JP	63	0.68	A	-	12	8	96	Single Option	-	-
127	Round Valley	NA	82	0.26	A	-	7	7	49	Single Option	-	-
128	Mendoza	SA	52	0.79	B	-	11	11	121	Single Option	-	-
129	New Britain	OC	77	0.37	A	-	50	15	750	Single Option	-	-
130	New Ireland	OC	46	0.92	B	-	48	23	1104	Single Option	-	-
131	Kettleman Hills	NA	12	0.94	B	-	22	6	132	Single Option	-	-
132	Nahanni-1	NA	60	0.93	B	-	25	15	375	Single Option	-	-
133	Constantine	AF	71	0.61	A	3.8	21	13	273	Disp. comp.	3.74E+02	10
134	Nahanni-2	NA	25	1.00	A	-	34	18	591	Disp. comp.	7.06E+02	73.1
135	Prince George	NA	40	0.77	B	-	6	8	48	Single Option	-	-
136	Mt Lewis	NA	79	0.44	A	-	5.5	4	22	Single Option	-	-
137	Hualien	AS	47	0.88	B	-	20	24	480	Single Option	-	-
138	N. Palm Springs	NA	46	0.67	A	9	20	13.3	266	Disp. comp.	3.17E+02	14.5

**Table A.2 (contd.) Rupture dimension parameters of the global dataset for crustal zones**

Event Id.	Name	CR	Dip	SOFP	Method for SOFP	SRL (km)	RL (km)	RW (km)	A (km <sup>2</sup> )	Remark	D compatible A from Mo (sq.km)	D (cm)
139	Oceanside	NA	46	0.92	B	-	8	7	56	Single Option	-	-
140	Chalfant Valley-01	NA	90	0.61	A	-	7.5	6	45	Disp. comp.	5.37E+01	31.5
141	Chalfant Valley-02	NA	55	0.41	A	15.8	15	8	120	Disp. comp.	1.43E+02	50.4
142	Kalamata	EU	51	0.21	B	15	15	14	210	Single Option	-	-
143	San Salvador	NA	85	0.50	A	-	8	7	56	Disp. comp.	6.68E+01	28.0
144	Hualien	AS	57	1.00	B	-	48	26	1248	Single Option	-	-
145	Omachi	JP	57	0.73	B	-	7	4	28	Single Option	-	-
146	Edgumbe	OC	35	0.08	B	18	13.0	10.2	132.6	Disp. comp.	1.58E+02	187.7
147	Whittier Narrows-01	NA	30	0.67	A	-	10.0	6.0	60	Disp. comp.	7.16E+01	50.5
148	Superstition Hills-01	NA	90	0.50	A	10	20.0	10.0	200	Disp. comp.	2.39E+02	33.5
149	Superstition Hills-02	AS	90	0.50	A	27	20.0	12.0	240	Disp. comp.	2.86E+02	84.3
150	Colorado Plateau	NA	79*	0.50	C	-	5	7	35	Single Option	-	-
151	Lancang Gengma	AS	88	0.30	A	35	80	20	1600	Not disp. comp	2.39E+03	70
152	Armenia	ME	67	0.81	B	25	38	11	418	Subsurface Pref.	-	-
153	Loma Prieta	NA	70	0.72	A	-	40.0	18.0	719.8	Disp. comp.	8.59E+02	108.1
154	Chenoua	AF	49	0.84	B	4	15	10	150	Subsurface Pref.	-	-
155	L. Tennyson	OC	89	0.50	C	-	8	5	40	Disp. comp.	4.02E+01	73
156	Izu-Oshima	JP	79	0.56	A	-	19	12	228	Single Option	-	-
157	Upland	NA	73	0.58	B	-	4	7	28	Single Option	-	-
158	Weber II	OC	40	0.92	C	-	14	12	168	Disp. comp.	1.70E+02	79



**Table A.2 (contd.) Rupture dimension parameters of the global dataset for crustal zones**

Event Id.	Name	CR	Dip	SOFP	Method for SOFP	SRL (km)	RL (km)	RW (km)	A (km <sup>2</sup> )	Remark	D compatible A from Mo (sq.km)	D (cm)
159	Rudbar-Tarom	ME	88	0.45	A	80	71.6	16.0	1146	Single Option	1.37E+03	310.5
160	Luzon	PH	88	0.52	A	120	120	20	2400	Single Option	-	-
161	Griva	EU	47	0.07	A	-	17.5	16	280	Disp. comp.	3.34E+02	15.8
162	Racha	ME	66	0.97	B	-	70	24	1680	Single Option	-	-
163	Sierra Madre	NA	50	0.96	A	-	4	5	20	Disp. comp.	2.00E+01	48.5
164	Erzincan	ME	63	0.41	A	30	29.0	8.0	232	Single Option	2.77E+02	146.4
165	Joshua Tree	NA	90	0.61	A	-	15	13	195	Single Option	-	-
166	Cape Mendocino	NA	14	0.88	A	-	20.0	28.0	559.7	Disp. comp.	6.68E+02	183.3
167	Big Bear	NA	70	0.48	A	-	18	12.5	225	TS96	-	-
168	Landers	NA	90	0.50	A	71	71.7	15.0	1075.1	Not disp. comp	1.58E+03	242.5
169	Little Skull Mtn	NA	70	0.11	A	-	6.0	6.0	36	Disp. comp.	4.30E+01	26.0
170	Eureka Valley	NA	50*	0.00	B	4.4	17	7	117	Subsurface Pref.	-	-
171	Northridge-01	NA	40	0.93	A	-	18	24	432	Disp. comp.	5.16E+02	78.6
172	Arthur's Pass	OC	47	0.92	C	-	16	12	192	Disp. comp.	1.97E+02	220
173	Double Springs	NA	81	0.36	A	-	10	7	70	Disp. comp.	8.35E+01	31.7
174	Kobe	JP	85	0.50	A	-	60	20	1200	Disp. comp.	1.43E+03	58.5
175	Kozani	EU	43	0.03	A	-	27	16	424	Disp. comp.	5.06E+02	29.4
176	Sakhalin	AS	79	0.56	B	-	60	15	900	Single Option	-	-
177	Dinar	ME	45	0.02	A	-	13	13	168	Disp. comp.	2.00E+02	74.5
178	Gulf of Aqaba	ME	78	0.50	A	-	54	25	1350	Disp. comp.	1.61E+03	146.5

**Table A.2 (contd.) Rupture dimension parameters of the global dataset for crustal zones**

Event Id.	Name	CR	Dip	SOFP	Method for SOFP	SRL (km)	RL (km)	RW (km)	A (km <sup>2</sup> )	Remark	D compatible A from Mo (sq.km)	D (cm)
179	Cass	OC	46	0.50	C	-	8	8	60	Disp. comp.	5.91E+01	150
180	Manyi	AS	69	0.58	B	-	175	15	2625	Single Option	-	-
181	Kocaeli	ME	88	0.50	A	-	138	20	2784	Disp. comp.	3.32E+03	207.2
182	Chi-Chi-04	AS	89	0.58	A	-	22	18	376	Disp. comp.	4.49E+02	16.6
183	Chi-Chi	AS	30	0.81	A	-	88	40	3539	Disp. comp.	4.22E+03	238.4
184	Chi-Chi-02	AS	50	0.94	A	-	19	13	247	Disp. comp.	2.95E+02	9.0
185	Chi-Chi-03	AS	10	0.94	A	-	10	11	110	Disp. comp.	1.31E+02	56.8
186	Chi-Chi-05	AS	70	0.94	A	-	18	19	332	Disp. comp.	3.97E+02	18.8
187	Chi-Chi-06	AS	30	0.94	A	-	29	20	580	Disp. comp.	6.92E+02	15.2
188	Hector Mine	NA	77	0.51	A	-	69	16	1118	Disp. comp.	1.33E+03	138.9
189	Duzce	ME	65	0.49	A	-	47	20	949	Disp. comp.	1.13E+03	169.4
190	Kokoxili (Kunlunshan)	AS	61	0.38	B	-	400	15	6000	Single Option	-	-
191	Nenana Mountain	NA	90	0.51	A	-	30	15	450	Disp. comp.	5.37E+02	78.1
192	Denali	NA	71	0.55	A	-	327	16	5085	Disp. comp.	6.07E+03	436.3

## APPENDIX B

### RECURRENCE RELATION PLOTS FOR SEISMIC SOURCES

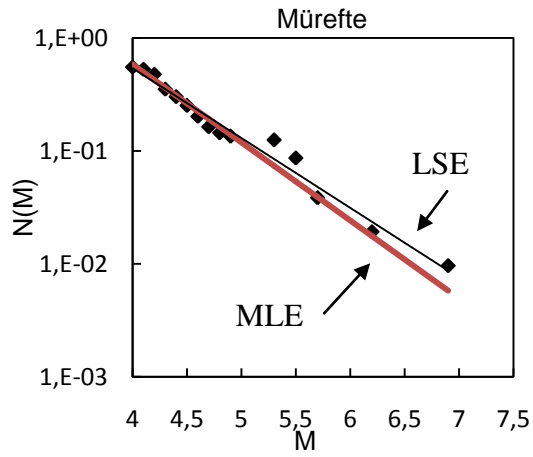


Figure B.1 Source Id # 1

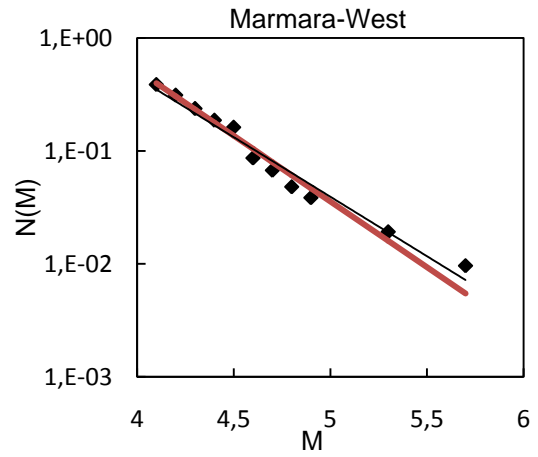


Figure B.2 Source Id # 2

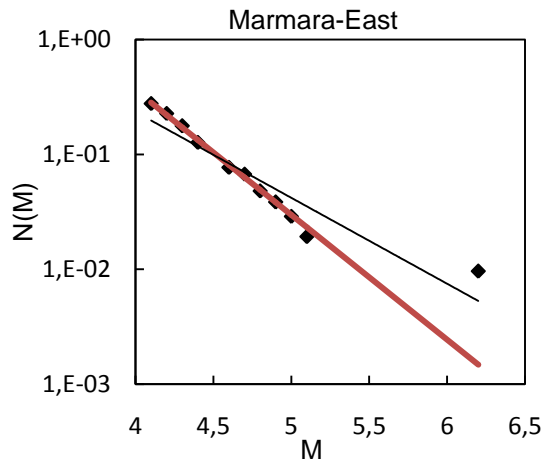


Figure B.3 Source Id # 3

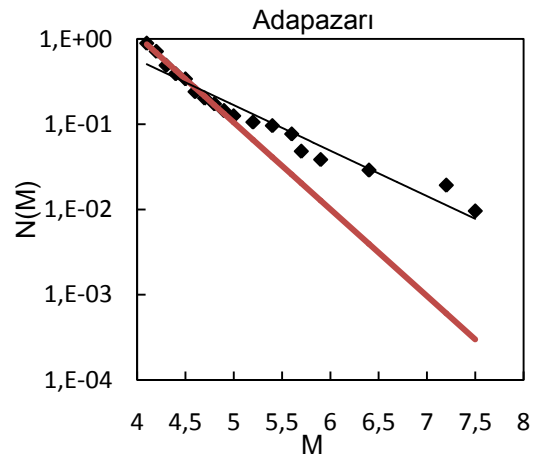
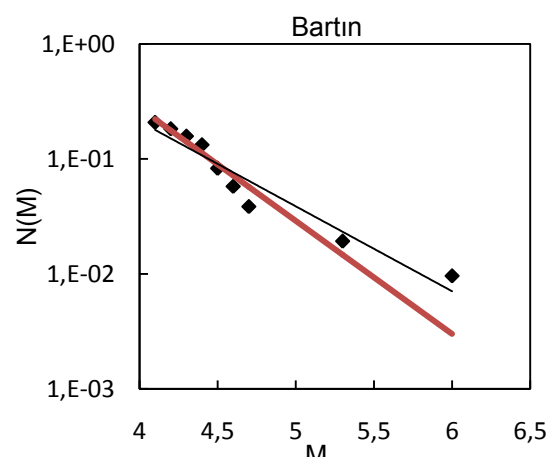
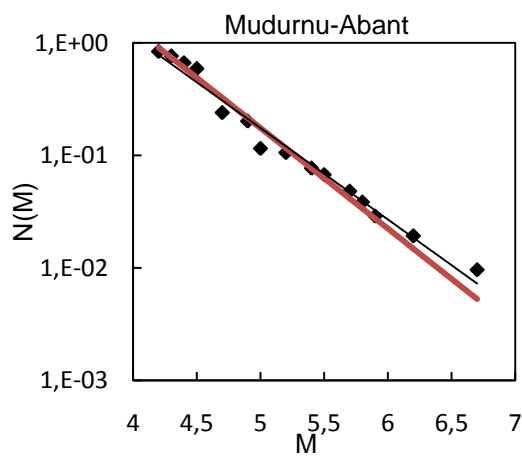
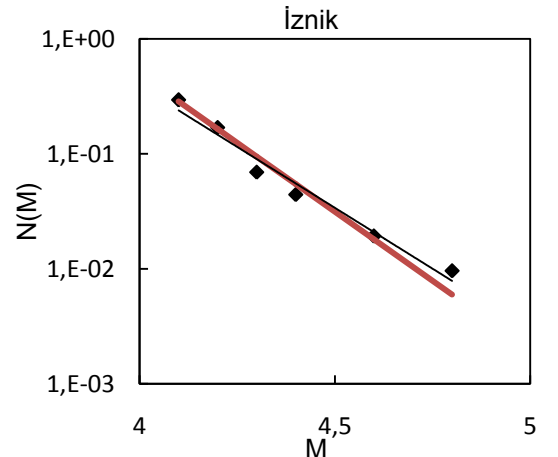
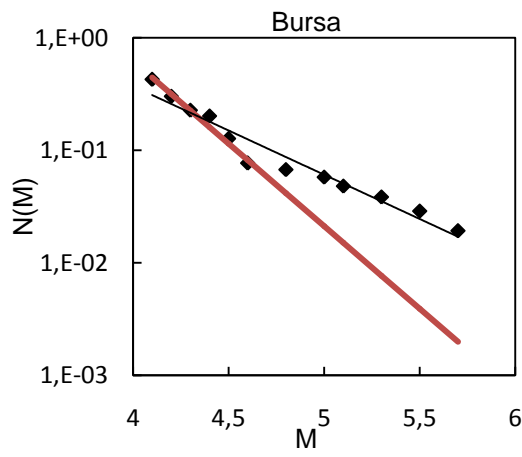
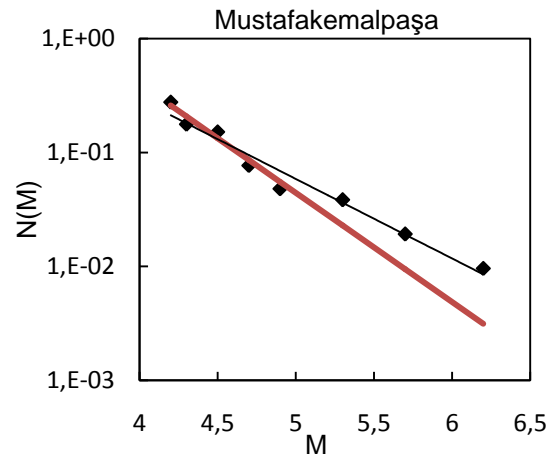
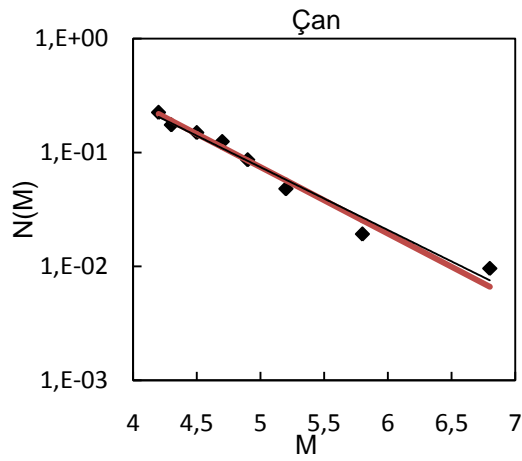
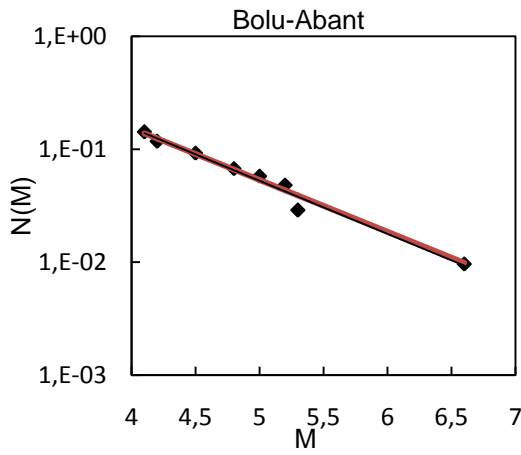
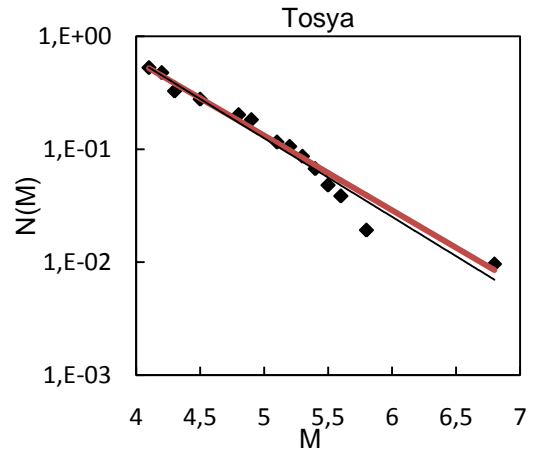


Figure B.4 Source Id # 4





**Figure B.11 Source Id # 14, 15**



**Figure B.12 Source Id # 16, 17**

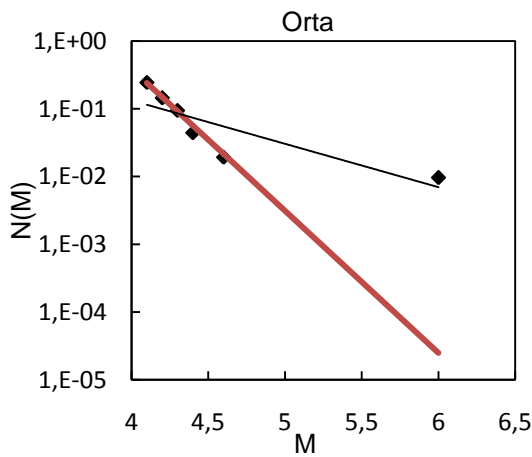


**Figure B.13 Source Id # 18**

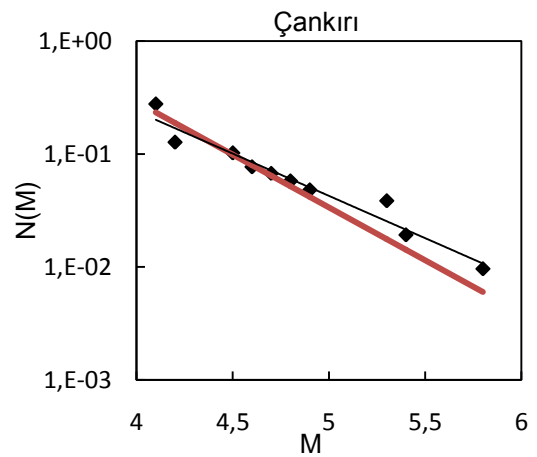


**Figure B.14 Source Id # 19**

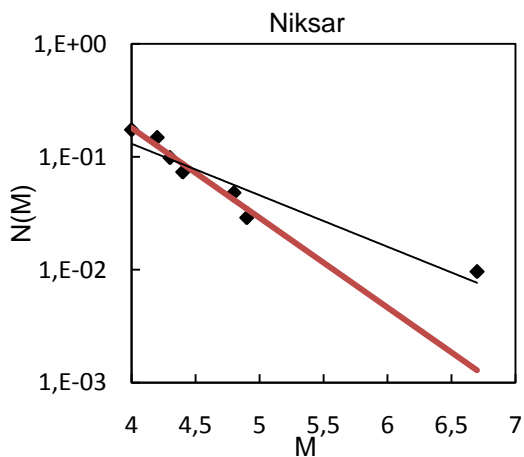


**Figure B.15 Source Id # 20**

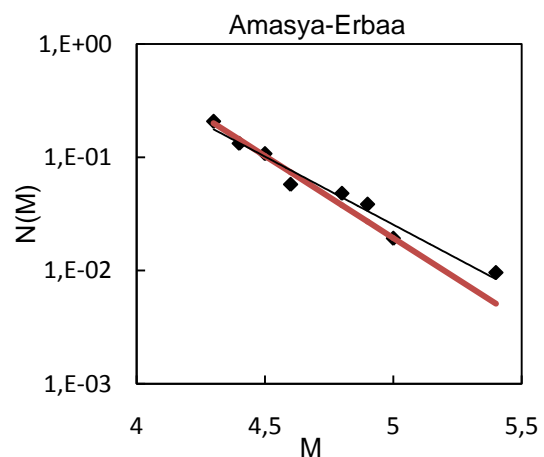


**Figure B.16 Source Id # 21, 61**

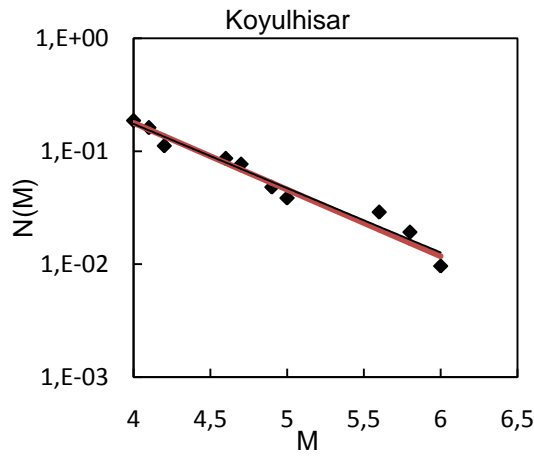


**Figure B.17 Source Id # 22**

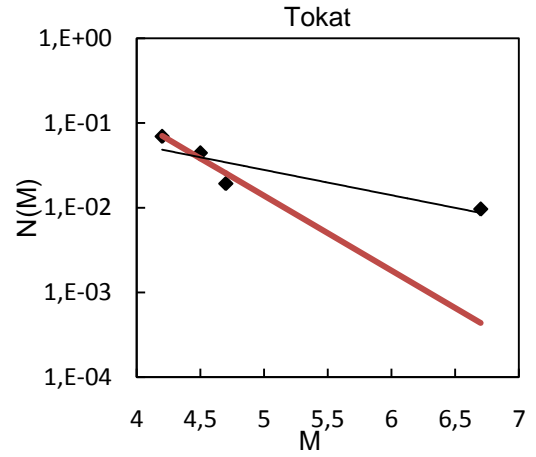


**Figure B.18 Source Id # 23**

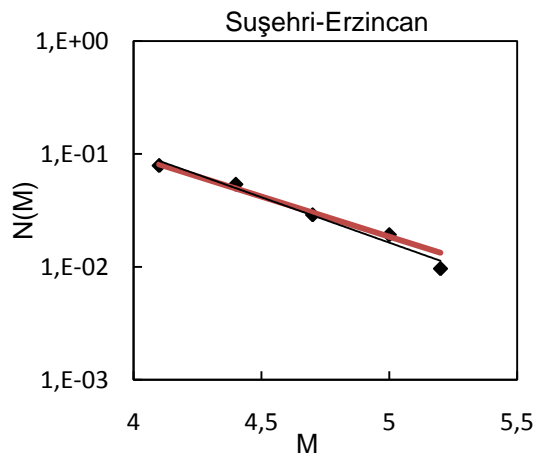


**Figure B.19 Source Id # 24, 25**

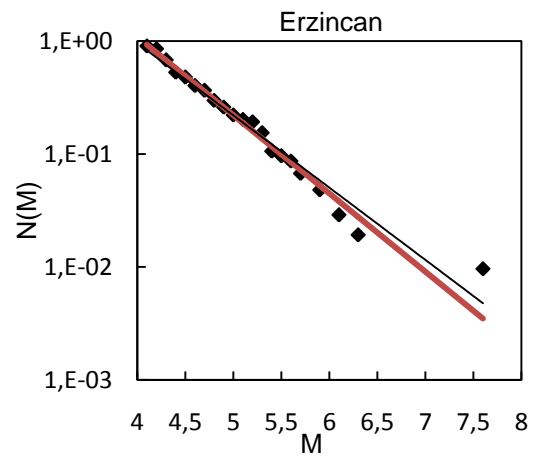


**Figure B.20 Source Id # 26**

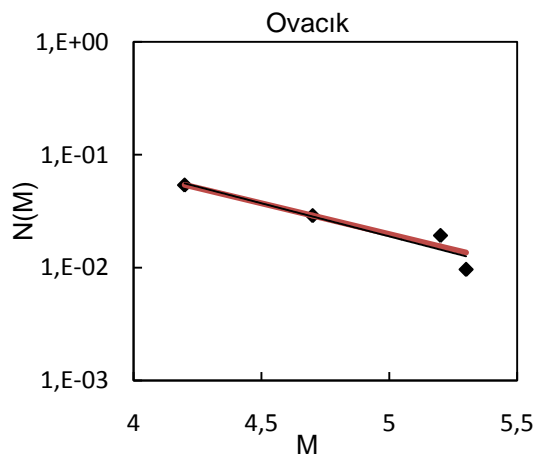


**Figure B.21 Source Id # 27**

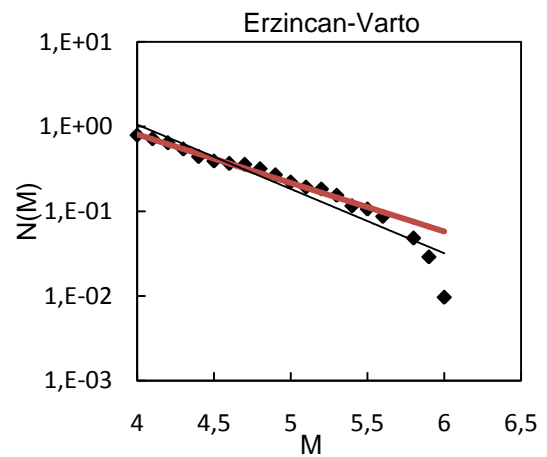


**Figure B.22 Source Id # 28**

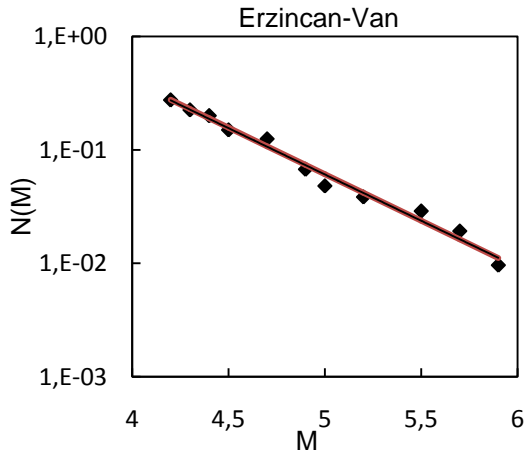


**Figure B.23 Source Id # 29**

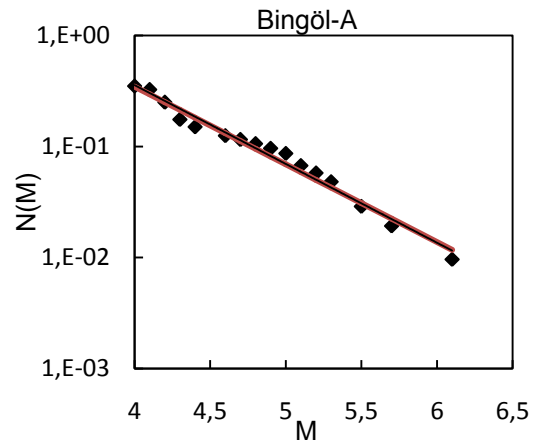


**Figure B.24 Source Id # 30**

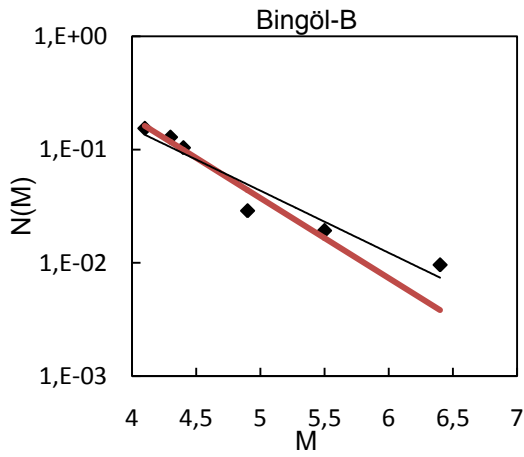


**Figure B.25 Source Id # 31**

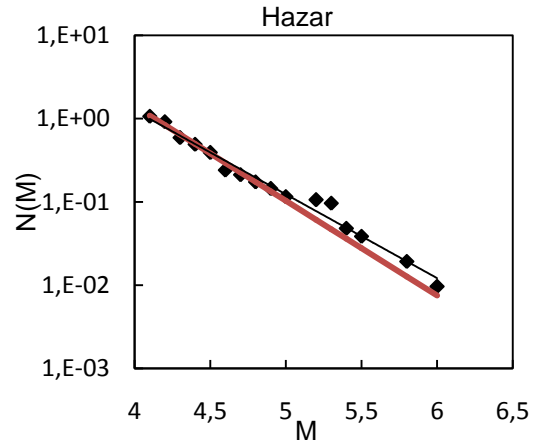


**Figure B.26 Source Id # 32**

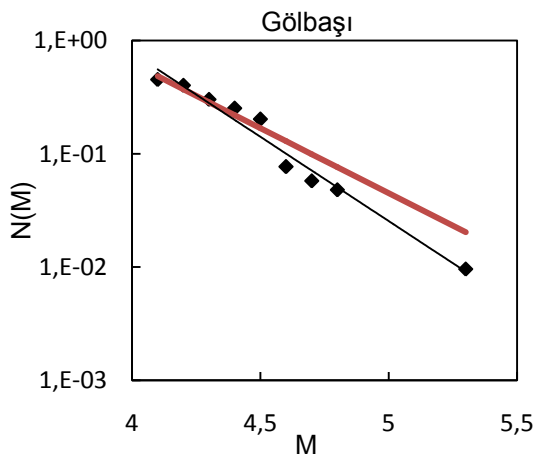


**Figure B.27 Source Id # 33, 34**

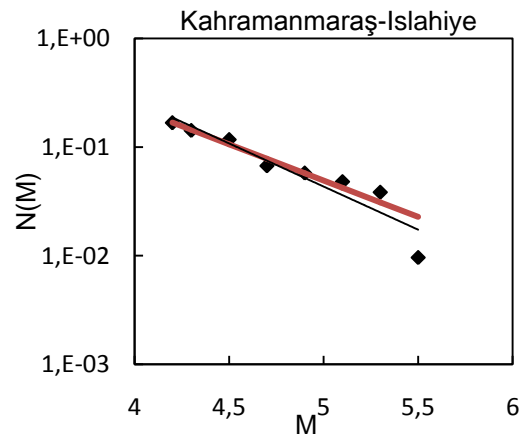


**Figure B.28 Source Id # 35, 36**

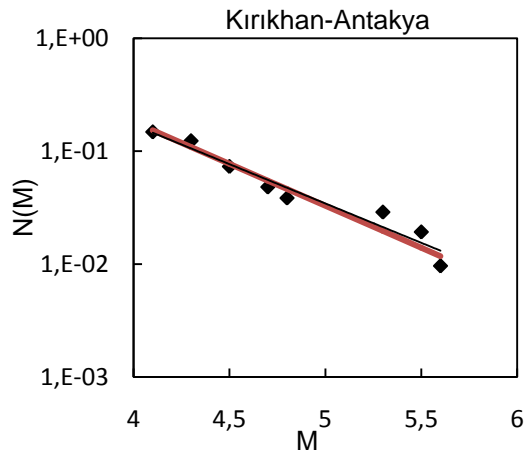


**Figure B.29 Source Id # 37**

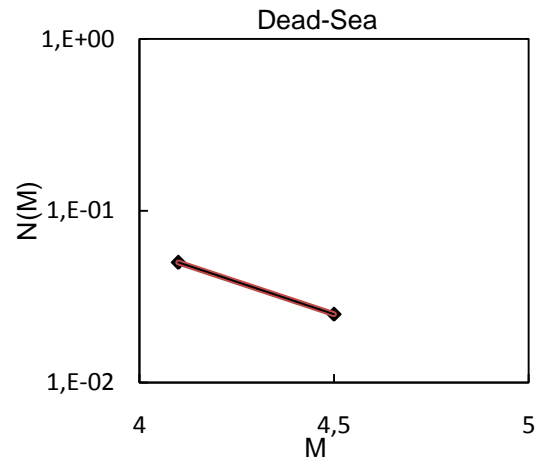


**Figure B.30 Source Id # 38, 39**

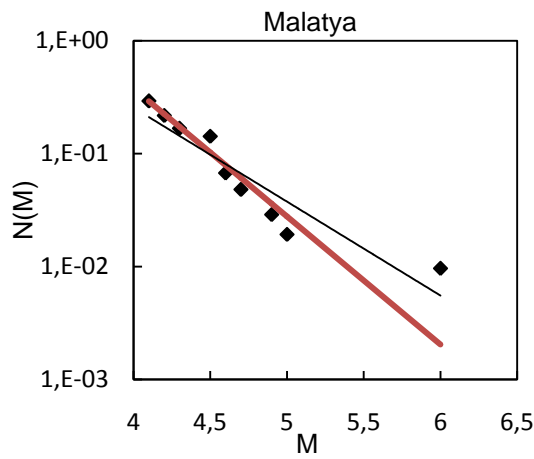


**Figure B.31 Source Id # 40**

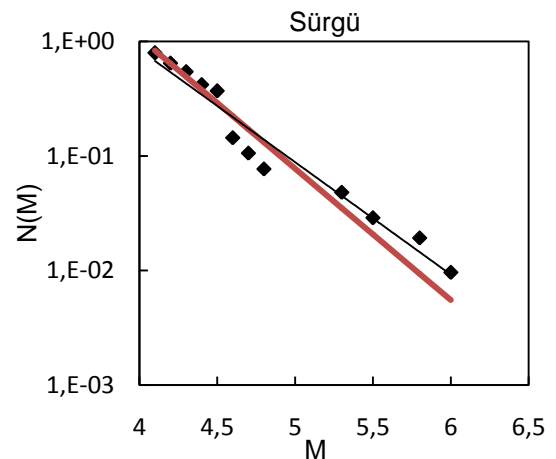


**Figure B.32 Source Id # 41, 42**

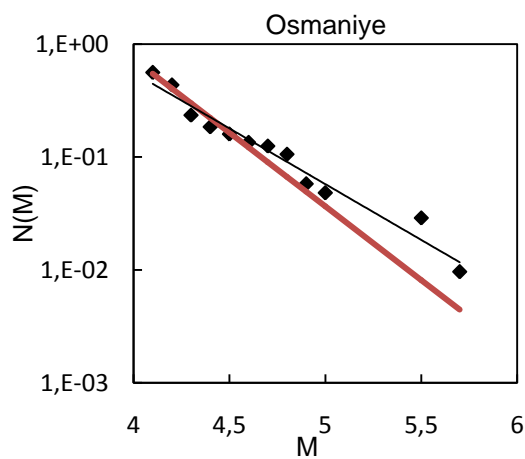


**Figure B.33 Source Id # 43**

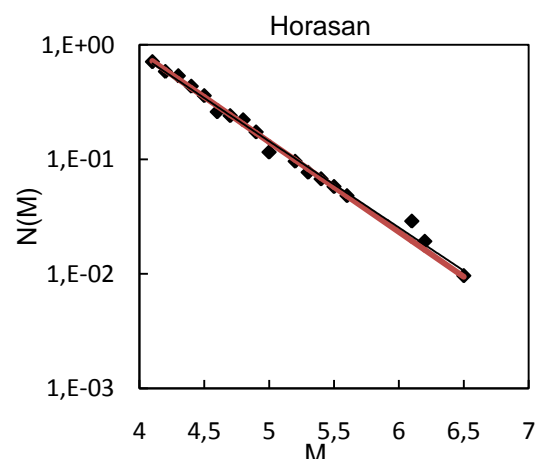


**Figure B.34 Source Id # 44**



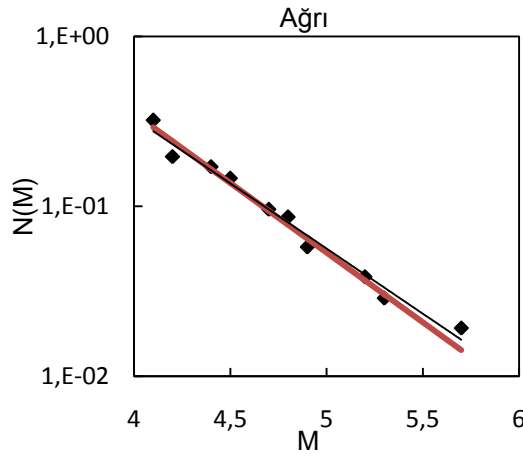


**Figure B.35 Source Id # 45**

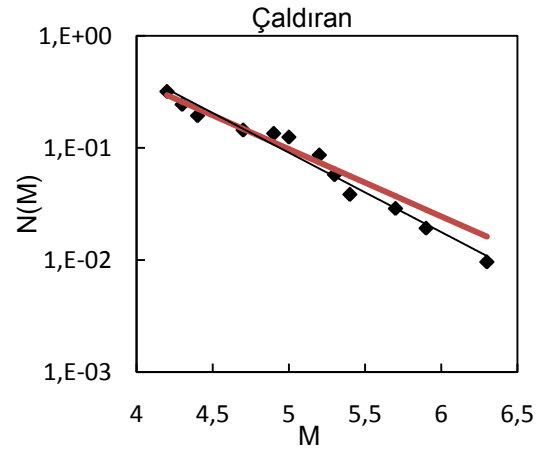


**Figure B.36 Source Id # 46**

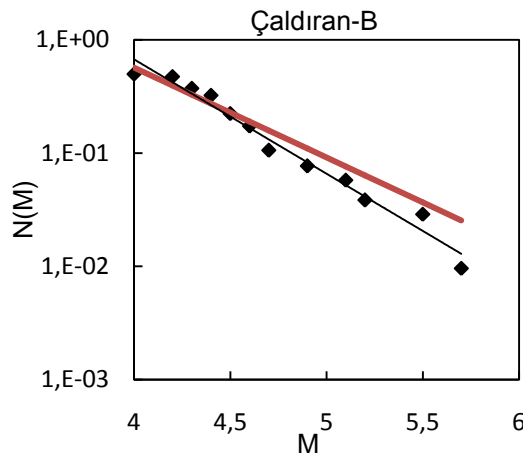


**Figure B.37 Source Id # 47**

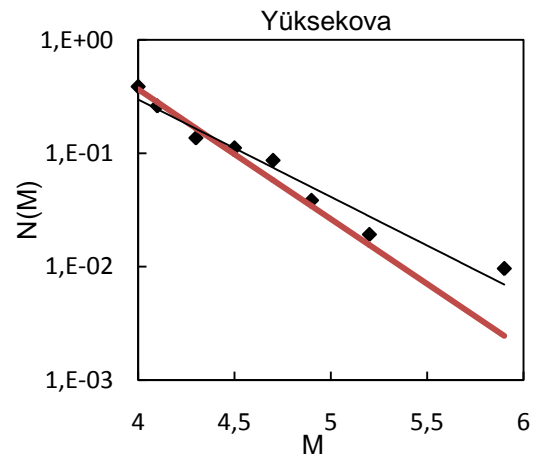


**Figure B.38 Source Id # 48, 49**

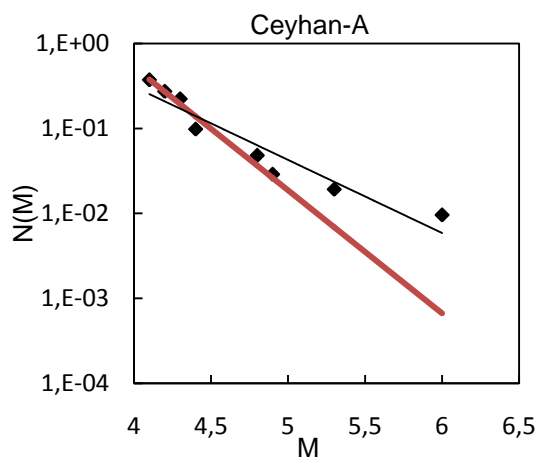


**Figure B.39 Source Id # 50**

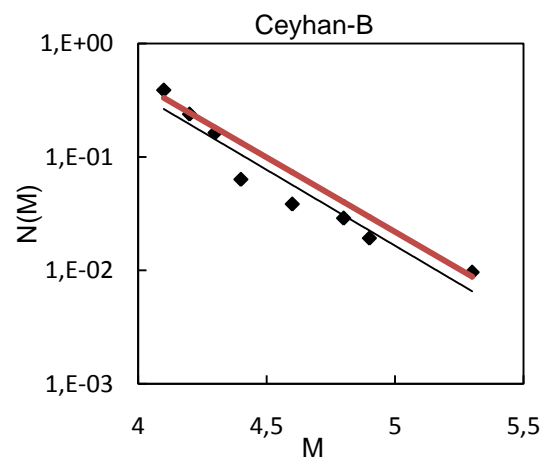


**Figure B.40 Source Id # 51**

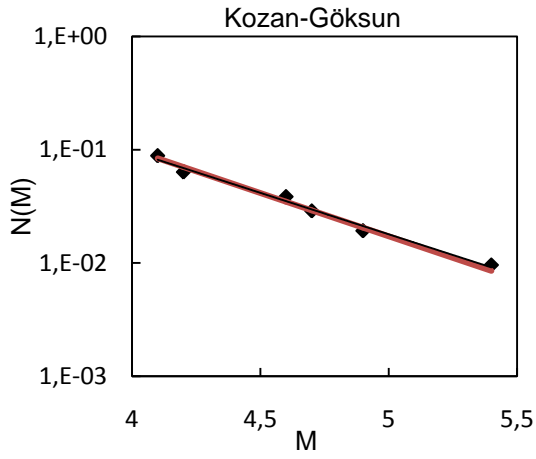


**Figure B.41 Source Id # 52**

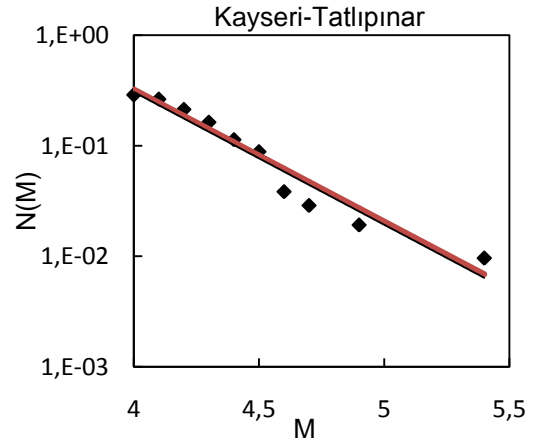


**Figure B.42 Source Id # 53, 54, 55, 56, 57**

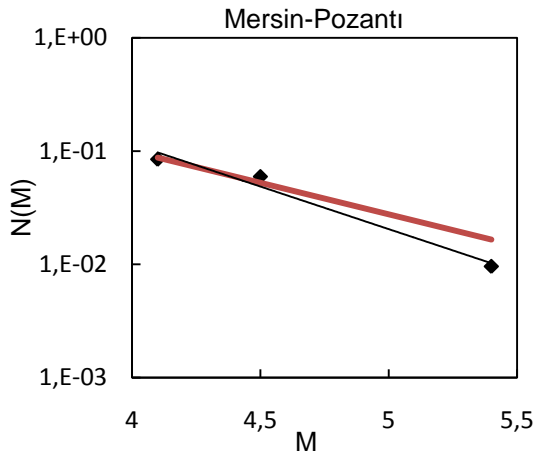


**Figure B.43 Source Id # 58, 59**

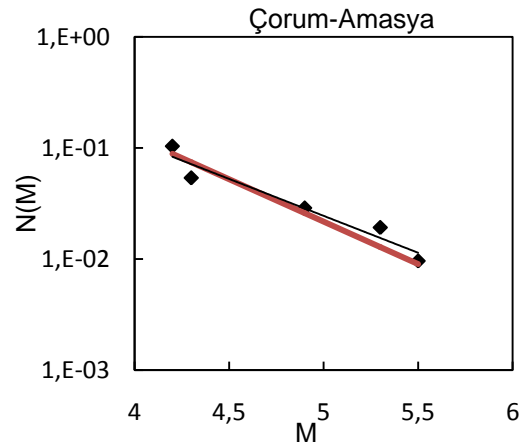


**Figure B.44 Source Id # 60**

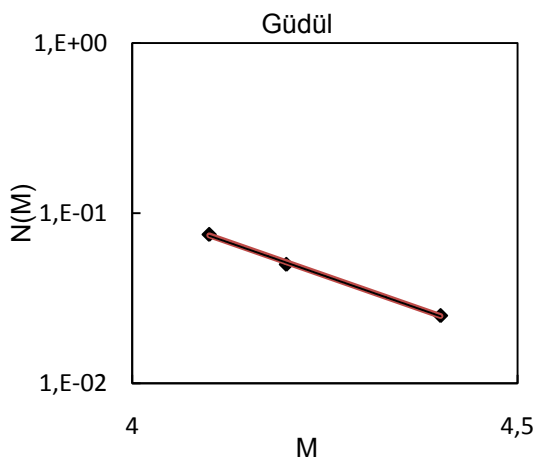


**Figure B.45 Source Id # 62**

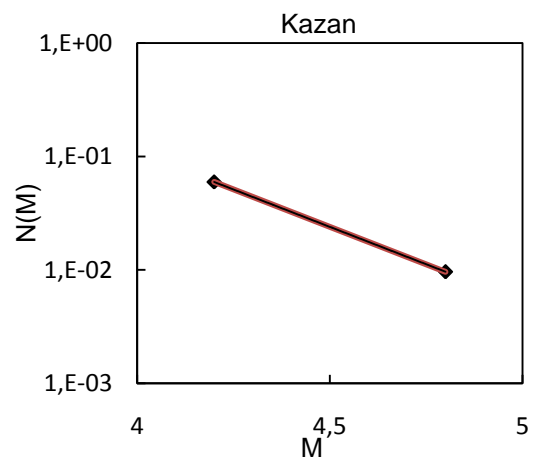


**Figure B.46 Source Id # 63**

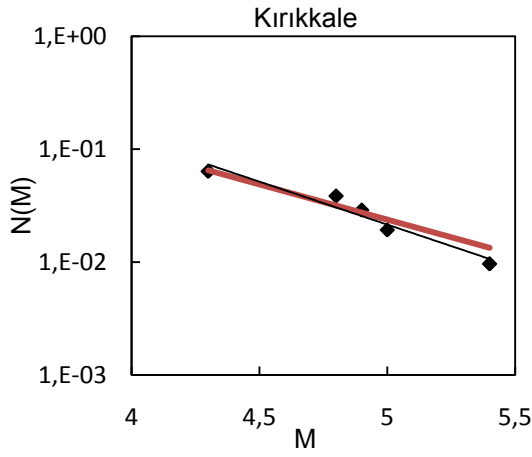


**Figure B.47 Source Id # 64**

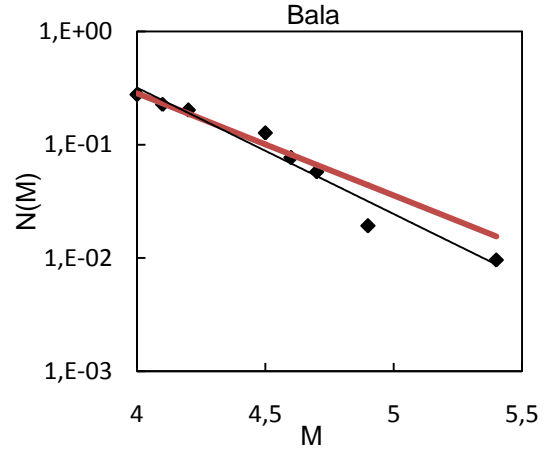


**Figure B.48 Source Id # 65**

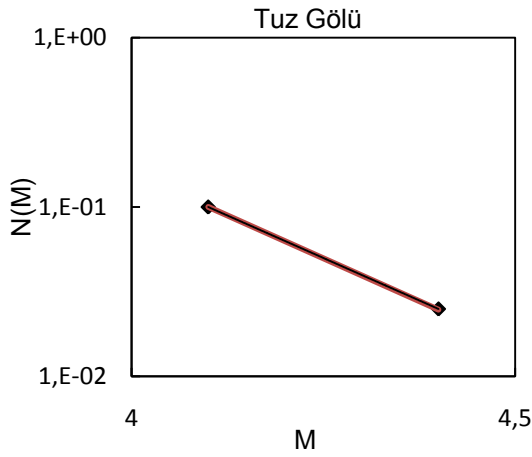


**Figure B.49 Source Id # 66, 67, 68, 69**

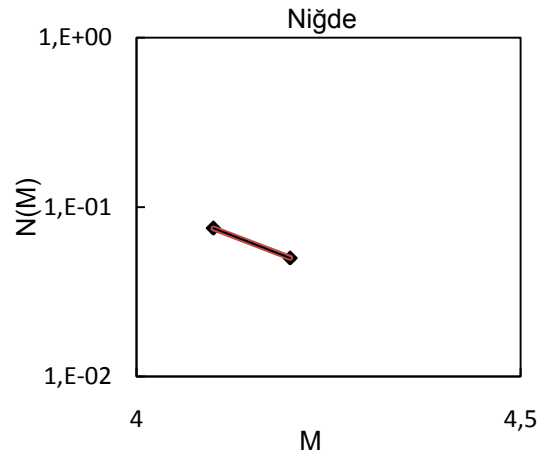


**Figure B.50 Source Id # 70**

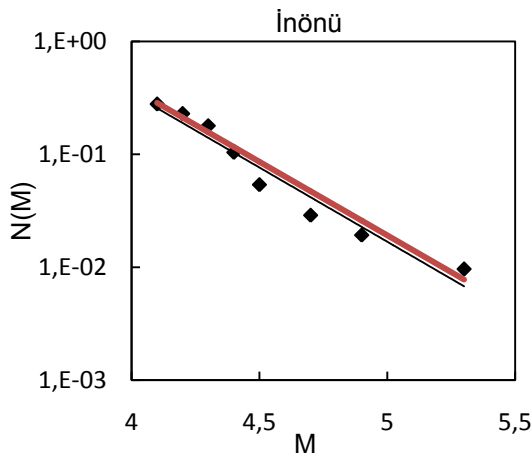


**Figure B.51 Source Id # 72**

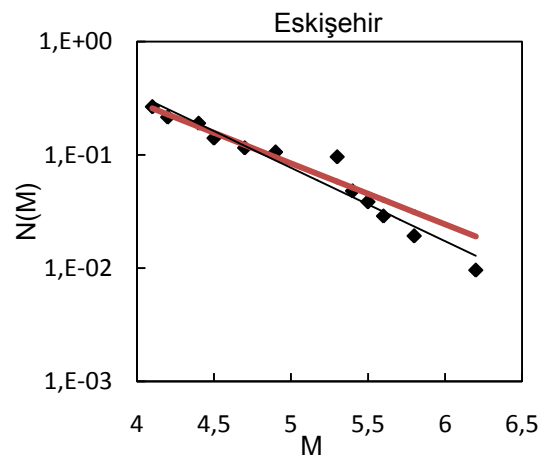


**Figure B.52 Source Id # 73, 74, 75**

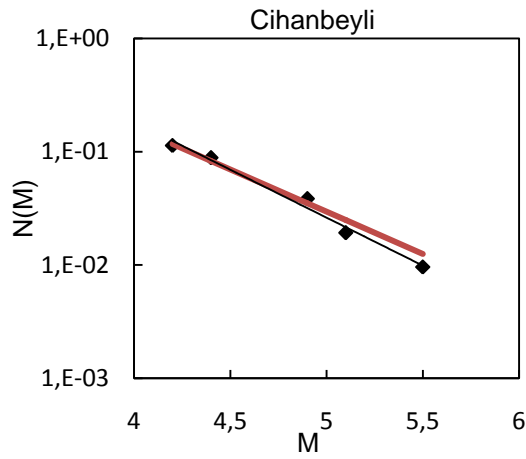


**Figure B.53 Source Id # 77, 78, 79, 80**

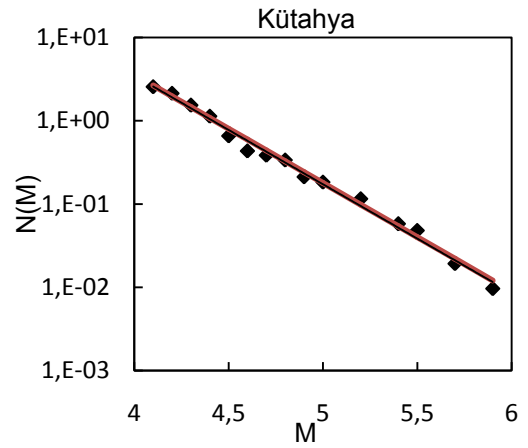


**Figure B.54 Source Id # 81**

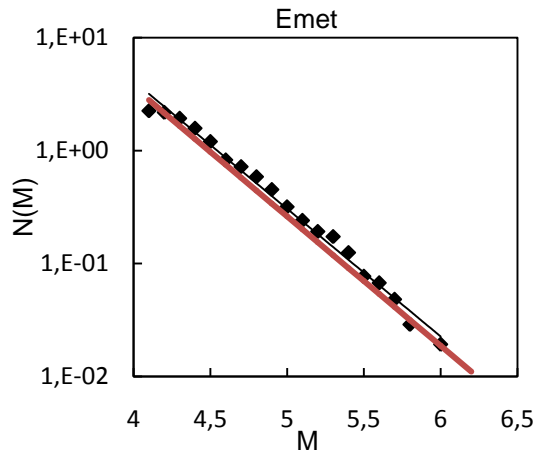


**Figure B.55 Source Id # 82**

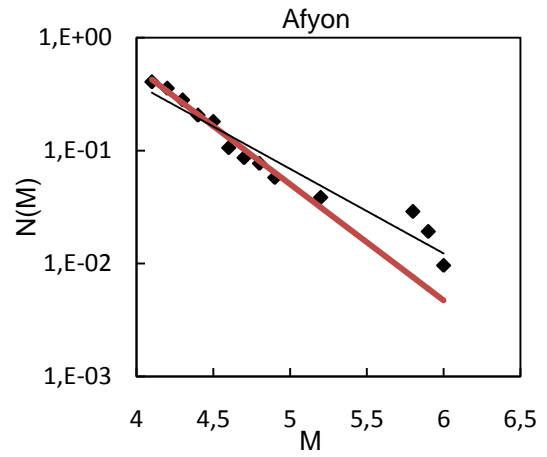


**Figure B.56 Source Id # 83**

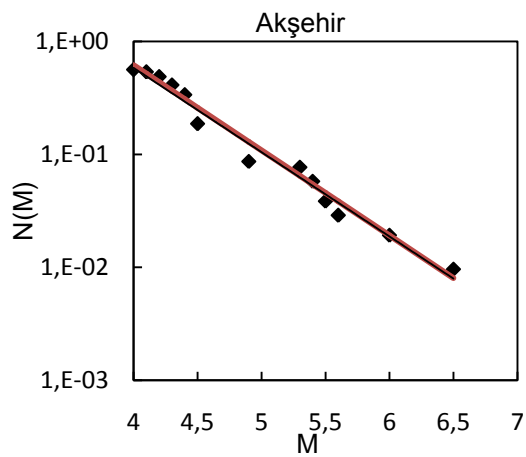


**Figure B.57 Source Id # 84**

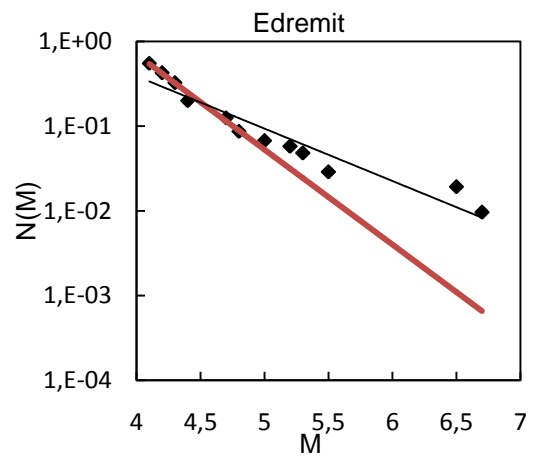


**Figure B.58 Source Id # 85**

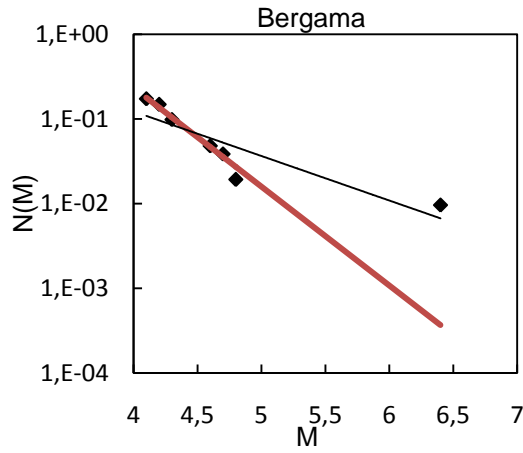


**Figure B.59 Source Id # 86**

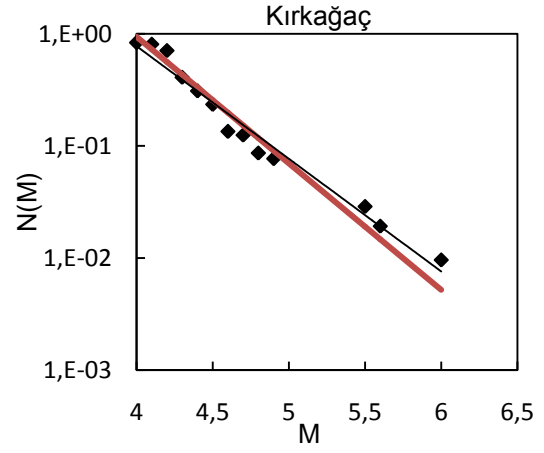


**Figure B.60 Source Id # 87**

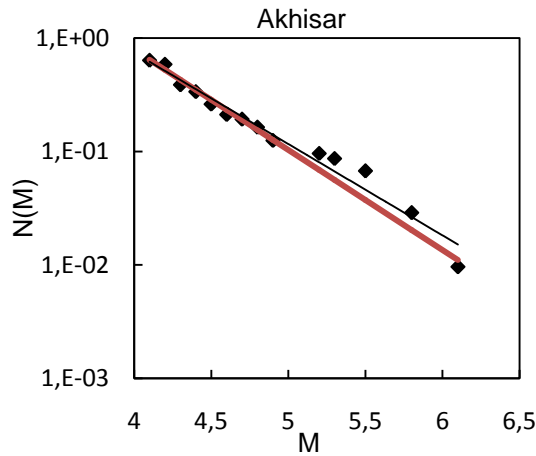


**Figure B.61 Source Id # 88, 89, 90, 91**

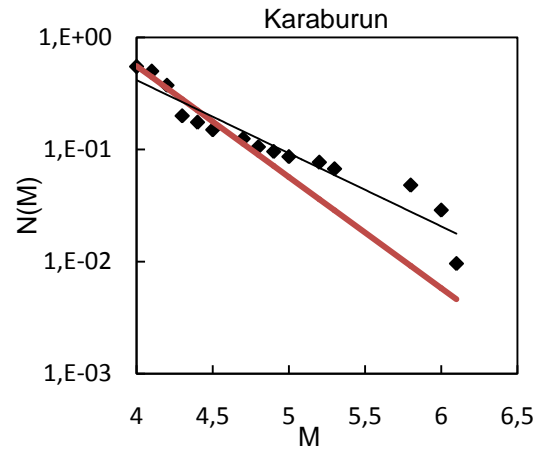


**Figure B.62 Source Id # 92**

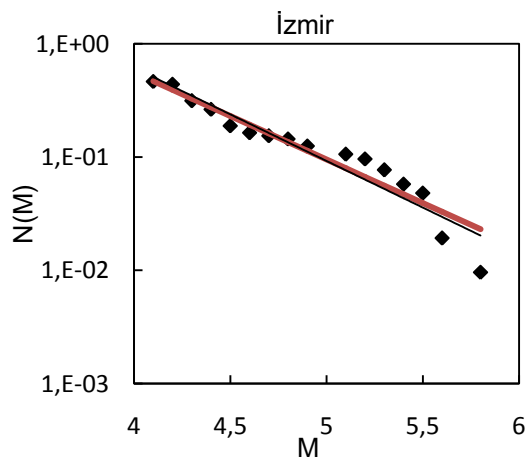


**Figure B.63 Source Id # 93**

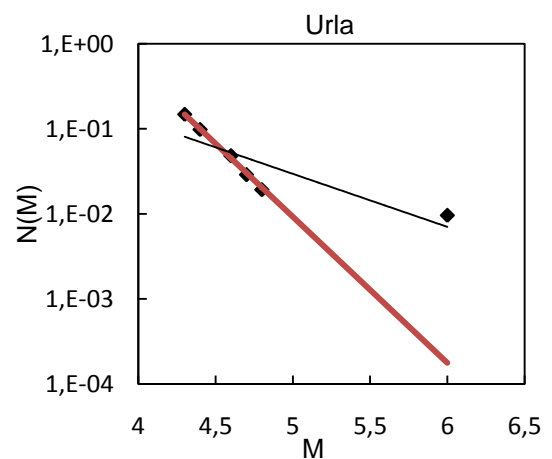


**Figure B.64 Source Id # 94**

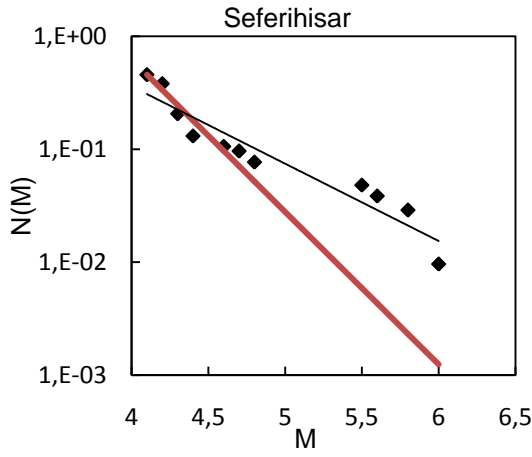


**Figure B.65 Source Id # 95**

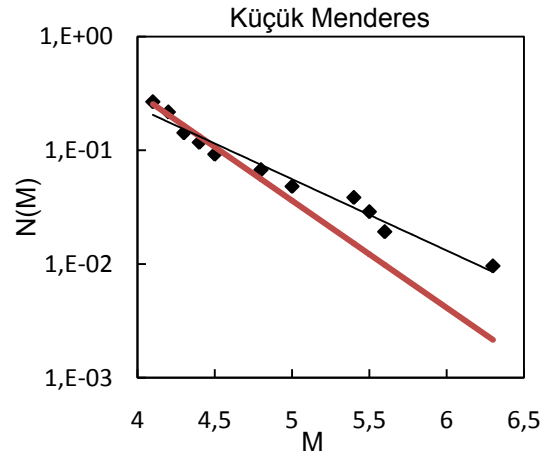


**Figure B.66 Source Id # 96**

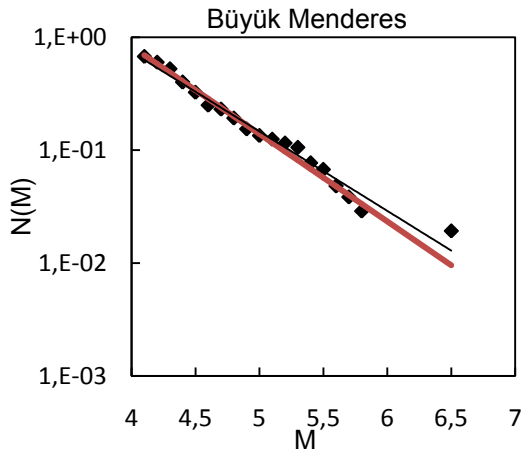


**Figure B.67 Source Id # 97, 98, 99,100, 101, 102**

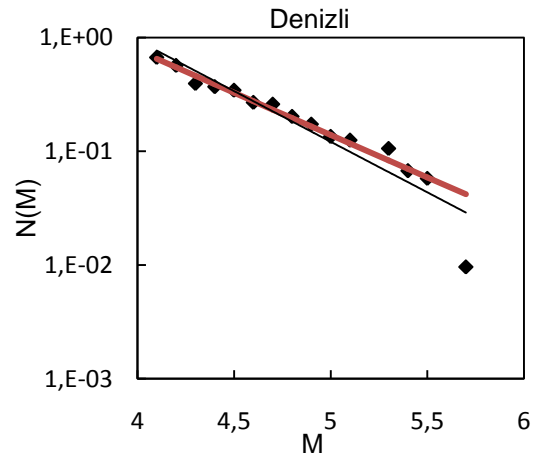


**Figure B.68 Source Id # 103, 104**

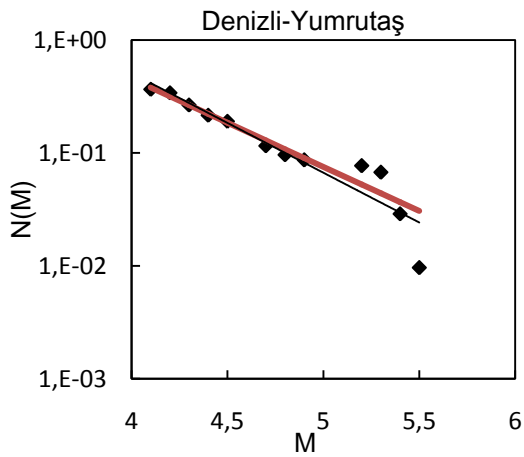


**Figure B.69 Source Id # 105**

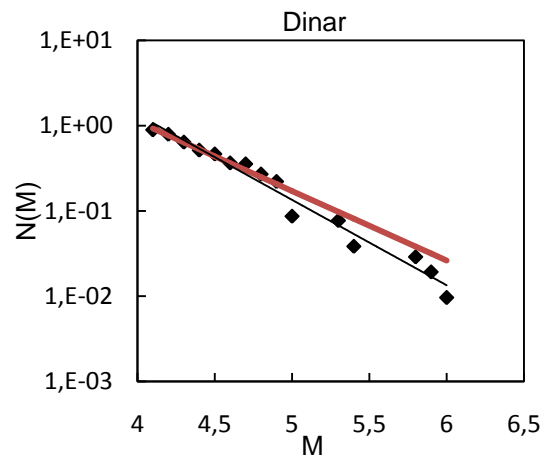


**Figure B.70 Source Id # 106, 107**

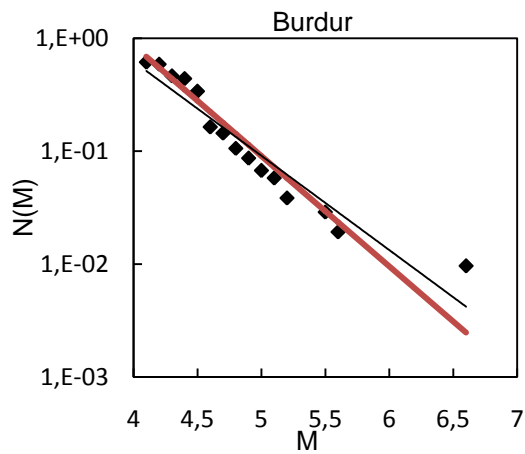


**Figure B.71 Source Id # 108, 109, 110**

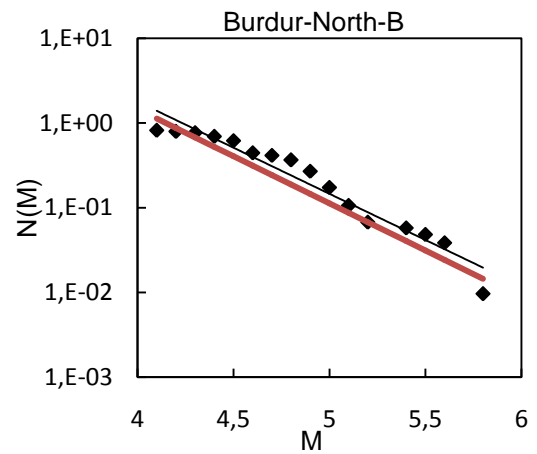


**Figure B.72 Source Id # 111**

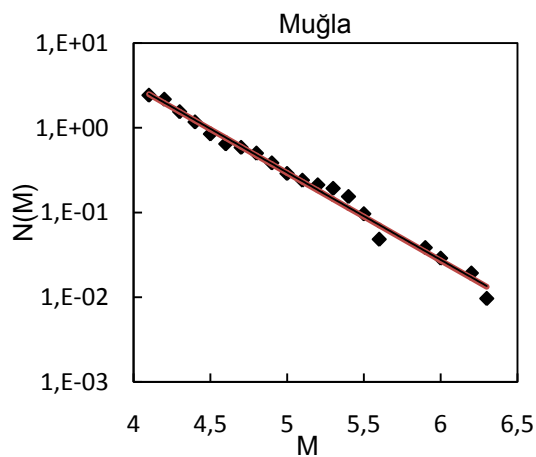


**Figure B.73 Source Id # 112**

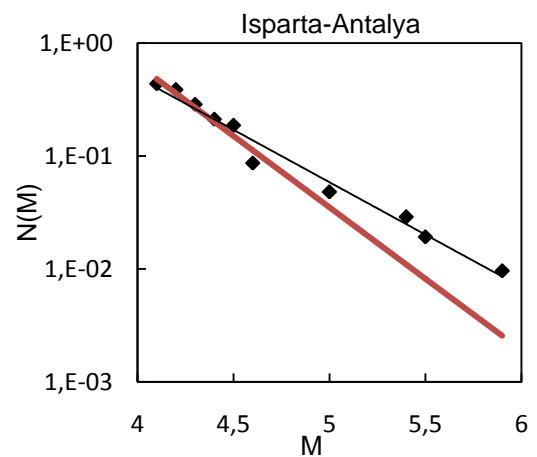


**Figure B.74 Source Id # 113**

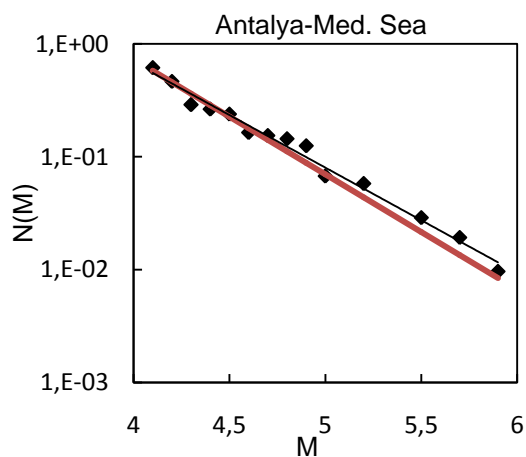


**Figure B.75 Source Id # 114, 115**

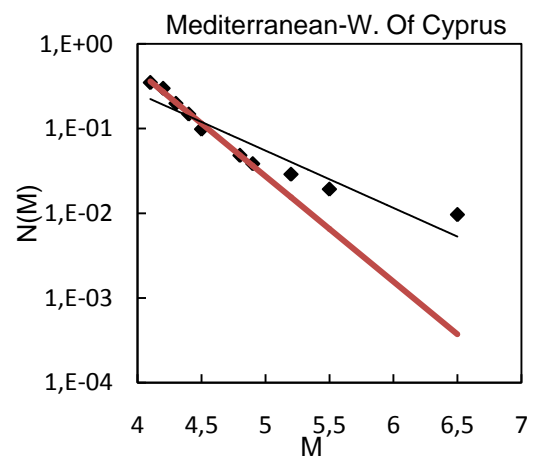


**Figure B.76 Source Id # 116**

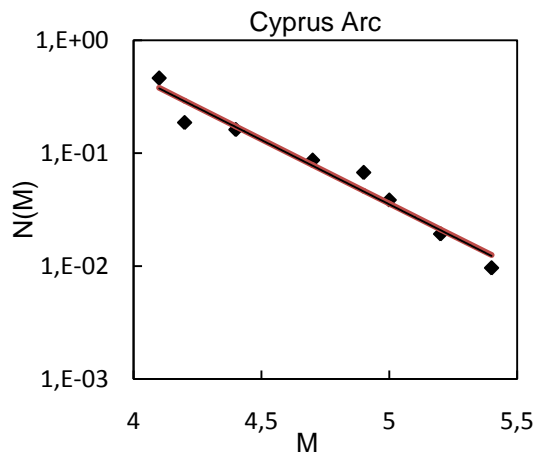


**Figure B.77 Source Id # 117**

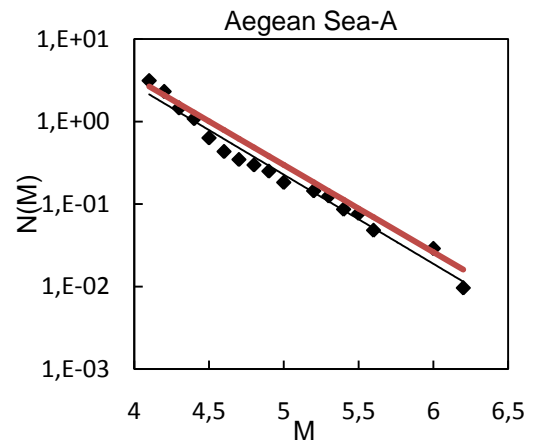


**Figure B.78 Source Id # 118**

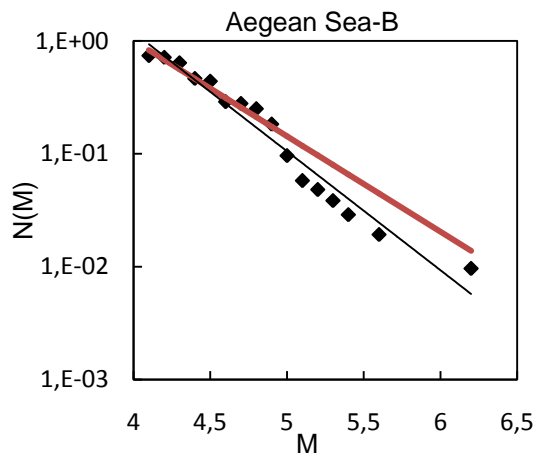


**Figure B.79 Source Id # 119**

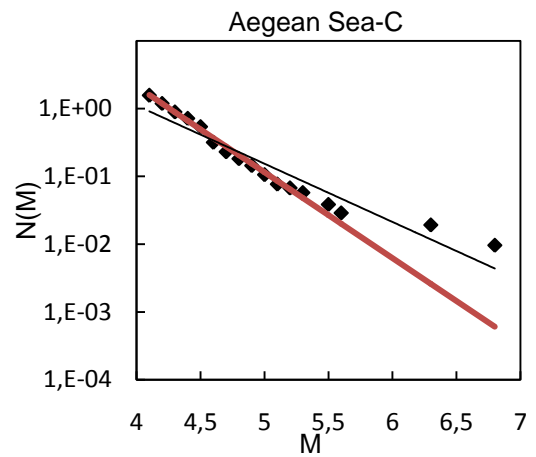


**Figure B.80 Source Id # 120**

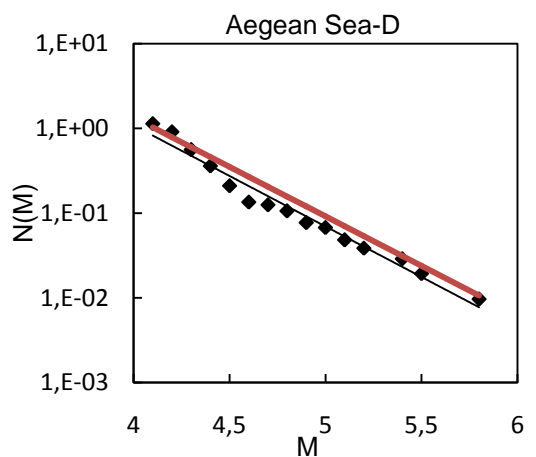


**Figure B.81 Source Id # 121**

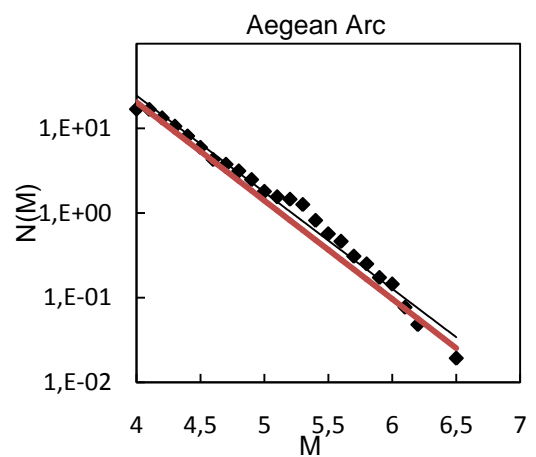


**Figure B.82 Source Id # 122**



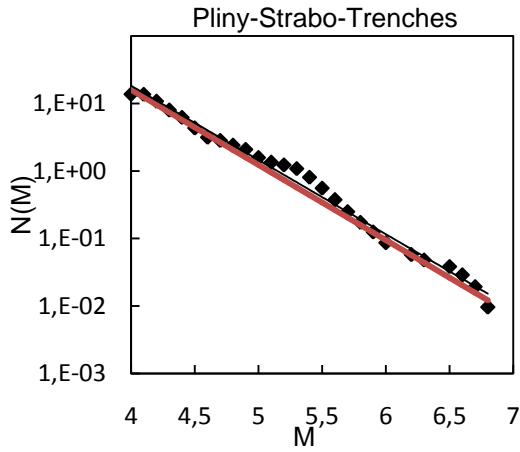


**Figure B.83 Source Id # 123**

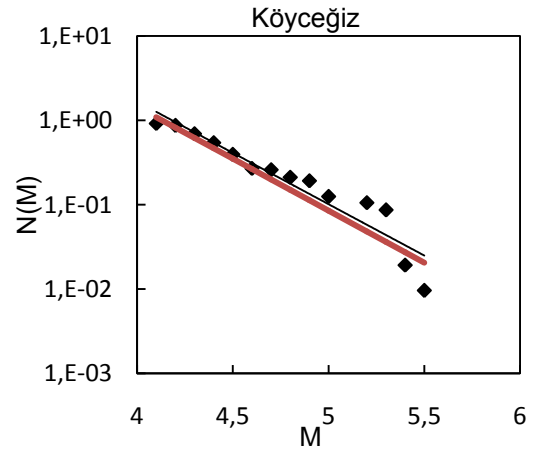


**Figure B.84 Source Id # 124**

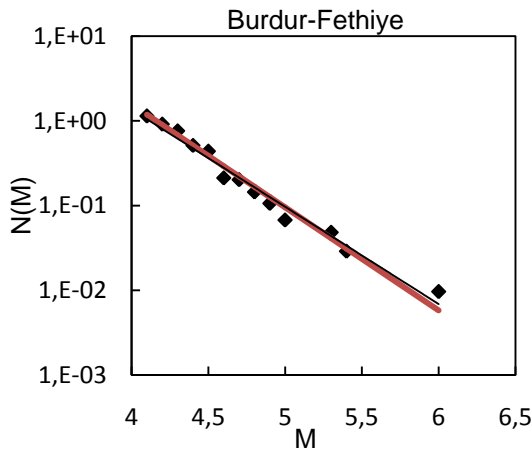


**Figure B.85 Source Id # 125**

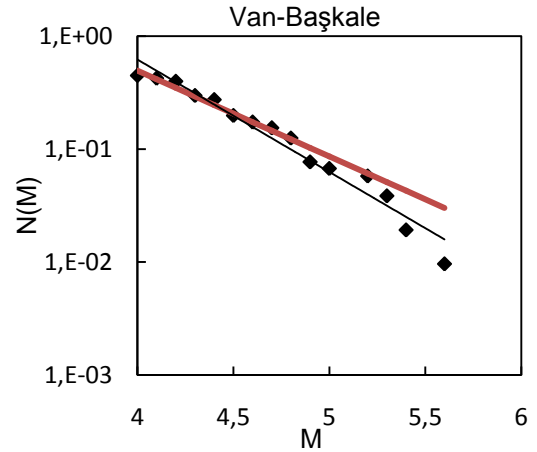


**Figure B.86 Source Id # 126**

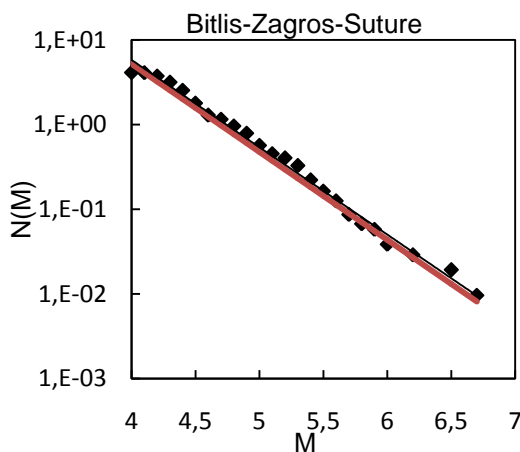


**Figure B.87 Source Id # 127**

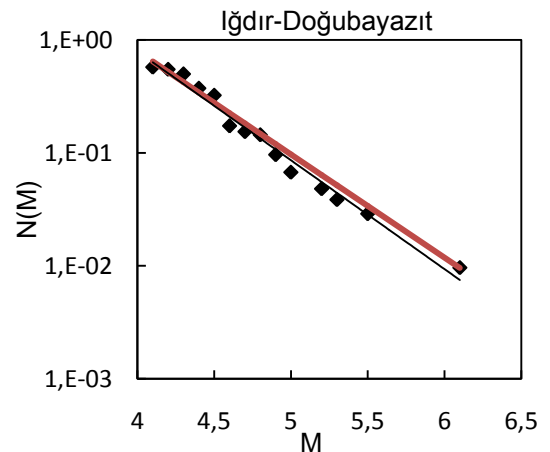


**Figure B.88 Source Id # 128**

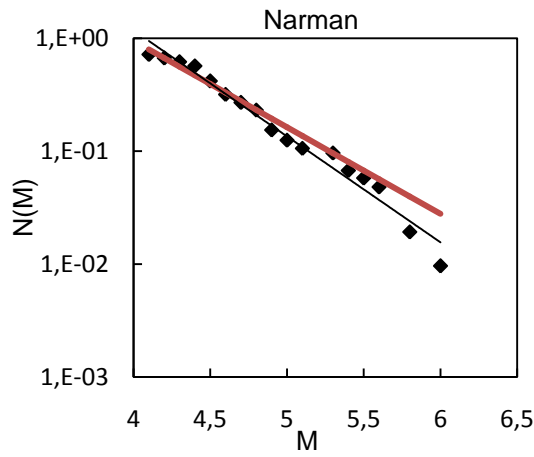


**Figure B.89 Source Id # 129**

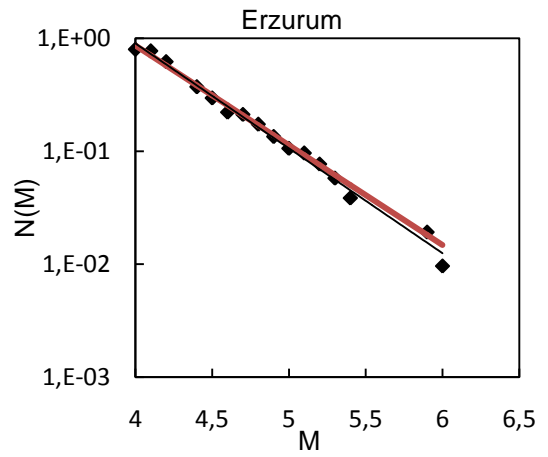


**Figure B.90 Source Id # 130**

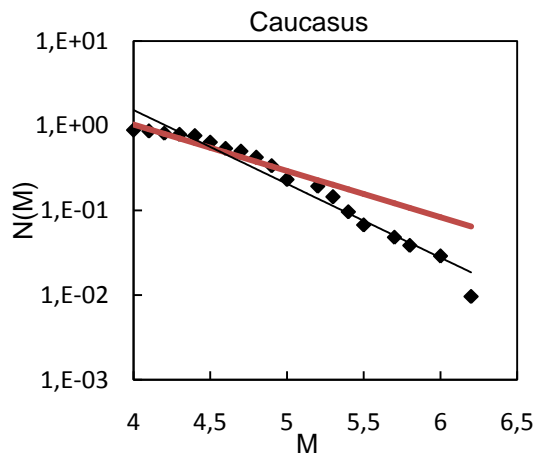


**Figure B.91 Source Id # 131**

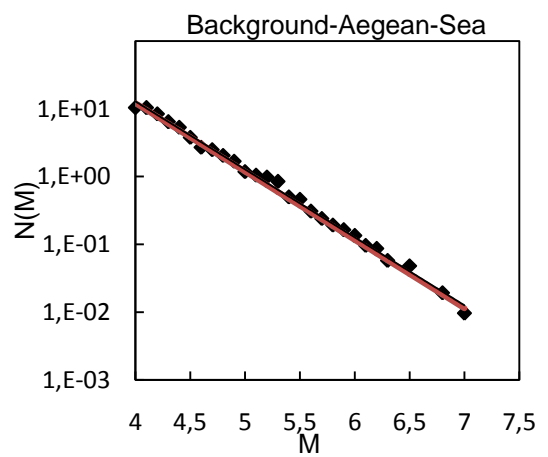


**Figure B.92 Source Id # 132**

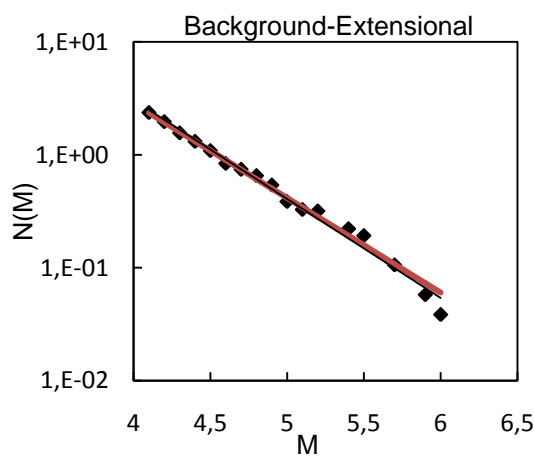


**Figure B.93 Source Id # 133**

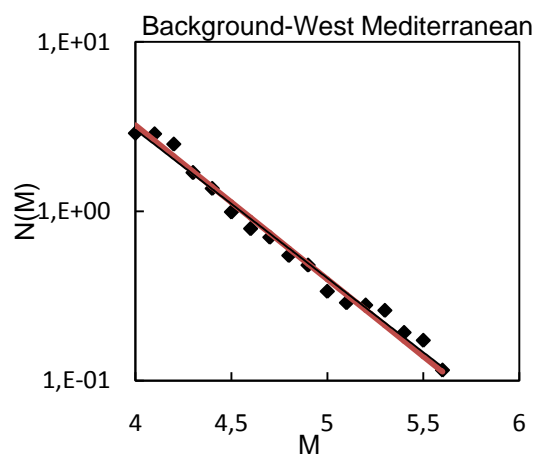


**Figure B.94 Source Id # 134**

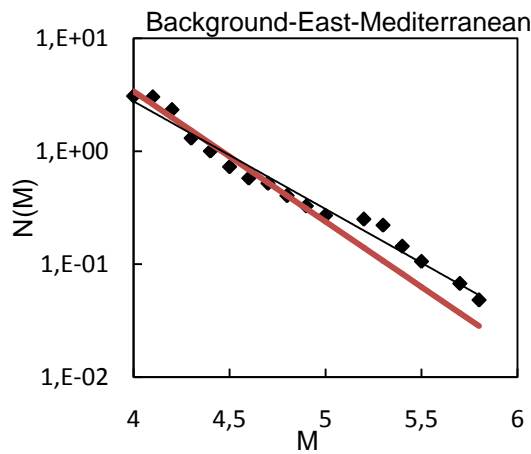


**Figure B.95 Source Id # 135**

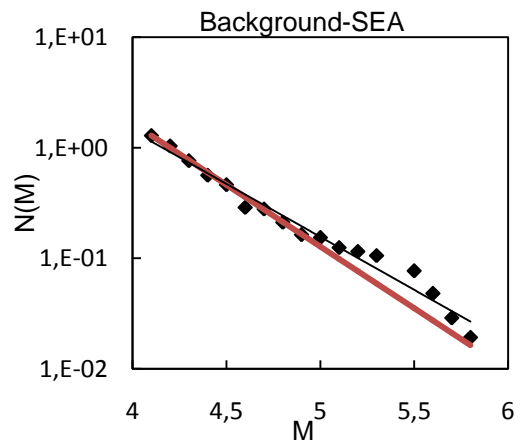


**Figure B.96 Source Id # 136**

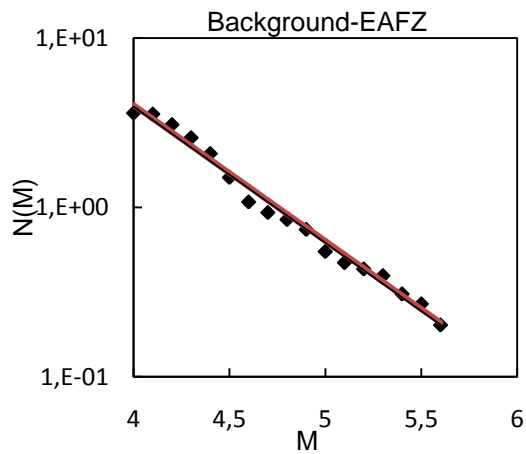


**Figure B.97 Source Id # 137**

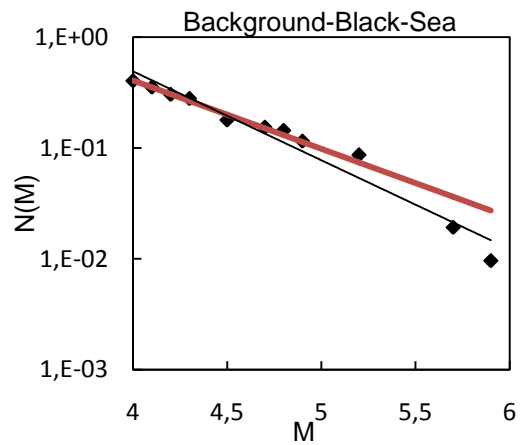


**Figure B.98 Source Id # 138**

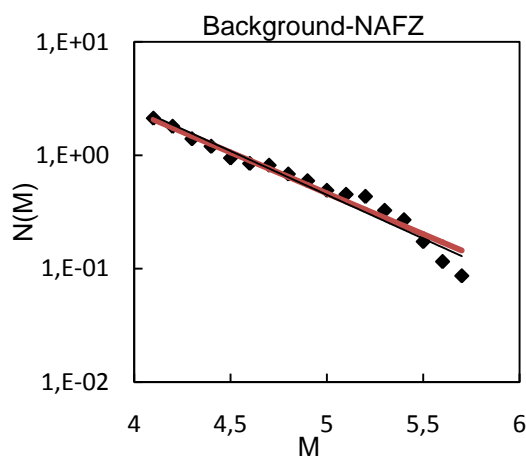


**Figure B.99 Source Id # 139**

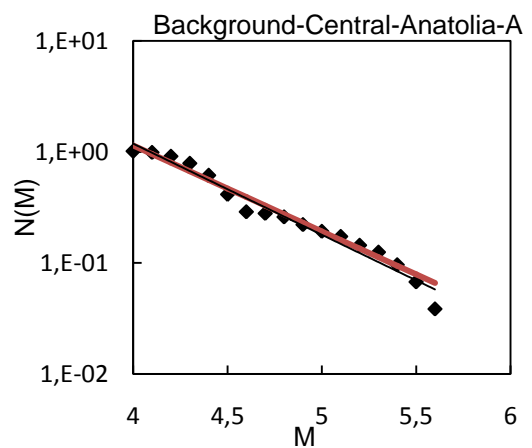


**Figure B.100 Source Id # 140**

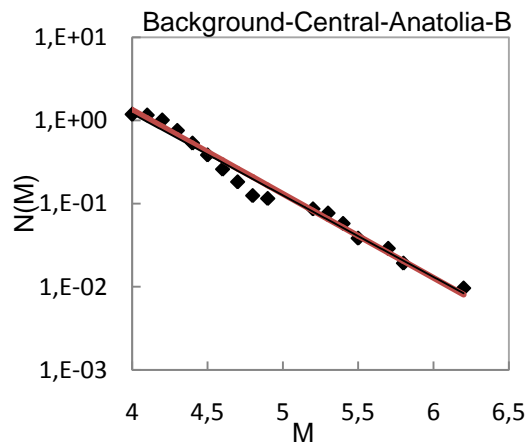


**Figure B.101 Source Id # 141**

## APPENDIX C

### PROPERTIES OF GENERIC SOIL PROFILES

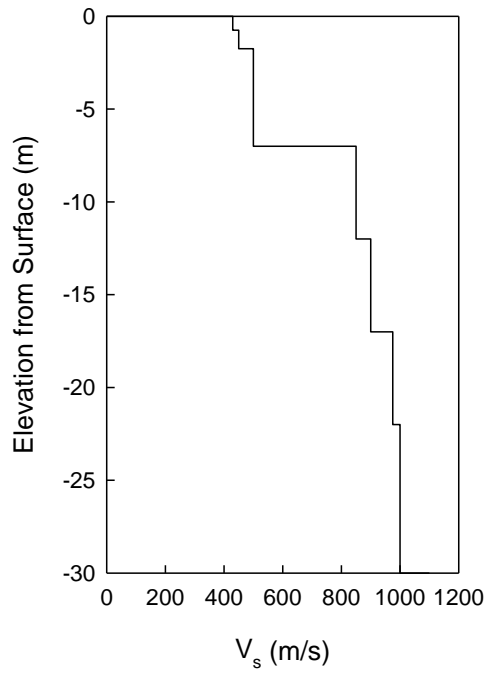


**Figure C.1 Shear wave velocity profile for generic site B1**

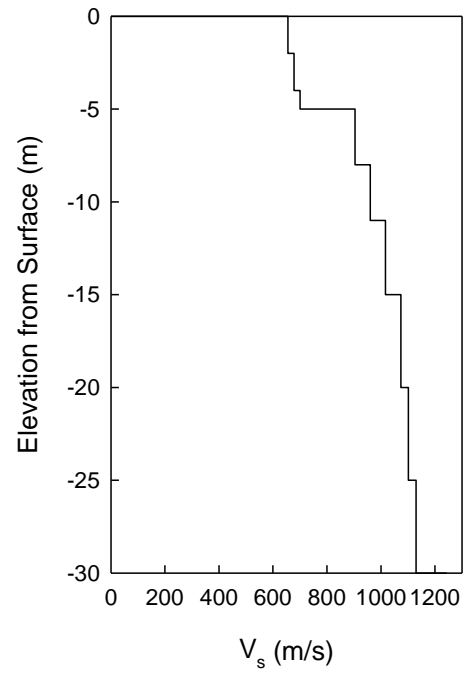


**Figure C.2 Shear wave velocity profile for generic site B2**

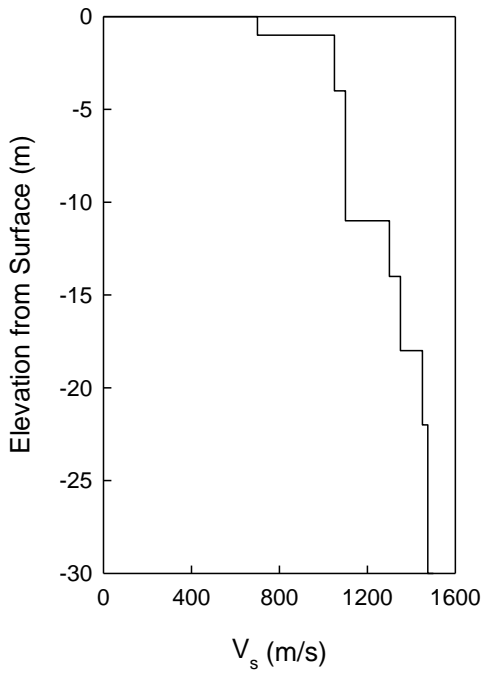


**Figure C.3 Shear wave velocity profile for generic site B3**

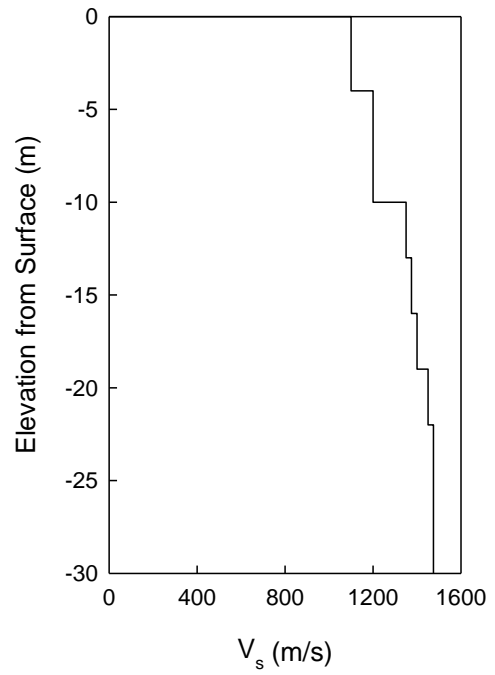


**Figure C.4 Shear wave velocity profile for generic site B4**

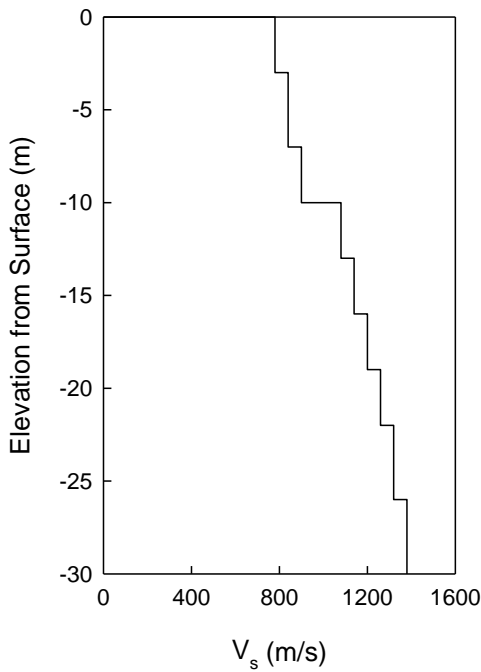


**Figure C.5 Shear wave velocity profile for generic site B5**

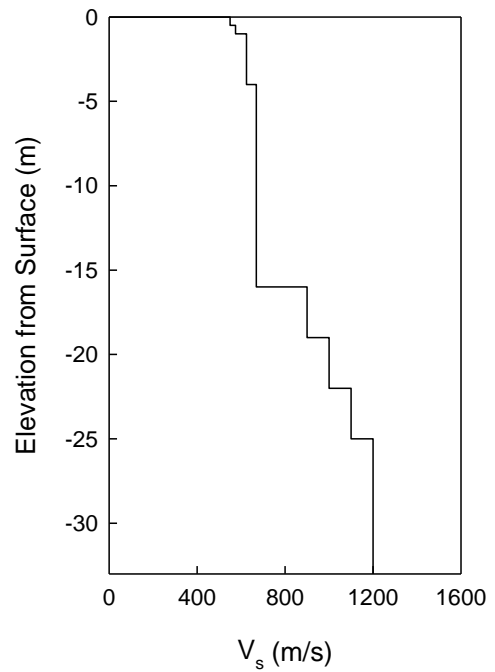


**Figure C.6 Shear wave velocity profile for generic site B6**

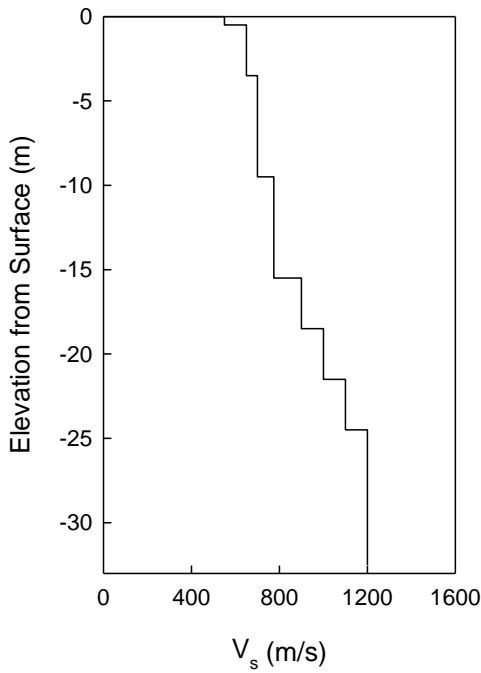


**Figure C.7 Shear wave velocity profile for generic site B7**

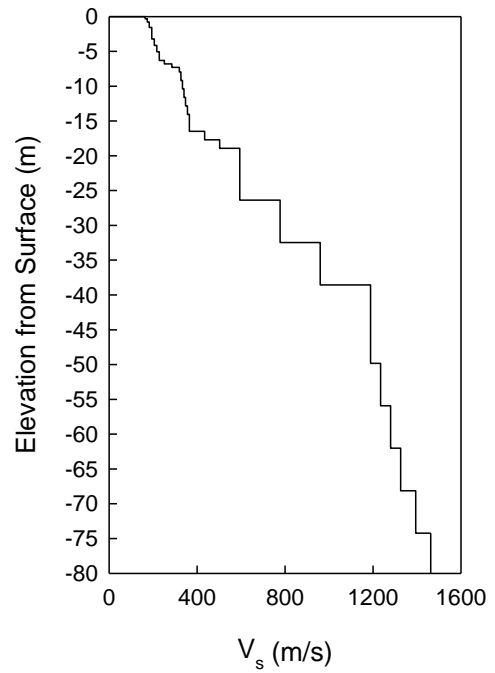


**Figure C.8 Shear wave velocity profile for generic site C1**

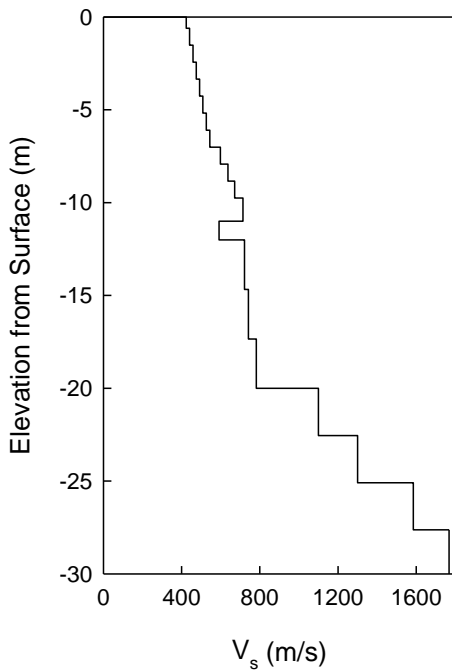


**Figure C.9 Shear wave velocity profile for generic site C2**

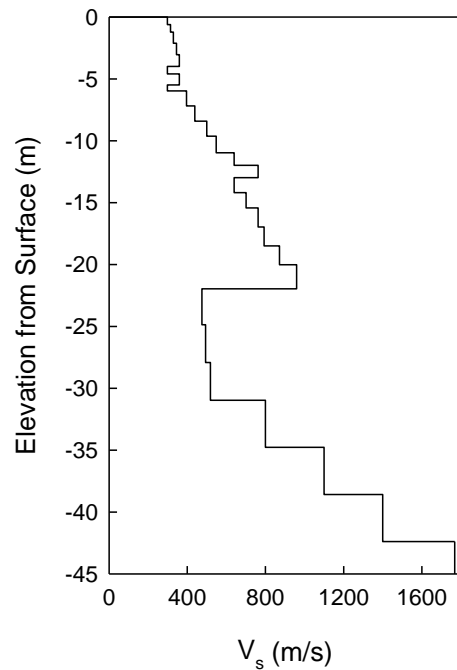


**Figure C.10 Shear wave velocity profile for generic site C3**

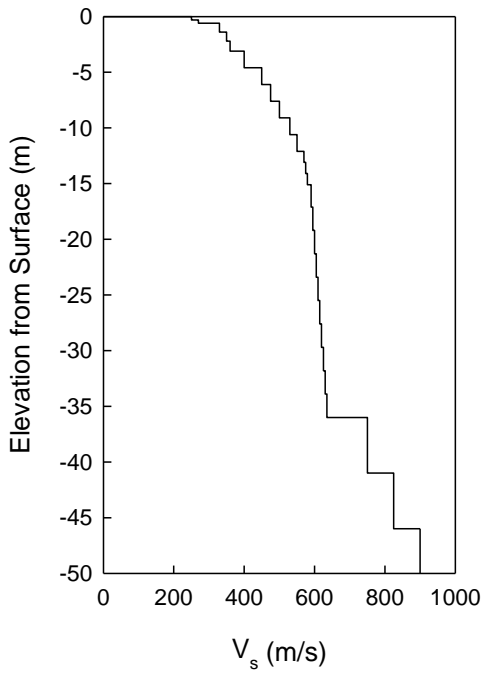


**Figure C.11 Shear wave velocity profile for generic site C4**

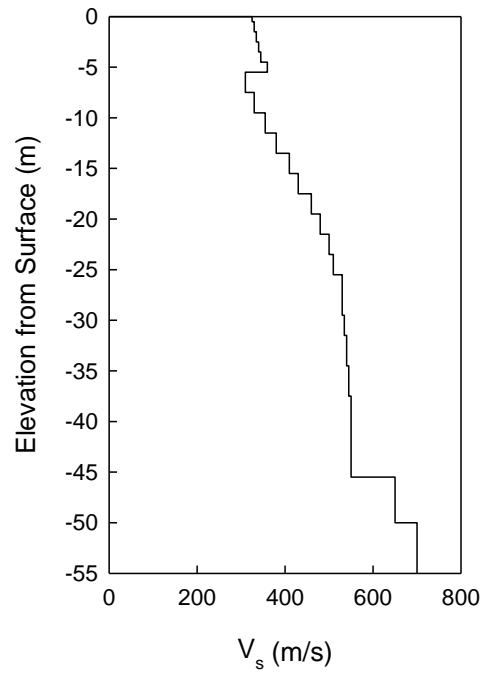


**Figure C.12 Shear wave velocity profile for generic site C5**

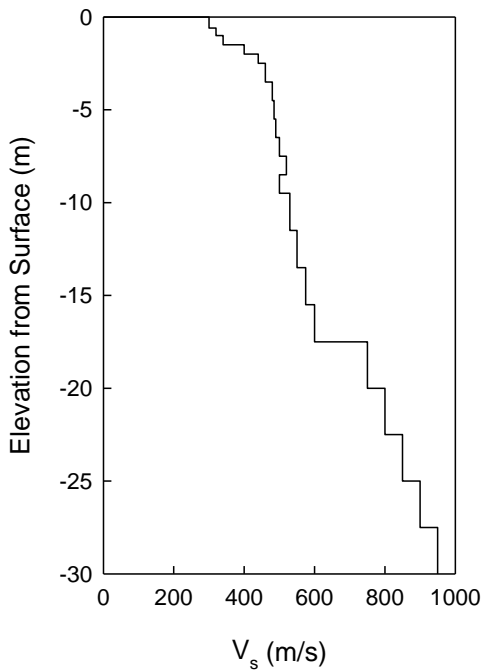


**Figure C.13 Shear wave velocity profile for generic site C6**

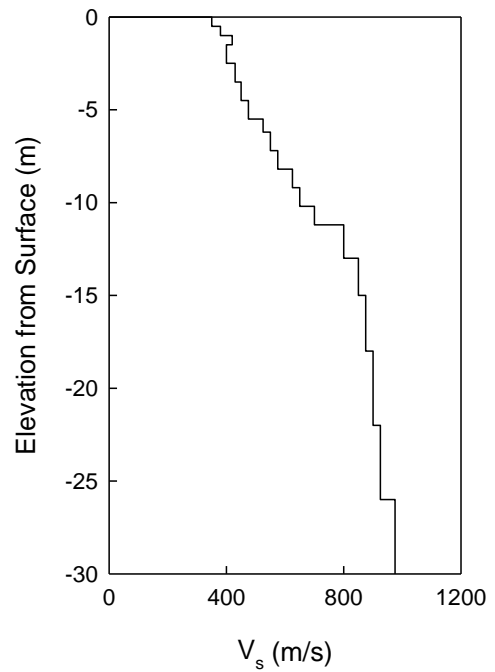


**Figure C.14 Shear wave velocity profile for generic site C7**



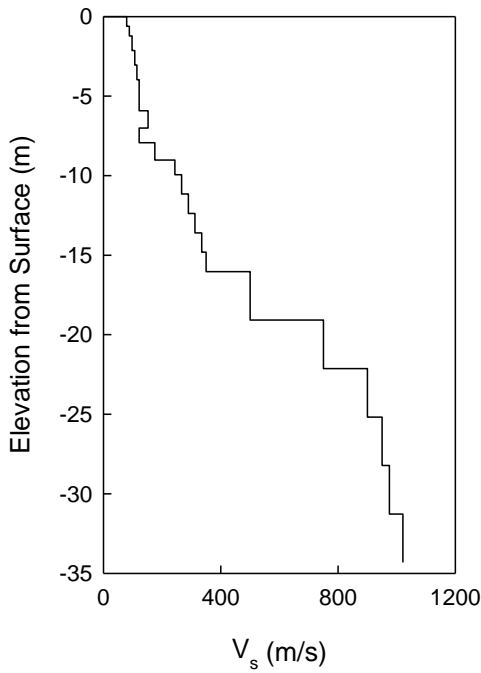


**Figure C.15 Shear wave velocity profile for generic site D1**

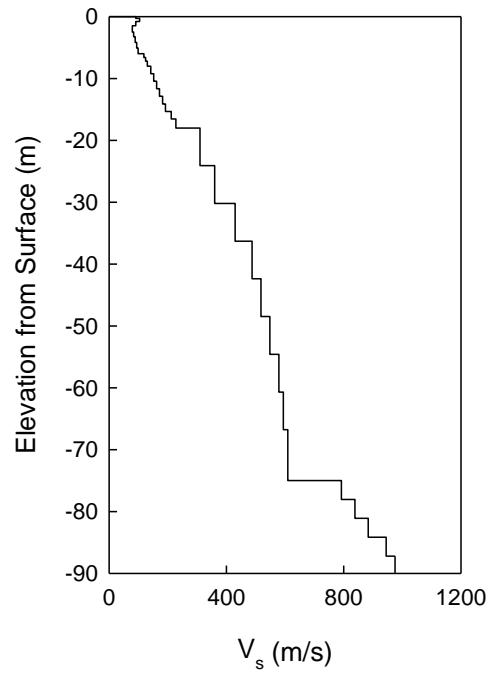


**Figure C.16 Shear wave velocity profile for generic site D2**

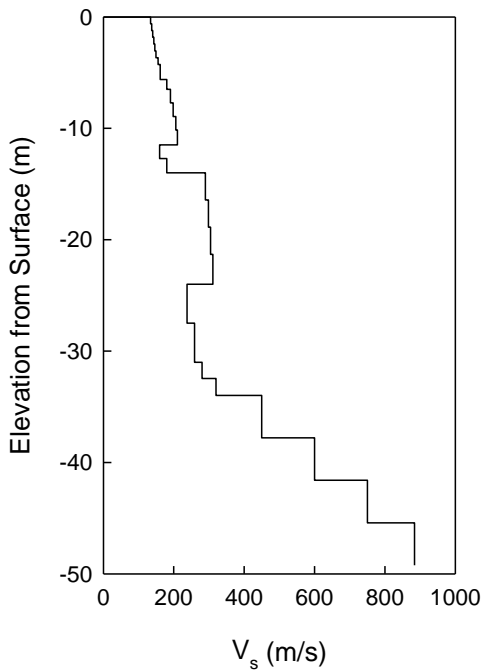


**Figure C.17 Shear wave velocity profile for generic site D3**

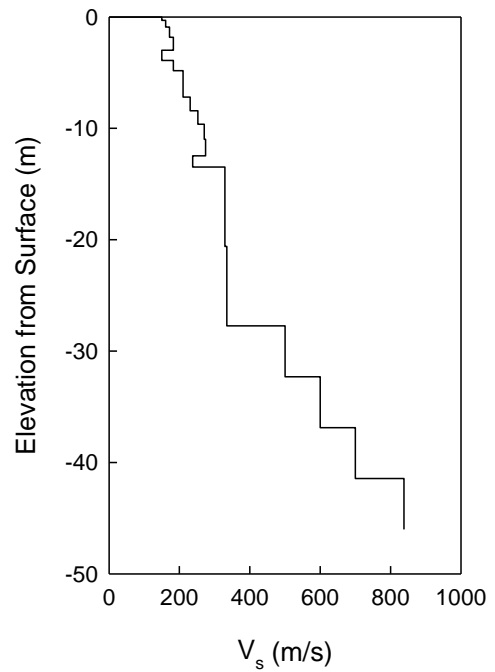


**Figure C.18 Shear wave velocity profile for generic site D4**

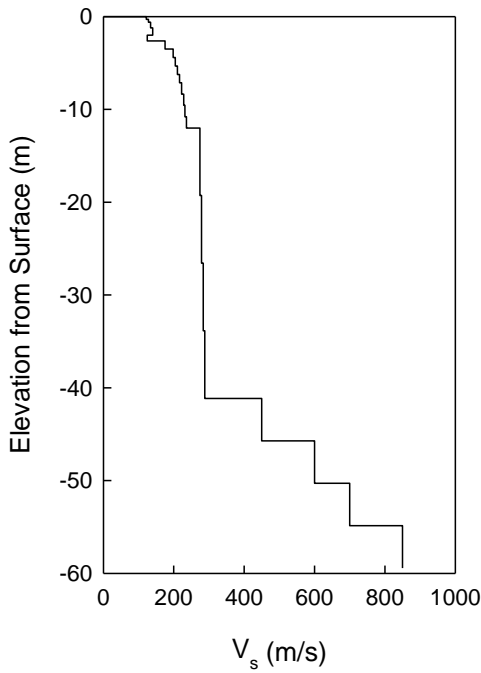


**Figure C.19** Shear wave velocity profile for generic site D5

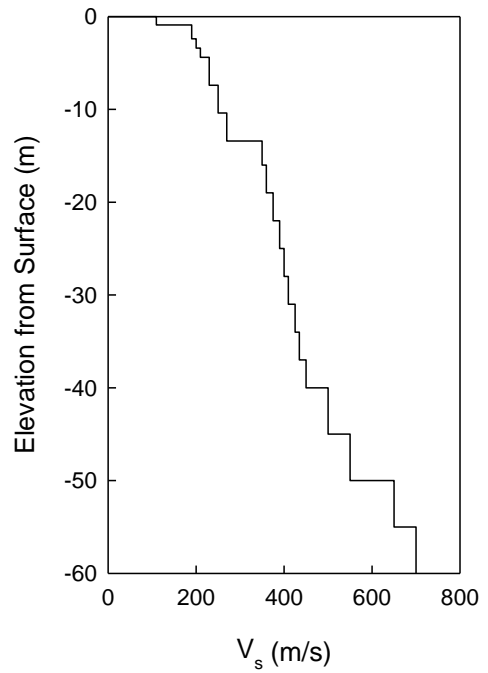


**Figure C.20** Shear wave velocity profile for generic site D6

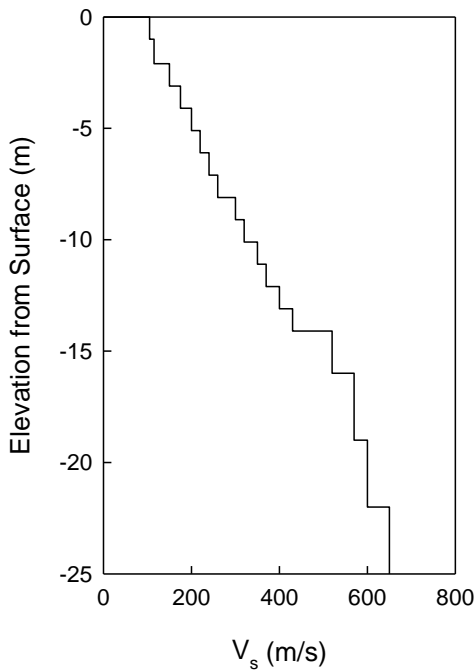


**Figure C.21** Shear wave velocity profile for generic site D7

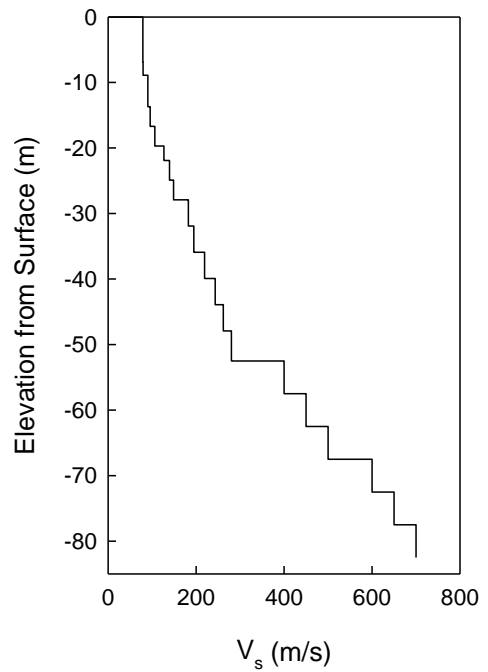


**Figure C.22** Shear wave velocity profile for generic site E1

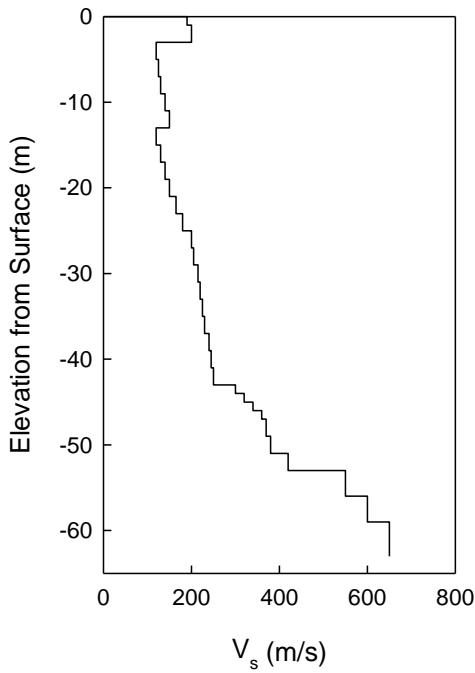


**Figure C.23 Shear wave velocity profile for generic site E2**

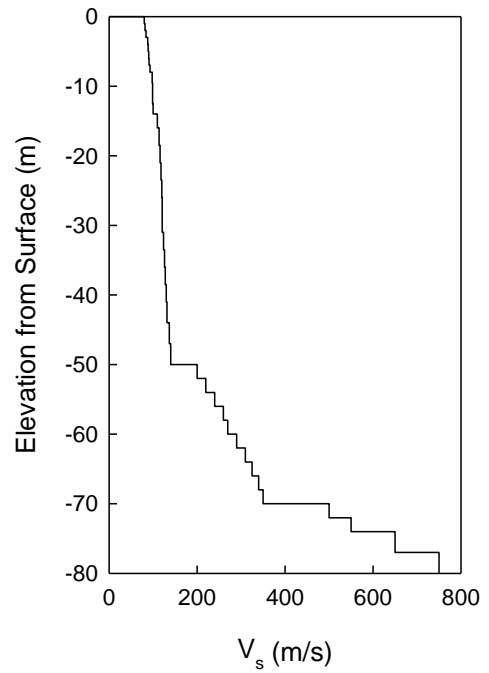


**Figure C.24 Shear wave velocity profile for generic site E3**

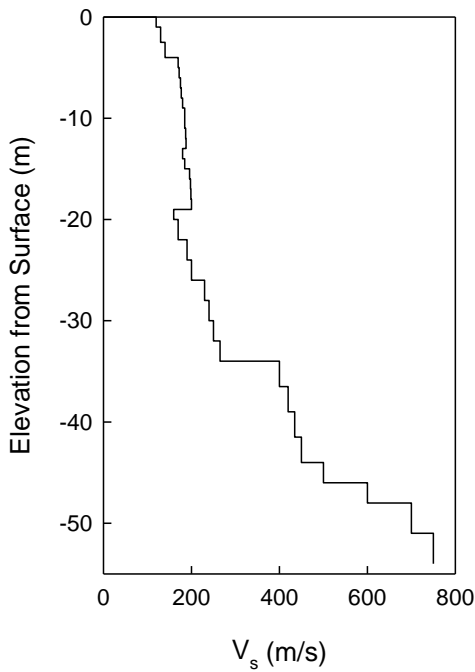


**Figure C.25 Shear wave velocity profile for generic site E4**

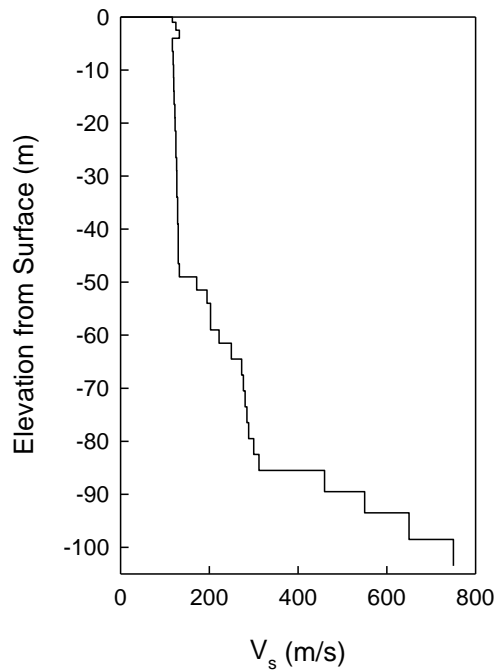


**Figure C.26 Shear wave velocity profile for generic site E5**

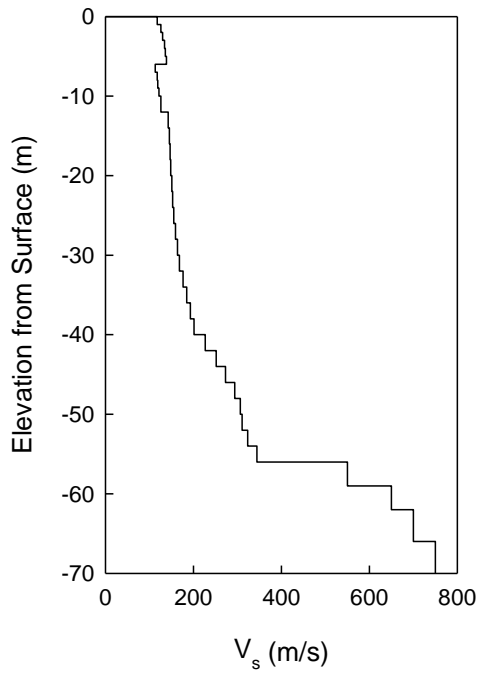


**Figure C.27 Shear wave velocity profile for generic site E6**

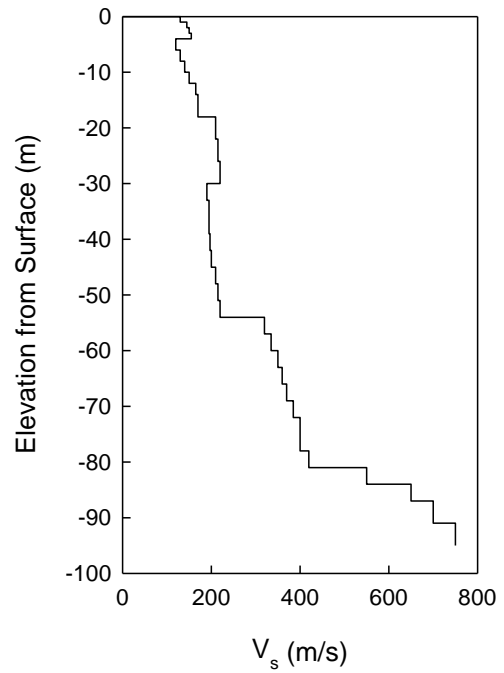


**Figure C.28 Shear wave velocity profile for generic site E7**

**Table C.1 Dynamic soil properites of generic site B1**

Layer No	Material ID	Layer Thickness (m)	Unit Weight (kN/m <sup>3</sup> )	V <sub>s</sub> (m/s)	Cumulative Depth (m)
1	Clay PI=20	0.75	18.9	430	0.75
2	Clay PI=20	1.00	18.9	450	1.75
3	W. Rock*	1.00	19.6	500	2.75
4	W. Rock*	1.00	19.6	500	3.75
5	W. Rock*	1.00	19.6	500	4.75
6	W. Rock*	1.00	19.6	500	5.75
7	W. Rock*	1.25	19.6	500	7.00
8	Rock	5.00	20.4	850	12.00
9	Rock	5.00	20.4	900	17.00
10	Rock	5.00	20.4	975	22.00
11	Rock	8.00	20.4	1000	30.00
12	Bedrock		20.4	1100	

\*: Weathered Rock

**Table C.2 Dynamic soil properites of generic site B2**

Layer No	Material ID	Layer Thickness (m)	Unit Weight (kN/m <sup>3</sup> )	V <sub>s</sub> (m/s)	Cumulative Depth (m)
1	W. Rock	1.00	18.9	655	1.00
2	W. Rock	1.00	18.9	655	2.00
3	W. Rock	1.00	19.6	678	3.00
4	W. Rock	1.00	19.6	678	4.00
5	W. Rock	1.00	19.6	701	5.00
6	Rock	3.00	20.4	904	8.00
7	Rock	3.00	20.4	961	11.00
8	Rock	4.00	20.4	1017	15.00
9	Rock	5.00	20.4	1074	20.00
10	Rock	5.00	20.4	1102	25.00
11	Rock	5.00	20.4	1130	30.00
12	Bedrock		20.4	1243	

**Table C.3 Dynamic soil properites of generic site B3**

Layer No	Material No	Layer Thickness (m)	Unit Weight (kN/m <sup>3</sup> )	V <sub>s</sub> (m/s)	Cumulative Depth (m)
1	Gravel	1.00	18.9	700	1.00
2	W. Rock	1.00	19.6	1050	2.00
3	W. Rock	1.00	19.6	1050	3.00
4	W. Rock	1.00	19.6	1050	4.00
5	W. Rock	1.00	19.6	1100	5.00
6	W. Rock	1.00	19.6	1100	6.00
7	W. Rock	1.00	19.6	1100	7.00
8	W. Rock	1.00	19.6	1100	8.00
9	W. Rock	1.00	19.6	1100	9.00
10	W. Rock	1.00	19.6	1100	10.00
11	W. Rock	1.00	19.6	1100	11.00
12	Rock	3.00	20.4	1300	14.00
13	Rock	4.00	20.4	1350	18.00
14	Rock	4.00	20.4	1450	22.00
15	Rock	4.00	20.4	1475	26.00
16	Rock	4.00	20.4	1475	30.00
17	Bedrock		20.4	1500	

**Table C.4 Dynamic soil properites of generic site B4**

Layer No	Material ID	Layer Thickness (m)	Unit Weight (kN/m <sup>3</sup> )	Vs (m/s)	Cumulative Depth (m)
1	W. Rock	1.00	19.6	1100	1.00
2	W. Rock	1.00	19.6	1100	2.00
3	W. Rock	1.00	19.6	1100	3.00
4	W. Rock	1.00	19.6	1100	4.00
5	W. Rock	1.00	19.6	1200	5.00
6	W. Rock	1.00	19.6	1200	6.00
7	W. Rock	1.00	19.6	1200	7.00
8	W. Rock	1.00	19.6	1200	8.00
9	W. Rock	1.00	19.6	1200	9.00
10	W. Rock	1.00	19.6	1200	10.00
11	Rock	3.00	20.4	1350	13.00
12	Rock	3.00	20.4	1375	16.00
13	Rock	3.00	20.4	1400	19.00
14	Rock	3.00	20.4	1450	22.00
15	Rock	4.00	20.4	1475	26.00
16	Rock	4.00	20.4	1475	30.00
17	Bedrock		20.4	1500	

**Table C.5 Dynamic soil properites of generic site B5**

Layer No	Material ID	Layer Thickness (m)	Unit Weight (kN/m <sup>3</sup> )	Vs (m/s)	Cumulative Depth (m)
1	W. Rock	1.00	19.6	780	1.00
2	W. Rock	1.00	19.6	780	2.00
3	W. Rock	1.00	19.6	780	3.00
4	W. Rock	1.00	19.6	840	4.00
5	W. Rock	1.00	19.6	840	5.00
6	W. Rock	1.00	19.6	840	6.00
7	W. Rock	1.00	19.6	840	7.00
8	W. Rock	1.00	19.6	900	8.00
9	W. Rock	1.00	19.6	900	9.00
10	W. Rock	1.00	19.6	900	10.00
11	Rock	3.00	20.4	1080	13.00
12	Rock	3.00	20.4	1140	16.00
13	Rock	3.00	20.4	1200	19.00
14	Rock	3.00	20.4	1260	22.00
15	Rock	4.00	20.4	1320	26.00
16	Rock	4.00	20.4	1380	30.00
17	Bedrock		20.4	1440	

**Table C.6 Dynamic soil properites of generic site B6**

Layer No	Material ID	Layer Thickness (m)	Unit Weight (kN/m <sup>3</sup> )	Vs (m/s)	Cumulative Depth (m)
1	Gravel	0.50	18.9	550	0.50
2	Gravel	0.50	18.9	575	1.00
3	W. Rock	1.00	19.6	625	2.00
4	W. Rock	1.00	19.6	625	3.00
5	W. Rock	1.00	19.6	625	4.00
6	W. Rock	1.00	19.6	670	5.00
7	W. Rock	1.00	19.6	670	6.00
8	W. Rock	1.00	19.6	670	7.00
9	W. Rock	1.00	19.6	670	8.00
10	W. Rock	1.00	19.6	670	9.00
11	W. Rock	1.00	19.6	670	10.00
12	W. Rock	1.00	19.6	670	11.00
13	W. Rock	1.00	19.6	670	12.00
14	W. Rock	1.00	19.6	670	13.00
15	W. Rock	1.50	19.6	670	14.50
16	W. Rock	1.50	19.6	670	16.00
17	Rock	3.00	20.4	900	19.00
18	Rock	3.00	20.4	1000	22.00
19	Rock	3.00	20.4	1100	25.00
20	Rock	4.00	20.4	1200	29.00
21	Rock	4.00	20.4	1200	33.00
22	Bedrock		20.4	1250	

**Table C.7 Dynamic soil properites of generic site B7**

Layer No	Material ID	Layer Thickness (m)	Unit Weight (kN/m <sup>3</sup> )	V <sub>s</sub> (m/s)	Cumulative Depth (m)
1	Gravel	0.50	18.9	550	0.50
2	W. Rock	1.00	19.6	650	1.50
3	W. Rock	1.00	19.6	650	2.50
4	W. Rock	1.00	19.6	650	3.50
5	W. Rock	1.00	19.6	700	4.50
6	W. Rock	1.00	19.6	700	5.50
7	W. Rock	1.00	19.6	700	6.50
8	W. Rock	1.00	19.6	700	7.50
9	W. Rock	1.00	19.6	700	8.50
10	W. Rock	1.00	19.6	700	9.50
11	W. Rock	1.00	19.6	775	10.50
12	W. Rock	1.00	19.6	775	11.50
13	W. Rock	1.00	19.6	775	12.50
14	W. Rock	1.00	19.6	775	13.50
15	W. Rock	1.00	19.6	775	14.50
16	W. Rock	1.00	19.6	775	15.50
17	Rock	3.00	20.4	900	18.50
18	Rock	3.00	20.4	1000	21.50
19	Rock	3.00	20.4	1100	24.50
20	Rock	4.00	20.4	1200	28.50
21	Rock	4.00	20.4	1200	32.50
22	Bedrock		20.4	1250	



**Table C.8 Dynamic soil properites of generic site C1**

Layer No	Material ID	Layer Thickness (m)	Unit weight (kN/m <sup>3</sup> )	V <sub>s</sub> (m/s)	Cumulative Depth (m)
1	Clay, PI=30	0.30	17.3	165	0.30
2	Clay, PI=30	0.49	17.3	174	0.79
3	Clay, PI=30	0.76	17.3	183	1.55
4	Clay, PI=15	0.76	17.3	194	2.32
5	Clay, PI=15	0.91	18.1	194	3.23
6	Clay, PI=15	0.91	18.1	206	4.15
7	Clay, PI=15	0.91	18.1	217	5.06
8	Clay, PI=15	1.25	18.1	229	6.31
9	Sand, <1 ksc	0.49	18.9	251	6.80
10	Sand, <1 ksc	0.49	18.9	286	7.28
11	Clay, PI=15	0.67	17.3	320	7.96
12	Clay, PI=15	1.22	17.3	327	9.17
13	Clay, PI=15	1.22	17.3	334	10.39
14	Clay, PI=15	1.22	17.3	341	11.61
15	Clay, PI=15	1.22	17.3	347	12.83
16	Clay, PI=15	1.22	17.3	357	14.05
17	Clay, PI=15	1.22	17.3	366	15.27
18	Sand, average	1.22	18.9	366	16.49
19	Sand, average	1.22	18.9	434	17.71
20	Sand, average	1.22	18.9	503	18.93
21	Sand, average	1.34	18.9	594	20.27
22	Sand, >3 ksc	6.10	18.9	594	26.37
23	Sand, >3 ksc	6.10	18.9	777	32.46
24	Sand, >3 ksc	6.10	18.9	960	38.56
25	Sand, >3 ksc	6.71	18.9	1189	45.26
26	Sand, >3 ksc	4.57	19.6	1189	49.83
27	Rock	6.10	19.6	1234	55.93
28	Rock	6.10	19.6	1280	62.03
29	Rock	6.10	20.4	1326	68.12
30	Rock	6.10	20.4	1394	74.22
31	Rock	6.10	20.4	1463	80.31
32	Bedrock		20.4	1600	80.31

**Table C.9 Dynamic soil properites of generic site C2**

Layer No	Material ID	Layer Thickness (m)	Unit Weight (kN/m <sup>3</sup> )	V <sub>s</sub> (m/s)	Cumulative Depth (m)
1	Clay, PI=15	0.61	17.3	424	0.61
2	Clay, PI=15	0.91	17.3	441	1.52
3	Clay, PI=15	0.91	17.3	458	2.44
4	Clay, PI=15	0.91	17.3	475	3.35
5	Clay, PI=15	0.91	17.3	492	4.27
6	Clay, PI=15	0.91	17.3	509	5.18
7	Clay, PI=15	0.91	17.3	526	6.10
8	Clay, PI=15	0.91	17.3	544	7.01
9	Sand, <1 ksc	0.91	18.9	599	7.92
10	Sand, <1 ksc	0.91	18.9	637	8.84
11	Sand, <1 ksc	0.91	18.9	672	9.75
12	Sand, <1 ksc	1.25	18.9	714	11.00
13	Clay, PI=30	1.01	17.3	592	12.01
14	Sand, average	2.67	19.6	722	14.68
15	Sand, average	2.67	19.6	742	17.34
16	Sand, average	2.67	19.6	782	20.01
17	Rock	2.54	19.6	1100	22.55
18	Rock	2.54	19.6	1300	25.09
19	Rock	2.54	19.6	1585	27.63
20	Rock	7.62	19.6	1768	35.25
21	Bedrock		20.4	2012	

**Table C.10 Dynamic soil properites of generic site C3**

Layer No	Material ID	Layer Thickness (m)	Unit Weight (kN/m <sup>3</sup> )	Vs (m/s)	Cumulative Depth (m)
1	Clay, PI=15	0.61	18.1	299	0.61
2	Clay, PI=15	0.61	18.1	314	1.22
3	Clay, PI=15	0.91	18.1	329	2.13
4	Clay, PI=15	0.91	18.1	344	3.05
5	Clay, PI=15	0.94	18.1	360	3.99
6	Sand, <1 ksc	0.61	18.9	299	4.60
7	Sand, <1 ksc	0.88	18.9	360	5.49
8	Clay, PI=40	0.49	17.3	299	5.97
9	Sand, <1 ksc	1.22	18.9	396	7.19
10	Sand, <1 ksc	1.22	18.9	439	8.41
11	Sand, <1 ksc	1.22	18.9	500	9.63
12	Sand, <1 ksc	1.34	18.9	549	10.97
13	Clay, PI=40	1.01	17.3	640	11.98
14	Clay, PI=40	1.01	17.3	762	12.98
15	Clay, PI=15	1.22	18.9	640	14.20
16	Clay, PI=15	1.22	18.9	701	15.42
17	Clay, PI=15	1.55	18.9	762	16.98
18	Gravel	1.52	19.6	792	18.50
19	Gravel	1.52	19.6	872	20.03
20	Gravel	1.95	19.6	960	21.98
21	Clay, PI=40	2.90	18.1	475	24.87
22	Clay, PI=40	3.05	18.1	494	27.92
23	Clay, PI=40	3.05	18.1	518	30.97
24	Rock	3.81	18.1	800	34.78
25	Rock	3.81	18.1	1100	38.59
26	Rock	3.81	19.6	1400	42.40
27	Rock	3.81	19.6	1768	46.21
28	Bedrock		20.4	2012	

**Table C.11 Dynamic soil properties of generic site C4**

Layer No	Material ID	Layer Thickness (m)	Unit Weight (kN/m <sup>3</sup> )	Vs (m/s)	Cumulative Depth (m)
1	Clay, PI=15	0.30	17.3	250	0.30
2	Clay, PI=15	0.30	17.3	270	0.60
3	Sand, <1 ksc	0.80	17.3	330	1.40
4	Sand, <1 ksc	0.80	17.3	350	2.20
5	Sand, <1 ksc	0.90	17.3	360	3.10
6	Clay, PI=20	1.50	18.9	400	4.60
7	Clay, PI=20	1.50	18.9	450	6.10
8	Clay, PI=20	1.50	18.9	475	7.60
9	Clay, PI=20	1.50	18.9	500	9.10
10	Clay, PI=20	1.50	18.9	530	10.60
11	Clay, PI=20	1.50	18.9	550	12.10
12	Sand, average	1.00	18.9	570	13.10
13	Sand, average	1.00	18.9	575	14.10
14	Sand, average	1.00	18.9	580	15.10
15	Clay PI=40	2.00	18.9	590	17.10
16	Clay PI=40	2.10	18.9	595	19.20
17	Clay PI=40	2.10	18.9	600	21.30
18	Clay PI=40	2.10	18.9	605	23.40
19	Clay PI=40	2.10	19.6	610	25.50
20	Clay PI=40	2.10	19.6	615	27.60
21	Clay PI=40	2.10	19.6	620	29.70
22	Clay PI=40	2.10	19.6	625	31.80
23	Clay PI=40	2.10	19.6	630	33.90
24	Clay PI=40	2.10	19.6	635	36.00
25	W. Rock	5.00	20.4	750	41.00
26	W. Rock	5.00	20.4	825	46.00
27	W. Rock	5.00	20.4	900	51.00
28	Bedrock		21.2	1000	

**Table C.12 Dynamic soil properites of generic site C5**

Layer No	Material ID	Layer Thickness (m)	Unit Weight (kN/m <sup>3</sup> )	V <sub>s</sub> (m/s)	Cumulative Depth (m)
1	Clay, PI=30	0.50	17.3	325	0.50
2	Clay, PI=30	1.00	17.3	330	1.50
3	Clay, PI=30	1.00	17.3	335	2.50
4	Clay, PI=20	1.00	17.3	340	3.50
5	Clay, PI=20	1.00	17.3	345	4.50
6	Clay, PI=20	1.00	17.3	360	5.50
7	Clay, PI=20	2.00	18.9	310	7.50
8	Clay, PI=20	2.00	18.9	330	9.50
9	Clay, PI=20	2.00	18.9	355	11.50
10	Clay, PI=20	2.00	18.9	380	13.50
11	Clay, PI=20	2.00	18.9	410	15.50
12	Clay, PI=20	2.00	18.9	430	17.50
13	Clay, PI=20	2.00	18.9	460	19.50
14	Clay, PI=20	2.00	18.9	480	21.50
15	Clay, PI=20	2.00	18.9	500	23.50
16	Clay, PI=20	2.00	18.9	510	25.50
17	Clay, PI=20	2.00	18.9	530	27.50
18	Clay, PI=20	2.00	18.9	530	29.50
19	Clay, PI=20	2.00	19.6	535	31.50
20	Clay, PI=20	3.00	19.6	540	34.50
21	Clay, PI=20	3.00	19.6	545	37.50
22	Clay, PI=20	3.00	19.6	550	40.50
23	Clay, PI=20	2.50	19.6	550	43.00
24	Clay, PI=20	2.50	19.6	550	45.50
25	W. Rock	4.50	20.4	650	50.00
26	W. Rock	5.00	20.4	700	55.00
27	Bedrock		20.4	750	

**Table C.13 Dynamic soil properites of generic site C6**

Layer No	Material ID	Layer Thickness (m)	Unit Weight (kN/m <sup>3</sup> )	V <sub>s</sub> (m/s)	Cumulative Depth (m)
1	Sand, <1 ksc	0.60	17.3	300	0.60
2	Sand, <1 ksc	0.40	17.3	320	1.00
3	Sand, <1 ksc	0.50	17.3	340	1.50
4	Sand, <1 ksc	0.50	18.9	400	2.00
5	Sand, <1 ksc	0.50	18.9	440	2.50
6	Sand, <1 ksc	1.00	18.9	460	3.50
7	Sand, <1 ksc	1.00	18.9	480	4.50
8	Sand, average	1.00	18.9	485	5.50
9	Sand, average	1.00	18.9	490	6.50
10	Sand, average	1.00	18.9	500	7.50
11	Sand, average	1.00	18.9	520	8.50
12	Clay, PI=20	1.00	18.9	500	9.50
13	Clay, PI=20	2.00	18.9	530	11.50
14	Clay, PI=20	2.00	19.6	550	13.50
15	Clay, PI=20	2.00	19.6	575	15.50
16	Clay, PI=20	2.00	19.6	600	17.50
17	W. Rock	2.50	19.6	750	20.00
18	W. Rock	2.50	19.6	800	22.50
19	W. Rock	2.50	19.6	850	25.00
20	W. Rock	2.50	19.6	900	27.50
21	W. Rock	2.50	19.6	950	30.00
22	Bedrock		20.4	1000	

**Table C.14 Dynamic soil properites of generic site C7**

Layer No	Material ID	Layer Thickness (m)	Unit Weight (kN/m <sup>3</sup> )	V <sub>s</sub> (m/s)	Cumulative Depth (m)
1	Sand, <1 ksc	0.50	17.3	350	0.50
2	Sand, <1 ksc	0.50	17.3	380	1.00
3	Sand, <1 ksc	0.50	17.3	420	1.50
4	Clay, PI=30	1.00	18.9	400	2.50
5	Clay, PI=30	1.00	18.9	430	3.50
6	Clay, PI=30	1.00	18.9	450	4.50
7	Clay, PI=30	1.00	18.9	475	5.50
8	Gravel	0.70	18.9	525	6.20
9	Gravel	1.00	18.9	550	7.20
10	Gravel	1.00	18.9	575	8.20
11	Gravel	1.00	18.9	625	9.20
12	Gravel	1.00	18.9	650	10.20
13	Gravel	1.00	18.9	700	11.20
14	W. Rock	1.80	19.6	800	13.00
15	W. Rock	2.00	19.6	850	15.00
16	W. Rock	3.00	19.6	875	18.00
17	W. Rock	4.00	19.6	900	22.00
18	W. Rock	4.00	19.6	925	26.00
19	W. Rock	4.00	19.6	975	30.00
20	Bedrock		20.4	1000	

**Table C.15 Dynamic soil properties of generic site D1**

Layer No	Material ID	Layer Thickness (m)	Unit Weight (kN/m <sup>3</sup> )	Vs (m/s)	Cumulative Depth (m)
1	Clay, PI=15	0.61	17.3	79	0.61
2	Clay, PI=15	0.61	17.3	88	1.22
3	Clay, PI=15	0.91	17.3	98	2.13
4	Clay, PI=15	0.91	17.3	107	3.05
5	Clay, PI=15	0.91	17.3	114	3.96
6	Clay, PI=15	1.04	17.3	122	5.00
7	Sand, <1 ksc	0.91	18.1	122	5.91
8	Sand, <1 ksc	1.10	18.1	152	7.01
9	Clay, PI=30	0.91	17.3	122	7.92
10	Clay, PI=30	1.10	17.3	175	9.02
11	Clay, PI=30	0.91	17.3	244	9.94
12	Clay, PI=30	1.22	17.3	267	11.16
13	Clay, PI=30	1.22	17.3	290	12.37
14	Clay, PI=30	1.22	17.3	312	13.59
15	Clay, PI=30	1.22	17.3	335	14.81
16	Clay, PI=30	1.22	17.3	351	16.03
17	W. Rock	3.05	19.6	500	19.08
18	W. Rock	3.05	19.6	750	22.13
19	W. Rock	3.05	19.6	900	25.18
20	W. Rock	3.05	19.6	950	28.22
21	W. Rock	3.05	20.4	975	31.27
22	W. Rock	3.05	20.4	1021	34.32
23	Bedrock		20.4	1067	



**Table C.16 Dynamic soil properties of generic site D2**

Layer No	Material ID	Layer Thickness (m)	Unit Weight (kN/m <sup>3</sup> )	Vs (m/s)	Cumulative Depth (m)
1	Sand, <1 ksc	0.30	18.1	91	0.30
2	Sand, <1 ksc	0.49	18.1	104	0.79
3	Clay, PI=30	0.70	17.3	91	1.49
4	Sand, <1 ksc	1.01	18.1	79	2.50
5	Clay, PI=15	0.76	17.3	84	3.26
6	Clay, PI=15	0.91	17.3	89	4.18
7	Clay, PI=15	0.91	17.3	94	5.09
8	Clay, PI=15	0.91	17.3	99	6.00
9	Sand, <1 ksc	0.61	18.1	119	6.61
10	Sand, <1 ksc	0.61	18.1	125	7.22
11	Sand, <1 ksc	0.79	18.1	131	8.02
12	Clay, PI=30	1.22	17.3	143	9.24
13	Clay, PI=30	1.22	17.3	153	10.45
14	Clay, PI=30	1.22	17.3	162	11.67
15	Clay, PI=30	1.22	17.3	172	12.89
16	Clay, PI=30	1.22	17.3	182	14.11
17	Clay, PI=30	1.22	17.3	192	15.33
18	Clay, PI=30	1.22	17.3	212	16.55
19	Clay, PI=30	1.46	17.3	228	18.01
20	Gravel	6.10	18.9	310	24.11
21	Gravel	6.10	18.9	360	30.21
22	Gravel	6.10	18.9	430	36.30
23	Gravel	6.10	18.9	488	42.40
24	Gravel	6.10	18.9	518	48.49
25	Gravel	6.10	18.9	549	54.59
26	Gravel	6.10	18.9	579	60.69
27	Gravel	6.10	18.9	594	66.78
28	Gravel	8.23	18.9	610	75.01
29	Rock	3.05	19.6	792	78.06
30	Rock	3.05	19.6	838	81.11
31	Rock	3.05	19.6	884	84.16
32	Rock	3.05	20.4	945	87.20
33	Rock	3.05	20.4	975	90.25
34	Bedrock		20.4	1067	

**Table C.17 Dynamic soil properties of generic site D3**

Layer No	Material ID	Layer Thickness (m)	Unit Weight (kN/m <sup>3</sup> )	Vs (m/s)	Cumulative Depth (m)
1	Sand, <1 ksc	0.61	18.1	134	0.61
2	Sand, <1 ksc	0.61	18.1	137	1.22
3	Sand, <1 ksc	0.61	18.1	140	1.83
4	Sand, <1 ksc	0.61	18.1	143	2.44
5	Sand, <1 ksc	0.61	18.1	146	3.05
6	Sand, <1 ksc	0.61	18.1	149	3.66
7	Sand, <1 ksc	0.61	18.1	155	4.27
8	Sand, average	0.73	18.1	162	5.00
9	Clay, PI=15	0.61	18.1	162	5.61
10	Clay, PI=15	0.88	18.1	180	6.49
11	Sand, average	1.22	18.9	191	7.71
12	Sand, average	1.22	18.9	198	8.93
13	Sand, average	1.22	18.9	206	10.15
14	Sand, average	1.34	18.9	210	11.49
15	Clay, PI=30	1.22	17.3	160	12.71
16	Clay, PI=30	1.28	17.3	180	13.99
17	Play, PI=15	2.44	18.1	290	16.43
18	Play, PI=15	2.44	18.1	299	18.87
19	Play, PI=15	2.44	18.1	305	21.31
20	Play, PI=15	2.68	18.1	311	23.99
21	Clay, PI=30	3.51	18.1	238	27.49
22	Clay, PI=30	3.51	18.1	259	31.00
23	Sand, >3 ksc	1.46	18.9	280	32.46
24	Sand, >3 ksc	1.52	18.9	320	33.99
25	W. Rock	3.81	19.6	450	37.80
26	W. Rock	3.81	19.6	600	41.61
27	Rock	3.81	19.6	750	45.42
28	Rock	3.81	19.6	884	49.23
29	Bedrock		20.4	1006	

**Table C.18 Dynamic soil properites of generic site D4**

Layer No	Material ID	Layer Thickness (m)	Unit Weight (kN/m <sup>3</sup> )	Vs (m/s)	Cumulative Depth (m)
1	Clay, PI=15	0.30	17.3	150	0.30
2	Clay, PI=15	0.61	17.3	161	0.91
3	Clay, PI=15	0.91	17.3	172	1.83
4	Clay, PI=15	1.16	17.3	183	2.99
5	Sand, <1 ksc	0.91	18.1	150	3.90
6	Sand, average	0.91	18.1	183	4.82
7	Sand, average	1.16	18.1	210	5.97
8	Clay, PI=15	1.22	17.3	210	7.19
9	Clay, PI=15	1.22	17.3	230	8.41
10	Clay, PI=15	1.22	17.3	252	9.63
11	Clay, PI=15	1.34	17.3	271	10.97
12	Clay, PI=15	1.49	17.3	274	12.47
13	Sand, average	1.01	19.6	238	13.47
14	Clay, PI=15	7.13	17.3	329	20.60
15	Clay, PI=15	7.13	17.3	335	27.74
16	W. Rock	4.57	19.6	500	32.31
17	W. Rock	4.57	19.6	600	36.88
18	W. Rock	4.57	19.6	700	41.45
19	Rock	4.57	19.6	838	46.02
20	Bedrock		20.4	1067	

**Table C.19 Dynamic soil properties of generic site D5**

Layer No	Material ID	Layer Thickness (m)	Unit Weight (kN/m <sup>3</sup> )	Vs (m/s)	Cumulative Depth (m)
1	Clay, PI=15	0.30	17.3	122	0.30
2	Clay, PI=15	0.30	17.3	128	0.61
3	Clay, PI=15	0.61	17.3	134	1.22
4	Clay, PI=15	0.79	17.3	140	2.01
5	Clay, PI=15	0.61	17.3	125	2.62
6	Clay, PI=15	0.88	17.3	175	3.51
7	Sand, <1 ksc	0.91	18.9	198	4.42
8	Sand, average	0.91	18.9	204	5.33
9	Sand, average	0.91	18.9	210	6.25
10	Sand, average	0.88	18.9	216	7.13
11	Sand, average	1.22	18.9	223	8.35
12	Sand, average	1.22	18.9	229	9.57
13	Sand, average	1.22	18.9	232	10.79
14	Sand, average	1.22	18.9	236	12.01
15	Clay, PI=15	7.28	17.3	274	19.29
16	Clay, PI=15	7.28	17.3	279	26.58
17	Clay, PI=15	7.28	17.3	283	33.86
18	Clay, PI=15	7.28	17.3	288	41.15
19	W. Rock	4.57	19.6	450	45.72
20	W. Rock	4.57	19.6	600	50.29
21	W. Rock	4.57	19.6	700	54.86
22	Rock	4.57	19.6	850	59.43
23	Bedrock		20.4	1050	

**Table C.20 Dynamic soil properites of generic site D6**

Layer No	Material ID	Layer Thickness (m)	Unit Weight (kN/m <sup>3</sup> )	Vs (m/s)	Cumulative Depth (m)
1	Clay, PI=20	0.45	17.3	110	0.45
2	Clay, PI=20	0.45	17.3	110	0.90
3	Sand, < 1ksc	1.50	17.3	190	2.40
4	Sand, < 1ksc	1.00	17.3	200	3.40
5	Sand, < 1ksc	1.00	17.3	210	4.40
6	Sand, average	3.00	17.3	230	7.40
7	Sand, average	3.00	17.3	250	10.40
8	Sand, average	3.00	17.3	270	13.40
9	Gravel	2.60	18.9	350	16.00
10	Gravel	3.00	18.9	360	19.00
11	Gravel	3.00	18.9	375	22.00
12	Gravel	3.00	18.9	390	25.00
13	Gravel	3.00	18.9	400	28.00
14	Gravel	3.00	18.9	410	31.00
15	Gravel	3.00	18.9	425	34.00
16	Gravel	3.00	18.9	435	37.00
17	Gravel	3.00	18.9	450	40.00
18	W. Rock	5.00	19.6	500	45.00
19	W. Rock	5.00	19.6	550	50.00
20	W. Rock	5.00	19.6	650	55.00
21	W. Rock	5.00	20.4	700	60.00
22	Bedrock		20.4	750	

**Table C.21 Dynamic soil properites of generic site D7**

Layer No	Material ID	Layer Thickness (m)	Unit Weight (kN/m <sup>3</sup> )	Vs (m/s)	Cumulative Depth (m)
1	Sand, <1 ksc	1.00	17.3	105	1.00
2	Sand, <1 ksc	1.10	17.3	115	2.10
3	Clay, PI=20	1.00	17.3	150	3.10
4	Clay, PI=20	1.00	17.3	175	4.10
5	Clay, PI=20	1.00	17.3	200	5.10
6	Clay, PI=20	1.00	17.3	220	6.10
7	Clay, PI=20	1.00	17.3	240	7.10
8	Clay, PI=20	1.00	17.3	260	8.10
9	Clay, PI=30	1.00	18.9	300	9.10
10	Clay, PI=30	1.00	18.9	320	10.10
11	Clay, PI=30	1.00	18.9	350	11.10
12	Clay, PI=30	1.00	18.9	370	12.10
13	Clay, PI=30	1.00	18.9	400	13.10
14	Clay, PI=30	1.00	18.9	430	14.10
15	W. Rock	1.90	19.6	520	16.00
16	W. Rock	3.00	19.6	570	19.00
17	W. Rock	3.00	19.6	600	22.00
18	W. Rock	3.00	19.6	650	25.00
19	Bedrock		20.4	750	

**Table C.22 Dynamic soil properites of generic site E1**

Layer No	Material ID	Layer Thickness (m)	Unit Weight (kN/m <sup>3</sup> )	Vs (m/s)	Cumulative Depth (m)
1	Clay, PI=15	2.00	17.3	79	2.00
2	Clay, PI=15	2.90	17.3	79	4.90
3	Clay, PI=30	2.00	17.3	79	6.90
4	Clay, PI=30	2.00	17.3	80	8.90
5	Clay, PI=30	2.60	17.3	91	11.50
6	Sand, average	2.20	18.1	91	13.70
7	Sand, average	3.00	18.1	96	16.70
8	Sand, >3 ksc	3.00	18.1	106	19.70
9	Sand, >3 ksc	2.20	18.9	127	21.90
10	Sand, >3 ksc	3.00	18.9	140	24.90
11	Sand, >3 ksc	3.00	18.9	149	27.90
12	Clay, PI=30	4.00	17.3	183	31.90
13	Clay, PI=30	4.00	17.3	195	35.90
14	Clay, PI=30	4.00	17.3	219	39.90
15	Clay, PI=30	4.00	17.3	244	43.90
16	Clay, PI=30	4.00	17.3	262	47.90
17	Clay, PI=30	4.60	17.3	280	52.50
18	W. Rock	5.00	19.6	400	57.50
19	W. Rock	5.00	19.6	450	62.50
20	W. Rock	5.00	19.6	500	67.50
21	W. Rock	5.00	19.6	600	72.50
22	W. Rock	5.00	20.4	650	77.50
23	W. Rock	5.00	20.4	700	82.50
24	Bedrock		20.4	750	

**Table C.23 Dynamic soil properites of generic site E2**

Layer No	Material ID	Layer Thickness (m)	Unit Weight (kN/m <sup>3</sup> )	V <sub>s</sub> (m/s)	Cumulative Depth (m)
1	Clay, PI=20	1.00	17.3	190	1.00
2	Clay, PI=20	1.00	17.3	200	2.00
3	Clay, PI=20	1.00	17.3	200	3.00
4	Clay, PI=40	2.00	17.3	120	5.00
5	Clay, PI=40	2.00	17.3	125	7.00
6	Clay, PI=40	2.00	17.3	130	9.00
7	Clay, PI=40	2.00	17.3	140	11.00
8	Clay, PI=40	2.00	17.3	150	13.00
9	Clay, PI=20	2.00	18.1	120	15.00
10	Clay, PI=20	2.00	18.1	130	17.00
11	Clay, PI=20	2.00	18.1	140	19.00
12	Clay, PI=20	2.00	18.1	150	21.00
13	Clay, PI=20	2.00	18.1	165	23.00
14	Clay, PI=20	2.00	18.1	180	25.00
15	Clay, PI=30	2.00	18.1	200	27.00
16	Clay, PI=30	2.00	18.1	205	29.00
17	Clay, PI=30	2.00	18.1	215	31.00
18	Clay, PI=30	2.00	18.1	220	33.00
19	Clay, PI=30	2.00	18.1	225	35.00
20	Clay, PI=30	2.00	18.1	230	37.00
21	Clay, PI=30	2.00	18.1	240	39.00
22	Clay, PI=30	2.00	18.1	245	41.00
23	Clay, PI=30	2.00	18.1	250	43.00
24	Sand, >3 ksc	1.00	18.9	300	44.00
25	Sand, >3 ksc	1.00	18.9	320	45.00
26	Sand, >3 ksc	1.00	18.9	340	46.00
27	Sand, >3 ksc	1.00	18.9	360	47.00
28	Sand, >3 ksc	2.00	18.9	370	49.00
29	Sand, >3 ksc	2.00	18.9	380	51.00
30	Sand, >3 ksc	2.00	18.9	420	53.00
31	W. Rock	3.00	19.6	550	56.00
32	W. Rock	3.00	19.6	600	59.00
33	W. Rock	4.00	19.6	650	63.00
34	Bedrock		20.4	750	



**Table C.24 Dynamic soil properites of generic site E3**

Layer No	Material ID	Layer Thickness (m)	Unit Weight (kN/m <sup>3</sup> )	V <sub>s</sub> (m/s)	Cumulative Depth (m)
1	Clay, PI=20	1.00	17.3	80	1.00
2	Clay, PI=20	1.00	17.3	82	2.00
3	Clay, PI=20	1.00	17.3	84	3.00
4	Clay, PI=20	1.00	17.3	88	4.00
5	Clay, PI=20	1.00	17.3	89	5.00
6	Clay, PI=20	1.00	17.3	90	6.00
7	Clay, PI=20	1.00	17.3	91	7.00
8	Clay, PI=20	1.00	17.3	93	8.00
9	Clay, PI=20	1.50	18.1	98	9.50
10	Clay, PI=20	1.50	18.1	99	11.00
11	Clay, PI=20	1.50	18.1	99	12.50
12	Clay, PI=20	1.50	18.1	100	14.00
13	Clay, PI=30	2.00	18.1	110	16.00
14	Clay, PI=30	2.50	18.1	114	18.50
15	Clay, PI=30	2.50	18.1	116	21.00
16	Clay, PI=30	2.50	18.1	118	23.50
17	Clay, PI=30	2.50	18.1	120	26.00
18	Clay, PI=30	2.50	18.1	121	28.50
19	Clay, PI=30	2.50	18.1	121	31.00
20	Clay, PI=30	2.50	18.1	124	33.50
21	Clay, PI=30	2.50	18.1	126	36.00
22	Clay, PI=30	2.50	18.1	128	38.50
23	Clay, PI=30	2.50	18.1	130	41.00
24	Clay, PI=30	3.00	18.1	132	44.00
25	Clay, PI=30	3.00	18.1	137	47.00
26	Clay, PI=30	3.00	18.1	140	50.00
27	Clay, PI=40	2.00	19.6	200	52.00
28	Clay, PI=40	2.00	19.6	220	54.00
29	Clay, PI=40	2.00	19.6	240	56.00
30	Clay, PI=40	2.00	19.6	260	58.00
31	Clay, PI=40	2.00	19.6	270	60.00
32	Clay, PI=40	2.00	19.6	290	62.00
33	Clay, PI=40	2.00	19.6	310	64.00
34	Clay, PI=40	2.00	19.6	325	66.00
35	Clay, PI=40	2.00	19.6	340	68.00
36	Clay, PI=40	2.00	19.6	350	70.00
37	W. Rock	2.00	19.6	500	72.00
38	W. Rock	2.00	19.6	550	74.00
39	W. Rock	3.00	19.6	650	77.00
40	Rock	3.00	19.6	750	80.00
41	Bedrock		20.4	850	

**Table C.25 Dynamic soil properties of generic site E4**

Layer No	Material ID	Layer Thickness (m)	Unit Weight (kN/m <sup>3</sup> )	Vs (m/s)	Cumulative Depth (m)
1	Sand, <1 ksc	1.00	17.3	120	1.00
2	Sand, <1 ksc	1.50	17.3	130	2.50
3	Sand, <1 ksc	1.50	17.3	140	4.00
4	Sand, <1 ksc	1.00	18.1	170	5.00
5	Sand, average	1.00	18.1	172	6.00
6	Sand, average	1.00	18.1	175	7.00
7	Sand, average	1.00	18.1	177	8.00
8	Sand, average	1.00	18.1	180	9.00
9	Sand, average	1.00	18.1	185	10.00
10	Sand, average	1.00	18.1	185	11.00
11	Sand, average	1.00	18.1	187	12.00
12	Sand, average	1.00	18.1	188	13.00
13	Sand, >3 ksc	1.00	18.1	180	14.00
14	Sand, >3 ksc	1.00	18.1	185	15.00
15	Sand, >3 ksc	1.00	18.1	196	16.00
16	Sand, >3 ksc	1.00	18.1	198	17.00
17	Sand, >3 ksc	1.00	18.1	199	18.00
18	Sand, >3 ksc	1.00	18.1	200	19.00
19	Sand, >3 ksc	1.00	18.9	160	20.00
20	Sand, >3 ksc	2.00	18.9	170	22.00
21	Sand, >3 ksc	2.00	18.9	190	24.00
22	Clay, PI=30	2.00	18.9	200	26.00
23	Clay, PI=30	2.00	18.9	230	28.00
24	Clay, PI=30	2.00	18.9	240	30.00
25	Gravel	2.00	18.9	250	32.00
26	Gravel	2.00	18.9	265	34.00
27	Gravel	2.50	18.9	400	36.50
28	Gravel	2.50	18.9	420	39.00
29	Gravel	2.50	18.9	435	41.50
30	Gravel	2.50	18.9	450	44.00
31	W. Rock	2.00	19.6	500	46.00
32	W. Rock	2.00	19.6	600	48.00
33	W. Rock	3.00	19.6	700	51.00
34	Rock	3.00	19.6	750	54.00
35	Bedrock		20.4	850	

**Table C.26 Dynamic soil properties of generic site E5**

Layer No	Material ID	Layer Thickness (m)	Unit Weight (kN/m <sup>3</sup> )	Vs (m/s)	Cumulative Depth (m)
1	Sand, <1 ksc	1.00	17.3	117	1.00
2	Sand, <1 ksc	1.50	17.3	125	2.50
3	Sand, <1 ksc	1.50	17.3	133	4.00
4	Sand, average	2.50	18.1	117	6.50
5	Sand, average	2.50	18.1	119	9.00
6	Sand, average	2.50	18.1	119	11.50
7	Sand, average	2.50	18.1	120	14.00
8	Sand, >3 ksc	2.50	18.1	121	16.50
9	Sand, >3 ksc	2.50	18.1	122	19.00
10	Sand, >3 ksc	2.50	18.1	123	21.50
11	Sand, >3 ksc	2.50	18.1	125	24.00
12	Sand, >3 ksc	2.50	18.1	125	26.50
13	Sand, >3 ksc	2.50	18.1	126	29.00
14	Sand, >3 ksc	2.50	18.1	127	31.50
15	Sand, >3 ksc	2.50	18.1	127	34.00
16	Sand, >3 ksc	2.50	18.1	129	36.50
17	Sand, >3 ksc	2.50	18.1	129	39.00
18	Sand, >3 ksc	2.50	18.1	130	41.50
19	Sand, >3 ksc	2.50	18.1	130	44.00
20	Sand, >3 ksc	2.50	18.1	130	46.50
21	Sand, >3 ksc	2.50	18.1	133	49.00
22	Sand, >3 ksc	2.50	18.9	172	51.50
23	Sand, >3 ksc	2.50	18.9	195	54.00
24	Sand, >3 ksc	2.50	18.9	203	56.50
25	Sand, >3 ksc	2.50	18.9	203	59.00
26	Sand, >3 ksc	2.50	18.9	222	61.50
27	Clay, PI=40	3.00	18.9	250	64.50
28	Clay, PI=40	3.00	18.9	273	67.50
29	Clay, PI=40	3.00	18.9	277	70.50
30	Clay, PI=40	3.00	18.9	281	73.50
31	Clay, PI=40	3.00	18.9	285	76.50
32	Clay, PI=40	3.00	18.9	289	79.50
33	Clay, PI=40	3.00	18.9	300	82.50
34	Clay, PI=40	3.00	18.9	312	85.50
35	W. Rock	4.00	19.6	460	89.50
36	W. Rock	4.00	19.6	550	93.50
37	W. Rock	5.00	19.6	650	98.50
38	Rock	5.00	19.6	750	103.50
39	Bedrock		20.4	850	

**Table C.27 Dynamic soil properties of generic site E6**

Layer No	Material ID	Layer Thickness (m)	Unit Weight (kN/m <sup>3</sup> )	Vs (m/s)	Cumulative Depth (m)
1	Sand, <1 ksc	1.00	17.3	118	1.00
2	Sand, <1 ksc	1.00	17.3	126	2.00
3	Sand, <1 ksc	1.00	17.3	130	3.00
4	Sand, <1 ksc	1.00	17.3	134	4.00
5	Sand, average	1.00	17.3	136	5.00
6	Sand, average	1.00	17.3	139	6.00
7	Sand, average	1.00	18.1	113	7.00
8	Sand, average	1.00	18.1	118	8.00
9	Sand, average	1.00	18.1	119	9.00
10	Sand, average	1.00	18.1	122	10.00
11	Sand, average	1.00	18.1	126	11.00
12	Sand, average	1.00	18.1	126	12.00
13	Sand, average	2.00	18.9	143	14.00
14	Sand, >3 ksc	2.00	18.9	145	16.00
15	Sand, >3 ksc	2.00	18.9	147	18.00
16	Sand, >3 ksc	2.00	18.9	149	20.00
17	Sand, >3 ksc	2.00	18.9	151	22.00
18	Sand, >3 ksc	2.00	18.9	153	24.00
19	Sand, >3 ksc	2.00	18.9	155	26.00
20	Sand, >3 ksc	2.00	18.9	160	28.00
21	Sand, >3 ksc	2.00	18.9	164	30.00
22	Sand, >3 ksc	2.00	19.6	168	32.00
23	Sand, >3 ksc	2.00	19.6	176	34.00
24	Sand, >3 ksc	2.00	19.6	185	36.00
25	Sand, >3 ksc	2.00	19.6	193	38.00
26	Sand, >3 ksc	2.00	19.6	202	40.00
27	Sand, >3 ksc	2.00	19.6	227	42.00
28	Sand, >3 ksc	2.00	19.6	252	44.00
29	Sand, >3 ksc	2.00	19.6	273	46.00
30	Sand, >3 ksc	2.00	19.6	294	48.00
31	Sand, >3 ksc	2.00	19.6	307	50.00
32	Sand, >3 ksc	2.00	19.6	311	52.00
33	Sand, >3 ksc	2.00	19.6	323	54.00
34	Sand, >3 ksc	2.00	19.6	344	56.00
35	W. Rock	3.00	20.4	550	59.00
36	W. Rock	3.00	20.4	650	62.00
37	W. Rock	4.00	20.4	700	66.00
38	W. Rock	4.00	20.4	750	70.00
39	Bedrock		20.4	900	

**Table C.28 Dynamic soil properites of generic site E7**

Layer No	Material ID	Layer Thickness (m)	Unit Weight (kN/m <sup>3</sup> )	V <sub>s</sub> (m/s)	Cumulative Depth (m)
1	Sand, <1 ksc	1.00	17.3	130	1.00
2	Sand, <1 ksc	1.00	17.3	145	2.00
3	Sand, <1 ksc	1.00	17.3	150	3.00
4	Sand, <1 ksc	1.00	17.3	155	4.00
5	Clay, PI=30	2.00	17.3	120	6.00
6	Clay, PI=30	2.00	17.3	130	8.00
7	Clay, PI=30	2.00	18.1	140	10.00
8	Clay, PI=30	2.00	18.1	150	12.00
9	Clay, PI=30	2.00	18.1	165	14.00
10	Clay, PI=30	2.00	18.1	170	16.00
11	Clay, PI=30	2.00	18.1	170	18.00
12	Clay, PI=50	2.00	18.1	210	20.00
13	Clay, PI=50	2.00	18.9	210	22.00
14	Clay, PI=50	2.00	18.9	215	24.00
15	Clay, PI=50	2.00	18.9	215	26.00
16	Clay, PI=50	2.00	18.9	220	28.00
17	Clay, PI=50	2.00	18.9	220	30.00
18	Sand, >3 ksc	3.00	18.9	190	33.00
19	Sand, >3 ksc	3.00	18.9	195	36.00
20	Sand, >3 ksc	3.00	18.9	195	39.00
21	Sand, >3 ksc	3.00	18.9	197	42.00
22	Sand, >3 ksc	3.00	19.6	200	45.00
23	Sand, >3 ksc	3.00	19.6	210	48.00
24	Sand, >3 ksc	3.00	19.6	215	51.00
25	Sand, >3 ksc	3.00	19.6	220	54.00
26	Gravel	3.00	19.6	320	57.00
27	Gravel	3.00	19.6	335	60.00
28	Gravel	3.00	19.6	350	63.00
29	Gravel	3.00	19.6	360	66.00
30	Gravel	3.00	19.6	370	69.00
31	Gravel	3.00	19.6	385	72.00
32	Gravel	3.00	19.6	400	75.00
33	Gravel	3.00	19.6	400	78.00
34	Gravel	3.00	19.6	420	81.00
35	W. Rock	3.00	20.4	550	84.00
36	W. Rock	3.00	20.4	650	87.00
37	W. Rock	4.00	20.4	700	91.00
38	Rock	4.00	20.4	750	95.00
39	Bedrock		20.4	900	

## APPENDIX D

### SUMMARY OF GMPE DATASET

#### Abbreviation List for Table Headers

Epi. Coord.	: Epicenter coordinate, determined by the KOERI catalog (degrees)
$\mu M$	: Mean earthquake moment magnitude
SOFP	: Style of faulting parameter
EQ.ID	: Event identification number for the given earthquake
HP (N-S)	: High-pass filter cutoff of the recorded north-south component (Hz)
LP (N-S)	: Low-pass filter cutoff of the recorded north-south component (Hz)
HP (E-W)	: High-pass filter cutoff of the recorded east-west component (Hz)
LP (E-W)	: Low-pass filter cutoff of the recorded east-west component (Hz)
$PGA_{soil}$	: Peak acceleration of the recorded component of ground motion (g)
$R_{epi}$	: Epicentral distance (km)
$R_{hyp}$	: Hypocentral distance (km)
$\mu R_{rup}$	: Median value of the closest distance to rupture plane (km)
$\sigma R_{rup}$	: Standard deviation of $R_{rup}$ for the given record
$\mu R_{jb}$	: Median value of the Joyner-Boore distance (km)
$\sigma R_{jb}$	: Standard deviation of Joyner-Boore distance for the given record
ERD	: Earthquake Res. Dept., General Directorate of Disaster Affairs
KOERI	: Kandilli Observatory Earthquake Research Institute
ITU	: İstanbul Technical University
IRIGM	: Universite Joseph Fourier, Grenoble, France
LDEO	: Lamont-Doherty Earth Observatory, Columbia University, USA
ISESD	: Internet Site for European Strong Motion Data
Final Selection:	NEHRP site class(es) for the specific station

**Table D.1 List of processed events from the Turkish strong motion database**

EQ.ID	YEAR	MO/DY	Time (GMT)	Earthquake Name	Epi. Coord. (N)	Epi. Coord. (E)	Focal depth (km)	$\mu\text{M}$	Number of Recordings
1	1976	08/19	01:12:40	Denizli	37.7100	29.0000	20.0	5.10	1
2	1976	11/24	12:22:00	Çaldıran	39.0500	44.0400	10.0	6.80	1
3	1977	10/05	05:34:43	Çerkeş	41.0200	33.5700	10.0	5.40	1
4	1977	12/09	15:53:37	İzmir	38.3500	27.2300	27.0	4.53	1
5	1977	12/16	07:37:29	İzmir	38.4100	27.1900	24.0	5.47	1
6	1978	09/21	19:37:48	Malatya	37.9700	38.5900	22.0	4.57	1
7	1979	04/11	12:14:27	Muradiye	39.1200	43.9100	44.0	5.03	1
8	1979	05/28	09:27:33	Bucak	36.4600	31.7200	111.0	6.03	1
9	1979	07/18	13:12:23	Dursunbey	39.6600	28.6500	7.0	5.34	1
10	1981	06/30	07:59:08	Hatay	36.1700	35.8900	63.0	4.63	1
11	1983	07/05	12:01:27	Biga	40.3300	27.2100	7.0	5.91	3
12	1983	10/30	04:12:28	Horasan-Narman	40.3500	42.1800	16.0	6.55	2
13	1984	03/29	00:06:01	Balıkesir	39.6400	27.8700	12.0	4.58	1
14	1984	06/17	07:48:00	Foça	38.8700	25.6800	3.0	5.25	1
15	1985	08/12	02:54:44	Kığı	39.9500	39.7700	29.0	4.88	1
16	1985	12/06	22:35:29	Köyceğiz	36.9700	28.8500	9.0	4.73	1
17	1986	05/05	03:35:38	Malatya	38.0200	37.7900	4.0	5.98	1
18	1986	06/01	06:43:09	Kuşadası	37.9600	27.3900	10.0	3.97	1

**Table D.1 (continued) List of processed events from the Turkish strong motion database**

EQ.ID	YEAR	MO/DY	Time (GMT)	Earthquake Name	Epi. Coord. (N)	Epi. Coord. (E)	Focal depth (km)	$\mu\text{M}$	Number of Recordings
19	1986	06/06	10:39:47	Sürgü (Malatya)	38.0100	37.9100	11.0	5.75	2
20	1988	04/20	03:50:07	Muradiye	39.1100	44.1200	48.0	5.29	1
21	1991	02/12	09:54:58	İstanbul	40.8000	28.8200	10.0	4.90	1
22	1992	02/12	15:55:11	Amasya	40.5800	35.8000	10.0	4.40	1
23	1992	03/13	17:18:39	Erzincan	39.7200	39.6300	23.0	6.58	3
24	1992	11/06	19:08:09	Seferihisar	38.1600	26.9900	17.0	5.90	3
25	1994	01/03	21:00:30	İslahiye	37.0000	35.8400	26.0	5.18	1
26	1994	05/24	02:05:36	Girit	38.6600	26.5400	17.0	5.33	1
27	1994	11/13	06:56:00	Köyceğiz	36.9700	28.8900	7.0	5.24	1
28	1995	01/29	04:16:57	Tercan	39.9800	40.9900	33.0	5.11	1
29	1995	02/26	11:33:25	Van	38.6000	43.3300	33.0	4.00	1
30	1995	04/13	04:08:00	Tekirdağ	40.8500	27.6700	12.0	4.82	1
31	1995	10/01	15:57:13	Dinar	38.1100	30.0500	5.0	6.17	3
32	1995	12/05	18:49:32	Erzincan	39.3500	40.2200	33.0	5.70	1
33	1996	04/02	07:59:20	Kuşadası	37.7800	26.6400	12.0	5.40	1
34	1996	08/14	01:55:02	Merzifon	40.7400	35.2900	17.0	5.66	2
35	1997	01/21	20:47:46	Buldan	38.1200	28.9200	9.0	5.15	1
36	1997	01/22	17:57:19	Hatay	36.1400	36.1200	23.0	5.49	2
37	1997	10/21	10:49:33	Sakarya	40.7000	30.4200	11.0	4.20	1



**Table D.1 (continued) List of processed events from the Turkish strong motion database**

EQ.ID	YEAR	MO/DY	Time (GMT)	Earthquake Name	Epi. Coord. (N)	Epi. Coord. (E)	Focal depth (km)	$\mu$ M	Number of Recordings
38	1997	10/25	00:38:41	Gelibolu	40.4900	26.4300	10.0	4.12	1
39	1998	04/04	16:16:47	Dinar	38.1200	30.0400	7.0	5.11	2
40	1998	04/13	19:56:28	Horasan	40.0300	42.0900	22.0	4.48	1
41	1998	06/27	13:55:51	Adana-Ceyhan	36.9600	35.5200	18.0	6.16	5
42	1998	07/09	17:36:47	Bornova	37.9500	26.7400	21.0	4.87	1
43	1999	08/17	00:01:39	Kocaeli	40.7600	29.9700	17.0	7.55	30
44	1999	11/11	14:41:24	Sapanca- Adapazarı	40.8100	30.2000	7.0	5.65	9
45	1999	11/12	16:57:20	Düzce	40.7960	31.1830	10.0	7.15	38
46	2000	06/06	02:41:51	Çankırı -Orta	40.7200	32.8700	10.0	5.98	1
47	2000	08/23	13:41:28	Hendek-Akyazı	40.6800	30.7100	15.3	5.32	4
48	2000	10/04	02:33:57	Denizli	37.9100	29.0400	8.4	4.83	1
49	2001	07/10	21:42:04	Erzurum-Pasinler	39.8273	41.6200	5.0	5.27	1
50	2001	08/26	00:41:12	Yığılca-Düzce	40.9455	31.5728	7.8	5.10	1
51	2001	12/02	04:11:45	Van	38.6170	43.2940	5.0	4.76	1
52	2002	02/03	07:11:28	Sultandağı-Çay	38.5733	31.2715	5.0	6.38	2
53	2002	12/14	01:02:44	Andırın	37.4720	36.2210	13.6	4.95	1
54	2003	03/10	04:10:07	Akyazı	40.7283	30.5900	4.4	3.60	1
55	2003	04/10	00:40:16	Seferihisar-Urla	38.2568	26.8345	15.8	5.76	1
56	2003	05/01	00:27:04	Bingöl	38.9400	40.5100	6.0	6.35	1

**Table D.1 (continued) List of processed events from the Turkish strong motion database**

EQ.ID	YEAR	MO/DY	Time (GMT)	Earthquake Name	Epi. Coord. (N)	Epi. Coord. (E)	Focal depth (km)	$\mu$ M	Number of Recordings
57	2003	05/21	08:21:50	Düzce	40.8700	30.9800	7.7	4.30	1
58	2003	06/09	17:44:03	Bandırma	40.2000	27.9700	14.7	4.67	1
59	2003	07/06	19:10:28	Saros Kör.	40.4200	26.2100	9.1	5.61	1
60	2003	07/23	04:56:02	Buldan-Denizli-1	38.1718	28.8533	5.0	5.19	2
61	2003	07/26	01:00:56	Buldan-Denizli-2	38.1100	28.8800	5.0	4.75	1
62	2003	07/26	08:36:49	Buldan-Denizli-3	38.1100	28.8900	4.3	5.41	2
63	2004	04/13	21:47:23	Bolu	40.7200	31.6290	5.0	4.34	1
64	2004	08/04	03:01:07	Çiftlikköy-Muğla-1	37.0238	27.6063	15.7	5.47	1
65	2004	12/20	23:02:15	Ula-Muğla	37.0000	28.2800	12.5	5.35	2
66	2005	01/23	22:36:06	Antalya-Kaş Aç.	35.7510	29.5730	12.1	5.77	1
67	2005	06/06	07:41:30	Karlıova	39.3880	40.9030	10.5	5.64	1
68	2005	10/17	09:46:56	Seferihisar-İzmir	38.2200	26.6500	18.6	5.80	1
69	2005	10/20	21:40:02	Seferihisar-İzmir	38.1500	26.6700	3.7	5.86	2
70	2006	02/08	05:24:26	Sakarya	40.7073	30.3779	4.1	3.70	1
71	2006	10/20	18:15:58	Manyas (Kuş Gölü)	40.2640	27.9840	13.0	4.95	1
72	2006	10/24	14:00:22	Gemlik Körfezi	40.4220	28.9930	7.9	4.98	9

**Table D.2 Key properties of processed strong motion records**

Record No	EQ ID	Faulting Style	SOFP	Station Id	HP (N-S) (Hz)	LP (N-S) (Hz)	HP (E-W) (Hz)	LP (E-W) (Hz)	PGA Soil N-S (g)	PGA Soil E-W (g)	R <sub>epi</sub> (km)	R <sub>hyp</sub> (km)	μR <sub>rup</sub> (km)	σR <sub>rup</sub> (km)	μR <sub>jb</sub> (km)	σR <sub>jb</sub> (km)
1	1	N	0.08	2	0.50	40	0.80	35	0.368	0.293	9.96	22.34	17.59	1.62	8.25	1.30
2	2	SS	0.57	98	0.25	25	0.25	25	0.094	0.066	49.06	50.06	47.78	0.79	47.37	0.55
3	3	SS	0.54	3	0.50	20	0.50	15	0.036	0.042	62.10	62.94	61.62	1.23	61.41	1.27
4	4	N	0.08	4	1.50	25	1.20	20	0.162	0.244	10.79	29.07	27.21	0.74	9.81	0.63
5	5	N	0.09	4	0.42	25	0.50	20	0.374	0.124	3.29	24.22	18.07	2.66	1.09	0.84
6	6	SS	0.48	6	1.00	25	1.20	25	0.014	0.037	47.39	52.14	50.09	0.97	46.49	0.97
7	7	SS	0.48	7	0.50	22	0.50	20	0.050	0.048	19.25	48.02	41.45	2.70	17.93	0.71
8	8	SS	0.48	8	0.80	25	0.60	22	0.019	0.016	150.12	186.56	175.44	4.64	145.23	5.48
9	9	N	0.03	9	0.30	30	0.36	30	0.177	0.238	8.38	10.90	5.58	1.45	4.74	1.78
10	10	NO	0.09	10	0.40	25	0.40	25	0.133	0.120	24.50	67.62	64.72	1.17	22.62	1.43
11	11	SS	0.46	12	0.24	25	0.40	25	0.052	0.050	55.25	55.75	51.75	1.89	51.65	1.94
12	11	SS	0.46	13	0.20	30	0.30	25	0.046	0.046	43.92	44.47	40.54	1.87	40.43	1.93
13	11	SS	0.46	15	0.40	20	0.50	22	0.023	0.037	76.73	76.87	72.31	6.47	72.30	6.47
14	12	SS	0.41	16	0.50	25	0.50	25	0.113	0.183	34.18	37.67	29.74	2.11	29.18	2.01
15	12	SS	0.41	18	0.60	25	0.50	20	0.023	0.015	92.97	94.50	86.02	9.77	85.96	9.90
16	13	NO	0.09	20	0.40	25	0.50	25	0.226	0.122	2.05	12.17	8.17	1.60	1.81	0.18
17	14	SS	0.48	22	0.60	25	0.70	15	0.019	0.024	96.43	96.55	94.30	3.25	94.20	3.23
18	15	SN	0.48	23	0.40	20	0.70	20	0.159	0.084	86.97	91.55	88.88	1.78	85.43	1.87
19	16	N	0.09	24	1.00	25	1.00	25	0.125	0.140	14.51	17.09	14.31	0.96	12.73	1.12
20	17	SS	0.55	25	0.12	20	0.20	20	0.123	0.077	29.65	29.85	23.97	5.73	23.85	5.78
21	18	N	0.09	26	0.50	25	0.70	25	0.049	0.103	15.63	18.54	17.63	0.55	14.84	0.43
22	19	SS	0.50	25	0.30	20	0.40	20	0.074	0.033	34.76	36.42	31.02	4.56	30.99	4.65

**Table D.2 (continued) Key properties of processed strong motion records**

Record No	EQ ID	Faulting Style	SOFP	Station Id	HP (N-S) (Hz)	LP (N-S) (Hz)	HP (E-W) (Hz)	LP (E-W) (Hz)	PGA Soil N-S (g)	PGA Soil E-W (g)	R <sub>epi</sub> (km)	R <sub>hyp</sub> (km)	μR <sub>rup</sub> (km)	σR <sub>rup</sub> (km)	μR <sub>jb</sub> (km)	σR <sub>jb</sub> (km)
23	19	SS	0.50	6	0.50	25	0.40	25	0.018	0.024	53.74	54.80	50.02	5.04	50.01	5.09
24	20	SS	0.59	7	0.50	10	0.70	15	0.041	0.047	33.63	58.61	52.39	2.56	32.26	1.10
25	21	NO	0.09	27	0.40	20	0.50	20	0.027	0.012	32.87	34.30	31.60	2.32	30.99	2.42
26	22	SS	0.48	29	0.50	25	0.60	25	0.031	0.029	10.09	14.19	11.28	1.10	9.23	1.44
27	23	SS	0.53	30	0.10	30	0.10	30	0.518	0.473	12.75	26.30	12.10	2.98	8.35	1.34
28	23	SS	0.53	32	0.30	25	0.40	20	0.068	0.082	76.36	79.80	70.60	5.75	70.07	5.98
29	23	SS	0.53	33	0.45	20	0.55	15	0.039	0.025	65.44	69.43	63.03	2.07	61.82	2.14
30	24	SS	0.47	34	0.30	25	0.60	25	0.016	0.042	61.76	64.09	57.82	5.62	57.46	5.84
31	24	SS	0.47	5	0.30	15	0.40	20	0.028	0.040	37.20	40.81	38.19	1.22	35.96	0.62
32	24	SS	0.47	26	0.32	35	0.34	35	0.091	0.069	41.20	44.50	37.37	4.79	36.80	5.16
33	25	SS	0.48	44	0.80	25	0.60	25	0.020	0.020	70.80	75.59	70.89	3.36	68.65	3.68
34	26	NO	0.25	22	0.50	15	0.40	15	0.035	0.048	19.00	25.51	21.30	1.74	16.23	1.79
35	27	N	0.61	24	0.35	30	0.40	20	0.076	0.089	18.07	19.40	15.54	1.67	15.17	1.78
36	28	SS	0.50	33	0.35	25	0.20	20	0.044	0.049	55.95	64.99	61.90	1.15	55.78	0.10
37	29	SS	0.48	35	0.20	25	0.30	25	0.030	0.016	12.43	35.25	32.70	1.02	11.80	1.03
38	30	SR	0.48	14	0.15	25	0.20	25	0.038	0.043	19.42	22.81	19.27	0.99	18.27	1.01
39	31	N	0.02	36	0.40	13	0.40	13	0.042	0.042	48.22	48.39	41.95	6.90	41.89	6.90
40	31	N	0.02	37	0.80	18	0.80	18	0.060	0.065	46.31	46.61	42.51	2.58	42.46	2.60
41	31	N	0.61	38	0.20	25	0.20	25	0.287	0.365	10.66	11.78	5.83	2.69	4.46	3.06
42	32	SS	0.21	31	0.09	25	0.10	25	0.030	0.024	74.88	81.81	75.00	4.55	71.38	5.19
43	33	NO	0.52	26	0.50	20	0.45	22	0.022	0.034	55.68	57.00	53.21	1.52	52.74	1.55
44	34	SS	0.52	28	0.10	30	0.20	20	0.027	0.057	46.90	49.95	46.05	2.17	44.02	2.10
45	34	SS	0.12	39	0.40	18	0.50	18	0.014	0.032	48.91	51.80	46.22	3.51	45.47	3.75
46	35	N	0.42	40	0.40	25	0.40	25	0.042	0.025	11.29	14.43	12.24	0.99	10.60	0.52

**Table D.2 (continued) Key properties of processed strong motion records**

Record No	EQ ID	Faulting Style	SOPF	Station Id	HP (N-S) (Hz)	LP (N-S) (Hz)	HP (E-W) (Hz)	LP (E-W) (Hz)	PGA Soil N-S (g)	PGA Soil E-W (g)	R <sub>epi</sub> (km)	R <sub>hyp</sub> (km)	μR <sub>rup</sub> (km)	σR <sub>rup</sub> (km)	μR <sub>jb</sub> (km)	σR <sub>jb</sub> (km)
47	36	SS	0.42	11	0.10	35	0.10	30	0.129	0.151	9.00	24.69	18.50	2.35	5.68	2.95
48	36	SS	0.42	44	0.20	25	0.30	20	0.030	0.024	108.83	111.01	106.65	5.11	105.30	5.31
49	37	SS	0.48	41	0.40	25	0.25	20	0.037	0.069	5.33	12.22	9.28	1.08	4.56	0.83
50	38	SS	0.48	42	0.60	20	0.70	20	0.020	0.019	21.42	23.65	22.59	0.37	21.23	0.09
51	39	N	0.08	38	0.25	20	0.25	25	0.138	0.142	12.00	13.90	10.70	1.96	10.23	2.33
52	39	N	0.08	37	0.40	30	0.50	25	0.024	0.023	46.46	47.01	44.77	0.96	44.64	0.97
53	40	SS	0.47	17	0.20	20	0.20	20	0.026	0.022	7.24	23.16	20.61	1.15	7.00	0.18
54	41	SS	0.58	43	0.10	25	0.12	30	0.224	0.285	27.66	33.02	22.72	3.94	21.21	4.38
55	41	SS	0.58	11	0.15	25	0.20	20	0.027	0.025	100.81	102.36	98.75	1.56	97.92	1.44
56	41	SS	0.58	44	0.35	20	0.30	20	0.017	0.020	99.48	101.34	95.27	4.86	94.43	4.93
57	41	SS	0.58	45	0.20	20	0.30	20	0.026	0.036	45.15	48.50	39.08	6.40	38.12	6.82
58	41	SS	0.58	46	0.20	15	0.30	15	0.135	0.114	84.08	86.07	78.25	6.17	78.03	6.24
59	42	SS	0.59	47	0.10	20	0.15	20	0.027	0.013	70.53	73.47	70.71	2.06	69.09	2.19
60	43	SS	0.59	48	0.08	20	0.08	15	0.319	0.362	99.77	101.50	99.70	0.48	99.34	0.25
61	43	SS	0.59	49	0.07	25	0.04	25	0.212	0.143	51.82	54.62	51.41	0.47	50.76	0.50
62	43	SS	0.59	50	0.03	25	0.02	25	0.248	0.185	110.27	111.73	107.79	0.72	107.29	0.69
63	43	SS	0.59	51	0.03	40	0.03	40	0.089	0.101	169.48	170.56	167.72	0.61	167.27	0.60
64	43	SS	0.59	52	0.02	25	0.08	25	0.103	0.106	94.41	95.95	76.68	5.53	75.92	5.46
65	43	SS	0.59	53	0.30	20	0.40	20	0.169	0.132	106.06	107.55	102.35	1.01	101.77	0.96
66	43	SS	0.59	54	0.02	40	0.02	40	0.085	0.084	99.91	101.48	97.13	0.77	96.60	0.74
67	43	SS	0.59	55	0.02	25	0.01	25	0.176	0.160	90.59	92.28	86.32	1.12	85.72	1.07
68	43	SS	0.59	56	0.20	25	0.20	30	0.059	0.109	75.29	77.30	74.45	0.49	73.88	0.51
69	43	SS	0.59	57	0.03	20	0.08	20	0.039	0.038	88.23	89.94	81.34	1.86	80.74	1.79
70	43	SS	0.59	58	0.07	25	0.07	25	0.347	0.257	17.29	24.27	17.27	0.48	16.55	0.50

**Table D.2 (continued) Key properties of processed strong motion records**

Record No	EQ ID	Faulting Style	SOFP	Station Id	HP (N-S) (Hz)	LP (N-S) (Hz)	HP (E-W) (Hz)	LP (E-W) (Hz)	PGA Soil N-S (g)	PGA Soil E-W (g)	R <sub>epi</sub> (km)	R <sub>hyp</sub> (km)	μR <sub>rup</sub> (km)	σR <sub>rup</sub> (km)	μR <sub>jb</sub> (km)	σR <sub>jb</sub> (km)
71	43	SS	0.59	59	0.03	25	0.02	40	0.104	0.164	97.74	99.34	94.74	0.82	94.16	0.79
72	43	SS	0.59	60	0.06	25	0.05	25	0.053	0.069	88.62	90.32	82.50	1.64	81.85	1.57
73	43	SS	0.59	61	0.09	25	0.03	25	0.045	0.039	88.67	90.37	80.72	2.18	80.12	2.11
74	43	SS	0.59	62	0.06	25	0.04	25	0.110	0.109	92.87	94.53	89.77	0.84	89.20	0.80
75	43	SS	0.59	63	0.03	25	0.03	25	0.128	0.095	91.78	93.45	88.14	0.97	87.54	0.92
76	43	SS	0.59	64	0.09	20	0.07	12	0.059	0.046	96.04	97.52	73.47	7.80	72.79	7.74
77	43	SS	0.59	27	0.20	25	0.07	25	0.051	0.047	87.36	89.09	81.45	1.58	80.78	1.52
78	43	SS	0.59	41	0.04	40	0.04	40	0.401	0.401	34.68	38.71	34.69	0.49	34.25	0.24
79	43	SS	0.59	65	0.07	13	0.09	12	0.050	0.064	149.26	150.07	103.92	39.69	103.91	39.82
80	43	SS	0.59	66	0.50	25	0.60	20	0.118	0.106	106.16	107.65	102.37	1.03	101.79	0.97
81	43	SS	0.59	67	0.20	20	0.20	20	0.095	0.108	171.67	172.74	170.20	0.56	169.73	0.56
82	43	SS	0.59	68	0.30	25	0.30	30	0.225	0.155	43.93	47.18	43.87	0.47	43.19	0.50
83	43	SS	0.59	69	0.15	30	0.10	25	0.123	0.136	79.79	81.73	68.88	3.14	68.25	3.13
84	43	SS	0.59	70	0.10	25	0.07	25	0.097	0.136	41.47	44.78	21.20	5.62	20.49	5.67
85	43	SS	0.59	71	0.10	30	0.10	30	0.161	0.230	4.56	17.60	4.53	0.58	3.76	0.50
86	43	SS	0.59	21	0.10	20	0.10	18	0.016	0.015	218.03	219.06	196.71	11.53	196.17	11.41
87	43	SS	0.59	47	0.10	10	0.10	10	0.009	0.011	348.08	348.73	317.00	25.38	316.54	25.28
88	43	SS	0.59	72	0.03	10	0.02	12	0.025	0.029	310.17	310.97	303.60	2.26	303.12	2.16
89	43	SS	0.59	14	0.20	25	0.20	25	0.035	0.037	208.09	209.06	206.77	0.53	206.34	0.55
90	44	SS	0.47	75	0.12	19	0.10	20	0.049	0.039	33.78	34.58	31.49	1.61	31.17	1.41
91	44	SS	0.47	58	0.20	25	0.20	25	0.019	0.025	37.16	37.91	34.31	1.65	33.99	1.50
92	44	SS	0.47	82	0.25	35	0.30	35	0.047	0.047	50.91	51.46	46.47	3.10	46.33	3.09
93	44	SS	0.47	81	0.24	20	0.20	25	0.031	0.042	35.00	35.75	30.77	2.38	30.57	2.36
94	44	SS	0.47	80	0.15	30	0.16	30	0.025	0.032	57.11	57.62	52.74	2.88	52.61	2.87

**Table D.2 (continued) Key properties of processed strong motion records**

Record No	EQ ID	Faulting Style	SOFP	Station Id	HP (N-S) (Hz)	LP (N-S) (Hz)	HP (E-W) (Hz)	LP (E-W) (Hz)	PGA Soil N-S (g)	PGA Soil E-W (g)	R <sub>epi</sub> (km)	R <sub>hyp</sub> (km)	μR <sub>rup</sub> (km)	σR <sub>rup</sub> (km)	μR <sub>jb</sub> (km)	σR <sub>jb</sub> (km)
95	44	SS	0.47	85	0.25	40	0.25	40	0.096	0.103	57.47	57.98	53.09	2.90	52.97	2.89
96	44	SS	0.47	83	0.17	20	0.20	25	0.047	0.033	53.16	53.70	48.74	3.07	48.60	3.06
97	44	SS	0.47	86	0.20	25	0.22	25	0.037	0.029	56.50	57.01	52.06	3.26	51.91	3.24
98	44	SS	0.47	41	0.25	25	0.20	25	0.236	0.363	17.22	18.60	13.15	3.04	12.78	2.99
99	45	SS	0.43	73	0.05	25	0.05	25	0.721	0.821	36.21	37.60	30.78	3.22	28.47	4.73
100	45	SS	0.43	48	0.06	50	0.08	50	0.357	0.537	6.03	11.67	3.20	2.33	0.00	1.15
101	45	SS	0.43	74	0.08	25	0.08	25	0.120	0.058	36.54	37.79	8.49	11.20	7.57	12.19
102	45	SS	0.43	54	0.08	12	0.08	12	0.017	0.017	199.93	200.76	196.66	2.14	196.59	2.07
103	45	SS	0.43	58	0.08	12	0.05	12	0.024	0.015	119.62	120.38	116.26	2.19	116.14	2.07
104	45	SS	0.43	75	0.08	15	0.06	15	0.035	0.045	115.61	116.38	111.94	2.20	111.81	2.07
105	45	SS	0.43	76	0.10	50	0.10	50	0.293	0.302	25.33	27.26	21.92	2.64	21.28	2.07
106	45	SS	0.43	77	0.40	50	0.40	50	0.813	1.112	26.82	28.65	23.22	2.62	22.63	2.07
107	45	SS	0.43	78	0.30	40	0.40	30	0.312	0.405	26.23	28.10	22.73	2.63	22.13	2.07
108	45	SS	0.43	79	0.06	40	0.06	40	0.116	0.073	14.88	17.94	11.87	3.03	10.65	2.07
109	45	SS	0.43	80	0.06	40	0.06	40	0.134	0.146	26.83	28.66	23.31	2.61	22.72	2.07
110	45	SS	0.43	81	0.06	40	0.06	40	0.053	0.028	48.09	49.19	44.92	2.37	44.62	2.07
111	45	SS	0.43	82	0.07	40	0.07	40	0.133	0.106	34.04	35.52	29.91	2.51	29.48	2.07
112	45	SS	0.43	83	0.08	40	0.08	40	0.255	0.113	31.67	33.25	27.58	2.54	27.11	2.07
113	45	SS	0.43	84	0.06	40	0.07	40	0.027	0.042	45.81	46.94	40.50	2.44	40.14	2.12
114	45	SS	0.43	85	0.15	40	0.10	40	0.480	0.981	26.55	28.40	22.98	2.62	22.38	2.07
115	45	SS	0.43	86	0.06	40	0.05	40	0.118	0.159	29.53	31.21	24.78	2.60	24.20	2.10
116	45	SS	0.43	87	0.05	20	0.09	20	0.041	0.042	162.76	163.53	158.46	2.18	158.37	2.10
117	45	SS	0.43	88	0.06	15	0.07	15	0.048	0.052	162.66	163.44	158.27	2.19	158.18	2.10
118	45	SS	0.43	69	0.40	25	0.40	25	0.024	0.023	55.91	56.74	34.54	7.83	33.93	7.82
119	45	SS	0.43	41	0.05	40	0.05	40	0.017	0.023	68.01	68.84	64.47	2.28	64.26	2.07

**Table D.2 (continued) Key properties of processed strong motion records**

Record No	EQ ID	Faulting Style	SOFP	Station Id	HP (N-S) (Hz)	LP (N-S) (Hz)	HP (E-W) (Hz)	LP (E-W) (Hz)	PGA Soil N-S (g)	PGA Soil E-W (g)	R <sub>epi</sub> (km)	R <sub>hyp</sub> (km)	μR <sub>rup</sub> (km)	σR <sub>rup</sub> (km)	μR <sub>jb</sub> (km)	σR <sub>jb</sub> (km)
120	45	SS	0.43	71	0.70	25	0.70	25	0.019	0.017	106.79	107.57	103.49	2.20	103.36	2.07
121	45	SS	0.43	70	0.30	25	0.40	25	0.019	0.020	130.00	130.71	121.06	3.21	120.97	3.14
122	45	SS	0.43	109	0.12	20	0.12	20	0.015	0.013	159.95	160.72	155.67	2.18	155.58	2.09
123	45	SS	0.43	110	0.04	20	0.06	20	0.027	0.022	160.36	161.13	156.10	2.18	156.01	2.09
124	45	SS	0.43	111	0.06	15	0.07	15	0.025	0.022	161.17	161.95	156.85	2.18	156.76	2.10
125	45	SS	0.43	112	0.07	18	0.07	18	0.019	0.019	161.82	162.60	157.53	2.18	157.44	2.09
126	45	SS	0.43	113	0.06	20	0.07	15	0.036	0.037	161.65	162.43	157.26	2.19	157.16	2.10
127	45	SS	0.43	114	0.05	20	0.07	20	0.023	0.028	163.96	164.74	159.74	2.18	159.65	2.09
128	45	SS	0.43	56	0.20	25	0.20	25	0.024	0.022	176.64	177.44	173.76	2.15	173.68	2.07
129	45	SS	0.43	65	0.03	12	0.04	12	0.016	0.023	183.51	183.81	157.51	21.46	157.35	21.48
130	45	SS	0.43	52	0.03	20	0.04	12	0.018	0.017	188.60	189.34	177.69	4.28	177.60	4.24
131	45	SS	0.43	55	0.02	20	0.04	25	0.035	0.025	189.52	190.33	185.90	2.15	185.83	2.08
132	45	SS	0.43	63	0.06	20	0.07	20	0.015	0.018	191.13	191.94	187.67	2.15	187.60	2.07
133	45	SS	0.43	62	0.08	12	0.06	12	0.023	0.029	192.61	193.43	189.27	2.15	189.19	2.07
134	45	SS	0.43	59	0.20	15	0.20	15	0.017	0.017	197.57	198.40	194.25	2.14	194.18	2.07
135	45	SS	0.43	53	0.04	20	0.08	20	0.015	0.017	205.49	206.35	202.15	2.14	202.08	2.07
136	45	SS	0.43	50	0.05	12	0.03	12	0.038	0.025	210.55	211.42	207.50	2.14	207.43	2.07
137	46	SS	0.24	3	0.08	25	0.07	40	0.065	0.066	10.62	14.57	8.41	2.48	7.42	2.48
138	47	SS	0.39	89	0.07	25	0.10	25	0.083	0.087	7.47	17.03	12.30	2.10	5.63	1.05
139	47	SS	0.39	48	0.10	30	0.08	40	0.023	0.017	41.24	44.02	39.16	2.05	38.21	2.20
140	47	SS	0.39	70	0.07	25	0.10	25	0.022	0.017	88.07	89.61	86.27	2.21	85.34	2.16
141	47	SS	0.39	41	0.12	15	0.20	15	0.021	0.026	28.55	32.43	30.21	1.74	27.19	1.13
142	48	N	0.09	1	0.35	30	0.25	30	0.050	0.066	12.52	15.06	12.55	1.59	11.10	2.07
143	49	SS	0.40	19	0.06	30	0.07	25	0.020	0.022	31.73	32.16	30.48	2.02	30.33	2.04
144	50	SS	0.63	73	0.60	35	0.60	35	0.194	0.128	22.43	23.69	19.91	2.26	19.68	2.25



**Table D.2 (continued) Key properties of processed strong motion records**

Record No	EQ ID	Faulting Style	SOFP	Station Id	HP (N-S) (Hz)	LP (N-S) (Hz)	HP (E-W) (Hz)	LP (E-W) (Hz)	PGA Soil N-S (g)	PGA Soil E-W (g)	R <sub>epi</sub> (km)	R <sub>hyp</sub> (km)	μR <sub>rup</sub> (km)	σR <sub>rup</sub> (km)	μR <sub>jb</sub> (km)	σR <sub>jb</sub> (km)
145	51	R	0.96	35	0.12	30	0.20	35	0.031	0.023	15.74	16.49	14.38	1.13	13.91	1.02
146	52	N	0.11	90	0.07	20	0.10	20	0.122	0.099	67.95	68.20	62.34	2.25	62.30	2.20
147	52	N	0.11	65	0.10	22	0.07	15	0.026	0.023	144.99	145.23	135.62	6.53	135.58	6.53
148	53	N	0.06	91	0.18	25	0.20	30	0.079	0.052	16.26	21.19	17.04	1.73	14.37	2.40
149	54	SS	0.50	89	0.15	25	0.25	25	0.027	0.035	7.01	8.27	7.40	0.42	6.60	0.49
150	55	SS	0.42	47	0.07	35	0.05	30	0.081	0.036	40.74	43.68	38.32	2.31	36.54	2.04
151	56	SS	0.45	92	0.20	25	0.10	25	0.520	0.330	4.81	7.68	4.31	1.27	3.31	0.69
152	57	SS	0.52	48	0.10	30	0.30	30	0.018	0.032	14.52	16.45	15.17	0.37	14.40	0.09
153	58	NO	0.23	93	0.30	35	0.20	35	0.033	0.022	15.44	21.29	17.44	1.52	14.00	2.16
154	59	SS	0.61	72	0.10	30	0.07	25	0.027	0.016	34.93	36.03	32.12	2.97	31.81	3.03
155	60	N	0.07	94	0.08	30	0.07	30	0.091	0.123	27.36	27.74	24.88	3.14	24.67	3.19
156	60	N	0.07	1	0.15	35	0.10	40	0.022	0.047	45.95	46.13	43.49	3.59	43.46	3.60
157	61	SS	0.44	94	0.07	30	0.10	30	0.049	0.036	20.13	20.69	19.06	1.42	18.93	1.44
158	62	SN	0.29	94	0.05	30	0.06	30	0.110	0.119	19.98	20.38	17.02	2.73	16.82	2.76
159	62	SN	0.29	1	0.10	15	0.10	15	0.025	0.025	38.38	38.55	35.31	4.40	35.17	4.43
160	63	SS	0.45	73	0.20	25	0.35	22	0.071	0.055	3.40	6.04	2.96	0.66	2.49	0.63
161	64	N	0.03	95	0.15	30	0.20	35	0.018	0.030	14.81	21.59	16.57	1.63	12.60	1.51
162	65	N	0.12	24	0.07	30	0.20	30	0.028	0.015	36.33	38.45	35.42	1.60	33.74	1.32
163	65	N	0.12	99	0.06	14	0.15	14	0.035	0.032	18.15	21.99	16.38	2.28	14.87	2.83
164	66	SS	0.44	96	0.10	20	0.10	22	0.026	0.025	80.18	81.08	75.61	6.97	75.01	7.11
165	67	SS	0.43	19	0.10	25	0.10	25	0.007	0.022	65.07	65.80	61.25	3.09	61.10	3.07
166	68	SS	0.42	47	0.15	25	0.06	25	0.023	0.019	56.75	59.72	55.88	1.28	54.97	1.32
167	69	SS	0.41	47	0.07	30	0.08	35	0.025	0.034	59.32	59.41	58.01	0.55	57.96	0.53
168	69	SS	0.41	97	0.10	25	0.10	25	0.013	0.022	80.66	80.68	79.73	0.34	79.68	0.33

**Table D.2 (continued) Key properties of processed strong motion records**

Record No	EQ ID	Faulting Style	SOFP	Station Id	HP (N-S) (Hz)	LP (N-S) (Hz)	HP (E-W) (Hz)	LP (E-W) (Hz)	PGA Soil N-S (g)	PGA Soil E-W (g)	R <sub>epi</sub> (km)	R <sub>hyp</sub> (km)	μR <sub>rup</sub> (km)	σR <sub>rup</sub> (km)	μR <sub>jb</sub> (km)	σR <sub>jb</sub> (km)
169	70	SS	0.48	41	0.30	25	0.35	25	0.086	0.077	3.32	5.27	3.88	0.48	2.90	0.65
170	71	SS	0.58	93	0.17	25	0.25	25	0.102	0.293	8.25	15.39	8.82	1.77	6.25	1.80
171	72	SN	0.29	100	0.20	25	0.20	20	0.038	0.029	29.11	30.11	27.02	1.42	26.88	1.44
172	72	SN	0.29	101	0.16	40	0.15	40	0.080	0.038	22.90	24.18	20.79	1.54	20.60	1.57
173	72	SN	0.29	102	0.10	20	0.10	25	0.164	0.183	12.76	15.01	12.13	0.83	11.83	0.75
174	72	SN	0.29	103	0.10	20	0.20	30	0.181	0.218	9.43	12.31	8.90	0.87	8.39	0.74
175	72	SN	0.29	104	0.13	18	0.10	20	0.070	0.104	15.90	17.77	14.51	0.83	14.19	0.79
176	72	SN	0.29	105	0.10	20	0.10	25	0.068	0.100	14.72	16.72	13.11	0.91	12.78	0.89
177	72	SN	0.29	106	0.15	30	0.10	30	0.031	0.045	25.25	26.49	23.45	1.04	23.28	1.05
178	72	SN	0.29	107	0.20	15	0.16	15	0.027	0.026	30.86	31.87	28.66	2.53	28.53	2.58
179	72	SN	0.29	108	0.20	25	0.25	20	0.038	0.027	29.77	30.80	27.55	2.84	27.45	2.89

**Table D.3 Key properties of strong motion recording stations**

St Id.	Station Name	Station Code	Station Coord. (N)	Station Coord. (E)	Station Operator	Info. Source	Instrument Model	Final Selection 1	Final Selection 2	Weight 1 (%)	Weight 2 (%)
1	Denizli Bay. ve İsk. Md.	DNZ_B	37.8125	29.1111	ERD	ERD	GSR-16	D		100	
2	Denizli Meteoroloji Md.	DNZ_A	37.7619	29.0921	ERD	ERD	SMA-1	D		100	
3	erkeş Meteoroloji İst.	CER	40.8149	32.8834	ERD	ERD	SMA-1	D		100	
4	İzmir Meteoroloji İst.	IZM_A	38.4333	27.1667	ERD	ERD	SMA-1	B		100	
5	İzmir Bayındırlık Mdrlę	IZM_B	38.4656	27.1623	ERD	ERD	SMA-1	D		100	
6	Malatya Bay. İsk. Md. (Meteor.)	MLT	38.3500	38.3460	ERD	ERD	SMA-1	D		100	
7	Muradiye Meteoroloji Md.	MUR	38.9901	43.7630	ERD	ERD	SMA-1	D		100	
8	Bucak Meteoroloji Md.	BCK	37.4610	30.5890	ERD	ERD	SMA-1	C		100	
9	Dursunbey Kandilli Gzlem Md.	DUR	39.5871	28.6255	ERD	ERD	SMA-1	C		100	
10	Hatay Bay. ve İsk. Md. (Valilik)	HTY_A	36.2025	36.1597	ERD	ERD	SMA-1	D		100	
11	Hatay Bay. ve İsk. Md.	HTY_B	36.2142	36.1597	ERD	ERD	SM-2/GSR16	D		100	
12	Edincik Kandilli Gozlem Mud.	EDC	40.3360	27.8610	ERD	ERD	SMA-1	C		100	
13	Gonen Meteoroloji Mud.	GNN	40.1140	27.6424	ERD	ERD	SMA-1	C		100	
14	Tekirdaę Bay. ve İsk. Md.	TKR_B	40.9793	27.5150	ERD	ERD	SMA-1	C		100	
15	Tekirdaę Meteoroloji Md	TKR_A	40.9793	27.5150	ERD	ERD	SM2/GSR16	C		100	
16	Horasan Meteoroloji İst.	HRS_A	40.0430	42.1730	ERD	ERD	SMA-1	D		100	
17	Horasan İle Tarım Md.	HRS_B	40.0415	42.1736	ERD	ERD	SM2	C		100	
18	Erzurum Meteoroloji Md.	ERZ_A	39.9055	41.2553	ERD	ERD	SMA-1	D	E	50	50
19	Erzurum Bay. ve İsk. Md.	ERZ_B	39.9030	41.2620	ERD	ERD	GSR-16	C		100	
20	Balıkesir Meteoroloji Md.	BLK_A	39.6391	27.8939	ERD	ERD	SMA-1	D		100	
21	Balıkesir Huzur Evi	BLK_B	39.6500	27.8569	ERD	ERD	GSR16	C		100	
22	Foa Gmrk Md.	FOC	38.6624	26.7586	ERD	ERD	SMA-1	B		100	
23	Kięi Meteoroloji Md.	KIG	39.3082	40.3485	ERD	ERD	SMA-1	C		100	

**Table D.3 Key properties of strong motion recording stations**

St Id.	Station Name	Station Code	Station Coord. (N)	Station Coord. (E)	Station Operator	Info. Source	Instrument Model	Final Selection 1	Final Selection 2	Weight 1 (%)	Weight 2 (%)
24	Köyceğiz Meteoroloji Müd.	KOY	36.9700	28.6868	ERD	ERD	SMA-1	C		100	
25	Gölbaşı Devlet Hastanesi	GOL	37.7810	37.6410	ERD	ERD	SMA-1	C		100	
26	Kuşadası Meteoroloji Müd.	KUS	37.8600	27.2650	ERD	ERD	SMA-1	C		100	
27	İstanbul Bay. ve İsk. Müd.	IST	41.0582	29.0095	ERD	ERD	SMA-1	B		100	
28	Amasya Bay. ve İsk. Müd.	AMS_B	40.6540	35.8340	ERD	ERD	SM-2	C		100	
29	Amasya Meteoroloji Müd.	AMS_A	40.6666	35.8351	ERD	ERD	SMA-1	C	D	25	75
30	Erzincan Meteoroloji. Müd.	ERC_A	39.7520	39.4870	ERD	ERD	SMA-1	E		100	
31	Erzincan Bay. ve İsk. Müd.	ERC_B	39.7430	39.5120	ERD	ERD	SSA-2	D		100	
32	Refahiye Kaymakamlık Binası	REF	39.9063	38.7706	ERD	ERD	SMA-1	C		100	
33	Tercan Meteoroloji Müd.	TER	39.7767	40.3910	ERD	ERD	SMA-1	D		100	
34	Ilıca Meteoroloji Müd.	ILI	38.3100	26.3100	ERD	ERD	MR-2002	C		100	
35	Van Bay. ve İsk. Müd.	VAN	38.5035	43.4018	ERD	ERD	SM-2	C		100	
36	Burdur Meteoroloji Müd.	BRD	37.7220	30.2940	ERD	ERD	SMA-1	D		100	
37	Çardak Sağlık Ocağı	CRD	37.8236	29.6672	ERD	ERD	SMA-1	C		100	
38	Dinar Meteoroloji Müd.	DIN	38.0599	30.1537	ERD	ERD	SMA-1	D		100	
39	Osmancık Belediye Binası	OSM	40.9763	34.8002	ERD	ERD	SMA-1	D		100	
40	Buldan Kaymakamlık Binası	BLD	38.0448	28.8336	ERD	ERD	SMA-1	D		100	
41	Sakarya Bay. ve İsk. Müd.	SKR	40.7371	30.3801	ERD	ERD	GSR-16	C		100	
42	Gelibolu Karayolları Şefliği	GL1	40.4233	26.6672	ERD	ERD	SMA-1	D		100	
43	Ceyhan Tarım İlçe Müdürlüğü	CYH	37.0500	35.8100	ERD	ERD	SMA-1	D		100	
44	İslahiye Meteoroloji Müd.	ISL	37.0255	36.6359	ERD	ERD	SMA-1	C		100	
45	Karataş Meteoroloji Müd.	KRT	36.5680	35.3901	ERD	ERD	SMA-1	C		100	
46	Mersin Meteoroloji Müd.	MRS	36.7810	34.6028	ERD	ERD	SMA-1	C		100	

**Table D.3 (continued) Key properties of strong motion recording stations**

St Id.	Station Name	Station Code	Station Coord. (N)	Station Coord. (E)	Station Operator	Info. Source	Instrument Model	Final Selection 1	Final Selection 2	Weight 1 (%)	Weight 2 (%)
47	Bornova Ege Üniversitesi Ziraat Fak. Dek.	BRN	38.4551	27.2267	ERD	ERD	GSR-16	D		100	
48	Düzce Meteoroloji Müd.	DZC	40.8436	31.1489	ERD	ISESD	SMA-1	D		100	
49	Gebze-Arçelik	ARC	40.8240	29.3610	KOERI	ISESD	GSR-16	C	D	50	50
50	Ambarlı-Termik Santrali	ATS	40.9810	28.6930	KOERI	ISESD	GSR-16	D	E	50	50
51	M. Ereğlisi: Botaş Gaz Terminali	BTS	40.9920	27.9800	KOERI	ISESD	GSR-16	C		100	
52	Bursa: Tofaş Fabrikası	BUR	40.2610	29.0680	KOERI	ISESD	GSR-16	C	D	50	50
53	Küçükçekmece	CNAK	41.0240	28.7590	KOERI	ISESD	GSR-16	C		100	
54	Yeşilköy: Havaalanı	DHM	40.9820	28.8200	KOERI	ISESD	GSR-16	C	D	75	25
55	Fatih: Fatih Türbesi	FAT	41.0197	28.9498	KOERI	ISESD	GSR-16	C	D	75	25
56	Heybeliada: Sanatoryum	HAS	40.8690	29.0880	KOERI	ISESD	GSR-16	B		100	
57	4. Levent: Yapı Kredi Plaza	YKP	41.0810	29.0110	KOERI	ISESD	GSR-16	B		100	
58	Yarımca: Petkim Tesisleri	YPT	40.7560	29.7650	KOERI	ISESD	GSR-16	D		100	
59	İstanbul: Ataköy	ATK	40.9890	28.8490	İTÜ	ISESD	SSA-2	D		100	
60	İstanbul: Mecidiyeköy	MCD	41.0650	28.9970	İTÜ	ISESD	SSA-2	B		100	
61	İstanbul: Maslak	MSK	41.1040	29.0190	İTÜ	ISESD	SSA-2	B		100	
62	İstanbul: Zeytinburnu	ZYT	40.9860	28.9080	İTÜ	ISESD	SSA-2	D		100	
63	İstanbul: Kocamustafapaşa	KMP	41.0030	28.9280	KOERI	ISESD	GSR-16	D		100	
64	Bursa: Sivil Savunma Müdürlüğü	BRS	40.1824	29.1276	ERD	ERD	GSR-16	C		100	
65	Kütahya Sivil Savunma Müd.	KUT	39.4193	29.9972	ERD	ERD	GSR-16	D		100	
66	Çekmece: Nükleer Santral Binası	CEK	41.0265	28.7587	ERD	ERD	SMA-1	D		100	
67	Ereğli: Kaymakamlık Binası	ERG	40.9730	27.9503	ERD	ERD	SMA-1	D		100	
68	Gebze: TÜBİTAK-MAM	GBZ	40.7863	29.4500	ERD	ERD	SMA-1	C		100	
69	Göynük: Devlet Hastanesi	GYN	40.3960	30.7830	ERD	ERD	SMA-1	D		100	
70	İzmit Karayolları Şefliği Mür.	IZN	40.4406	29.7175	ERD	ERD	SMA-1	D		100	
71	İzmit: Meteoroloji Müd.	IZT	40.7668	29.9167	ERD	ERD	SMA-1	B		100	
72	Çanakkale: Meteoroloji İstasyonu	CNK	40.1415	26.3995	ERD	ISESD	GSR-16	D		100	

**Table D.3 (continued) Key properties of strong motion recording stations**

St Id.	Station Name	Station Code	Station Coord. (N)	Station Coord. (E)	Station Operator	Info. Source	Instrument Model	Final Selection 1	Final Selection 2	Weight 1 (%)	Weight 2 (%)
73	Bolu Bay. ve İsk. Müd.	BOL	40.7457	31.6073	ERD	ISESD	GSR-16	D		100	
74	Mudurnu: Kaymakamlık Binası	MDR	40.4684	31.2099	ERD	ISESD	SMA-1	D		100	
75	Gölcük	GLCK	40.7260	29.8150	İTÜ	ISESD	SSA-2	D		100	
76	IRIGM Station No. 487	487	40.7490	30.8890	IRIGM	ISESD	-	B	C	50	50
77	IRIGM Station No. 496	496	40.7420	30.8730	IRIGM	ISESD	-	B	C	50	50
78	IRIGM Station No. 498	498	40.7460	30.8790	IRIGM	ISESD	-	B	C	50	50
79	LDEO Station No. C1058 BV	C1058	40.7550	31.0150	LDEO	ISESD	TERRATEK-320	C		100	
80	LDEO Station No. C1059 FP	C1059	40.7450	30.8720	LDEO	ISESD	TERRATEK-320	B	C	50	50
81	LDEO Station No. C1060 BU	C1060	40.7770	30.6130	LDEO	ISESD	TERRATEK-320	B		100	
82	LDEO Station No. C1061	C1061	40.7200	30.7920	LDEO	ISESD	TERRATEK-320	C		100	
83	LDEO Station No. C1062 FI	C1062	40.7230	30.8200	LDEO	ISESD	TERRATEK-320	C		100	
84	LDEO Station No. C0362 CH	C0362	40.6700	30.6660	LDEO	ISESD	TERRATEK-320	B	C	75	25
85	LDEO Station No. C0375 VO	C0375	40.7430	30.8760	LDEO	ISESD	TERRATEK-320	B	C	50	50
86	LDEO Station No. D0531 WF	D0531	40.7030	30.8550	LDEO	ISESD	TERRATEK-320	B		100	
87	Hastane (Yalova)	HAST	40.6530	29.2630	KOERI-Iran	ISESD	SSA-12	E		100	
88	Hilal (Yalova)	HIL	40.6470	29.2650	KOERI-Iran	ISESD	SSA-12	E		100	
89	Akyazı Orman İşletme Müd.	AKY	40.6703	30.6225	ERD	ERD	GSR-18	D		100	
90	Afyon Bay. ve İsk. Müd.	AFY	38.7760	30.5340	ERD	ERD	SM-2	D		100	
91	Andırın Tufan Paşa İlkokulu	AND	37.5701	36.3574	ERD	ERD	GSR-16	C		100	
92	Bingöl Bay. ve İsk. Müd.	BNG	38.8971	40.5032	ERD	ERD	GSR-16	C		100	

**Table D.3 (continued) Key properties of strong motion recording stations**

St Id.	Station Name	Station Code	Station Coord. (N)	Station Coord. (E)	Station Operator	Info. Source	Instrument Model	Final Selection 1	Final Selection 2	Weight 1 (%)	Weight 2 (%)
93	Bandırma Bölge Trafik Den. Müd.	BND	40.3381	27.9869	ERD	ERD	GSR-16	C		100	
94	Denizli-Sarayköy Jeoterm. İşl. Müd.	DAT1	37.9326	28.9248	ERD	ERD	ETNA	D		100	
95	Bodrum Meteoroloji Müd.	BDR	37.0330	27.4400	ERD	ERD	GSR-16	C		100	
96	Finike Meteoroloji Müd.	FNK	36.3022	30.1463	ERD	ERD	SM-2	D		100	
97	Manisa Bay. ve İsk. Müd.	MNS	38.6126	27.3814	ERD	ERD	SM-2	D		100	
98	Maku	MAK	39.2942	44.5133	BHRC	ISESD	-	C		100	
99	Marmaris GUR-18	MRM	36.8394	28.2448	ERD	ERD	GSR-18	C		100	
100	Bursa Köy Hizmetleri 17. Bölge Müd. Misafirhane Bahçesi	BYT01	40.1822	29.1297	ERD	ERD	ETNA	C		100	
101	Bursa Afet Yönetim Merkezi	BYT02	40.226	29.075	ERD	ERD	ETNA	D	E	50	50
102	Kurtul Koyu Muhtarlık Bahçesi (Gemlik)	BYT04	40.3632	29.1222	ERD	ERD	ETNA	D		100	
103	Engürücük Köyü Askeri Veteriner Okulu Bahçesi	BYT05	40.394	29.098	ERD	ERD	ETNA	C		100	
104	Umurbey Sağlık Meslek Lisesi Bahçesi	BYT06	40.4100	29.1799	ERD	ERD	ETNA	C		100	
105	Gemlik Endüstri Meslek Lisesi Bahçesi	BYT07	40.4251	29.1666	ERD	ERD	ETNA	D		100	
106	Cargill Tarım Sanayi Fabrikası	BYT08	40.42220	29.2909	ERD	ERD	ETNA	D		100	
107	Su Gören Köyü - Et ve Süt Ürünleri Fabrikası	BYT11	40.5641	29.306	ERD	ERD	ETNA	C		100	
108	Soğucak Köyü Afet Konutları	BYT12	40.58990	29.26680	ERD	ERD	ETNA	D		100	
109	Girne (Yalova)	GIR	40.6560	29.2960	KOERI	ISESD	GSR-12	E		100	
110	Kaşif (Yalova)	KAS	40.6570	29.2910	KOERI	ISESD	SSA-12	E		100	
111	Bahcevan (Yalova)	BAH	40.6520	29.2820	KOERI	ISESD	SSA-12	E		100	
112	Bağlaraltı (Yalova)	BAG	40.6540	29.2740	KOERI	ISESD	SSA-12	E		100	
113	Rüzgar (Yalova)	RUZ	40.6470	29.2770	KOERI	ISESD	SSA-12	E		100	
114	Tar (Yalova)	TAR	40.6580	29.2480	KOERI	ISESD	SSA-12	E		100	

## CURRICULUM VITAE

### PERSONAL INFORMATION

Surname, Name : Yunatçı, Ali Anıl  
Nationality : Turkish (TC)  
Date and Place of Birth : 08 August 1978, Ankara  
Marital Status : Married  
Phone : +90 312 210 54 68  
Fax : +90 312 210 54 01  
Email : yunatci@gmail.com

### EDUCATION

2000 – 2003 METU Civil Engineering, Geotechnical Engineering, MS  
1995 – 1999 Gazi University, Civil Engineering, BS  
1988 – 1995 TED Ankara College Foundation High School

### WORK EXPERIENCE

2002 – 2010 METU Department of Civil Engineering Research/Teaching Assistant

### FOREIGN LANGUAGES

English

### PUBLICATIONS

**Yunatçı, A., and Cetin, K. O., (2009)**, "Seismic Hazard Assessment: An Evaluation for the Design of Critical Structures ", *2nd National Dam Safety Symposium and Exhibition*, Osmangazi University, May 13-15, 2009, Eskisehir, Turkey

**Cetin, K. O., Unsal, S., and Yunatçı, A., (2009)**, "An Integrated Seismic Hazard Framework for Assessing the Liquefaction Triggering of Dam Foundation Soils", *2nd National Dam Safety Symposium and Exhibition*, Osmangazi University, May 13-15, 2009, Eskisehir, Turkey

**Cetin, K. O., Yargici, V., and Yunatçı, A. A., (2009)**, Assessment of Buried Pipeline Performance During the 1999 Duzce Earthquake, Turkey, *ASCE Pipelines 2009*, San Diego, CA, August 16-19

**Unsal, S., Yunatçı, A., and Cetin, K. O. (2009)**, "An Integrated Seismic Hazard Framework for Assessing the Liquefaction Triggering of Dam Foundation Soils",



*International Conference on Performance-Based Design in Earthquake Geotechnical Engineering*, IS-Tokyo 2009, Tsukuba, June 15-17, 2009, Japan

**Yunatçı, A. A., and Cetin, K. O. (2008)**, “Site Specific Ground Response Analysis Integrated Within Probabilistic Seismic Hazard Framework”, *Proceedings, International Congress on Advances in Civil Engineering*, 15-17 September 2008, Eastern Mediterranean University, Famagusta, N. Cyprus.

**Bilge, H. T., Yunatçı, A. A., Unutmaz, B., Yunatçı, I., and Cetin, K. O., (2007)**, "Soil Liquefaction Triggering Behaviour Under Cyclic Sea Wave Loads", *6th National Symposium on Coastal Engineering*, 25-28 October 2007, İzmir, Turkey (in Turkish).

**Yunatçı, A. A., Cetin, K. O. (2007)**, " Site Specific Seismic Response And Soil Liquefaction Triggering Assessment Integrated Within Probabilistic Seismic Hazard Framework", *6th National Conference on Earthquake Engineering*, 16-20 September 2007, İstanbul Technical University, İstanbul, Turkey (in Turkish).

**Yunatçı, A. A., and Cetin, K. O. (2007)**, “Probabilistic seismic hazard analysis for Buyuk Karacay Dam and HEPP”, *1<sup>st</sup> National Dam Safety Symposium and Exhibition*, May 28-30 2007, Ankara, Turkey (in Turkish).

**Yunatçı, A. A., and Cetin, K. O. (2006)**, “Impact of Attenuation Models on Probabilistic Seismic Hazard Analysis: A Case Study for Bursa City, Turkey”, *Proceedings of the 8th U.S. National Conference on Earthquake Engineering*, April 18-22, San Francisco, California, USA.

**Yunatçı, A. A., and Özkan, M. Y., (2004)**, “A Model Study on the Seismic Behaviour of Laterally Braced Sheet Pile Walls”, in *Proceedings, 11<sup>th</sup> International Conference on Soil Dynamics and Earthquake Engineering, 3<sup>rd</sup> International Conference on Earthquake Geotechnical Engineering*, 7-9 January, 2004, Berkeley, California, USA, Vol. 1, pp. 235-242

**Cetin, K. O., Yunatçı, A. A., Çağlı, S., Gülkökar, T., Aktaş, R., Altınışık, F., Çelik, S., Arabacı, H. M., and Çekmeceli, M., (2004)**, “GIS-based Probabilistic Seismic Hazard and Soil Liquefaction Initiation Assessment for the City of Bursa. *10<sup>th</sup> National Conference of Soil Mechanics and Foundation Engineering*, September 16-17, 2004, İstanbul Technical University, İstanbul, pp.479-489 (in Turkish).

**Yunatçı, A. A., Çalışan, O., and Özkan, M. Y., (2003)**, “Behaviour and Design Methods of Retaining Structures Under Seismic Loads”, *Yapı Dünyası*, May 2003, No: 86, pp. 50-56. (in Turkish)

**Yunatci, A. A., (2003),** “A Model Study on the Seismic Behavior of Laterally Braced Sheet Pile Walls”, MSc. Thesis, METU Graduate School of Natural and Applied Sciences, January 2003, 130 pages.